Journal of Sensors

Fiber and Integrated Waveguide-Based Optical Sensors

Guest Editors: Valerio Pruneri, Christos Riziotis, Peter G. R. Smith, and Athanasios Vasilakos

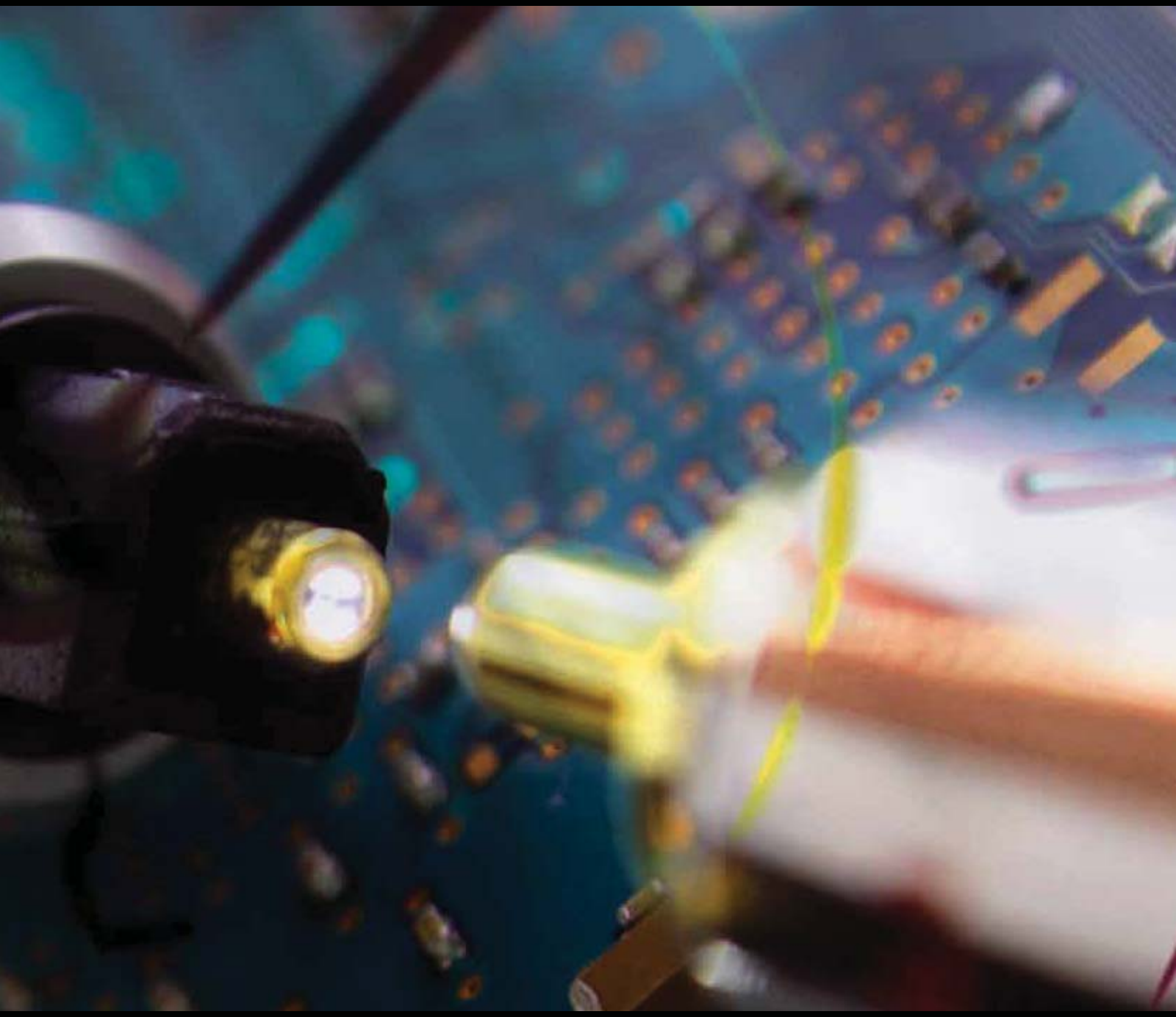

Fiber and Integrated Waveguide-Based Optical Sensors

Journal of Sensors

Fiber and Integrated Waveguide-Based Optical Sensors

Guest Editors: Valerio Pruneri, Christos Riziotis, Peter G. R. Smith, and Athanasios Vasilakos

Contents

Hindawi Publishing Corporation
Journal of Sensors
Volume 2009, Article ID 171748, 3 pages
doi:10.1155/2009/171748

Editorial

Fiber and Integrated Waveguide-Based Optical Sensors

Valerio Pruneri,[1] Christos Riziotis,[2] Peter G. R. Smith,[3] and Athanasios Vasilakos[4]

[1] *The Institute of Photonic Sciences (ICFO) and ICREA, Mediterranean Technology Park, Avenue del Canal Olímpic s/n, 08860 Castelldefels (Barcelona), Spain*
[2] *Photonics for Nanoapplications Laboratory, Theoretical and Physical Chemistry Institute, National Hellenic Research Foundation (NHRF), 48 Vassileos Constantinou Avenue, 11635 Athens, Greece*
[3] *Optoelectronics Research Centre, University of Southampton, Southampton SO17 1BJ, UK*
[4] *Department of Electrical and Computer Engineering, National Technical University of Athens, 15780 Athens, Greece*

Correspondence should be addressed to Christos Riziotis, riziotis@eie.gr

Received 15 December 2009; Accepted 15 December 2009

Over the last years, a large part of the activity in applied photonics and especially in fiber or integrated waveguide-based devices has been transferred partially from the photonics telecommunications industry towards the optical sensors research. Further to the necessity due to telecommunications sector turn down, it has been proven that this shift has been welcomed by the development in relevant industrial sectors (pharmaceutical, medical) where new requirements for very accurate control of the manufacturing process are required. This increasing research effort on all-optical sensors' technology, combined with emerging and demanding applications, has demonstrated a promising technological platform characterized by unique sensitivity, compactness, reliability, electromagnetic immunity, and low cost, promoting them to a preferable solution for real-world applications, from mechanical sensing to chemical/biochemical and pharmaceutical industry. The inherent also capability of photonics technology for the efficient sensing-signal transmission through optical fibers suggests an enhanced functionality from a system's perspective, by enabling the high-speed interconnection of multiple remote sensing points, either through a single readout and administration unit, or through a distributed network. Furthermore the need for development of large-scale ad hoc sensor networks requires reliable autonomous and controllable sensing nodes and optical sensors exhibit very attractive and unique characteristics to play key role in this area. Emerging technologies combining new design concepts and operational approaches such as microstructured fibers (PCFs), tapered nanofibers, Bragg gratings, and long-period gratings, interferometric devices, as well as Surface Plasmon Resonance (SPR) devices have shown a strong impetus for novel applications. A critical issue which could dramatically enhance the performance of such functional devices is the use of novel polymers and nanostructured materials able to improve the sensitivity and expand also sensors selectivity range.

This special issue is completely devoted in this dynamic area of optical sensors, aiming to broadly cover aspects such as material properties, fabrication techniques, modeling, optimization, and novel applications. Hosting 17 representative papers demonstrates successful engineering of novel fiber and planar optical sensors for a variety of applications such as physical, chemical, and biosensing. Selected papers have been invited in order to provide the state of the art and current trends in distinct hot areas.

The issue begins with a group of review papers on key fiber-based sensor categories, with the first invited paper from Gupta and Kumar which gives an up-to-date review on fiber optic-based surface plasmon resonance sensors demonstrating applications in measuring various physical, chemical, and biochemical parameters. Various designs of the fiber optic SPR probe were reported there for the enhancement of sensors' sensitivity. The second invited paper by Skorobogatiy presents a comprehensive review on microstructured optical fiber and photonic bandgap (PBG) fiber-based resonant optical sensors. Two sensor architectures are discussed where in the first one were employed hollow core photonic bandgap fibers where core-guided mode is strongly confined in the analyte-filled core. The second sensor case employed metalized photonic

bandgap waveguides and fibers, where core-guided mode was phase matched with a plasmon propagating at the metalized fiber/analyte interface. Operational regions of the resonant sensors are reviewed covering a wide range of wavelengths from the visible to terahertz. Canning presents in his invited paper the state-of-the-art work on sensors based on Bragg gratings and microstructured fibers. The paper presents the current situation and the measurements challenges with temperature and strain and discusses as well novel engineering concepts such as an integrated lab in a fiber. Another architecture based on modal interferometers on PCFs is reviewed by Villatoro et al. as a solution for highly sensitive sensors of low thermal sensitivity and applications ranging from strain, temperature, to refractive index and volatile organics. Sagnac, Mach-Zehnder, or Michelson-like interferometers can be fabricated by different postprocessing techniques such as grating inscription, tapering or cleaving, and splicing. Margulis et al. propose in their invited research paper a novel and alternative interferometric architecture based on the plurality of individual fiber preforms drawn together but nearly maintaining their original shape. The potential temperature independence and the ease of splicing of Gemini fibers make them an attractive solution for sensors development in a monolithic-robust multicore fiber design.

The following three papers present architectures and applications of PCFs for physical parameters sensing. The first paper by Ju and Jin is an invited review on photonic crystal fibers utilizing either long-period gratings or in-fiber modal interferometers for strain and temperature sensing. The paper suggests that air-silica PCF sensors are comparable or better than those implemented in conventional single-mode fibers but the temperature sensitivities of the PCF sensors are much lower. Next paper by Larrion et al. presents a novel configuration of a temperature sensor based on a PCF with quantum dot nanocoatings in its inner holes, deposited by means of the Layer-by-Layer technique. The paper studies for a temperature range from -40 to 70°C the optical properties of these sensors and introduces also the consideration of the full width at half maximum (FWHM) as a new insightful characterization parameter. Another configuration of a temperature sensor with a low-cost amplitude interrogation technique is presented in the paper by Torres-Peiro et al. based on the cutoff properties of the fundamental mode in a liquid filled Y-shaped Ge-doped microstructured fiber. The sensitivity is mainly determined by the thermo-optic coefficient of the filling liquids and values of 25 nm/$^{\circ}$C with detection limit of about 0.001°C are reported.

The next three papers present different approaches for measuring also physical parameters but using conventional fibers. The invited review by Yamashita presents a novel wide and fast wavelength-swept fiber laser architecture for dynamic and accurate fiber sensing, based on the dispersion tuning technique, by modulating the loss/gain in the dispersive laser cavity. Kuang et al. present in their invited review a low-cost platform based on plastic optical fibers-POF for the quite important area of Structural Health Monitoring (SHM). Between different possible schemes, the intensity-based interrogation capability of POF sensors provides additional a very favorable solution of low-cost SHM systems implementation. The next paper by Pinet gives from an industrial and applications perspective the state-of-the-art situation on miniaturized sensors based on Fabry-Perot fiber optic implementation. This alternative architecture provides a mature and reliable technology for strain, temperature, pressure, displacement, or refractive index measurements, and with a lot of applications ranging from industrial to medical.

The following three papers are devoted to fiber optic based chemical and biosensing, where the first invited paper by Dagenais presents a promising sensor based on an etched Bragg grating functionalized with glucopyranosyl-siloxane conjugate in order to interact selectively with glucose binding proteins, altering thus the surface's refractive index. Next paper by Carvalho et al. presents a hollow-core PCF for detecting low levels of methane. A prototype is demonstrated in a portable system incorporating an interrogation scheme based on the Wavelength Modulation Spectroscopy technique. In the next paper by Andres et al., another simple technique based on single mode fiber at 850 nm is presented, where a long-period grating as an equivalent 3 dB beam is used to form a coaxial-Michelson modal interferometer. Direct dipping of the sensor head in water solutions permits the measure of small refractive index changes.

The final group of papers is devoted to the integrated optics approach which offers a promising technological platform towards robust and multifunctional sensors physically compatible with microfluidics. The invited paper by Kashyap reviews the state of the art on Surface Plasmon Resonance-based devices focusing especially on their integrated platform approach as a route for low cost, mass production, disposable sensors. The next paper by Sparrow et al. reviews the emerging class of integrated Bragg grating-based sensors, and examines in detail the architecture, fabrication, and applications of special sensors' chips fabricated by the flexible direct UV writing technique on silica-on-silicon wafers. A variety of applications ranging from temperature, refractive index, chemical, and biosensing are described and also indicative specific problems in food industry for monitoring long-term industrial process such as fermentation are demonstrated. The final invited paper is by Mayeh et al. describing another class of integrated devices, based on the operational principle of slotted multimode interference (MMI). The paper presents design and modeling results towards the tuning of the device in order to detect protein-based molecules or water-soluble chemical or biological materials. Fabrication of the device has been demonstrated in silicon oxynitride (SiON) as highly stable to the reactivity with biological agents and processing chemicals.

Introducing this special issue to the Journal of Sensors, we would like to thank all the authors for their prompt and valuable contributions and also the reviewers for their critical help, necessary to achieve a high level of papers' quality and make thus possible the completion of this special issue. Also we would like to thank the Editor in Chief Professor Francisco J. Arregui and the Editorial Board for approving this special issue as well as the Journal's staff for their

professionalism and effective consideration of all the details during the preparation of the issue.

Valerio Pruneri
Christos Riziotis
Peter G.R. Smith
Athanasios Vasilakos

Hindawi Publishing Corporation
Journal of Sensors
Volume 2009, Article ID 979761, 12 pages
doi:10.1155/2009/979761

Review Article

Surface Plasmon Resonance-Based Fiber Optic Sensors: Principle, Probe Designs, and Some Applications

B. D. Gupta and R. K. Verma

Department of Physics, Indian Institute of Technology Delhi, New Delhi 110016, India

Correspondence should be addressed to B. D. Gupta, bdgupta@physics.iitd.ernet.in

Received 26 January 2009; Accepted 2 June 2009

Recommended by Christos Riziotis

Surface plasmon resonance technique in collaboration with optical fiber technology has brought tremendous advancements in sensing of various physical, chemical, and biochemical parameters. In this review article, we present the principle of SPR technique for sensing and various designs of the fiber optic SPR probe reported for the enhancement of the sensitivity of the sensor. In addition, we present few examples of the surface plasmon resonance- (SPR-) based fiber optic sensors. The present review may provide researchers valuable information regarding fiber optic SPR sensors and encourage them to take this area for further research and development.

1. Introduction

Surface plasmon resonance (SPR) is one of the most promising optical techniques that find applications in different fields. The first sensing application of SPR technique was reported in 1983 [1]. Since then, numerous SPR sensing structures for chemical and biochemical sensing have been reported. In SPR technique, a TM (transverse magnetic) or p-polarized light causes the excitation of electron density oscillations (known as surface plasmon wave, SPW) at the metal-dielectric interface. When the energy as well as the momentum of both, the incident light and SPW, match, a resonance occurs which results in a sharp dip in the reflected light intensity. The resonance condition depends on the angle of incidence, wavelength of the light beam, and the dielectric functions of both the metal as well as the dielectric. If the wavelength is kept constant and the angle of incidence is varied, then the sharp dip appears at a particular angle and the method is called angular interrogation. In another method, called spectral or wavelength interrogation, the angle of the incident beam is kept constant and the wavelength is varied. In this method, resonance occurs at a particular wavelength. The resonance parameter (angle or wavelength) depends on the refractive index of the dielectric medium. Change in refractive index changes the value of the resonance parameter. To excite surface plasmons, generally, a prism is used [2–9]. The prism-based SPR sensing device has a number of shortcomings such as its bulky size and the presence of various optical and mechanical (moving) parts. Further, the prism-based SPR sensing device cannot be used for remote sensing applications. These shortcomings can be overcome if an optical fiber is used in place of prism. The additional advantage of optical fiber is that the SPR probe can be miniaturized which can be advantageous for samples which are available in minute quantity or are costly. Due to these advantages the surface plasmon resonance-based optical fiber sensors have drawn a lot of attention [10–23]. Both experimental and theoretical investigations have been reported in literature on the SPR-based fiber optic sensors. The performance of these sensors is, generally, evaluated in terms of sensitivity and signal-to-noise ratio (or detection accuracy). As is known, the higher the values of these parameters, the better is the sensor.

The present review begins with a section on principle of the sensing technique. The section includes the description of the performance parameters of the sensor: sensitivity and signal-to-noise ratio or detection accuracy. In the next section, we present the simplest SPR-based fiber optic sensor and discuss its modulation scheme. Section 4 of the present

review deals with various designs of the SPR probe studied to enhance the performance of the fiber optic sensor. The designs include tapered, U-shaped and side-polished. The advantages of bimetallic coatings, addition of dopants in fiber core and the choice of the metals for coating have been discussed in the same section. In the last section, we review some of the SPR-based fiber optic sensors in details that have been reported in literature.

2. Principle

A metal-dielectric interface supports charge density oscillations along the interface which are called surface plasma oscillations. The quantum of these oscillations is given the name as surface plasmon. The surface plasmons are accompanied by a longitudinal (TM- or p-polarized) electric field which decays exponentially in metal as well as in dielectric medium. The electric field has its maximum at metal-dielectric interface. The TM-polarization and exponential decay of electric field are found by solving the Maxwell equation for semi-infinite media of metal and dielectric with an interface of metal-dielectric. The propagation constant (K_{SP}) of the surface plasmon wave propagating along the metal-dielectric interface is given by

$$K_{SP} = \frac{\omega}{c}\left(\frac{\varepsilon_m \varepsilon_s}{\varepsilon_m + \varepsilon_s}\right)^{1/2}, \quad (1)$$

where ε_m and ε_s are the dielectric constants of metal and the dielectric medium, respectively, ω is the frequency of incident light, and c is the velocity of light. From (1) it may be noted that the propagation constant of surface plasmon wave depends on the dielectric constants of both the metal and the dielectric medium.

The surface plasmons can be excited by light with same polarization state as that of surface plasmons. The propagation constant (K_s) of the light wave with frequency ω propagating through the dielectric medium is given by

$$K_s = \frac{\omega}{c}\sqrt{\varepsilon_s}. \quad (2)$$

Since $\varepsilon_m < 0$ (for metal) and $\varepsilon_s > 0$ (for dielectric), for a given frequency, the propagation constant of surface plasmon (K_{SP}) is greater than that of the light wave in dielectric medium (K_s). To excite surface plasmons, two propagation wave-vectors should be equal. Hence, the direct light cannot excite surface plasmons at a metal-dielectric interface. To excite surface plasmons the momentum and hence the wave vector of the exciting light in dielectric medium should be increased. This can be done if instead of a direct light, evanescent wave is used to excite the surface plasmons. To obtain the evanescent wave for the excitation of surface plasmons, a prism with high dielectric constant is used.

When a light beam is incident through one of the two sides of the prism at an angle greater than the critical angle at prism-air interface the total internal reflection of light beam takes place. In the condition of total internal reflection light beam does not return exactly from the interface. Instead it returns after penetrating in the lower refractive index medium (air in this case). The field in the lower refractive index medium is called evanescent field and the wave corresponding to this is called evanescent wave. The evanescent wave propagates along the prism-air interface and decays exponentially in the rarer medium (air). The propagation constant of the evanescent wave at prism-air interface is given by

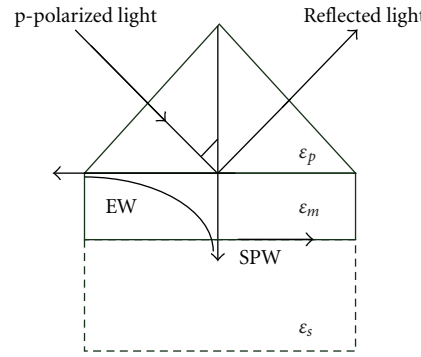

Figure 1: Kretschmann configuration for the excitation of surface plasmon at metal-dielectric interface [23]. © IEEE.

$$K_{ev} = \frac{\omega}{c}\sqrt{\varepsilon_p}\sin\theta, \quad (3)$$

where ε_p represents the dielectric constant of the material of the prism and θ is the angle of incidence of the beam. Increase in the dielectric constant of the prism increases the propagation constant of the evanescent wave and hence this can be made equal to propagation constant of the surface plasmon wave to satisfy the surface plasmon resonance condition. Kretschmann and Reather [24] devised a prism-based configuration, shown in Figure 1, to excite the surface plasmons using evanescent wave. In this configuration the base of the glass prism is coated with a thin layer of metal (typically around 50 nm). The metal layer is kept in direct contact with the dielectric medium of lower refractive index (such as air or some other dielectric sample). When a p-polarized light beam is incident through the prism on the prism-metal layer interface at an angle θ equal to or greater than the critical angle, the evanescent wave is produced at the prism-metal interface. The excitation of surface plasmons occurs when the wave vector of evanescent wave exactly matches with that of the surface plasmons of similar frequency. This occurs at a particular angle of incidence θ_{res}. Thus the resonance condition for surface plasmon resonance is

$$\frac{\omega}{c}\sqrt{\varepsilon_p}\sin\theta_{res} = \frac{\omega}{c}\left(\frac{\varepsilon_m \varepsilon_s}{\varepsilon_m + \varepsilon_s}\right)^{1/2}. \quad (4)$$

The excitation of surface plasmons at metal/dielectric interface results in the transfer of energy from incident light to surface plasmons, which reduces the intensity of the reflected light. If the intensity of the reflected light is measured as a function of angle of incidence θ for fixed values of frequency, metal layer thickness and dielectric layer thickness then a

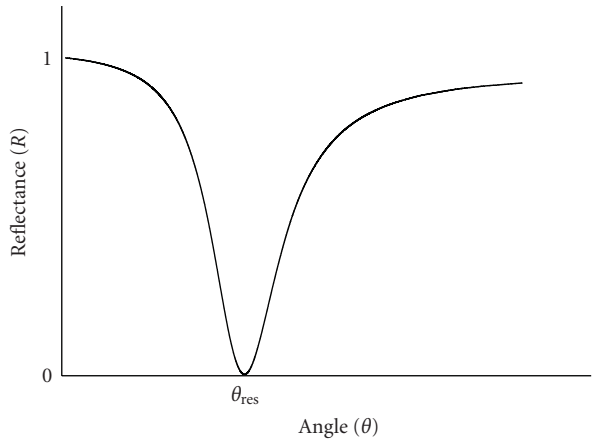

Figure 2: SPR spectrum [23]. © IEEE.

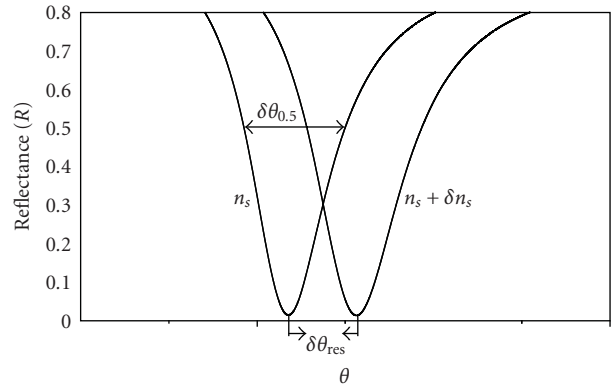

Figure 3: SPR spectra for two different refractive indices of the sensing layer [23]. © IEEE.

sharp dip is observed at resonance angle, θ_{res}, due to an efficient transfer of energy to surface plasmons as shown in Figure 2. The minimum of the reflected intensity can be quantitatively described with the help of Fresnel's equations for the three-layer system.

For a given frequency of the light source and the dielectric constant of metal film one can determine the dielectric constant (ε_s) of the sensing layer adjacent to metal layer using (4) if the value of the resonance angle (θ_{res}) is known. The resonance angle is experimentally determined by using angular interrogation method. It is very sensitive to variation in the refractive index of the sensing layer. Increase in refractive index of the sensing layer increases the resonance angle.

Sensitivity and detection accuracy or signal-to-noise ratio (SNR) are the two parameters that are used to analyze the performance of an SPR sensor. For the best performance both the parameters should be as high as possible. Sensitivity of an SPR sensor utilizing angular interrogation method depends on the amount of shift of the resonance angle with a change in the refractive index of the sensing layer. For a given refractive index change if the shift in resonance angle increases this means an increase in the sensitivity of the sensor.

Figure 3 shows a plot of reflectance as a function of angle of incidence of the light beam for sensing layer with refractive indices n_s and $n_s + \delta n_s$. Increase in refractive index by δn_s shifts the resonance angle by $\delta\theta_{res}$. Thus the sensitivity of an SPR sensor utilizing angular interrogation method is defined as

$$S_n = \frac{\delta\theta_{res}}{\delta n_s}. \tag{5}$$

The detection accuracy or the SNR of an SPR sensor depends on how accurately and precisely the sensor can detect the resonance angle and hence, the refractive index of the sensing layer. The narrower the width of the SPR curve, the higher is the detection accuracy. Therefore, if $\delta\theta_{0.5}$ is the angular width of the SPR curve corresponding to reflectance 0.5, the detection accuracy of the sensor is assumed to be inversely proportional to $\delta\theta_{0.5}$ (Figure 3). The SNR of the SPR sensor with angular interrogation is, thus, defined as [25]

$$\text{SNR} = \frac{\delta\theta_{res}}{\delta\theta_{0.5}}. \tag{6}$$

3. Fiber Optic SPR-Based Sensors

In the case of a prism-based SPR sensor evanescent wave required to excite surface plasmons is resulted due to the total internal reflection taking place at the prism-metal interface when the angle of incidence of the beam is greater than the critical angle. The evanescent wave is also present in an optical fiber because the light guidance in an optical fiber occurs due to the total internal reflection of the guided ray at the core-cladding interface. In the case of optical fiber the evanescent wave propagates along the core-cladding interface. Therefore, to design an SPR-based fiber optic sensor, the prism can be replaced by the core of an optical fiber. To fabricate an SPR-based fiber optic sensor, the silicon cladding from a small portion of the fiber, preferably from the middle, is removed and the unclad core is coated with a metal layer. The metal layer is further, surrounded by a dielectric sensing layer as shown in Figure 4. In an SPR-based fiber optic sensor, all the guided rays are launched and hence, instead of angular interrogation, spectral interrogation method is used. The light from a polychromatic source is launched into one of the ends of the optical fiber. The evanescent field produced by the guided rays excites the surface plasmons at the metal-dielectric sensing layer interface. The coupling of evanescent field with surface plasmons strongly depends on wavelength, fiber parameters, probe geometry, and the metal layer properties. Unlike prism-based SPR sensor, the number of reflections for most of the guided rays is greater than one in SPR-based fiber optic sensor geometry. The smaller the angle of incidence at the interface, the larger is the number of reflections per unit length in the fiber. In addition, the number of reflections for any ray also depends on the length of the sensing region

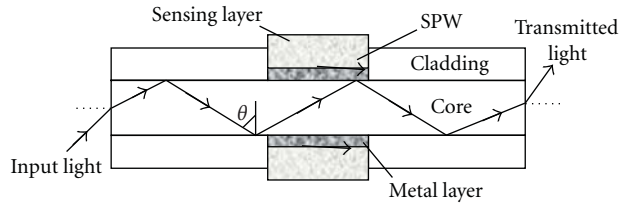

Figure 4: A typical probe of an SPR-based fiber optic sensor [23]. © IEEE.

and the fiber core diameter. The number of reflections is one of the important parameters that affect the width of the SPR curve. The intensity of the light transmitted after passing through the SPR sensing region is detected at the other end of the fiber as a function of wavelength. The SPR spectrum thus obtained is similar in shape to that shown in Figure 2. The sensing is accomplished by observing the wavelength corresponding to the dip in the spectrum (called resonance wavelength). A plot of resonance wavelength with the refractive index of the sensing layer is the calibration curve of the SPR sensor. The sensitivity and the detection accuracy are determined in the same way as determined in the case of angular interrogation. The angles are replaced by wavelengths in the definitions of sensitivity and detection accuracy.

4. SPR Probe Designs

Sensitivity, detection accuracy, reproducibility, and operating range of a sensor are the important parameters to compare it with other sensors. The best sensor is the one that has high sensitivity, detection accuracy and operating range, in addition to giving reproducible results. To achieve this various modifications have been carried out in the design of fiber optic SPR probe. We review some of these modifications in what follows.

4.1. Bimetallic Coating. For metallic coating on prism base or fiber core either silver or gold is used. Gold demonstrates a higher shift of resonance parameter to change in refractive index of sensing layer and is chemically stable. Silver, on the other hand, displays a narrower width of the SPR curve causing a higher SNR or detection accuracy. The sharpness of the resonance curve depends upon the imaginary part of the dielectric constant of the metal. Silver having the larger value of the imaginary part of the dielectric constant shows narrower width of the SPR curve causing a higher SNR or detection accuracy. On the other hand, the shift of the resonance curve depends on the real part of the dielectric constant of the metal. The real part of the dielectric constant is large in the case of gold than the silver and hence gold demonstrates a higher shift of resonance parameter to change in refractive index of sensing layer. The chemical stability of silver is poor due to its oxidation. The oxidation of silver occurs as soon as it is exposed to air and especially to water, which makes it difficult to give a reproducible result and hence the sensor remains unreliable for practical applications. Therefore, the treatment of silver surface by a thin and dense cover is required. In this regard, a new structure of resonant metal film based on bimetallic layers (gold as outer) on the prism base with angular interrogation method was reported [25]. The new structure displayed a large shift of resonance angle as gold film, and also showed narrower resonance curve as silver film along with the protection of silver film against oxidation. The same structure with spectral interrogation was extended to SPR-based optical fiber sensor for the selected and all guided rays configurations [19]. The sensitivity and SNR were evaluated numerically for different ratios of the thicknesses of silver and gold layers. Figures 5(a) and 5(b) show the variations of SNR and sensitivity with percentage of silver in bimetallic combination, respectively [19]. As expected the SNR increases with the increase in the silver thickness. The variation is almost the same for both kinds of launching but the values of SNR for all guided rays launching are about 1.5 times higher than those corresponding to selected rays launching. As far as sensitivity is concerned, it decreases as the silver layer thickness increases or gold layer thickness decreases. Its variation with silver thickness is almost same in the two cases but in terms of values, the selected ray launching has higher value than the all guided rays launching case.

4.2. Choice of Metals. The capability of other metals such as copper (Cu) and aluminium (Al) for SPR sensor applications has also been analyzed. Both metals have the ability to be used for an SPR sensor. The copper has some limitations like silver. It is chemically vulnerable against oxidation and corrosion, therefore, its protection is required for a stable sensing application. The SPR sensing capabilities of different bimetallic combinations made out of Ag, Au, Al, and Cu were theoretically investigated for the design of SPR-based fiber optic sensors [26]. Figures 6(a) and 6(b) show the variation of sensitivity and SNR with the ratio of inner layer thickness to total bimetallic thickness for different bimetallic combinations, respectively [26]. The figure predicts that the sensor with single gold layer is the most sensitive whereas the sensor with single aluminium layer is the least. Further, Cu-Al combination provides the minimum sensitivity for any ratio of their corresponding thickness values. In all the combinations with gold, Ag-Au and Cu-Au combinations provide good sensitivity for the small thickness of the inner layer while the Au-Al combination provides larger sensitivity than all other combinations for the larger thickness of inner gold layer. It implies that a thick Au layer with very thin cover of Al layer (around 2–4 nm) provides quite a large sensitivity. As far as variation of SNR with inner layer fraction is concerned, Cu-Al is better among all the bimetallic combinations while the Ag-Au combination provides the minimum values of SNR. To achieve highest SNR, one should choose a thin Cu layer and a much thicker covering of Al layer. This study implies that there is no single combination of metals that provides high values of both SNR and sensitivity simultaneously.

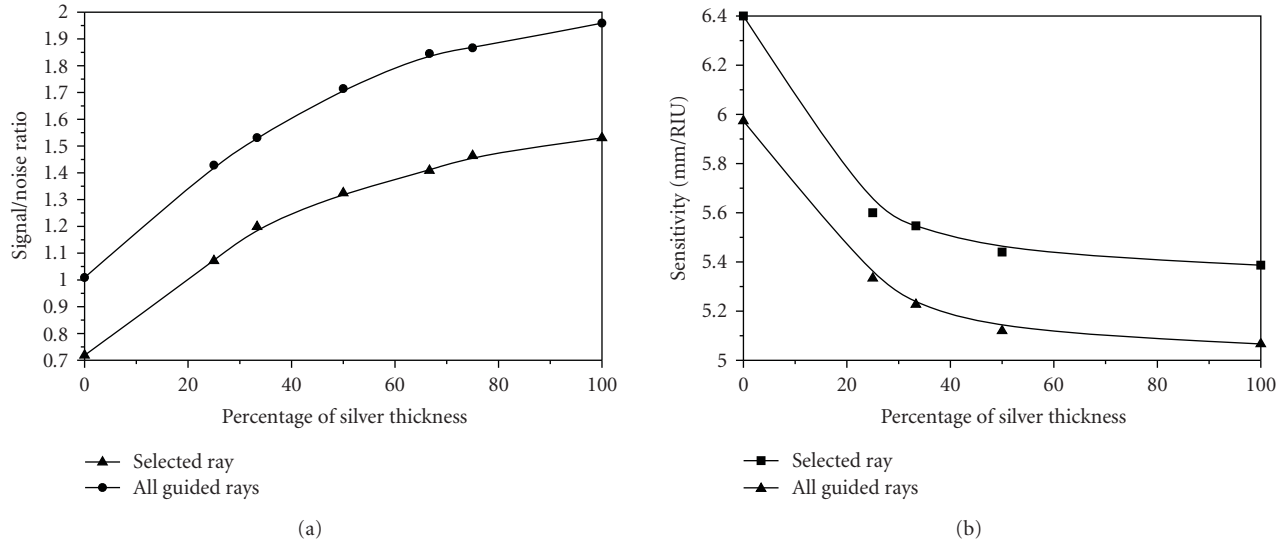

Figure 5: Variation of (a) signal-to-noise ratio and (b) sensitivity with percentage of silver in bimetallic layer for two different kinds of light launching [19]. © Elsevier.

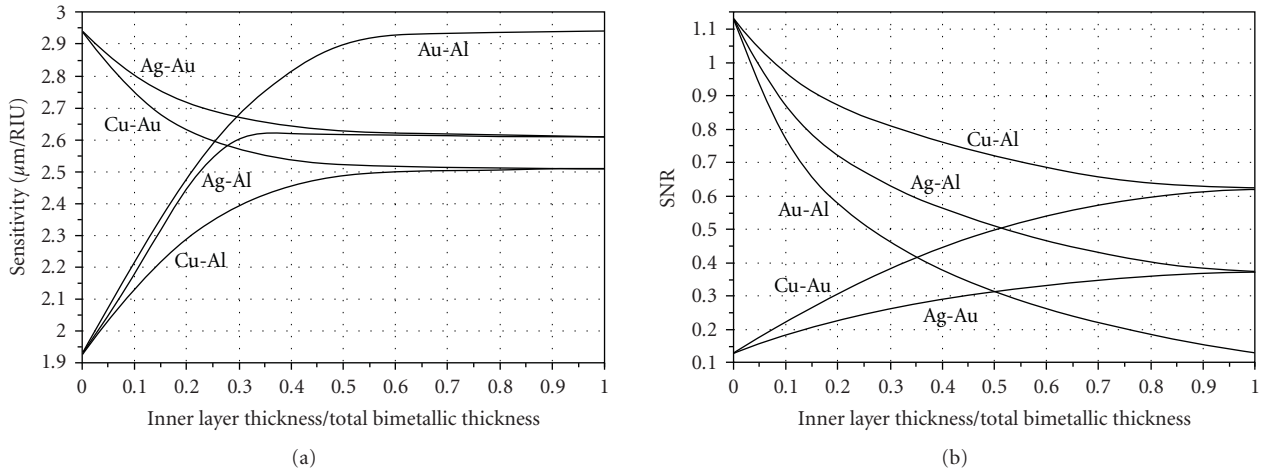

Figure 6: Variation of (a) sensitivity and (b) SNR with inner layer fraction for different bimetallic combinations [26]. © AIP.

4.3. Effect of Dopants. It may be noted from (4) that the SPR condition depends upon the refractive index of the material of the fiber core. Therefore, if an optical fiber is fabricated by adding dopants in the fiber core the sensitivity of the sensor can be enhanced or tuned. Generally, an optical fiber with pure silica core is used for SPR-based sensors. Sharma et al. [27] carried out theoretical modeling and analysis of SPR-based fiber optic sensor to evaluate the effect of dopants on the sensitivity and SNR. Germanium oxide (GeO_2), boron oxide (B_2O_3), and phosphorus pent-oxide (P_2O_5) were used as dopants for pure silica. Figure 7 shows the variation of sensitivity with the refractive index of the sensing layer for different dopants with concentrations [27]. The simulation predicts an increase of about 50% in sensitivity between B_2O_3 (5.2) and GeO_2 (19.3) dopants. Moreover, as the doping concentration of GeO_2 is increased from a low of 6.3 mole % to a high of 19.3 mole %, a noticeable decrease in sensor's sensitivity is obtained. Further, the effect of dopants on the sensitivity of the fiber optic SPR sensor was reported to be same irrespective of whether a single metal layer or a bimetallic configuration is used.

4.4. Tapered Probe. Several groups have worked on the improvement of the sensitivity of a fiber optic SPR sensor by changing the shape or the geometry of the fiber optic SPR probe. Tapering the fiber optic SPR probe was one of the modifications reported in literature [18, 28]. A typical tapered fiber optic SPR probe is shown in Figure 8 [29]. The uses of dual-tapered and tetra-tapered fiber optic SPR probes for gas and liquid sensing have also been reported [18]. Changing the profile of the tapered SPR probe also affects the sensitivity of the sensor. Surface plasmon resonance-based tapered fiber optic sensor with three different taper profiles,

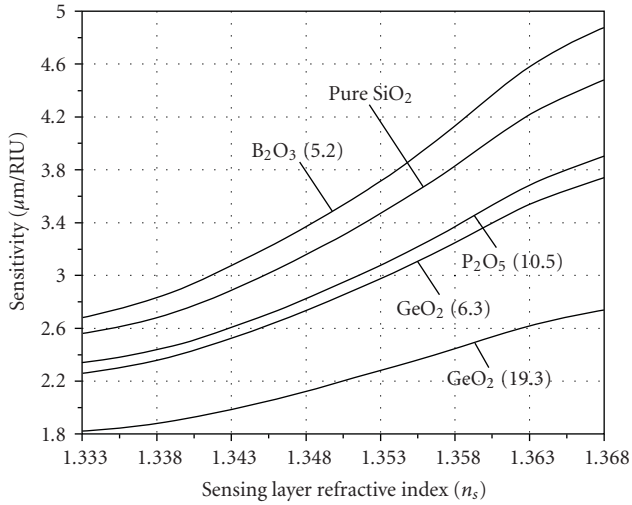

Figure 7: Variation of sensitivity with sensing layer refractive index. A: Silica doped with GeO_2 (19.3); B: Silica doped with GeO_2 (6.3); C: Silica doped with P_2O_5 (10.5); D: Pure silica with no doping; and E: Silica doped with B_2O_3 (5.2). Numbers in brackets are the molar concentrations of dopant in mole % [27]. © Elsevier.

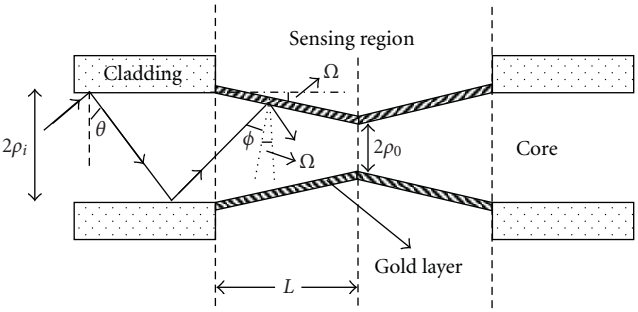

Figure 8: A typical SPR-based fiber optic sensor with tapered probe [29]. © Elsevier.

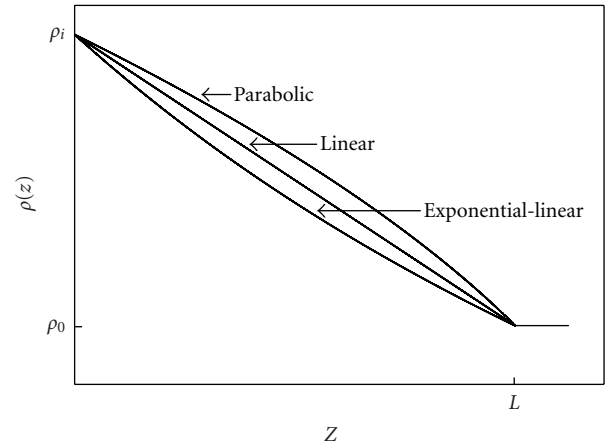

Figure 9: Three different taper profiles showing the linear, parabolic, and exponential-linear [29]. © Elsevier.

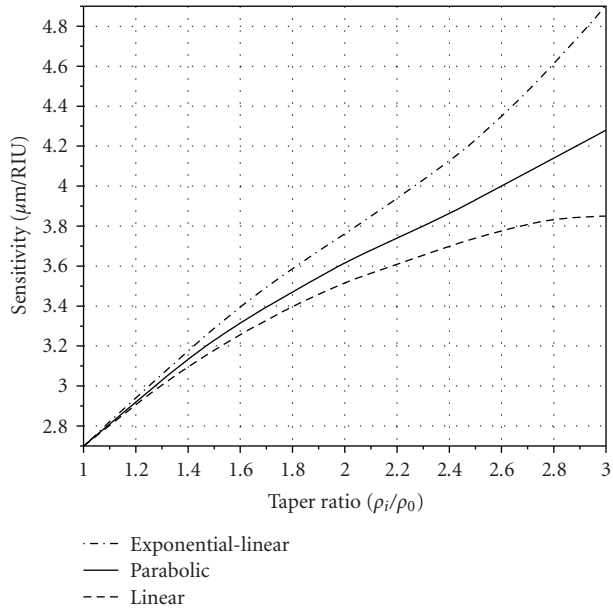

Figure 10: Variation of sensitivity with taper ratio for three different taper profiles [29]. © Elsevier.

namely, linear, parabolic, and exponential-linear, shown in Figure 9, was analyzed theoretically [29]. Figure 10 shows the variation of the sensitivity of the tapered fiber optic SPR probe with taper ratio for these three taper profiles [29]. Theoretical analysis predicts an increase in the sensitivity with the increase in the taper ratio. The study further shows that, for a given taper ratio, the exponential-linear taper profile provides the maximum sensitivity. The increase in sensitivity occurs because of the decrease in the angle of incidence of the guided rays with the normal to the core-cladding interface in the tapered region.

To further enhance the sensitivity, an SPR probe of uniform core (with metallic coating) sandwiched between two unclad tapered fiber regions, shown in Figure 11, was proposed [30]. The taper region 1 brings down the angles of the bound rays in the fiber close to the critical angle of the unclad tapered region while the taper region 2 reconverts the angles of these rays to their initial values so that all the guided rays can propagate up to the output end of the fiber. This was achieved by choosing the minimum allowed value of the radius of the uniform core in the sensing region. In the sensing region rays propagate close to the critical angle of the region. Figure 12 shows the variation of sensitivity with taper ratio for this kind of probe [30]. The sensitivity increases with an increase in the taper ratio as reported in other studies [29]. However, a significant sensitivity enhancement of more than 5 times was obtained for a taper ratio of 2.0 in comparison to conventional (TR = 1) fiber optic SPR sensor.

4.5. U-Shaped. The angle of incidence of the ray with the normal to the core-cladding interface can be brought close to the critical angle by using a U-shaped probe. An SPR-based fiber optic sensor with uniform semimetal coated U-shaped probe, shown in Figure 13, was analyzed using a bi-dimensional model [31]. To make the analysis simpler, all

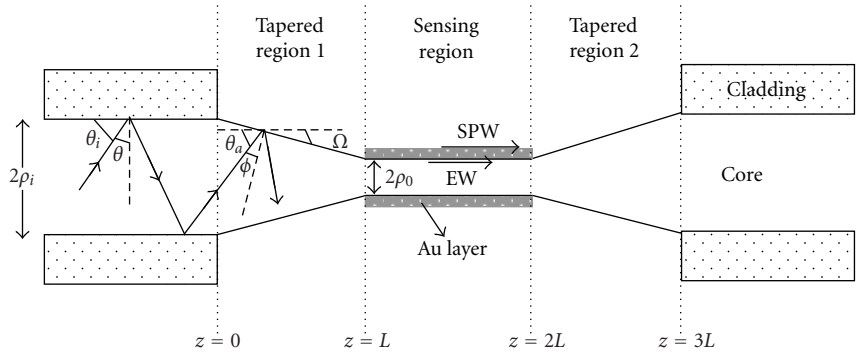

Figure 11: A novel SPR-based fiber optic sensor. Sensing probe of uniform core radius is sandwiched between two tapered fiber regions [30]. © IEEE.

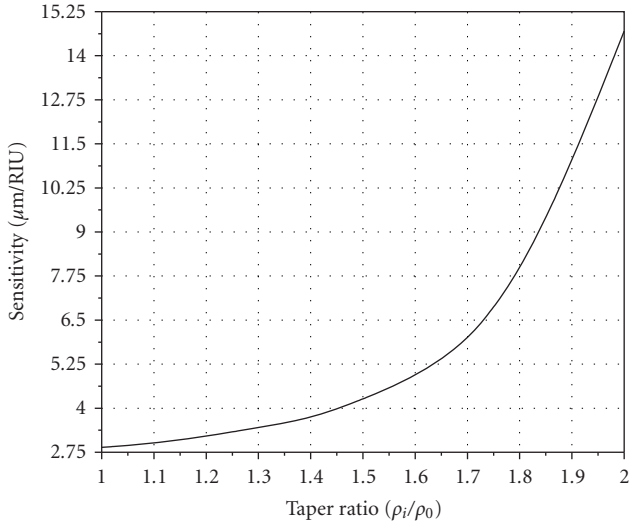

Figure 12: Variation of sensitivity of the SPR-based fiber optic sensor with taper ratio [30]. © IEEE.

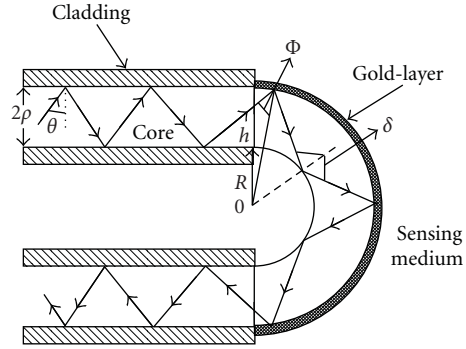

Figure 13: A typical U-shaped fiber optic SPR probe [31]. © IOP.

the guided rays of the p-polarized light launched in the fiber and their electric vectors were assumed to lie in the plane of bending of the U-shaped probe. Figure 14 shows the variation of the sensitivity of the probe with bending radius for different values of the sensing length of the probe. Increase in sensitivity with the decrease in the bending radius was obtained. The increase in sensitivity was up to a certain value of the bending radius below that it starts decreasing sharply. The decrease in sensitivity occurs because the angle of incidence of the last ray becomes less than the critical angle required for a ray to be guided in the bent region. Thus, there exists an optimum value of the bending radius at which the sensitivity of the SPR sensor based on U-shaped probe acquires a maximum value. The trend of variation was same for all the three values of the sensing length used. This is due to the independence of the angle of incidence on the sensing length. For a given bending radius the sensitivity increases as the sensing length increases. The increase in sensitivity, as mentioned earlier, is due to the decrease in the angle of incidence. The decrease in angle of incidence increases the number of reflections which causes the broadening of SPR curve and hence the decrease in the detection accuracy or SNR of the sensor. The enhancement in sensitivity obtained was much more compared to the decrease in the detection accuracy and hence the decrease in detection accuracy can be tolerated. In fact the maximum sensitivity achieved was several times more than that reported for an SPR-based fiber optic tapered probe.

4.6. Side-Polished Fiber. The SPR probes reported above use multimode optical fibers. A single mode fiber has also been used to fabricate fiber optic SPR probe. Surface plasmon resonance sensor using side-polished single mode optical fiber and a thin metal over layer is shown in Figure 15 [32]. The design of the probe is slightly different from that shown in Figure 4. In this configuration, the guided mode propagating in the fiber excites the surface plasmon wave at the interface between the metal and a sensing medium. The resonance occurs if the two modes are closely phase matched. Such single-mode optical fiber based SPR sensor is more sensitive and more accurate in comparison to those with multi-mode optical fibers. However, their fabrication is much more complex and sophisticated compared with those that use multi-mode fibers. The advantage of side-polished half block SPR sensor is that it requires a very small amount of sample for measuring the refractive index.

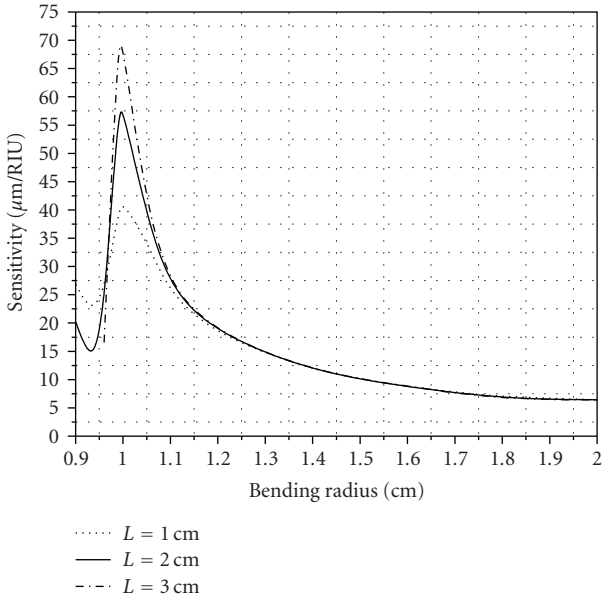

Figure 14: Variation of sensitivity with bending radius for three different values of the sensing length [31]. © IOP.

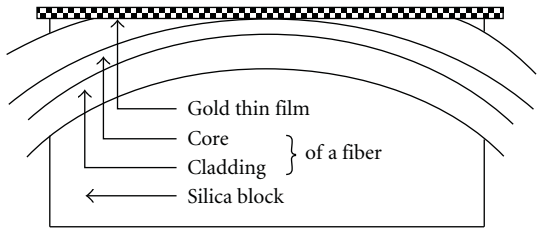

Figure 15: Side-polished single mode fiber optic SPR probe [23]. © IEEE.

Recently SPR-based side-polished multimode optical fiber sensors have been reported [33, 34]. In these sensors the fiber was side-polished until half the core was closed. This increased the sensing area which is an advantage. Apart from side-polished single mode fiber, D-type single mode optical fibers have also been used for sensing applications utilizing SPR technique [35, 36]. These fibers also improve sensitivity. The other designs for SPR-based fiber optic sensor includes SPR probe at one of the ends of the fiber with the reflecting end face [37, 38] and a fiber tip [39, 40]. The photonic band-gap fiber based SPR sensors have also been reported very recently [41, 42].

4.7. Effect of Skew Rays. Most of the theoretical studies on fiber optic SPR sensors using ray optics and reported in literature do not consider skew rays in the analysis. These studies consider the propagation of only meridional rays in the fiber that makes the analysis simpler. However, apart from meridional rays, skew rays also exist in the fiber depending on the light launching conditions. These rays follow a helical path inside the fiber. To specify the trajectory of a skew ray, a second angle (known as skewness angle), in addition to the inclination of the ray with the axial direction of the fiber, is required. Recently, the effect of skew rays on the sensitivity and the SNR of a fiber optic SPR sensor were studied using spectral interrogation method [43]. Figures 16(a) and 16(b) show the variation of sensitivity and SNR with skewness parameter, respectively [43]. Both the sensitivity and the SNR decrease as the value of skewness parameter increases irrespective of the metal used for coating. The sensitivity is better in the case of gold whereas silver demonstrates better SNR as expected. The decrease in sensitivity for highest value of skewness parameter is about 6% in the case of both the metals. The effect of skew rays is more on SNR than on the sensitivity. In the case of gold film it is about 40% while in the case of silver it is around 30%.

5. Some Applications

The surface plasmon resonance-based fiber optic sensors have large number of applications for quantitative detection of chemical and biological species. These include food quality, medical diagnostics and environmental monitoring. These are detected by changing the refractive index of the medium around the metallic coating. The measurand changes the refractive index of the medium directly or indirectly. Here we present few SPR-based fiber optic sensors.

5.1. Temperature. Since the refractive index of a medium depends on its temperature, the SPR technique can be applied to sense the temperature of a medium. The temperature sensor based on surface plasmon resonance was proposed using a coupling prism and angular interrogation mode of operation [44]. It was suggested that for SPR technique to be used in temperature sensing, the sensing layer of large thermo-optic coefficient (such as titanium dioxide or silicon acrylate) should be used. Further, the penetration of surface plasmon wave should be restricted only to metal and sensing layers by taking an appropriate thickness of the two layers. The analysis was later extended to SPR-based fiber optic remote sensor for temperature detection [45]. The sensing layer was assumed to be of TiO_2 (titanium dioxide). The outermost ambient medium was chosen as air, which adds to the flexibility of the sensor's design. Figure 17 shows the variation in resonance wavelength with temperature for silver and gold [45]. For both the metals, resonance wavelength shifts to shorter side with the increase in the temperature. However, there is no appreciable difference in resonance wavelength (and hence, in temperature sensitivity) for two metals used. This was suggested to be due to the similarity in the variation of physical properties of both the metals with temperature. Figure 18 depicts the corresponding variation in SPR curve width with temperature [45]. The SPR curve width increases with the increase in the temperature. This was reported to happen because the imaginary (absorption) part of the metal dielectric function increases with temperature. The effect of other parameters such as numerical aperture and the ratio of sensing region length to fiber core diameter on the sensitivity and detection accuracy were also reported.

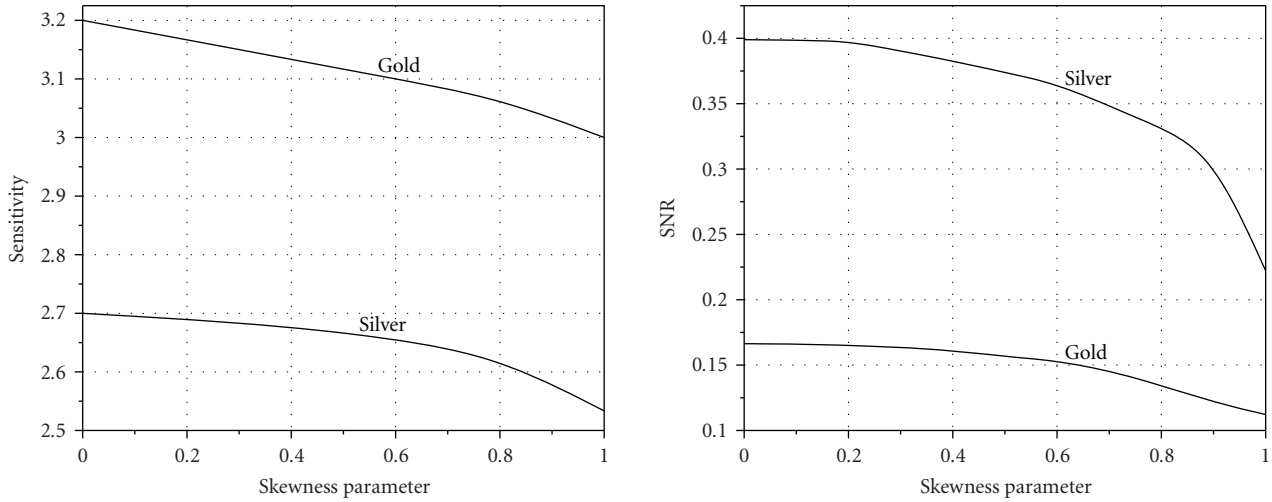

(a) (b)

Figure 16: Variation of (a) Sensitivity and (b) SNR of an SPR-based fiber optic sensor with skewness parameter for two different metals [43]. © OSA.

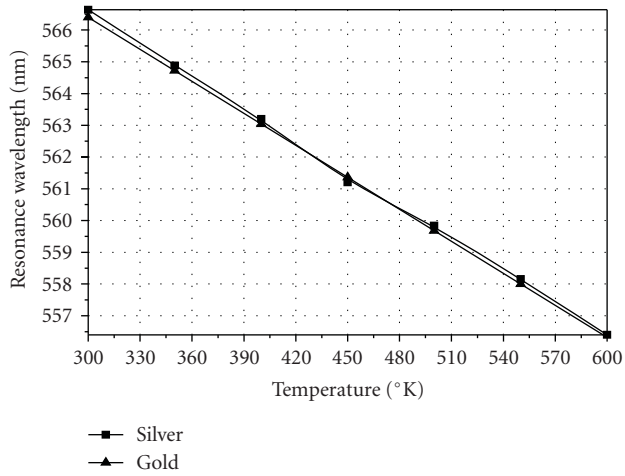

Figure 17: Variation of resonance wavelength with temperature for two metals: silver and gold [45]. © Elsevier.

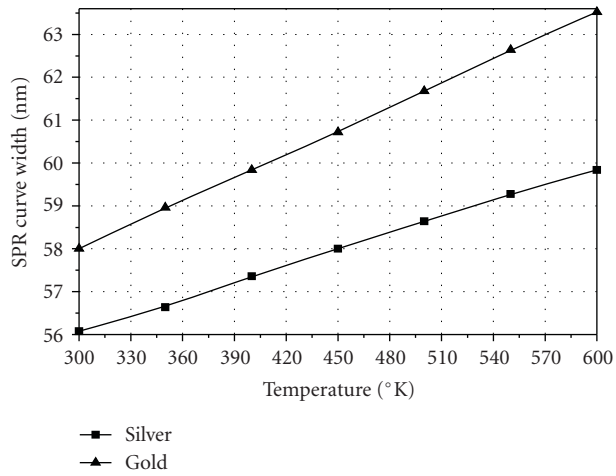

Figure 18: Variation of SPR curve width with temperature for two metals: silver and gold [45]. © Elsevier.

It was also reported that the fiber with smaller numerical aperture provides larger detection accuracy without affecting the temperature sensitivity. Similarly, the small values of the ratio of sensing region length to fiber core diameter give high detection accuracy. For SPR-based fiber optic temperature sensor smaller sensing region and highly multimode optical fiber was recommended.

5.2. Naringin. The processing of citrus fruit juice has faced formidable problems in terms of bitterness, thereby affecting its consumer acceptability. The bitterness is caused by excessive naringin contents in fruit juice. The presence of naringin in fruit juice can be detected using an SPR-based fiber optic sensor. An SPR-based fiber optic sensor relying on spectral interrogation method was reported for the detection of naringin [21]. The SPR probe was prepared by immobilizing the enzyme naringinase on the silver-coated core of the optical fiber. To immobilize, gel entrapment technique was used. The experimental set up for the characterization of the SPR-based fiber optic sensor is shown in Figure 19 [21]. Light from a broadband source (tungsten halogen lamp) was focused on the input face of the fiber using a circular slit and a microscope objective. The probe was mounted in a flow cell to keep the sample around the probe. The spectral distribution of the transmitted power for the sample around the probe was determined using a monochromator, a silicon detector and a power meter. The spectral distribution of transmitted light so obtained for a sample was divided by the corresponding spectral distribution obtained without any sample around the probe. The resultant SPR spectrum so obtained does not depend on the source spectral

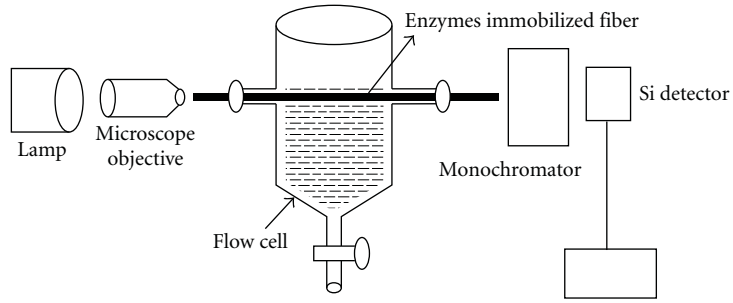

Figure 19: Experimental set up of the SPR-based fiber optic sensor [21]. © Elsevier.

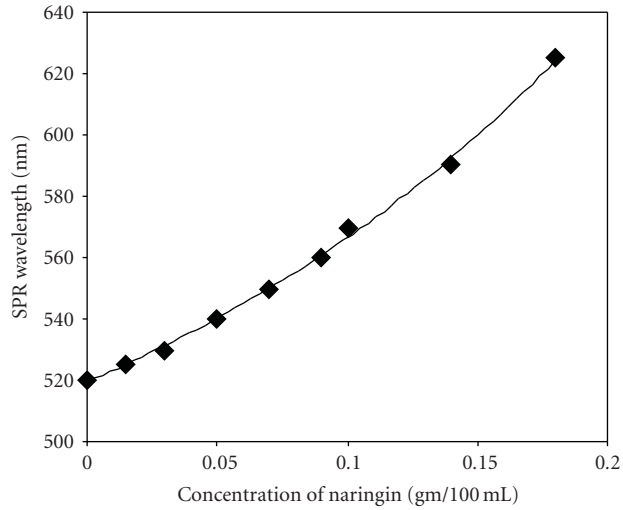

Figure 20: Variation of resonance wavelength with the concentration of naringin in buffer solution [21]. © Elsevier.

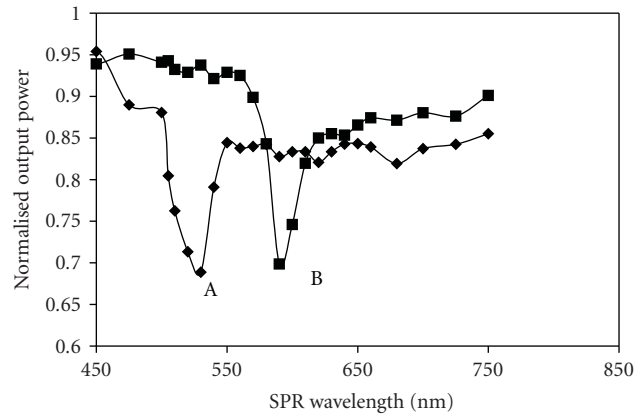

Figure 21: Variation of normalized output power as a function of wavelength for a substrate concentration (2.5 mM) and 1.0 μM concentration of pesticide (A) without enzyme and (B) with enzyme (B) [46]. © Elsevier.

output, spectral sensitivity of photodetector and the spectral absorbance of the fiber. From the SPR spectrum resonance wavelength was determined. The calibration curve of the SPR-based fiber optic sensor obtained for the detection of naringin is shown in Figure 20 [21]. As the concentration of naringin increases the resonance wavelength increases. The increase in resonance wavelength was reported to be due to an increase in the refractive index of the immobilized layer which may occur due to the formation of a complex of naringin with the enzyme naringinase in the film.

5.3. Pesticides. Surface plasmon resonance-based fiber optic sensor for the detection of organophosphate pesticide, chlorphyrifos, was also reported recently using similar experimental method as used for the detection of naringin [46]. The probe was prepared by immobilizing acetylcholinesterase enzyme on the silver-coated core of the fiber. The principle of detection of pesticide was slightly different from that of naringin. It was based on the principle of competitive binding of the pesticide (acting as an inhibitor) for the substrate (acetlythiocholine iodide) to the enzyme. Figure 21 shows SPR spectra for pesticide concentration of 1.0 μM and a substrate concentration of 2.5 mM for the two cases (A) without enzyme (control experiment) and (B) with enzyme in the film [46]. The dip in control experiment occurs due to the refractive index of the gel. The difference in two spectra implies that the enzyme is playing a role in changing the refractive index of the gel in the presence of pesticide. The resonance wavelength was obtained around 590 nm for 1.0 μM pesticide concentration. Figure 22 shows the calibration curve of the sensor [46]. The trend is opposite to that reported for the detection of naringin. In this case, the SPR wavelength decreases with the increase in the concentration of the pesticide for the fixed concentration of the substrate. The results appear to be due to the decrease in the refractive index of the film as the concentration of pesticide increases.

Surface plasmon resonance-based fiber optic sensors have also been reported for other chemical species. These include measurements of salinity in water [22, 37], refractive indices of alcohols [17], BSA [34], vapor and liquid analyses [18]. In addition a single-mode waveguide surface plasmon resonance sensor has been developed for biomolecular interaction analysis [47]. Recently, fiber optic SPR sensors have been reported that uses either a series of long period grating [48] or Bragg grating [49]. The advantage of these designs is that these offer multiple sensing channels capability.

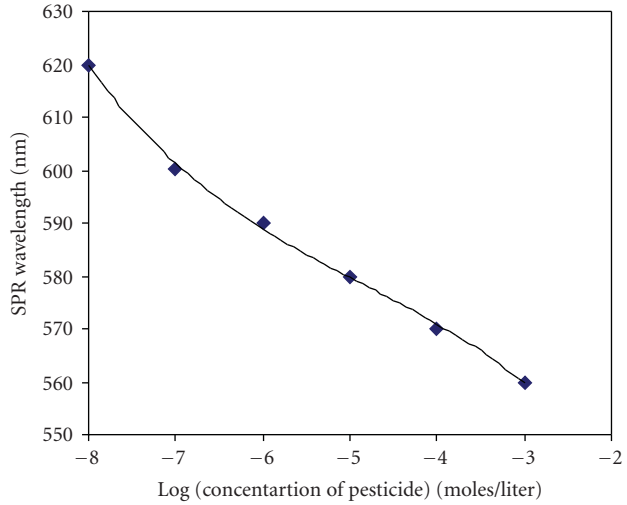

FIGURE 22: Calibration curve of SPR-based fiber optic pesticide sensor [46]. © Elsevier.

6. Summary

In this review article we have first described the principle of surface plasmon resonance technique. The technique is well established and will remain unchanged for years. In the beginning, the technique was used for prism-based SPR sensors but later when the advantages of optical fiber were realized, it was applied to optical fiber based sensors. Recently there have been significant advancements in both the design of fiber optic SPR sensors and strategies for the enhancement of the performance of the sensors particularly sensitivity. The probe designs include tapered, U-shaped, and side-polished fibers. These developments are likely to drive future trends in the research and development of optical fiber sensors. The unique optical properties of metal nanoparticles have also attracted the sensor community to develop localized surface plasmon resonance- (LSPR-) based sensors. The LSPR-based sensors have few advantages over bulk SPR-based sensors. However, the pace of collaboration of LSPR with optical fiber for sensing is at present slow but may gain momentum in coming years.

Acknowledgment

The present work is partially supported by the Department of Science and Technology (India).

References

[1] B. Liedberg, C. Nylander, and I. Lunström, "Surface plasmon resonance for gas detection and biosensing," *Sensors and Actuators*, vol. 4, pp. 299–304, 1983.

[2] J. van Gent, P. V. Lambeck, H. J. M. Kreuwel, et al., "Optimization of a chemooptical surface plasmon resonance based sensor," *Applied Optics*, vol. 29, pp. 2843–2849, 1990.

[3] E. Stenberg, B. Persson, H. Roos, and C. Urbaniczky, "Quantitative determination of surface concentration of protein with surface plasmon resonance using radiolabeled proteins," *Journal of Colloid and Interface Science*, vol. 143, no. 2, pp. 513–526, 1991.

[4] G. Dougherty, "A compact optoelectronic instrument with a disposable sensor based on surface plasmon resonance," *Measurement Science and Technology*, vol. 4, no. 6, pp. 697–699, 1993.

[5] S. Ekgasit, A. Tangcharoenbumrungsuk, F. Yu, A. Baba, and W. Knoll, "Resonance shifts in SPR curves of nonabsorbing, weakly absorbing, and strongly absorbing dielectrics," *Sensors and Actuators B*, vol. 105, no. 2, pp. 532–541, 2005.

[6] J.-J. Chyou, C.-S. Chu, F.-C. Chien, et al., "Precise determination of the dielectric constant and thickness of a nanolayer by use of surface plasmon resonance sensing and multiexperiment linear data analysis," *Applied Optics*, vol. 45, no. 23, pp. 6038–6044, 2006.

[7] H. P. Chiang, C.-W. Chen, J. J. Wu, et al., "Effects of temperature on the surface plasmon resonance at a metal-semiconductor interface," *Thin Solid Films*, vol. 515, no. 17, pp. 6953–6961, 2007.

[8] J. Le Person, F. Colas, C. Compere, et al., "Surface plasmon resonance in chalcogenide glass-based optical system," *Sensors and Actuators B*, vol. 130, no. 2, pp. 771–776, 2008.

[9] W. Feng, L. Shenye, P. Xiaoshi, C. Zhuangqi, and D. Yongkun, "Reflective-type configuration for monitoring the photobleaching procedure based on surface plasmon resonance," *Journal of Optics A*, vol. 10, no. 9, Article ID 095102, 2008.

[10] R. C. Jorgenson and S. S. Yee, "A fiber-optic chemical sensor based on surface plasmon resonance," *Sensors and Actuators B*, vol. 12, no. 3, pp. 213–220, 1993.

[11] R. D. Harris and J. S. Wilkinson, "Waveguide surface plasmon resonance sensors," *Sensors and Actuators B*, vol. 29, no. 1–3, pp. 261–267, 1995.

[12] W. B. Lin, N. Jaffrezic-Renault, A. Gagnaire, and H. Gagnaire, "The effects of polarization of the incident light-modeling and analysis of a SPR multimode optical fiber sensor," *Sensors and Actuators A*, vol. 84, no. 3, pp. 198–204, 2000.

[13] R. Slavík, J. Homola, J. Ctyroký, and E. Brynda, "Novel spectral fiber optic sensor based on surface plasmon resonance," *Sensors and Actuators B*, vol. 74, no. 1–3, pp. 106–111, 2001.

[14] M. Piliarik, J. Homola, Z. Maníková, and J. Ctyroký, "Surface plasmon resonance sensor based on a single-mode polarization-maintaining optical fiber," *Sensors and Actuators B*, vol. 90, no. 1–3, pp. 236–242, 2003.

[15] D. J. Gentleman, L. A. Obando, J.-F. Masson, J. R. Holloway, and K. S. Booksh, "Calibration of fiber optic based surface plasmon resonance sensors in aqueous systems," *Analytica Chimica Acta*, vol. 515, no. 2, pp. 291–302, 2004.

[16] A. K. Sharma and B. D. Gupta, "Absorption-based fiber optic surface plasmon resonance sensor: a theoretical evaluation," *Sensors and Actuators B*, vol. 100, no. 3, pp. 423–431, 2004.

[17] M. Mitsushio, S. Higashi, and M. Higo, "Construction and evaluation of a gold-deposited optical fiber sensor system for measurements of refractive indices of alcohols," *Sensors and Actuators A*, vol. 111, no. 2-3, pp. 252–259, 2004.

[18] Y.-C. Kim, W. Peng, S. Banerji, and K. S. Booksh, "Tapered fiber optic surface plasmon resonance sensor for analyses of vapor and liquid phases," *Optics Letters*, vol. 30, no. 17, pp. 2218–2220, 2005.

[19] A. K. Sharma and B. D. Gupta, "On the sensitivity and signal to noise ratio of a step-index fiber optic surface plasmon resonance sensor with bimetallic layers," *Optics Communications*, vol. 245, no. 1–6, pp. 159–169, 2005.

[20] B. D. Gupta and A. K. Sharma, "Sensitivity evaluation of a multi-layered surface plasmon resonance-based fiber optic sensor: a theoretical study," *Sensors and Actuators B*, vol. 107, no. 1, pp. 40–46, 2005.

[21] Rajan, S. Chand, and B. D. Gupta, "Fabrication and characterization of a surface plasmon resonance based fiber-optic sensor for bittering component—Naringin," *Sensors and Actuators B*, vol. 115, no. 1, pp. 344–348, 2006.

[22] N. Diaz-Herrera, O. Esteban, M. C. Navarrete, M. Le Haitre, and A. Gonzalez-Cano, "In situ salinity measurements in seawater with a fibre-optic probe," *Measurement Science and Technology*, vol. 17, no. 8, pp. 2227–2232, 2006.

[23] A. K. Sharma, R. Jha, and B. D. Gupta, "Fiber-optic sensors based on surface plasmon resonance: a comprehensive review," *IEEE Sensors Journal*, vol. 7, pp. 1118–1129, 2007.

[24] E. Kretchmann and H. Reather, "Radiative decay of non-radiative surface plasmons excited by light," *Naturforsch*, vol. 23, pp. 2135–2136, 1968.

[25] S. A. Zynio, A. V. Samoylov, E. R. Surovtseva, V. M. Mirsky, and Y. M. Shirshov, "Bimetallic layers increase sensitivity of affinity sensors based on surface plasmon resonance," *Sensors*, vol. 2, no. 2, pp. 62–70, 2002.

[26] A. K. Sharma and B. D. Gupta, "On the performance of different bimetallic combinations in surface plasmon resonance based fiber optic sensors," *Journal of Applied Physics*, vol. 101, no. 9, Article ID 093111, 6 pages, 2007.

[27] A. K. Sharma, Rajan, and B. D. Gupta, "Influence of dopants on the performance of a fiber optic surface plasmon resonance sensor," *Optics Communications*, vol. 274, no. 2, pp. 320–326, 2007.

[28] B. Grunwald and G. Holst, "Fibre optic refractive index microsensor based on white-light SPR excitation," *Sensors and Actuators A*, vol. 113, no. 2, pp. 174–180, 2004.

[29] R. K. Verma, A. K. Sharma, and B. D. Gupta, "Surface plasmon resonance based tapered fiber optic sensor with different taper profiles," *Optics Communications*, vol. 281, no. 6, pp. 1486–1491, 2008.

[30] R. K. Verma, A. K. Sharma, and B. D. Gupta, "Modeling of tapered fiber-optic surface plasmon resonance sensor with enhanced sensitivity," *IEEE Photonics Technology Letters*, vol. 19, no. 22, pp. 1786–1788, 2007.

[31] R. K. Verma and B. D. Gupta, "Theoretical modeling of a bi-dimensional U-shaped surface plasmon resonance based fibre optic sensor for sensitivity enhancement," *Journal of Physics D*, vol. 41, Article ID 095106, 2008.

[32] J. Homola and R. Slavik, "Fibre-optic sensor based on surface plasmon resonance," *Electronics Letters*, vol. 32, no. 5, pp. 480–482, 1996.

[33] H.-Y. Lin, W.-H. Tsai, Y.-C. Tsao, and B.-C. Sheu, "Side-polished multimode fiber biosensor based on surface plasmon resonance with halogen light," *Applied Optics*, vol. 46, no. 5, pp. 800–806, 2007.

[34] Y.-C. Lin, Y.-C. Tsao, W.-H. Tsai, T.-S. Hung, K.-S. Chen, and S.-C. Liao, "The enhancement method of optical fiber biosensor based on surface plasmon resonance with cold plasma modification," *Sensors and Actuators B*, vol. 133, no. 2, pp. 370–373, 2008.

[35] M.-H. Chiu, C.-H. Shih, and M.-H. Chi, "Optimum sensitivity of single-mode D-type optical fiber sensor in the intensity measurement," *Sensors and Actuators B*, vol. 123, no. 2, pp. 1120–1124, 2007.

[36] M.-H. Chiu and C.-H. Shih, "Searching for optimal sensitivity of single-mode D-type optical fiber sensor in the phase measurement," *Sensors and Actuators B*, vol. 131, no. 2, pp. 596–601, 2008.

[37] D. J. Gentleman and K. S. Booksh, "Determining salinity using a multimode fiber optic surface plasmon resonance dip-probe," *Talanta*, vol. 68, no. 3, pp. 504–515, 2006.

[38] H. Suzuki, M. Sugimoto, Y. Matsui, and J. Kondoh, "Effects of gold film thickness on spectrum profile and sensitivity of a multimode-optical-fiber SPR sensor," *Sensors and Actuators B*, vol. 132, no. 1, pp. 26–33, 2008.

[39] K. Kurihara, H. Ohkawa, Y. Iwasaki, O. Niwa, T. Tobita, and K. Suzuki, "Fiber-optic conical microsensors for surface plasmon resonance using chemically etched single-mode fiber," *Analytica Chimica Acta*, vol. 523, no. 2, pp. 165–170, 2004.

[40] T. Abrahamyan and Kh. Nerkararyan, "Surface plasmon resonance on vicinity of gold-coated fiber tip," *Physics Letters A*, vol. 364, no. 6, pp. 494–496, 2007.

[41] A. Hassani and M. Skorobogatiy, "Design criteria for microstructured-optical-fiber-based surface-plasmon-resonance sensors," *Journal of the Optical Society of America B*, vol. 24, no. 6, pp. 1423–1429, 2007.

[42] B. Gauvreau, A. Hassani, M. F. Fehri, A. Kabashin, and M. Skorobogatiy, "Photonic bandgap fiber-based surface plasmon resonance sensors," *Optics Express*, vol. 15, no. 18, pp. 11413–11426, 2007.

[43] Y. S. Dwivedi, A. K. Sharma, and B. D. Gupta, "Influence of skew rays on the sensitivity and signal-to-noise ratio of a fiber-optic surface-plasmon-resonance sensor: a theoretical study," *Applied Optics*, vol. 46, no. 21, pp. 4563–4569, 2007.

[44] S. K. Ozdemir and G. Turhan-Sayan, "Temperature effects on surface plasmon resonance: design considerations for an optical temperature sensor," *Journal of Lightwave Technology*, vol. 21, no. 3, pp. 805–814, 2003.

[45] A. K. Sharma and B. D. Gupta, "Theoretical model of a fiber optic remote sensor based on surface plasmon resonance for temperature detection," *Optical Fiber Technology*, vol. 12, no. 1, pp. 87–100, 2006.

[46] Rajan, S. Chand, and B. D. Gupta, "Surface plasmon resonance based fiber-optic sensor for the detection of pesticide," *Sensors and Actuators B*, vol. 123, no. 2, pp. 661–666, 2007.

[47] T. Matsushita, T. Nishikawa, H. Yamashita, J. Kishimoto, and Y. Okuno, "Development of new single-mode waveguide surface plasmon resonance sensor using a polymer imprint process for high-throughput fabrication and improved design flexibility," *Sensors and Actuators B*, vol. 129, no. 2, pp. 881–887, 2008.

[48] Y.-J. He, Y.-L. Lo, and J.-F. Huang, "Optical-fiber surface-plasmon-resonance sensor employing long-period fiber gratings in multiplexing," *Journal of the Optical Society of America B*, vol. 23, no. 5, pp. 801–811, 2006.

[49] B. Spackova, M. Piliarik, P. Kvasnicka, C. Themistos, M. Rajarajan, and J. Homola, "Novel concept of multi-channel fiber optic surface plasmon resonance sensor," *Sensors and Actuators B*, vol. 139, no. 1, pp. 199–203, 2009.

Hindawi Publishing Corporation
Journal of Sensors
Volume 2009, Article ID 524237, 20 pages
doi:10.1155/2009/524237

Review Article

Microstructured and Photonic Bandgap Fibers for Applications in the Resonant Bio- and Chemical Sensors

Maksim Skorobogatiy

Département de Génie Physique, Ecole Polytechnique de Montreal, C. P. 6079, succ. Centre-ville, Montréal, QC, Canada H3C 3A7

Correspondence should be addressed to Maksim Skorobogatiy, maksim.skorobogatiy@polymtl.ca

Received 3 March 2009; Accepted 2 June 2009

Recommended by Christos Riziotis

We review application of microstructured and photonic bandgap fibers for designing resonant optical sensors of changes in the value of analyte refractive index. This research subject has recently invoked much attention due to development of novel fiber types, as well as due to development of techniques for the activation of fiber microstructure with functional materials. Particularly, we consider two sensors types. The first sensor type employs hollow core photonic bandgap fibers where core guided mode is confined in the analyte filled core through resonant effect in the surrounding periodic reflector. The second sensor type employs metalized microstructured or photonic bandgap waveguides and fibers, where core guided mode is phase matched with a plasmon propagating at the fiber/analyte interface. In resonant sensors one typically employs fibers with strongly nonuniform spectral transmission characteristics that are sensitive to changes in the real part of the analyte refractive index. Moreover, if narrow absorption lines are present in the analyte transmission spectrum, due to Kramers-Kronig relation this will also result in strong variation in the real part of the refractive index in the vicinity of an absorption line. Therefore, resonant sensors allow detection of minute changes both in the real part of the analyte refractive index (10^{-6}–10^{-4} RIU), as well as in the imaginary part of the analyte refractive index in the vicinity of absorption lines. In the following we detail various resonant sensor implementations, modes of operation, as well as analysis of sensitivities for some of the common transduction mechanisms for bio- and chemical sensing applications. Sensor designs considered in this review span spectral operation regions from the visible to terahertz.

1. Introduction

R&D into fiber-optic bio- and chemosensors (FOSs) has made a lot of progress during the last ten years. This is due to the appealing properties of FOS such as immunity to electromagnetic interference, safety in explosive environments, and potential to provide continuous quantitative and qualitative real-time analysis. Chemically sensitive thin films deposited on selected areas of optical fibers can influence the propagation of light in such fibers depending on the presence or absence of chemical molecules in the surrounding environment [1]. A wide range of optical sensors has been developed for selective biomolecule detection. Most of them have reliability issues as they employ very fragile antibodies as sensing elements. These sensors include high refractive index waveguides [2], surface plasmon resonance sensors [3], resonant mirrors [4], and classical fiber-optical sensors [5, 6]. Most optical sensors are based on evanescent wave sensing, where the perturbations in the refractive index close to the sensor surface are probed by the exponentially decaying optical wave. Such sensors have proven to be highly sensitive in detection of small targets such as proteins and viruses, but they experience difficulties in detecting larger targets such as bacteria (0.5–5 μm) since in that case much larger penetration of the evanescent field into analyte is required [7].

Microstructured Optical Fibers (MOFs), and Photonic Bandgap (PBG) fibers which are a subset of MOFs, promise a viable technology for the mass production of highly integrated and intelligent sensors in a single manufacturing step. In standard total internal reflection (TIR) fiber-based evanescent-wave sensors the fiber polymer jacket is stripped and the fiber cladding is polished to the core in order to obtain an overlap between the optical field and analyte,

with sensor sensitivity proportional to such an overlap. Compared to the conventional solid core optical fibers, MOFs offer a number of unique advantages in sensing applications. A defining feature of a microstructured fiber is the presence of air holes running along its entire length. Fiber optical properties are then determined by the size, shape, and relative position of the holes. Particularly, a unique ability of MOFs is to accommodate biological and chemical samples in gaseous or liquid forms inside of the air holes in the immediate vicinity of the fiber core [8–10]. In this context a MOF is used simultaneously as a light guide and as a fluidic channel. The MOF's unique architecture makes it a very promising sensing platform for chemical and biological detection. First, MOFs naturally integrate optical detection with the mirofluidics, allowing for continuous on-line monitoring of dangerous samples in real-time without exposing the personnel to danger. In addition, the samples can be transferred in the enclosed MOF optofluidic system for further confirmation analysis, for example, polymerase chain reactions (PCRs) if needed. Such channels can be further functionalized with biorecognition layers that can bind and progressively accumulate target biomolecules, thus enhancing sensor sensitivity and specificity. Second, the MOF hole size is in sub-100 μm rage, leading to very small fluid samples required for sensing. Third, MOF-based sensors can be coiled into long sensing cells ($\sim$10 m), thus dramatically increasing their sensitivity. The same is impossible to achieve with traditional TIR fiber sensors as side polishing step limits sensor length to several cm. Forth, the desired MOFs can be mass-produced using commercial fiber draw tower in a very cost-effective manner. Fifth, the MOFs can potentially be scaled up into a two-dimensional array with small dimensions, which is suitable for making into portable point-of-care devices for simultaneous on-site detection of different kinds of analytes. Sixth, Photonic Bandgap fibers can be designed to guide light directly in their analyte-field hollow cores [11]. In such fibers light-analyte coupling is considerably stronger than that in evanescent sensors.

In this paper we review several MOF and PBG fiber-based resonant optical sensors, which have recently invoked strong interest due to development of novel fiber types, as well as due to development of techniques for activation of the fiber microstructure with functional materials. In resonant sensors one typically employs fibers with strongly nonuniform spectral transmission characteristics that are sensitive to changes in the real part of the analyte refractive index. Moreover, if narrow absorption lines are present in the analyte transmission spectrum, due to Kramers-Kronig relation this will also result in strong variation in the real part of the refractive index in the vicinity of an absorption line. Therefore, resonant sensors allow detection of minute changes both in the real part of the analyte refractive index, as well as in the imaginary part of the analyte refractive index in the vicinity of absorption lines. Although the operational principle of almost all fiber-based resonant sensors relies on strong sensitivity of the fiber transmission losses to the value of the analyte refractive index, particular transduction mechanism for biodetection can vary. Consider, for example, the case of a hollow core PBG fiber featuring an analyte filled core. In one sensor implementation one can label the target biomolecules with highly absorbing particles of known absorption spectra, such as metal nanoparticles or quantum dots. The presence of such particles in the aqueous fiber core can then be quantified by detecting appearance of the absorption lines in the fiber transmission spectrum, or through resonant changes in the fiber transmission losses induced by variations in the real part of the core refractive index. In another implementation, a functional layer that binds specific biomolecules can be deposited on the inside of the hollow fiber core. Biomolecule binding events to such a layer can then be detected through resonant changes in the fiber transmission losses induced by variations in the real part of the layer refractive index.

In what follows we discuss two types of resonant sensors. One such sensor type relies on changes in the radiation losses of a leaky core mode due to changes in the real part of an analyte refractive index. Such a leaky mode is typically confined inside an analyte filled fiber core by a resonant reflector cladding. The term "leaky mode" generally refers to the guidance mechanism where the effective refractive index of a propagating mode is smaller than that of the fiber cladding. Such unusual modes are called leaky modes as, outside of a waveguide core, they do not exhibit a traditional evanescent decay into the cladding, but rather they radiate slowly (leak) into the cladding. Unlike in the case of common TIR fibers, leaky modes in PBG fibers are confined by the bandgap of a microstructured reflector. For a particular value of an analyte refractive index geometry of such a fiber is chosen to provide strong optical confinement of the leaky core mode. An example of a resonant sensor described above is a photonic bandgap fiber featuring a hollow core filled with analyte. When changing the real part of an analyte refractive index, resonant condition for mode confinement will change, resulting in strong changes in the modal radiation loss (see Figure 1(a)). Detection of changes in the transmitted intensities can be then reinterpreted in terms of the changes in the real part of an analyte refractive index. Interestingly, the same sensor can also be used in a standard nonresonant interrogation mode for the detection of changes in the imaginary part of the analyte refractive index (analyte absorption), see Figure 1(b). Even when operated in a nonresonant regime, sensitivity of the hollow core PBG fiber-based sensors is, generally, superior to that of traditional TIR fiber-based sensors due to greatly improved modal overlap with analyte.

Second sensor type considered in this review is operated in the vicinity of a phase matching wavelength between a Gaussian-like core-guided-mode and some other (high-order) mode that shows high sensitivity of its propagation properties to changes in the real part of the analyte refractive index Figure 1(b). For example, by activating fiber surface with a thin metal layer, at a specific resonant wavelength one can induce strong optical loss of a core-guided-mode due to coupling to an absorbing plasmon mode propagating at the metal/analyte interface. As plasmon mode is largely delocalized in the analyte region, wavelength of phase

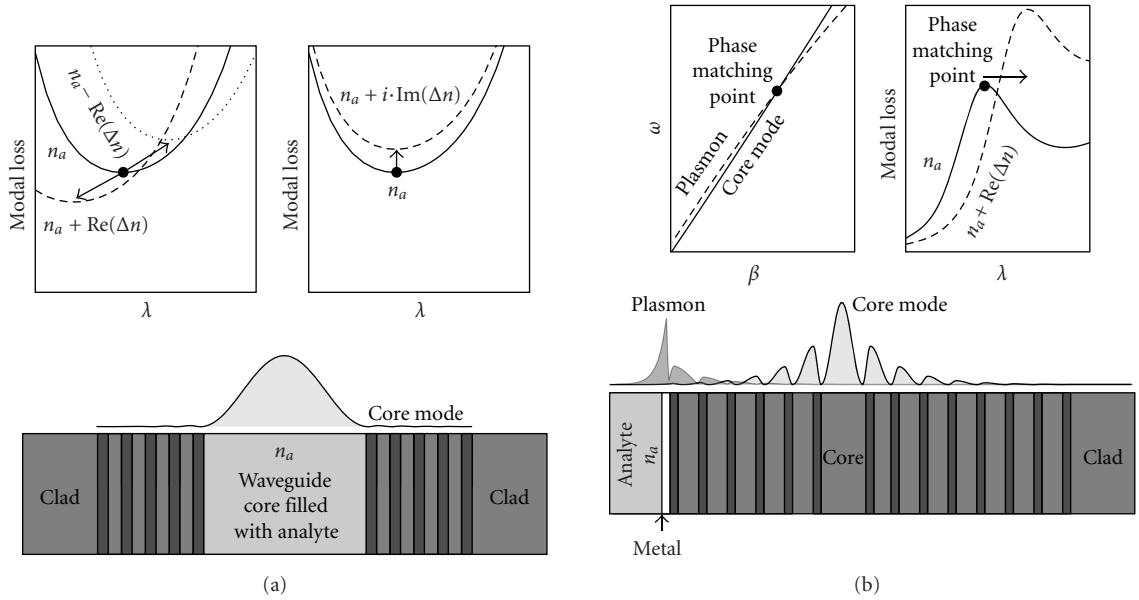

Figure 1: Operational principles and schematics of the two types of the resonant optical sensors. (a) Analyte-filled hollow photonic bandgap fiber-based sensor. Transmission loss through such a sensor is very sensitive to the values of both the real and imaginary parts of the analyte refractive index. (b) Sensor operating near the phase matching point of a core-guided-mode and a second mode featuring large overlap with the analyte region. In the case of a phase matching with a plasmon mode, propagation loss of a core-guided-mode is strongly dependent on the real part of the analyte refractive index.

matching between the two modes will be very sensitive to the value of the real part of analyte refractive index.

2. Detection Strategies for Absorption-Based Sensors

We now remind the reader some general facts about amplitude-based and spectral-based detection methodologies. Particularly, we focus on fiber-based sensors that rely on detection of changes in the transmitted light intensity in the presence of a target analyte.

In the amplitude-based detection methodology one operates at a fixed wavelength λ and records changes in the amplitude of a signal, which are then reinterpreted in terms of changes in the analyte refractive index. To characterize sensitivity of a fiber-based sensor of length L, one employs an amplitude sensitivity function $S_a(\lambda, L)$, which is defined as a relative change in the intensity $P(\delta, \lambda, L)$ of a transmitted light for small changes in the measurand δ. Note that δ can be any parameter that influences transmission properties of a fiber sensor. This includes concentration of absorbing particles in the analyte, thickness of a biolayer that can change due to capture of specific biomolecules, as well as real or imaginary parts of the analyte refractive index. Amplitude sensitivity is then defined as

$$S_a(\lambda, L) = \lim_{\delta \to 0} \frac{P(\delta, \lambda, L) - P(0, \lambda, L)}{\delta \cdot P(0, \lambda, L)} = \frac{\partial P(\delta, \lambda, L)/\partial \delta|_{\delta=0}}{P(0, \lambda, L)}. \quad (1)$$

Denoting, $\alpha(\delta, \lambda)$ to be the fiber propagation loss at a fixed value δ of a measurand, light intensity at the fiber output can be written as:

$$P(\delta, \lambda, L) = P_{\mathrm{in}}(\lambda) \exp(-\alpha(\delta, \lambda) L), \quad (2)$$

where $P_{\mathrm{in}}(\lambda)$ is the light intensity launched into a fiber. Substituting (2) into (1), amplitude sensitivity function can be then expressed as:

$$S_a(\lambda, L) = \frac{\partial \alpha(\delta, \lambda)}{\partial \delta|_{\delta=0} \cdot L} - . \quad (3)$$

As follows from (3), sensor sensitivity is proportional to the sensor length L. In turn, as follows from (2), the maximal sensor length is limited by the absorption loss of a fiber. Defining $P_{\mathrm{det}}(\lambda)$ to be the power detection limit at which changes in the light intensity can still be detected reliably, the maximal sensor length allowed by the power detection limit can be calculated from (2) as

$$L = \frac{\log(P_{\mathrm{in}}(\lambda)/P_{\mathrm{det}}(\lambda))}{\alpha(0, \lambda)}. \quad (4)$$

Defining $\eta_{\mathrm{det}}(\lambda) = \log(P_{\mathrm{in}}(\lambda)/P_{\mathrm{det}}(\lambda))$, maximal sensitivity allowed by the power detection limit can be written using (3) as

$$S_a(\lambda) = -\eta_{\mathrm{det}}(\lambda) \frac{\partial \alpha(\delta, \lambda)/\partial \delta|_{\delta=0}}{\alpha(0, \lambda)}. \quad (5)$$

In all the simulations that follow we assume that $\eta_{\mathrm{det}}(\lambda) = 1$, which allows us to characterize an inherent sensitivity of a sensor system, while separating it from the issue of a power

budget that might bring additional sensitivity enhancement. Finally, given sensor amplitude sensitivity, to estimate sensor resolution of a measurand δ, one can use expression (1). Assuming that the minimal detectable relative change in the signal amplitude is $(\Delta P/P)_{\min}$ (which is typically on the order of 1% if no advanced electronics is used), then the minimum value of a measurand that can be detected by such a sensor is

$$\delta_{\min} = \frac{(\Delta P/P)_{\min}}{S_a(\lambda)}. \tag{6}$$

Another popular sensing methodology is spectral-based. It uses detection of displacements of spectral singularities in the presence of a measurand with respect to their positions for a zero level of a measurand. This sensing approach is particularly effective in the resonant sensor configurations that feature sharp transmission or absorption peaks in their spectra. Defining $\lambda_p(\delta)$ to be the position of a peak in a sensor transmission spectrum as a function of a measurand value δ, spectral sensitivity function can be defined as

$$S_\lambda = \frac{\partial\lambda(\delta)}{\partial\delta|_{\delta=0}}. \tag{7}$$

Given sensor spectral sensitivity, to estimate sensor resolution of a measurand δ, one can use expression (7). Thus, assuming that the minimal detectable spectral shift in the peak position is $(\Delta\lambda_p)_{\min}$ (which is typically on the order of 0.1 nm in the visible spectral range if no advanced optical detection is used), then the minimum value of a measurand that can be detected by such a sensor is

$$\delta_{\min} = \frac{\left(\Delta\lambda_p\right)_{\min}}{S_\lambda}. \tag{8}$$

3. Sensing Using Analyte-Filled Hollow Core Photonic Bandgap Fibers

We now describe the first resonant sensor type based on hollow core photonic bandgap fibers filled with analyte. In their crossection PBG fibers can contain periodic sequence of micron-sized layers of different materials [11, 12] (Figure 2(a)), periodically arranged micron-sized air voids [13–15] (Figure 2(b)), or rings of holes separated by nanosupports [16, 17] (Figure 2(c)). PBG fibers are currently available in silica glass, polymer and specialty soft glass implementations. The key functionality of such fibers is their ability to guide light directly in the hollow or liquid-filled cores with refractive index smaller than the refractive index of a surrounding cladding material. Unlike microstructured fibers, PBG fibers confine light in their hollow cores by photonic bandgap effect, rather than by total internal reflection. Practically, bandgaps are defined as frequency regions of enhanced fiber transmission, and they are the result of destructive interference of the core-guided light inside of the fiber-microstructured cladding. When launching spectrally broad light into a PBG fiber, only the spectral components guided by the fiber bandgaps will reach the fiber end, while all the spectral components not located within the bandgaps will be irradiated out near the fiber coupling end. Moreover, even in the absence of fiber material losses, core-guided-modes always exhibit radiation loss. This is a direct consequence of guidance in a core with refractive index smaller than that of a cladding. As we will soon see, core mode radiation loss can be very sensitive to the value of the real part of the refractive index of the material filling the fiber core, which can be utilized for sensor applications. Finally, PBG fibers have a tendency to improve the beam quality of guided light, while being effectively single mode in the limit of long propagation distances. This is a consequence of the fact that radiation losses (and, generally, absorption losses too) of the core-guided-modes of a PBG fiber are strongly differentiated with only a few low-order modes having small propagation losses. Thus, when exciting several modes at the fiber input end, only the modes having the lowest losses will survive till the fiber end. For historical reference we mention that before the invention of the all-dielectric PBG fibers, guidance in the hollow core fibers has been demonstrated in the context of metal coated capillaries [18, 19].

We now detail some of the advantages offered by the hollow core PBG fibers for sensing applications. One has to distinguish two modes of operation of such sensors. First, is sensing of changes in the imaginary part of the analyte refractive index (analyte absorption) by detecting the presence and strength of the narrow absorption bands in the fiber transmission spectrum. This is the simplest, nonresonant application of the hollow PBG fibers for optical sensing in which one only takes advantage of large overlap of the core-guided leaky mode with analyte. In such sensors, signal strength due to analyte absorption, as well as sensor sensitivity are directly proportional to the sensor length. Recently, several experimental implementations of such absorption-based sensors have been demonstrated [10, 20–23]. Second mode of operation of a PBG fiber-based sensor is sensing of changes in the real part of the analyte refractive index by detection of shifts in the fiber bandgap position. As it will be explained in the following, such a sensor operates in the resonant regime with sensitivity that is largely independent of the sensor length.

3.1. Nonresonant Sensing. Classic perturbation theory considerations [24] predicts that changes in the effective refractive index of a guided mode Δn_{eff} are related to the changes in the refractive index Δn_a of analyte infiltrating the fiber, through the overlap factor f defined as

$$\begin{aligned} \Delta n_{\text{eff}} &= \Delta n_a \cdot f = \text{Re}(\Delta n_a) \cdot f + i \cdot \text{Im}(\Delta n_a) \cdot f \\ f &= \frac{\int_{\text{analyte}} dA|\mathbf{E}|^2}{\text{Re}\left(\hat{\mathbf{z}} \cdot \int_{\text{crossection}} dA\mathbf{E}_t^* \times \mathbf{H}_t\right)}, \end{aligned} \tag{9}$$

where $\mathbf{E}_t, \mathbf{H}_t$ are the transverse electromagnetic fields of a fiber mode, while $\mathbf{E}$ is a complete electric field of a mode. Strictly speaking, expression (9) is only valid for the truly guided square integrable modes of the Total Internal Reflection (TIR) fibers. In the case of hollow-core PBG fibers

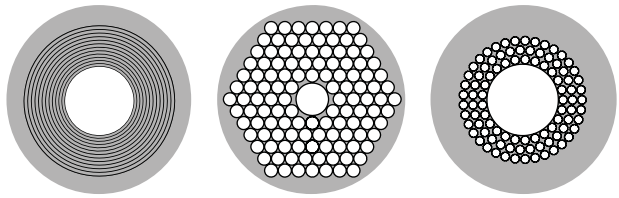

Figure 2: Various types of hollow core photonic bandgap fibers. (a) Bragg fiber featuring large hollow core surrounded by a periodic sequence of high and low refractive index layers. (b) Photonic crystal fiber featuring small hollow core surrounded by a periodic array of large air holes. (c) Microstructured fiber featuring medium size hollow core surrounded by several rings of small air holes separated by nano-size bridges.

the leaky modes are, generally, nonsquare integrable [25]. In this case, however, expression (9) can still be used but only approximatively. Particularly, to avoid divergence in the denominator of (9), one performs integration only over the finite fiber crossection limited by the interface between the multilayer reflector and a cladding. For the hollow core PBG fibers, detailed simulations show that f is typically larger than 0.9. The value of an overlap increases rapidly when the fiber core size increases, reaching values higher than 0.99 for even the moderate core sizes $R_{\text{core}} \sim 5$–$10\,\lambda$. Such a high value of the overlap factor is explained by high confinement of the guided mode in the fiber core (see, e.g., energy flux distribution of the core-guided-mode in the inset of Figure 1(a)).

Expression (9) is fundamental for the analysis of nonresonant absorption-based sensors. Consider, for example, a microstructured or a hollow core fiber filled with aqueous solution. One possible biosensor implementation utilizing such fibers can, for example, monitor presence and concentration of specific biomolecules labeled by highly absorbing nanoparticles. In such a sensor biomolecules in the aqueous solution are purged through the fiber microstructure. Defining C to be the concentration (measurand; $\delta = C$ in (1)) of the absorbing particles mixed with analyte, and assuming that nano-particle bulk absorption per unit of concentration is $\alpha_C(\lambda)$, while fiber loss in the absence of nanoparticles is $\alpha_f(\lambda)$, then total fiber loss in the presence of absorbing nanoparticles can be written using (9) as

$$\alpha(C,\lambda) = \alpha_f(\lambda) + f \cdot C \cdot \alpha_C(\lambda). \tag{10}$$

In derivation of (10) we used the fact that $\text{Im}(\Delta n_a) \sim C \cdot \alpha_C$, $\alpha(C,\lambda) \sim \text{Im}(n_{\text{eff}})$. By substituting (10) into (5), we now find expression for the maximal nonresonant sensor sensitivity to changes in the nano-particle concentration:

$$S_a(\lambda) = -f\frac{\alpha_C(\lambda)}{\alpha_f(\lambda)}. \tag{11}$$

Note that as nano-particle absorption $\alpha_C(\lambda)$ is completely independent from the fiber loss $\alpha_f(\lambda)$ in the absence of nanoparticles, sensitivity (11) of a nonresonant sensor is, thus, directly proportional to the fiber length $L \sim 1/\alpha_f(\lambda)$. Consequently, to increase sensor sensitivity one has to simply work with longer fibers featuring low propagation loss.

3.2. Resonant Sensing. Note that expression (9), when applied to PBG fibers, does not account for the spectral shift of the PBG fiber bandgap (see Figure 1(a)) due to changes in the real part of the refractive index of an analyte filling the fiber core. In fact, for the hollow-core PBG fibers in place of (9) one has to use the following modified expression:

$$\Delta n_{\text{eff}} = \text{Re}(\Delta n_a) \cdot f + i[\text{Im}(\Delta n_a) \cdot f + \text{Re}(\Delta n_a) \cdot f_{\text{rad}}]. \tag{12}$$

Here, f_{rad} is a radiation factor that describes changes in the radiation losses of a photonic bandgap guided mode due to spectral shift of a fiber bandgap caused by changes in the real part of the refractive index of an analyte filling the fiber core.

To understand the radiation loss contribution in (12) one has to recall the principles of design and operation of the hollow-core PBG fibers. Consider, as an example, the case of a hollow core plastic Bragg fiber featuring a water filled core (refractive index n_w) surrounded by a Bragg reflector (Figure 3(a)) made of a periodic sequence of two optically different materials with refractive indices n_l, n_h which are assumed to be purely real [11, 26]. We now design Bragg reflector to feature the fundamental bandgap in the visible at $\lambda_0 = 0.5\,\mu$m. The reflector layer thicknesses d_l, d_h have to be chosen in a very specific way as to guarantee the destructive interference of guided light in the periodic fiber cladding, hence efficient modal confinement in the fiber hollow core. Particularly, by choosing the reflector layer thicknesses to satisfy the quarter wave condition:

$$d_{l,h} = \frac{\lambda_0}{4\sqrt{n_{l,h}^2 - \text{Re}\,(n_{\text{core}})^2}}, \tag{13}$$

one guarantees that the fundamental bandgap of a Bragg reflector is centered in the near vicinity of a design wavelength λ_0 [25].

We now consider particular implementation of a Bragg fiber having the core of radius $R_{\text{core}} = 25\,\mu$m surrounded by 6 reflector layers with $n_h = 1.6$, $n_l = 1.4$ and the layer thicknesses given by (13), where $n_{\text{core}} = 1.34$. In Figure 2(b) in thick solid curve we present propagation loss of the fundamental Gaussian-like HE_{11} core mode of a Bragg fiber. In fact, HE_{11} mode plays a key role in the operation of a majority of the hollow-core based sensors as it is the easiest mode to excite with an external Gaussian-like laser source.

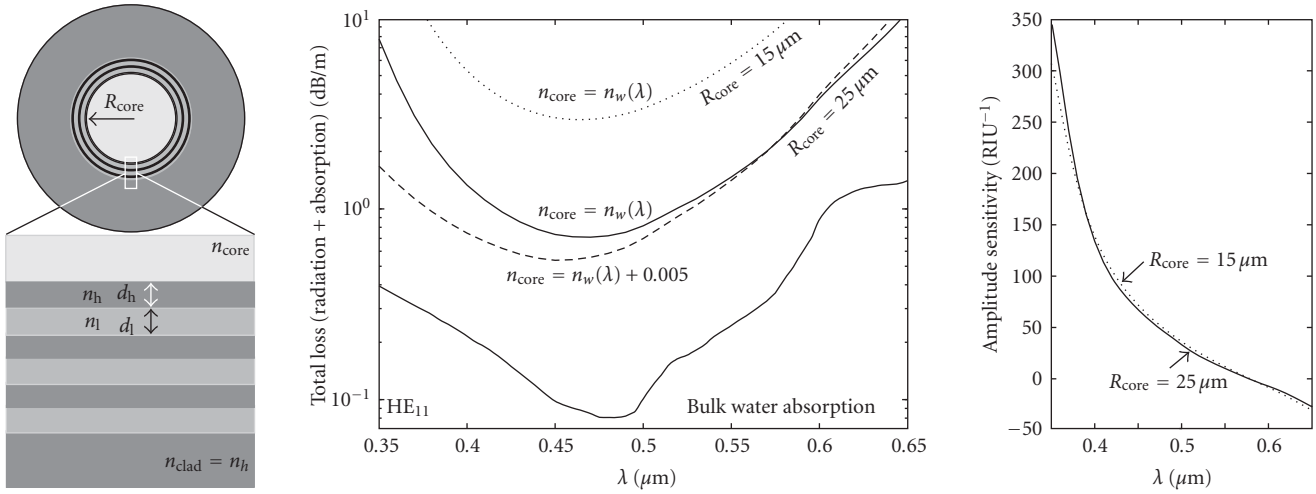

FIGURE 3: Refractive index sensors based on hollow core PBG Bragg fibers. (a) Schematic of a hollow core Bragg fiber filled with aqueous analyte of refractive index $n_w(\lambda)$. (b) Radiation-dominated propagation loss of a core-guided HE_{11} mode for two Bragg fibers with core radii $R_{core} = 25\,\mu m$ (solid curve) and $R_{core} = 15\,\mu m$ (thin dashed curve). When analyte refractive index changes, so does the radiation loss of a fiber core mode (thick dashed curve). For the reference, in thin solid line we present absorption loss of distilled water in the visible. (c) Maximal amplitude sensitivity of the analyte filled Bragg fiber-based sensor for the two values of the fiber core radius. Note that amplitude sensitivity is almost independent of the fiber core radius.

While total propagation loss is a sum of the modal radiation and absorption losses, this particular fiber is operating in the Radiation-dominated regime; for comparison, bulk absorption loss of water is presented in Figure 3(b) in thin solid line. We note that modal propagation loss reaches its minimum at the center of a photonic bandgap at ~0.46 μm, while increasing rapidly towards the edges of a bandgap. When changing the real part of the refractive index of an analyte filling the fiber core, resonant condition (13) is no longer satisfied, thus leading to spectral displacement of the fiber bandgap (a thick dashed line in Figure 3(b)). Therefore, even for small changes in the analyte refractive index, due to spectral shift in the position of a reflector bandgap, fiber propagation loss can vary substantially. Moreover, due to resonant nature of bandgap guiding, bandgap shift due to changes in the real part of the analyte refractive index can have a substantially stronger effect on the propagation losses of a core-guided-mode than changes in the absorption coefficient of an analyte. Particularly, in (13) one can calculate that at the operational wavelength of 0.5 μm, $f \simeq 1$, while $f_{rad} \simeq 2.4 \cdot 10^{-4}$. Therefore, change of 1 dB/m loss in the analyte absorption coefficient ($\mathrm{Im}(\Delta n_a) \simeq 0.9 \cdot 10^{-8}$), or change of $\mathrm{Re}(\Delta n_a) \simeq 3.8 \cdot 10^{-5}$ in the real part of the analyte refractive index, result in the same 1 dB/m change in the modal propagation loss.

We now investigate amplitude and spectral sensitivities of the hollow-core PBG fiber-based sensors. In Figure 3(c) we present amplitude sensitivity (5) of a Bragg fiber-based sensor to changes in the real part of the analyte refractive index $\delta = \mathrm{Re}(\Delta n_a)$. Note that sensitivity varies strongly as a function of the wavelength of operation, increasing rapidly towards the bandgap edges. Inside of a bandgap and in the vicinity of a design wavelength, amplitude sensitivity is on the order of $S_a \sim 100\,\mathrm{RIU}^{-1}$. Assuming that 1% of change in the amplitude of a transmitted light can be detected reliably, this results in sensor resolution of $\mathrm{Re}\,(\Delta n_a)_{min} \sim 10^{-4}$ RIU. Finally, in the vicinity of a bandgap center at 470 nm the total fiber loss is ~0.7 dB/m, thus defining the maximal sensor length to be on the order of ~6 m.

In a similar fashion, spectral sensitivity can be defined using (7) by detecting spectral shift in the bandgap center (wavelength of the fiber lowest loss) resulting in a spectral sensitivity $S_\lambda \sim 5300$ nm/RIU. Assuming that 0.1 nm spectral shift in the position of a bandgap center can be detected reliably, this results in the sensor resolution of $\mathrm{Re}\,(\Delta n_a)_{min} \sim 2 \cdot 10^{-5}$ RIU, which is comparable to the resolution achieved by the amplitude method.

Interestingly, maximal sensitivity of a resonant hollow-core PBG fiber sensor does not depend strongly on the fiber length. To demonstrate that, in Figure 3(b) we also present losses of an HE_{11} mode of a hollow core Bragg fiber, with a core radius $R_{core} = 15\,\mu m$ and otherwise identical parameters to the Bragg fiber with $R_{core} = 25\,\mu m$. Note that losses of a smaller core fiber are almost 10 times as high as losses of a larger core fiber. This signifies that the maximal sensor length for a smaller core fiber is almost 10 times shorter than the length of a sensor based on a larger core fiber. In Figure 3(c) we also plot the maximal sensitivity (5) of a Bragg fiber-based sensor with a core radius $R_{core} = 15\,\mu m$ and note that it is almost identical to that of a larger core fiber. This interesting, while somewhat counterintuitive result is a direct consequence of the fact that in PBG fibers operating in the Radiation-dominated regime, fiber propagation loss and radiation factor are not independent parameters. Particularly, starting from (12), and assuming that the fiber loss for a neutral analyte is $\alpha_f(\lambda)$,

then PBG fiber absorption loss $\alpha(\Delta n_a, \lambda)$ in the presence of changes in the real part of the analyte refractive index is described by:

$$\alpha(\Delta n_a, \lambda) = \alpha_f(\lambda) + \frac{4\pi}{\lambda} \mathrm{Re}(\Delta n_a) \cdot f_{\mathrm{rad}}. \quad (14)$$

In the case of Bragg fibers operating in the Radiation-dominated regime one generally finds that $f_{\mathrm{rad}} \sim \alpha_f(\lambda)$. Therefore, maximal amplitude sensitivity as defined by (5) will not depend on the fiber loss, and as a consequence, it will not depend on the sensor length. This finding promises a significant advantage of PBG fiber based resonant sensors compared to their conventional absorption-based counterparts. Particularly, compact and highly sensitive sensors that utilize short PBG fiber pieces and that do not require fiber coiling are more convenient to use, and easier to maintain than their conventional counterparts that utilize long coiled fibers.

4. Surface Plasmon Resonance-Based Fiber Sensors

In this section we describe another type of a resonant sensor operating in the vicinity of a phase matching point between a Gaussian-like core mode of a fiber (waveguide) and another mode that has strong overlap with analyte region (see the inset of Figure 1(b)). In what follows, the mode that has strong overlap with analyte is assumed to be a plasmonic wave propagating on the metalized fiber surface facing analyte.

Propagating at the metal/dielectric interface, surface plasmons [27] are extremely sensitive to changes in the refractive index of the dielectric. This feature constitutes the core of many Surface Plasmon Resonance (SPR) sensors. Typically, these sensors are implemented in the Kretschmann-Raether prism geometry where p-polarized light is launched through a glass prism and reflected from a thin metal (Au, Ag) film deposited on the prism facet [28]. The presence of a prism allows phase matching of an incident electromagnetic wave with a plasmonic wave at the metal/ambient dielectric interface at a specific combination of the angle of incidence and wavelength. Mathematically, phase matching condition is expressed as an equality between the plasmonvector and a projection of the wavevector of an incident wave along the interface. Since plasmon excitation condition depends resonantly on the value of the refractive index of an ambient medium within 100–300 nm from the interface, the method enables, for example, detection, with unprecedented sensitivity, of biological binding events on the metal surface [29]. The course of a biological reaction can then be followed by monitoring angular [29, 30], spectral [31] or phase [32, 33] characteristics of the reflected light. However, the high cost and large size of commercially available systems makes them useful mostly in a laboratory, while many important field and other applications still remain out of the reach for this method.

Using optical waveguides and fibers instead of bulk prism configuration in plasmonic sensors offers miniaturization, high degree of integration and remote sensing capabilities. In fiber and waveguide-based sensors, one launches the light into a waveguide core and then uses coupling of a guided mode with a plasmonic mode to probe for the changes in the ambient environment. To excite efficiently a surface plasmon, the phase matching condition between a plasmon and a waveguide mode has to be satisfied, which mathematically amounts to the equality between their modal propagation constants (effective refractive indices). Over the past decade, driven by the need for miniaturization of SPR sensors, various compact configurations enabling coupling between optical waveguide modes and surface plasmonic waves have been investigated. Among others, metalized single mode, multimode and polarization maintaining waveguides and fibers, metalized tapered fibers, metalized fiber Bragg gratings [34–49] and, recently, solid core microstructured fibers [50–52], as well as planar photonic crystal waveguides [53] have been studied. In the majority of fiber implementations (with an exception of microstructured fibers), one typically strips fiber polymer jacket and polishes off fiber cladding until fiber core is exposed; then, a metal layer is deposited directly onto a fiber core. Thus functionalized surface of a fiber core is then exposed to an analyte.

Ideally, one would use a single mode fiber or waveguide with all the power traveling in a single Gaussian-like core mode operating near the point of resonant excitation of the plasmon [37, 54–58]. Gaussian shape of a core mode is important as it is best suited for the excitation by standard Gaussian laser sources. Near the point of phase matching, most of the energy launched into a waveguide core mode should be efficiently transferred into a plasmon mode. However, in the Total Internal Refraction (TIR) single mode waveguides with low refractive index-contrast, coupling with a plasmon is realized at essentially grazing angles of modal incidence on the metal layer. As follows from the basic SPR theory, coupling at such grazing incidence angles leads to an inevitable decrease of sensitivity of the SPR method. In principle, high index-contrast single mode waveguides (see Figure 4(a)) could be employed to increase the angle of modal incidence on the interface. However, in the single mode waveguide-based sensors, phase matching between plasmon and fundamental waveguide mode is typically hard to realize. This is related to the fact that the effective refractive index of a core-guided-mode is close to the refractive index of the core material, which is typically larger than 1.45 due to practical material limitations. The effective refractive index of a plasmon is close to the refractive index of an ambient medium which is typically air $n_a = 1$ (gas sensing) or water $n_a = 1.33$ (biological sensing). Thus, large discrepancy in the effective refractive indices makes phase matching between the two modes hard to achieve, with an exception of the high frequencies $\lambda < 600$ nm, where the plasmon dispersion relation starts deviating towards higher refractive indices. Thus, due to practical limitation on the lowest value of the waveguide core and cladding refractive indices, single mode TIR waveguide-based sensors were demonstrated almost exclusively in the visible where phase matching condition is easier to enforce.

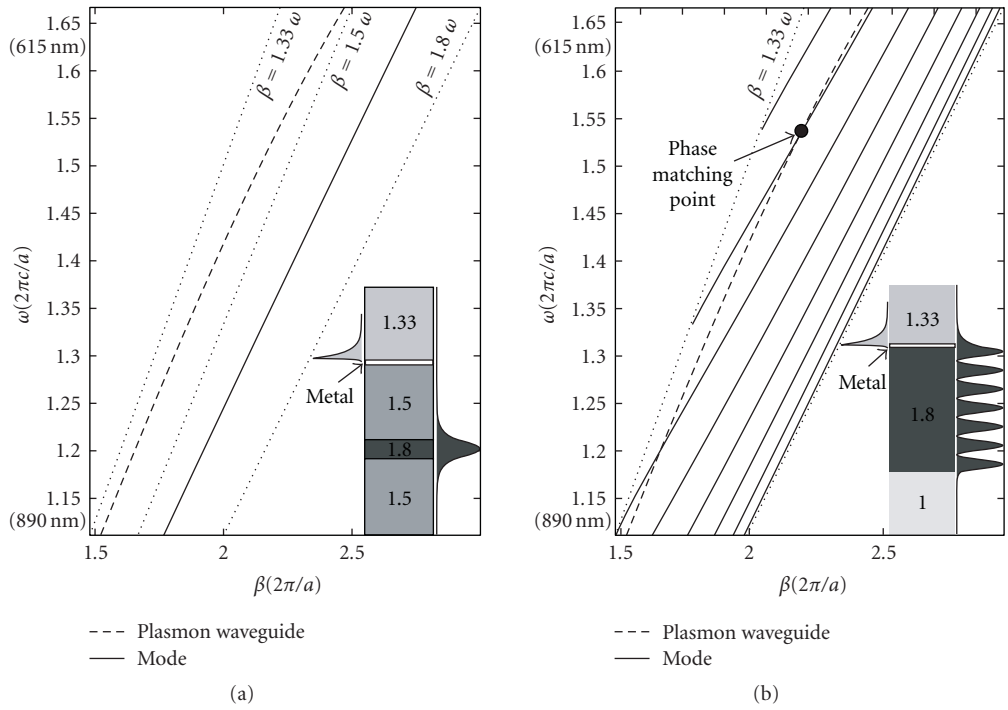

Figure 4: Band diagrams and schematics of various SPR-based integrated sensor implementations. (a) Single mode waveguide-based sensor. Dispersion relations of a core-guided-mode (solid) and a plasmon (thick dashed). Inset-sensor schematic; $|H_{\|}|^2$ of a plasmon (a) and a core mode (b). (b) Multimode waveguide-based sensor. Dispersion relations of the core modes (solid) and a plasmon (thick dashed). Inset-coupler schematic; $|H_{\|}|^2$ of a plasmon (a) and a high-order mode (b) at the phase matching point (black circle).

Problems with phase matching and loss of sensitivity due to shallow angles of incidence could be, in principle, alleviated by using multimode waveguides [45–49] presented in Figure 4(b). If launched properly, modal effective propagation angles in such waveguides can be much steeper, also resulting in smaller effective refractive indices. However, in multimode waveguides, a large number of higher-order modes can be phase matched with a plasmon. Thus, sensitivity and stability of such sensors depend crucially on launch conditions. Moreover, as spatial field distribution in a Gaussian-like laser source is typically not well matched with the field distributions of higher-order modes of a multimode waveguide, only a small fraction of energy can be efficiently launched into such modes, thus resulting again in decreased sensitivity.

5. Plasmon-Assisted Sensing Using Solid Core Microstructured Fibers

To alleviate the problem of phase matching of the fiber core mode and a plasmon one approach is to introduce additional geometrical features into the fiber core that could allow tuning of the fiber core mode effective refractive index [51, 59]. As mentioned before, in the case of aqueous or gaseous analytes the core mode effective refractive index has to be lowered to match that of a plasmon. As a first example of a fiber where tuning by design can be effectively achieved we consider a solid core microstructured optical fiber shown in Figure 5(a). Such a MOF is comprised of a solid core surrounded by a ring of six air holes of diameter d_1 which are placed at the vertices of a hexagon with vertice-to-vertice distance Λ. The ring of holes works as a low refractive index cladding enabling mode guidance in the fiber core. To lower the refractive index of a core-guided-mode a small air hole of diameter d_c is introduced into the fiber core center. In place of a single hole, an array of smaller holes can be used similarly to [60]. Finally, two large semicircular channels of size d_2 surround the microstructured fiber core region. During sensor operation these channels are filled with analyte, and in what follows we assume that the analyte under study is distilled water with $n_a \simeq 1.33$. On a fiber core side the channels are covered with a thin gold film of thickness $d_{\text{gold}} \simeq 40\,\text{nm}$–$60\,\text{nm}$ to enable plasmon excitation at the gold/analyte interface. Coupling strength between the core mode and plasmon is strongly influenced by the size d_1 of the holes surrounding the fiber core, (larger hole sizes result in a weaker coupling). We assume that MOF is made of a silica glass with refractive index given by one of the standard Sellmeier-type fits $n_{\text{glass}} \simeq 1.46$ [61]. Finally, the dielectric constant of gold is approximated by the Drude model:

$$\varepsilon_{\text{gold}}(\lambda_c) = \varepsilon_\infty - \frac{\left(\lambda/\lambda_p\right)^2}{1 + i(\lambda/\lambda_t)}, \tag{15}$$

where the choice $\varepsilon_\infty = 9.75$, $\lambda_t = 13\,\mu\text{m}$, $\lambda_p = 0.138\,\mu\text{m}$ presents one of the many possible fits of the experimental data.

As a concrete example we consider MOF with the following parameters $\Lambda = 2\,\mu$m, $d_c = 0.5\,\Lambda$, $d_1 = 0.6\,\Lambda$, $d_2 = 0.8\,\Lambda$, $d_{\text{gold}} = 40$ nm.

Finite element method with PML boundaries was used to find complex propagation constants of the core-guided and plasmonic modes. A typical fiber-based plasmonic sensor operates in the vicinity of a phase matching point between the core-guided-mode and a plasmon localized at the metalized surface. Figure 5(b) we present dispersion relations of the core-guided-mode (thick solid line) and a plasmon (thick dashed line). Phase matching point is located at 640 nm where the difference between the modal refractive indexes is the smallest. Detailed simulations show that by changing the size of a central hole in the range $d_c = 0.35\,\Lambda$–$0.55\,\Lambda$, or by changing diameters of the six holes in the range $d_1 = 0.6\,\Lambda$–$0.7\,\Lambda$, one can readily tune the effective refractive index of the fundamental mode by 0.01 RIU which is equivalent to 30 nm spectral tuning of the position of a plasmonic peak. Energy flux distributions in the vicinity of a phase matching point (insets (I,II) in Figure 5(b) allow clear differentiation of the nature of the two modes as being the core mode (inset (I)) and plasmonic mode (inset (II)). Due to symmetry, only a quarter of the fiber crossection is presented in the insets. In the vicinity of a phase matching point the two modes become strongly mixed (inset (III) in Figure 5(c)), with losses of a core-guided-mode increasing dramatically due to the energy transfer into the lossy plasmon mode. Core mode losses calculated as $\text{Im}(n_{\text{eff}})$ are presented in Figure 5(b) in a thin solid line. For the reference, losses in [dB/m] are defined as $\alpha[\text{dB/m}] = (40\,\pi\,\text{Im}(n_{\text{eff}}))/(\ln(10)\lambda[\text{m}])$.

As explained earlier, detection of changes in the propagation loss of a core-guided-mode at the point of its phase matching with a plasmon constitutes the core of many SPR sensor implementations. We now detail plasmon-based transduction mechanism in greater details. In Figure 6(a) we present losses of the fundamental core-guided-mode in the wavelength range of $0.5\,\mu$m–$1.3\,\mu$m for the same MOF design as discussed earlier. Solid line corresponds to the case of a pure analyte with $n_a \simeq 1.33$ and it features two plasmonic excitation peaks located at 640 nm and 1120 nm. To demonstrate potential of this fiber for sensing, we present in a dashed line losses of the core-guided-mode for the case when the analyte refractive index is changed to $n_a \simeq 1.335$. As seen from Figure 6(a) position of the first plasmonic peak (at shorter wavelengths) shifts by as much as 10 nm, which is readily detectable. From the amount of shift in the position of a plasmonic peak one can, in principle, extract the value of changes in the analyte refractive index. This transduction mechanism is commonly used for the detection of the analyte bulk refractive index changes, as well as monitoring of formation of the nanometer-thin biolayers on top of a metalized sensor surface.

Interestingly, when analyte refractive index is varied the position of the second plasmonic peak in Figure 6(a) stays mostly unchanged. Therefore, such a peak cannot be used for sensing changes in analyte refractive index. Nevertheless, presence of such a peak is very useful as it serves as a natural reference in the measurements, which simplifies greatly data acquisition and data interpretation. To understand better the nature of the two plasmonic peaks, in the insets of Figure 6(a) we present energy flux distributions in the core-guided core modes evaluated at the first and second plasmonic peaks. From the pictures one notices that at the first peak (inset (I), Figure 6(a)) the plasmon contribution to the hybrid mode is delocalized in the analyte region, while at the second peak (inset (II), Figure 6(a)) the plasmon contribution to the hybrid mode is delocalized mostly in the fiber cladding. This explains why spectral position of the first peak is considerably more sensitive to the changes in the analyte refractive index than that of a second peak.

Finally, in Figure 6(b) we present amplitude sensitivity of the MOF sensor to changes in the real part of the analyte refractive index as defined in (5) ($\delta = \text{Re}(\Delta n_a)$). Sensor sensitivities are calculated for several values of the gold layer thickness. Maximal sensitivity $S_a \sim 180\,\text{RIU}^{-1}$ is achieved for a 40 nm thick gold film. Assuming that 1% of change in the amplitude of a transmitted light can be detected reliably, this results in sensor resolution of $\text{Re}\,(\Delta n_a)_{\text{min}} \sim 6 \cdot 10^{-5}$ RIU. Finally, at the wavelength of maximal sensor sensitivity at 665 nm the total fiber loss is ~150 dB/cm, thus defining the maximal sensor length to be on the order of ~1 mm. In passing we note that plasmon being a surface excitation is very sensitive to the thickness of a metallic layer. This can be used to study metal nanoparticle binding events on the metallic surface of a sensor [62]. This mode of sensor operation can be of interest, for example, to the monitoring of concentration of metal nanoparticles attached to the photosensitive drugs in the photodynamic cancer therapy [63].

6. Plasmon-Assisted Sensing Using Solid Core Photonic Bandgap Fibers

As mentioned in the previous section, introduction of additional geometrical features into the fiber core could allow tuning of the fiber core mode effective refractive index. However, in the case of TIR-microstructured fibers the tuning range, while significant (0.01 RIU as shown in the previous section), is not sufficient to alleviate the problem of phase matching of the fiber core mode and a plasmon. The problem of phase matching becomes especially pronounced in the case of low refractive index analytes. In what follows, we detail design principles of the photonic bandgap fiber and waveguide-based SPR sensors, and show that in such sensors the fundamental Gaussian-like leaky core mode can be phase matched with a plasmon at any desired wavelength of operation from the visible to mid-IR, and for any value of the analyte refractive index. Effectively, PBG waveguide-based sensors integrate advantages of both the multimode and single mode waveguide-based SPR sensors by being able to reduce the core mode refractive index to any desired value (even 0), while operating with a Gaussian-like core mode.

To remind the reader, the term "leaky mode" generally refers to the guidance mechanism where the effective refractive index of a propagating mode is smaller than that of the waveguide cladding. Such unusual modes are called

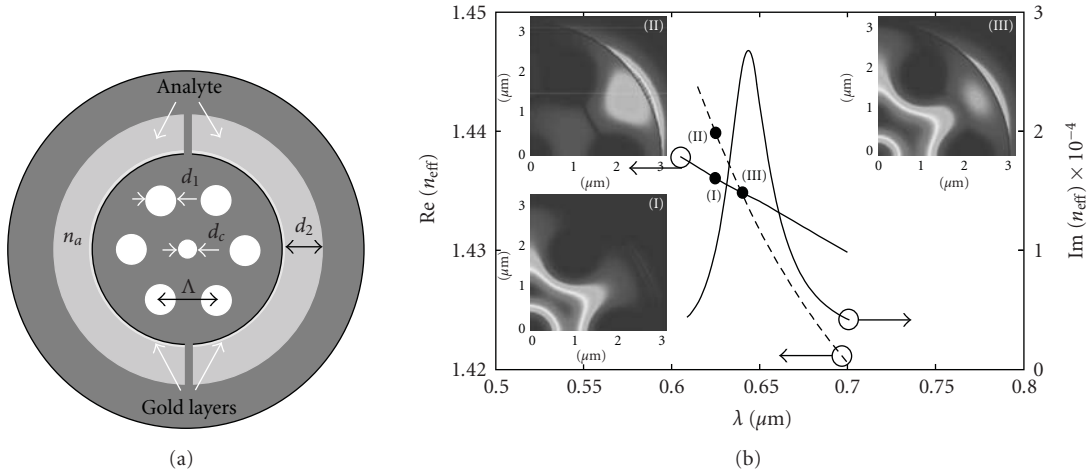

Figure 5: (a)Schematics of a MOF-based SPR sensor. The fiber comprises six air holes surrounding a solid fiber core. These holes form a microstructured cladding with low effective refractive index. A smaller hole is introduced in the core center to enable tunability of the core mode effective refractive index to facilitate phase matching with a plasmon. Two large semicircular metalized channels are integrated into the fiber structure to enable efficient microfluidic flow of analyte and plasmon excitation at the metal/analyte interface. (b) Dispersion relations of a core-guided-mode (thick solid line) and a surface plasmon (thick dashed line) in the vicinity of the phase matching point. Insets (I), (II) show energy fluxes of the core-guided and plasmon modes close to the phase matching point. Transmission loss of a core-guided-mode (thin solid line) exhibits strong increase at the phase matching point due to efficient mixing with a plasmon as confirmed by its energy flux distribution (inset (III)).

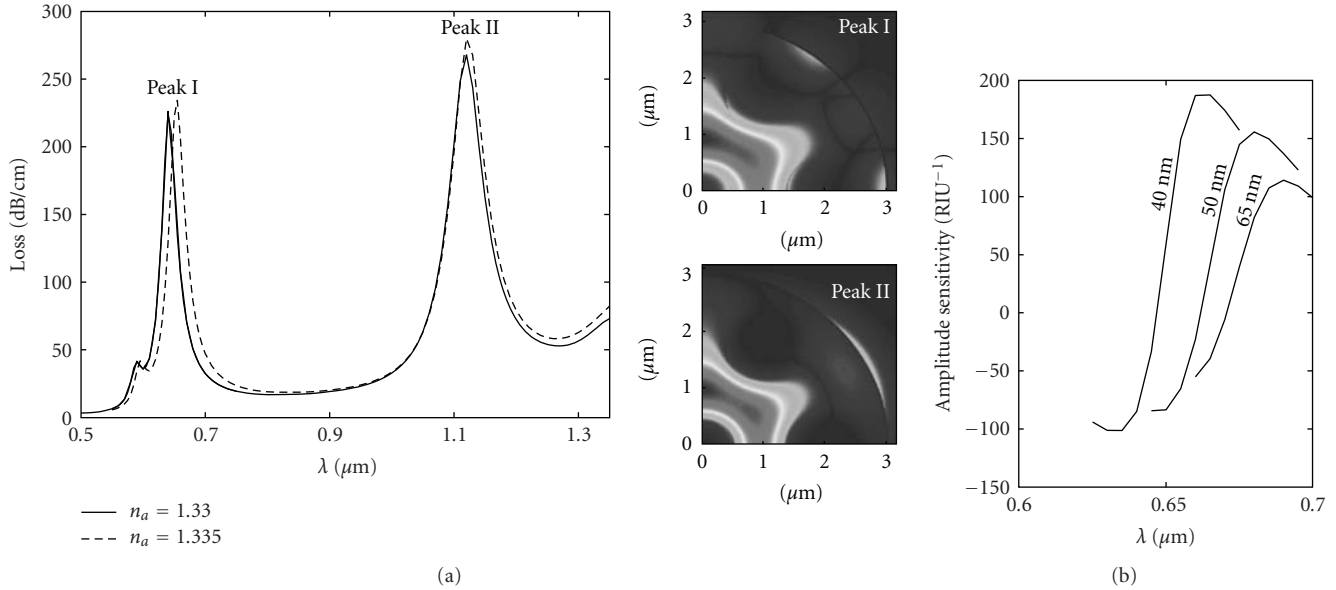

Figure 6: Calculated loss spectra of the fundamental core-guided-mode of a metalized MOF. Loss spectrum (solid curve) features several attenuation peaks corresponding to the excitation of plasmonic modes on the surface of metalized channels filled with aqueous analyte of refractive index 1.33. By changing the analyte refractive index (dotted curve), resonant attenuation peaks corresponding to the points of phase matching between the core-guided and plasmon modes shift. In the insets, energy flux of a core-guided-mode is presented at the two absorption peaks. Spectral position of the peak I is the most sensitive of the two peaks to changes in the analyte refractive index. This is because the corresponding core mode is coupled to a plasmon with a strong presence in the analyte region in contrast to the peak II at which plasmonic mode is predominantly extended into the cladding region.

leaky modes as, outside of a waveguide core, they do not exhibit a traditional evanescent decay into the cladding, but rather they radiate slowly (leak) into the cladding. Unlike in the case of common TIR waveguides, leaky modes in photonic crystal waveguides are confined by the bandgap of a photonic crystal reflector. As a consequence, the effective refractive index of the fundamental (lowest loss) leaky core mode can be designed to be arbitrarily smaller than that of a waveguide core material, thus enabling phase matching with a plasmon at any desired frequency. Moreover, the lowest loss

leaky core mode typically exhibits a Gaussian-like intensity distribution in the waveguide core region, thus enabling convenient excitation by a Gaussian beam of an external light source. Using the fundamental (lowest loss) leaky mode for sensing gives the additional advantage of an effectively single mode propagation regime. In particular, when a set of modes is excited at a sensor input, higher-order leaky modes radiate out faster than a fundamental mode. Consequently, after a certain propagation distance, only the fundamental mode is left in the waveguide core. Finally, the effective angle of modal incidence onto a metal film, and hence sensitivity, can be varied at will by a proper selection of the waveguide core and reflector materials.

6.1. SPR Sensors Using Planar Photonic Bandgap Waveguides. To demonstrate the principles of operation of photonic bandgap waveguide-based SPR sensors we start by considering plasmon excitation by a Gaussian-like TM-polarized mode of a planar photonic crystal waveguide (see Figure 7(a)), in which light confinement in a lower refractive index core is achieved by a surrounding multilayer reflector. TM polarization of the electromagnetic field in a planar multilayer assumes a single magnetic field component $|H_{\|}|^2$ directed parallel to the plane of a multilayer, while the electric field component is confined to a plane perpendicular to the multilayer.

The photonic crystal waveguide under consideration consists of 27 alternating layers having refractive indices $n_h = 2.0$, and $n_l = 1.5$. The core layer is layer number 12; having refractive index $n_c = n_l$. Analyte (first cladding) is water $n_a = 1.332$ bordering a 50 nm layer of gold. The substrate refractive index is 1.5. Theory of planar photonic crystal waveguides with infinite reflectors where $n_c = n_l$ [64], predicts that, for a design wavelength λ_c, the effective refractive index $n_{\text{eff}}(\lambda_c)$ of the fundamental TE and TM core-guided-modes can be designed at will, as long as $0 < n_{\text{eff}} < n_l$, by choosing the reflector layer thicknesses as

$$d_{l,h} = \frac{\lambda_c}{4\sqrt{n_{l,h}^2 - n_{\text{eff}}^2}}, \tag{16}$$

and by choosing the core layer thickness as $d_c = 2d_l$. Moreover, for this choice of n_c, the field distribution in the core is always Gaussian-like for TE-polarized modes, while for TM-polarized modes it is Gaussian-like as long as $n_{\text{eff}}^2 > \varepsilon_l\varepsilon_h/(\varepsilon_l + \varepsilon_h)$ [64]. By choosing the effective refractive index of a core mode to be that of a plasmon, a desired phase matching condition is achieved. For a waveguide with a finite reflector, the same design principle holds approximately. Thus, for an operating wavelength of $\lambda = 640$ nm, considered in this example, phase matching is achieved when the photonic crystal waveguide is designed using $\lambda_c = 635$ nm and $\text{Re}(n_{\text{eff}}(\lambda_c)) = 1.46$ in (16). A reasonable approximation to the $n_{\text{eff}}(\lambda_c)$ is a value of the effective refractive index of a plasmonic wave propagating at a planar gold-analyte interface:

$$n_{\text{eff}}(\lambda_c) = \left(\frac{\varepsilon_{\text{gold}}(\lambda_c)\cdot\varepsilon_a(\lambda_c)}{\varepsilon_{\text{gold}}(\lambda_c) + \varepsilon_a(\lambda_c)}\right)^{1/2}, \tag{17}$$

where ε_a is the dielectric constant of an analyte and $\varepsilon_{\text{gold}}$ is the dielectric constant of the gold layer approximated by the Drude model (15).

In Figure 7(b) we present band diagram of a planar photonic crystal waveguide-based SPR sensor. All the simulations are performed using standard transfer matrix theory on a complete system that includes both the waveguide and metal layer. Gray regions signify bulk states of a periodic reflector. The clear region is a TM bandgap where no extended into the reflector states are found. The thick solid line, which is almost parallel to the band gap edges, marked as "core mode" is a dispersion relation of a Gaussian-like leaky core mode with most of its modal energy concentrated in the low refractive index core. The dashed line marked as "plasmon" represents the dispersion relation of a plasmonic mode. Most of the plasmon energy is concentrated at the metal/analyte interface.

Near the phase matching point, fields of a core-guided-mode contain strong plasmonic contribution. As plasmon exhibits very high propagation loss, the loss of a core mode (upper plot in Figure 7(c)) will also exhibit a sharp increase near the phase matching point with a plasmon. An important aspect of the proposed setup is the freedom of adjusting the loss of a core mode. As leaky mode decays exponentially fast with respect to distance into the multilayer reflector, coupling strength between the plasmon and core modes can be controlled by changing the number of reflector layers situated between the waveguide core and a metal film. Ultimately, higher coupling strength leads to higher modal losses, hence, shorter sensor length. When the real part of the analyte refractive index is varied, the plasmon dispersion relation displaces accordingly, thus leading to a shift in the position of the phase matching point with a core-guided-mode. Consequently, in the vicinity of the phase matching point, transmission loss of a core-guided-mode varies strongly with changes in the analyte refractive index (see the upper part of Figure 7(c)).

We would like to point out that what is identified as a "core mode" in all the figures in this paper is in fact a waveguide supermode that includes both the core-guided-mode and plasmonic contribution. Since the plasmon mode is extremely lossy, only a small mixing of this mode with the core mode is necessary to achieve sensing. We found pertinent to also show on the graphs what a plasmonic mode looks like near the phase matching point, although this mode by itself is not used in our sensing arrangements. Depending on the designs, the plasmon contribution to the evanescent tail of a core mode is not always visible on the field distribution plots as only the real components of the modes are truly phase matched.

The simplest mode of operation of a waveguide-based SPR sensor is detection of small changes in the bulk refractive index of an analyte. Similarly to the case of hollow core PBG fiber-based sensors, there are two main modalities of SPR detection-amplitude-based and spectral-based. In both methodologies sensing is enabled through detection of changes in the location of a sharp plasmonic loss peak which spectral position is strongly dependent on the value of the ambient refractive index. In the amplitude-based

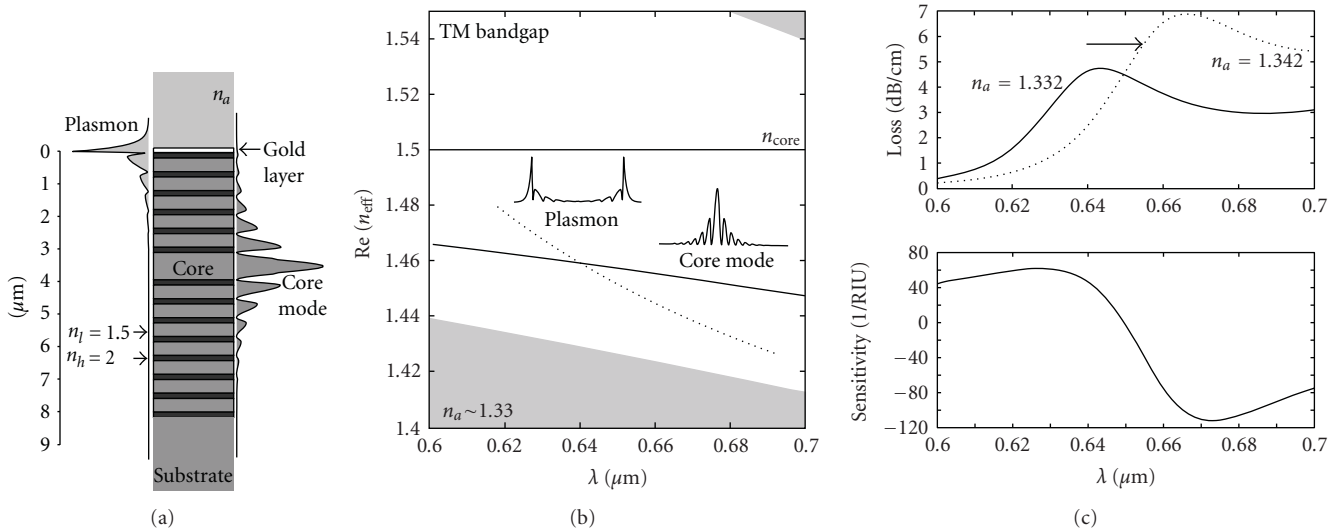

FIGURE 7: Planar photonic bandgap waveguide-based SPR sensor. (a) Schematic of a sensor. Low refractive index core is surrounded by the periodic photonic crystal reflector. Top side of the reflector is goldplated for plasmon excitation. Gold layer is bordered by aqueous analyte. $|H_{\|}|^2$ field distribution in the fundamental core mode is shown on the right, while field distribution in a plasmonic mode is show on the left of a sensor schematic. (b) Band diagram of sensor modes. Dispersion relation and field distribution of the fundamental core mode (thick solid curve), and plasmonic mode (dashed curve). TM bandgap of a periodic reflector is shown as a clear region, while gray regions correspond to the continuum of the bulk reflector states. By design, the effective refractive index of a core-guided-mode can be made significantly smaller than that of the waveguide core material. (c) Upper part: solid curve shows loss of a waveguide core mode near the phase matching point with a plasmon at which modal loss peaks. Dashed line shows shift of the modal loss curve when refractive index of the analyte is varied. Lower part: dependence of the sensor amplitude sensitivity on wavelength.

approach, all the amplitude measurements are performed at a single wavelength near the center of a plasmonic peak. The advantage of this method is its simplicity and low cost, as no spectral manipulation is required. The disadvantage is a smaller dynamic range and lower sensitivity when compared to the wavelength interrogation approach, in which the whole transmission spectra are taken and compared before and after the change in the analyte has occurred. We now use expression (5) to define sensor amplitude sensitivity with respect to changes in the real part of an analyte refractive index. In (5) the measurand δ is $\text{Re}(\Delta n_a)$, and $\alpha(\delta, \lambda)$ is propagation loss of a core-guided-mode presented at the top of Figure 7(c). At the bottom of Figure 7(c) we present amplitude sensitivity of a PBG waveguide-based SPR sensor as a function of the wavelength of operation. Maximal sensitivity is achieved at 673 nm and is equal to 112 RIU^{-1}. It is typically a safe assumption that 1% change in the transmitted intensity can be detected reliably, which leads to a sensor resolution of $9 \cdot 10^{-5}$ RIU. In the wavelength interrogation mode, changes in the analyte refractive index are detected by measuring displacement of a plasmonic peak center wavelength λ_p as a function of the value of an analyte refractive index. Sensor sensitivity is then defined by expression (7), where $\delta = \text{Re}(\Delta n_a)$. We find that the spectral sensitivity of a PBG waveguide-based sensor is 2300 nm $\cdot$ RIU^{-1}. Assuming that a 0.1 nm change in the position of a resonance peak can be detected reliably, sensor resolution of $4.3 \cdot 10^{-5}$ RIU is obtained.

Finally, sensor length is always in the range $L \sim 1/\alpha(\delta, \lambda)$. In the vicinity of plasmonic peak shown in Figure 7(c) typical sensor length is $L \sim 1$ cm. Detailed simulations also show that similarly to the case of resonant sensing using hollow core PBG fibers, sensitivity of a PBG waveguide-based plasmonic sensor is only weakly dependent on the sensor length. Particularly, by varying the number of reflector layers separating the waveguide core and gold layer one can vary the overall sensor length from sub-mm to several cm without changing significantly the sensor sensitivity.

In the rest of this section we present theoretical study of SPR sensor designs based on photonic bandgap fibers, rather than planar waveguides. Advantages of fiber based sensors over their planar counterparts include lower manufacturing cost, possibility of distributed sensing, and incorporation of microfluidics into the fiber structure directly at the fiber drawing step. In what follows we demonstrate an SPR sensor using solid core PBG Bragg fiber operating at 760 nm, as well as an SPR sensor using honeycomb lattice photonic bandgap fiber operating at 1060 nm.

6.2. SPR Sensors Using Photonic Bandgap Bragg Fibers. We start by describing solid core Bragg fiber-based SPR sensor for detection in aqueous analytes. In such a sensor a thin gold layer is deposited on the outer surface of a Bragg fiber in direct contact with an analyte. By tailoring the dispersion relation of the core-guided-mode of a Bragg fiber, phase matching with a plasmon can be obtained at any wavelength in the visible and near-IR. The mode of operation in such a sensor is a Gausian-like HE_{11} core mode. Effective refractive index of such a mode is matched with that of a plasmon by the proper choice of the fiber core size. The choice of an HE_{11}

mode over the other modes is motivated by the ease of its excitation using common Gaussian laser sources.

As an example we consider solid core photonic crystal Bragg fibers made of two materials with refractive indices $n_l = 1.42$ and $n_l = 1.6$. Prototypes of such fibers have been recently fabricated in our group by using a poly(vinylene difloride) (PVDF)/polycarbonate (PC) material combination [65]. In such fibers, a solid core of refractive index n_l is surrounded by N alternating high and low refractive index reflector layers of thicknesses d_l, and d_h (see Figure 8(a)). In a manner similar to the planar multilayer waveguides, reflector layer thicknesses are given by the quarter wave condition (16), where λ_c is an operating wavelength, and $n_{\text{eff}}(\lambda_c)$ is a desired effective refractive index of a core-guided-mode at that wavelength. Although such a choice of the reflector parameters guarantees bandgap guidance at λ_c of a mode with effective refractive index $n_{\text{eff}}(\lambda_c)$, however, it does not guarantee existence of such a mode. One way of positioning a core mode dispersion relation inside of the reflector bandgap is by varying the fiber core diameter d_c. Namely, in the large core diameter Bragg fibers with $d_c \gg \lambda_c$, effective refractive index of the fundamental core mode is close to that of the core material. By decreasing the fiber core size, one can consistently reduce the core mode effective refractive index, and, eventually, position it in the middle of the reflector bandgap. Moreover, in the context of SPR sensing, λ_c also corresponds to the wavelength of phase matching between plasmon and a core-guide mode. Therefore, a good approximation to $n_{\text{eff}}(\lambda_c)$ of a core-guided-mode is that of the effective refractive index of a plasmonic wave propagating at a planar gold-analyte interface given by (17). With these choices of $n_{\text{eff}}(\lambda_c)$ and d_c we are still left with one free parameter, which is the number of layers N in the Bragg reflector. In metalized Bragg fibers, guided modes incur additional losses due to high absorption in the metal film. When operating within bandgap of a Bragg fiber reflector, the fields of leaky core modes decay exponentially fast into the reflector. Therefore, modal presence in the metal layer also decreases exponentially fast when increasing the number of reflector layers. Thus, the choice of the number of reflector layers primarily effects the core mode propagation loss, and, consequently, sensor length. As was mentioned earlier, PBG fiber-based sensor sensitivity is only weekly dependent on sensor length. Therefore, without the loss of sensitivity, one would choose a small enough number of reflector layers, so that the resultant fiber is short enough to prevent the necessity of coiling and simplify sensor handling.

In Figure 8 we present an example of a solid core PBG fiber-based SPR sensor. By choosing the fiber core size to be small, one can considerably reduce the effective refractive index of the core mode. This enables plasmonic excitation at longer wavelengths in the near-IR. In Figure 8(a) we show cross-section of a small-core Bragg fiber-based sensor, as well as energy flux distributions in the HE_{11} core mode and plasmonic mode. Reflector layer thicknesses are chosen according to (16), where $\lambda_c = 760\,\text{nm}$, $n_l = 1.42$, $n_h = 1.6$, and $n_{\text{eff}} = 1.39$, thus resulting in $n_l = 654\,\text{nm}$, $n_l = 240\,\text{nm}$. Fiber core diameter is $d_c = 1.8\,\mu\text{m}$. The total number of layers is $N = 12$. For the fundamental Gaussian-like mode, the amount of energy in the core is 78%. In Figure 8(b) we present the band diagram of the modes of thus defined Bragg fiber sensor. Common TM, TE bandgap of a corresponding infinitely periodic Bragg reflector is presented as a clear region, while gray regions define a continuum of reflector bulk states. In a small core Bragg fiber, the effective refractive index of the core-guided HE_{11} mode (thick solid line) can be considerably smaller than the refractive index of a core material (thin solid line). Dispersion relation of a plasmon mode is shown as thick dashed line. In this particular case, the dispersion relation of the core-guided-mode is shifted towards the lower edge of the reflector bandgap, therefore, the core mode (solid curve in Figure 8(a)) and plasmonic mode (dashed curve in Figure 8(a)) penetrate significantly into the reflector. Phase matching between the core and plasmonic modes is achieved at 758 nm. In the upper plot of Figure 8(c), propagation loss of the core-guided-mode is presented as a function of the wavelength. As seen from this plot, core mode loss peaks at the wavelength of phase matching with plasmon mode. In the lower plot of Figure 8(c), we present amplitude sensitivity (5) of a solid core Bragg fiber-based SPR sensor with respect to changes in the real part of the analyte refractive index. Maximal sensitivity is achieved at 788 nm and is equal to $293\,\text{RIU}^{-1}$. Assuming that a 1% change in the transmitted intensity can be detected reliably, this leads to a sensor resolution of $3.4 \cdot 10^{-5}$ RIU. Finally, we find that the corresponding spectral sensitivity (7) is $10^4\,\text{nm} \cdot \text{RIU}^{-1}$. Assuming that a 0.1 nm change in the position of a resonance peak can be detected reliably, this leads to a sensor resolution of $9.8 \cdot 10^{-6}$ RIU. The sensor length in this case is in a 1 cm range.

6.3. SPR Sensors Using Photonic Bandgap Honeycomb Fibers. In the two previous subsections we have presented design strategies for the SPR sensors based on a PBG Bragg waveguide and a PBG Bragg fiber. In principle, any photonic bandgap fiber can be used in place of a Bragg fiber to develop such sensors. In this section we present an example of a SPR sensor based on a solid core honeycomb PBG fiber.

In Figure 9(a) schematic of a honeycomb photonic crystal fiber-based SPR sensor is presented. The design parameters are chosen as follows, the center-to-center distance between adjacent holes is $\Lambda = 0.77\,\mu\text{m}$, the cladding hole diameter is $d = 0.55\,\Lambda$, the diameter of the hole in the core center is $d_c = 0.35\,\Lambda$. The fiber is made of silica glass with a refractive index of $n_{\text{glass}} = 1.45$, the core and cladding holes are filled with air $n_{\text{air}} = 1$, while the large semicircular channels are plated with a 40 nm thick layer of gold and filled with an aqueous analyte $n_a = 1.32$. The central hole in the fiber core lowers its effective refractive index compared to that of a silica cladding. Under certain conditions, such a core can support a mode confined by the bandgap of the honeycomb reflector. The core-guided-mode in such a fiber is analogous to that of the small solid core Bragg fiber discussed earlier. Guided by the bandgap of the fiber reflector, the effective refractive index of the core mode can be made much lower than that of the silica material.

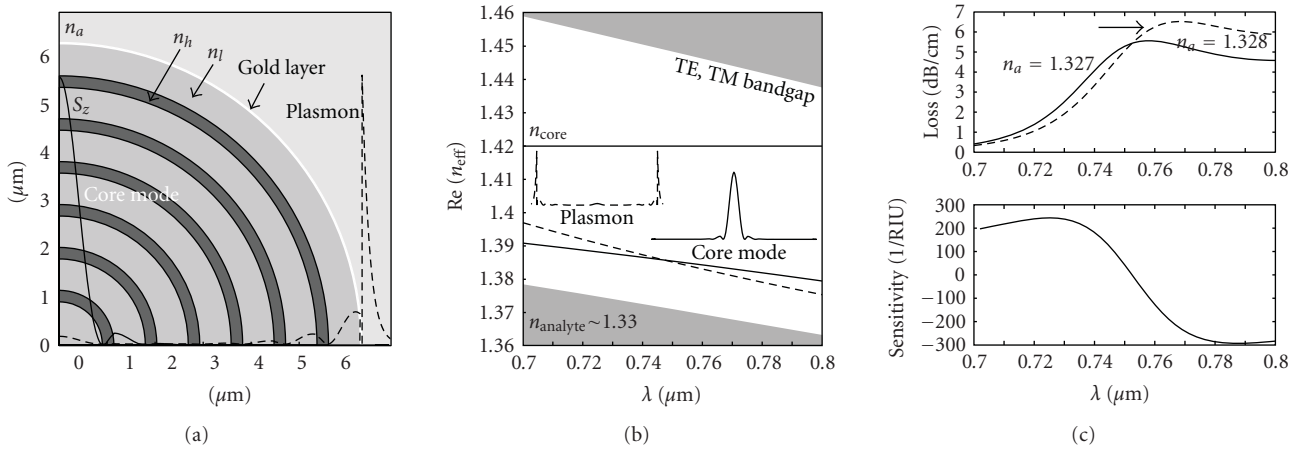

Figure 8: Small solid core PBG Bragg fiber-based SPR sensor. (a) Schematic of a sensor. Low refractive index core is surrounded by the concentric photonic crystal reflector. Reflector exterior is goldplated for plasmon excitation. Gold layer is bordered by aqueous analyte. Energy flux distribution across the fiber cross-section is shown as a solid curve for the fundamental core mode, and as a dashed curve for the plasmonic mode. (b) Band diagram of the sensor modes. Dispersion relation of the fundamental core mode (thick solid curve), and plasmonic mode (dashed curve). TE, TM bandgap of a periodic planar reflector is shown as a clear region, while gray regions correspond to the continuum of bulk reflector states. In a small core Bragg fiber, effective refractive index of the fundamental core mode can be much smaller than refractive index of the core material. (c) Upper plot: solid curve shows loss of the fundamental core mode near the phase matching point with plasmon. Modal loss reaches its maximum at the phase matching wavelength. Dashed line corresponds to the shifted modal loss curve when the analyte refractive index is varied. Lower plot: sensor amplitude sensitivity as a function of wavelength.

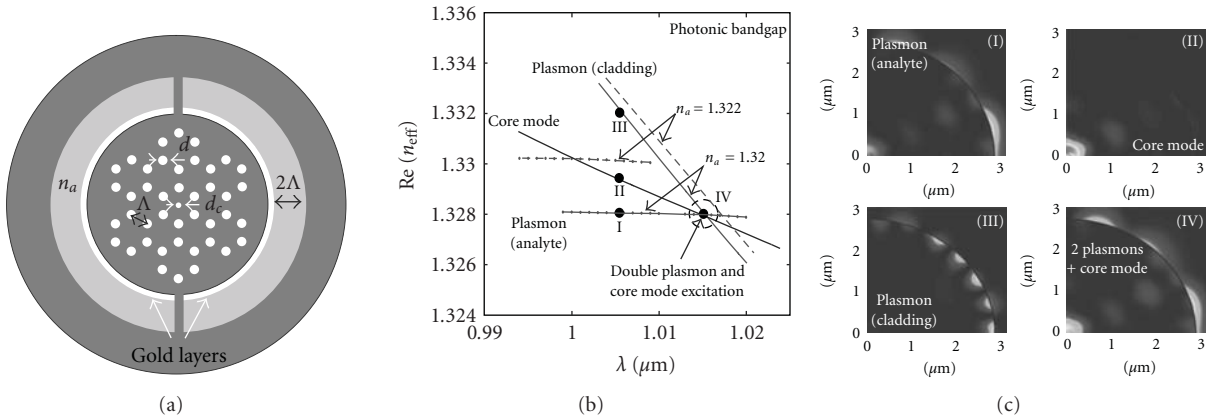

Figure 9: Solid core honeycomb photonic crystal fiber-based SPR sensor. (a) Schematic of a sensor. Solid fiber core having a small central hole is surrounded with a honeycomb photonic crystal reflector. Two large channels are integrated to implement analyte access to the fiber reflector region. The channels are goldplated for plasmon excitation. The gold layer is bordered by an aqueous analyte. (b) Band diagram of sensor modes. Dispersion relation of the fundamental core mode (thick solid curve), analyte bound plasmonic mode (dashed curve with circles), and cladding bound plasmonic mode (dashed curve). The bandgap of an infinitely periodic reflector is shown as a clear region. (c) The energy flux distributions across the fiber cross-section are shown for the fundamental core mode (II) as well as the analyte and cladding bound plasmon modes (I,III) outside of the phase matching region. The energy flux distribution is also shown for the fundamental core mode at the phase matching point (IV) showing strong mixing of the fundamental core mode with plasmonic modes.

Moreover, as in the case of photonic crystal Bragg fibers, radiation loss of a bandgap guided core mode can be reduced by adding more layers into the honeycomb reflector. The main reason why we chose a honeycomb structure of the fiber reflector is because it enables a very large photonic bandgap [66, 67], thus simplifying considerably phase matching of the core-guided and plasmonic modes.

Unlike planar metal/dielectric interface that supports a single plasmonic excitation, finite size, microstructured metal layer separating two dielectrics can support multiple plasmonic modes [51, 52]. Thus, when tracking losses of a core-guided fiber mode as a function of wavelength, one typically observes several plasmonic peaks corresponding to phase matching between the core mode and various plasmonic modes. Particularly, one of the plasmonic modes will have most of its energy concentrated in one of the neighboring dielectrics, while the other plasmonic excitation will have most of its energy concentrated in the other

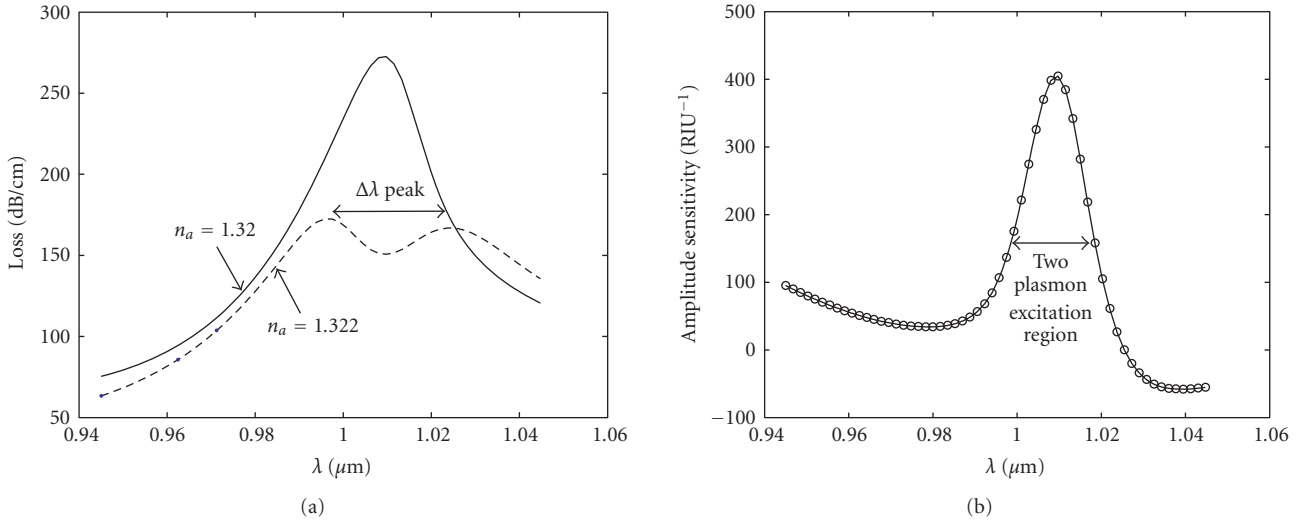

Figure 10: Sensitivity of the honeycomb photonic crystal fiber-based SPR sensor. (a) The solid curve shows loss of the fundamental core mode near the degenerate phase matching point with two plasmonic modes and $n_a = 1.32$. Due to degeneracy, only one peak is distinguishable in the loss curve. Dashed line shows splitting of the degeneracy in plasmonic modes when the analyte refractive index is changed to $n_a = 1.322$. (b) Dependence of the sensor amplitude sensitivity on wavelength.

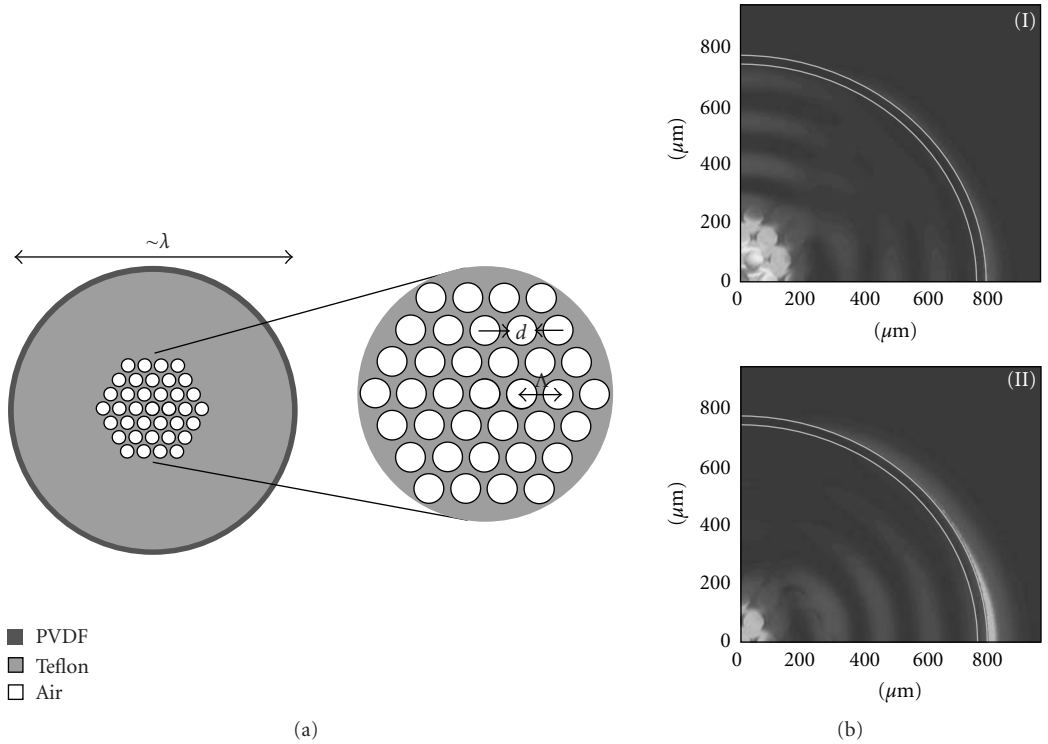

Figure 11: (a) Schematic of a porous THz fiber with a PVDF layer facing gaseous analyte. (b) Longitudinal energy flux distribution across the fiber crossection for the core-guided-mode far from the phase matching point with a Pseudoplasmon (I), and in the vicinity of a phase matching point with a Pseudoplasmon (II).

neighboring dielectric. In principle, simultaneous detection of changes in several plasmonic peaks can improve sensor sensitivity; additionally it gives a natural reference point in the measurements.

In the case of a honeycomb photonic crystal fiber-based sensor we design the fiber so that two plasmonic peaks are degenerate at 1009 nm with $n_a = 1.32$. Figure 9(b) shows the dispersion relations of the Gaussian-like core mode (thick solid line), analyte bound plasmonic mode (thin solid line with circles) and cladding bound plasmonic mode (thick solid line). These dispersion relationes are positioned well inside the bandgap of an infinite honeycomb reflector,

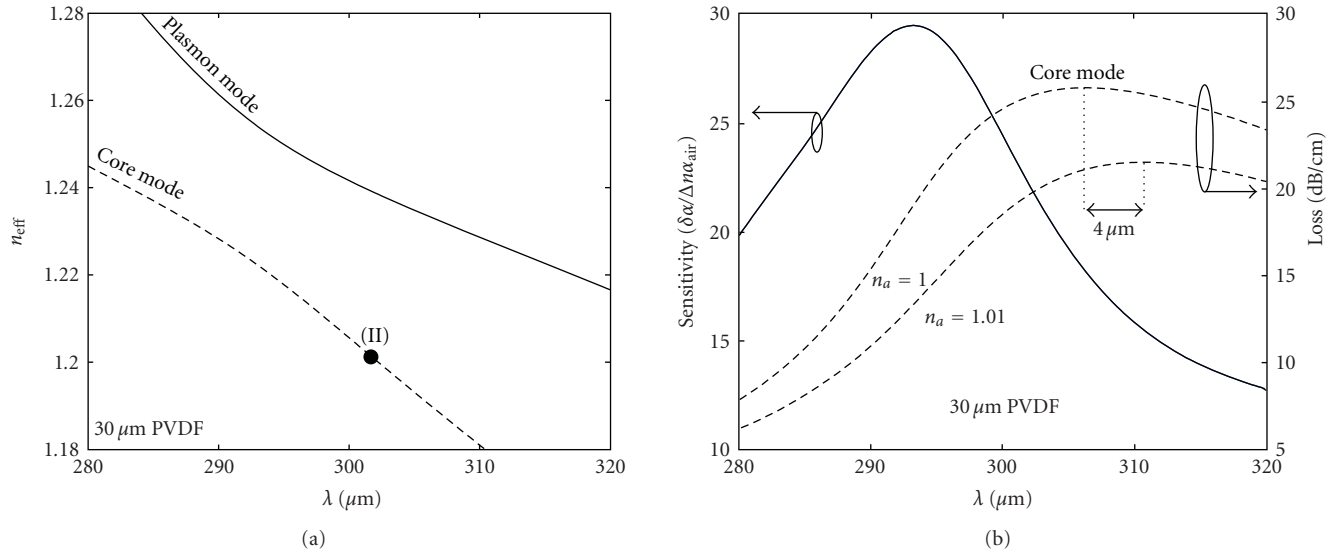

Figure 12: (a) Avoided crossing of the dispersion relations of the fundamental core mode (dashed curve) and a THz plasmon-like excitation (thin solid curve) in a porous fiber with a PVDF layer. (b) Losses of a core-guided-mode for two values of the gaseous analyte refractive index (dashed curves). A corresponding amplitude sensitivity curve for a sensor of the refractive index of a gaseous analyte is presented as a thick solid curve.

which can be confirmed by the plane wave method [67]. Corresponding flux distributions of the core-guided and plasmonic modes are presented in Figure 9(c). The core mode loss shows a single plasmonic peak (solid curve in Figure 10(a). When the refractive index of the analyte is varied, this affects the two plasmonic dispersion relations differently. Particularly, the analyte bound plasmon mode is affected much strongly by the changes in the analyte refractive index than the cladding bound plasmonic mode. As a result, degeneracy is lifted, and two closely spaced plasmonic peaks appear in the core mode loss curve (dashed curve in Figure 10(a)). For example, a 0.002 change in the analyte refractive index splits a single plasmonic peak into two peaks separated by 27.5 nm. This permits a novel spectral detection technique, where relative peak separation can be used to characterize changes in the real part of the analyte refractive index. By defining spectral sensitivity as

$$S_\lambda = \lim_{\Delta n_a \to 0} \frac{\lambda_{\text{peak2}}(n_a + \Delta n_a) - \lambda_{\text{peak1}}(n_a + \Delta n_a)}{\Delta n_a}, \qquad (18)$$

we find spectral sensitivity of $1.4 \cdot 10^4$ nm $\cdot$ RIU^{-1}. It is typically a safe assumption that a 0.1 nm change in the position of a resonance peak can be detected reliably, which results in a sensor resolution of $7.2 \cdot 10^{-6}$ RIU, which is, to our knowledge, the highest reported spectral sensitivity of an aqueous fiber-based SPR sensor.

Finally, in Figure 10(b), we present the amplitude sensitivity of the proposed honeycomb photonic crystal fiber-based sensor as defined by (5). The maximal sensitivity is achieved at 1009 nm and equals to 400 RIU^{-1}. It is typically a safe assumption that a 1% change in the transmitted intensity can be detected reliably, which leads to a sensor resolution of $2.5 \cdot 10^{-5}$ RIU. It is interesting to note that for this sensor design, the sensitivity curve has a single maximum, unlike the sensitivity curves associated with the Bragg fiber designs reported in the preceding section. Sensor length in this case is in 1 mm range.

7. Pseudoplasmon-Assisted Sensing Using Highly Porous Microstructured Fibers and Ferroelectric Layers in Terahertz Spectral Range

In this final section we present an alternative approach to phase matching (at any desirable wavelength) a core-guided fiber mode with a plasmon. This approach is especially useful in the case of very low refractive index analytes, such as gases. As gaseous analytes have refractive index close to 1, and as plasmon effective refractive index is generally close to that of an analyte, it becomes especially challenging to ensure that the effective refractive index of a core-guided-mode is low enough to match that of a plasmon. One way to lower the core mode effective refractive index is to work with subwavelength fibers or highly porous fibers that guide light while having a substantial fraction of their modal field located in the gaseous cladding. Unfortunately, subwavelength fibers in the visible and even in the mid-IR spectral range are difficult to fabricate and work with as their dimensions are smaller than a fraction of a μm. However, in the terahertz (THz) spectral range (also known as far-IR) that covers 30 μm–3000 μm wavelengths, the subwavelength fiber size is in tens or even hundreds of μm, thus making such fibers easy to manufacture and handle [68].

An example of a subwavelength THz fiber that supports a mode with very low effective refractive index is presented in Figure 11(a). The fiber shown is a Teflon rod of 1480 μm

Table 1

Sensor type	operation λ	Amplitude sensitivity S_a[RIU^{-1}]	Sensor resolution (1% det. limit) Re(Δn_a)[RIU]	Spectral sensitivity S_λ[nm/RIU]	Sensor resolution (0.1 nm det. limit) Re(Δn_a)[RIU]
Analyte-filled hollow core Bragg fiber (no metal). Section 3.2.	anywhere in the visible	100	10^{-4}	5300	$2 \cdot 10^{-5}$
Metalized MOF. Section 5.	640 nm (Vis)	180	$6 \cdot 10^{-5}$		
Metalized planar PBG waveguide. Section 6.1	673 nm (Vis)	112	$9 \cdot 10^{-5}$	2300	$4.3 \cdot 10^{-5}$
Metalized solid core Bragg fiber. Section 6.2	788 nm (Vis-IR)	293	$3.4 \cdot 10^{-5}$	10000	$9.8 \cdot 10^{-6}$
Metalized PBG photonic crystal fiber. Section 6.3.	1009 nm (IR)	400	$2.5 \cdot 10^{-5}$	14000	$7.2 \cdot 10^{-6}$
PVDF-activated highly porous subwave-length fiber. Section 7.	292 μm (THz)	29	$3.4 \cdot 10^{-4}$		

diameter having porous core in the form of 4 layers of hexagonally arranged subwavelength holes filled with air. The hole-to-hole distance (the pitch) is considered to be $\Lambda = 86\,\mu$m, while the hole diameter is $d = 76\,\mu$m. The refractive indices of Teflon and air are 1.59 and 1.0 respectively. From outside, the teflon fiber is covered with a 30 μm thick layer of a ferroelectric plastic (Polyvinylidene fluoride (PVDF)) facing air. PVDF is a ferroelectric semicrystalline polymer with a small absolute value of permittivity in the visible and near-IR regions. However, in the THz region the dielectric function of ferroelectric PVDF exhibits a resonance

$$\varepsilon_{\mathrm{PVDF}}(\omega) = \varepsilon_{\mathrm{opt}} + \frac{\left(\varepsilon_{\mathrm{dc}} - \varepsilon_{\mathrm{opt}}\right)\omega_{\mathrm{TO}}^2}{\omega_{\mathrm{TO}}^2 - \omega^2 + i\gamma\omega}, \tag{19}$$

where, according to [69], $\varepsilon_{\mathrm{opt}} = 2.0$, $\varepsilon_{\mathrm{dc}} = 50.0$, $\omega_{\mathrm{TO}} = 0.3$ THz, $\gamma = 0.1$ THz. In the wavelength range between 100 μm (3 THz) and 700 μm (~0.43 THz) the real part of the refractive index of PVDF is less than one, while the imaginary part is positive and mostly larger than one. Therefore, the real part of the PVDF dielectric constant is negative and by analogy with the behavior of metals in the visible range, PVDF layer is expected to support a plasmon-like excitation, which we call a Pseudoplasmon.

As detailed in [68], introduction of subwavelength holes in the fiber core allows to lower dramatically the effective refractive index of the core-guided-mode. This, in turn, makes phase matching possible between the core-guided-mode and a THz Pseudoplasmon propagating at the PVDF/air interface [70]. Furthermore, outside of the phase matching point, most energy in the Gaussian-like core mode is guided in the subwavelength holes (as seen in the inset (I) of Figure 11(b)), thus resulting in greatly reduced modal absorption loss. In Figure 12 we present dispersion relation and losses of a core-guided and Pseudoplasmon modes. Particularly, Figure 12(a) presents the effective refractive index of the core-guided and Pseudoplasmon modes as a function of wavelength. Avoided mode crossing between the two modes around the wavelength of 300 μm is clearly visible. In the inset (II) of Figure 11(b) we show field distribution in a hybrid mode in the vicinity of a phase matching point (point (II) in Figure 12(a)). From the plot, contributions from both the core-guided-mode and a Pseudoplasmon are clearly visible. In Figure 12(b), losses of a core-guided-mode near the point of avoided crossing are shown for two values of the analyte refractive index $n_a = 1.0$ and $n_a = 1.01$. Losses of a core-guided-mode peak (~25 dB/cm) at the point of phase matching with a Pseudoplasmon, while being much lower (<10 dB/cm) outside of the phase matching region. In these simulations Teflon material is considered lossless compared to PVDF, which is justified as

the bulk absorption loss of Teflon is reported to be as low as ~1.3 dB/cm.

Finally, in Figure 12(b) we present amplitude sensitivity of the porous-core fiber-based sensor to changes in the real part of the analyte refractive index (see definition (5)). The maximal sensitivity is achieved at 292 μm and equals to 29 RIU^{-1}. Assuming that 1% change in the transmitted intensity can be reliably detected, sensor resolution of $3.4 \cdot 10^{-4}$ RIU is predicted. Sensor length in this case is in 1 cm range.

8. Discussions

First, we would like to comment on the limitations of theoretical estimates of the sensor detection limits. Throughout the paper we assumed, for example, that the spectral detection method allows detection of 0.1 nm changes in the position of resonant absorption peaks. If a resonant peak preserves its shape when the refractive index of analyte changes, then sensor resolution is only determined by the resolution of a spectrometer. This is indeed the case in our theoretical simulations. However, if noise is present, such as thermal noise, nonhomogeneity in the analyte refractive index etc., then the peak shape at maxima could change unpredictably between measurements, thus limiting the sensor resolution. The same argument applies to amplitude sensing where measurements are performed at the wavelength of strongest change in the waveguide loss. In our theoretical estimates we used spectral resolution of 0.1 nm and an amplitude resolution of 1% reflecting the available experimental body of work in resonant sensors. We note that these optical detection limits were achieved in real sensor systems of moderate complexity and cost.

Another important question regarding proposed sensors is about complexity of their practical implementation. As most of the presented designs use nanothick metallic layers deposited on the inner or outer surfaces of the fiber microstructure the question is about experimental technique that can allow such metallization. After the first paper on resonant MOF-based plasmonic sensors [53] there have been several reports of fabrication of the metal-coated and metal-filled photonic crystal fibers. Particularly, in [71] the authors reported deposition of thin metallic layers of silver on the inner walls of micron-sized holes of a MOF using chemical deposition via precipitation from a reduction reaction. In [72] the same reduction reaction was used to create silver nanoparticles on the microstructure walls. In [73] the authors used high pressure chemical deposition process to deposit nanoparticles and nanothick layers of silver onto the inner walls of the microstructured fibers. In [74] the authors have codrawn a copper rod sealed in a silica tube, then inserted a thus drawn copper/silica wire into a silica fiber preform and redraw it again to get a MOF with selectively metalized holes. Finally, the first demonstration of a photonic bandgap fiber-based plasmonic sensor was presented in [75] where the authors deposited gold layer onto the outer surface of a tapered Bragg fiber. A rapid progress in the fabrication of metalized MOFs and POFs makes us to believe that various sensors presented in this work indeed have a strong practical potential.

9. Conclusions

In conclusion, we have reviewed microstructured optical fiber and photonic bandgap (PBG) fiber-based resonant optical sensors of changes in the real part of the analyte refractive index. Particularly, we have considered two sensors types. One sensor type employed hollow core photonic bandgap fibers where core-guided-mode is strongly confined in the analyte-filled core. Another sensor type employed metalized photonic bandgap waveguides and fibers, where core-guided-mode was phase matched with a plasmon propagating at the metalized fiber/analyte interface. All the sensor types described in the paper showed strong resonant dependence of the fiber absorption on the value of the analyte refractive index, leading to the 10^{-6}–10^{-4} RIU resolution in the real part of the aqueous and gaseous analyte refractive index (assuming amplitude or spectral interrogation techniques). In both sensor types the length is designable and can range from submillimeters to several meters. Surprisingly, we have discovered that the maximal sensor sensitivity is largely independent of the sensor length. Finally, operational regions of the resonant sensors reviewed in this work spanned a wide range of wavelengths from the visible to terahertz.

To summarize the results of this paper, we also present a table of performance parameters of all the resonant sensor designs considered in this paper. In all but the last designs we assume an aqueous analyte of $n_a \approx 1.32$, while in the case of THz sensor we assume a gaseous analyte $n_a \approx 1$.

References

[1] A. MacLean, C. Moran, W. Johnstone, B. Culshaw, D. Marsh, and P. Parker, "Detection of hydrocarbon fuel spills using a distributed fibre optic sensor," *Sensors and Actuators A*, vol. 109, no. 1-2, pp. 60–67, 2003.

[2] N. Kim, I.-S. Park, and W.-Y. Kim, "Salmonella detection with a direct-binding optical grating coupler immunosensor," *Sensors and Actuators B*, vol. 121, no. 2, pp. 606–615, 2007.

[3] S. Balasubramanian, I. B. Sorokulova, V. J. Vodyanoy, and A. L. Simonian, "Lytic phage as a specific and selective probe for detection of *Staphylococcus aureus*—a surface plasmon resonance spectroscopic study," *Biosensors and Bioelectronics*, vol. 22, no. 6, pp. 948–955, 2007.

[4] H. J. Watts, C. R. Lowe, and D. V. Pollard-Knight, "Optical biosensor for monitoring microbial cells," *Analytical Chemistry*, vol. 66, no. 15, pp. 2465–2470, 1994.

[5] D. R. DeMarco and D. V. Lim, "Direct detection of *Escherichia coli* 0157:H7 in unpasteurized apple juice with an evanescent wave biosensor," *Journal of Rapid Methods and Automation in Microbiology*, vol. 9, no. 4, pp. 241–257, 2001.

[6] J. R. E. Shepard, Y. Danin-Poleg, Y. Kashi, and D. R. Walt, "Array-based binary analysis for bacterial typing," *Analytical Chemistry*, vol. 77, no. 1, pp. 319–326, 2005.

[7] M. Zourob, S. Mohr, B. J. T. Brown, P. R. Fielden, M. B. McDonnell, and N. J. Goddard, "An integrated metal clad

leaky waveguide sensor for detection of bacteria," *Analytical Chemistry*, vol. 77, no. 1, pp. 232–242, 2005.

[8] J. B. Jensen, P. E. Hoiby, G. Emiliyanov, O. Bang, L. H. Pedersen, and A. Bjarklev, "Selective detection of antibodies in microstructured polymer optical fibers," *Optics Express*, vol. 13, no. 15, pp. 5883–5889, 2005.

[9] J. M. Fini, "Microstructure fibres for optical sensing in gases and liquids," *Measurement Science and Technology*, vol. 15, no. 6, pp. 1120–1128, 2004.

[10] S. O. Konorov, A. M. Zheltikov, and M. Scalora, "Photonic-crystal fiber as a multifunctional optical sensor and sample collector," *Optics Express*, vol. 13, no. 9, pp. 3454–3459, 2005.

[11] E. Pone, C. Dubois, N. Guo, et al., "Drawing of the hollow all-polymer Bragg fibers," *Optics Express*, vol. 14, no. 13, p. 5838, 2006.

[12] B. Temelkuran, S. D. Hart, G. Benoit, J. D. Joannopoulos, and Y. Fink, "Wavelength-scalable hollow optical fibres with large photonic bandgaps for CO_2 laser transmission," *Nature*, vol. 420, no. 6916, pp. 650–653, 2002.

[13] J. C. Knight, T. A. Birks, P. St. J. Russell, and J. G. Rarity, "Bragg scattering from an obliquely illuminated photonic crystal fiber," *Applied Optics*, vol. 37, no. 3, pp. 449–452, 1998.

[14] P. St. J. Russell, "Photonic-crystal fibers," *Journal of Lightwave Technology*, vol. 24, no. 12, pp. 4729–4749, 2006.

[15] C. M. Smith, N. Venkataraman, M. T. Gallagher, et al., "Low-loss hollow-core silica/air photonic bandgap fibre," *Nature*, vol. 424, no. 6949, pp. 657–659, 2003.

[16] G. Vienne, Y. Xu, C. Jakobsen, et al., "Ultra-large bandwidth hollow-core guiding in all-silica Bragg fibers with nano-supports," *Optics Express*, vol. 12, no. 15, pp. 3500–3508, 2004.

[17] A. Argyros, M. A. van Eijkelenborg, M. C. J. Large, and I. M. Bassett, "Hollow-core microstructured polymer optical fiber," *Optics Letters*, vol. 31, no. 2, pp. 172–174, 2006.

[18] J. A. Harrington, "Review of IR transmitting, hollow waveguides," *Fiber and Integrated Optics*, vol. 19, no. 3, pp. 211–227, 2000.

[19] Y. W. Shi, K. Ito, Y. Matsuura, and M. Miyagi, "Multiwavelength laser light transmission of hollow optical fiber from the visible to the mid-infrared," *Optics Letters*, vol. 30, no. 21, pp. 2867–2869, 2005.

[20] Y. L. Hoo, W. Jin, H. L. Ho, J. Ju, and D. N. Wang, "Gas diffusion measurement using hollow-core photonic bandgap fiber," *Sensors and Actuators B*, vol. 105, no. 2, pp. 183–186, 2005.

[21] C. Charlton, B. Temelkuran, G. Dellemann, and B. Mizaikoff, "Midinfrared sensors meet nanotechnology: trace gas sensing with quantum cascade lasers inside photonic band-gap hollow waveguides," *Applied Physics Letters*, vol. 86, no. 19, Article ID 194102, 3 pages, 2005.

[22] F. M. Cox, A. Argyros, and M. C. J. Large, "Liquid-filled hollow core microstructured polymer optical fiber," *Optics Express*, vol. 14, no. 9, pp. 4135–4140, 2006.

[23] S. Smolka, M. Barth, and O. Benson, "Highly efficient fluorescence sensing with hollow core photonic crystal fibers," *Optics Express*, vol. 15, no. 20, pp. 12783–12791, 2007.

[24] A. W. Snyder and J. Love, *Optical Waveguide Theory*, Springer, London, UK, 2nd edition, 2008.

[25] S. G. Johnson, M. Ibanescu, M. Skorobogatiy, et al., "Low-loss asymptotically single-mode propagation in large-core omniguide fibers," *Optics Express*, vol. 9, no. 13, pp. 748–779, 2001.

[26] M. Skorobogatiy, "Efficient antiguiding of TE and TM polarizations in low-index core waveguides without the need for an omnidirectional reflector," *Optics Letters*, vol. 30, no. 22, pp. 2991–2993, 2005.

[27] V. M. Agranovich and D. L. Mills, *Surface Polaritons: Electromagnetic Waves at Surfaces and Interfaces*, North-Holland, Amsterdam, The Netherlands, 1982.

[28] E. Kretschmann and H. Raether, "Radiative decay of non radiative surface plasmons excited by light," *Naturforschung A*, vol. 23, p. 2135, 1968.

[29] B. Liedberg, C. Nylander, and I. Lundström, "Surface plasmon resonance for gas detection and biosensing," *Sensors and Actuators*, vol. 4, pp. 299–304, 1983.

[30] J. Melendez, R. Carr, D. U. Bartholomew, et al., "A commercial solution for surface plasmon sensing," *Sensors and Actuators B*, vol. 35, no. 1–3, pp. 212–216, 1996.

[31] L.-M. Zhang and D. Uttamchandani, "Optical chemical sensing employing surface plasmon resonance," *Electronics Letters*, vol. 24, no. 23, pp. 1469–1470, 1988.

[32] A. V. Kabashin and P. I. Nikitin, "Surface plasmon resonance interferometer for bio- and chemical-sensors," *Optics Communications*, vol. 150, no. 1–6, pp. 5–8, 1998.

[33] A. N. Grigorenko, P. I. Nikitin, and A. V. Kabashin, "Phase jumps and interferometric surface plasmon resonance imaging," *Applied Physics Letters*, vol. 75, no. 25, pp. 3917–3919, 1999.

[34] M. Manuel, B. Vidal, R. López, et al., "Determination of probable alcohol yield in musts by means of an SPR optical sensor," *Sensors and Actuators B*, vol. 11, no. 1–3, pp. 455–459, 1993.

[35] R. Alonso, J. Subias, J. Pelayo, F. Villuendas, and J. Tornos, "Single-mode, optical-fiber sensors and tunable wavelength filters based on the resonant excitation of metal-clad modes," *Applied Optics*, vol. 33, no. 22, pp. 5197–5201, 1994.

[36] J. Homola, "Optical fiber sensor based on surface plasmon excitation," *Sensors and Actuators B*, vol. 29, no. 1–3, pp. 401–405, 1995.

[37] A. J. C. Tubb, F. P. Payne, R. B. Millington, and C. R. Lowe, "Single-mode optical fibre surface plasma wave chemical sensor," *Sensors and Actuators B*, vol. 41, no. 1–3, pp. 71–79, 1997.

[38] J. Homola, J. Čtyrocký, M. Skalský, J. Hradilová, and P. Kolárová, "A surface plasmon resonance based integrated optical sensor," *Sensors and Actuators B*, vol. 39, no. 1–3, pp. 286–290, 1997.

[39] A. Díez, M. V. Andrés, and J. L. Cruz, "In-line fiber-optic sensors based on the excitation of surface plasma modes in metal-coated tapered fibers," *Sensors and Actuators B*, vol. 73, no. 2-3, pp. 95–99, 2001.

[40] M. Piliarik, J. Homola, Z. Maníková, and J. Čtyroký, "Surface plasmon resonance sensor based on a single-mode polarization-maintaining optical fiber," *Sensors and Actuators B*, vol. 90, no. 1–3, pp. 236–242, 2003.

[41] D. Monzón-Hernández, J. Villatoro, D. Talavera, and D. Luna-Moreno, "Optical-fiber surface-plasmon resonance sensor with multiple resonance peaks," *Applied Optics*, vol. 43, no. 6, pp. 1216–1220, 2004.

[42] D. Monzón-Hernández and J. Villatoro, "High-resolution refractive index sensing by means of a multiple-peak surface plasmon resonance optical fiber sensor," *Sensors and Actuators B*, vol. 115, no. 1, pp. 227–231, 2006.

[43] H. Suzuki, M. Sugimoto, Y. Matsui, and J. Kondoh, "Fundamental characteristics of a dual-colour fibre optic SPR sensor," *Measurement Science and Technology*, vol. 17, no. 6, pp. 1547–1552, 2006.

[44] S. J. Al-Bader and M. Imtaar, "Optical fiber hybrid-surface plasmon polaritons," *Journal of the Optical Society of America B*, vol. 10, p. 83, 1993.

[45] R. C. Jorgenson and S. S. Yee, "A fiber-optic chemical sensor based on surface plasmon resonance," *Sensors and Actuators B*, vol. 12, no. 3, pp. 213–220, 1993.

[46] A. Trouillet, C. Ronot-Trioli, C. Veillas, and H. Gagnaire, "Chemical sensing by surface plasmon resonance in a multimode optical fibre," *Pure and Applied Optics*, vol. 5, no. 2, pp. 227–237, 1996.

[47] J. Čtyrocký, J. Homola, P. V. Lambeck, et al., "Theory and modelling of optical waveguide sensors utilising surface plasmon resonance," *Sensors and Actuators B*, vol. 54, no. 1, pp. 66–73, 1999.

[48] M. Weisser, B. Menges, and S. Mittler-Neher, "Refractive index and thickness determination of monolayers by multi mode waveguide coupled surface plasmons," *Sensors and Actuators B*, vol. 56, no. 3, pp. 189–197, 1999.

[49] B. D. Gupta and A. K. Sharma, "Sensitivity evaluation of a multi-layered surface plasmon resonance-based fiber optic sensor: a theoretical study," *Sensors and Actuators B*, vol. 107, no. 1, pp. 40–46, 2005.

[50] B. T. Kuhlmey, K. Pathmanandavel, and R. C. McPhedran, "Multipole analysis of photonic crystal fibers with coated inclusions," *Optics Express*, vol. 14, no. 22, pp. 10851–10864, 2006.

[51] A. Hassani and M. Skorobogatiy, "Design of the microstructured optical fiber-based surface plasmon resonance sensors with enhanced microfluidics," *Optics Express*, vol. 14, no. 24, pp. 11616–11621, 2006.

[52] B. Gauvreau, A. Hassani, M. F. Fehri, A. Kabashin, and M. Skorobogatiy, "Photonic bandgap fiber-based surface plasmon resonance sensors," *Optics Express*, vol. 15, no. 18, pp. 11413–11426, 2007.

[53] M. Skorobogatiy and A. V. Kabashin, "Photon crystal waveguide-based surface plasmon resonance biosensor," *Applied Physics Letters*, vol. 89, no. 14, Article ID 211641, 2006.

[54] C. R. Lavers and J. S. Wilkinson, "A waveguide-coupled surface-plasmon sensor for an aqueous environment," *Sensors and Actuators B*, vol. 22, no. 1, pp. 75–81, 1994.

[55] R. D. Harris and J. S. Wilkinson, "Waveguide surface plasmon resonance sensors," *Sensors and Actuators B*, vol. 29, no. 1–3, pp. 261–267, 1995.

[56] M. N. Weiss, R. Srivastava, and H. Groger, "Experimental investigation of a surface plasmon-based integrated-optic humidity sensor," *Electronics Letters*, vol. 32, no. 9, pp. 842–843, 1996.

[57] J. Dostáleka, J. Tyrokýa, J. Homola, et al., "Surface plasmon resonance biosensor based on integrated optical waveguide," *Sensors and Actuators B*, vol. 76, no. 1–3, pp. 8–12, 2001.

[58] A. K. Sheridan, R. D. Harris, P. N. Bartlett, and J. S. Wilkinson, "Phase interrogation of an integrated optical SPR sensor," *Sensors and Actuators B*, vol. 97, no. 1, pp. 114–121, 2004.

[59] A. Hassani and M. Skorobogatiy, "Design criteria for microstructured-optical-fiber-based surface-plasmon-resonance sensors," *Journal of the Optical Society of America B*, vol. 24, no. 6, pp. 1423–1429, 2007.

[60] C. M. B. Cordeiro, M. A. R. Franco, G. Chesini, et al., "Microstructured-core optical fibre for evanescent sensing applications," *Optics Express*, vol. 14, no. 26, pp. 13056–13066, 2006.

[61] I. H. Malitson, "Interspecimen comparison of the refractive index of fused silica," *Journal of the Optical Society of America*, vol. 55, pp. 1205–1209, 1965.

[62] S. Patskovsky, A. V. Kabashin, and M. Meunier, "Near-infrared surface plasmon resonance sensing on a Si platform with nanoparticle-based signal enhancement," *Optical Materials*, vol. 27, no. 5, pp. 1093–1096, 2005.

[63] L. O. Cinteza, T. Y. Ohulchanskyy, Y. Sahoo, E. J. Bergey, R. K. Pandey, and P. N. Prasad, "Diacyllipid micelle-based nanocarrier for magnetically guided delivery of drugs in photodynamic therapy," *Molecular Pharmaceutics*, vol. 3, no. 4, pp. 415–423, 2006.

[64] M. Skorobogatiy, "Efficient antiguiding of TE and TM polarizations in low-index core waveguides without the need for an omnidirectional reflector," *Optics Letters*, vol. 30, no. 22, pp. 2991–2993, 2005.

[65] Y. Gao, N. Guo, B. Gauvreau, et al., "Consecutive solvent evaporation and co-rolling techniques for polymer multilayer hollow fiber preform fabrication," *Journal of Materials Research*, vol. 21, no. 9, pp. 2246–2254, 2006.

[66] T. Murao, K. Saitoh, and M. Koshiba, "Design of air-guiding modified honeycomb photonic band-gap fibers for effectively single-mode operation," *Optics Express*, vol. 14, no. 6, pp. 2404–2412, 2006.

[67] S. E. Barkou, J. Broeng, and A. Bjarklev, "Silica-air photonic crystal fiber design that permits waveguiding by a true photonic bandgap effect," *Optics Letters*, vol. 24, no. 1, pp. 46–48, 1999.

[68] T. Hidaka, H. Minamide, H. Ito, J.-I. Nishizawa, K. Tamura, and S. Ichikawa, "Ferroelectric PVDF cladding terahertz waveguide," *Journal of Lightwave Technology*, vol. 23, no. 8, pp. 2469–2473, 2005.

[69] A. Hassani, A. Dupuis, and M. Skorobogatiy, "Low loss porous terahertz fibers containing multiple subwavelength holes," *Applied Physics Letters*, vol. 92, no. 7, Article ID 071101, 2008.

[70] A. Hassani, A. Dupuis, and M. Skorobogatiy, "Porous polymer fibers for low-loss Terahertz guiding," *Optics Express*, vol. 16, no. 9, pp. 6340–6351, 2008.

[71] X. Zhang, R. Wang, F. M. Cox, B. T. Kuhlmey, and M. C. J. Large, "Selective coating of holes in microstructured optical fiber and its application to in-fiber absorptive polarizers," *Optics Express*, vol. 15, no. 24, pp. 16270–16278, 2007.

[72] X. Yang and L. Wang, "Silver nanocrystals modified microstructured polymer optical fibres for chemical and optical sensing," *Optics Communications*, vol. 280, no. 2, pp. 368–373, 2007.

[73] A. C. Peacock, A. Amezcua-Correa, J. Yang, P. J. A. Sazio, and S. M. Howdle, "Highly efficient surface enhanced Raman scattering using microstructured optical fibers with enhanced plasmonic interactions," *Applied Physics Letters*, vol. 92, no. 14, Article ID 141113, 2008.

[74] J. Hou, D. Bird, A. George, S. Maier, B. T. Kuhlmey, and J. C. Knight, "Metallic mode confinement in microstructured fibres," *Optics Express*, vol. 16, no. 9, pp. 5983–5990, 2008.

[75] L. Ma, T. Katagiri, and Y. Matsuura, "Surface-plasmon resonance sensor using silica-core Bragg fiber," *Optics Letters*, vol. 34, no. 7, pp. 1069–1071, 2009.

Hindawi Publishing Corporation
Journal of Sensors
Volume 2009, Article ID 871580, 17 pages
doi:10.1155/2009/871580

Review Article

Properties of Specialist Fibres and Bragg Gratings for Optical Fiber Sensors

John Canning

Interdisciplinary Photonics Laboratories, School of Chemistry, University of Sydney, Sydney, NSW 2006, Australia

Correspondence should be addressed to John Canning, j.canning@usyd.edu.au

Received 4 March 2009; Accepted 9 June 2009

Recommended by Christos Riziotis

The advent of optical fibres based on air holes running along their entirety opens up new directions in addressing various properties relevant to sensing, including the temperature/strain challenge of optical fibre sensors. This paper looks at the measurement challenges associated with temperature and strain, examines the potentially unique functionality structured fibre designs with and without gratings open up, and briefly describes some current research directions within conventional fibre and grating technologies.

1. Introduction

The projected market size of optical fiber sensors generally is expected to exceed $US 1.6 billion in 2014, up from the 2007 figure of $US 235 million [1]. Grating technologies are increasingly pervasive within this market finding applications ranging from biomedical, chemical, and cosmetic [2–6] to structural health monitoring (SHM) of buildings, vehicles, aircraft, bridges, trains, and windmills [7–19]. Two important characteristics dominate the criteria of gratings for sensing applications: temperature and strain/pressure sensitivity, both of which are affected by the type of optical fibre and the performance parameters not only of the grating itself but also of the type of fibre and the required packaging.

Traditionally, the separation of the intertwined temperature and strain response has been done using reference grating elements to calibrate out one or the other parameter. However, innovations in new fibre design, largely centred on structured fibre technology [20], offer radically new solutions that may circumvent the need for secondary reference gratings. The ability to tailor the hole distribution in general allows an incomparable flexibility in fibre design and in parameter control, not just of temperature and strain but of many others. For example, by adjusting the crystal lattice parameters of a photonic crystal fibre appropriately, unique composite system properties providing multiple functions, such as dual dispersion compensation and Raman amplification [21], are possible. By controlling the hole distribution and size, mechanical (including acoustic and pressure response) properties are altered as well as even more basic properties such as strain optic coefficient. Inserting material gives greater scope for adjusting composite system properties such as the effective thermo-optic coefficient of zero, ideal for zero temperature gratings [22, 23]. The recent demonstration of microfilling a structured optical fibre with three separated laser dyes around the core of the fibre [24] reveals the full potential of structured fibres, particularly bringing the speculative prospect of the "lab-in-a-fibre" [25] closer to reality. Grating technology will inevitably contribute to such functionality—it will, as noted, also benefit the separation of temperature measurements with the grating, the most immediate area where practical progress using structured optical fibre gratings will likely be seen.

2. Structured Optical Fibres and the Evanescent Field

Figure 1 illustrates three contemporary examples of interest to the sensing community: the first is a single mode "photonic crystal fibre" [27] (so-called because of the periodic lattice although diffractive effects are clearly observed at short

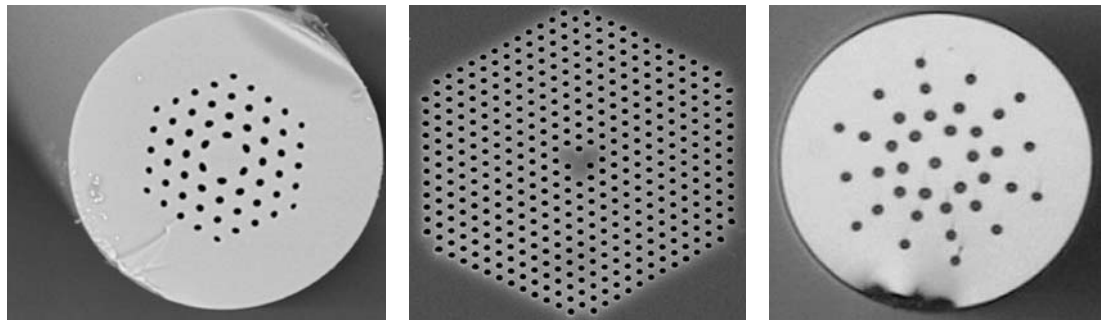

(a) (b) (c)

Figure 1: Examples of common structured optical fibres into which gratings have been written: (a) low loss (<4 dB/km) 4-ring all-silica photonic crystal optical fibre; (b) 12-ring photonic crystal fibre with triangular core and photosensitive, high NA step-index germanosilicate centre; and (c) a simple Fresnel fibre.

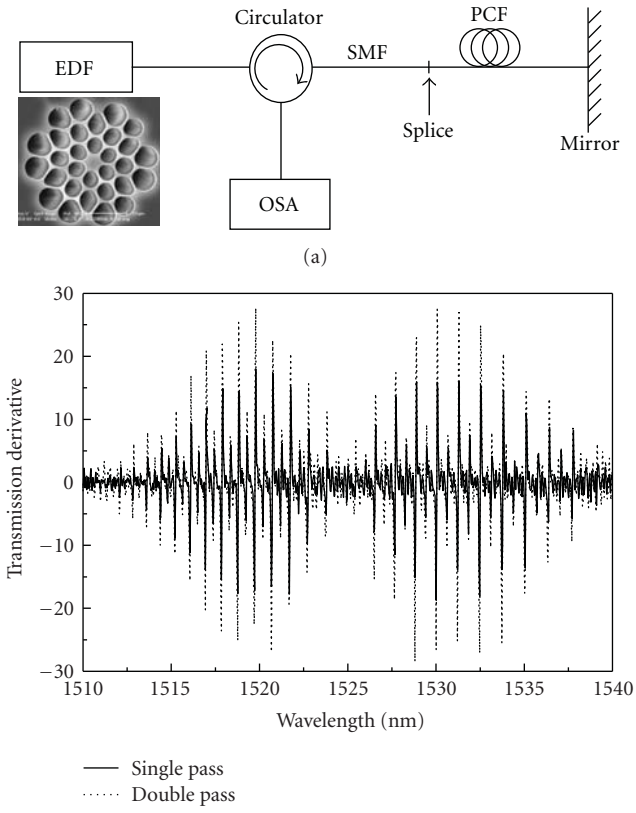

Figure 2: All-fibre add-drop acetylene reference cell using a photonic crystal fibre (a). Spectra for both single pass and double pass of the cell are shown (b) [26]. (EDF-erbium doped fibre source, OSA-optical spectrum analyser, SMF-standard single mode fibre smf 28, PCF-photonic crystal fibre: scanning electron microscope image of cross-section shown above y-axis).

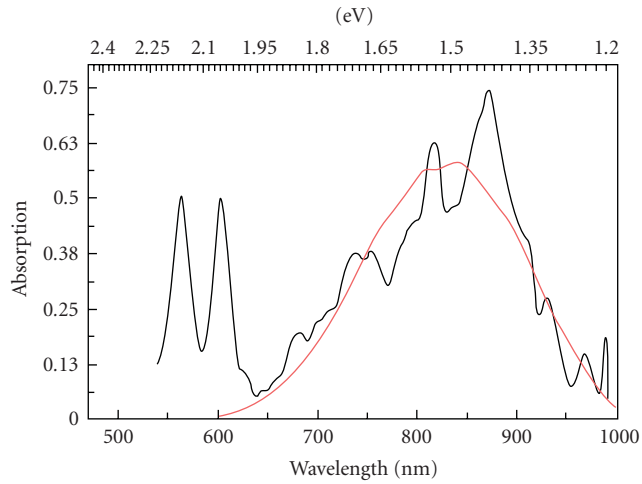

Figure 3: Absorption measurement of PCF containing a porphyrin thin film deposited on the surfaces of its holes in DMF: (length = 50 cm, absorption rescaled to 25 cm) the typical Q-band (559 and 599 nm) is observed along with a new near-IR band (660–930) nm. Numerical simulation is shown in red for a typical charge transfer band. More details can be found in [5].

wavelengths—see, e.g., [28, 29]); the second is a photonic crystal fibre with a highly nonlinear and photosensitive core surrounding by a triangle of silica which supports an unusual additional mode, and the latter is a Fresnel fibre [30], where propagation is diffractive and the mode peak intensity is surprisingly well localised in the hole centre. Perhaps more interesting still, light is partially focused at the output [30–32], from which small phase zone plates can be fabricated [33].

An important consideration for exploiting the structure within these fibres is the penetration depth, and overlap integral, of the evanescent field within the holes. Within a conventional photonic crystal fibre (a structured fibre with a regular periodic array of holes determining the cladding without necessarily having significant diffractive effects at the sensor probe wavelength), the evanescent field overlapping with the holes is a key determinant of the effective interaction lengths possible. A typical "endlessly single mode" fibre usually has an overlap integral that is too low to be of significant use so the air fraction tends to be increased. Generally, a few per cent overlap at 1500 nm becomes useful; the figure increases towards the red and decreases towards

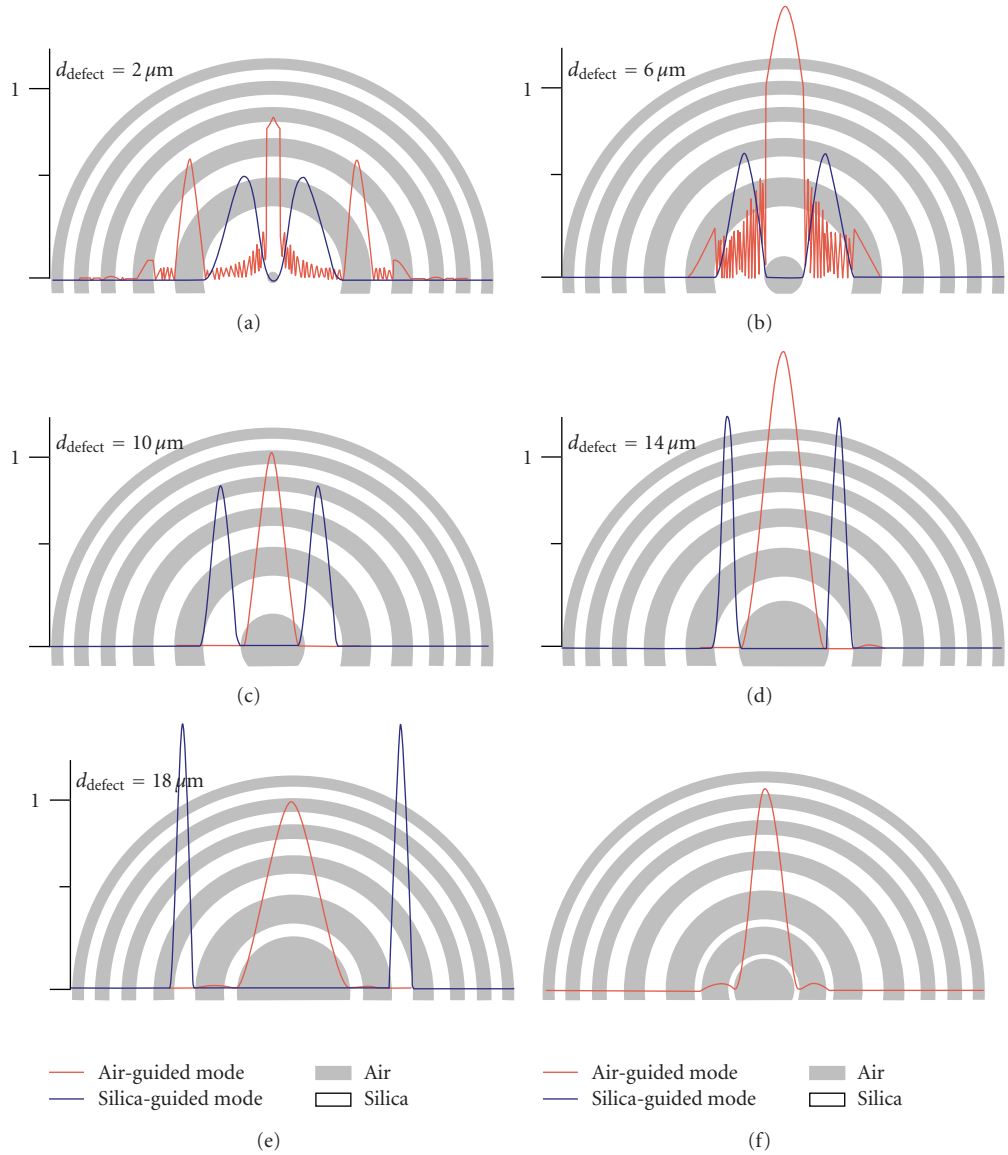

FIGURE 4: (a)–(f). Numerical simulation of (red) optical localisation in varying hole size within a bandgap Fresnel fibre and (blue) optical localisation within the silica. As the hole size becomes smaller (a and b), a step-like discontinuity arising from the interface boundary is observed [34]. There appears to be enhanced field localisation of the evanescent field in addition to that expected from the far-field phase diffraction of the Fresnel structure.

the blue. Notably, the bulk of the evanescent field lies within the first 60–100 nm from the surface—it is often not recognised that the probing field is therefore highly concentrated close to the near field regime, making it an ideal tool for exploring interface effects but also a potentially problematic issue when comparing to bulk references. On this scale what sometimes appears to have no detectable interaction with a silica surface in free space can sometimes be picked up over long interaction lengths complicating any analysis that relies on bulk sample, or indeed short path length, interactions. Therefore, whilst for many species this is not a problem, for others, particularly those associated with biodiagnostics where surface interactions are not unexpected, the issue may be both problematic and opportunistic. For example, to highlight this point, an overlap of a few percent is sufficient to perform numerous sensing and device experiments. Figure 2 shows a double-pass add-drop all-fibre acetylene gas reference cell made with a photonic crystal fibre, filled with low pressure acetylene, and with a few percent field overlap with the first ring of holes in the near IR [26]. A cross-section of the fibre is shown for comparison with Figure 1(a). In this case, there is no observable difference between these measurements and bulk, consistent with the expectation that acetylene does not react with the glass surface. On the other hand, an identical fibre was also used to make the first direct observation of charge transfer between porphyrins and silica [5], a molecular interface effect which has not been previously observed. This added effect generates a large

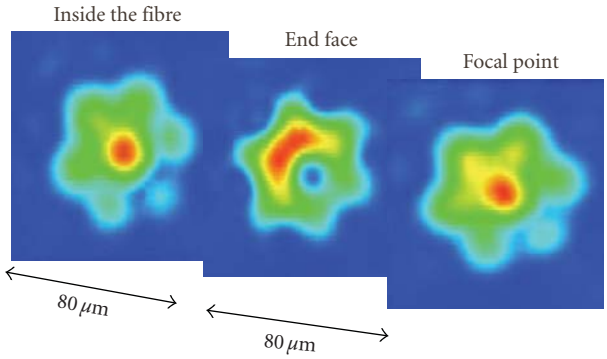

Figure 5: Near field profile of the end of the Fresnel fibre shown in Figure 1(c). The centre profile is the end face, and the other profiles are imaged using an objective lens within and beyond the fibre, respectively. Complex interfering supermodes are observed including one with tight optical localisation within the hole.

near IR band (Figure 3) which needs to be considered if porphyrins are to be used in biodiagnostics that operate in this region, for example.

A solution for writing gratings is to introduce a photosensitive core, as in the second example illustrated in Figure 1(b). This is often done by preparing a standard optical preform using MCVD and then etching out the core (typically close to 1mm in diameter) before inserting into the structured optical fibre preform. Whilst this process clearly introduces a standard photosensitive core and makes grating writing easy, the benefits of single-material fibres are lost and the added complication of further confinement away from the holes by a step index needs to be dealt with. This latter problem can in part be handled by making the photosensitive region much smaller than the effective mode field diameter and, consequently, such fibres often have smaller cores.

Numerical simulation of a Fresnel fibre with decreasing hole size in the centre that showed a highly localised peak intensity within the hole is possible once subwavelength dimensions were reached [34]. This localisation arises as a result of the impedance matching required at the interface between two materials of different refractive indices and on the lower index side the electric field, E, scales as the square of the ratio of the index contrast, n_1/n_2 (E proportional $(n_1/n_2)^2$. The higher the index contrast the more significant the effect—in silicon photonic crystal waveguides this forms the basis for very sensitive nanoparticles detection and biosensing on a chip [35–38]. Figure 4 shows the simulation for the Fresnel fibre. In any case, optical localisation over the hole is observed experimentally at larger sizes attributed to the diffractive properties of the Fresnel fibres [30–32]. Other work also supported very tight optical localisation within a silica structured photonic crystal fibre using a subwavelength hole [39]. All these forms of optical localisation phenomena have significant potential for enhancing sensitivity in many applications that require small volumes and high interaction with optical fields, such as biodiagnostics applications. For example, localisation of light is central to developing metal free optical microscopy both in the far and near fields [40].

Figure 5 shows the near field profile of experimentally observed localised light within a Fresnel fibre (Figure 1(c)) with a central air hole which is smaller than the effective mode wavelength. Also observed is the ring mode associated with the silica ring region around the central hole, as expected from simulation. There is evidence that the two localised propagating fields (modes) interfere every 80 μm within this fibre sample. The localization of the evanescent field within the central air hole is difficult to observe since the resolution is diffraction limited. In contrast to so-called "photonic bandgap" fibres, a key advantage of this type of optical field is that there remains sufficient silica in the surrounding ring into which useful gratings can be written (shown later). (These "photonic bandgap" fibres are essentially diffractive fibres with only a partial bandgap; the index contrast is usually too small to have anything more than a small angular stopgap, which is analogous to diffractive fibres such as Bragg and Fresnel fibres.) These gratings can therefore be used to perform additional spectrally selective monitoring of samples probed by the high field within the central hole (in contrast to the much poorer overlap in the cladding holes). Quasicrystal fibres such as Fresnel fibres rely on simplifying the design based on the circular nature of the waveguide. Periodic lattices associated with 3D structures are unnecessary—instead designs based on omnidirectional filters allow much broader stopgaps. For example, the fibre in Figure 1(c) has a bandgap over 1000 nm wide [41]. These fibres also lead to significantly lower losses since the resonant coupling between interstitial regions (both in terms of optical field within and or at the interface of the glass regions, perhaps as surface modes) is reduced, as discussed later.

From the few examples illustrated above, the potential and challenges of structured optical fibres, which can generate complex propagation, can clearly benefit by the inscription of wavelength selective components such as Bragg gratings. Grating writing, therefore, within nonphotosensitive, pure silica, single material fibre becomes of paramount importance if many of these unique features are fully retained. In this particular paper, the focus is on specific silica-based Bragg grating technologies that address new directions in the temperature/strain challenge of optical fibre sensor gratings in conventional and structured optical fibres. This will serve to highlight the potential to sensing.

3. Temperature and Strain

Grating sensors rely on a shift, $\Delta\lambda_B$, in the resonance wavelength, λ_B, arising from either strain, $\varepsilon = \Delta l/l$, and/or temperature, T. This is because ε affects a change in resonance through both spatial changes in period, Λ, and refractive index, n, whilst T largely affects a refractive index change (although this is also affected by changes in stress between the core and cladding as a result of different thermal expansion coefficients, which in turn affects the stress contribution to refractive index change). In general, the relationship which binds strain and temperature with the grating resonance wavelength can be described simply in

one equation (see, e.g., [42]):

$$\frac{\Delta\lambda_{\mathbf{B}}}{\lambda_B} = \frac{\Delta n}{n} + \frac{\Delta\Lambda}{\Lambda} = (1-\rho)\varepsilon + \kappa T, \quad (1)$$

where ρ is the elasto-optic coefficient of the fibre, and κ is the thermo-optic coefficient. The particular expression for studying specific stain parameters introduced by pressure can be obtained by noting Poisson's ratio and expanding the series if necessary. This expression forms the basis for nearly all Bragg grating-based optical fibre sensor applications.

4. Conventional Step Index Fibres

For nearly all practical cases using conventional silicate-based optical fibres, it is assumed that the fibre parameters are approximately those of pure bulk silica, which are well known ($\rho \sim 0.22, \kappa \sim 5\times10^{-6}$). If the tolerable experimental error bars are sufficiently large, or a self-calibration reference is implemented for each sensor, then this is an acceptable approximation. However, it is just that—in reality, the actual response profiles that are obtained cannot be fitted so nicely by such a simplification—estimates of both strain optic and thermo-optic coefficients based on optical fibre work therefore often vary noticeably not only from bulk measurements but also between laboratories. This may come as a surprise, but this variation cannot be readily calibrated out using a universal standard—each fibre is genuinely different depending on how it was fabricated, by whom (an element of black magic sometimes comes into play!), what dopants are employed, and sometimes by what lathe system is used. In practice, there is an additional term that affects the values to (1)—frozen in mechanical pressures and strains. For instance, the axial strain generated by the fibre drawing process alone can be described as [43, 44]

$$\sigma_z \approx \frac{F}{2\pi}\left[\frac{\eta}{\int_0^R \eta(r)rdr} - \frac{E}{\int_0^R E(r)rdr}\right], \quad (2)$$

where F = drawing force/tension, h = viscosity, and E is the Young's modulus. This strain increases with drawing tension, viscosity, or decreasing E. Consequently, the processing history becomes important in determining the optical fibre's mechanical properties, which are in turn dependent on the type and quantity of dopants used. These dopants also clearly affect the local refractive index of the core and, therefore, the confinement of the optical mode which in turn affects the measurands.

For most normal optical fibres made from germanosilicate, for example, optical fibre drawing conditions are selected that happen to produce a certain range of tensile stresses arising from the fact that conventional fibres are composite systems determined by two differing glass compositions between core and cladding. It is entirely possible to obtain the reverse—mechanical stress can be of opposite sign and exceed magnitude of thermal stress and lead to compressive stress at the interface depending on preparation conditions, impurities, and dopants [45, 46]. For example, under very high drawing tensions, compressive stresses can be generated.

Equally important to the frozen-in mechanical stresses are the subsequent thermo-elastic stresses arising from differences in thermal expansion coefficient between core and cladding. The expansion coefficient for SiO_2 is typically $\sim 0.55\times10^{-6}$ but this can be changed substantially by adding dopants. Adding 20 mol% of GeO_2 increases this to 2.8×10^{-6} whilst adding only 12 mol% of P_2O_5 increases this to 2×20^{-6}. This changes the temperature dependence of the fibre and in combination with the effects of frozen-in mechanical stresses means even fibres with identical recipes can vary between each other substantially. Table 1 summarises some of the thermal expansion coefficients, α, per mol % of common dopant added [47]. Interestingly enough, using materials with large negative expansion coefficients in sufficient concentrations can open up pathways to designing glass hosts that have reduced, zero or negative temperature dependence, an alternative to subsequent mechanical tensile stress—based packaging of optical fibre Bragg gratings currently sold commercially. Not considering the frozen-in mechanical stresses, only 5 mol% of TiO_2 is required to cancel out the positive temperature dependence of SiO_2. Of course, an important consideration is whether the dopant can be readily introduced and whether it will impact on the desired properties of the optical fibre, including photosensitivity. For this latter case, the almost ubiquitous material chosen is GeO_2 and often codoped with B_2O_3 to facilitate better mixing into the silica glass network and to lower the refractive index step. Standard grating writing within these fibres takes advantage of highly coherent frequency doubled Ar^+ lasers to generate arbitrary grating profiles using a computer controlled free space interferometer. This level of sophistication was developed for the telecommunications industry where alternative filters to etalon-based thin films were needed to achieve superior performance. Inevitably, such technology would find applications in chemical sensing diagnostics since a filter designed to filter out a specific molecular absorption or emission band can be readily made. This has been particularly useful already for those species with overlapping bands in existing telecoms windows, such as OH a problematic source in spectroscopic studies of the night sky. Fibre grating filters promise to displace current thin film etalon filters [48], for example.

For active sensor devices based on rare earth ions, it is often preferable to avoid these dopants since they have a deleterious impact on the longevity of the upper level lifetimes crucial for laser and amplifier performance, particularly in codopeded systems such as Er^{3+}/Yb^{3+} that are more exposed to phonon decoupling. For these, preferable dopants include P_2O_5 for reduced decoupling of the upper level excited states although at the expense of higher scattering losses and lower fibre thermal tolerance. For higher power laser operation and power handling generally, Al_2O_3 is the preferred dopant. Mixing and phase separation are two important considerations when optimising optical fibre functionality because the issue of loss is critical for most

Table 1: Thermal expansion coefficients (per degree Celsius) for common glass dopants used in conventional optical fibres.

Dopant	α ($\times 10^{-6}$/mol%)
P_2O_5	1.3
GeO_2	0.7
B_2O_3	0.7
F	−0.02
TiO_2	−1.0

functional applications, especially long distributed sensor systems that consist of numerous components.

Another important dopant that has not been considered in detail in the past (at least with respect to grating writing) is OH impurities. OH impurities are known to give rise to compressive stresses [45, 46]. It is almost certain that the formation of OH acts to create an internal pressure within the glass that can help offset tensile stresses, if not exceed them. The ramifications for a well-known photosensitive enhancing procedure—hydrogen loading—are significant. OH formation is often a by-product of conventional grating writing and its formation conveniently accounts for the induced index changes through Kramers-Kronig analysis [49]. The effect of mechanical stress within the fibre is not widely considered. On the other hand, it seems highly plausible that this mechanical effect contributes substantially to the total index change possible by alleviating the stresses that might otherwise restrict normal type I grating formation (where stresses have been observed to increase directly at the core-cladding interface [50, 51]). Furthermore, it seems crucial that this effect takes place for type Ip (or type IA) positive gratings [52]. There is no doubt that the complexity and range of grating writing opportunities [52] across the type I spectrum are dependent on all these processing conditions and dopant properties. If this insight is correct, we can actually begin to make predictions of additional effects one might expect using other dopants, for example, Cl is also known to reduce the thermal expansion coefficient of the core [53, 54] and is a standard drying material used in MCVD optical fibre fabrication. If used appropriately, axial stress during fibre fabrication may be reduced. If standard germanosilicate optical fibres are considered, by reducing the total frozen-in stresses into the final fibre, it is likely that the photosensitivity of type I gratings can be substantially optimised, with potentially important outcomes such as improved thermal stability. Likewise, the impact on higher processed gratings such as negative index gratings and regenerated gratings bears consideration.

Clearly, in addition to changing the mechanical and thermal response parameters of a fibre Bragg grating, there remains substantial scope for tailoring the photosensitive response of conventional optical fibres. Conversely, there has been considerable work in tailoring the grating writing process itself to the medium—the advent of 193 nm laser applied to optical fibre Bragg gratings, in particular, extends the application to many other materials, including important phosphosilicate and aluminosilicate systems that benefit fibre lasers [59–61]. New lasers, especially femtosecond lasers

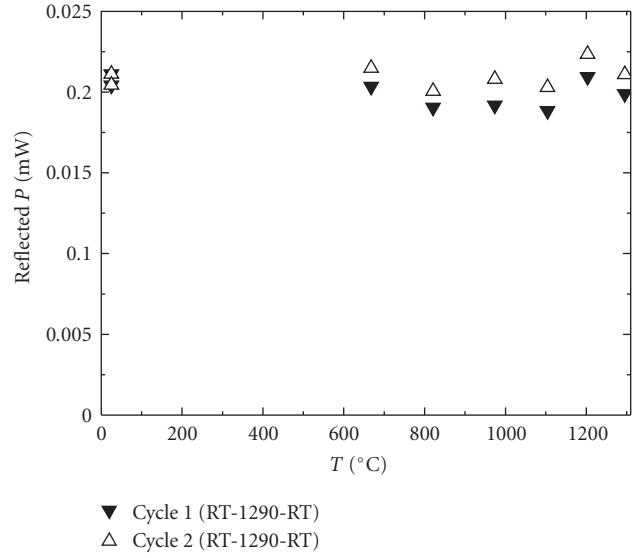

Figure 6: Temperature performance of a regenerated grating (10% T) in a telecom matched photosensitive germanosilicate core optical fibre. Two full cycles from room temperature to 1295 °C are shown [55].

that depend less on the dopants and more on the damage threshold to affect index change [62, 63], promise to have a similar impact. Below the damage threshold, the exploration of photosensitivity into other materials for conventional fibre Bragg gratings has meant that in parallel a large number of new processing recipes allow the properties of Bragg gratings themselves to be tailored substantially—for a review of these photosensitive mechanisms see [52].

Most conventional fibres, therefore, have an inbuilt stress (or pressure) that adds or detracts to the actual sensitivity of the component. The strain and temperature curves as a function of applied pressure will in all likelihood vary across fibres from recipe to recipe and composition to composition, a problem that raises interesting challenges for the definition and measurement standards, international bodies must eventually determine if there are to be universal generic sensor elements. Differences between laboratories are often attributed to arising from variable experimental parameters rather than, potentially, from differences in the mechanical and thermal parameters between fibres.

4.1. Extreme Gratings. As an illustration how conventional optical fibres remain far from exhausted in terms of novel research and direction for grating sensors, and how little is still understood in terms of the underlying photosensitive mechanism of even the most thoroughly investigated type I gratings, it is worth examining recent reports of gratings in conventional fibres that survive repeated cycling at ultrahigh temperature (>1000 °C) [55, 64, 65]. These so-called regenerated gratings presently outperform all other gratings—despite the expansive growth in new writing recipes and formulations, these results were obtained by taking ordinary type 1 gratings and thermally processing them with an appropriate recipe where the temperature

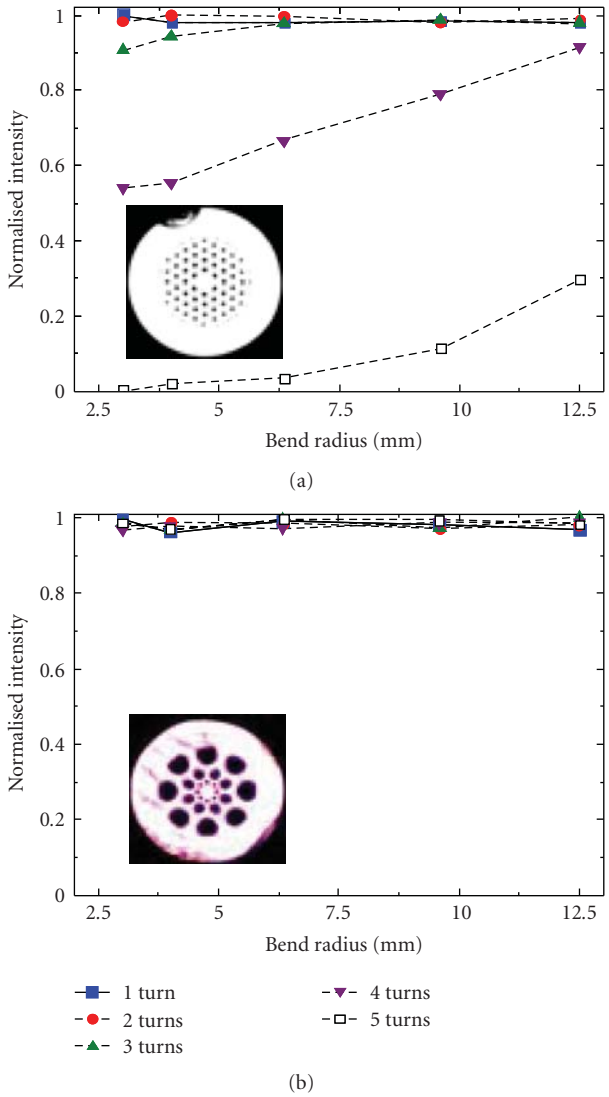

FIGURE 7: Observed bend loss as function of bend radii for (a) regular photonic crystal fibre and (b) "fractal" (or chirped Fresnel) fibre [56].

is ramped to ~ 9000 °C and the regenerated grating allowed to evolve. The final regenerated 5 mm long grating can be as strong as 25% transmission and can be cycled repeatedly as high as a temperature of 1295 °C with full recovery at room temperature [55], as illustrated in Figure 6. The grating can outlast the fibre itself, that is, whilst the fibre becomes brittle at such temperatures and often breaks, no observable impact on the grating spectra is noted. A simple diffusion model alone, based on hydrogen bonding and oscillating reactions, therefore, seems unlikely to suffice to explain these results. H is crucial for any diffusive process, particularly via OH transfer. One argument rests on the formation of molecular water as a mean of displacing oxygen, which would not normally be possible [64], based on a modified oxygen diffusion model [66]. However, such a transfer implies that substantive oxygen-deficient silica is created, which would likely lead to a crystallisation of

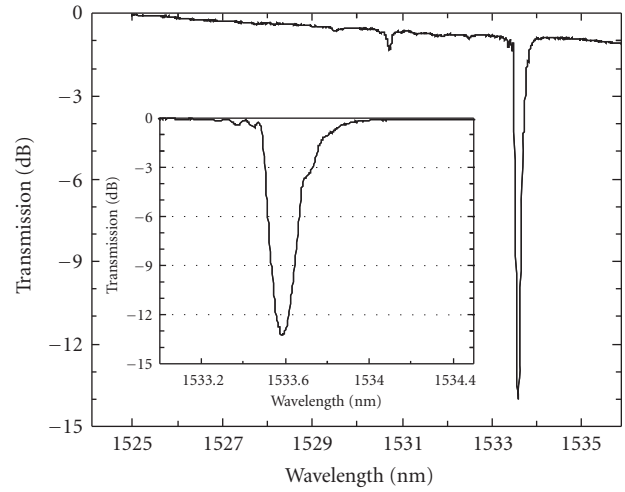

FIGURE 8: Grating in pure silica single material photonic crystal fibre [57]. Some evidence of birefringence ($< \times 10^{-5}$) is observed in this example.

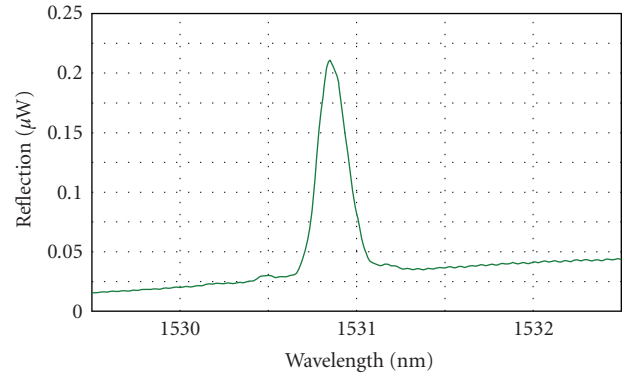

FIGURE 9: Reflection spectra of a 5 dB strong grating within the Fresnel fibre shown in Figure 1(c) [58]. The optical intensity of a propagating mode peaks in the core hole.

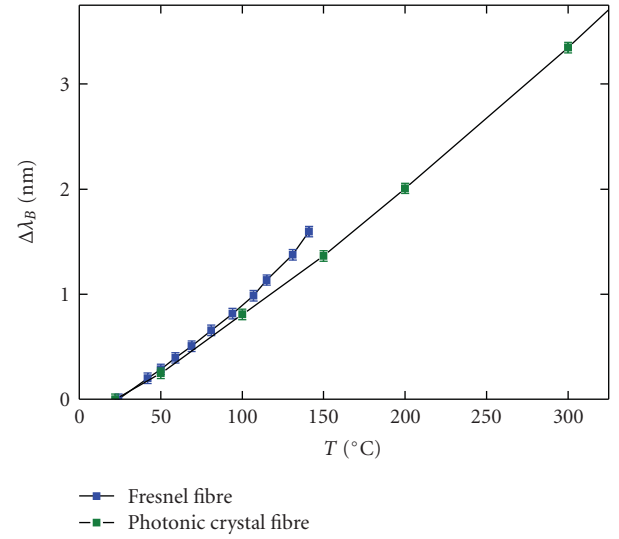

FIGURE 10: Temperature dependence of the fundamental mode within two types of structured optical fibre [58].

silicon or structural transformation to a larger bond angle polymorph, both of which would give rise to large scattering and large index changes. Alternatively, the seed grating with hydrogen allows a different glass quenching and relaxation to occur in the processed regions that give rise to, perhaps, a crystallised or amorphous grating structure of similar tetrahedral properties. This remains the subject of ongoing work. Nevertheless, these gratings can now be applied to ultrahigh temperature applications including temperature monitoring of smelters, furnaces, and engines.

5. Single Material Structured Fibres

Equation (1), along with the discussion above, would suggest that single material optical fibres will have much less variability to parameters and, in particular, the effective thermo-optic coefficient should be lower. The possibility that such fibres might form the basis for more reproducibility between laboratories, amongst many other applications, makes the idea of single material fibres especially attractive. This reduced temperature dependence of such fibres has recently been verified many times in many ways, not only with Bragg gratings, but also for long period gratings in single material photonic crystal fibres [67] and, particularly attractive, linearly and spun birefringent photonic crystal fibres and devices utilizing them [68–73]. Modal interferometers using a short length of single material photonic crystal fibre [74] have also been used as a temperature insensitive strain sensor [75]. Specifically, structured optical fibres based on air holes running along their entire length have one other key advantage not possible with conventional fibre technology based on dopants. Essentially, step index propagation can be achieved by a reduced average cladding index determined by the distribution of air holes.

The structured optical fibre is made up of so-called leaky modes where the normal confinement boundaries defining modes in convention step index fibres are less defined because there is leakage between the holes. In perfectly periodic lattices this leakage translates into coupling between the interstitial regions, both in terms of optical field within the region and the optical field at the interface (sometimes described in terms of surface modes), and the surprising possibility of having complex cladding supermodes with close to equal or, in some cases, higher effective index than the core mode. In fact, this problem is almost certainly the reason why in terms of low loss fibres one would not use a periodic structure. Bend loss in particular is significantly worse for a periodic lattice fibre than even conventional step-index fibre with substantially lower NA (this beggars the explanation of what NA means in such fibres?). On the other hand, by removing the periodic lattice and preventing interstitial optical coupling of light, quasiperiodic or other nonperiodic Fresnel and "Fractal" fibre designs have been shown to reduce bend loss so effectively that they outperform conventional fibres. Zero bend loss is possible [56], as shown in Figure 7. For many sensor and other device applications this is a highly desirable property and allows tight bending of optical fibres. This net result also shows fundamentally the difference between higher-order modes and fundamental modes within photonic crystal fibres—the loss differential can be huge.

Given that, in the first instance, the fundamental leaky mode of the structured fibre has a k vector along the fibre axis and therefore the role of leakage loss is somewhat suppressed, the fundamental mode may not be so distinctive in behavior to that of the step index analog. This forms the justification for the step-index approximation of simple structured fibres where the cladding index is, on average, lower than the core index. In contrast, when higher-order modes are present they will be significantly affected by leakage loss and greater access to the evanescent field within the holes—a property which opens up new opportunities for sensing applications. For example, because the difference between index and loss is large between the fundamental and higher-order mode of a two-mode structured optical fibre, it is possible to exploit this to create an internal reference for a Bragg grating. This was done using, instead, an active grating structure in the form of a DFB fibre laser [76]. Equivalent intermodal interference within photonic crystal fibres has also been demonstrated [74], and this needs to be considered when short devices are fabricated.

The ability to write gratings in single material fibres was first demonstrated using 193 nm from an ArF laser [57]. A key challenge that needed to be overcome was the large attenuation of the writing beam through scattering of the lattice structure—a comprehensive description of these processes can be found in [77]. Figure 8 shows the first such grating in a regular photonic crystal fibre (similar to that in Figure 1(a)). An immediate advantage is the absence of cladding modes since the index is not confined solely to the core. For conventional fibre technology, a photosensitive matched cladding needs to be custom designed to achieve a similar result. Figure 9 also highlights another important example—a 5 dB strong grating within a Fresnel fibre [58]. Although the optical mode has a large amount of optical filed interacting within the hole, the fibre design is such that there is sufficient propagation within the silica ring region into which the grating is inscribed so as to see the grating. By making the field smaller the optical localisation of evanescent light into the hole can be exploited for extremely sensitive biodiagnostics and chemical sensors.

5.1. Temperature Response

5.1.1. Fresnel Versus Photonic Crystal Fibre. Figure 10 shows the relative wavelength shift of a Bragg grating written by 2-photon excitation within a single material all-silica Fresnel fibre (Figure 1(c) and Figure 8) and a similar single material, single mode, all-silica 4-ring photonic crystal fibre (Figure 1(a)) as a function of temperature [58]. Below 100 °C the Fresnel fibre has a slightly higher temperature dependence, or effective thermo-optic coefficient, $(1/n_{\text{eff1}})(\partial n_{\text{eff1}}/\partial \text{T}) = 7.8 \times 10^{-6}/^{\circ}\text{C}$ compared to the photonic crystal fibre of $6.5 \times 10^{-6}/^{\circ}\text{C}$, although both are very close to that of pure silica $\sim 6 \times 10^{-6}/^{\circ}\text{C}$ [47]. There is a quadratic dependence on this effective thermo-optic

coefficient, which is particularly pronounced for the Fresnel fibre. This is directly attributable to mode field confinement by the air holes as the index of the glass changes and, hence, great care must be taken when interpreting and comparing the temperature dependence between structured optical fibres. The apparent observation of a sharp transition within the Fresnel fibre may characterize a cut-off condition for propagation which is especially sensitive in the Fresnel fibre given the larger dependence on diffractive propagation. As noted previously, the role of surface optical field localization also remains unclear.

The illustrated results reflect, overall, huge scope to adjust both the fibre design and fibre parameters and control properties such as the temperature dependence. This can be applied to enhance various configurations of thermally tunable devices using structured fibres, active or passive, and gratings, for example. For sensing applications this control over the temperature dependence can be used to help separateing the intertwined relationship between temperature and strain. Single material fibres have other advantages, for example, given that the index contrast with air is sufficiently high, properties such as form birefringence can be readily introduced into these fibres. Form birefringence within a single material fibre is free of the temperature problem associated with two materials of different thermal expansion coefficient—fibre that has a zero temperature dependence of birefringence from −20 to +800 °C has been demonstrated [68]. These results were extended to a spun version of this fibre [72] which has important applications, amongst many, within electric field sensors and gyroscopes, where a critical parameter is packaging to isolate the system from temperature fluctuations. These two can be combined with Bragg gratings for enhanced and multifunctional properties.

5.1.2. Fundamental versus Higher-Order Modes. The stronger evanescent field interaction of the higher-order with the air holes can allow the fundamental mode to be used as a relative reference arm, an attractive all-in-one fibre solution. This possibility was recently extended to DFB fibre laser operation where lasing could be obtained on the fundamental mode or the higher-order mode, using a doped aluminosilicate core to further confine the fundamental mode away from the holes [56]. Such active grating structures allow enhanced resonance detection of many measurands, for example, it is an important approach to make optical fibres sufficiently sensitive for undersea acoustic detection [78, 79]. Below the lasing threshold, such a structure was used to study strain and temperature within structured optical fibres [80]. The effective indices of the two modes give rise to two distinct grating peaks (Figure 11). The modes are determined by the corresponding fractional powers (η) of each mode within the higher index doped region (0.002) and in the surrounding silica. Leakage phenomena play an important part in determining and defining the mode field radius and, therefore, the fractional distribution of light of the modes either in the doped core or in the silica. Those modes with large transverse vector components will be sensitive to changes in the hole shape and stress between the holes in the

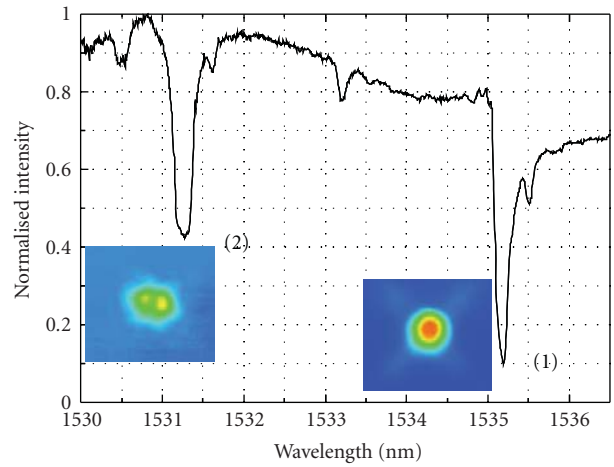

Figure 11: Transmission spectrum of a two-photon written Bragg gratings within a two-mode 4-ring photonic crystal fibre. (1)—fundamental mode; (2)—higher-order mode and the dip in the centre is some cross coupling between the two arises from some asymmetry in transverse profile of the induced index change [80].

structure arising from, for example, tensile or compressive stress applied along the fiber.

But it is also clear that this sensitivity will depend on air fraction, the regularity of the lattice, the constituent materials, and the type of index guidance. For example, the Fresnel fibre described earlier has much less air fraction, no regularity, is single material all-silica, and the mode is largely determined by diffractive guidance even for the fundamental mode rather than an average step-index like effect. On the other hand, related diffractive coupling loss is a characteristic of regular photonic crystal fibres with the smallest microbends. Therefore, a comparison of both temperature and strain effects of the fundamental mode within a single material Fresnel fibre and a single-material photonic crystal fibre will further illustrate just how much flexibility in design exists by controlling structure alone.

From Figure 11, the transmission spectrum of a 4-ring photonic crystal fiber with a fibre grating has two reflection bands corresponding with the two modes it is designed to support, one at longer wavelengths (1535.2 nm) for the fundamental mode, and the other ~ 4 nm at shorter wavelengths for the higher-order mode. Figure 12 shows the obtained temperature dependencies for each mode—both grating transmission bands are found to have a similar linear variation with temperature. These results are in accordance with the material properties of the fiber, since the thermal expansion coefficient, α_{SiO2}, of the fiber ($\alpha_{SiO2} \sim 0.55 \times 10^{-6}$ for silica) is an order of magnitude smaller than the thermo-optic coefficient—for germanium-doped silica core fiber this is $(1/n_{eff})(\partial n_{eff}/\partial T) \sim 8.6 \times 10^{-6}$, which serves as a reference value [81]. From the grating response as a function of temperature, the fundamental mode wavelength dependence is $\partial\lambda_{B1}/\partial T = 19.72$ pm/°C, and for 1535.2 nm of $\partial\lambda_{B2}/\partial T = 20.14$ pm/°C. These correspond to $(1/n_{eff1})(\partial n_{eff1}/\partial T) = 12.9\times10^{-6}\,°C^{-1}$, and $(1/n_{eff2})(\partial n_{eff2}/\partial T) = 12.8\times10^{-6}\,°C^{-1}$ which are nearly double that of pure silica although similar

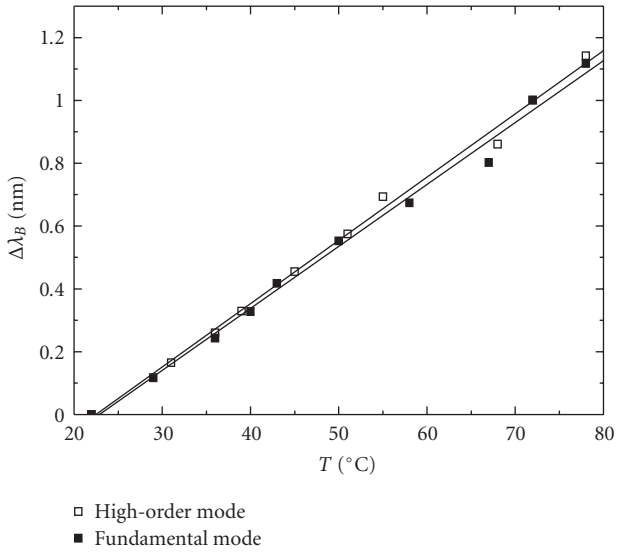

Figure 12: Temperature dependence of the two modes of the fibre described in Figure 11 [80].

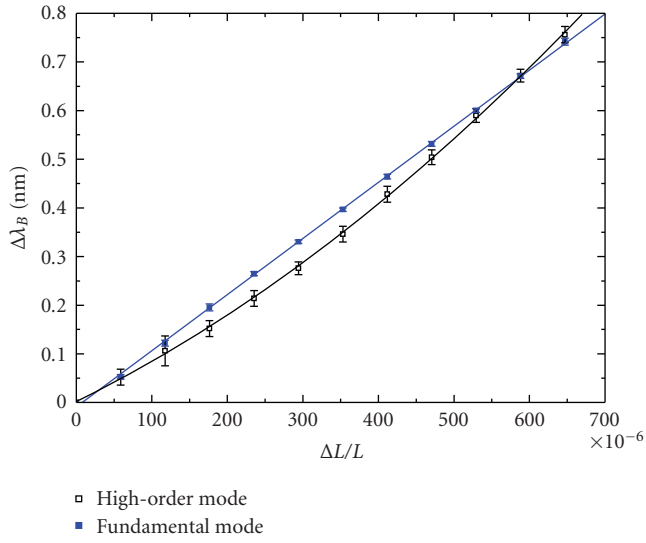

Figure 13: Wavelength shift versus applied longitudinal strain on the Er^{3+} doped, aluminosilicate dual mode photonic crystal fibre. A quadratic dependence is observed for the higher-order mode [80, 84].

to doped optical fibres. This larger value is due to the Er^{3+}-doped aluminosilicate core, and it is not surprising that the higher-order mode, which sees more silica, has a slightly lower value. Therefore, the composite system behavior is expected on the basis of constituent component materials.

5.2. Strain Dependence. In contrast to the temperature dependencies, there is a difference between the fundamental mode and the higher-order mode of the previous Er^{3+} doped aluminosilicate photonic crystal fibre. The observed shift with applied strain in the Bragg wavelength corresponding to the fundamental mode (Figure 13) has a linear behavior ($\partial\lambda_{B1}/\partial\varepsilon = 1.2\,\text{pm}/\mu\varepsilon$). However, the shorter Bragg wavelength, corresponding to the higher-order mode, has nonlinear behavior described by a quadratic dependence. Unlike conventional fibers, the higher-order leaky modes (in particular) of a photonic crystal fiber are sensitive to changes in stress between the holes and both the hole size and shape as well as the ratio of the hole diameter over the hole pitch, d/Λ [82]. The compression of the first ring, in part arising as the solid core resists the compressive force, leads to an increase in d/Λ with positive strain (applied tension). This problem is a well-known one that also contributes to hole deformation of the first ring during fiber fabrication if not addressed [83]. By increasing d/Λ, the modal confinement loss decreases, leading to improved confinement of the mode. This alters the fractions of power, η, in the center of the core and in both the silica ring and cladding. Since the effective index is dependent on this fraction, there is an additional shift in the Bragg wavelength ($\lambda_B = 2n_{\text{eff}}d$) that deviates the curve from linearity. Given that the changes are based on circular confinement and therefore mode area, to first approximation a quadratic dependence ($\lambda \propto a\varepsilon + b\varepsilon^2$) is expected and observed [80]. The strain-optic coefficient, therefore, reduces to $\partial\lambda_{B1}/\partial\varepsilon = a + 2b\varepsilon$. Further, the grating strength is also dependent on this fraction [$\kappa = \tan h^2(\pi \triangle \nu L\eta/\lambda)$ and we expect to observe a change in grating strength as a function of strain. The air structure itself becomes integral to defining the material properties and in this context is indistinguishable from a composite material. Therefore, the whole medium can be considered a unique super-structured material (SSM) with properties that can be tailored by tailoring the refractive index in a way analogous to tailoring the atomic distribution of constituents and their fractions in composite systems.

In contrast to this fibre, and despite the large interaction of the sensitive fundamental diffractive mode with the structure given its reduced confinement and the absence of an insulating step index core, the Fresnel fibre has a linear dependence with strain, as shown in Figure 14 [58, 84]. This is explained by the very low air fraction and the irregular arrangement of holes that prevent a sponge-like structure susceptible to compressive effects that sufficiently affect the mode overlap with the holes.

The most obvious application of this work is to enable a simple distinction between strain and temperature from the perspective of controlling strain instead of temperature. The ability to remove, or unravel, the strain contribution is a key problem in fibre sensing with gratings generally and structured optical fibres offer a unique pathway to resolving this.

6. Refractive Index Measurements Using Photonic Crystal Fibres

As a consequence of the high core-cladding index contrast, the contribution to mode propagation from, for example, a periodic arrangement of holes is negligible when the wavelength of light is larger than the bridge thickness

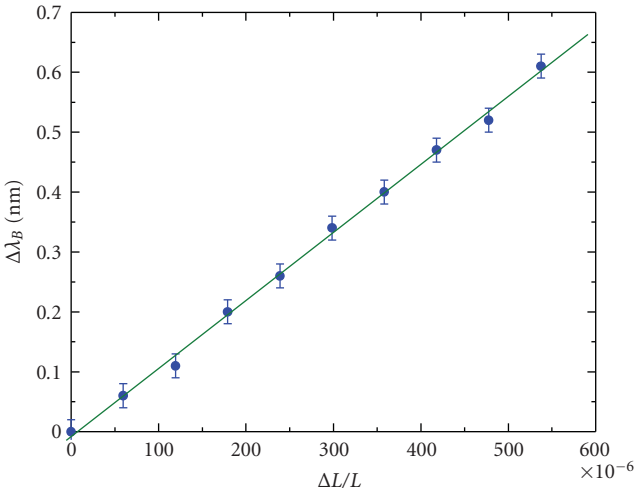

Figure 14: Wavelength shift versus applied longitudinal strain on the Fresnel fibre. No higher-order mode is observed in this fibre [58].

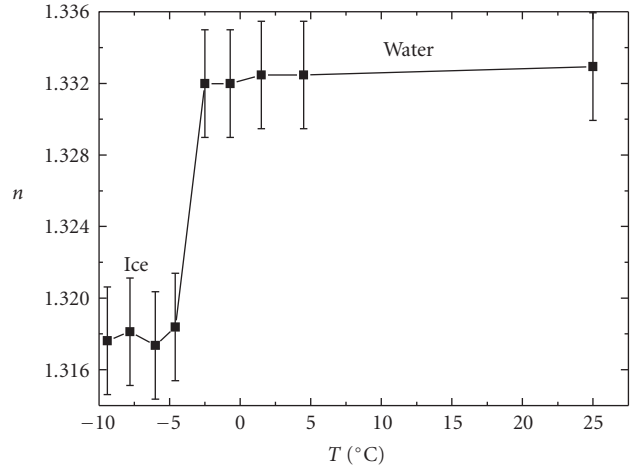

Figure 15: Refractive index measurement of the water and ice 1 h before, during, and after freezing [29].

between the holes but smaller than the core diameter. On the other hand, for less confined modes or when the wavelength of light is commensurate or smaller than the interstitial hole spacing, as well as the core size itself, a periodic lattice provides phase conditions that allow coherent scattering of light and therefore diffractive confinement [85]. This resonant phenomenon has been observed in bending loss tests where light leaks out from the core and is launched into the cladding, generating a short wavelength cutoff in the fibre transmission band [28]. Given that this property is unique to periodically structured optical fibres, it can be exploited in a unique fashion to measure the properties of what is placed into the holes.

The short wavelength cutoff is sensitive to the perturbations applied to the fibre as well as the index of the material within the hole. In fact, such regular coupling of light between the interstitial regions of a regular lattice structured fibre plays a key role in high bend loss characteristic of such fibres [56]. The best way to prevent this is therefore to remove the crystalline regularity of this lattice thereby spoiling the coupling—zero bend loss has been demonstrated using a chirped Fresnel fibre (or fractal fibre) [56]. Such optical fibres were also ideal as the basis for tapered structured fibres for efficient metal free near field microscopy [86], an important tool for diagnostic analysis which removes the problems of plasmon coupling in metal coated tips.

A 1D variation of this diffractive scattering problem was observed within air-clad optical fibres. It arose from the regular corrugations of the surrounding air hole ring [87]. These particular fibres are especially important for astrophotonics and imaging applications because they can have extraordinarily high numerical apertures as a result of approaching the idealised air ring fibre. Recently, careful consideration to the effect on focal ratio degradation (FRD) was reported [88]—whilst no significant impact from diffractive scattering was noted, scattering generally off the corrugated surface was observed to give rise to degradation in FRD.

For the crystal lattice fibre, the corrugations associated with densification gratings produce the necessary coupling to the lattice through scattering [29]. The condition for the wavelength dependence of this scattering will be sensitive to what is in the air channels—in effect a diagnostic tool for measuring refractive index is possible. The refractive index of ice was measured this way, confirming how a simple Bragg condition suffices to describe the processes at short wavelengths. Therefore, the refractive index of the material within the holes, n_h, is given by [29]

$$n_h = \frac{n_{\text{core}} \cos[\sin^{-1}(\lambda m/2n\Lambda)] - x_{\text{SiO}_2} n_{\text{SiO}_2}}{x_h} \quad (3)$$

where $n_{\text{cladding}} = x_h n_h + x_{\text{SiO2}} n_{\text{SiO2}}$, x_{SiO2} and x_h are the fractions of silica and holes that make up the cladding, m is the grating order, Λ is the lattice pitch, and n_{SiO_2} is the index of SiO_2. Figure 15 shows the calculated refractive index of water determined from the transmission band edge shift in the visible to longer wavelengths as a function of temperature. Freezing is observed to occur at a lower temperature than zero, $\sim -3\,^{\circ}\text{C}$, consistent with very high pressures induced within the microchannel. To lower the m.p. of ice by such an amount requires a local pressure >30 Mpa [89], giving an indication of the high effective pressures that can be generated within micro-and nanocapillaries of ice 1 h, which has ~9% volume increase from the liquid state. This has important implications for micro-and nanofluidics. The calculated refractive index for the frozen ice is in agreement within error with that of ice 1 h as expected.

It is also possible to determine the refractive index of a material within the holes by monitoring the effective temperature dependence of an inscribed grating—the index, and its temperature dependence, can be extracted from the effective thermo-optic coefficient (or dn/dT) of the fibre and its effective overlap derived form reference samples used to calibrate the sensor. Such a method was used to determine the thermo-optic coefficient of perfluoroheptane, which was not available in the literature [22]. Figure 16 shows the measurement of effective index change as a function of

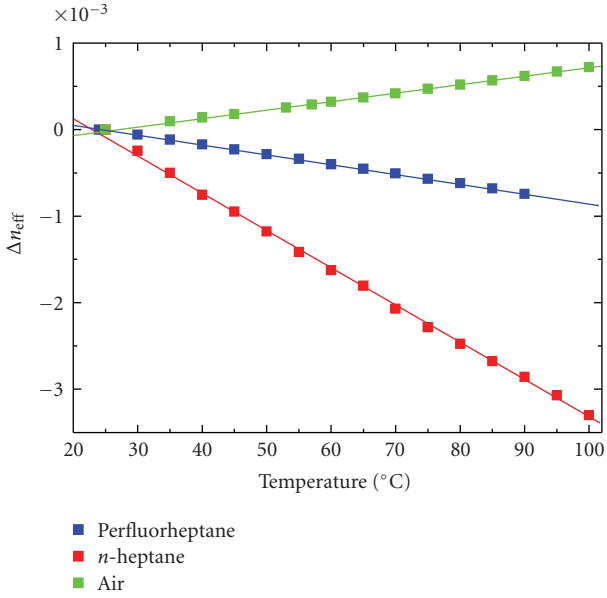

FIGURE 16: Effective index determined from shift in Bragg wavelength as a function of temperature. Heptane is used a reference to determine the actual dn/dT of perfluoroheptane as [22].

temperature for both the unknown perfouroheptane and the known heptane. Substituting H for F in heptane significantly reduces the negative thermo-optic coefficient of the organic molecular system.

7. Other Examples Based on Filling Structured Optical Fibres

Filling of structured optical fibres has already produced simple but interesting all-fibre results. These include the demonstration of substantially enhanced stimulated Raman scattering (SRS) within a photonic bandgap fibre using hydrogen gas [90]. Simply using structured fibres as a cell for direct optical detection of gases such as methane and acetylene has also been demonstrated [91, 92]. For these latter applications it is clear that side access of the fibre, either by etching, laser ablation [93–96], or ion beam processing [97] will become important. Straightforward functional devices using liquid crystals have also been demonstrated, some of which have already been described earlier. A critical factor in taking this relatively straightforward approach to device fabrication to another level that truly differentiates structured optical fibres has been the development of selective filling, initially by filling the core only of a diffractive Fresnel fibre [98]. The techniques for allowing this to be done laid the foundation for the first true material engineering of an optical fibre by superposing the properties of three different materials without mixing them [24], a critical step to demonstrating the feasibility of lab-in-a-fibre technology [25] where multiple functionality, perhaps using all the above examples in the one fibre along with gratings and various other components, becomes possible. Optical localisation at the interface may play a critical role in condensing the feature sizes possible within a complex lab-in-a-fibre system, including the incorporation of semiconductors, polymers, and soft glasses to help raise the index contrast. A schematic of the potential lab-in-a fibre system is shown in Figure 17.

8. Conclusions

The purpose of the paper was to highlight some of the properties of the new generation optical fibres and gratings that are coming to fruition whilst also showing that conventional fibre technologies retain huge potential for further development. Starting with step index structured fibres [20], through to proposed Bragg bandgap fibres [99], demonstrated in structured form [100], to the step-index crystal lattices developed in a similar direction [101] and the subsequent bandgap fiber experimental results [102] based on theoretical designs [103], with later experimental results more convincing [104], to the quasicrystal, zone plate Fresnel fibres [30–34, 84, 105], structured fibres have the potential for extending optical fibre capability well beyond conventional technologies. Nevertheless, the literature database for both conventional and structured optical fibres is now so large and rapidly growing that it is impossible to do fair justice to all examples developed. The select few chosen here, largely air-structured fibres, are aligned with the perspective of exploiting these new trends.

Material science is clearly an increasingly important determinant for application specific devices and systems. Given the wide exploration space into new materials, especially soft glasses and polymers, the paper has focussed specifically on silica-related technologies as these remain by far the most mature and practical with regards to applications within the sensing industries. However, in some areas these other materials (ranging from disposable and soluble cellulose fibres for biodiagnostics [106] through arbitrary structured fibre cross-section using polymer extrusion [107] to soft glasses for infrared operation [108, 109] through to semiconductor optical fibres [110] including new silicon core silica-based fibres [111]) will have an important role to play. In this respect, it is worth digressing and commenting briefly on the next material system heralded for fibre Bragg gratings sensor work: polymer fibres.

Grating writing in other materials is sometimes, in relation to the work done in silica, contentious. Recent demonstrations of gratings in polymer structured fibres, for example, are shown in reflection only because they have been virtually undetectable in transmission [112, 113], similar to initial work in regenerated gratings [64]. Further, in addition to the very large losses associated with these structured polymer fibres, mostly made of polymethylmethacrylate (PMMA), there is evidence that the gratings written into them are made up of periodic UV oxidation of the polymer in air along the fibre—in addition to observable coloration with longer exposures, when nitrogen was used to displace air no gratings were able to be inscribed [113]. In contrast, however, some interesting results in solid polymer fibre with a special photosensitiser such as trans-4-stilbenemethanol [112–115] do promise potential applications in biomedicine

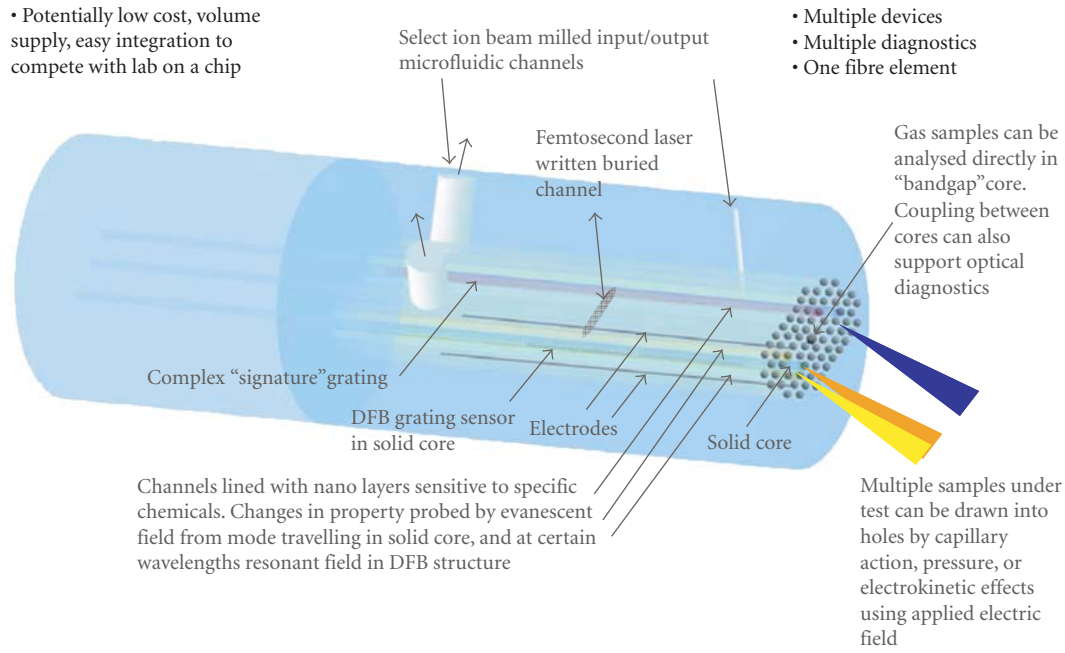

Figure 17: Schematic of multiple functionality within a possible future lab in a fibre.

where some organic compatibility is required. (The issue of biocompatibility is a complex one that needs full peer review within the medical community, particularly given the increased range of materials, and dopants, being proposed for biomedical applications that often involve invasive procedures within organic tissue.) This is significant progress from the first results in polymer fibre [116] where high propagation losses made implementation impossible. It is clear, nonetheless, to anyone who has worked in this area that there still remains enormous materials work to advance polymer fibre gratings to applications. A key problem that has to be investigated is deformation and the impact on long-term performance—this is particularly problematic for structured polymer optical fibres which have been proposed by the author and others for LAN networks. On the other hand, this detrimental aspect of polymer structured optical fibres has been exploited to make effective point sensors for the first force measurements within orthodontic applications [3, 117]. The ability to incorporate polymer (or other materials including silicon [111]) materials within and around silica structured fibres, including photosensitive systems, offers a simple interim solution for biocompatible applications as well as a viable access route to the large strain and thermo-optic coefficients of polymers (recall the use of organic fluids within structured silica fibre for such effects).

With regards to grating writing in soft glasses, this should see relatively straightforward success, since index changes should be easy to achieve using visible laser light to access the band edge and/or specific defect sites, although little work has yet been reported in fibre form. The question of long-term stability, however, will likely pose further material challenges.

The future of the silica fibre Bragg grating, therefore, as the lynch pin for optical fibre sensing looks bright. New writing technologies, such as femtosecond laser processing, continue to be explored—these enable writing in almost any material, for example, and the technologies have been covered in greater detail within other reviews [52, 61–63, 76]. Meanwhile, a structured optical fibre potentially allows, using both air holes and filled glass systems, unprecedented custom tailoring of both a fibre and a gratings properties in terms of genuine composite material engineering. Despite all these new developments and promises, however, type I grating writing within conventional fibres continues to persist as an active starting point for new grating research. Regenerated gratings that operate in excess of 1200 °C are a novel highlight. These "conventional" gratings are particularly attractive as they retain many important practical features of conventional fibres that the new generation of fibres has yet to fulfil: low splice losses, low propagation losses, no interior contamination with breaks, and general overall simplicity and compatibility with existing maintenance technology. Further, the grating writing process using CW 244 nm light remains the most commercially accepted and by far the most advanced, enabling any spectral filter design for numerous applications. On the other hand, new structured fibres offer alternative routes to solve many of the problems of existing conventional fibres. The decision of which technology to use will depend on whether the maturity of practical conventional fibre technology can be outweighed by new functionality that structured fibres offer for a specific application. The optimistic longer-term directions for sensing, epitomised by the potential of lab-in-a-fibre technology, look promising indeed. On the other hand, for many applications simplicity is central to a working

design—a good example that also highlights the potential of structured fibre technology is a simple hydrostatic pressure sensor based on a grating written into a germanosilicate core fibre with two large side holes [118]. Simply breaking the symmetry of the fibre using holes breaks the isotropic response to hydrostatic pressure and allows induced grating birefringence to serve as direct, and effective, monitor of pressure. The sensitivity can obviously be enhanced with a passive or active resonant structure.

Acknowledgments

The author would like to acknowledge various students, staff, and colleagues. In particular the following: Nathaniel Groothoff, Kevin Cook, Michael Stevenson, Jacob Fenton, Mattias Aslund from IPL; Cicero Martelli now at the Mechanical Engineering Department, PUC, Rio Brazil; Hypolito Kalinowski and Alexandre Pohl from the Federal University of Technology, Curitiba, Parana, Brazil; John Holdsworth from the Mathematical and Physical Sciences School, Newcastle University, Newcastle, NSW, Australia; Somnath Bandyopadhyay from the Central Glass and Ceramic Research Institute (CGCRI), Kolkata, India; Henrick Sorenson, formerly Centre COM, DTU, now at Koheras A/S, Denmark, Hans Deyerl formerly Centre COM, DTU, now with Chemnitz university of Technology, Germany, Martin Kristensen formerly Centre COM, DTU, now with iNANO, Arhus university, Denmark and other colleagues from Research Centre COM (now DTU Fotonik, Department of Photonic Engineering, Denmark) and many others. Funding for this work came from the Australian Research Council through its Discovery Project scheme and the Department of Education, Science and Training (DEST), Australia through its International Science Linkages programs.

References

[1] BCC, "Fiber Optic Sensors," (Report code: 1AS002D), 2009, http://www.photonics.com.

[2] H. J. Kalinowski, I. Abeb, J. A. Simõesc, and A. Ramosc, "Application of fibre Bragg grating sensors in biomechanics," in *Trends in Photonics*, J. Canning, Ed., chapter 10, Research Signpost, Kerala, India, 2008.

[3] M. S. Milczewski, J. C. Cardozo da Silva, L. Carvalho, J. Canning, and H. J. Kalinowski, "Optical fiber sensors in dentistry," in *Trends in Photonics*, J. Canning, Ed., chapter 11, Research Signpost, Kerala, India, 2008.

[4] F. I. Baldini and A. G. Mignani, "Biomedical fibre optic sensors," in *Handbook of Optical Fibre Sensing Technology*, J. M. López-Higuera, Ed., Wiley Interscience, Chichester, UK, 2002.

[5] C. Martelli, J. Canning, J. R. Reimers, et al., "Evanescent-field spectroscopy using structured optical fibers: detection of charge-transfer at the porphyrin-silica interface," *Journal of the American Chemical Society*, vol. 131, no. 8, pp. 2925–2933, 2009.

[6] I. Latka, W. Ecke, B. Hoefer, T. Frangen, R. Willsch, and A. Reutlinger, "Micro bending beam based optical fiber grating sensors for physical and chemical measurands," in *Proceedings of the 17th International Conference on Optical Fibre Sensors*, vol. 5855 of *Proceedings of SPIE*, pp. 94–97, Bruges, Belgium, May 2005.

[7] W. Du, X. M. Tao, H. Y. Tam, and C. L. Choy, "Fundamentals and applications of optical fiber Bragg grating sensors to textile structural composites," *Composite Structures*, vol. 42, no. 3, pp. 217–229, 1998.

[8] R. Willsch, W. Ecke, and H. Bartelt, "Optical fiber grating sensor networks and their application in electric power facilities, aerospace and geotechnical engineering," in *Proceedings of the 15th Optical Fiber Sensors Conference Technical Digest (OFS '02)*, pp. 49–54, Portland, Ore, USA, May 2002.

[9] B. Lee, "Review of the present status of optical fiber sensors," *Optical Fiber Technology*, vol. 9, no. 2, pp. 57–79, 2003.

[10] I. Latka, W. Ecke, B. Höfer, C. Chojetzki, and A. Reutlinger, "Fiber optic sensors for the monitoring of cryogenic spacecraft tank structures," in *Photonics North 2004: Photonic Applications in Telecommunications, Sensors*, vol. 5579 of *Proceedings of SPIE*, pp. 195–204, Ottawa, Canada, November 2004.

[11] W. Ecke, K. Schroeder, M. Kautz, et al., "On-line characterization of impacts on electrical train current collectors using integrated optical fiber grating sensor network," in *Smart Structures and Materials 2005: Smart Sensor Technology and Measurement Systems*, vol. 5758 of *Proceedings of SPIE*, pp. 114–123, San Diego, Calif, USA, March 2005.

[12] K. Schroeder, W. Ecke, J. Apitz, E. Lembke, and G. Lenschow, "A fibre Bragg grating sensor system monitors operational load in a wind turbine rotor blade," *Measurement Science and Technology*, vol. 17, no. 5, pp. 1167–1172, 2006.

[13] J. C. Cardozo da Silva, C. Martelli, H. J. Kalinowski, E. Penner, J. Canning, and N. Groothoff, "Dynamic analysis and temperature measurements of concrete cantilever beam using fibre Bragg gratings," *Optics and Lasers in Engineering*, vol. 45, no. 1, pp. 88–92, 2007.

[14] A. C. L. Wong, P. A. Childs, R. Berndt, T. Macken, G.-D. Peng, and N. Gowripalan, "Simultaneous measurement of shrinkage and temperature of reactive powder concrete at early-age using fibre Bragg grating sensors," *Cement and Concrete Composites*, vol. 29, no. 6, pp. 490–497, 2007.

[15] H. Soejima, T. Ogisu, H. Yoneda, Y. Okabe, N. Takeda, and Y. Koshioka, "Demonstration of detectability of SHM system with FBG/PZT hybrid system in composite wing box structure," in *Sensors and Smart Structures Technologies for Civil, Mechanical, and Aerospace Systems*, vol. 6932 of *Proceedings of SPIE*, San Diego, Calif, USA, March 2008.

[16] V. G. M. Annamdas, Y. Yang, and H. Liu, "Current development in fiber Bragg grating sensors and their applications," in *Sensors and Smart Structures Technologies for Civil, Mechanical, and Aerospace Systems*, vol. 6932 of *Proceedings of SPIE*, San Diego, Calif, USA, March 2008.

[17] M. Majumder, T. K. Gangopadhyay, A. K. Chakraborty, K. Dasgupta, and D. K. Bhattacharya, "Fibre Bragg gratings in structural health monitoring—present status and applications," *Sensors and Actuators A*, vol. 147, no. 1, pp. 150–164, 2008.

[18] J. A. Epaarachchi, J. Canning, and M. Stevenson, "Investigation of the response of embedded Near Infrared FBG (830 nm) sensors in glass fibre composites," in *Proceedings of 19th International Conference on Optical Fibre Sensors*, vol. 7004 of *Proceedings SPIE*, 2008.

[19] A. C. L. Wong, P. A. Childs, and G.-D. Peng, "Spectrally coded multiplexing techniques in fibre-optic sensor systems,"

in *Trends in Photonics*, J. Canning, Ed., chapter 8, Research Signpost, Kerala, India, 2008.

[20] P. Kaiser and H. W. Astle, "Low-loss single-material fibers made from pure fused silica," *Bell System Technical Journal*, vol. 53, no. 6, pp. 1021–1039, 1974.

[21] K. Digweed-Lyytikainen, C. A. de Francisco, D. Spadoti, et al., "Photonic crystal optical fibers for dispersion compensation and Raman amplification: design and experiment," *Microwave and Optical Technology Letters*, vol. 49, no. 4, pp. 872–874, 2007.

[22] H. R. Sørenson, J. Canning, J. Lægsgaard, K. Hansen, and P. Varming, "Control of the wavelength dependent thermo-optic coefficients in structured fibres," *Optics Express*, vol. 14, no. 14, pp. 6428–6433, 2006.

[23] N. Mothe, D. Pagnoux, H. Phan, et al., "Thermal wavelength stabilization of Bragg gratings photowritten in hole-filled microstructured optical fibers," *Optics Express*, vol. 16, no. 23, pp. 19018–19033, 2008.

[24] J. Canning, M. Stevenson, T. K. Yip, S. K. Lim, and C. Martelli, "White light sources based on multiple precision selective micro-filling of structured optical waveguides," *Optics Express*, vol. 16, no. 20, pp. 15700–15708, 2008.

[25] J. Canning, "New trends in structured optical fibres for telecommunications and sensing," in *Proceedings of the 5th International Conference on Optical Communications and Networks and the 2nd International Symposium on Advances and Trends in Fiber Optics and Applications (ICOCN/ATFO '06)*, Chengdu, China, 2006.

[26] C. Martelli, J. Canning, and B. Ashton, "Add drop gas reference cell with acetylene," in *Proceedings of the Optical Fiber Sensors Conference (OFS '06)*, Cancun, Mexico, 2006.

[27] A. Bjarklev, J. Broeng, and A. S. Bjarklev, *Photonic Crystal Fibres*, Kluwer Academic Publishers, Dordrecht, The Netherlands, 2003.

[28] D. Kácik, I. Turek, I. Martincek, J. Canning, and K. Lyytikäinen, "The role of diffraction in determining the short wavelength losses edge of photonic crystal fibres," in *Proceedings of the Australian Conference on Optical Fibre Technology (ACOFT '05)*, Sydney, Australia, 2005.

[29] C. Martelli, J. Canning, M. Kristensen, and N. Groothoff, "Refractive index measurement within a photonic crystal fibre based on short wavelength diffraction," *Sensors*, vol. 7, no. 11, pp. 2492–2498, 2007.

[30] J. Canning, "Fresnel optics inside optical fibres," in *Photonics Research Developments*, Nova Science Publishers, Hauppauge, NY, USA, 2009.

[31] J. Canning, E. Buckley, and K. Lyytikäinen, "Propagation in air by field superposition of scattered light within a Fresnel fibre," *Optics Letters*, vol. 28, no. 4, pp. 2330–2332, 2003.

[32] J. Canning, E. Buckley, and K. Lyytikäinen, "Multiple source generation using air-structured optical waveguides for optical field shaping and transformation within and beyond the waveguide," *Optics Express*, vol. 11, no. 4, pp. 347–358, 2003.

[33] J. Canning, E. Buckley, and K. Lyytikäinen, "All-fibre phase-aperture zone plate fresnel lenses," *Electronics Letters*, vol. 39, no. 3, pp. 311–312, 2003.

[34] C. Martelli and J. Canning, "Fresnel fibres with core-defects for optical sensing," in *Proceedings of Optical Fiber Sensors Conference (OFS '06)*, Cancun Mexico, 2007, postdeadline paper, reproduced in C. Martelli, *PhD dissemination*, University of Sydney, 2007.

[35] V. R. Almeida, Q. Xu, C. A. Barrios, and M. Lipson, "Guiding and confining light in void nanostructure," in *Optics Letters*, vol. 29, no. 11, pp. 1209–1211, June 2004.

[36] B. Schmidt, V. Almeida, C. Manolatou, S. Preble, and M. Lipson, "Nanocavity in a silicon waveguide for ultrasensitive nanoparticle detection," *Applied Physics Letters*, vol. 85, no. 21, pp. 4854–4856, 2004.

[37] N. Skivesen, A. Têtu, M. Kristensen, J. Kjems, L. H. Frandsen, and P. I. Borel, "Photonic-crystal waveguide biosensor," *Optics Express*, vol. 15, no. 6, pp. 3169–3176, 2007.

[38] N. Skivesen, J. Canning, M. Kristensen, C. Martelli, A. Tetu, and L. H. Frandsen, "Photonic crystal waveguide-based biosensor," in *Proceedings of Optical Fiber Communication/National Fiber Optic Engineers Conference (OFC/NFOEC '08)*, pp. 1–3, San Diego, Calif, USA, February 2008.

[39] G. S. Wiederhecker, C. M. B. Cordeiro, F. Couny, et al., "Field enhancement within an optical fibre with a subwavelength air core," *Nature Photonics*, vol. 1, no. 2, pp. 115–118, 2007.

[40] C. M. Rollinson, S. M. Orbons, S. T. Huntington, et al., "Metal-free scanning optical microscopy with a fractal fiber probe," *Optics Express*, vol. 17, no. 3, pp. 1772–1780, 2009.

[41] C. Martelli, J. Canning, and K. Lyytikäinen, "Water core Fresnel fibre," *Optics Express*, vol. 13, no. 10, pp. 3890–3895, 2005.

[42] S. Donati, *Electro-Optical Instrumentation: Sensing and Measuring with Lasers*, Prentice-Hall, Englewood Cliffs, NJ, USA, 2004.

[43] U. C. Paek and C. R. Kurkjian, "Calculation of cooling rate and induced stresses in drawing of optical fibers," *Journal of the American Ceramic Society*, vol. 58, no. 7-8, pp. 330–335, 1975.

[44] G. W. Scherer and A. R. Cooper, "Thermal stresses in clad-glass fibers," *Journal of the American Ceramic Society*, vol. 63, no. 5-6, pp. 346–347, 1980.

[45] Y. Park, T.-J. Ahn, Y. H. Kim, W.-T. Han, U.-C. Paek, and D. Y. Kim, "Measurement method for profiling the residual stress and the strain-optic coefficient of an optical fiber," *Applied Optics*, vol. 41, no. 1, pp. 21–26, 2002.

[46] B. H. Kim, Y. Park, D. Y. Kim, U. C. Paek, and W.-T. Han, "Observation and analysis of residual stress development resulting from OH impurity in optical fibers," *Optics Letters*, vol. 27, no. 10, pp. 806–808, 2002.

[47] O. V. Mazurin, M. V. Streltsina, and T. P. Shvaiko-Shvaikovskaya, *Handbook of Glass Data Part A: Silica Glass and Binary Silicate Glasses*, vol. 15 of *Physical Sciences Data*, Elsevier, Amsterdam, The Netherlands, 1983.

[48] J. Bland-Hawthorn, M. Englund, and G. Edvell, "New approach to atmospheric OH suppression using an aperiodic fibre Bragg grating," *Optics Express*, vol. 12, no. 24, pp. 5902–5909, 2004.

[49] B. Leconte, W.-X. Xie, M. Douay, et al., "Analysis of color-center-related contribution to Bragg grating formation in Ge:SiO_2 fiber based on a local Kramers-Kronig transformation of excess loss spectra," *Applied Optics*, vol. 36, no. 24, pp. 5923–5930, 1997.

[50] H. G. Limberger, P.-Y. Fonjallaz, R. P. Salathé, and F. Cochet, "Compaction- and photoelastic-induced index changes in fiber Bragg gratings," *Applied Physics Letters*, vol. 68, no. 22, pp. 3069–3071, 1996.

[51] N. H. Ky, H. G. Limberger, R. P. Salathé, F. Cochet, and L. Dong, "UV-irradiation induced stress and index changes during the growth of type-I and type-IIA fiber gratings," *Optics Communications*, vol. 225, no. 4–6, pp. 313–318, 2003.

[52] J. Canning, "Fibre gratings and devices for sensors and laser," *Laser and Photonics Reviews*, vol. 2, no. 4, pp. 275–289, 2008.

[53] P. K. Bachmann, W. Hermann, H. Wehr, and D. U. Wiechert, "Stress in optical waveguides. 1: preforms," *Applied Optics*, vol. 25, no. 7, pp. 1093–1098, 1986.

[54] P. K. Bachmann, W. Hermann, H. Wehr, and D. U. Wiechert, "Stress in optical waveguides. 2: fibers," *Applied Optics*, vol. 26, no. 7, pp. 1175–1182, 1987.

[55] J. Canning, M. Stevenson, S. Bandyopadhyay, and K. Cook, "Extreme silica optical fibre gratings," *Sensors*, vol. 8, no. 10, pp. 6448–6452, 2008.

[56] C. Martelli, J. Canning, B. Gibson, and S. Huntington, "Bend loss in structured optical fibres," *Optics Express*, vol. 15, no. 26, pp. 17639–17644, 2007.

[57] N. Groothoff, J. Canning, E. Buckley, K. Lyttikainen, and J. Zagari, "Bragg gratings in air-silica structured fibers," *Optics Letters*, vol. 28, no. 4, pp. 233–235, 2003.

[58] N. Groothoff, C. Martelli, J. Canning, and K. Lyytikäinen, "Fibre Bragg grating in Fresnel fibre with temperature and strain characterisation," in *Proceedings of Australian Conference on Optical Fibre Technology (ACOFT '05)*, Sydney, Australia, 2005.

[59] J. Albert, B. Malo, F. Bilodeau, et al., "Photosensitivity in Ge-doped silica optical waveguides and fibers with 193-nm light from an ArF excimer laser," *Optics Letters*, vol. 19, no. 6, pp. 387–389, 1994.

[60] J. Canning, H. G. Inglis, M. G. Sceats, and P. Hill, "Transient and permanent gratings in phosphosilicate optical fibers produced by the flash condensation technique," *Optics Letters*, vol. 20, p. 2189, 1995.

[61] J. Canning, "Gratings and grating devices in structured fibres using 193nm from an ArF laser," in *Proceedings of the OSA Topical Meeting: Bragg Gratings, Photosensitivity and Poling (BGPP '07)*, Quebec City, Canada, 2007, (invited).

[62] J. Canning, Ed., *Proceedings of the 1st International Workshop on Multiphoton Processes in Glass and Glassy Materials*, Darlington Centre, University of Sydney, Sydney, Australia.

[63] S. J. Mihailov, D. Grobnic, C. W. Smelser, P. Lu, R. B. Walker, and H. Ding, "Bragg grating inscription using femtosecond laser sources," in *Trends in Photonics*, J. Canning, Ed., chapter 4, Research Signpost, Kerala, India, 2008.

[64] B. Zhang and M. Kahriziet, "High temperature resistance fiber Bragg grating temperature sensor fabrication," *IEEE Sensors Journal*, vol. 7, pp. 586–590, 2007.

[65] S. Bandyopadhyay, J. Canning, M. Stevenson, and K. Cook, "Ultra-high temperature regenerated gratings in boron codoped germanosilicate optical fibre using 193 nm," *Optics Letters*, vol. 33, no. 16, pp. 1917–1919, 2008.

[66] M. Fokine, "Formation of thermally stable chemical composition gratings in optical fibers," *Journal of the Optical Society of America B*, vol. 19, no. 8, pp. 1759–1765, 2002.

[67] H. Dobb, K. Kalli, and D. J. Webb, "Temperature-insensitive long period grating sensors in photonic crystal fibre," *Electronics Letters*, vol. 40, no. 11, pp. 657–658, 2004.

[68] A. Michie, J. Canning, K. Lyytikäinen, M. Åslund, and J. Digweed, "Temperature independent highly birefringent photonic crystal fibre," *Optics Express*, vol. 12, no. 21, pp. 5160–5165, 2004.

[69] D.-H. Kim and J. U. Kang, "Sagnac loop interferometer based on polarization maintaining photonic crystal fiber with reduced temperature sensitivity," *Optics Express*, vol. 12, no. 19, pp. 4490–4495, 2004.

[70] C.-L. Zhao, X. Yang, C. Lu, W. Jin, and M. S. Demokan, "Temperature-insensitive interferometer using a highly birefringent photonic crystal fiber loop mirror," *IEEE Photonics Technology Letters*, vol. 16, no. 11, pp. 2535–2537, 2004.

[71] M. J. F. Digonnet, H. K. Kim, S. Blin, V. Dangui, and G. S. Kino, "Sensitivity and stability of an air-core fiber-optic gyroscope," in *Optical Fiber Sensors*, OSA Technical Digest (CD), Optical Society of America, 2006, paper ME1.

[72] A. Michie, J. Canning, I. Bassett, et al., "Spun elliptically birefringent photonic crystal fibre," *Optics Express*, vol. 15, no. 4, pp. 1811–1816, 2007.

[73] X. Dong, H. Y. Tam, and P. Shum, "Temperature-insensitive strain sensor with polarization-maintaining photonic crystal fiber based Sagnac interferometer," *Applied Physics Letters*, vol. 90, no. 15, Article ID 151113, 3 pages, 2007.

[74] D. Káčik, I. Turek, I. Martinček, J. Canning, N. A. Issa, and K. Lyytikäinen, "Intermodal interference in a photonic crystal fibre," *Optics Express*, vol. 12, no. 15, pp. 3465–3470, 2004.

[75] J. Villatoro, V. Finazzi, V. P. Minkovich, V. Pruneri, and G. Badenes, "Temperature-insensitive photonic crystal fiber interferometer for absolute strain sensing," *Applied Physics Letters*, vol. 91, no. 9, Article ID 091109, 2007.

[76] N. Groothoff, C. Martelli, and J. Canning, "A dual wavelength distributed feedback fibre laser," *Journal of Applied Physics*, vol. 103, Article ID 013101, 2008.

[77] J. Canning, N. Groothoff, K. Cook, et al., "Gratings in structured optical fibres," *Laser Chemistry*, vol. 2008, Article ID 239417, 2008.

[78] C. K. Kirkendall and A. Dandridge, "Overview of high performance fibre-optic sensing," *Journal of Physics D*, vol. 37, no. 18, pp. R197–R216, 2004.

[79] S. Foster, A. Tikhomirov, M. Englund, H. Inglis, G. Edvell, and M. Milnes, "A 16 channel fibre laser sensor array," in *Proceedings of the Australian Conference on Optical Fibre Technology (ACOFT '06)*, pp. 40–42, Melbourne, Australia, 2006.

[80] C. Martelli, J. Canning, N. Groothoff, and K. Lyytikäinen, "Strain and temperature characterization of photonic crystal fiber Bragg gratings," *Optics Letters*, vol. 30, no. 14, pp. 1785–1787, 2005.

[81] M. Janos and J. Canning, "Permanent and transient resonances thermally induced in optical fibre Bragg gratings," *Electronics Letters*, vol. 31, no. 12, pp. 1007–1009, 1995.

[82] D. Ferrarini, L. Vincetti, M. Zoboli, A. Cucinotta, and S. Selleri, "Leakage properties of photonic crystal fibers," *Optics Express*, vol. 10, no. 23, pp. 1314–1319, 2002.

[83] K. Lyytikäinen, *Control of complex structural geometry in optical fibre drawing*, Ph.D. thesis, School of Physics and Interdisciplinary Photonics Laboratories, The University of Sydney, Sydney, Australia, 2004.

[84] C. Martelli, J. Canning, N. Groothoff, and K. Lyttikainen, "Bragg gratings in photonic crystal fibres: strain and temperature characterisation," in *Proceedings of the 17th International Conference on Optical Fibre Sensors*, M. Voet, R. Willsch, W. Ecke, J. Jones, and B. Culshaw, Eds., vol. 5855 of *Proceedings of SPIE*, Bellingham, Wash, USA, 2005.

[85] J. Canning, "Diffraction-free mode generation and propagation in optical waveguides," *Optics Communications*, vol. 207, no. 1–6, pp. 35–39, 2002.

[86] C. M. Rollinson, S. M. Orbons, S. T. Huntington, et al., "Metal-free scanning optical microscopy with a fractal fibre probe," *Optics Express*, vol. 17, no. 3, pp. 1772–1780, 2009.

[87] M. Åslund, J. Canning, S. D. Jackson, A. Teixeira, and K. Lyytikäinen, "Diffraction in air-clad fibres," *Optics Express*, vol. 13, no. 14, pp. 5227–5233, 2005.

[88] M. Åslund and J. Canning, "Air-clad fibres for astronomical instrumentation: focal-ratio degradation," *Experimental Astronomy*, vol. 24, no. 1–3, pp. 1–7, 2009.

[89] V. F. Petrenko and R. W. Whitworth, *Physics of Ice*, Oxford University Press, New York, NY, USA, 2002.

[90] F. Benabid, J. C. Knight, G. Antonopoulos, and P. St. J. Russell, "Stimulated Raman scattering in hydrogen-filled hollow-core photonic crystal fiber," *Science*, vol. 298, no. 5592, pp. 399–402, 2002.

[91] T. Ritari, J. Tuominen, H. Ludvigsen, et al., "Gas sensing using air-guiding photonic bandgap fibers," *Optics Express*, vol. 12, no. 17, pp. 4080–4087, 2004.

[92] Y. L. Hoo, W. Jin, H. L. Ho, J. Ju, and D. N. Wang, "Gas diffusion measurement using hollow-core photonic bandgap fiber," *Sensors and Actuators B*, vol. 105, no. 2, pp. 183–186, 2005.

[93] J. Canning, E. Buckley, N. Groothoff, B. Luther-Davies, and J. Zagari, "UV laser cleaving of air-polymer structured fibre," *Optics Communications*, vol. 202, no. 1–3, pp. 139–143, 2002.

[94] J. Canning, E. Buckley, N. Groothoff, and S. Huntington, "Laser sculpting and shaping of air-polymer structured fibres," in *Proceedings Australian Conference on Optical Fibre Technology (ACOFT '03)*, Melbourne, Australia, 2003.

[95] H. Lehmann, S. Brueckner, J. Kobelke, G. Schwotzer, K. Schuster, and R. Willsch, "Toward photonic crystal fiber based distributed chemosensors," in *Proceedings of the 17th International Conference on Optical Fibre Sensors*, vol. 5855 of *Proceedings of SPIE*, pp. 419–422, 2005.

[96] Y. Lai, K. Zhou, L. Zhang, and I. Bennion, "Fabrication of micro-channels in optical fibers using femtosecond laser pulses and selective chemical etching," *Optics Letters*, vol. 31, p. 2559, 2006.

[97] C. Martelli, P. Olivero, J. Canning, N. Groothoff, B. Gibson, and S. Huntington, "Micromachining structured optical fibres using focussed ion beam (FIB) milling," *Optics Letters*, vol. 32, no. 12, pp. 1575–1577, 2007.

[98] C. Martelli, J. Canning, and K. Lyytikainen, "Water core Fresnel fibre," *Optics Express*, vol. 13, no. 10, pp. 3890–3895, 2005.

[99] P. Yeh, A. Yariv, and E. Maron, "Theory of Bragg fiber," *Journal of the Optical Society of America*, vol. 68, no. 9, pp. 1196–1201, 1978.

[100] G. Vienne, Y. Xu, C. Jakobsen, et al., "Ultra-large bandwidth hollow-core guiding in all-silica Bragg fibers with nano-supports," *Optics Express*, vol. 12, no. 15, pp. 3500–3508, 2004.

[101] J. Knight, T. Birks, P. St. J. Russell, and D. M. Atkins, "All-silica singlemode optical fiber with photonic crystal cladding," *Optics Letters*, vol. 21, no. 19, pp. 1547–1549, 1996.

[102] J. C. Knight, J. Broeng, T. A. Birks, and P. St. J. Russell, "Photonic band gap guidance in optical fibers," *Science*, vol. 282, no. 5393, pp. 1476–1478, 1998.

[103] J. Broeng, S. E. Barkou, and A. Bjarklev, "Waveguiding by the photonic bandgap effect," in *Proceedings of the Topical Meeting on Electromagnetic Optics*, pp. 67–68, EOS, hyeres, France, 1998.

[104] N. Venkataramn, M. T. Gallagher, C. M. Smith, et al., "Low loss (13dB/km) air core photonic bandgap fibre," in *Proceedings of the European Conference on Optical Communications (ECOC '02)*, Copenhagen, Denmark, 2002, PD1.1.

[105] C. Martelli and J. Canning, "Fresnel fibres with omni-directional zone cross-sections," *Optics Express*, vol. 15, no. 7, pp. 4281–4286, 2007.

[106] A. Dupuis, N. Guo, Y. Gao, et al., "Prospective for biodegradable microstructured optical fibers," *Optics Letters*, vol. 32, no. 2, pp. 109–111, 2007.

[107] M. Mignanelli, K. Wani, J. Ballato, S. Foulger, and P. Brown, "Polymer microstructured fibers by one-step extrusion," *Optics Express*, vol. 15, no. 10, pp. 6183–6189, 2007.

[108] J. S. Sanghera and I. D. Aggarwal, Eds., *Infrared Fiber Optics*, CRC Press, Boca Raton, Fla, USA, 1998.

[109] H. Ebendorff-Heidepriem and T. M. Monro, "Extrusion of complex preforms for microstructured optical fibers," *Optics Express*, vol. 15, no. 23, pp. 15086–15092, 2007.

[110] S. D. Hart, G. R. Maskaly, B. Temelkuran, P. H. Prideaux, J. D. Joannopoulos, and Y. Fink, "External reflection from omnidirectional dielectric mirror fibers," *Science*, vol. 296, no. 5567, pp. 510–513, 2002.

[111] J. Ballato, T. Hawkins, P. Foy, et al., "Silicon optical fiber," *Optics Express*, vol. 16, no. 23, pp. 18675–18683, 2008.

[112] D. Webb, in *Proceedings of the 1st Asia Pacific Optical Fibre Sensors Conference (APOS '08)*, Chengdu, China, 2008, invited talk.

[113] C. Zhang, K. Carroll, D. J. Webb, et al., "Recent progress in polymer optical fibre gratings," in *Proceedings of the 19th International Conference on Optical Fibre Sensors*, vol. 7004 of *Proceedings of SPIE*, April 2008.

[114] J. M. Yu, X. M. Tao, and H. Y. Tam, "Trans-4-stilbenemethanol-doped photosensitive polymer fibers and gratings," *Optics Letters*, vol. 29, no. 2, pp. 156–158, 2004.

[115] X.-M. Tao, J.-M. Yu, and H.-Y. Tam, "Photosensitive polymer optical fibres and gratings," *Transactions of the Institute of Measurement and Control*, vol. 29, no. 3-4, pp. 255–270, 2007.

[116] H. Y. Liu, H. B. Liu, G. D. Peng, and P. L. Chu, "Observation of type I and type II gratings behavior in polymer optical fiber," *Optics Communications*, vol. 220, no. 4–6, pp. 337–343, 2003.

[117] M. S. Milczeswki, H. J. Kalinowski, J. C. C. Silva, J. A. Simões, J. Canning, and C. Martelli, "Determination of orthodontics forces using optic fibre sensors," in *Proceedings of the 83rd Congress of the European Orthodontics Society (EOS '07)*, Berlin, Germany, 2007.

[118] C. Jewart, K. P. Chen, B. McMillen, et al., "Sensitivity enhancement of fiber Bragg gratings to transverse stress by using microstructural fibers," *Optics Letters*, vol. 31, no. 15, pp. 2260–2262, 2006.

Hindawi Publishing Corporation
Journal of Sensors
Volume 2009, Article ID 747803, 11 pages
doi:10.1155/2009/747803

Review Article

Highly Sensitive Sensors Based on Photonic Crystal Fiber Modal Interferometers

Joel Villatoro,[1] Vittoria Finazzi,[1] Gonçal Badenes,[1] and Valerio Pruneri[1,2]

[1] *Institut de Ciencies Fotoniques (ICFO), Mediterranean Technology Park, Castelldefels, 08860 Barcelona, Spain*
[2] *Institució Catalana de Recerca i Estudis Avançats (ICREA), 08010 Barcelona, Spain*

Correspondence should be addressed to Joel Villatoro, joel.villatoro@icfo.es

Received 23 March 2009; Accepted 19 May 2009

Recommended by Christos Riziotis

We review the research on photonic crystal fiber modal interferometers with emphasis placed on the characteristics that make them attractive for different sensing applications. The fabrication of such interferometers is carried out with different post-processing techniques such as grating inscription, tapering or cleaving, and splicing. In general photonic crystal fiber interferometers exhibit low thermal sensitivity while their applications range from sensing strain or temperature to refractive index and volatile organic compounds.

1. Introduction

Optical interferometers have played an important role in both fundamental and applied research during the past two centuries. The famous Young's double-slit experiment, for example, provided experimental support to the wave theory of light which had important consequences in physics, optics, and science in general. On the other hand, Abraham Michelson demonstrated the high resolution of an interferometer when it is used for metrology applications.

Fiber optics technology offers many degrees of freedom and some advantages such as stability, compactness, and no moving parts, for the construction of different types of interferometers [1–3]. Different types of fibers exist and can be used to build interferometers. Two different approaches are commonly followed. One consists of splitting and recombining two monochromatic optical beams that propagate in different fibers. These two-arm interferometers typically require several meters of optical fibers and one or two couplers [1–3]. The other approach consists of exploiting the relative phase displacement between two modes, typically the first two modes like the LP_{01} and LP_{11}, or the HE_{11} and HE_{21}. Interferometers based on the latter approach are known as *modal interferometers*. These have inherent advantages when compared to their two-arm counterparts. Since the modes propagate in the same path, the susceptibility to environmental fluctuations is reduced. In addition, one requires controlling only two or more modes. The compactness and simplicity of modal interferometers have gained considerable attention in many research groups. Here we review the different alternatives reported so far to construct all-fiber modal interferometers with photonic crystal fibers (PCFs). These fibers are characterized by a complex pattern of microscopic air-holes in the transverse plane that runs all over the fiber [4, 5]. The holey structure gives PCFs unique guiding mechanisms and modal properties that are not possible with conventional optical fibers. For this reason we focus only on PCF modal interferometers.

The unique properties of PCFs have intrigued the sensor community. Many research groups around the world have investigated different schemes which exploit the properties or structure of PCFs with a view to developing new optical sensors. Like a conventional optical fiber the propagation properties of a PCF can be modulated by external parameters such as strain, temperature, and pressure. However, they can also be modulated with liquids or gases infiltrated into the voids of the PCF, see for example [6]. It is, therefore, desirable to investigate new schemes which exploit the properties of PCFs with a view to developing new optical sensors. The construction of PCF-based interferometers in particular is interesting owing to their proven high sensitivity

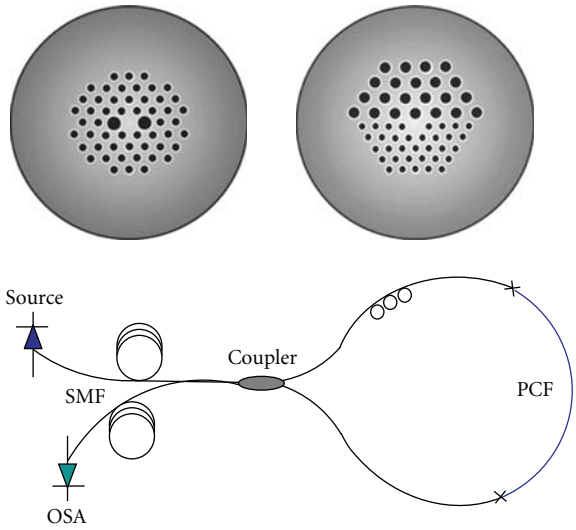

Figure 1: The top figures show the cross-sections of polarization maintaining PCF (top-left) or high birefringence PCF (top-right), taken from [6]. The bottom drawing is a diagram of the Sagnac interferometer. OSA stands for optical spectrum analyzer, SMF for single mode fiber, and PCF for photonic crystal fiber.

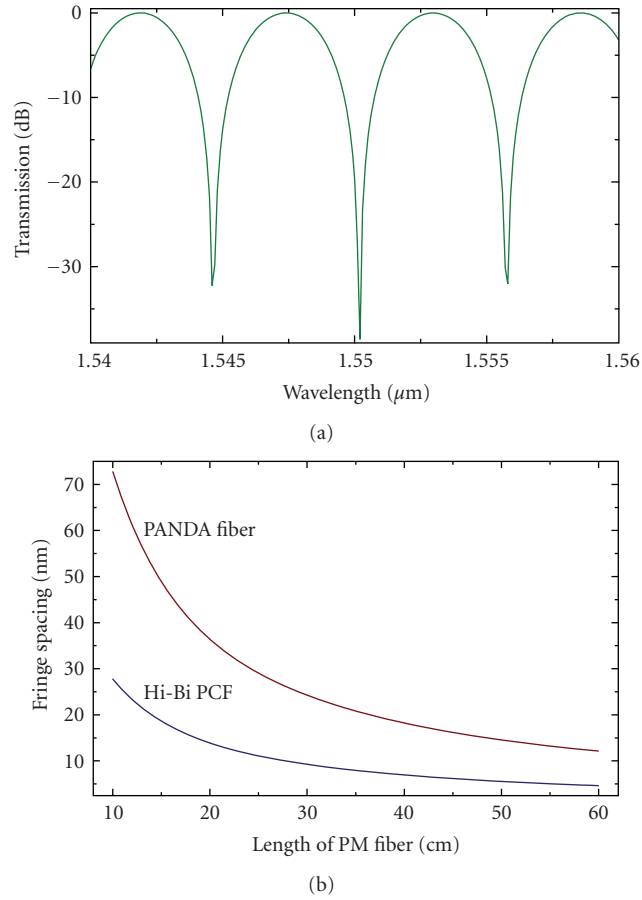

Figure 2: (a) Theoretical transmission spectrum of a Sagnac interferometer built with 500 mm of Hi-Bi PCF described in [15]. (b) Fringe spacing as a function of the length of fiber. The period of a Sagnac interferometer built with PANDA fiber is also shown for comparison.

and their broad range of applications. To the authors' best knowledge, the first attempt to construct an interferometer with a PCF was reported in 2001 by MacPherson et al. [7]. They used a dual-core photonic crystal fiber in which the two cores played the role of arms of a Mach-Zehnder interferometer. Since then other authors have reported a variety of interferometers built with different types of PCFs in which the relative phase displacement between two modes is exploited.

Two modes can be excited in a short piece of PCF or standard optical fiber under critical launching and polarization conditions which is impractical for optical sensing [8–13]. To overcome these drawbacks, the microstructure of the PCF can be designed to support only two modes [14], or to use long period gratings, tapering, or splicing techniques. The interesting features of PCF modal interferometers built with the later techniques are compactness, low temperature sensitivity, broad operation wavelength range, and high stability over time. All these properties are important for unambiguous measurement of the interferometer phase, and hence the parameter being sensed. The different approaches to build compact modal interferometers with PCFs will be reviewed in the following paragraphs placing emphasis on the characteristics that make them attractive for different sensing applications.

2. PCFs in Fiber Loop Mirrors

One configuration that has been widely explored consists of a structure where a relatively short length of polarization maintaining (PM) or high birefringence (Hi-Bi) PCF is inserted in a fiber loop mirror, see Figure 1. This configuration is also known as Sagnac interferometer. Basically, in this interferometer the input wave is split into two by the 3-dB coupler. The two modes counterpropagate through the same waveguide and then they are subsequently recombined by the same coupler. The resulting transmission spectrum is determined by the relative phase difference introduced to the two orthogonal guided modes. The phase difference between the modes depends on the wavelength, the group birefringence, and the length of the HiBi or PM fiber. The interference of the counterpropagating modes will be constructive or destructive, depending principally on the birefringence of the waveguide. The transmission spectrum of the Sagnac interferometer is approximately a periodic function of the wavelength. The average wavelength spacing ($\Delta\lambda$) between consecutive transmission peaks is $\Delta\lambda \approx \lambda^2/(\Delta n_g L)$, being λ the wavelength, Δn_g the group birefringence of the HiBi fiber, and L the length of Hi-Bi or PM PCF. An additional advantage of the Sagnac interferometer is that it typically exhibits high extinction ratio which is useful to track the position of the interference peaks.

Figure 2 shows the theoretical transmission spectrum over 20 nm of a Sagnac interferometer built with 50 cm

of commercially available Hi-Bi PCF which has $\Delta n_g = 8.65 \times 10^{-4}$ for $\lambda = 1550\,\text{nm}$, see [15]. The calculated fringe spacing as a function of the length of PCF is also shown. For comparison the corresponding $\Delta\lambda$ for a Sagnac interferometer built with PM fiber, commercially known as PANDA fiber ($\Delta n_g = 3.3 \times 10^{-4}$ for $\lambda = 1550\,\text{nm}$), is also given in the figure. Since the birefringence of Hi-Bi PCFs is in general larger than that of conventional Hi-Bi fibers then Sagnac interferometers will exhibit much shorter periods than their counterparts built with standard optical fibers. This property helps to construct more compact Sagnac interferometers with PCFs.

Note that the two interfering modes in the Sagnac interferometers are exposed to the same environment. This makes the interferometer insensitive to ambient temperature. Unlike conventional polarization maintaining fibers (bow-tie, elliptical core, or PANDA), which contain at least two different glasses each with a different thermal expansion coefficient, thereby causing the polarization of the propagation wave to vary with temperature, the PCF birefringence is highly insensitive to temperature because it is made of a single material. Therefore temperature-insensitive Sagnac interferometers built with PCFs are expected. The experiments carried out independently by different researchers confirmed low temperature sensitivity ($\sim$0.3 pm/°C) in this type of interferometer [15, 16]. The studies carried out on the thermal sensitivity of Sagnac interferometer revealed that Hi-Bi and PM PCFs had, respectively, 30 and 45 times smaller temperature dependence than that of their conventional fiber counterparts [15, 16].

The development of temperature-insensitive sensors based on PCF Sagnac interferometers was natural. So far different sensors for physical parameters such as strain, pressure or curvature had been demonstrated [15–20]. The sensitivities of these sensors depend critically on the type of PCF. For example, strain sensors exhibit sensitivities ranging from 0.23 to 1.2 pm/$\mu\varepsilon$ [16, 17] while their thermal sensitivity is really low, of the order of 0.3 pm/°C. However, when compared to other fiber-based strain sensors PCF Sagnac interferometers probably are not really competitive. They require several centimeters of PCF, from 8.6 to 56 cm, which is nearly an order of magnitude longer than that of the popular fiber Bragg grating strain sensors. Another disadvantage is the high loss caused when splicing Hi-Bi PCFs to standard optical fiber and the intrinsic losses of the PCF. The overall losses can be of the order of 10 dB.

Recently, a novel Hi-Bi photonic crystal fiber consisting of half region composed by large diameter holes and the other half containing small diameter holes (see Figure 1) was proposed for bend sensing in a Sagnac interferometer [20]. It was found that the sensor exhibited maximum sensitivity when the large holes were compressed. Insensitivity to temperature and longitudinal strain were also observed. Also a photonic band gap PCF with elliptical core was demonstrated in a Sagnac interferometer for strain and temperature sensing [21]. These recent works reflect the variety of possibilities that PCFs offer to construct Sagnac interferometers.

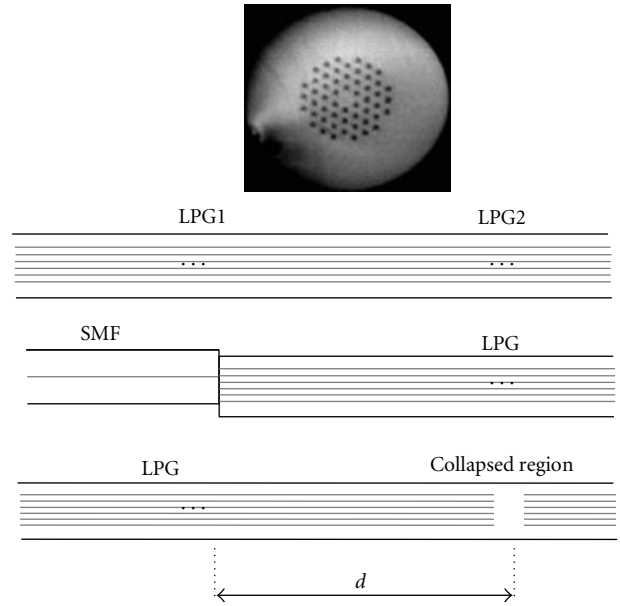

Figure 3: Micrograph of the cross-section of the typical PCF employed to build interferometers with LPGs. Diagrams of interferometers based on two LPGs in series, a misaligned point end together with an LPG, and an LPG together with a collapsed region in the PCF. The separation between the splitting gratings and recombining element is denoted by d.

3. Interferometers Built with Long Period Gratings

A long period grating (LPG) is a periodic modulation of the core refractive index whose period is much larger than the wavelength [22]. LPG are used to induce the mode coupling between a codirectional propagating core mode (LP_{01}) and cladding modes (LP_{0m}), where $m = 2, 3, 4, \ldots$ at discrete wavelengths. The transmission spectrum of an LPG exhibits dips at the wavelengths corresponding to resonances with various cladding modes. The resonance wavelength λ_r depends on the period of the LPG (usually denoted by Λ) and the difference between the effective refractive indices of the core and cladding modes. Since these modes propagate at different phase velocities, therefore, in-fiber interferometers can be implemented with a pair of LPGs—they were first studied using conventional optical fibers, see for example [23–30]. A popular configuration is to use two identical LPGs in cascade, see Figure 3. The first LPG couples part of the core mode power into a forward-propagating cladding mode and the second LPG recombines the two modes. The two LPGs function as beam-splitter/combiner and the core and the cladding modes travel through two independent paths along the same fiber. The resulting interference pattern of an interferometer formed with two LPGs in series exhibits sharp interference fringes. To a good approximation the fringe spacing ($\Delta\lambda$) can be given as $\Delta\lambda = \lambda_r^2/(\Delta n_{\text{eff}} d)$, where Δn_{eff} is the effective index difference between core and cladding modes and d the separation between the gratings [24].

The idea of constructing interferometers with LPGs has been extrapolated to PCFs, but unlike conventional Ge-doped single-mode fibers, in which UV-induced LPGs can be fabricated, PCFs have no photosensitivity because they are composed of pure silica. Therefore new ways to fabricate interferometers with LPGs in PCFs had been explored. The essential idea behind an LPG-based interferometer is that half of the fundamental LP_{01} core mode should be coupled to a cladding mode at the first LPG and half of the cladding mode should be coupled back to the core mode at the second LPG. Thus, for an all-PCF interferometer, one has to form two 3-dB LPGs with identical transmission spectra. It is difficult to form two identical 3-dB LPGs not only in PCF but also in standard optical fiber.

One of the approaches to achieve LPGs in photonic crystal fiber consists of pressing a section of the PCF with a periodic grooved plate [31, 32]. The length and period of the grooved plate as well as its width determines the transverse pressure applied on the PCF. Periodic pressure on the fiber surface induces periodic index changes in the fiber. The efficiency of the mode coupling between the core mode and a cladding mode varies with pressure. LPGs with proper lengths and periods have to be selected such that mode coupling occurs at the predetermined wavelength [31, 32]. The advantage of this type technique is that it is easy to form two identical LPGs, and therefore, it is easy to control the properties of the interferometer. However, the control is manual which severely limits the reproducibility of the devices.

As an alternative to the above approach a combination of a misaligned splicing point (MSP) and an LPG was proposed to form all-PCF interferometers [32]. The MSP can be formed, for example, by using a commercial fusion splicer in manual operation. The MSP acts as a light splitter which couples a part of the core-mode power into the cladding modes so that it may replace the first LPG in an LPG pair to form an interferometer. In principle the formation of the MSP is easier, moreover, it is permanent. Another alternative that was proposed consists of combining a single LPG and a short region of the PCF in which the airholes are collapsed [33]. In this case the LPG was imprinted with the electric arc discharge of a fusion splicer by using the point-by-point technique. The air holes of the PCF collapsed over a microscopic region behaves like a recombining element. Since the LPG and the collapsed section are permanent very sensitive interferometers can be effectively implemented. By adjusting the separation between the collapsed region and the LPG the spectral properties of the interferometer, specifically the interference fringe spacing, can be easily controlled. This type of interferometer was investigated for strain sensing applications. A sensitivity of 1.8 pm/$\mu\varepsilon$ was found which is slightly higher that the typical sensitivity of an FBG (1.2 pm/$\mu\varepsilon$) [33].

More recently the fabrication of LPG-based PCF interferometers was demonstrated in which the gratings are inscribed by using a high-frequency CO_2 laser [34]. By controlling the coupling coefficients of the two LPGs to be 3 dB, sharp interference fringes due to coherent mixing of the core and the cladding mode were obtained around the resonant wavelength of the LPGs. The temperature and strain sensitivities for the interferometers were measured. The former was found to be equal to 42.4 pm/°C per meter which suggests that with a separation between the two LPGs of 25 mm the interferometer can exhibit sensitivity of only 1.06 pm/°C. The strain sensitivity was found to be $\sim$2.6 pm/$\mu\varepsilon$ which is higher than that of a Sagnac interferometer or that of FBGs.

It should be pointed out that the type of PCF preferred for LPG-based interferometers is the so called endlessly single mode PCF whose cross-section is shown in Figure 3. In this PCFs $\Delta n_{\text{eff}} \approx 3 \times 10^{-3}$ at 1550 nm which suggests that $\Delta\lambda$ can be in the range between 27 to 5.5 nm when the separation d between the gratings varies from 3 to 15 cm. This means that compact interferometers can be fabricated with LPGs with the advantage that no coupler is required. Some drawbacks of LPG-based PCF interferometers are the relatively high insertion loss. The later originates from the loss caused by the splicing of the PCF with the SMF, the deformation of the PCF microstructure to inscribe the gratings, the misaligning or collapsed point, and so forth. All these factors also give rise to interferometers with slightly distorted interference fringes. This may make difficult the positional tracking of the interference peaks or dips which is crucial in sensing applications.

4. Interferometers Built Tapered PCFs

PCF combined with tapering technology can result in compact interferometers with interesting features. Tapering basically consists of stretching the fiber while it is heated over a localized zone. When tapering a PCF the diameter of the fiber and the relative size of the airholes can be scaled down, depending on the PCF design these variations have multiple applications, see, for example, [35–39]. During the tapering the voids of the PCF can be intentionally collapsed around the heated zone which allows interferometers with interesting features. This idea was demonstrated some years ago by one of the present authors and collaborators [40–45]. By collapsing the air holes, a short zone of the PCF is transformed into a solid unclad multimode optical fiber, see Figure 4. As a consequence, the fundamental mode of the PCF is coupled to the modes of the solid fiber. The beating between the modes makes the transmission of the taper versus wavelength to exhibit an oscillatory pattern. By controlling the taper diameter and its length one can tailor the performance of the interferometer in a similar manner than those based on tapered conventional fibers [46, 47]. Tapering dual core fiber or photonic bandgap PCF also allows the development of interferometers [48, 49] but in these cases the voids of the PCF are not collapsed.

The interference patterns observed in tapered PCFs with collapsed airholes is a consequence of a phenomenon of mode coupling and beating. The single-mode holey fiber is gradually transformed into a solid unclad multimode fiber of diameter ρ_w and length L_0 (or viceversa), see Figure 4. In the contracting zone of the taper the fundamental HE_{11} mode of the PCF couples to the HE_{1m} modes supported

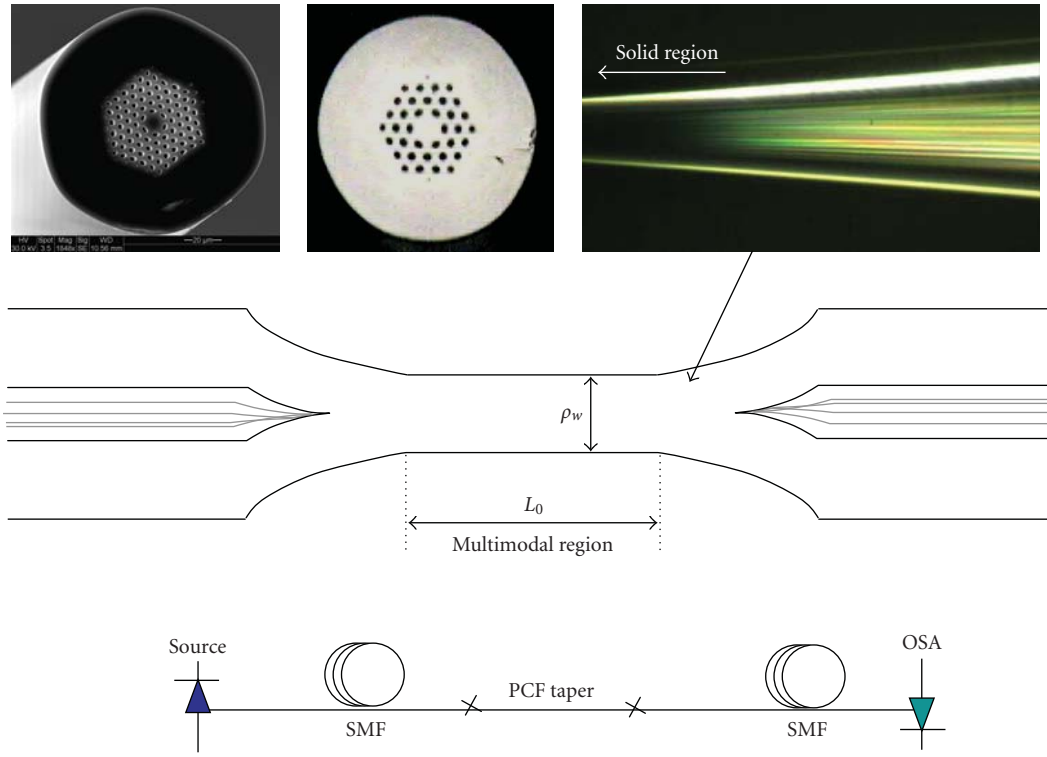

FIGURE 4: The top micrographs are the cross-section of some PCFs employed to fabricate tapers and the lateral view of the expanding zone of a taper. The middle drawing is a diagram of interferometers built with tapered PCFs. L_0 and ρ_w are, respectively, the length and width of the taper waist. The bottom drawing represents the transmission measuring setup.

by the multimode fiber. The HE_{1m} modes have propagation constants β_{1m}. In the region of the tapered PCF of constant diameter the HE_{1m} modes beat or interfere but no coupling occurs. After propagating such a beating length the modes accumulate phase difference. The expanding zone of the taper recombines the multiple modes of the solid fiber to core modes of the PCF. Therefore, a tapered PCF with collapsed air-holes can be considered as an interferometer. The contracting and expanding zones are equivalent to couplers or beam splitters and the modes of the beating region can be considered as arms of the interferometer. The transmission spectra of these modal interferometers also exhibit a series of maxima and minima, analogous to those of the Sagnac interferometers or the LPGs-based ones. However, for thick tapers ($\rho_w > 15\,\mu$m) the interference pattern does not vary sinusoidally with wavelength [40–44]. If the PCF is tapered down to diameters between 3 to 5 microns, then only two higher-order modes (HE_{05} and HE_{06}) survive [45]. The fringe spacing ($\Delta\lambda$) in this case is $\sim \Delta\lambda = \lambda^2/(\Delta n_{\text{eff}} L_0)$, being λ the wavelength of the source, Δn_{eff} the effective index difference between the modes participating in the interference and L_0 can be taken as the length of the taper waist. For two higher-order modes Δn_{eff} is large; therefore, the period of the interference pattern of a PCF microtaper can be very short, even for compact devices.

In PCF microtapers $\Delta n_{\text{eff}} \approx 0.5$ which is about two orders or magnitude larger than Δn_{eff} or Δn_g of LPG-based or Sagnac PCF interferometers, as mentioned above.

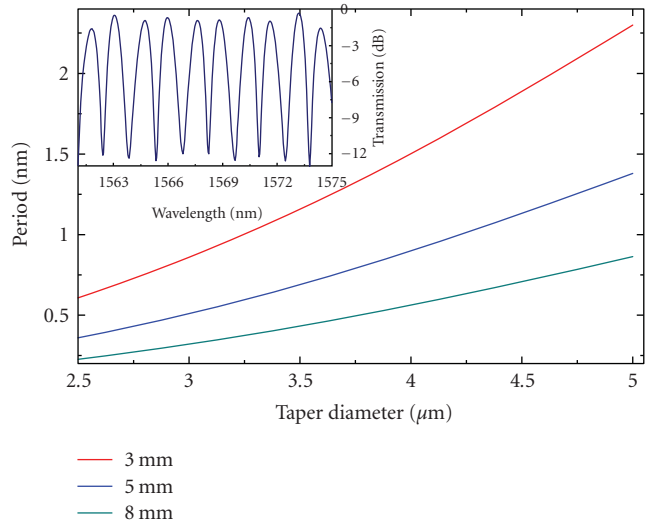

FIGURE 5: Predicted period of the interferometers at 1550 nm as a function of the diameter of the micro tapers for different lengths of their waist. The inset shows the experimental transmission spectrum of a 5 μm-thick taper in which the average fringe separation is 1.4 nm and the width of the fringes is around 0.9 nm.

Figure 5 shows the estimated period as a function of the taper diameter for some values of L_0. It can be noted that interferometers with nanometer and even sub-nanometer

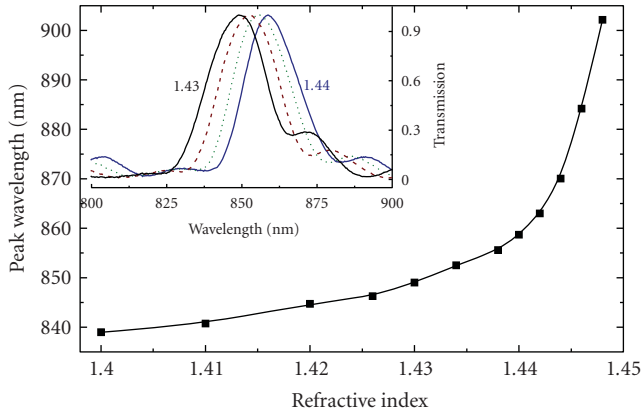

Figure 6: Position of the peak as a function of the external index observed in a 30 μm-thick taper. (Inset) Transmission spectra around 850 nm of the taper immersed into Cargille oils with indexes of 1.430, 1.434, 1.438, and 1.440.

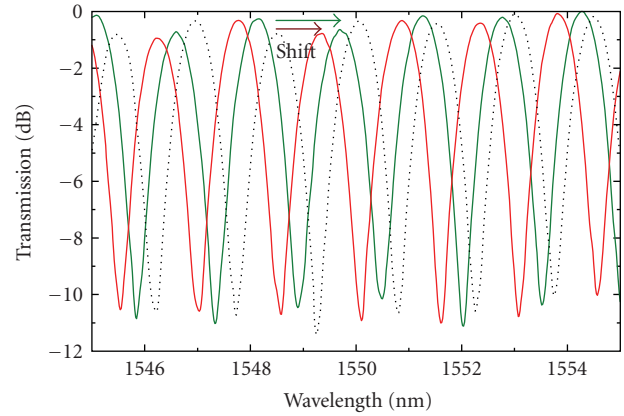

Figure 7: Normalized transmission spectra of an interferometer with diameter of 5 μm and waist of 5 mm in length when the external media were air (dotted line), vapor molecules of isopropyl alcohol (red line), and vapor molecules of acetone (green line). The arrows indicate the direction of the shift.

fringe spacing can be fabricated. The figure, for example, shows the transmission spectrum observed in a 5 μm-thick device in which the fringe spacing is only 1.4 nm, that is, a $\sim \lambda/1100$. At shorter wavelengths, the fringes are even closer. These features are important for sensing applications since narrow fringes or peaks help to improve the accuracy and resolution of any sensor.

The modes in PCF tapers are sensitive to the external medium. The interference pattern can be shifted if the external refractive index changes which suggest that the tapers can be used for refractometric applications [40]. In the inset of Figure 6 we show the observed transmission spectra of a 30 μm-thick taper for different refractive indexes of the external medium. The figure also shows the position of the highest peak as a function of the index. It can be noted that the device exhibits larger shifts as the index of the external medium approaches that of the PCF. In the 1.435–1.448 range the shift is ~50 nm which suggests that a resolution of the order of 3×10^{-5} can be achieved (assuming that a shift of 100 pm can be resolved). At longer wavelength the resolution may be higher [40] but the advantage at shorter wavelengths (around 850 nm) is that cost-effective light sources and spectrometers are commercially available. The results shown in Figure 6 demonstrate that PCF taper-based refractive index sensors can compete with others based on other technologies.

If a tapered PCF is subjected to strain the interference pattern also shifts, thus making possible the development of strain sensors [41]. The sensitivity of these strain sensors is considerably high (~5.3 pm/$\mu\varepsilon$) while the dynamic range is really broad. Strain up 8000 $\mu\varepsilon$ was demonstrated in [41]. The temperature sensitivity was found to be of the order of 12 pm/°C. A remarkable feature of PCF tapers is that they can withstand ultra-high temperature, up to 1000°C, with minimal degradation thus making possible the sensing of high temperature [42].

In addition to physical parameters taper-based PCF interferometers can also be exploited for gas and chemical sensing since the evanescent waves of the modes reach the external environment [43]. The solid region of the taper can be coated with gas-permeable layers thus making possible the detection of different gases. The detection of low concentration of hydrogen at room temperature was demonstrated in which a thin layer of Pd was deposited on the taper waist. More recently it was demonstrated that if a PCF consisting of 3 rings of air holes is tapered down to 3 to 5 microns, the fiber becomes sensitive to some chemical compounds without the need of any permeable material [45]. Figure 7, for example, shows the response of a 5 μm-thick taper in air and when it was exposed to vapors of isopropyl alcohol and acetone. It can be observed that the interference patterns shift to longer wavelengths. A red shift was also observed when the taper was exposed to vapors of ethyl and methyl alcohol, methylene chloride, and chloroform [45]. In all cases the interference pattern was returned to its original position when the VOCs were removed.

5. Interferometers Built via Micro-Holes Collapsing

More recently, new interferometers based on microhole collapse have been demonstrated [50–55]. This technique is really simple since it only involves cleaving and splicing, processes that can be carried out in any fiber-optics laboratory. The key element in these interferometers is a microscopic region in which the voids of the PCF are fully collapsed. Basically, the collapsed region is what allows the excitation of two modes in the PCF. The appeal of the interferometers fabricated with this approach is that the devices can be used for a variety of applications ranging from sensing strain (and all the parameters that can be translated to strain) or temperature to refractive index (biosensing) and volatile organic compounds (VOCs). In addition, the devices are compact, robust, and highly stable over time. For their interrogation

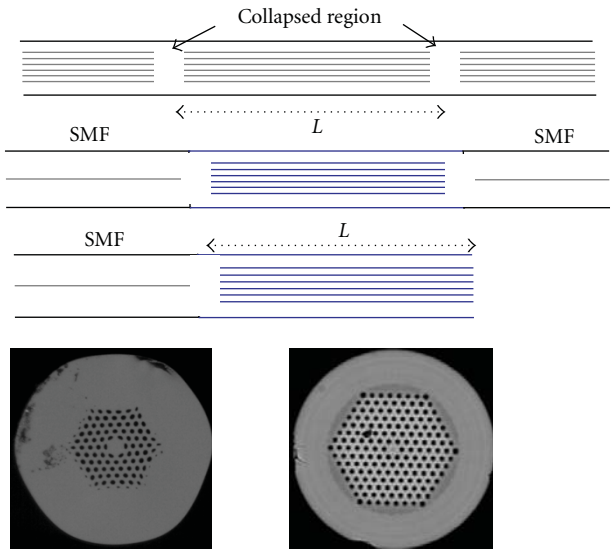

Figure 8: Diagrams of PCF interferometers built via microhole collapsing. The bottom images are the cross section of some PCFs employed in this type of interferometers. L is the length pf PCF or length between the collapsed regions.

a light emitting diode (LED) and a conventional fiber Bragg grating (FBG) interrogator or spectrum analyzer or a tunable laser and a single photodetector can be employed.

It is known that when splicing together two PCFs, or a PCF and a conventional optical fiber, with the standard electric-arc method, the air-holes of the PCF collapse completely in the vicinity of the splice [56, 57]. The length of the collapsed region is typically less than 300 or 400 μm. This is not a serious drawback of fusion splices since it may introduce minimal losses. The collapsing of the voids in a short region makes the fundamental PCF mode to spread out since it reaches a piece of coreless fiber, see Figure 9. The broadening of the fundamental mode can be estimated by using a Gaussian beam approximation [56]. According to it the fiber's mode field diameter (MFD) at any z (the direction of propagation) depends on the wavelength (λ) of the guided light, the refractive index n_1 of the medium (pure silica in our case), and the light spot size (ω_0) as

$$\text{MFD} = 2\omega_0\sqrt{1+\left(\frac{z\lambda}{n_1\pi\omega_0^2}\right)^2}. \quad (1)$$

If we assume that the solid region starts at $z = 0$, see Figure 9, then at the end of the solid region, let us say at $z_1 = 300\,\mu m$, according to (1), the MFD practically quadruplicates when $\lambda = 1.55\,\mu$m and triplicates when $\lambda = 0.85\,\mu$m. This means that the enlarged mode does not reach the surface of the collapsed region and it is therefore insensitive to the external medium. At $z \sim 300\,\mu$m the enlarged mode reaches a piece of PCF of length L in which two modes can be excited. In Figure 9, for example, we show the transverse component of the electric field of two core modes. The calculations were performed using finite-element method (COMSOL Multiphysics) applied to the

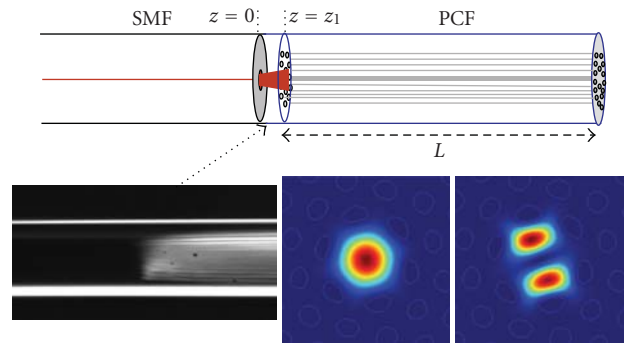

Figure 9: Diagram of SMF-PCF splice illustrating the broadening of the fundamental mode. The bottom images are a micrograph of the PCF in the vicinity of the splice and the transverse components of the electric field of the LP_{01}- and LP_{11}-like modes of a real PCF.

index profile based on the 5-ring PCF shown in Figure 8. The silica index was modeled using the known Sellmeier equation whereas the index of the holes was equal to 1 (air) to 1.1. After the PCF, the excited modes reach another solid piece of glass, that is, the other collapsed end of PCF. They will thus further diffract and will be recombined into core mode through the filtering of the subsequent SMF or PCF. Since the modes propagate at different phase velocities, thus in a certain length of PCF the modes accumulate a differential phase shift. The phase velocities and the phase difference are wavelength-dependent; therefore, the optical power transmitted (or reflected) by the device will be maximum at certain wavelengths and minimum at others.

The different configurations reported so far are illustrated in Figure 8. One of the first architectures that was demonstrated consisted of a PCF with two collapsed regions separated a few centimeters [50, 51]. Later on a short section of PCF longitudinally sandwiched between standard single mode fibers was proposed [52, 53]. The advantage of this configuration is that the modal properties of the PCF are exploited but the interrogation is carried out with conventional optical fibers, thus leading to more cost-effective interferometers. More recently, a stub of PCF with cleaved end fusion spliced at the distal end of a single mode fiber was demonstrated [54, 55]. In this case the interferometer operates in reflection and a single circulator or coupler is needed to interrogate the device. It is important to point out that the properties, and consequently the applications of the interferometer depend on the type of PCF.

The interferometers fabricated via micro-holes collapsing exhibit truly sinusoidal and stable interference spectra which are observed over a broad wavelength range (~800 nm). Figure 10, for example, shows the interference patterns observed in devices operating in transmission and reflection mode. The period or fringe spacing ($\Delta\lambda$) of these interferometers is $\Delta\lambda \approx \lambda^2/(\Delta n_{\text{eff}}L)$, being Δn_{eff} the effective refractive index difference between the modes participating in the interference. Such modes can be two core modes or a core and a cladding mode, depending on the PCF employed. L is the length of PCF or the length between collapsed regions, see Figure 8. The period or fringe spacing in these

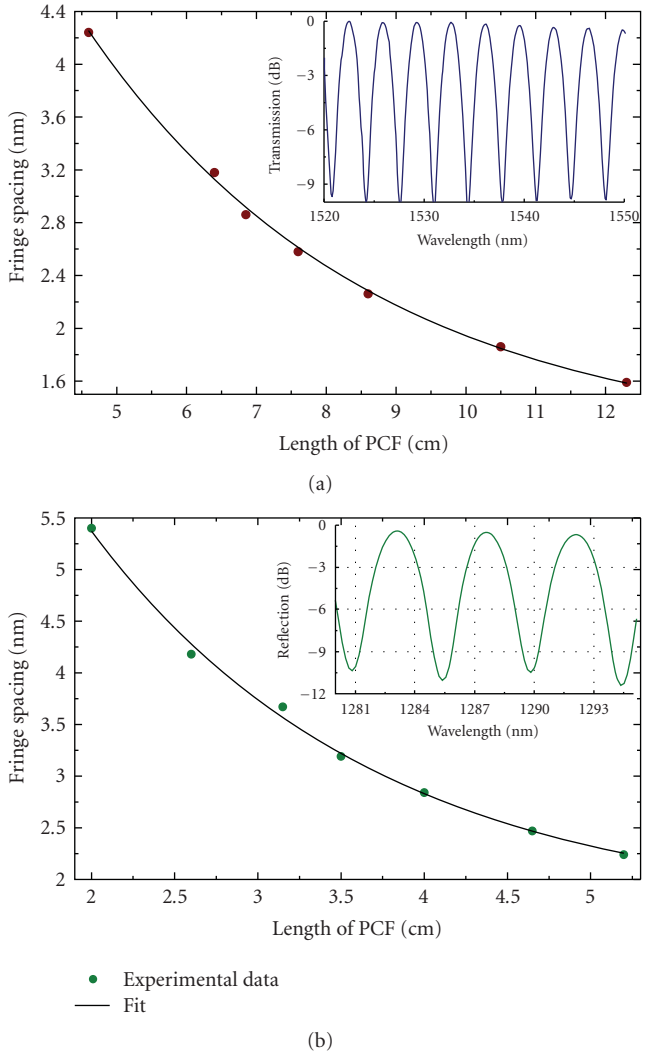

Figure 10: (a) Fringe spacing as a function of the length of PCF observed in interferometers operating in transmission mode. The inset shows the spectrum of an interferometer with $L = 75$ mm. (b) Period as a function of L observed in devices operating in reflection mode. The inset shows the spectrum of a device with $L = 26$ mm. In both cases the fringe spacing was measured at 1550 nm.

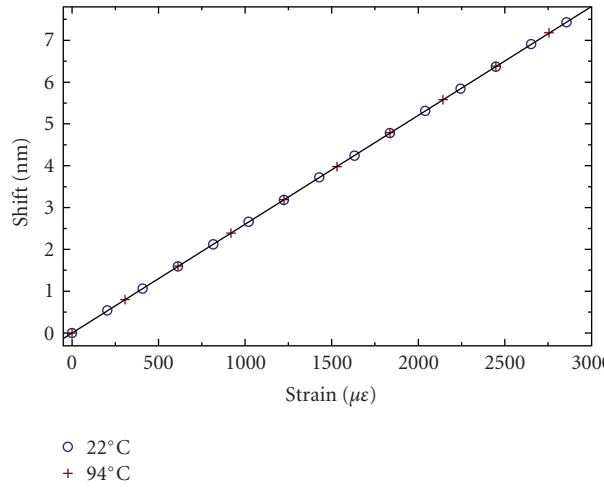

Figure 11: Shift of the interference pattern as a function of strain observed at room temperature and 94°C. The measurements were carried out at 1550 nm with a device with $L = 10.53$ mm.

interferometers can be controlled easily with the length of PCF between the two splices.

PCF interferometers fabricated via microhole collapsed exhibit some important features that are important for optical sensing. In general the performance, stability, and temperature dependence of a modal interferometer depend critically on the element that excites and recombines the modes. In interferometers built via microhole collapsing the excitation and recombination of modes is carried out with permanent and stable splices. These do not degrade over time or with temperature, thus interferometers with high stability are achievable. Their thermal sensitivity depends on the type of PCF one uses as well as the length of fiber. It is low, it can go from ~5 to ~10 pm/°C. In some applications no temperature compensation may be needed. For example, in Figure 11 we show the shift as a function of the applied strain observed in a device fabricated with 10.53 cm of 5-ring PCF at different temperatures. Note that the behavior of the interferometer is similar which demonstrates that no temperature compensation is required. The strain sensitivity of this device is 2.6 pm/$\mu\varepsilon$ which is higher than that of other PCF interferometric strain sensors.

As mentioned before, the features of the interferometers depend on the microstructure of the PCF. For example, by splicing a PCF consisting of seven rings of holes (LMA-8 from Crystal Fibre), then core and cladding modes are excited [53, 54]. Cladding modes, for example, are sensitive to the external environment, thus making possible the detection of samples present on the surface of the PCF. In this case the interaction is solely with the cladding modes since the core mode is isolated from the external environment. The interaction of the cladding modes with the external index changes Δn_{eff}, and consequently the phase difference. As a result, the position of the interference peaks and valleys change, or equivalently the interference pattern shifts. Therefore by monitoring the interference pattern wavelength shift one can infer the external refractive index and its changes. For example, the inset of Figure 12 shows the transmission spectra over 30 nm observed in an interferometer fabricated with $L = 17$ mm when it was in air (refractive index of 1) and in a liquid with index of 1.330. The figures also show the shifts measured as a function the external index. It is worth noting that the range of refractive indices that can be measured is quite broad, from 1.33 (aqueous environments) to 1.44 (biomolecules). The resolution of is estimated to be $\sim 2.9 \times 10^{-4}$ in the 1.40–1.44 range [53].

When the interferometers operate in reflection mode novel sensing applications are possible. For example, an in-reflection interferometer fabricated by fusion splicing a stub of 5-ring PCF (see Figure 8) at the distal end of a standard optical fiber (Corning SMF-28) can be used

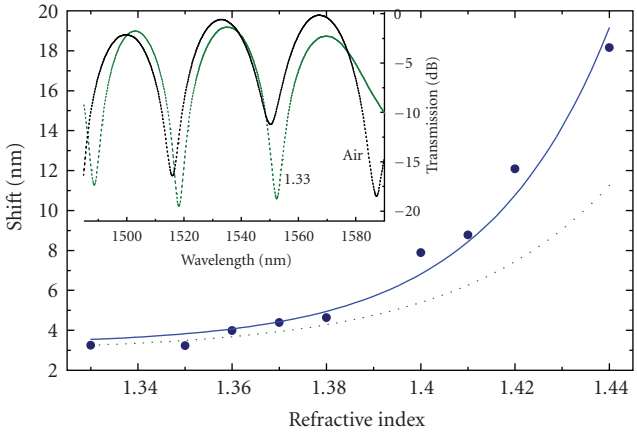

Figure 12: Shift of the interference pattern as a function of the external refractive index observed in a device with $L = 17$ mm. The circles are experimental data and the continuous line is a fitting to the data. The measurements were carried out in the 1490–1590 nm wavelength range.

to detect different volatile organic compounds at room temperature. The key point here is to leave the voids of the PCF open to allow infiltration of some gases, chemical vapor, or molecules. The interaction of the compounds with the interfering modes takes place in the first rings of voids which have a total volume in the picolitters range [55]. Figure 13 for example shows the shift of an interferometer in which L was 37 mm when exposed to vapor of acetone in closed and open chamber. Figure 13(a) was collected by evaporating 5 μl of acetone in a closed container. The shift increases owing to the presence of the vapor. The fact that the curve plateaus indicates that the chamber was properly sealed. Figure 13(b) was collected by evaporating 75 μL of acetone in an open container. Note that the interferometer saturates owing to the limited volume of the voids. They can house a maximum number of molecules. The interferometer slowly returns to its original position which indicates the reversibility of the devices. The response time of the device is long because the experiments were carried at normal conditions. In addition, the infiltration of the acetone vapor into the microscopic voids of the PCF is a diffusion process which is typically slow.

We would like to point out that the combination of different fibers to form interferometers has been investigated during many years [58–61]. In these cases the splicing is critical since it determines the splitting and/or recombination of the interfering beams or mores. The selection of the fiber in which two modes are excited is also crucial.

6. Conclusions and Outlook

Photonic crystal fibers are at the forefront of fiber optics technology. These fibers offer different possibilities for the fiber optic sensing field as demonstrated by different works reported in the past few years. PCFs offer different alternatives for the fabrication of modal interferometers,

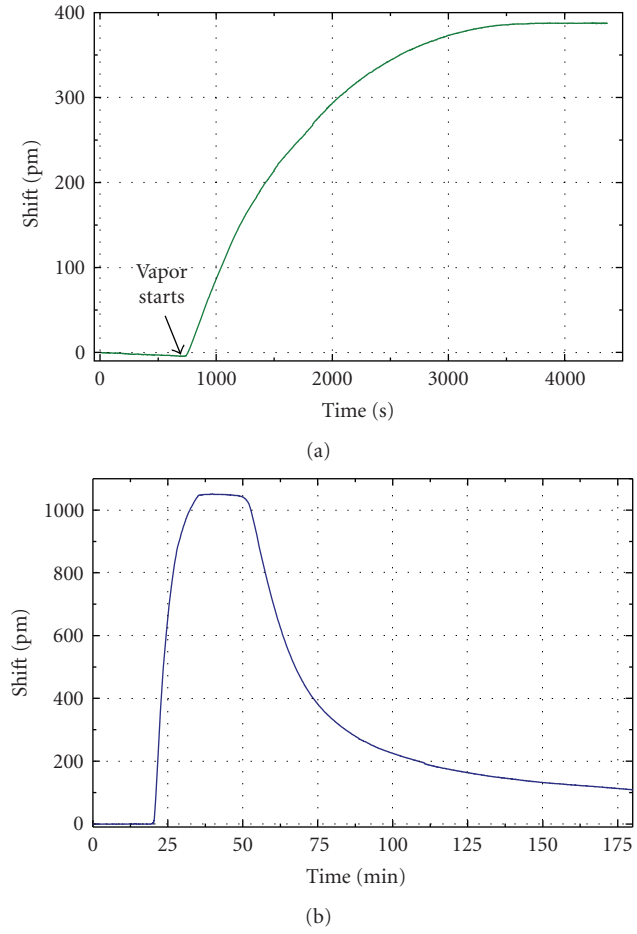

Figure 13: Shift observed in a 37 mm-long interferometer when exposed to acetone vapor in closed (LHS) and open container (RHS). The measurements were carried out at 1310 nm.

Sagnac-, and Mach-Zehnder- or Michelson-like ones. Most of them can also be implemented with standard optical fiber but PCFs give them important advantages such as low thermal sensitivity, broad operation wavelength range, or high stability over time. However, other cases have no counterparts in conventional fibers. Interferometers that exploit the diffraction caused by a short region with collapsed voids, for example, are completely new. In this case the holey microstructure of the PCF is fully exploited. It will, therefore be no surprise if some of the interferometers reviewed in this paper end as innovative commercial products in the near future or at least represent new solutions to old problems (temperature compensation) in optical sensing.

Acknowledgments

This work was carried out with the financial support of the Spanish MEC through grant TEC2006-10665/MIC and the "Ramón y Cajal" program. The authors are grateful to Vladimir P. Minkovich and D. Monzón-Hernández for their valuable help.

References

[1] D. A. Jackson and J. D. C. Jones, "Interferometers," in *Optical Fiber Sensors: Systems and Applications*, B. Culshaw and J. Dakin, Eds., pp. 239–280, Artech House, Norwood, Mass, USA, 1989.

[2] J. D. C. Jones, "Interferometry and polarimetry for optical sensing," in *Handbook of Optical Fibre Sensing Technology*, J. M. López-Higuera, Ed., pp. 227–245, John Wiley & Sons, West Sussex, UK, 2002.

[3] F. T. S. Yu and S. Yin, Eds., *Fiber Optic Sensors*, Marcel & Dekker, New York, NY, USA, 2002.

[4] P. St. J. Russell, "Photonic-crystal fibers," *IEEE Journal of Lightwave Technology*, vol. 24, pp. 4729–4749, 2006.

[5] A. Bjarklev, J. Broeng, and A. S. Bjarklev, *Photonic Crystal Fibres*, Kluwer Academic Publishers, Boston, Mass, USA, 2003.

[6] O. Frazao, J. L. Santos, F. M. Araujo, and L. A. Ferreira, "Optical sensing with photonic crystal fibers," *Laser & Photonics Reviews*, vol. 2, pp. 449–459, 2008.

[7] W. N. MacPherson, M. J. Gander, R. McBride, et al., "Remotely addressed optical fibre curvature sensor using multicore photonic crystal fibre," *Optics Communications*, vol. 193, no. 1–6, pp. 97–104, 2001.

[8] D. Káčik, I. Turek, I. Martinček, J. Canning, N. A. Issa, and K. Lyytikäinen, "Intermodal interference in a photonic crystal fibre," *Optics Express*, vol. 12, no. 15, pp. 3465–3470, 2004.

[9] J. Ju, W. Jin, and M. S. Demokan, "Two-mode operation in highly birefringent photonic crystal fiber," *IEEE Photonics Technology Letters*, vol. 16, no. 11, pp. 2472–2474, 2004.

[10] M. R. Layton and J. A. Bucaro, "Optical fiber acoustic sensor utilizing mode-mode interference," *Applied Optics*, vol. 18, no. 5, pp. 666–670, 1979.

[11] M. Spajer, B. Carquille, and H. Maillotte, "Application of intermodal interference to fibre sensors," *Optics Communications*, vol. 60, no. 5, pp. 261–264, 1986.

[12] T. A. Eftimov and W. J. Bock, "Sensing with a LP_{01}-LP_{02} intermodal interferometer," *Journal of Lightwave Technology*, vol. 11, no. 12, pp. 2150–2156, 1993.

[13] T.-J. Chen, "A novel two-mode fiber-optic interferometer based on HE_{11}-TE_{01} modal interference utilizing a liquid-crystal-clad fiber modal filter," *Optics Communications*, vol. 261, no. 1, pp. 43–50, 2006.

[14] W. Jin, Z. Wang, and J. Ju, "Two-mode photonic crystal fibers," *Optics Express*, vol. 13, no. 6, pp. 2082–2088, 2005.

[15] C.-L. Zhao, X. Yang, C. Lu, W. Jin, and M. S. Demokan, "Temperature-insensitive interferometer using a highly birefringent photonic crystal fiber loop mirror," *IEEE Photonics Technology Letters*, vol. 16, no. 11, pp. 2535–2537, 2004.

[16] D.-H. Kim and J. U. Kang, "Sagnac loop interferometer based on polarization maintaining photonic crystal fiber with reduced temperature sensitivity," *Optics Express*, vol. 12, no. 19, pp. 4490–4495, 2004.

[17] X. Dong, H. Y. Tam, and P. Shum, "Temperature-insensitive strain sensor with polarization-maintaining photonics crystal fiber based on Sagnac interferometer," *Applied Physics Letters*, vol. 90, no. 15, Article ID 151113, 3 pages, 2007.

[18] O. Frazao, J. M. Baptista, and J. L. Santos, "Temperature independent strain sensor based on a Hi-Bi photonic crystal fiber loop mirror," *IEEE Journal Sensors*, vol. 7, pp. 1453–1455, 2007.

[19] H. Y. Fu, H. Y. Tam, L.-Y. Shao, et al., "Pressure sensor realized with polarization-maintaining photonic crystal fiber-based Sagnac interferometer," *Applied Optics*, vol. 47, no. 15, pp. 2835–2839, 2008.

[20] O. Frazão, J. Baptista, J. L. Santos, and P. Roy, "Curvature sensor using a highly birefringent photonic crystal fiber with two asymmetric hole regions in a Sagnac interferometer," *Applied Optics*, vol. 47, no. 13, pp. 2520–2523, 2008.

[21] G. Kim, T. Cho, K. Hwang, et al., "Strain and temperature sensitivities of an elliptical hollow-core photonic bandgap fiber based on Sagnac interferometer," *Optics Express*, vol. 17, no. 4, pp. 2481–2486, 2009.

[22] V. Bhatia and A. M. Vengsarkar, "Optical fiber long-period grating sensors," *Optics Letters*, vol. 21, no. 9, pp. 692–694, 1996.

[23] B. H. Lee and J. Nishii, "Self-interference of long-period fibre grating and its application as temperature sensor," *Electronics Letters*, vol. 34, no. 21, pp. 2059–2060, 1998.

[24] B. H. Lee and J. Nishii, "Dependence of fringe spacing on the grating separation in a long-period fiber grating pair," *Applied Optics*, vol. 38, no. 16, pp. 3450–3459, 1999.

[25] O. Duhem, J. F. Henninot, and M. Douay, "Study of in fiber Mach-Zehnder interferometer based on two spaced 3-dB long period gratings surrounded by a refractive index higher than that of silica," *Optics Communications*, vol. 180, no. 4, pp. 255–262, 2000.

[26] T. Allsop, R. Reeves, D. J. Webb, I. Bennion, and R. Neal, "A high sensitivity refractometer based upon a long period grating Mach-Zehnder interferometer," *Review of Scientific Instruments*, vol. 73, no. 4, pp. 1702–1705, 2002.

[27] S. W. James, I. Ishaq, G. J. Ashwell, and R. P. Tatam, "Cascaded long-period gratings with nanostructured coatings," *Optics Letters*, vol. 30, no. 17, pp. 2197–2199, 2005.

[28] I. D. Villar, M. Achaerandio, F. J. Arregui, and I. R. Matias, "Generation of selective fringes with cascaded long-period gratings," *IEEE Photonics Technology Letters*, vol. 18, no. 13, pp. 1412–1414, 2006.

[29] P. L. Swart, "Long-period grating Michelson refractometric sensor," *Measurement Science and Technology*, vol. 15, no. 8, pp. 1576–1580, 2004.

[30] D. W. Kim, Y. Zhang, K. L. Cooper, and A. Wang, "In-fiber reflection mode interferometer based on a long-period grating for external refractive-index measurement," *Applied Optics*, vol. 44, no. 26, pp. 5368–5373, 2005.

[31] J. H. Lim, H. S. Jang, K. S. Lee, J. C. Kim, and B. H. Lee, "Mach-Zehnder interferometer formed in a photonic crystal fiber based on a pair of long-period fiber gratings," *Optics Letters*, vol. 29, no. 4, pp. 346–348, 2004.

[32] X. Yu, P. Shum, and X. Dong, "Photonic-crystal-fiber-based Mach-Zehnder interferometer using long-period gratings," *Microwave and Optical Technology Letters*, vol. 48, no. 7, pp. 1379–1383, 2006.

[33] H. Y. Choi, K. S. Park, and B. H. Lee, "Photonic crystal fiber interferometer composed of a long period fiber grating and one point collapsing of air holes," *Optics Letters*, vol. 33, no. 8, pp. 812–814, 2008.

[34] J. Ju, W. Jin, and H. L. Ho, "Compact in-fiber interferometer formed by long-period gratings in photonic crystal fiber," *IEEE Photonics Technology Letters*, vol. 20, no. 23, pp. 1899–1901, 2008.

[35] S. T. Huntington, J. Katsifolis, B. C. Gibson, et al., "Retaining and characterizing nano-structure within tapered air-silica structured optical fibers," *Optics Express*, vol. 11, pp. 98–104, 2003.

[36] H. C. Nguyen, B. T. Kuhlmey, E. C. Magi, et al., "Tapered photonic crystal fibers: properties, characterization and applications," *Applied Physics B*, vol. 81, pp. 377–387, 2005.

[37] J. Hu, B. S. Marks, C. R. Menyuk, et al., "Pulse compression using a tapered microstructure optical fiber," *Optics Express*, vol. 14, no. 9, pp. 4026–4036, 2006.

[38] S. Laflamme, S. Lacroix, J. Bures, and X. Daxhelet, "Understanding power leakage in tapered solid core microstructured fibers," *Optics Express*, vol. 15, no. 2, pp. 387–396, 2007.

[39] M.-L. V. Tse, P. Horak, F. Poletti, and D. J. Richardson, "Designing tapered holey fibers for soliton compression," *IEEE Journal of Quantum Electronics*, vol. 44, no. 2, pp. 192–198, 2008.

[40] V. P. Minkovich, J. Villatoro, D. Monzón-Hernández, S. Calixto, A. B. Sotsky, and L. I. Sotskaya, "Holey fiber tapers with resonance transmission for high-resolution refractive index sensing," *Optics Express*, vol. 13, no. 19, pp. 7609–7614, 2005.

[41] J. Villatoro, V. P. Minkovich, and D. Monzón-Hernández, "Temperature-independent strain sensor made from tapered holey optical fiber," *Optics Letters*, vol. 31, no. 3, pp. 305–307, 2006.

[42] D. Monzón-Hernández, V. P. Minkovich, and J. Villatoro, "High-temperature sensing with tapers made of microstructured optical fiber," *IEEE Photonics Technology Letters*, vol. 18, pp. 511–513, 2006.

[43] V. P. Minkovich, D. Monzón-Hernández, J. Villatoro, and G. Badenes, "Microstructured optical fiber coated with thin films for gas and chemical sensing," *Optics Express*, vol. 14, no. 18, pp. 8413–8418, 2006.

[44] V. P. Minkovich, D. Monzón-Hernández, J. Villatoro, A. B. Sotsky, and L. I. Sotskaya, "Modeling of holey fiber tapers with selective transmission for sensor applications," *Journal of Lightwave Technology*, vol. 24, no. 11, pp. 4319–4328, 2006.

[45] D. Monzón-Hernández, V. P. Minkovich, J. Villatoro, M. P. Kreuzer, and G. Badenes, "Photonic crystal fiber microtaper supporting two selective higher-order modes with high sensitivity to gas molecules," *Applied Physics Letters*, vol. 93, no. 8, Article ID 081106, 3 pages, 2008.

[46] X. Daxhelet, J. Bures, and R. Maciejko, "Temperature-independent all-fiber modal interferometer," *Optical Fiber Technology*, vol. 1, no. 4, pp. 373–376, 1995.

[47] K. Q. Kieu and M. Mansuripur, "Biconical fiber taper sensors," *IEEE Photonics Technology Letters*, vol. 18, pp. 2239–2241, 2006.

[48] L. Yuan, J. Yang, Z. Liu, and J. Sun, "In-fiber integrated Michelson interferometer," *Optics Letters*, vol. 31, no. 18, pp. 2692–2694, 2006.

[49] A. Ozcan, A. Tewary, M. J. F. Digonnet, and G. S. Kino, "Observation of mode coupling in bitapered air-core photonic bandgap fibers," *Optics Communications*, vol. 271, no. 2, pp. 391–395, 2007.

[50] J. Villatoro, V. P. Minkovich, V. Pruneri, and G. Badenes, "Simple all-microstructured-optical-fiber interferometer built via fusion splicing," *Optics Express*, vol. 15, no. 4, pp. 1491–1496, 2007.

[51] H. Y. Choi, M. J. Kim, and B. H. Lee, "All-fiber Mach-Zehnder type interferometers formed in photonic crystal fiber," *Optics Express*, vol. 15, no. 9, pp. 5711–5720, 2007.

[52] J. Villatoro, V. Finazzi, V. P. Minkovich, V. Pruneri, and G. Badenes, "Temperature-insensitive photonic crystal fiber interferometer for absolute strain sensing," *Applied Physics Letters*, vol. 91, no. 9, Article ID 091109, 3 pages, 2007.

[53] R. Jha, J. Villatoro, G. Badenes, and V. Pruneri, "Refractometry based on a photonic crystal fiber interferometer," *Optics Letters*, vol. 34, no. 5, pp. 617–619, 2009.

[54] R. Jha, J. Villatoro, and G. Badenes, "Ultrastable in reflection photonic crystal fiber modal interferometer for accurate refractive index sensing," *Applied Physics Letters*, vol. 93, no. 19, Article ID 191106, 3 pages, 2008.

[55] J. Villatoro, M. P. Kreuzer, R. Jha, et al., "Photonic crystal fiber interferometer for chemical vapor detection with high sensitivity," *Optics Express*, vol. 17, no. 3, pp. 1447–1453, 2009.

[56] B. Bourliaguet, C. Paré, F. Émond, A. Croteau, A. Proulx, and R. Vallée, "Microstructured fiber splicing," *Optics Express*, vol. 11, no. 25, pp. 3412–3417, 2003.

[57] A. D. Yablon and R. T. Bise, "Low-loss high-strength microstructured fiber fusion splices using GRIN fiber lenses," *IEEE Photonics Technology Letters*, vol. 17, no. 1, pp. 118–120, 2005.

[58] J. Canning and A. L. G. Carter, "Modal interferometer for in situ measurements of induced core index change in optical fibers," *Optics Letters*, vol. 22, no. 8, pp. 561–563, 1997.

[59] Q. Li, C.-H. Lin, P.-Y. Tseng, and H. P. Lee, "Demonstration of high extinction ratio modal interference in a two-mode fiber and its applications for all-fiber comb filter and high-temperature sensor," *Optics Communications*, vol. 250, no. 4–6, pp. 280–285, 2005.

[60] Q. Wang and G. Farrell, "All-fiber multimode-interference-based refractometer sensor: proposal and design," *Optics Letters*, vol. 31, no. 3, pp. 317–319, 2006.

[61] Y. Jung, S. Kim, D. Lee, and K. Oh, "Compact three segmented multimode fibre modal interferometer for high sensitivity refractive-index measurement," *Measurement Science and Technology*, vol. 17, no. 5, pp. 1129–1133, 2006.

Hindawi Publishing Corporation
Journal of Sensors
Volume 2009, Article ID 196380, 7 pages
doi:10.1155/2009/196380

Research Article

Gemini Fiber for Interferometry and Sensing Applications

E. Zetterlund, A. Loriette, C. Sterner, M. Eriksson, H. Eriksson-Quist, and W. Margulis

Department of Fiber Photonics, Acreo, Electrum 236, 16440 Stockholm, Sweden

Correspondence should be addressed to W. Margulis, walter.margulis@acreo.se

Received 6 April 2009; Accepted 11 May 2009

Recommended by Valerio Pruneri

A novel type of fiber for sensing applications is introduced based on a plurality of individual fiber preforms drawn together but maintaining their original shape. The individual cores of the Gemini fiber can be addressed at input and output ends through splicing to stand-alone fibers. Thermal coupling between cores is sufficient to eliminate relative thermal effects. Fabrication, coupling and fiber Bragg grating (FBG) studies are discussed. The possibility to connect in a single splice more than one fiber to the Gemini fiber is introduced as being highly advantageous. A conventional splicer can be used, the loss is acceptable and the operation takes minutes. Sensing with Gemini fibers is discussed mainly with the incorporation of fiber Bragg gratings. Another advantage of the concept of the Gemini fiber discussed is the possibility to make monolithic fiber interferometers of nearly equal arm lengths. A large number of new options are opened by the monolithic multicore fiber design, where access to individual cores is straightforward.

1. Introduction

Multicore optical fibers [1] find a great number of applications in sensing beyond endoscopy. Various measurands have been monitored with the information extracted from the propagation of light in different cores [2–7]. The close proximity of the waveguides allows for equalizing thermal perturbations, and the temperature dependence is nearly eliminated by working with the difference between signals traveling in neighboring cores. Multicore fibers used in bend and torsion sensing can be employed in the determination of the path taken by a moving fiber incorporating a number of fiber Bragg gratings (FBGs), the reflected wavelengths indicating the bend experienced by the fiber along its path [8]. The input and output access to the individual cores, however, pose a severe coupling limitation. It has not been possible, so far, to splice individual fibers to the each core and guarantee low loss coupling. Various ingenious mounting schemes have been devised to make optical coupling possible [9–11], but they are generally lossy and costly, not particularly robust and ultimately far from ideal. Coupling at the input and output ends is so problematic that it significantly restricts the use of multicore fibers. In other applications, such as in telecom and pumping fiber lasers, independently drawn fibers are brought together in a ribbon or with low index coating materials [12]. Here, accessing the individual cores is straightforward, but the thermal and mechanical contact between fibers that would be useful for sensing is limited.

In the present letter, we describe a novel type of fiber for sensing applications. A single fiber is drawn from a number of individual fiber preforms and except for a narrow connecting glass bridge, the original individual circular cross-sections are maintained. A Gemini fiber is then obtained that has Siamese character. Addressing the individual cores at input and output ends thus becomes easier, through splicing to stand-alone fibers. Although thermal coupling is weaker than in a conventional multicore fiber, the easier access to the cores is greatly advantageous, and the structure is a good compromise for various sensing applications. Fabrication, coupling and fiber Bragg grating (FBG) studies are discussed in the following. Other advantages of this concept, including the possibility to make monolithic fiber interferometers of nearly equal arm lengths are also touched upon. The general name given for this type of structure is the Gemini fiber, and complementing information (e.g., G4) indicates the number of cores available.

Figure 1: Preform of Gemini fiber G4, where four individual standard telecom fiber preforms are mounted together and drawn into a monolithic fiber with four easily accessed ports.

2. Fiber Fabrication

The fabrication of the Gemini fiber starts from the fixation of a number of close proximity preforms, which can have standard or special cross-section. Figure 1 shows one such arrangement, in which four standard telecommunications single-mode preforms are stacked. After drawing each preform results in an individual single mode fiber barely in contact with the neighboring fibers, as shown in Figure 1. Drawing is carried out without pressure control, but the furnace temperature (~1900°C) is slightly lower than in standard fiber manufacture. The automatic diameter control unit normally used while drawing is not used for feedback. This is necessary, since the width of the Gemini fiber seen from various angles varies, and the viewing angle changes during fiber drawing. When necessary, the temperature of the furnace is adjusted to prevent the dimensions of the fiber from drifting.

Four Gemini fiber types are illustrated in Figures 2(a)–2(d) with scanning electron microscope pictures. These are (a) a Gemini fiber (G2), (b) a two-core Gemini fiber with holes (G2H), (c) a Gemini fiber composed from four individual preforms (G4) shown in Figure 1, and (d) a Gemini fiber composed of four individual preforms and a middle rod (G4M). All individual preforms have circular shape and circular cores (except for the middle rod in Figure 2(d) that is coreless). Some form alteration was observed while drawing, in particular for the first Gemini fiber pulled G2 (Figure 2(a)). The measured distance between core centers in the G2 fiber is 135 μm instead of the expected 125 μm (8% distortion). This can be attributed almost entirely to the creation during drawing of the glass bridge connecting the individual halves of the fiber. The four individual diameters measured in G4 by fitting circles to the cross-section in Figure 2(d) are 71.8 μm, 72.7 μm, 72.5 μm, and 72.0 μm. The distance between opposite core centers in two directions is 102.7 μm and 101.5 μm. The four individual diameters measured in G4M by fitting circles to the cross section in Figure 2(d) are 81.4 μm, 80.0 μm, 82.6 μm, and 81.0 μm.

3. Accessing Individual Cores

Two approaches are used for accessing the individual cores of the Gemini fibers. Here, work carried out with the Gemini fiber G2 is described in more detail. Etching is the first approach. From the cross-section seen in Figure 2(a) it is clear that the thin bridge connecting the individual waveguides is etched away relatively early if the fiber is immersed in HF. Two independent fibers result from this process, which can be spliced to standard fibers at both ends for input and output coupling. The time taken for separating two independent fibers was 18 minutes in a 40% concentration HF solution. A photo illustrating an etched Gemini fiber G2 is shown in Figure 3.

It is advantageous to strengthen the separation point, and UV curing glue (Wellomer UV 2010) is appropriate for this purpose. The two fiber sections can then be mounted, cleaved and spliced individually. It is found, however, that the cross-section of the two independent fibers resulting from etching the G2 is not circular, but maintains an edged profile. Even if the etching time is increased to 50 minutes, the two independent fiber sections are not circular. Three splicing options become available, those of automatically aligning the fibers to be spliced by imaging the claddings, the cores, or alternatively perform a manual splice. When the etched fiber sections are automatically aligned to the standard fiber from the cladding profile, a large mean loss of 1.7 dB is measured for the splice with a large standard deviation (2.1 dB). The lowest value obtained for the loss using this splice procedure is 0.36 dB. Figure 4 illustrates one example of such a splice.

When the cores are automatically aligned, the minimum loss obtained improves to 0.14 dB with a standard deviation of 0.87 dB, but splicing was only successful in approximately half of the cases. Finally, when a manual aligning procedure is used, the mean loss is 0.53 dB, the standard deviation 0.56 dB and the minimal loss measured is as low as 0.05 dB. All splices carried out manually were successful. One disadvantage of splicing individually the separated fiber sections to standard fibers is the long length of unprotected fiber created. Besides, whenever a fiber section breaks or a splice is unsuccessful, at least one additional fiber needs to be recleaved to approximately equalize the lengths, or in the worst case start the etching procedure again. As a whole, the etching procedure described for separating the individual waveguides gives acceptable results. However, it involves many steps, including coating removal, etching, fixing, cleaving, manual splicing four times and final mounting. The total time estimated for these operations carried out manually is at present in excess of three hours.

The second approach developed for accessing the individual cores of the Gemini fiber to independent standard telecom fibers is to perform a single automated fusion splice

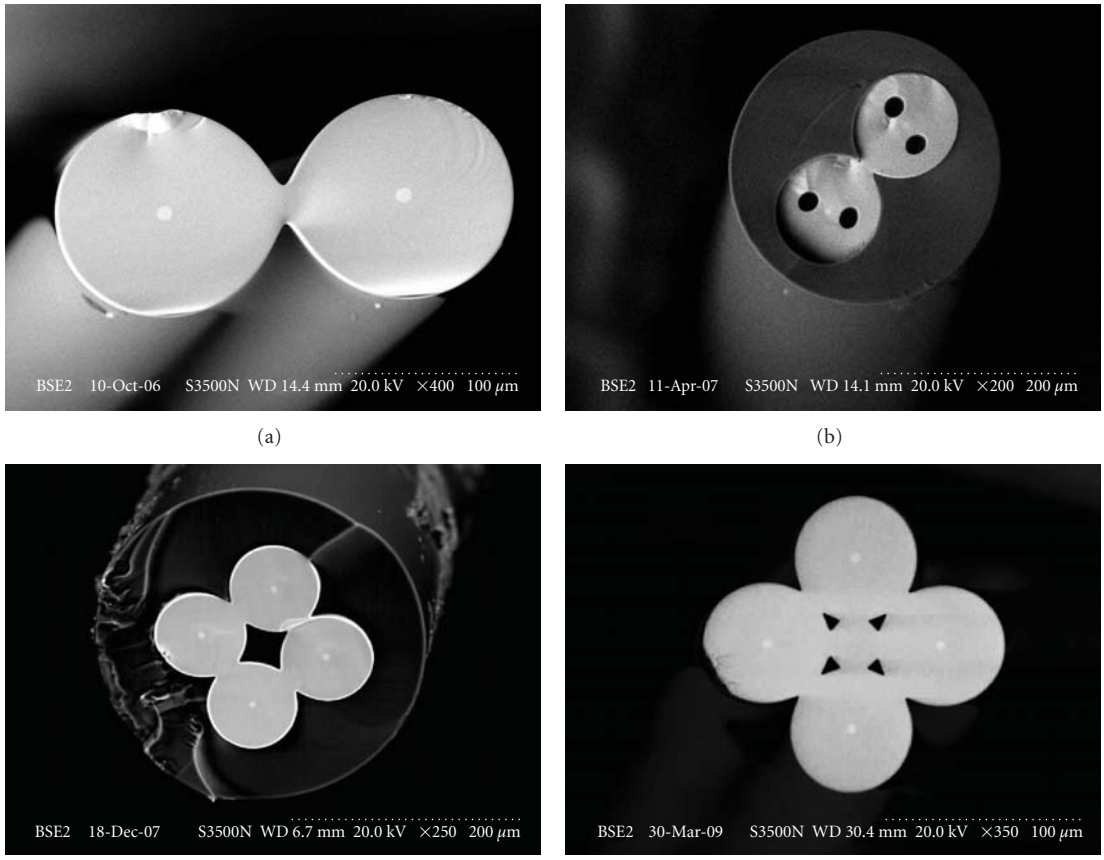

Figure 2: SEM pictures of Gemini fibers. (a) Gemini fiber G2; (b) Gemini fiber with holes (G2H); (c) Fiber G4; and (d) Gemini fiber G4M with a glass rod in the middle.

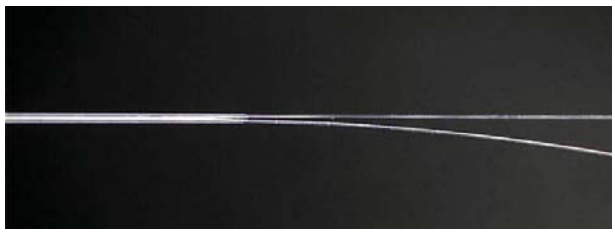

Figure 3: Gemini fiber G2 where etching is used to separate the arms for splicing to standard telecom fiber. After separation, the splitting point is reinforced with UV curing glue.

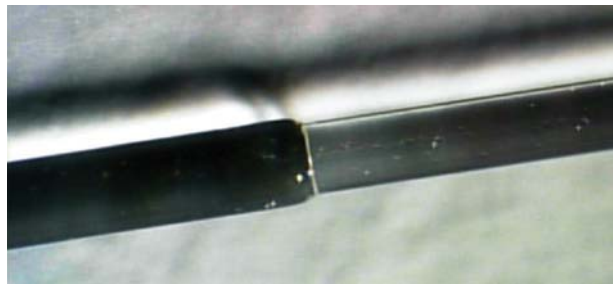

Figure 4: One of the two waveguides of the Gemini fiber G2 spliced to a standard telecom fiber through automatic alignment between cladding images.

of various fibers in parallel. This procedure is also studied in some detail for the Gemini fiber G2. With this procedure, one exploits the ability to cleave well the Gemini fiber with a conventional cleaver, producing a fiber with various waveguides of equal length (as seen in Figure 2). Here, the entire process of addressing the individual cores is reduced to a couple of splices. The handling time is dramatically reduced. The resulting component becomes rugged with the use of conventional splice protectors. The main disadvantage of a single splice to each side of the Gemini fiber is that no individual fiber adjustment becomes possible. While this is easier when the core separation is exactly 125 μm because the individual fibers are placed in contact with each other, mounting individual standard telecom fibers in parallel separated by a few microns requires a special fixture. For splicing the Gemini fiber G2 available in this work where the core center separation is 135 μm, an appropriate fiber holder was fabricated with two grooves separated by 135 μm. The result gives typically a loss below 1 dB per splice, but a loss below 0.5 dB has also been achieved for each one of the

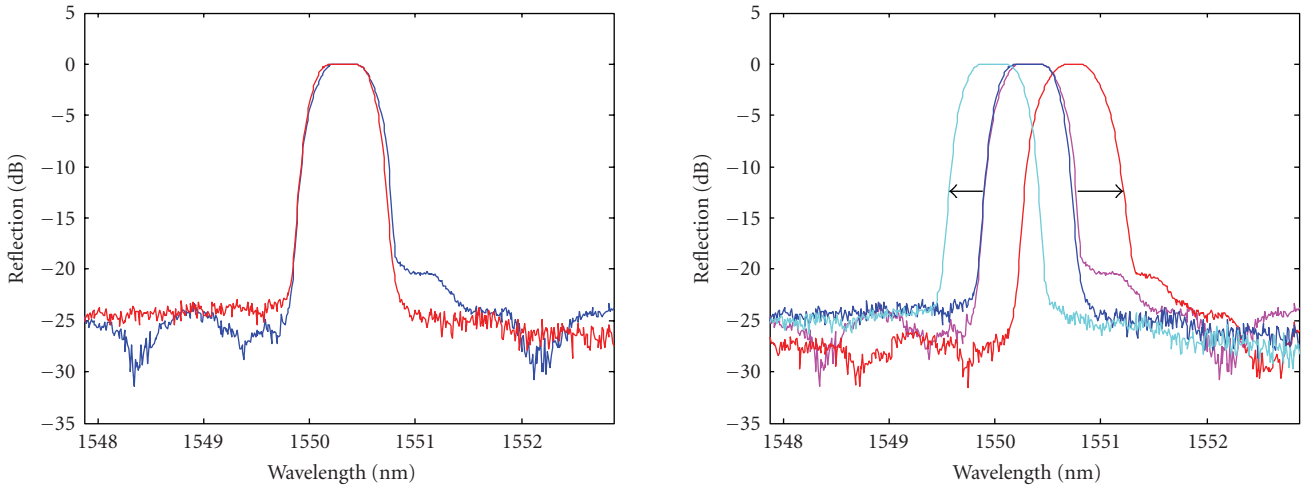

Figure 5: (a) Two fiber Bragg gratings written one in each core of a Gemini G2 fiber. (b) Upon bending, one grating shifts to shorter wavelengths while the other one shifts to longer wavelengths.

pair of fibers spliced to the Gemini G2 fiber. The total splice procedure to each Gemini fiber end here takes ~15 minutes if the loss is considered acceptable.

4. Sensing with Bragg Gratings

One of the most interesting applications of the Gemini fiber concept involves writing Bragg gratings in the various cores. Similarly to conventional multicore fibers, the sensitivity to temperature of the various waveguides is similar, and if the temperature varies all gratings shift equally in wavelength. However, a bend around the neutral axis cause the FBG to shift to longer wavelengths when the waveguide is elongated and to shorter wavelengths when it is compressed [13–15]. It is thus possible to determine optically the strain or stress to which the fiber is subjected. By translating other measurands such as pressure or acceleration to a bend, the Gemini fiber can be employed in various sensing applications. Here, we describe preliminary studies of Gemini fibers (G2) with fiber Bragg gratings.

The qualitative behavior of the Gemini G2 fiber is illustrated in Figure 5. A fiber Bragg grating is written in each one of the (in this case two) cores. The process is done sequentially, one grating at a time. The fiber is previously H_2-loaded at 150 atm for two weeks at room temperature. UV exposure is carried out in an interferometer with 244 nm radiation from a frequency doubled CW Ar^+ laser delivering ~23 mW. In the particular example here, the 1.2-cm long unchirped Hamming apodized FBGs are both centered at ~1550 nm, are ~0.5 nm broad and relatively strong (~25 dB) after 7 identical exposures.

Upon bending around its own axis, one grating shifts to longer wavelengths and the other one to shorter wavelengths, as seen in Figure 5. In order to carry out a more quantitative measurement, another pair of gratings was recorded in a piece of Gemini fiber G2, which after recording was mounted with UV curing glue on a flexible beam [13–15]. The piece of G2 fiber is displaced from the axis of the beam so as to result in a large wavelength shift when the beam is bent. The wavelengths of the two gratings are matched at 1555 nm at room temperature with the beam straight.

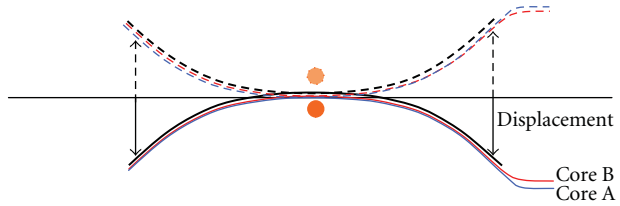

Figure 6: Schematic diagram of FBG bending set-up. Solid drawings indicate compression and dashed stretching. The scheme is not in scale.

Figure 6 shows the schematic set-up used to study the response to a bend (displacement) of FBGs written in a Gemini G2 fiber. The bend is introduced by displacing the two extremes of the beam while keeping the center fixed as seen in Figure 6. A 5 mm displacement here corresponds to a bend radius of 25 cm. Negative values mean that the gratings are elongated and positive displacements correspond to compression.

Figure 7 illustrates the tuning of the Bragg wavelengths for the two FBG of this device. The parabolic (black and red) curves shown are the best fit to the data (squares for core A and circles for core B) of the Bragg wavelength when the beam is bent. A tuning range of 16 nm is covered with a displacement D in the range $-2\,\text{mm} < D < +10\,\text{mm}$, where D is measured 5 cm from the center of the grating. Figure 7 also gives the difference in Bragg wavelengths for cores A and B measured when the bend is increased. A well-behaved and monotonic shift is observed (blue triangles), indicating that this difference can be used as an optical measurement

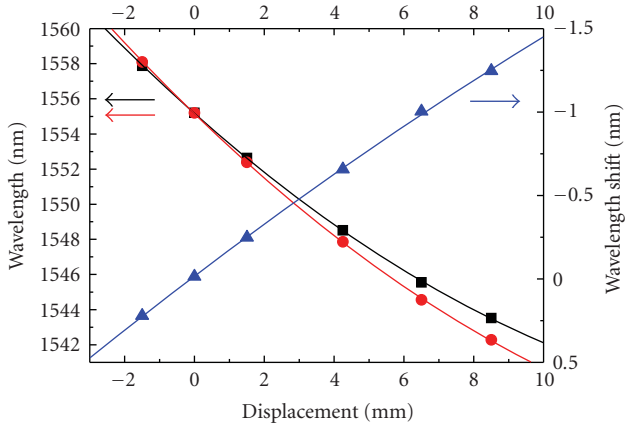

FIGURE 7: Bend tuning a Gemini S2 fiber with two FBGs. Both Bragg wavelengths shift by >14 nm. Triangles show the difference between the two waveguides. Measurements carried out at room temperature.

of the displacement. This device broke before temperature measurements could be carried out.

A third device was then manufactured in Gemini G2 fiber, where the two Bragg wavelengths do not overlap (λ_A = 1533.3 nm and λ_B = 1535.5 nm at 25°C). This device was mounted as schematically shown in Figure 6 and heated with a lamp. The temperature of the arrangement was monitored with a thermocouple in close proximity to the FBGs. No particular precaution was taken to equalize the temperature at the waveguides, equalization relying only on the close proximity of the cores. Figure 8(a) shows a plot of the Bragg wavelengths for both cores at 25°C, 35°C and 45°C, where D is measured 13.5 cm from the center of the grating. The solid curves are again parabolic fits to the data. In contrast to the behavior in Figure 7, here the second derivative of the solid lines is negative. The reason for this difference is not understood at present, but is likely to be associated to the exact position in relation to the axis of the beam at which the Gemini device is glued, which is largely uncertain and strongly affects the response of the gratings. It is clear from Figure 8(a) that the peak wavelengths change both with the bend (displacement) and with temperature. The sensitivity to temperature measured is 32 pm/Kelvin. This is approximately 3 times larger than expected for a free-standing FBG, indicating that the plastic beam and glue dominate the temperature dependence. A similar problem is likely to be found in most applications where a Gemini fiber G2 is to be used for sensing. The relative wavelength shift, that is, the difference between the shifts for the two cores is determined for various bends at three temperatures. It is hoped that the temperature dependence can be cancelled out exactly, and only the bend (displacement) remains. Figure 8(b) illustrates the three curves obtained at 25°C, 35°C and 45°C from the subtraction of the pair of blue curves (triangles), red curves (circles) and black curves (squares). A set of three monotonic curves is obtained, relating the wavelength to the displacement. The curves nearly overlap, indicating that the temperature effects can be cancelled from the information from both cores. The maximum deviation measured amounts to 0.5%. Thus, it is concluded that the bend can be determined from the difference in Bragg wavelengths for the two gratings. It should be remarked that the Gemini G2 fiber tends to bend naturally in such a way that both cores (FBGs) are affected equally much. In order to have one core stretching more than the other when bending, the fiber needs to be mounted on a beam and fixated (e.g., by gluing). The G4 fiber, on the other hand, can be easily bent in various directions and the fixation requirements are relaxed.

From these preliminary experiments it can be concluded that the Gemini fibers can be used with fiber Bragg gratings for sensing bends and displacement. Temperature effects can be removed using the information acquired from both cores.

5. Interferometry with Gemini Fiber

One interesting potential application of the Gemini fiber is in the embodiment of a monolithic fiber interferometer. The structure of the fibers fabricated in the drawing tower (cf. Figure 2) is well suited for the manufacture of fusion couplers. Thus, the easy access to each core, the possibility to taper a Gemini fiber locally to allow for coupling between cores and the rigid structure which guarantees equal arm lengths and minimizes polarization uncertainty provide for a useful broadband fiber interferometer. Potential applications include electrically driven fiber switches and modulators and add-drop multiplexers [16–18].

A preliminary experiment was carried out to make a coupler in Gemini G2 fiber. A Vytran LDS-1250 splicing/tapering machine with a 3-mm tungsten element is employed. The computer driven procedure consists first of a fusion stage, when the heated zone is scanned over a 10 mm section of the G2 fiber so that the waveguides start fusing together. This process takes 1500 seconds, and a fusion coefficient [19, 20] 0.45 is obtained (i.e., the normalized ratio of the structure reducing from 2 to 1.73). The fusion stage is followed by tapering stage, when the fused zone is simultaneously heated and pulled to become thinner. The process takes 2000 seconds and generates an adiabatic structure. Because of the nonoptimal coupler fabrication process and in particular the metal oxide layer deposited on the taper, the excess loss incurred is ~3.3 dB. This is unacceptably high for a commercial device, but still usable for characterization of the Gemini fiber. The optical set-up used is for monitoring the process is illustrated in Figure 9.

The fabrication of the coupler in a Gemini fiber implies in the creation of a Michelson interferometer [21], where the back reflection is obtained from the fiber cleave. If the interferometer is probed with a white light source, the bandwidth obtained indicates how well the two optical paths match. Figure 10 illustrates the result of such a measurement. The extinction measured is 14 dB. From the 50 nm FWHM bandwidth, the optical path difference inferred for the 40-cm long device is 12.8 μm (i.e., 32 μm/m). It is possible that the path unbalance is created either at the coupler or at the end cleave. However, if the unbalance is assigned entirely to a difference in propagation constants between the two fiber

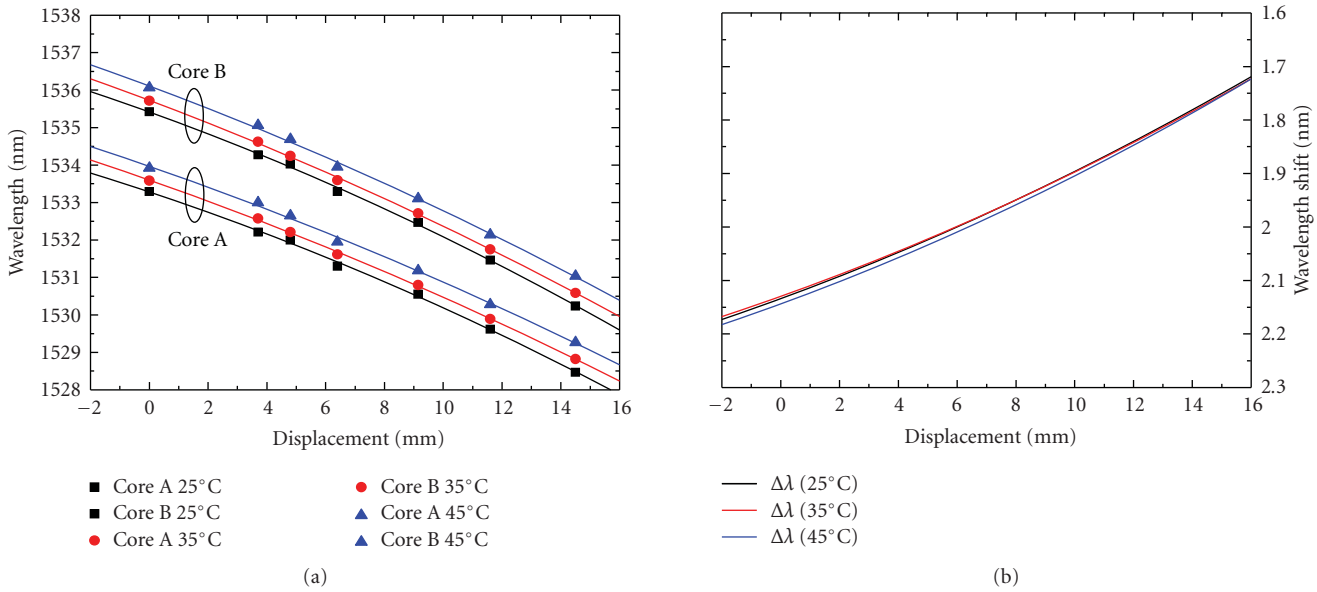

Figure 8: (a) Bragg wavelength λ_A and λ_B measured for cores A and B when a piece of Gemini fiber G2 with FBGs is compressed (positive values of the displacement) and stretched (negative values) at 25°C, 35°C and 45°C. (b) Relative wavelength shift $\lambda_B - \lambda_A$ at three temperatures. The displacement is associated to wavelength and the temperature dependence is small.

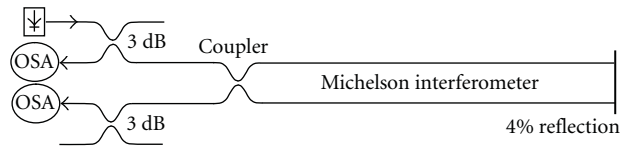

Figure 9: Arrangement used for the fabrication and characterization of fused fiber couplers and interferometers in Gemini G2 fiber.

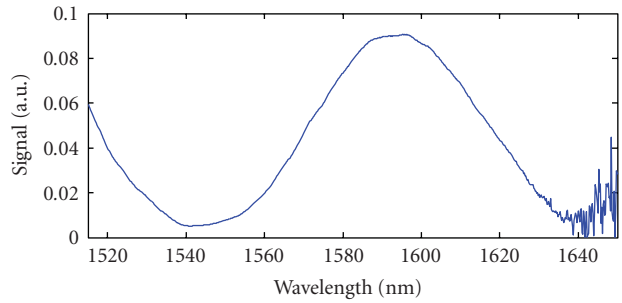

Figure 10: Measurement of the optical bandwidth of a 40 cm long fiber interferometer on a linear scale. The FWHM is ~50 nm.

cores, a mode index difference of 3×10^{-5} is obtained. This is an upper limit for the inequality of the two waveguides in the Gemini fiber G2.

Other characterization measurements were carried out. The differential group delay (DGD) of 2 m long section of Gemini G2 and G2H fiber is measured to be ~27 fs and ~74 fs, respectively, and the polarization dependent loss (PDL) of G2 for the same length is 0.1 dB. These low values are perhaps not surprising considering that the fibers are made from standard telecommunication preforms.

6. Conclusions

A novel fiber configuration is introduced in this work, based on a plurality of individual fiber preforms drawn together but nearly maintaining their original shape. This concept can be extended to the case where the preforms are unequal, for instance, with one arm drawn from a single-mode and the other from a microstructured, doped or multimode preform. Coupling is studied in the present work and the possibility to connect in a single splice more than one fiber to the Gemini fiber is introduced as being highly advantageous. A conventional splicer can be used, the loss is acceptable and the operation takes minutes. Sensing with Gemini fibers is discussed mainly with the incorporation of fiber Bragg gratings. The temperature dependence of devices made from this fiber type can be removed almost entirely by using the information collected from both cores. Interferometry is also briefly discussed, although it can be appreciated that a large number of new options are opened by the monolithic multicore fiber design, where access to individual cores is straightforward.

Acknowledgments

It is a pleasure to acknowledge the valuable input of Suzanne Lacroix on the procedure to be used for the fabrication of fused couplers used in this work. Help by Oleksandr Tarasenko, Erik Petrini, Per Helander and Håkan Olsson at Acreo is also greatly appreciated.

References

[1] A. Méndez and T. S. Morse, Eds., *Specialty Optical Fibers Handbook*, chapter 6.4, Elsevier, Amsterdam, The Netherlands, 1st edition, 2007.

[2] J. W. Arkwright, S. J. Hewlett, G. R. Atkins, and B. Wu, "High-isolation demultiplexing in bend-tuned twin-core fiber," *Journal of Lightwave Technology*, vol. 14, no. 7, pp. 1740–1745, 1996.

[3] M. J. Gander, E. A. C. Galliot, R. McBride, and J. D. C. Jones, "Bend measurement using multicore optical fiber," in *Optical Fiber Sensors*, OSA Technical Digest Series, Optical Society of America, 1997, OWC6.

[4] M. J. Gander, D. Macrae, E. A. C. Galliot, et al., "Two-axis bend measurement using multicore optical fibre," *Optics Communications*, vol. 182, no. 1–3, pp. 115–121, 2000.

[5] G. M. H. Flockhart, W. N. MacPherson, J. S. Barton, J. D. C. Jones, L. Zhang, and I. Bennion, "Two-axis bend measurement with Bragg gratings in multicore optical fiber," *Optics Letters*, vol. 28, no. 6, pp. 387–389, 2003.

[6] G. M. H. Flockhart, G. A. Cranch, and C. K. Kirkendall, "Differential phase tracking applied to Bragg gratings in multicore fibre for high accuracy curvature measurement," *Electronics Letters*, vol. 42, no. 7, pp. 17–18, 2006.

[7] M. Silva-Lopez, C. Li, W. N. MacPherson, et al., "Differential birefringence in Bragg gratings in multicore fiber under transverse stress," *Optics Letters*, vol. 29, no. 19, pp. 2225–2227, 2004.

[8] C. G. Askins, T. F. Taunay, G. A. Miller, et al., "Inscription of fiber Bragg gratings in multicore fiber," in *Bragg Gratings, Photosensitivity and Poling in Glass Waveguides (BGPP '07)*, p. JWA39, Quebec, Canada, 2007.

[9] S. B. Poole and J. D. Love, "Single-core fibre to twin-core fibre connector," *Electronics Letters*, vol. 27, pp. 1559–1560, 1991.

[10] R. R. Thomson, H. T. Bookey, N. D. Psaila, et al., "Ultrafast-laser inscription of a three dimensional fan-out device for multicore fiber coupling applications," *Optics Express*, vol. 15, no. 18, pp. 11691–11697, 2007.

[11] L. Yuan, Z. Liu, J. Yang, and C. Guan, "Bitapered fiber coupling characteristics between single-mode single-core fiber and single-mode multicore fiber," *Applied Optics*, vol. 47, no. 18, pp. 3307–3312, 2008.

[12] A. B. Grudinin, D. N. Payne, P. W. Turner, et al., "Multi-fiber arrangements for high power fiber lasers and amplifiers," US patent 6826335, November 2004.

[13] T. Imai, T. Komukai, and M. Nakazawa, "Dispersion tuning of a linearly chirped fiber Bragg grating without a center wavelength shift by applying a strain gradient," *IEEE Photonics Technology Letters*, vol. 10, no. 6, pp. 845–847, 1998.

[14] S. Y. Set, B. Dabarsyah, C. S. Goh, et al., "A widely tunable fiber Bragg grating with a wavelength tunability over 40 nm," in *Proceedings of the Optical Fiber Communication Conference and Exhibit (OFC '01)*, vol. 1, pp. MC4-1–MC4-3, 2001.

[15] C. S. Goh, M. R. Mokhtar, S. A. Butler, S. Y. Set, K. Kikushi, and M. Ibsen, "Wavelength tuning of fiber Bragg grating over 907 nm using a simple tuning package," *IEEE Photonics Technology Letters*, vol. 15, no. 4, pp. 557–559, 2003.

[16] R. Kashyap, *Fiber Bragg gratings*, chapter 6.4, Academic Press, New York, NY, USA, 1st edition, 1999.

[17] P. Yvernault, D. Mechin, E. Goyat, L. Brilland, and D. Pureur, "Fully functional optical add & drop multiplexer using twin-core fiber based Mach-Zehnder interferometer with photoimprinted fiber Bragg gratings," in *Proceedings of the Optical Fiber Communication Conference and Exhibit (OFC '01)*, vol. 3, pp. WDD92-1–WDD92-3, 2001.

[18] W. Margulis, O. Tarasenko, and N. Myrén, "Electrooptical fibers," in *Photonics North*, P. Mathieu, Ed., vol. 6343 of *Proceedings of SPIE*, Quebec, Canada, 2006, 634319.

[19] E. Pone, X. Daxhelet, and S. Lacroix, "Refractive index profile of fused-tapered fiber couplers," *Optics Express*, vol. 12, no. 13, pp. 2909–2918, 2004.

[20] E. Pone, X. Daxhelet, and S. Lacroix, "Refractive index profile of fused-fiber couplers cross-section," *Optics Express*, vol. 12, no. 6, pp. 1036–1044, 2004.

[21] R. Kashyap and B. K. Nayar, "An all single-mode fiber Michelson interferometer sensor," *Journal of Lightwave Technology*, vol. 1, no. 4, pp. 619–624, 1983.

Hindawi Publishing Corporation
Journal of Sensors
Volume 2009, Article ID 476267, 10 pages
doi:10.1155/2009/476267

Review Article

Photonic Crystal Fiber Sensors for Strain and Temperature Measurement

Jian Ju and Wei Jin

Department of Electrical Engineering, The Hong Kong Polytechnic University, Hung Hom, Kowloon, Hong Kong

Correspondence should be addressed to Wei Jin, eewjin@polyu.edu.hk

Received 27 February 2009; Accepted 27 May 2009

Recommended by Christos Riziotis

This paper discusses the applications of photonic crystal fibers (PCFs) for strain and temperature measurement. Long-period grating sensors and in-fiber modal interferometric sensors are described and compared with their conventional single-mode counterparts. The strain sensitivities of the air-silica PCF sensors are comparable or higher than those implemented in conventional single-mode fibers but the temperature sensitivities of the PCF sensors are much lower.

1. Introduction

Recently, there has been great interest in the development of photonic crystal fibers (PCFs) and related devices and sensors. PCFs are typically made of single silica material and comprised of a solid or hollow core surrounded by a periodic array of air holes running along their length [1]. PCFs may be regarded as falling into two broad categories: the index-guiding PCFs (IG-PCFs) and the photonic bandgap fibers (PBFs). In IG-PCFs, the effective refractive index of the microstructured cladding is reduced by the introduction of the air columns to below the index of the central core, and this makes it possible to guide light in the core by a modified form of total internal reflection. Figures 1(a) and 1(b) show two examples of such IG-PCFs. They are endlessly single-mode PCFs (Figure 1(a)) [2] that support only the fundamental mode over the entire wavelength range, and highly birefringent (Hi-Bi) PCFs (Figure 1(b)) [3] that have a high birefringence and a low temperature dependence of the birefringence. In PBFs, light is confined to a lower index core by reflection from the photonic crystal cladding, which possesses out of plane photonic bandgaps and does not allow light signals with certain wavelengths and propagation constants to escape from the central core. Figures 1(c) and 1(d) show, respectively, an air-silica PBF with an air core [4] and an all solid PBF with a silica core and a cladding comprising of an array of higher index rods (Ge-doped silica) in a silica matrix [5].

The emergence of PCFs opens the door for new possibilities in ultra-broadband transmission, high-power optical fiber amplifiers and lasers, optical fiber sensors, and so forth. PCF sensors in various forms have been demonstrated for the measurement of strain [7], temperature [8], refractive index [9], bending [10], and gas concentration [11]. In this paper, we describe mainly two classes of PCF-based sensors, that is, in-fiber long-period grating (LPG) sensors and in-fiber modal interferometric sensors; we discuss their applications for strain and temperature measurement.

2. Long-Period Grating Sensors

An LPG is formed by periodical perturbing the refractive index or waveguide geometry longitudinally along the length of an optical fiber, with a typical period from several hundreds micrometers to 1 mm. An LPG couples light resonantly from the fundamental core mode to forward propagating cladding modes. The resonant wavelength λ_{res} of an LPG with period Λ is determined by the phase matching condition [12]:

$$\lambda_{\text{res}} = (n_{\text{co}} - n_{\text{cl,m}}).\Lambda, \tag{1}$$

where n_{co} and $n_{\text{cl,m}}$ are the effective indices of the fundamental core mode and the mth cladding mode, respectively. The

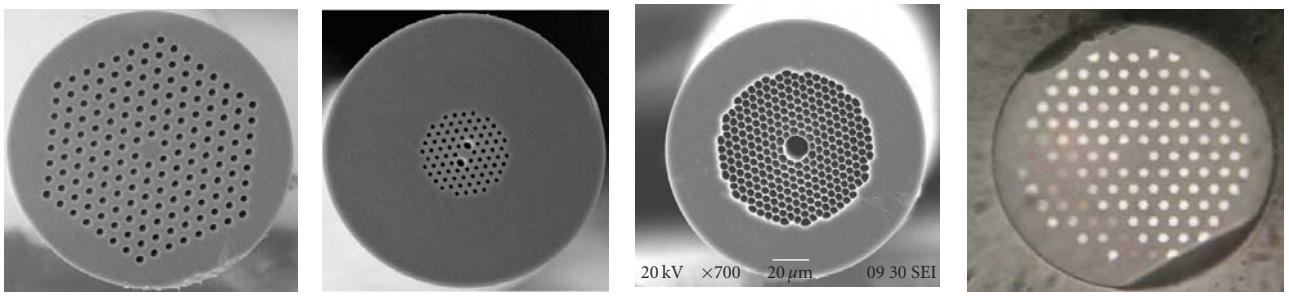

Figure 1: Scanning electron micrographs of different PCF cross-sections. (a) a large-mode-area air-silica endlessly single-mode PCF, (b) an air-silica highly birefringent PCF, (c) an air-silica air-core PBF. These PCFs are from Crystal Fiber A/S [6] (d) an all-solid PBF [5].

cladding modes have higher loss than the core mode, leading to attenuation bands in the transmission spectrum.

Conventional single-mode fibers (SMFs) have Ge-doped cores that are photosensitive and LPGs in such fibers can be formed by periodical perturbing the core refractive index by UV illumination through an amplitude mask or a point-by-point writing technique. LPGs in SMFs have been investigated extensively for applications such as wavelength filters, gain flatteners for EDFAs, and sensors.

PCFs are typically made of a single material (silica) which has no photosensitivity; inscription of PCFs by direct UV irradiation is then difficult. However, LPGs in PCFs have been made by use of nonphotochemical inscription techniques such as CO_2 laser irradiation [7], electrical arc discharge [8], external mechanical pressure [13], and femtosecond laser radiation [14].

2.1. LPGs in IG-PCFs. Figure 2(b) shows the side view of an LPG created on a large-mode-area endlessly single-mode PCF (LMA-10) with its cross-section shown in Figure 2(a). The LPG was fabricated by use of a pulsed CO_2 laser with a setup described in [7]. Observable notches or grooves were created along the surface of the PCF, indicating considerable collapsing of the air-holes in the cladding region. The LPG has 40 periodic notches along the fiber, and the period is 410 μm. The transmission spectrum of the LPG, as shown in Figure 3, has double resonant peaks from 1200 to 1700 nm, corresponding to coupling of two different cladding modes. The resonant wavelengths of LPGs in such PCFs were found to decrease with the grating period, which is contrary to that in a conventional SMF.

LPGs with a similar transmission spectrum as shown in Figure 3 can be made with no visible physical deformation (notches) on the surface of the PCFs. The creation of such LPGs requires lower CO_2 laser energy density, and in such a LPG, the perturbation of the fiber geometry is negligible and the index perturbation of the glass material is believed to play a significant role in the formation of the LPGs.

The responses of the resonant wavelength to tensile strain are very different for LPGs with and without visible notches [7]. Figure 4 shows the strain and temperature responses of the LPG (LPG_1) shown in Figure 2 and a similar LPG (LPG_2) with the same grating length and pitch but no

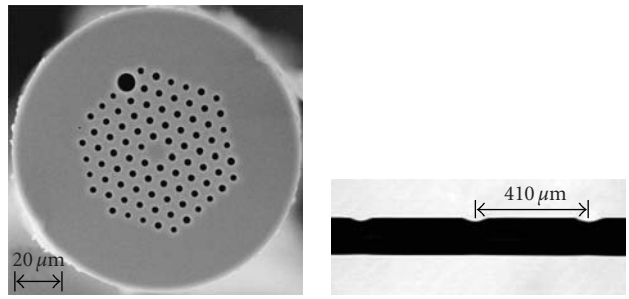

Figure 2: (a) Scanning electron micrograph of the cross-section of LMA-10 PCF, (b) photograph of the LPG with periodic notches [7].

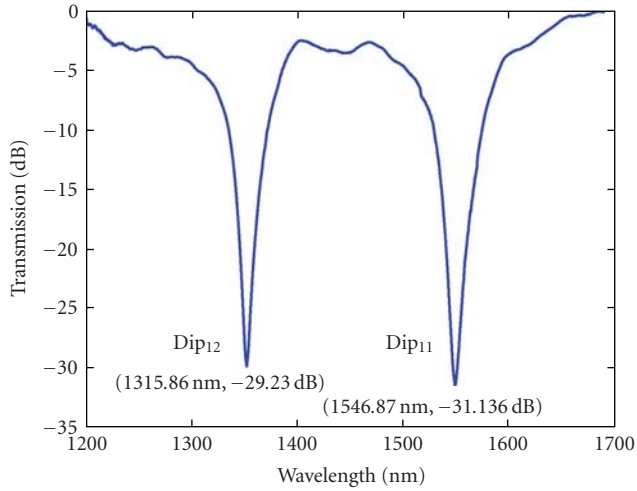

Figure 3: Transmission spectrum of a 40-notch LPG.

observable notches on the fiber surface. LPG_2 was fabricated by use of the same CO_2 laser setup as for LPG_1 but a lower dosage of CO_2 irradiation. The strain sensitivity of the LPG with notches (-7.6 pm/$\mu\varepsilon$) is about 25 times higher than the LPG without physical deformation (-0.31 pm/$\mu\varepsilon$). The temperature sensitivities of the two LPGs are approximately the same. The asymmetrical structure caused by the periodic

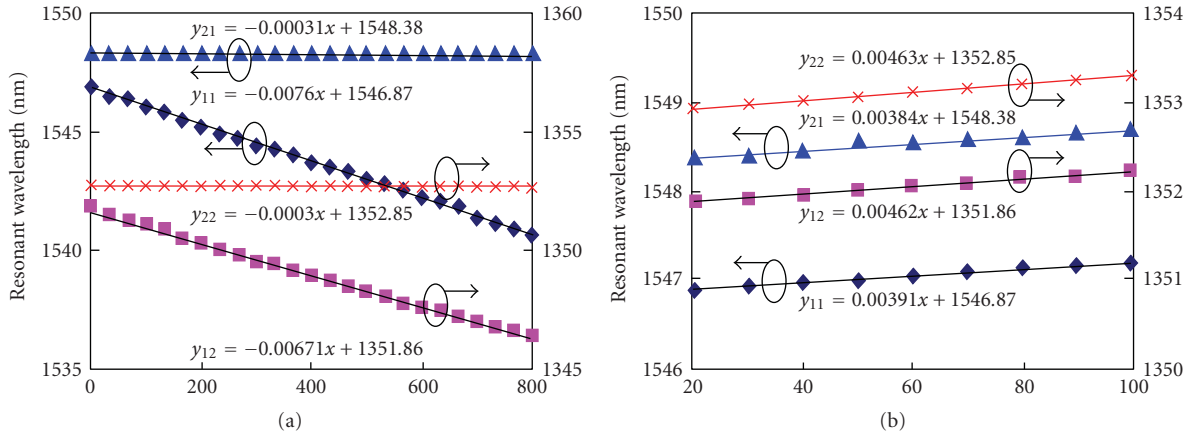

FIGURE 4: Variation of resonant wavelength of a LPG with notches (LPG_1) and a similar LPG without notches (LPG_2) with (a) tensile strain, and (b) temperature ♦: Dip_{11} of LPG_1, ■: Dip_{12} of LPG_1, ▲: Dip_{21} of LPG_2, ×: Dip_{22} of LPG_2 [7].

notches introduces microbend when the LPG is axially stretched, which effectively enhanced the refractive index change of the LPGs with notches. The CO_2-laser-notched LPGs on PCFs also demonstrated very strong polarization dependent loss (PDL) and can be used as in-fiber polarizers with good temperature stability [15]. The large PDL may be attributed to the side exposure of CO_2 laser, which introduces asymmetrical index profile in the fiber cross-section.

Table 1 lists the strain and temperature sensitivities of some PCF-based LPGs fabricated by CO_2 laser and electric arc discharge techniques. The sensitivities of SMF-based LPGs are also listed in the table for comparison. The exceptional low temperature dependence of the LPG is regarded as the results of single material used for PCF. As both the cladding and core modes are mostly distributed in the silica, they show similar responses to the temperature change. The very small temperature sensitivity makes them useful for strain measurement with negligible temperature cross-sensitivity.

2.2. LPGs in PBFs. LPGs were also fabricated in hollow-core (HC) PBFs [19]. Figure 5(c) shows the side view of an LPG made on an HC PBF (HC-1550-02) in which periodic notches are created along the fiber. The cross-section, as shown in Figure 5(b), of the PBF at the notched region is asymmetric due to the collapse of air holes and the ablation of glass on one side of the fiber. The outer rings of air holes in the cladding, facing to the CO_2 laser irradiation, were largely deformed; however, little or no deformation was observed in the innermost ring of air-holes and in the hollow core.

Figure 5(d) shows the measured transmitted spectrum of a 40-period LPG. The 3 dB bandwidth is ~5.6 nm, which is much narrower than that of the LPGs with the same number of grating periods in conventional SMFs and in IG-PCFs [7, 16]. The insertion loss of the LPG is very low (<0.3 dB), because most light is guided in the hollow-core where no deformation was observed.

Both refractive index perturbation of the glass material and the changes in air-hole sizes, shapes, and locations may contribute to the formation of the LPG. However, as most light power of the fundamental mode (>95%) is in the air region, the effect of refractive index variation of the glass material on the mode index is expected to be smaller than that for conventional fibers and solid core IG-PCFs. On the other hand, as shown in Figure 5(b), the deformation of air-holes in the cladding is obvious, which changes the air-filling fraction and the waveguide structure and perturbs the mode fields and effective indexes of the core, surface, and cladding modes. There could also be weak deformation of the hollow-core, although it is not observable in our experiments. We believe that the periodic perturbation of the waveguide geometry is the dominant factor that causes resonant mode coupling, although the induced refractive index variation may also contribute a little.

A number of LPGs with different pitches and the same number of grating periods were written in the PBG fiber and the measured resonant wavelength as functions of the grating pitch is shown in Figure 5(e), the resonant wavelength decreases with the increase in grating pitch, which is opposite to the LPGs in the conventional SMFs [16, 17]. For each of the LPGs, two attenuation pits, as shown in Figure 5(e), were observed within 1500 to 1680 nm, indicating that the fundamental mode is coupled to two different higher-order (surface-like) modes.

The responses of the LPG in the air-core PBF to strain, temperature, bend, and external refractive index are measured, and the results are shown in Figure 6. The wavelength sensitivity to strain (−0.830 pm/$\mu\varepsilon$) is similar to that of LPGs in IG-PCFs or conventional SMFs (Table 1), and the temperature sensitivity (~2.9 pm/°C) is one to two orders of magnitude less than those of the LPGs in the conventional SMFs. In addition, the wavelength sensitivity to bend is three to four orders of magnitude less than those of the LPGs in the conventional SMFs, and it is insensitive to the external refractive index changes. The LPG in HC-PBF may be used as a strain sensor without cross-sensitivity to temperature, curvature, and external refractive index.

Table 1: Strain and temperature sensitivities of LPGs in IG-PCFs by different methods.

Inscriptionmethod	Period (μm)	Length (mm)	Wavelength (nm)	dλ/dε (pm/$\mu\varepsilon$)	dλ/dT (pm/°C)	Reference
CO_2 laser (with grooves)	410	16.4	1546.87	−7.6	3.91	[5]
CO_2 laser (without grooves)	410	16.4	1548.38	−0.31	3.84	[5]
Arc discharge	400	37.6	1668	−2.5	3.4	[6]
Arc discharge	1000	19.0	1403	−2.08	2.2	[6]
CO_2 laser*			1526.5	−0.45	58	[16]
UV exposure*	320		1573.1	7.31	46	[17]
Arc discharge*	540		1580	~1.5	66–73	[18]

*Conventional single-mode fiber-based LPG.

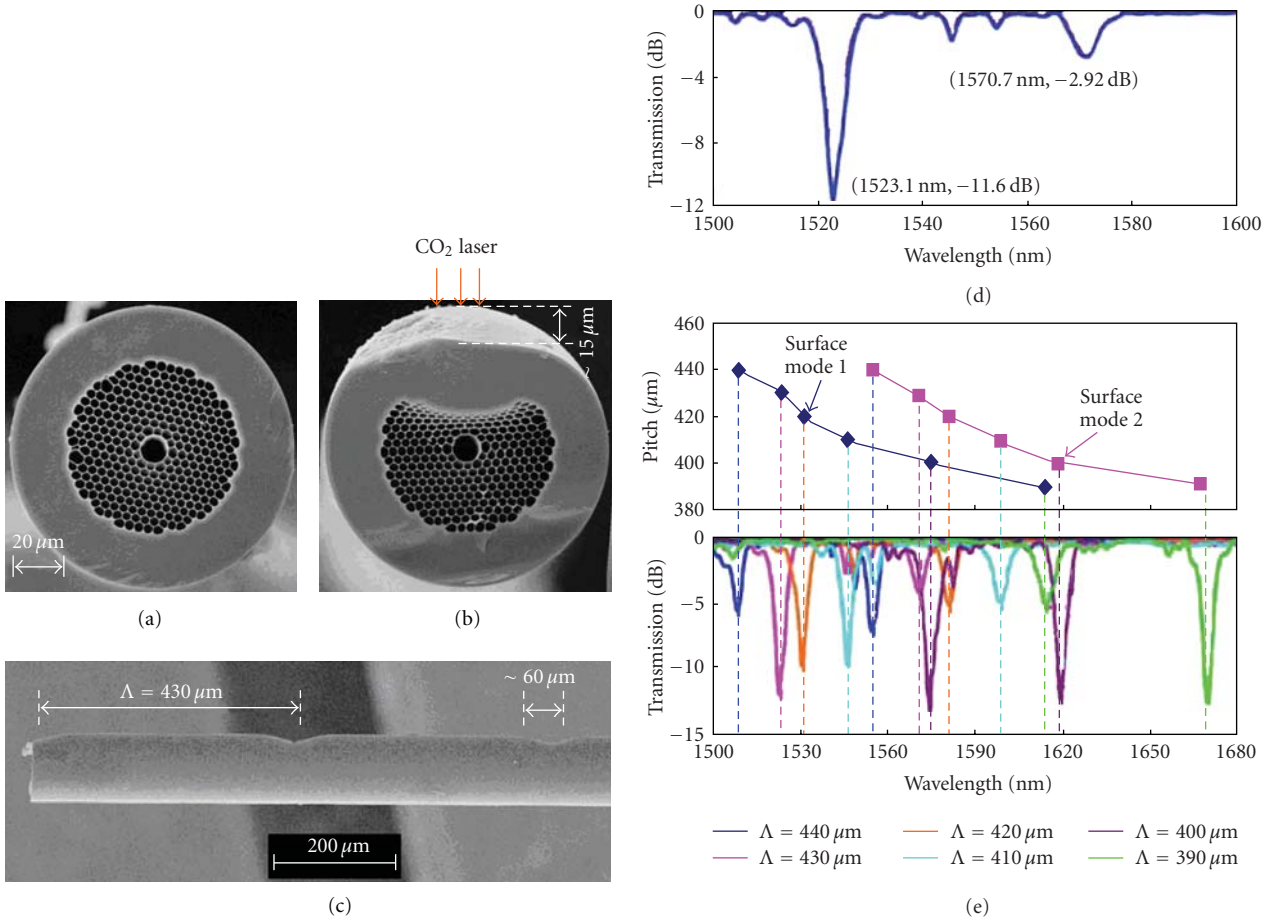

Figure 5: Scanning electron micrographs of PBF cross-sections (a) before and (b) after CO_2 laser irradiation. (c) Periodic notches created on the surface of the PBF. (d) The transmitted spectrum of LPG with 40 periods and a grating pitch of 430 μm. (e) Variation of LPG resonant wavelengths with grating pitch (upper panel) and the corresponding transmission spectrums (lower panel) [19].

LPGs were also inscribed in all-solid PBG PCF (Figure 1(c)) by the UV exposure method [5]. The all-solid PBG PCF has a solid central silica core region and a microstructured cladding region where higher index Ge-doped silica rods are embedded into silica background. The resonant wavelength of the LPG experiences a red shift when the temperature is increased, and the temperature sensitivity is measured to be 19.1 pm/°C. This value is higher than those of the PCFs made from a single material.

3. Modal Interferometric Sensors

Interferometric sensors have been explored in sensing largely because of their high sensitivities to a broad range of parameters. The modal interferometers in which the interferometric phase difference is accumulated by considering the difference in the effective refractive indices of different fiber modes have been widely investigated. They are attractive for several reasons, including small size, flexibility, as well as the reduced thermal sensitivity in view of the small difference of the

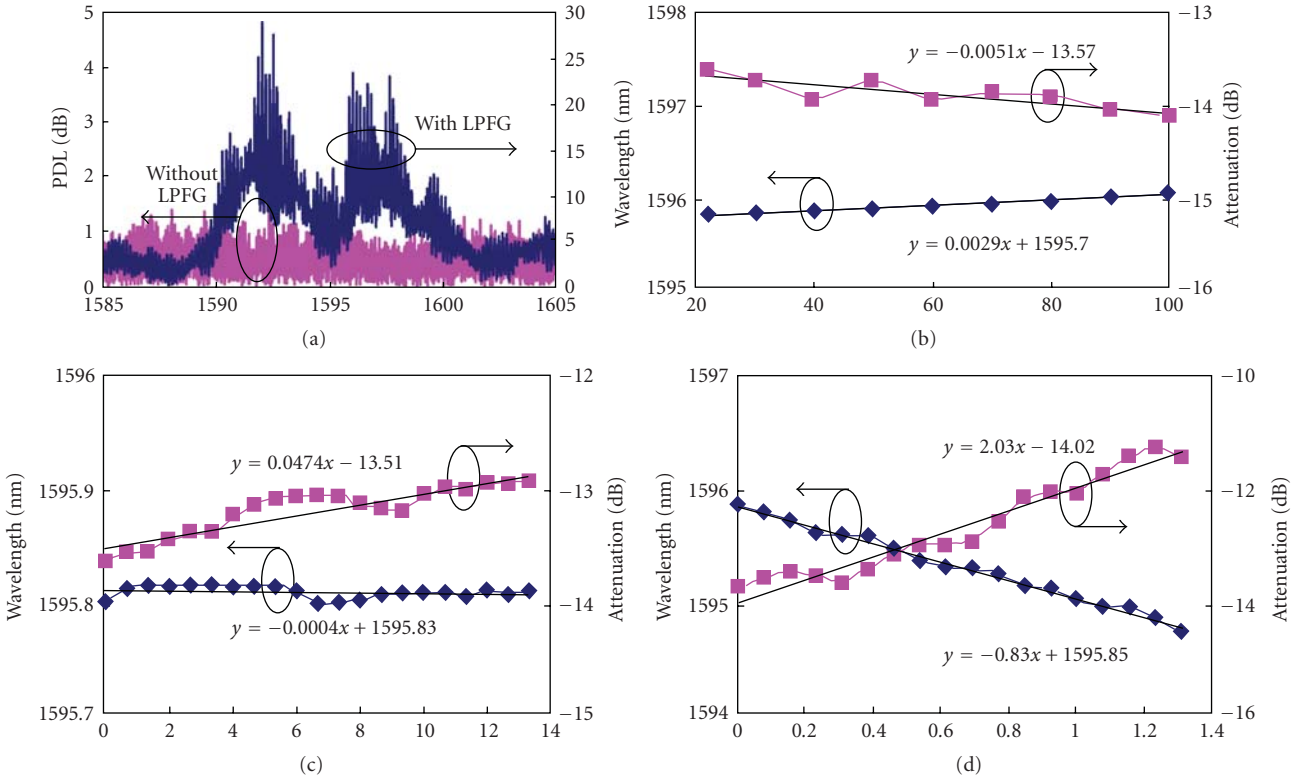

Figure 6: (a) PDL of PBF with and without an LPG. Measured resonant wavelength and peak transmitted attenuation of the LPG as functions of temperature (b), curvature (c), and tensile strain (d) [19].

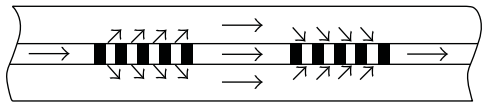

Figure 7: A typical MZI configuration.

thermo-optic coefficients of different modes as they travel the same length of optical fibers. In this section, modal interferometers based on different types of modes in IG-PCFs will be described and their application to the strain and temperature measurement will be discussed.

3.1. Core/Cladding Modal Interferometer. A core/cladding modal interferometer utilizes the interference between a core mode and a copropagating cladding mode, which is also referred as in-fiber Mach-Zehnder interferometer (MZI). It has been widely used for wavelength filtering and optical sensing [20, 21]. In the typical MZI configuration as shown in Figure 7, two cascaded LPGs are commonly used with the first LPG couples part of the core mode power into a forward-propagating cladding mode and the second LPG combines the two modes, resulting in sharp interference fringes. The two LPGs serve as beam-splitter/combiner and the core and the cladding modes travel through two independent paths along the same fiber.

A variety of PCF-based MZIs have been demonstrated with modifications on the basic MZI configuration. The first PCF-based MZI has two nearly identical LPGs which are formed by applying periodic mechanical stress to the PCF [22]. Alternatively, all-PCF MZIs can also be formed by offset-splicing combined with partial collapsing of air-holes [23], or by using a single LPG in combination with a short section of PCF where air-holes are fully collapsed [24]. With the advancement of LPG writing technique by using pulsed CO_2 laser, the resonant wavelength and attenuation of the LPG can be precisely controlled, which allows compact in-fiber MZI with low insertion loss to be developed on PCF [25].

Figure 8 shows the wavelength domain interference fringes of an in-fiber MZI formed by a pair of LPGs fabricated directly on PCF by use of a pulsed CO_2 laser. The measured strain and temperature responses of the interference peak wavelength at 1646 nm are shown in Figure 9. The strain sensitivity is $-2.6\,\text{pm}/\mu\varepsilon$, which agrees with the results reported in elsewhere ($-2.28\,\text{pm}/\mu\varepsilon$ at 1560 nm in [23], and $-2.80\,\text{pm}/\mu\varepsilon$ at 1550 nm in [24]) and is about 5 times higher than that for an MZI fabricated on a standard SMF ($+0.445\,\text{pm}/\mu\varepsilon$, Figure 9(b)) with the same CO_2 laser technique and two times higher than that of a typical fiber Bragg grating (FBG) sensor. The temperature sensitivity of the MZI is measured to be $42.4\,\text{pm}/^\circ\text{C}\cdot\text{m}$, which is almost 30 times lower than that of the MZI in the SMF ($1215.56\,\text{pm}/^\circ\text{C}\cdot\text{m}$, Figure 9(a)) [25].The very small temperature sensitivity may be attributed to the single material property of the PCF, which results in similar

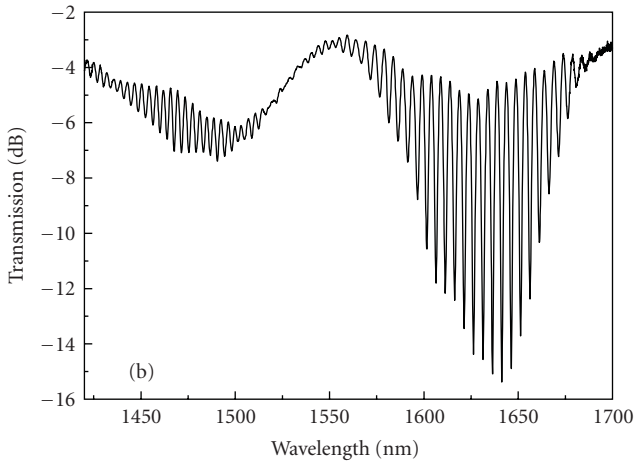

Figure 8: The transmission spectrum of a PCF-MZI with a cavity length of 190 mm [25].

response of the core and cladding modes to temperature. The MZI on PCF may be potentially used as a temperature-insensitive strain sensor and as stable multichannel filter with low temperature dependence.

3.2. Two-Mode PCF Interferometer. It is possible to make in-fiber devices based in the interference between the two core modes. This however requires the use of a two-mode fiber, that is, a fiber that supports only two core modes, to avoid interference with other core modes. Conventional step-index two-mode optical fibers have been investigated for various device applications such as wavelength filters, frequency shifters, switches, interferometric strain, and temperature measurement. However, the wavelength range of the two-mode operation for conventional fibers is typically less than 150 nm [26], which limit the potential applications of the two-mode devices.

It has been shown that an air-silica IG-PCF with a cross-section similar to Figure 1(b) can be designed to operate as a two-mode fiber over the entire low-loss transmission window of the silica glass [27]. This would allow the creation of extremely broadband two-mode fiber devices and sensors.

We investigated theoretically and experimentally the modal properties of the commercial high birefringent (Hi-Bi) PCF as shown in Figure 1(b) (PM-1550, Crystal Fiber A/S [6]) and found it operating as a two-mode fiber over wavelength range from below 543 to 1400 nm, although it guides only the fundamental mode at 1550 nm. Figure 10 shows the transverse mode field patterns of the four nondegenerate approximately linearly polarized (LP) modes at 1330 nm, which were calculated by using a full-vector finite element method (FEM). By analogy to the elliptical core fiber, these four modes are labeled as $LP_{01}{}^{x}$, $LP_{01}{}^{y}$, $LP_{11}{}^{x}$(even), and $LP_{11}{}^{y}$(even) modes. The superscripts x and y correspond to the x- and y-polarizations, respectively. It is interesting to notice that this Hi-Bi PCF is capable to suppress the LP_{11}(odd) modes. The wide two-mode wavelength range and the stable lobe orientation make it possible to built stable two-mode devices and interferometric sensors with long length of fibers.

A two-mode fiber sensor uses a differential interferometric scheme where the interference between the LP_{01} and the LP_{11}(even) modes of the fiber leads to a varying two-lobe pattern in the output. When the LP_{01} and LP_{11}(even) modes with the same polarization state are excited equally in the Hi-Bi PCF, the output radiation pattern will be a superposition of the contribution from the two modes and will be a function of the relative phase difference φ between them. For a change in φ of 2π there will be one complete oscillation of the intensity pattern.

An external disturbance, for example, strain or temperature, applied on the PCF two-mode interferometer leads to a differential phase shift between these two modes, resulting in an oscillation of the two-lobe pattern. A spatial demodulator monitoring one of the two-lobe patterns converts this oscillation into an intensity variation. When only the x- or y-polarization of LP_{01} and LP_{11} modes was excited at the entrance, a quasisinusoidal intensity waveform is obtained after the spatial demodulator.

3.2.1. Two-Mode PCF Strain Sensor. Figure 11 is a schematic of the experimental setup used to study the strain response of the two-mode PCF interferometer. Light from a laser was coupled into a piece of Hi-Bi PCF (PM-1550, Crystal Fiber A/S) with an alignment system consisting of a pair of lenses, a polarizer, a fiber holder, and a 5-dimensional translation stage. The PCF has a total length of ∼1 meter and is epoxy-bounded to a fixed stage and a translation stage. The 50 cm PCF in between the two stages can be axially strained through a computer controlled translation stage. An infrared TV camera with lens removed is placed near the output of the fiber to monitor one of two lobes of the far-field intensity patterns, as indicated in the rectangular region in the right panel of Figure 11. Alternatively, it is possible to use a lead-out fiber which is offset from the two-mode PCF to pick up the maximum contrast ratio in the intensity of the two-lobe output.

Experiments were conducted with different semiconductor lasers with wavelengths of 650, 780, 850, 980, and 1310 nm. Figure 12 shows the measured intensity variation at one of the lobes at 1310 nm when the PCF was elongated from 0 to 2 mm. The curves from top to bottom correspond, respectively, to polarizer set to 0°, 90°, and 45°, in respect to the x-axis as shown in the right panel of Figure 11. At 0° and 90°, the intensity variation is due to the interference of LP_{01} and LP_{11}(even) modes for the x- and y-polarizations, respectively. At a launch angle of 45° respective to the principle axis of PCF, the two sets of interference patterns, corresponding to two orthogonal polarizations, are superimposed, resulting in an amplitude-modulated wave as shown in the lower graph of Figure 12.

The strain sensitivities for orthogonal polarizations, which are defined as the rate of change of the phase difference between the two modes with respect to strain, are shown in Figure 13. The strain sensitivities have linear relationship

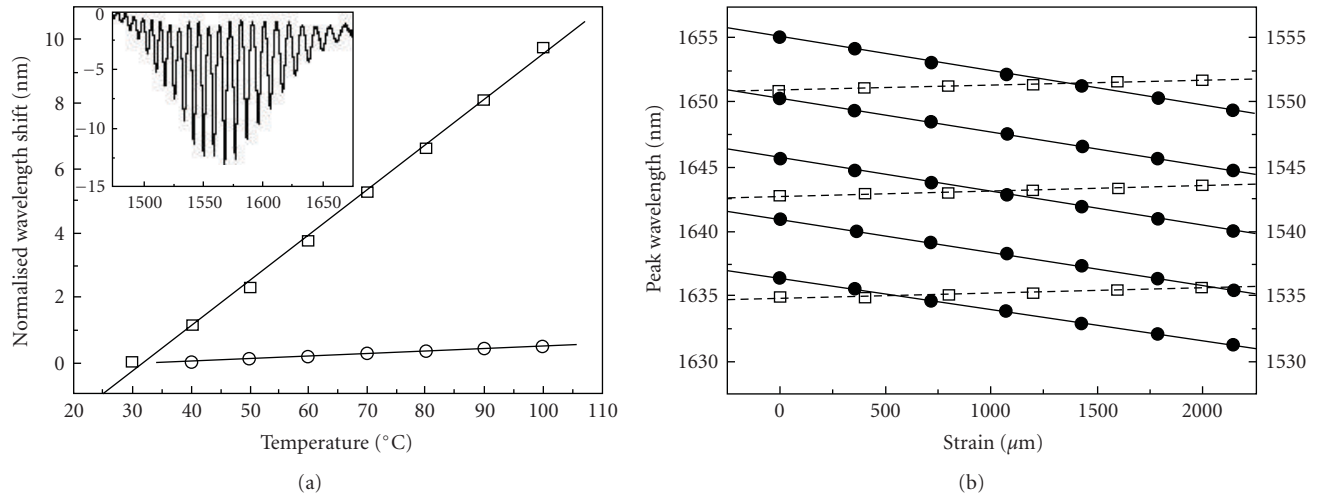

Figure 9: (a) Temperature responses of the PCF-MZI with transmission spectrum in Figure 8 (circular points) and an SMF-MZI with output spectrum shown in the inset (rectangular points). Solid lines: linear fits. (b) Strain responses of the interference peaks as functions of strain (PCF-MZI: left axis, filled circles, SMF-MZI: right axis, open squares). The solid and dash lines are the corresponding linear fits for the PCF-MZI and SMF-MZI [25].

with the optical wavelength, and higher sensitivity is achieved at longer wavelength.

3.2.2. Two-Mode PCF Temperature Sensor. The experimental setup used for studying the temperature response is similar to that shown in Figure 11, except that a section of PCF (~1.8 meters) was heated by putting it inside an oven. Measurements were performed for both the x- and y-polarizations. Figure 14 shows an example of the output intensity of the two-mode interferometer at 1310 nm as a function of oven temperature when the input polarization is aligned to the x-axis. One complete cycle in the intensity variation corresponds to a 2π change in the phase difference between the LP_{01} and LP_{11}(even) modes. We noticed that the period of the intensity oscillation is not constant during the temperature range from 20°C to 120°C, and the period is obviously larger at lower temperatures, indicating that the interferometer shows a nonlinear response to the temperature changes. The temperature sensitivity η, defined as the rate of change of phase difference $\Delta\phi$ between the two modes with respect to temperature T per unit length of sensing fiber, is given by

$$\eta = \frac{1}{L} \cdot \frac{\Delta\phi}{\Delta T}, \tag{2}$$

where L is the fiber length placed inside the oven. The measured average temperature sensitivities as functions of wavelength within the temperature range from 20°C to 120°C are shown in Figure 15. The temperature sensitivities of two-mode PCF sensor are slightly different for the x- and y-polarizations. And the values are in general smaller than those of the conventional elliptical core two-mode fibers [29].

The extremely broad two-mode wavelength range and the unusual wavelength-dependent temperature sensitivity of the two-mode PCF sensor provide a useful means for strain and temperature discrimination. As shown in Figure 13, the strain sensitivities increase linearly with wavelength and are significantly different (~15%) for the two orthogonal polarizations. The temperature sensitivities have nonmonotonic dependence on wavelength (Figure 15) and are similar for both polarizations. A temperature-independent strain measurement can then be realized by operating the interferometer at two wavelengths where the temperature sensitivities are the same, and taking a differential measurement. On the other hand, it is possible to use the two-mode sensor for simultaneous measurement of strain and temperature by operating at two properly chosen optical wavelengths.

4. Conclusions

In conclusion, PCF provides a new platform for the development of optical fiber sensors. It allows for LPGs with exceptional low temperature coefficient to be created, while the strain sensitivity can be significantly enhanced by carving visible grooves on the surface of the fiber. The LPG fabricated in the HC-PBF has many advantages compared with those in conventional SMFs and index-guiding PCFs such as insensitivity to temperature, bending, and external refractive index. It is also possible to construct an interferometric strain or temperature sensor by utilizing the interference between the fundamental core mode and cladding mode or a higher-order core mode. The core/cladding mode interferometric sensor based on PCF has higher strain sensitivity and lower temperature sensitivity than its SMF counterpart. The interference between two core modes of PCF can be operated over a broader wavelength range than conventional two-mode fibers. The strain sensitivity of two-mode PCF sensor is comparable to that of the conventional two-mode sensors and shows a linear relationship with optical wavelength. The

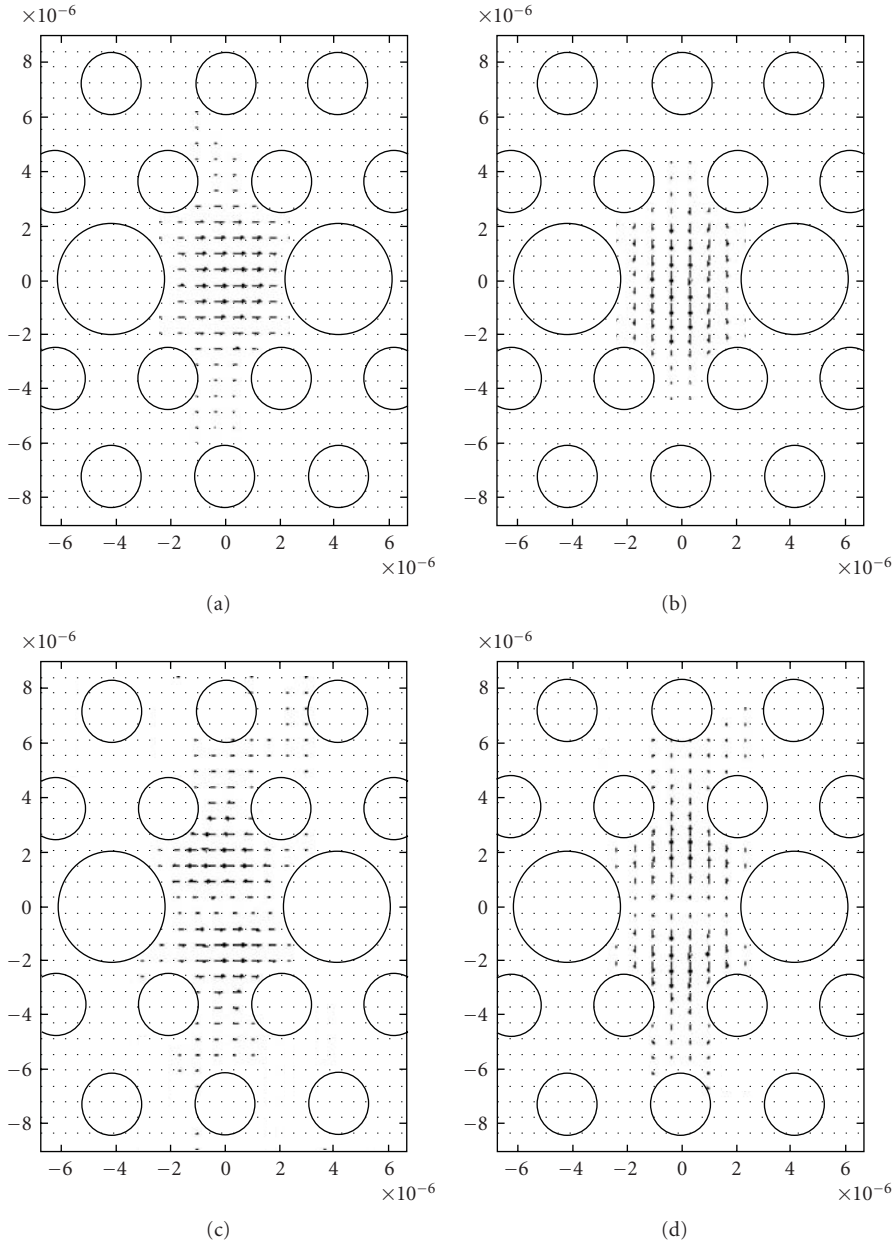

Figure 10: Transverse electric field distribution of (a) $LP_{01}{}^{x}$, (b) $LP_{11}{}^{y}$, (c) $LP_{01}{}^{x}$ (even), and (d) $LP_{11}{}^{y}$ (even) modes for an Hi-Bi PCF operating at 1.3 μm.

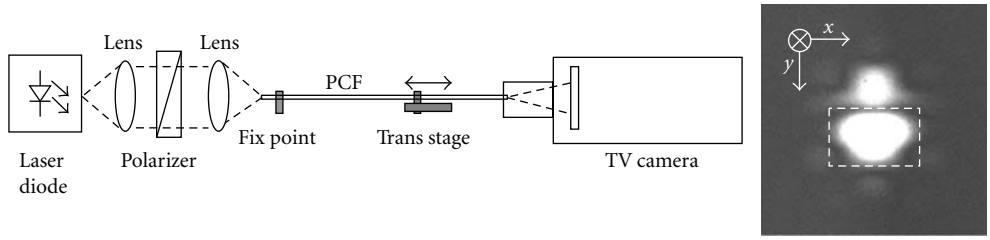

Figure 11: Experimental setup for strain measurement and far-field intensity pattern.

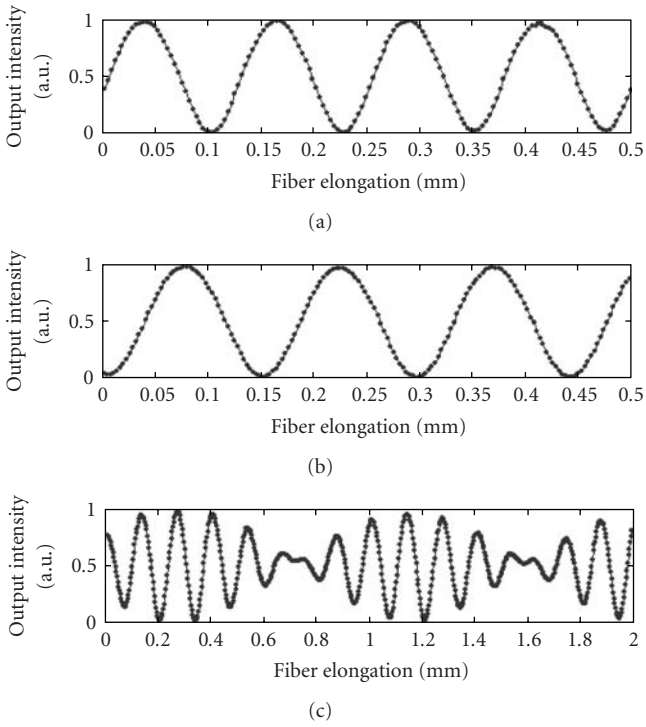

Figure 12: Experimental results for different launch angles of 0°, 90°, and 45° (from top to bottom) [28].

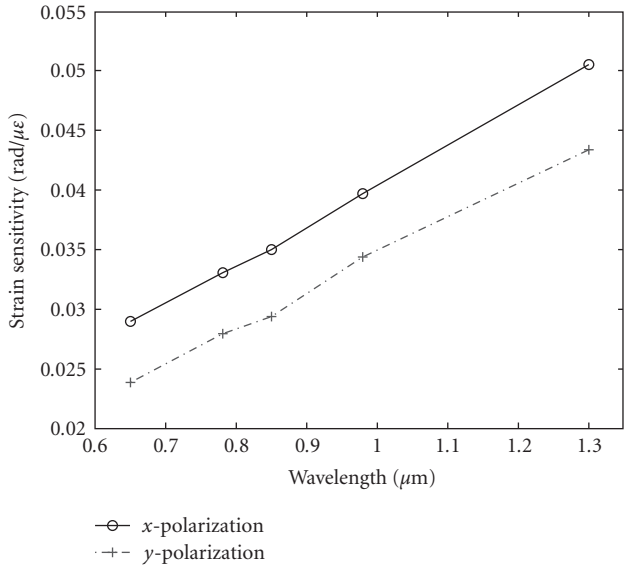

Figure 13: Strain sensitivity as function of wavelength.

temperature sensitivity of the two-mode PCF sensor is in general smaller than that of the conventional elliptical core two-mode fiber sensors and has a nonmonotonic relationship with optical wavelength, which may be employed for temperature-independent strain sensing by operating at two wavelengths with similar temperature coefficients.

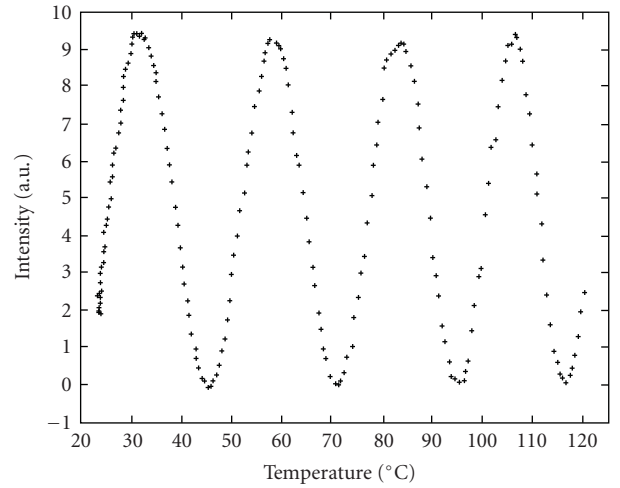

Figure 14: Experimental results showing the periodic intensity variation with temperature. (λ = 1310 nm, x-polarization) [30].

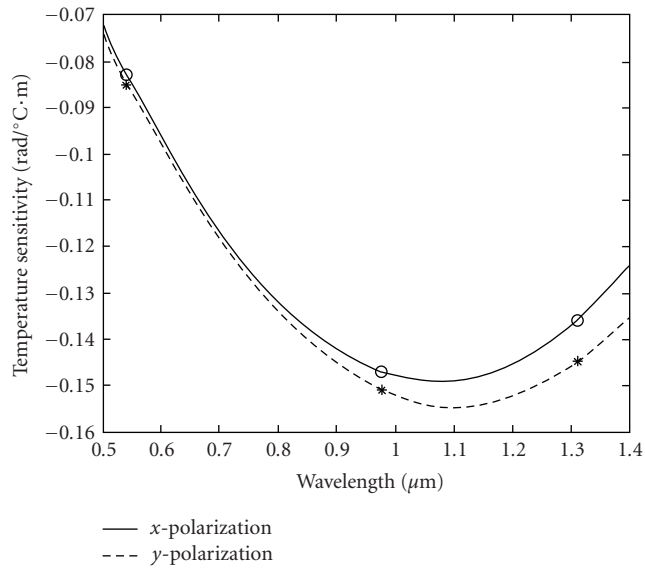

Figure 15: Measured temperature sensitivity for x-polarization (circle) and y-polarization (star) as a function of optical wavelength. Solid and dashed lines are curve fitting results of the measured data [30].

Acknowledgments

The research work was partially supported by NSF of China through Grant 60629401, and the Hong Kong SAR Government through GRF Grants PolyU 5182/07E.

References

[1] P. Russell, "Photonic crystal fibers," *Science*, vol. 229, pp. 258–362, 2003.

[2] T. A. Birks, J. C. Knight, and P. St. J. Russell, "Endlessly single-mode photonic crystal fiber," *Optics Letters*, vol. 22, no. 13, pp. 961–963, 1997.

[3] K. Suzuki, H. Kubota, S. Kawanishi, M. Tanaka, and M. Fujita,

"Optical properties of a low-loss polarization-maintaining photonic crystal fiber," *Optics Express*, vol. 9, no. 13, pp. 676–680, 2001.

[4] R. F. Cregan, B. J. Mangan, J. C. Knight, et al., "Single-mode photonic band gap guidance of light in air," *Science*, vol. 285, no. 5433, pp. 1537–1539, 1999.

[5] L. Jin, Z. Wang, Y. Liu, G. Kai, and X. Dong, "Ultraviolet-inscribed long period gratings in all-solidnphotonic bandgap fibers," *Optics Express*, vol. 16, no. 25, pp. 21119–21131, 2008.

[6] http://www.nktphotonics.com.

[7] Y.-P. Wang, L. Xiao, D. N. Wang, and W. Jin, "Highly sensitive long-period fiber-grating strain sensor with low temperature sensitivity," *Optics Letters*, vol. 31, no. 23, pp. 3414–3416, 2006.

[8] H. Dobb, K. Kalli, and D. J. Webb, "Measured sensitivity of arc-induced long-period grating sensors in photonic crystal fibre," *Optics Communications*, vol. 260, no. 1, pp. 184–191, 2006.

[9] Y. Zhu, Z. He, and H. Du, "Detection of external refractive index change with high sensitivity using long-period gratings in photonic crystal fiber," *Sensors and Actuators B*, vol. 131, no. 1, pp. 265–269, 2008.

[10] Z. He, Y. Zhu, and H. Du, "Effect of macro-bending on resonant wavelength and intensity of long-period gratings in photonic crystal fiber," *Optics Express*, vol. 15, no. 4, pp. 1804–1810, 2007.

[11] Y. L. Hoo, W. Jin, C. Shi, H. L. Ho, D. N. Wang, and S. C. Ruan, "Design and modeling of a photonic crystal fiber gas sensor," *Applied Optics*, vol. 42, no. 18, pp. 3509–3515, 2003.

[12] A. M. Vengsarkar, P. J. Lemaire, J. B. Judkins, V. Bhatia, T. Erdogan, and J. E. Sipe, "Long-period fiber gratings as band-rejection filters," *Journal of Lightwave Technology*, vol. 14, no. 1, pp. 58–64, 1996.

[13] J. H. Lim, K. S. Lee, J. C. Kim, and B. H. Lee, "Tunable fiber gratings fabricated in photonic crystal fiber by use of mechanical pressure," *Optics Letters*, vol. 29, no. 4, pp. 331–333, 2004.

[14] A. A. Fotiadi, G. Brambilla, T. Ernst, S. A. Slattery, and D. N. Nikogosyan, "TPA-induced long-period gratings in a photonic crystal fiber: inscription and temperature sensing properties," *Journal of the Optical Society of America B*, vol. 24, no. 7, pp. 1475–1481, 2007.

[15] Y.-P. Wang, L. Xiao, D. N. Wang, and W. Jin, "In-fiber polarizer based on a long-period fiber grating written on photonic crystal fiber," *Optics Letters*, vol. 32, no. 9, pp. 1035–1037, 2007.

[16] Y.-J. Rao, Y.-P. Wang, Z.-L. Ran, and T. Zhu, "Novel fiber-optic sensors based on long-period fiber gratings written by high-frequency CO_2 laser pulses," *Journal of Lightwave Technology*, vol. 21, no. 5, pp. 1320–1327, 2003.

[17] V. Bhatia and A. M. Vengsarkar, "Optical fiber long-period grating sensors," *Optics Letters*, vol. 21, no. 9, pp. 692–694, 1996.

[18] G. Rego, R. Falate, O. Ivanov, and J. L. Santos, "Simultaneous temperature and strain measurements performed by a step-changed arc-induced long-period fiber grating," *Applied Optics*, vol. 46, no. 9, pp. 1392–1396, 2007.

[19] Y.-P. Wang, W. Jin, J. Ju, et al., "Long period gratings in air-core photonic bandgap fibers," *Optics Express*, vol. 16, no. 4, pp. 2784–2790, 2008.

[20] X. J. Gu, "Wavelength-division multiplexing isolation fiber filter and light source using cascaded long-period fiber gratings," *Optics Letters*, vol. 23, no. 7, pp. 509–510, 1998.

[21] K. T. V. Grattan and B. T. Meggitt, *Optical Fiber Sensor Technology; Vol. 2: Devices and Technology*, Chapman & Hall, London, UK, 1998.

[22] J. H. Lim, H. S. Jang, K. S. Lee, J. C. Kim, and B. H. Lee, "Mach-Zehnder interferometer formed in a photonic crystal fiber based on a pair of long-period fiber gratings," *Optics Letters*, vol. 29, no. 4, pp. 346–348, 2004.

[23] H. Y. Choi, M. J. Kim, and B. H. Lee, "All-fiber Mach-Zehnder type interferometers formed in photonic crystal fiber," *Optics Express*, vol. 15, no. 9, pp. 5711–5720, 2007.

[24] H. Y. Choi, K. S. Park, and B. H. Lee, "Photonic crystal fiber interferometer composed of a long period fiber grating and one point collapsing of air holes," *Optics Letters*, vol. 33, no. 8, pp. 812–814, 2008.

[25] J. Ju, W. Jin, and H. L. Ho, "Compact in-fiber interferometer formed by long-period gratings in photonic crystal fiber," *IEEE Photonics Technology Letters*, vol. 20, no. 23, pp. 1899–1901, 2008.

[26] B. Y. Kim, J. N. Blake, S. Y. Huang, and H. J. Shaw, "Use of highly elliptical core fibers for two-mode fiber devices," *Optics Letters*, vol. 12, pp. 729–731, 1987.

[27] W. Jin, Z. Wang, and J. Ju, "Two-mode photonic crystal fibers," *Optics Express*, vol. 13, no. 6, pp. 2082–2088, 2005.

[28] J. Ju, W. Jin, and M. S. Demokan, "Two-mode operation in highly birefringent photonic crystal fiber," *IEEE Photonics Technology Letters*, vol. 16, no. 11, pp. 2472–2474, 2004.

[29] S.-Y. Huang, J. N. Blake, and B. Y. Kim, "Perturbation effects on mode propagation in highly elliptical core two-mode fibers," *Journal of Lightwave Technology*, vol. 8, no. 1, pp. 23–33, 1990.

[30] J. Ju, Z. Wang, W. Jin, and M. S. Demokan, "Temperature sensitivity of a two-mode photonic crystal fiber interferometric sensor," *IEEE Photonics Technology Letters*, vol. 18, no. 20, pp. 2168–2170, 2006.

Hindawi Publishing Corporation
Journal of Sensors
Volume 2009, Article ID 932471, 6 pages
doi:10.1155/2009/932471

Research Article

Photonic Crystal Fiber Temperature Sensor Based on Quantum Dot Nanocoatings

Beatriz Larrión, Miguel Hernáez, Francisco J. Arregui, Javier Goicoechea, Javier Bravo, and Ignacio R. Matías

Electrical and Electronic Engineering Department, Public University of Navarre, Campus Arrosadía s/n, 31006 Pamplona, Spain

Correspondence should be addressed to Beatriz Larrión, beatriz.larrion@unavarra.es

Received 3 March 2009; Accepted 16 April 2009

Recommended by Valerio Pruneri

Quantum dot nanocoatings have been deposited by means of the Layer-by-Layer technique on the inner holes of Photonic Crystal Fibers (PCFs) for the fabrication of temperature sensors. The optical properties of these sensors including absorbance, intensity emission, wavelength of the emission band, and the full width at half maximum (FWHM) have been experimentally studied for a temperature range from −40 to 70°C.

1. Introduction

In the past few years, new optical fibers have been developed in order to get lower nonlinearity, lower attenuation, and unique waveguiding properties. This is the case of Photonic Crystal Fibers (PCFs), also called holey fibers, which contain arrays of tiny air holes along their structure and allow, among other new applications, the fabrication of new optical fiber sensors. In 1995, Birks et al. proposed a fiber with air holes along its length that could guide light through this structure with interesting properties [1, 2]. Nowadays the PCF has become a subject of extensive research and has opened a new range of possible applications.

The structure of the PCF enables to have different types of fibers such as endless single mode, double clad, germanium or rare earth doped, high birefringence, and many others with particular features due to its manufacturing flexibility. This variety of choices permits the use of PCF in numerous applications such as sensors which measure physical parameters (temperature, pressure, force, etc.), chemical compounds in gas and liquids, and even biosensors [3–7]. In a PCF a fraction of the modal field is located within the holes of the fiber. This allows, by means of the evanescent field interaction, the measurement of different gases, liquids, or biological samples, only if these materials to be measured are placed in the holes of the PCFs. The possibility of coating the holes with sensing materials also exists. However, due to the technical challenge that implies the deposition of thin films on the inner part of the air holes, there is only a small number of works about sensors with this type of sensing coatings [8, 9]. One of the main contributions presented in this paper is the deposition of a sensing thin film with a thickness of few nanometers inside the holes of a PFC, instead of the classical approach, which consists of filling these holes with the liquid or gas.

More specifically, a PCF temperature sensor based on QD has been fabricated by means of the Layer-by-Layer (LbL) technique for the first time. An experimental study of the optical properties of these QD-based sensors has been performed focused in the optical absorbance, emission intensity, emission peak wavelength, and a feature which had not been studied before in literature, the dependence of the full width at half maximum (FWHM) of QD emission bands with the temperature.

2. Experimental

The deposition technique proposed here is the LbL method, technique which enables the building of nanostructured films in surfaces with complex shapes such as, in this case, the walls of the small cylindrical holes of the PCF. The technique is based on the attraction between oppositely charged polyelectrolytes. Its main advantage is the possibility

of controling the thickness of the coating on the nanometer scale, building the film by creating bilayers of both cationic and anionic solutions consecutively [10–14]. More specifically, in order to fabricate temperature sensing nanofilms inside the holes of the PCF, quantum dots (QDs) have been used as one of the colloids of the deposition process.

QDs are semiconductor nanocrystals with particle diameters typically from 1 to 12 nm, which have also attracted great interest in the last years due to their very appealing optical properties. QDs can be excited in a broad range of wavelengths and, at the same time, have a narrow emission spectrum. Moreover, the center wavelength of the emission peak depends on the geometrical size of the QD; therefore, the emission wavelength can be tuned by changing the size of the nanocrystals. This gives a large choice of emission wavelengths [12, 15, 16]. In fact, QDs have been already proposed for diverse applications such as biological labels, optical sensors, solar cells, photodetectors, lasers, and many other uses [17–24]. In addition, the emission spectrum of QDs changes gradually depending on temperature [25]. The emission intensity decreases, and the emission bands move to higher wavelengths when temperature increases. Due to these features, QDs are an excellent material for temperature sensing [25–28].

2.1. Materials. The polymeric materials used to build the nanostructured coatings were poly(diallyl dimethylammonium chloride) (PDDA) and poly(acrylic acid) (PAA), both purchased from Sigma-Aldrich. Water-based solutions of these materials were prepared at a concentration of 1%wt., and their pHs were adjusted to 8.0 and 6.0, respectively. These solutions were filtered using 0.45 μm pore size syringe filters before starting the film deposition.

The CdSe quantum dots (QDs) used in these experiments have a 5 nm diameter and emit in the red region of the visible spectrum (620 nm approximately). These water soluble QDs were supplied by the American Dye Source Inc. and are functionalized with carboxylic groups. The concentration of the QD aqueous solutions was 0.025%wt, and the pH was adjusted to 8.0. These solutions were also filtered with a 0.45 μm pore diameter filter.

All the solutions were prepared with 18.2 M$\Omega\cdot$cm deionized (DI) water from a Barnstead Diamond system.

2.2. Sensor Fabrication. The sensing nanofilms were deposited on the inner air holes of a PCF LMA-20 purchased from Thorlabs Inc. This fiber has a 229 μm diameter, and it is optimized for a single mode operation in the 600–1000 nm wavelength range. The fiber microstructure with the air holes can be observed in the cross section image shown in Figure 1. The diameter of the holes is 6.4 μm, and the separation between the centers of adjacent holes is 13.2 μm.

As mentioned in the introduction the LbL technique is used to fabricate the nanofilms on the inner part of the PCF holes. This method is based on the consecutive exposure of the substrate to cationic and anionic solutions in a repetitive sequence. The different charged particles are adsorbed by electrostatic attraction.

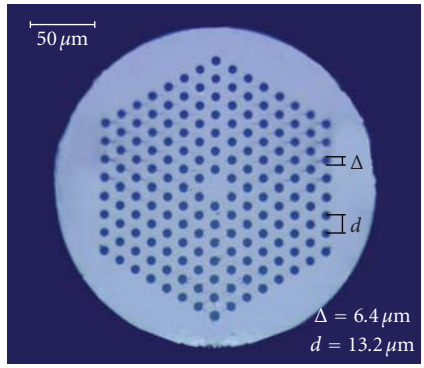

Figure 1: PCF LMA-20 cross section.

The sensing film has to be coated on the inner part of the PCF, and in order to achieve this, a segment of PCF has to be fixed to a 5 mL syringe with a 0.5 mm diameter needle using an epoxy resin. This helps the fluids flow through the segment of fiber and removes the solutions from it. The length of the fiber piece is nearly 6 cm.

To begin the LbL process, a previous bilayer of PDDA and PAA is created on the substrate to enhance the adhesion of the successive layers to the fiber. The segment of the PCF is filled with the cationic PDDA solution with the help of the syringe, and during 3 minutes the solution is left inside the fiber to let the molecules be adsorbed by the inner surface of the microtubes. After the liquid is removed from the fiber, then, the PCF is filled with DI water which removes any rest of the previous solution that could remain still inside the fiber. Once this cleaning process is made, the same procedure is repeated with the PAA solution, which corresponds to the anionic layer.

After the first bilayer, PAA is replaced with QD, and the previously explained process is repeated. The final sensing nanofilm consists of 20 bilayers of PDDA and QD. More details of the LbL process can be found in literature [10, 12–14, 26, 27, 29].

When the coating process is finished, the PCF segment is left into a vacuum oven during 15 minutes at 90°C in a nitrogen atmosphere. The fiber is then cleaved using a VYTRAN automatic cleaver to obtain smooth cut surfaces in both extremes. A PCF segment of 2.5 cm with the QD coating is the piece used to make the temperature sensors.

In order to encapsulate the QD film inside the holes of the PCF, the sensor is created by splicing two multimode fibers (MMFs) (200 μm diameter core and 230 μm diameter cladding) to the PCF segment. The end of each MMFs is also cut using a Fujikura CT-20 cleaver. An Ericsson FSU-905 splicing unit is then used to splice both MMF to the PFC segment. The fusion process with this unit is divided in three parts. The fusion parameters are conveniently selected in order to get a robust fusion between the MMF and the PCF without collapsing the holes of the PCF. Figure 2 shows a microscope picture of the splice between the PCF and the MMF.

Consequently, the QD films deposited on the inner surfaces of the holes are encapsulated as long as they are

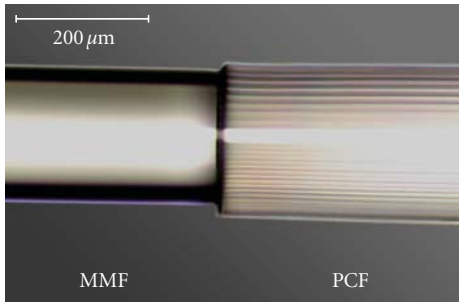

Figure 2: Microscope image of the PCF-MMF splices.

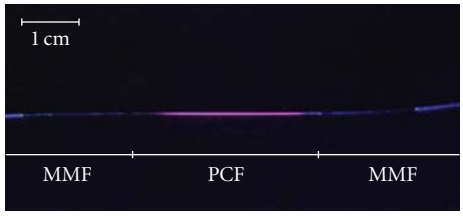

Figure 3: Picture of the LMA20 segment spliced to the MMF fibers under UV illumination. In the middle region the red quantum dots' fluorescence from the PCF inner holes can be seen.

protected against the exterior media and environmental agents such as oxygen. When the sensor fabrication is completed, the fluorescence of QD can be clearly observed by illuminating it with a simple UV-light, as it can be seen in Figure 3.

3. Results

In order to study the behavior of the sensors with the temperature, two different sets of experiments have been performed. The first one is intended for the QD absorption spectrum observation and the other one for the study of the emission properties. The setup depicted in Figure 4 was used to perform all the tests. The type of the light source to be used depends on the experiment: a broadband light source is used for the absorption experiments, and a laser is utilized for the emission studies. This light source is connected to a mode scrambler which is used to achieve a stable power by means of avoiding intermodal interference. Then, the PCF sensor is connected in line to this optical fiber. Light from the source passes through the mode scrambler and excites the quantum dots deposited into the sensor. The optical signal from the sensor (the excitation light and the emission light as well) is collected in a spectrometer (USB-2000 FLG, Oceanoptics). Between the sensor and the spectrometer, a high-pass filter is used to limit the excitation signal from the light source which can mask the emission light from the QD.

3.1. Absorption Study. Surprisingly, although optical absorption spectrum is an important QD feature which can also be used for sensing temperature, as was proposed in earliers publications [30], there are few works related to temperature sensors based on QD which study the variation of optical

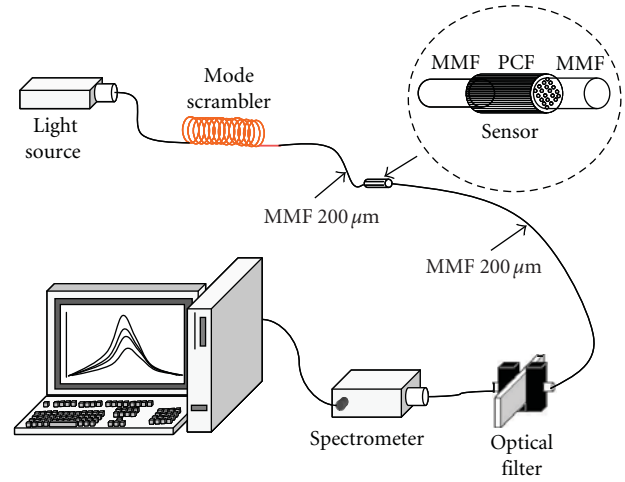

Figure 4: Experimental setup used to collect the optical response from the sensor.

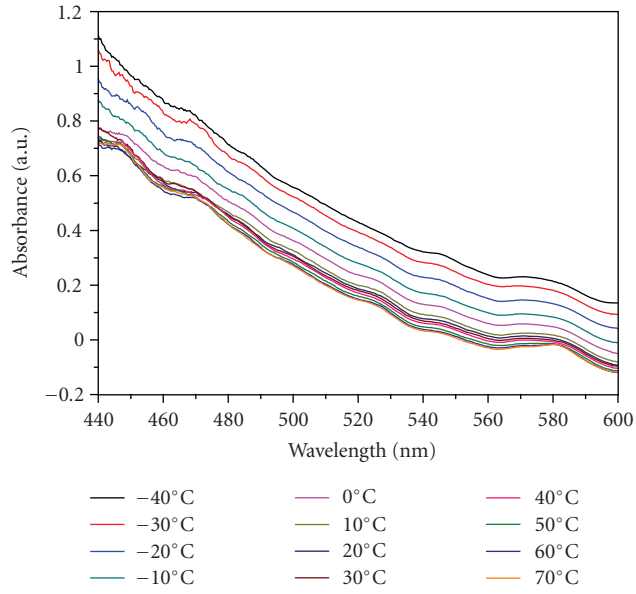

Figure 5: Absorption spectra at different temperatures (−40 to +70°C).

absorption for temperature sensing [31]. In order to measure this parameter, a lowpass optical filter and a deuterium and halogen white light source (Oceanoptics DH 2000) were used in the Figure 4 setup. This source supplies a stable spectrum in the wavelength range from 215 to 1700 nm. The sensor was introduced into a climatic chamber (Angelantoni), and the temperature was varied from −40 to 70°C. Absorption spectra at different temperatures are shown in Figure 5.

As can be seen in Figure 5, absorbance decreases when temperature rises. In Figure 6, the average absorbance between 500 and 520 nm at different temperatures is shown.

The experimental data of Figure 6 can be fitted to an exponential curve with a correlation factor of $R^2 = 0.985$. The average sensibility of this measurement method is 0.0027 a.u./°C, and its value in the worst case is 0.0004 a.u./°C for the range of higher temperatures.

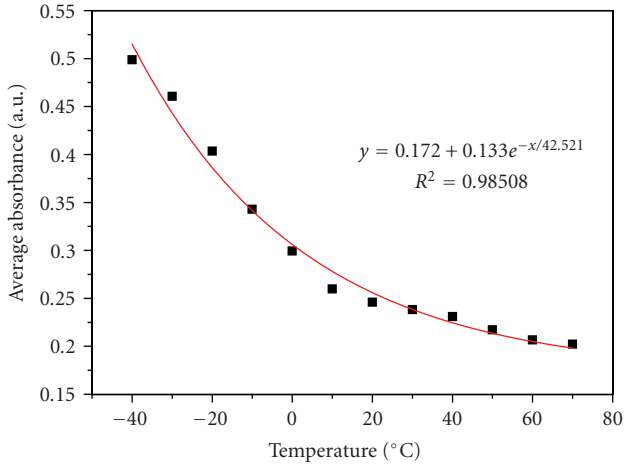

Figure 6: Average absorbance from 500 to 520 nm at different temperatures.

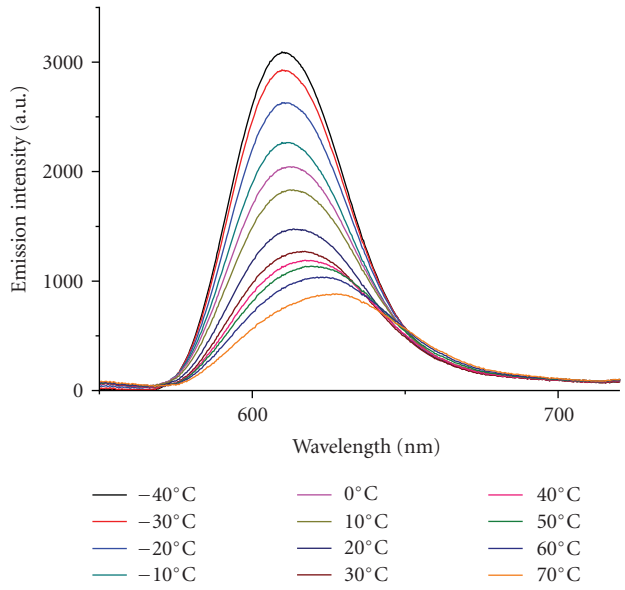

Figure 7: Fluorescent emission curves variation with temperature.

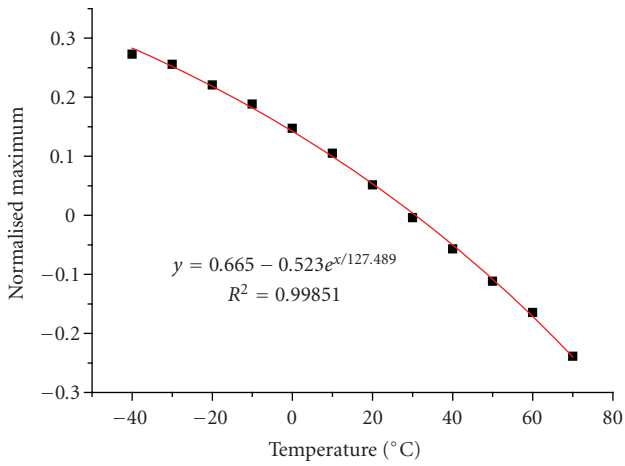

Figure 8: Normalized emission maxima.

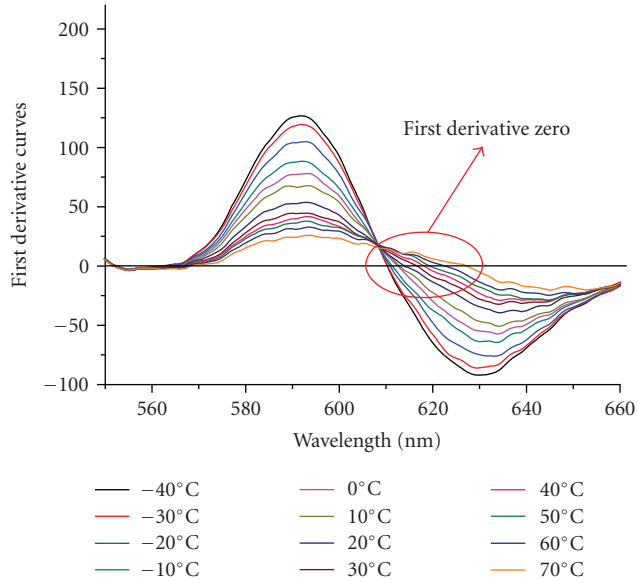

Figure 9: First derivative curves obtained from the emission spectra showed in Figure 5.

3.2. Emission Study. As it was previously commented, different emission properties of the sensor have been studied. With this aim, the QDs were excited using an Omnichrome Laser tuned at 470 nm. The spectrometer registers the QD emission peak which, due to their quantum confinement properties, decreases in intensity when the temperature rises. This feature is shown in Figure 7, where each curve has been taken at different temperatures from −40 to 70°C. It is important to realize that not only the maximum peak of the curve changes with the temperature. The wavelength and the width of this peak are increased as far as the temperature rises. Therefore, there are three features of the quantum dots emission peak which could be used to detect temperature variations: maximum values of each emission peak, wavelength of these values, and bandwidth of these peaks.

To study the maximum of the quantum dots emission peaks, a normalization method applied by Jorge et al. in a previous study [28] was utilized. It is based on taking two intensity signals (S_1 and S_2) corresponding to two 5 m spectral windows on opposite sides of the emission peak and applying a normalization according to $(S_1 - S_2)/(S_1 + S_2)$. The result of this normalization is proportional to the temperature and independent of the power fluctuations of the light source. In Figure 8, the evolution of this normalized maximum with temperature can be seen. These data can be approximated by an exponential signal with a correlation factor of $R^2 = 0.998$, rather better than the obtained absorption spectra measured in the precedent section. In some previous works [26–28, 30], the sensors apparently showed a linear behavior due to the narrower temperature range used. The average sensitivity of this sensor is $0.00465°C^{-1}$, and the sensitivity in the worst case is $0.001732°C^{-1}$ corresponding to the lower temperature values.

Another method to measure temperature with this sensor is based on monitoring the emission peak wavelength. The

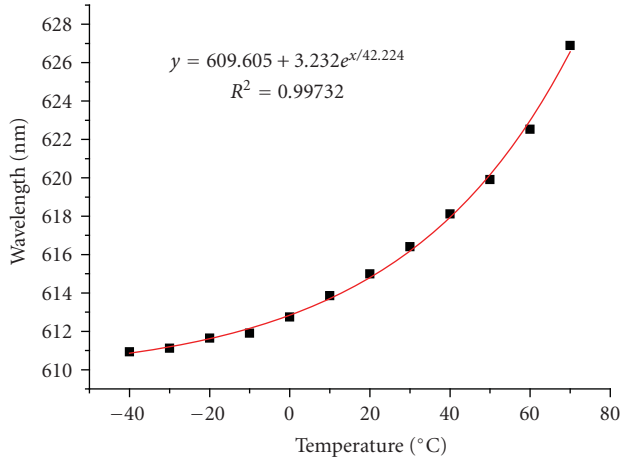

Figure 10: Emission peak wavelength at different temperatures.

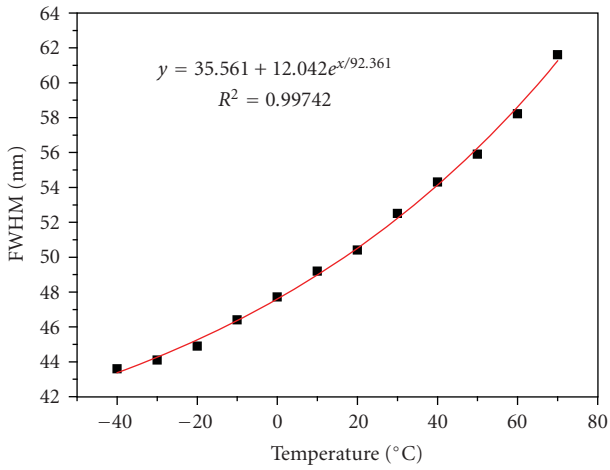

Figure 11: FWHM variation with temperature.

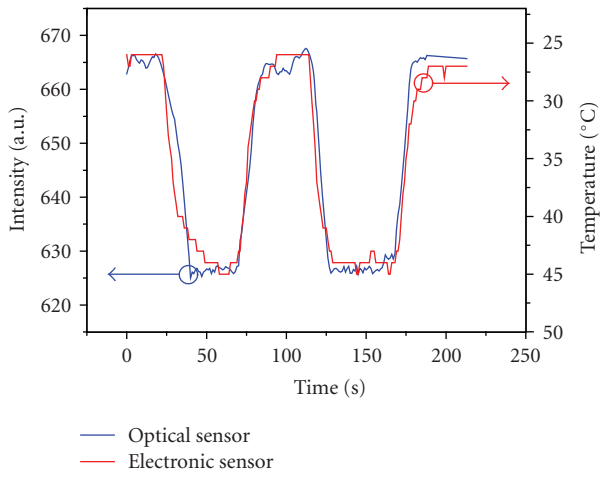

Figure 12: Dynamic behavior of the thermocouple (electronic) and the PCF QD-based (optical) sensors. The intensity measurement of y-axis is the average of the maximum intensity values between 600 and 640 nm.

emission peak shifts to higher wavelengths when the temperature rises, as is seen in Figure 7. Since the emission band does not provide a narrow peak to measure, it is necessary to develop a systematic method to calculate the emission peak wavelength, which matches with the maximum intensity. To reach this goal, a simple method based on the first derivative to detect the maxima of the emission curves is performed. Firstly, the derivative curves shown in Figure 9 are obtained from the graph in Figure 7. The first derivative curves reach the value of zero at the wavelengths which correspond to the maximum values of each emission spectrum as demonstrated in Figure 9. These wavelengths are plotted in Figure 10, having again an exponential fit with a good correlation factor of $R = 0.99732$. The average sensitivity of this method is 0.1451 nm/°C, and the worst sensitivity is 0.0195 nm/°C for the lower temperature range. The emission intensity and the emission peak wavelength give a lower sensitivity at lower temperatures whereas the absorption has the opposite behavior (higher sensitivity at lower temperatures). Combining the absorption with either the emission intensity or the peak wavelength, the sensitivity of these devices could be balanced in the whole range of temperatures.

In addition, a new emission feature was observed: the spectral width of the emission band shows temperature dependence. Taking advantage of this, the Full Width at Half Maximum (FWHM) of the emission band, a very popular parameter for the characterization of lasers, can be used as a sensing magnitude. The FWHM variation with temperature and its exponential approximation can be seen in Figure 10. The sensitivity of this method has an average value of 0.1636 nm/°C, and its minimum value of 0.05 nm/°C corresponds to low temperatures. To our knowledge, this is the first time that the FWHM is used as a sensing parameter in QD-based sensors.

Finally, in order to verify for the dynamic behavior of the devices, the temperature sensor is subjected to sharp temperature changes between 25 and 45°C. The QD sensor and a commercial sensor (a K thermocouple based device) are placed together and monitored at the same time to compare both responses. The QD emission magnitude measured is the average of the maximum intensity values between 600 and 640 nm. In Figure 12 the responses of the QD sensor and the thermocouple are shown. The rise time and fall time of both devices are similar, as seen in the graph. They are also similar to the times observed in previous works by Bravo et al. [26].

4. Conclusion

In this work a temperature sensor has been fabricated by the deposition of quantum dot films inside the holes of a Photonic Crystal Fiber by means of the Layer-by-Layer technique for the first time. The optical absorption, the emission intensity, and emission peak wavelength have shown a clear exponential behavior in the range from −40 to +70°C. It was observed that the measurement of the optical absorption can be used as a complementary method to improve the sensitivity at lower temperatures of the methods based on the emission properties. In addition, it has been

proposed, for the first time in literature, the utilization of a parameter based on the spectral width of the emission band, the FWHM, in QD-based sensors.

Acknowledgments

This work was supported in part by the Spanish CICYT-FEDER Research Grant TEC2006-12170/MIC. The authors are in debt to Jesus Arigita for all his previous experiments made for this project.

References

[1] T. A. Birks, P. J. Roberts, P. S. J. Russell, D. M. Atkin, and T. J. Shepherd, "Full 2-D photonic bandgaps in silica/air structures," *Electronics Letters*, vol. 31, no. 22, pp. 1941–1943, 1995.

[2] J. C. Knight, T. A. Birks, P. S. J. Russell, and D. M. Atkin, "All-silica single-mode optical fiber with photonic crystal cladding," *Optics Letters*, vol. 21, no. 19, pp. 1547–1549, 1996.

[3] H. L. Ho, Y. L. Hoo, W. Jin, et al., "Optimizing microstructured optical fibers for evanescent wave gas sensing," *Sensors and Actuators B*, vol. 122, no. 1, pp. 289–294, 2007.

[4] Y. L. Hoo, W. Jin, C. Shi, H. L. Ho, D. N. Wang, and S. C. Ruan, "Design and modeling of a photonic crystal fiber gas sensor," *Applied Optics*, vol. 42, no. 18, pp. 3509–3515, 2003.

[5] P. E. Hoiby, L. B. Nielsen, J. B. Jensen, T. P. Hansen, A. Bjarklev, and L. H. Pedersen, "Molecular immobilization and detection in a photonic crystal fiber," vol. 5317 of *Proceedings of SPIE*, pp. 220–223, 2004.

[6] W. Ye, L. L. Irene, C. R. Shuang, and P. Z. Jian, "Temperature sensor based on iodine-doped hollow core photonic crystal fiber," in *Proceedings of the International Conference on Microwave and Millimeter Wave Technology (ICMMT '08)*, vol. 2, pp. 890–892, 2008.

[7] W. J. Bock, J. Chen, T. Eftimov, and W. Urbanczyk, "A photonic crystal fiber sensor for pressure measurements," *IEEE Transactions on Instrumentation and Measurement*, vol. 55, no. 4, pp. 1119–1123, 2006.

[8] V. P. Minkovich, D. Monzón-Hernández, J. Villatoro, and G. Badenes, "Microstructured optical fiber coated with thin films for gas and chemical sensing," *Optics Express*, vol. 14, no. 18, pp. 8413–8418, 2006.

[9] Y. Ruan, T. C. Foo, S. Warren-Smith, et al., "Antibody immobilization within glass microstructured fibers: a route to sensitive and selective biosensors," *Optics Express*, vol. 16, no. 22, pp. 18514–18523, 2008.

[10] G. Decher, "Fuzzy nanoassemblies: toward layered polymeric multicomposites," *Science*, vol. 277, no. 5330, pp. 1232–1237, 1997.

[11] M. T. Crisp and N. A. Kotov, "Preparation of nanoparticle coatings on surfaces of complex geometry," *Nano Letters*, vol. 3, no. 2, pp. 173–177, 2003.

[12] F. J. Arregui, I. R. Matías, and R. O. Claus, "Optical fiber sensors based on nanostructured coatings fabricated by means of the layer-by-layer electrostatic self-assembly method," vol. 6619 of *Proceedings of SPIE*, 2007.

[13] J. Goicoechea, F. J. Arregui, J. M. Corres, and I. R. Matias, "Study and optimization of self-assembled polymeric multilayer structures with neutral red for pH sensing applications," *Journal of Sensors*, vol. 2008, Article ID 142854, 7 pages, 2008.

[14] R. K. Iler, "Multilayers of colloidal particles," *Journal of Colloid and Interface Science*, vol. 21, no. 6, pp. 569–594, 1966.

[15] A. P. Alivisatos, "Semiconductor clusters, nanocrystals, and quantum dots," *Science*, vol. 271, no. 5251, pp. 933–937, 1996.

[16] J. M. Costa-Fernandez, "Optical sensors based on luminescent quantum dots," *Analytical and Bioanalytical Chemistry*, vol. 384, no. 1, pp. 37–40, 2006.

[17] D. C. Oertel, M. G. Bawendi, A. C. Arango, and V. Bulović, "Photodetectors based on treated CdSe quantum-dot films," *Applied Physics Letters*, vol. 87, no. 21, pp. 1–3, 2005.

[18] T. J. Bukowski and J. H. Simmons, "Quantum dot research: current state and future prospects," *Critical Reviews in Solid State and Materials Sciences*, vol. 27, no. 3-4, pp. 119–142, 2002.

[19] I. L. Medintz, H. T. Uyeda, E. R. Goldman, and H. Mattoussi, "Quantum dot bioconjugates for imaging, labelling and sensing," *Nature Materials*, vol. 4, no. 6, pp. 435–446, 2005.

[20] A. R. Clapp, E. R. Goldman, H. Tetsuo Uyeda, E. L. Chang, J. L. Whitley, and I. L. Medintz, "Monitoring of enzymatic proteolysis using self-assembled quantum dot-protein substrate sensors," *Journal of Sensors*, vol. 2008, Article ID 797436, 10 pages, 2008.

[21] M. Bruchez Jr., M. Moronne, P. Gin, S. Weiss, and A. P. Alivisatos, "Semiconductor nanocrystals as fluorescent biological labels," *Science*, vol. 281, no. 5385, pp. 2013–2016, 1998.

[22] V. L. Colvin, M. C. Schlamp, and A. P. Alivisatos, "Light-emitting diodes made from cadmium selenide nanocrystals and a semiconducting polymer," *Nature*, vol. 370, no. 6488, pp. 354–357, 1994.

[23] P. Jorge, M. A. Martins, T. Trindade, J. L. Santos, and F. Farahi, "Optical fiber sensing using quantum dots," *Sensors*, vol. 7, no. 12, pp. 3489–3534, 2007.

[24] K. E. Sapsford, T. Pons, I. L. Medintz, and H. Mattoussi, "Biosensing with luminescent semiconductor quantum dots," *Sensors*, vol. 6, no. 8, pp. 925–953, 2006.

[25] G. W. Walker, V. C. Sundar, C. M. Rudzinski, A. W. Wun, M. G. Bawendi, and D. G. Nocera, "Quantum-dot optical temperature probes," *Applied Physics Letters*, vol. 83, no. 17, pp. 3555–3557, 2003.

[26] J. Bravo, J. Goicoechea, J. M. Corres, F. J. Arregui, and I. R. Matias, "Encapsulated quantum dot nanofilms inside hollow core optical fibers for temperature measurement," *IEEE Sensors Journal*, vol. 8, no. 7, pp. 1368–1374, 2008.

[27] G. De Bastida, F. J. Arregui, J. Goicoechea, and I. R. Matias, "Quantum dots-based optical fiber temperature sensors fabricated by layer-by-layer," *IEEE Sensors Journal*, vol. 6, no. 6, pp. 1378–1379, 2006.

[28] P. A. S. Jorge, M. Mayeh, R. Benrashid, P. Caldas, J. L. Santos, and F. Farahi, "Quantum dots as self-referenced optical fibre temperature probes for luminescent chemical sensors," *Measurement Science and Technology*, vol. 17, no. 5, pp. 1032–1038, 2006.

[29] F. J. Arregui, I. R. Matias, J. Goicoechea, and I. del Villar, *Sensors Based on Nanostructured Materials*, Springer, New York, NY, USA.

[30] M. L. Redígolo, W. A. Arellano, L. C. Barbosa, C. H. Brito Cruz, C. L. Cesar, and A. M. De Paula, "Temperature dependence of the absorption spectra in CdTe-doped glasses," *Semiconductor Science and Technology*, vol. 14, no. 1, pp. 58–63, 1999.

[31] C. Sifuentes, Y. O. Barmenkov, A. N. Starodumov, V. N. Filippov, and A. A. Lipovskii, "Application of CdSe-nanocrystallite-doped glass for temperature measurements in fiber sensors," *Optical Engineering*, vol. 39, no. 8, pp. 2182–2186, 2000.

Hindawi Publishing Corporation
Journal of Sensors
Volume 2009, Article ID 417540, 5 pages
doi:10.1155/2009/417540

Research Article

Temperature Sensor Based on Ge-Doped Microstructured Fibers

Salvador Torres-Peiró, Antonio Díez, José Luis Cruz, and Miguel Vicente Andrés

Departamento de Física Aplicada-ICMUV, Universidad de Valencia, Dr. Moliner 50, 46100 Burjassot, Spain

Correspondence should be addressed to Miguel Vicente Andrés, miguel.andres@uv.es

Received 1 February 2009; Revised 14 May 2009; Accepted 8 July 2009

Recommended by Valerio Pruneri

The fundamental mode cutoff properties of Ge-doped microstructured fibers, filled with a liquid, permit the implementation of wavelength- and amplitude-encoded temperature sensors with an ultra-high sensitivity. The cutoff wavelength changes with temperature, and the thermo-optic coefficient of the liquid determines the sensitivity of the sensor. Sensitivity as high as 25 nm/°C is reported. In addition, simple amplitude interrogation techniques can be implemented using the same sensor heads.

1. Introduction

A number of different approaches have been investigated along the last decades for the measurement of temperature using fiber-optics: Optical-scattering, fluorescence, interferometry, optical absorption, and so forth [1, 2]. In-fiber Bragg gratings (FBGs) have been extensively investigated because they present several potential advantages: the robustness of wavelength codification, easy multiplexing, small size, and low cost [3]. The typical temperature sensitivity of FBG is 13 pm/°C at 1550 nm, and it can be increased significantly by coating the FBG with other materials. A sensitivity of 108 pm/°C has been reported by coating the FBG with a polymer [4]. Using long period gratings (LPGs) larger sensitivities can be obtained (310 pm/°C was reported in [5]).

Other wavelength-encoded temperature sensors, that exhibit larger sensitivities than standard FBG, have been reported. The resonant coupling between the core-mode and the cladding modes in a special fiber with a multi-cladding structure has been used to make a temperature sensor, reporting a sensitivity of 240 pm/°C [6]. The temperature dependence of coupling coefficients in an optical fiber coupler with a special coating permitted to achieve 170 pm/°C sensitivity [7]. Finally, higher sensitivities, as high as 3.2 nm/°C, have been reported using short multimode fiber interferometers [8, 9].

Microstructured optical fibers open new opportunities to develop fiber sensors. Theoretical analysis of photonic crystal fiber sensors based on FBG and LPG predicts temperature sensitivities up to 60 pm/°C [10]. Specially designed Fabry-Perot cavities formed with photonic crystal fibers have demonstrated sensitivities as high as 170 pm/°C [11].

Here we develop some details on the exploitation of a new concept, recently presented, of wavelength-encoded temperature sensor based on the temperature dependence of the cutoff wavelength of the fundamental mode in a liquid-filled Ge-doped microstructured fiber [12]. Photonic crystal fibers with a Ge-doped core have some appealing properties: (i) low-loss splicing to standard fibers, (ii) easy photoinscription of fiber gratings using conventional techniques, and (iii) good guidance when the holes are collapsed to build in-fiber gas o liquid cells. In addition, cutoff of the fundamental mode is produced when the holes are filled with liquids, as if it were a conventional depressed-index fiber [13]. Modifications of the characteristics of the liquids lead to changes of the guidance properties of the fiber, in particular, the cutoff wavelength shifts.

In our experiments, a sensitivity as high as 25 nm/°C is achieved, which is about three orders of magnitude higher than the sensitivity of standard FBG, two orders of magnitude higher than the sensitivity of the best fiber gratings, and about one order of magnitude higher the values reported for multimode fiber interferometers. In addition

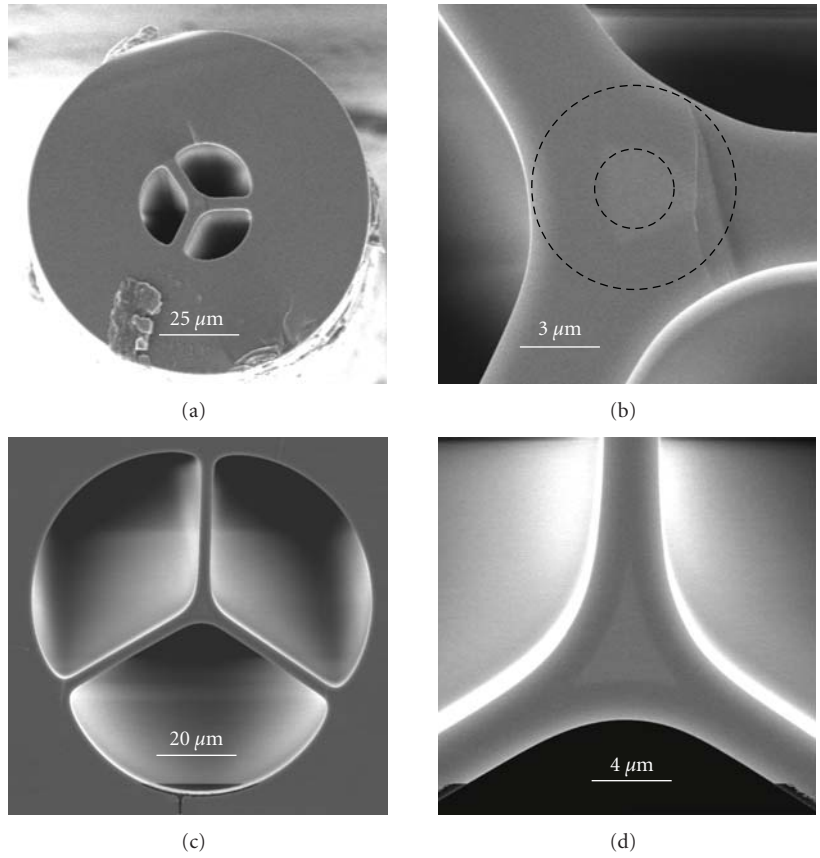

Figure 1: SEM images of fiber 1 (a) and (b) and fiber 2 (c) and (d).

to the wavelength-encoded configuration of the temperature sensor, we report here the amplitude interrogation of these devices. In this case, very simple experimental arrangements are required, preserving a high resolution.

2. Principle

The fiber that was used in our experiments is a Y-shaped Ge-doped microstructured fiber. This fiber has three big holes, which makes straightforward the procedure to fill the fiber with a liquid. In addition, the Y-shaped fiber can be designed to have rather small core, hence, a strong interaction with the liquids filling the fiber due to the presence of intense evanescent fields in the holes. The fiber was fabricated in our laboratory with a Ge-doped core using the conventional stack and draw technique [12]. Figure 1 shows the scanning electron microscope (SEM) images of the two fibers reported here, with a detail of the core region. In the case of fiber 1, two circles have been drawn on the image. The small circle is adjusted to have the same area that the triangular shaped Ge-doped region at the centre of the fiber, while the second circle is tangent to the three holes and defines what we call the first effective cladding of the fiber. The doped core had a Ge concentration to raise a step-index profile with a numerical aperture (NA) of 0.29. The first cladding surrounding the core was pure silica. Table 1 summarizes the basic parameters of the two fibers used in our experiments: the diameter of the circle that corresponds to the Ge-doped core (d), the diameter of the first effective cladding (D), the outer diameter of the fiber (OD), the holes' area (A_H), and the silica bridges thickness (d_B). The two fibers were singlemode when filled with liquids with a refractive index around 1.44.

Table 1: Basic parameters of the fibers.

	d (μm)	D (μm)	OD (μm)	A_H (μm^2)	d_B (μm)
Fiber 1	3.3	8	110	1000	4.4
Fiber 2	3.3	6	136	3570	2

The liquids that we used for these experiments were provided by Cargille (series A) and have a nominal refractive index (RI) value of 1.46, 1.47, and 1.48, measured at 589 nm and 25°C. The temperature coefficient of these liquids, provided by the manufacturer, is about $-4\times10^{-4}\,^{\circ}\mathrm{C}^{-1}$. Thus, when one fiber is filled with one of these liquids, the cutoff of the fundamental mode takes place at a given wavelength, as a function of the refractive index value. Figure 2 shows the typical transmission spectra for four devices with different lengths: 2, 18, 22, and 35 cm. They have been measured with a broadband unpolarized light source and an optical spectrum analyzer (OSA). The devices of 2 and 22 cm length

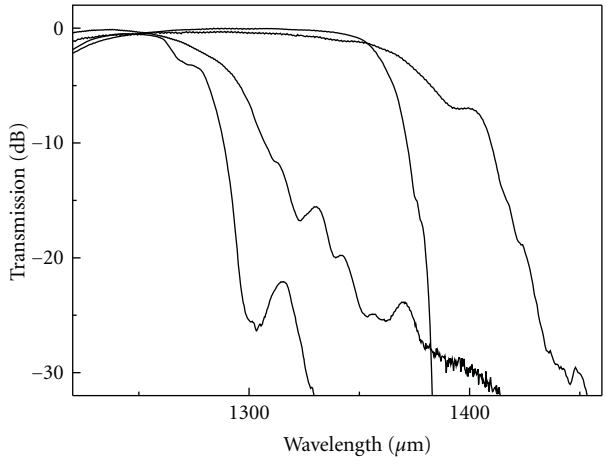

Figure 2: Transmission spectra of four sensor heads with different lengths, from left to right: 22, 2, 35, and 18 cm.

were prepared with fiber 2 (see Table 1) and filled with a liquid of RI = 1.475 (a mixture of two liquids: 50% of 1.47 and 50% of 1.48), while the devices of 18 and 35 cm length were filled with RI = 1.47, and they were prepared with fiber 2 and fiber 1, respectively. After filling the holes, both ends of the fiber were spliced to standard singlemode fiber. We can see that the losses increase dramatically beyond the cutoff wavelength, even in the case of the short sensor. Though most of the results that we will present here have been obtained with devices that were about 20 cm long, this figure demonstrates that sensor heads ten times shorter can be used if it is required. At present, the optimization of the short sensor heads has not been concluded yet.

The operation principle of the temperature sensor was discussed in a previous publication [12]. The cutoff is produced when the dispersion curve of the fundamental mode intersects the dispersion curve of the liquid, that has a refractive index between the refractive index of silica and the refractive index of the Ge-doped silica. When the temperature changes, the thermo-optic coefficient of the liquid dominates the properties of the device, since silica has a coefficient 40 times smaller. A small change of the refractive index of the liquid shifts the point of intersection and produces a large change of the cutoff wavelength. The calculations of the cutoff wavelength as a function of temperature, using the step-index model, predict a linear response within the temperature range of our experiments, $[-10, 60]^\circ$C.

3. Experimental Results and Discussion

In order to illustrate the basic characteristics of these devices as temperature sensors, Figure 3(a) shows the transmission spectra of a sensor head that was prepared by filling 18 cm of fiber 2 (see Table 1) with liquid of RI 1.47. In this experiment the temperature was adjusted from 15°C to

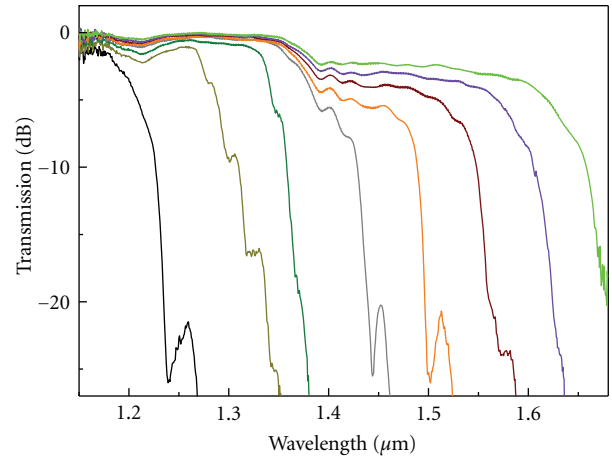

(a)

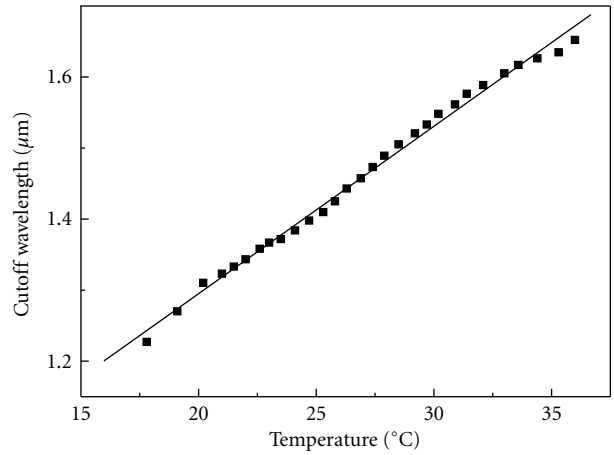

(b)

Figure 3: (a) Transmission spectra of a sensor head, with 18 cm length, at different temperatures, from left to right: 17.8, 20.2, 22.6, 25.8, 27.9, 30.2, 33.0, and 36.8°C. (b) Calibration of this sensor head: cutoff wavelength as a function of temperature.

35°C and the cutoff wavelength shifted from 1.2 μm to 1.65 μm. This sensor head is the shortest that we have fully calibrated. Figure 3(b) gives the result of the calibration of the temperature response of this sensor head, taking the cutoff wavelength at the point the transmission drops 10 dB. The sensitivity is ~25 nm/°C, the same that was reported in [12] for longer devices.

Since the sensitivity is very high, one can preserve a good detection limit while using low resolution OSA. According to the 25 nm/°C slope, a low-cost OSA with a resolution of 1 nm would permit to achieve a detection limit of 0.04°C, while the use of an OSA with 20 pm resolution would push the detection limit down to 0.001°C. The use of liquids with higher thermo-optic coefficients could increase the sensitivity. Transparent polymers are, as well, good candidates to implement compact and stable sensor heads with even higher sensitivity.

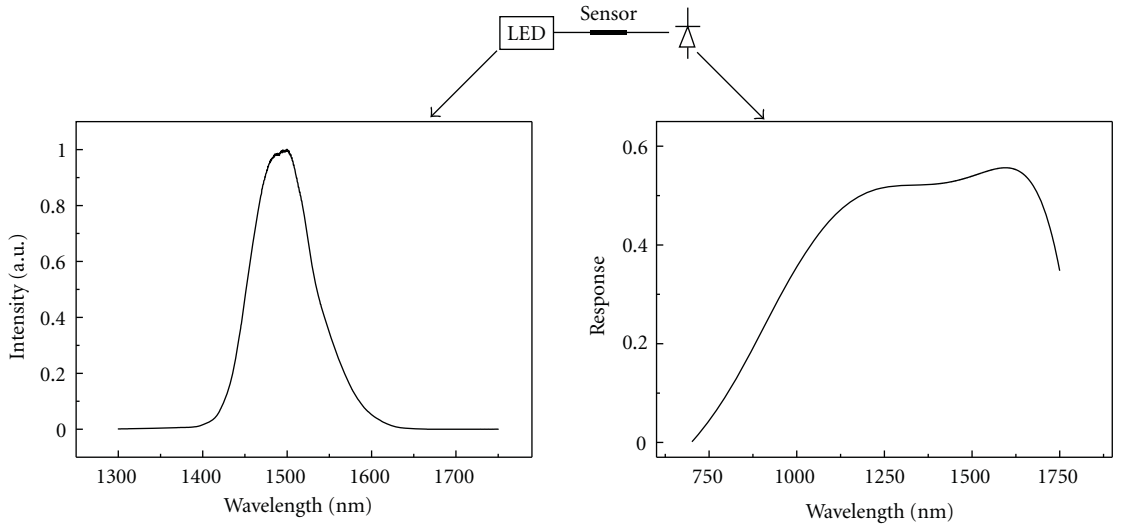

Figure 4: Schematic diagram of the sensor arrangement for amplitude interrogation. Optical spectrum of the LED and spectral response of the photodiode.

4. Amplitude Interrogation

One of the valuable characteristics of the previously reported temperature sensors is the wavelength codification of the sensor information. However, in some cases, one might be interested in using the simplest as possible interrogation technique. In such a case, our sensor heads permit the implementation of simple amplitude interrogation techniques. Figure 4 is a schematic diagram of the sensor arrangement that we have implemented to study the amplitude response of the sensors. A broadband source, either a light emitting diode (LED) or a halogen lamp (HL), was used to illuminate the sensor heads, and a photodiode was used to measure the transmitted power. Figure 4 includes the optical spectrum of the LED and the spectral response of the photodiode.

The amplitude response of the sensor is determined by the combination of the transmission characteristics of the sensor head as a function of temperature, the spectrum of the broadband light source, and the spectral response of the photodiode. Figure 5 gives two examples: (a) using a LED and (b) using an HL. In both cases, the sensor head was implemented using a section of fiber 2 and filling 31 cm with a liquid of RI = 1.47. The smaller bandwidth of the LED makes the response to exhibit saturation, with a maximum slope of $0.127^{\circ}C^{-1}$, while in the case of the HL the response is approximately linear ($\sim 0.022^{\circ}C^{-1}$). If we assume that the minimum relative amplitude change that we can detect is one thousandth, then the detection limit will be lower than $0.05^{\circ}C$.

Figure 6 is a simulation of the response that should be obtained using the sensor reported in Figure 3 and measuring the transmission of a laser centred at 1510.25 nm. The slope at $28.5^{\circ}C$ is $0.353^{\circ}C^{-1}$. Thus, if we assume that the transmittance can be measured with a resolution of one thousandth, then the detection limit would be $0.003^{\circ}C$. The characteristics of this sensor configuration could be used for temperature stabilization. Changing the wavelength of the

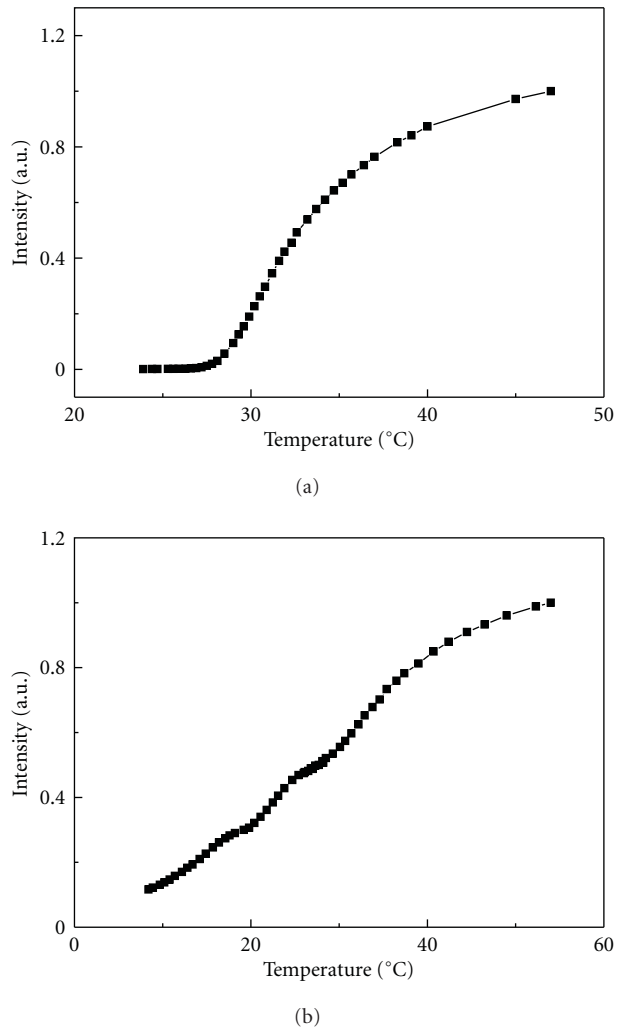

Figure 5: Calibration of the relative amplitude response of a sensor: (a) using a LED and (b) using a halogen lamp.

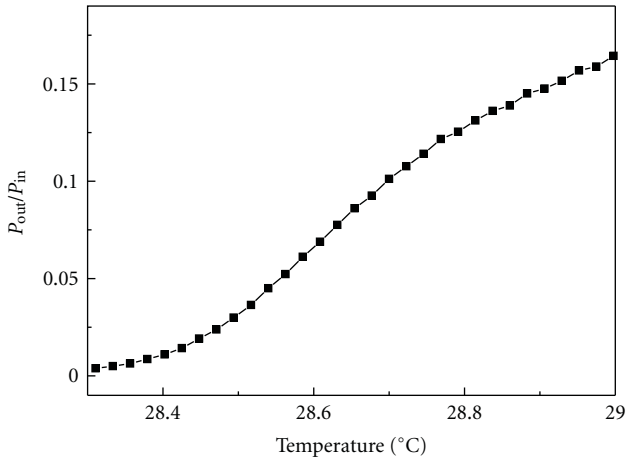

Figure 6: Transmittance of a sensor head at 1510.25 nm as a function of temperature.

laser, one could select the temperature of stabilization of the system.

5. Conclusion

Photonic crystal fibers open new opportunities by exploiting the unique properties that these fibers exhibit. Here we have exploited new possibilities based on the cutoff properties of the fundamental mode of Ge-doped photonic crystal fibers. Our experiments have been carried out using different Ge-doped Y-shaped microstructured fibers, and sensor heads of different lengths and filled with different liquids have been implemented. The sensitivity is mainly determined by the thermo-optic coefficient of the liquids that fill the fibers. A sensitivity of 25 nm/°C is reported, and a detection limit of about 0.001°C is estimated, when using the wavelength-encoded configuration. The sensor heads permit simple amplitude interrogation techniques to be implemented with high sensitivities and low detection limits.

Acknowledgment

This work has been financially supported by the Ministerio de Ciencia e Innovación of Spain (Project TEC2008-05490).

References

[1] B. Culshaw and J. Dakin, *Optical Fiber Sensors: Systems and Applications*, Artech House, 1989.
[2] K. T. V. Grattan and Z. Y. Zhang, *Fiber Optic Fluorescence Thermometry*, Chapman & Hall, 1995.
[3] Y. J. Rao, "In-fibre Bragg grating sensors," *Measurement Science and Technology*, vol. 8, no. 4, pp. 355–375, 1997.
[4] L. Jin, W. Zhang, H. Zhang, et al., "An embedded FBG sensor for simultaneous measurement of stress and temperature," *IEEE Photonics Technology Letters*, vol. 18, no. 1, pp. 154–156, 2006.
[5] S. K. A. K. Bey, T. Sun, and K. T. V. Grattan, "Optimization of a long-period grating-based Mach-Zehnder interferometer for temperature measurement," *Optics Communications*, vol. 272, no. 1, pp. 15–21, 2007.
[6] F. Pang, W. Xiang, H. Guo, et al., "Special optical fiber for temperature sensing based on cladding-mode resonance," *Optics Express*, vol. 16, no. 17, pp. 12967–12972, 2008.
[7] H. Guo, F. Pang, X. Zeng, N. Chen, Z. Chen, and T. Wang, "Temperature sensor using an optical fiber coupler with a thin film," *Applied Optics*, vol. 47, no. 19, pp. 3530–3534, 2008.
[8] E. B. Li, X. L. Wang, and C. Zhang, "Fiber-optic temperature sensor based on interference of selective higher-order modes," *Applied Physics Letters*, vol. 89, Article ID 091119, 2006.
[9] E. Li and G. D. Peng, "Wavelength-encoded fiber-optic temperature sensor with ultra-high sensitivity," *Optics Communications*, vol. 281, no. 23, pp. 5768–5770, 2008.
[10] L. Rindorf and O. Bang, "Sensitivity of photonic crystal fiber grating sensors: biosensing, refractive index, strain, and temperature sensing," *Journal of the Optical Society of America B*, vol. 25, no. 3, pp. 310–324, 2008.
[11] H. Y. Choi, K. S. Pack, S. J. Park, U. C. Paek, B. H. Lee, and E. S. Choi, "Miniature fiber-optic high temperature sensor based on a hybrid structured Fabry-Perot interferometer," *Optics Letters*, vol. 33, no. 21, pp. 2455–2457, 2008.
[12] S. Torres-Peiró, A. Díez, J. L. Cruz, and M. V. Andrés, "Fundamental-mode cutoff in liquid-filled Y-shaped microstructured fibers with Ge-doped core," *Optics Letters*, vol. 33, no. 22, pp. 2578–2580, 2008.
[13] L. G. Coen, D. Marcuse, and W. L. Mammel, "Radiating leaky-mode losses in singlemode lightguides with depressed-index claddings," *IEEE Transactions on Microwave Theory and Techniques*, vol. 30, pp. 1455–1460, 1982.

Hindawi Publishing Corporation
Journal of Sensors
Volume 2009, Article ID 572835, 12 pages
doi:10.1155/2009/572835

Review Article

Wide and Fast Wavelength-Swept Fiber Laser Based on Dispersion Tuning for Dynamic Sensing

Shinji Yamashita, Yuichi Nakazaki, Ryosei Konishi, and Osamu Kusakari

Department of Electrical Engineering and Information Systems, The University of Tokyo, 7-3-1 Hongo, Bunkyo-ku, Tokyo 113-8656, Japan

Correspondence should be addressed to Shinji Yamashita, syama@ee.t.u-tokyo.ac.jp

Received 13 February 2009; Accepted 12 June 2009

Recommended by Christos Riziotis

We have developed a unique wide and fast wavelength-swept fiber laser for dynamic and accurate fiber sensing. The wavelength tuning is based on the dispersion tuning technique, which simply modulates the loss/gain in the dispersive laser cavity. By using wideband semiconductor optical amplifiers (SOAs), the sweep range could be as wide as ~180 nm. Since the cavity contains no mechanical components, such as tunable filters, we could achieve very high sweep rate, as high as ~200 kHz. We have realized the swept lasers at three wavelength bands, 1550 nm, 1300 nm, and 800 nm, using SOAs along with erbium-doped fiber amplifiers (EDFAs), and in two laser configurations, ring and linear ones. We also succeeded in applying the swept laser for a dynamic fiber-Bragg grating (FBG) sensor system. In this paper, we review our researches on the wide and fast wavelength-swept fiber lasers.

1. Introduction

Wavelength-tunable lasers are versatile both in telecom and sensing applications. For the sensing applications, wide tuning range is needed to improve the spatial resolution and/or measurement range, and fast tuning (sweep) is required to enhance the measurement speed for dynamic sensing. Figure 1 shows two examples of wavelength-swept laser-based sensing systems, fiber Bragg grating (FBG) sensor system (Figure 1(a)) [1] and optical coherence tomography (OCT) system (Figure 1(b)) [2]. In the FBG sensor system, the strain or temperature change is decoded as the shift of the Bragg wavelength of the FBG in the position. Since multipoint sensing is achieved by multiplexing FBGs in wavelength, the tuning range determines the number of FBGs ($\propto$ measurement range). In case of dynamic FBG sensing, such as vibrations, the tuning speed has to be faster than the vibration. For the FBG sensor system, 1550 nm wavelength region is mostly used because the fiber loss is minimum and telecom components are readily available. In the OCT system, scattered and reflected light from the object under test, typically a living tissue, is resolved in the frequency domain by interference with the reference light, whose spatial resolution is inversely proportional to the tuning range. For the three-dimensional (3D) OCT measurement, the laser beam has to be deflected and scanned spatially. Thus, the dynamic and high-resolution 3D-OCT measurement requires extremely wide tuning range over 100 nm, and extremely fast sweep rate over 100 kHz. For the retinal OCT, 1300 nm wavelength region is mostly chosen in order to compromise the scattering (strong at shorter wavelength) and water absorption (large at longer wavelength). It should be noted that such swept lasers do not have to be CW ones, but can be the pulsed ones as long as the interference is assured.

Many kinds of wavelength-swept lasers, either laser diode- (LD-) based or fiber laser-based, have been proposed so far. External cavity tunable LDs are commercially available at several wavelength bands and has wide tuning range over 100 nm [3], but the tuning speed is not fast because the tuning is achieved by the rotation of the bulk grating. The most widely used wavelength-swept lasers consist of a wide gain medium, and a fast tunable optical filter, as illustrated in Figure 2(a). The wide gain medium is typically a semiconductor optical amplifier (SOA) or an erbium-doped fiber amplifier (EDFA). EDFAs can output high

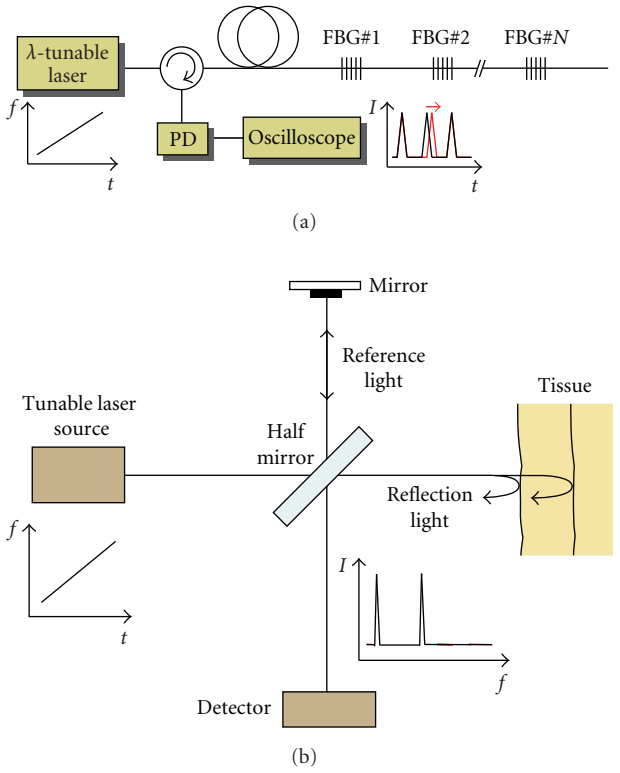

FIGURE 1: Wavelength-swept laser-based sensing systems (a) FBG sensor system (b) OCT system.

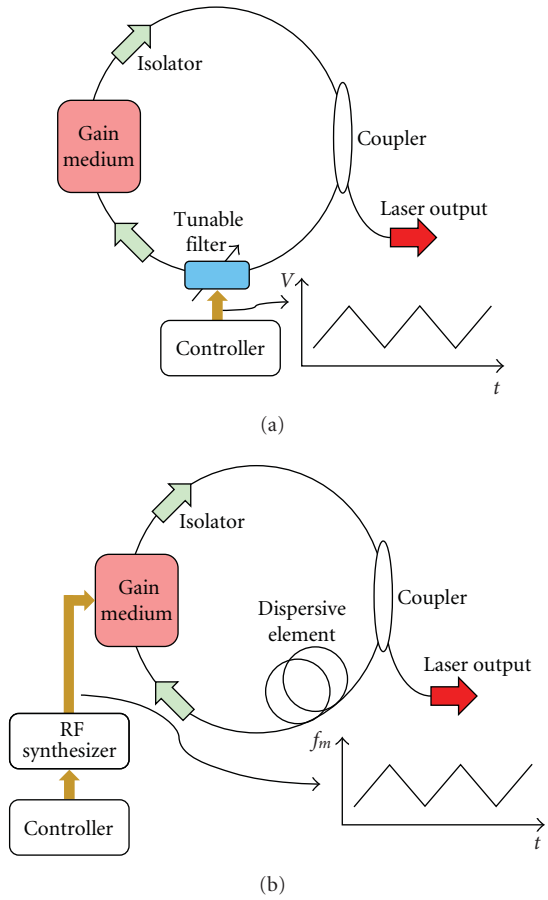

FIGURE 2: Wavelength-swept fiber lasers: (a) tunable filter-based laser (b) dispersion-tuned laser.

power and EDFA-based lasers can be tunable over 80 nm [4], but its wavelength band is limited to 1550 nm. So the more preferred gain medium for sensing applications is the SOA, which can work at many wavelength bands (1550 nm, 1300 nm, 1000 nm, and 800 nm) with wide gain bandwidth over 100 nm. As for sweep speed, there are two limiting factors, one is the sweep speed of the optical filters, and the other is the photon lifetime in the laser cavity, which is inversely proportional to the cavity length. There have been several fast tunable optical filters, such as piezo-transducer- (PZT-) based tunable Fabry-Perot filters (FFP) [5], and polygonal mirror scanners [6]. They are basically mechanically tunable filters, in which the sweep speed is normally limited below a few tens of kHz by the mechanical movements. FFPs have been shown to be able to be swept much faster, a few hundreds of kHz, by utilizing the resonance of specially-designed PZT [7], but the endurance of the PZT in the resonant mode is not clear. In terms of the second limiting factor, the cavity length, the SOA-based lasers are more advantageous than the EDFA-based lasers since the cavity can be shorter. As a different approach to this issue, so-called Fourier-domain mode locking (FDML) has been proposed recently, in which the sweep time is set to be equal to one round trip time of the cavity [7]. With the FDML, 105 nm tuning range and 290 kHz sweep rate have been achieved, but the endurance of the FFP in such high speed is still in question.

In this review paper, we present our proposed novel and different type of wide and fast wavelength-tunable fiber laser [8]. It uses the same gain medium with the conventional swept fiber lasers, but does not use any tunable filters. The tuning mechanism of our swept laser is so-called "dispersion tuning" technique, which simply modulates the loss/gain in the dispersive laser cavity, as illustrated in Figure 2(b). By using wideband SOAs, the sweep range could be as large as ~180 nm. Since the cavity contains no mechanical components, such as tunable filters, we could achieve very high sweep rate, as high as ~200 kHz. We have realized the swept lasers at three wavelength bands, 1550 nm, 1300 nm, and 800 nm, using SOAs along with EDFAs, and in two laser configurations, ring and linear ones. We also succeeded in applying the swept laser for dynamic FBG sensors. We review our researches on the wide and fast wavelength-swept fiber lasers.

2. Principle of Dispersion Tuning

The laser cavity has discrete longitudinal resonance modes. The resonance condition of the ring cavity is expressed as

$$\beta(\omega_K)L = 2K\pi, \tag{1}$$

where K is an integer expressing the mode number, $\beta(\omega)$ denotes the propagation constant at an angular frequency

ω, ω_K is the angular frequency of the Kth resonance mode, and L is the cavity length. However, (1) can be transformed to

$$(\beta(\omega_{K+1}) - \beta(\omega_K))L = 2\pi. \tag{2}$$

Spacing between adjacent modes or the free-spectral range (FSR) F of the laser cavity is expressed, using the relation $\beta = n\omega/c$ as

$$F = \frac{\omega_{K+1} - \omega_K}{2\pi} = \frac{c}{nL}, \tag{3}$$

where n is the effective refractive index in the cavity, and c is the speed of light in the vacuum. Note that n is assumed to be a constant in deriving (3).

In the fiber laser cavity, L is long, thus the spacing between adjacent modes is small. Here we assume $\omega_{K+1} - \omega_K \ll \omega_K$, then (2) becomes

$$(\omega_{K+1} - \omega_K)\frac{d\beta}{d\omega}L = 2\pi. \tag{4}$$

However, (4) leads to another but more general expression of FSR as

$$F = \left[\frac{d\beta}{d\omega}L\right]^{-1}. \tag{5}$$

We can lock the lasing modes and generate a short pulse train by applying the modulation at a frequency, which is well known as the active mode locking technique [9]. The modulation frequency f_m to the cavity has to match with an integer (N) times of the FSR ($= N \times F$), where N is the order of harmonics (harmonic mode locking). Without the chromatic dispersion in the cavity, F is a constant over entire frequency. In this case, the lasing occurs at the gain peak wavelength, regardless whether the modes are locked or not.

When the chromatic dispersion exists in the laser cavity, F becomes dependent on the frequency, $F(\omega)$. By expanding $\beta(\omega)$ around a frequency ω_0 with the Taylor series, (5) becomes

$$\begin{aligned} F(\omega) &= \frac{1}{L}\left[\beta_1 + \beta_2(\omega - \omega_0) + \frac{1}{2}\beta_3(\omega - \omega_0)^2 + \cdots\right]^{-1} \\ &\approx F_0\left[1 - \frac{\beta_2}{\beta_1}\Delta\omega - \frac{1}{2}\frac{\beta_3}{\beta_1}\Delta\omega^2 - \cdots\right], \end{aligned} \tag{6}$$

where $F_0 = 1/(\beta_1 L)$, which is the initial FSR at $\omega = \omega_0$, and $\triangle\ \omega = \omega - \omega_0$. Here we assumed that terms containing $\Delta\omega$ are much smaller than the first term. Neglecting the higher order chromatic dispersion ($\beta_3, \beta_4, \ldots$), the change of the FSR from F_0 by the change of frequency, $\Delta F(\omega)$, is expressed as

$$\Delta F(\omega) = -F_0\frac{\beta_2}{\beta_1}\Delta\omega. \tag{7}$$

However, (7) implies that the FSR is enlarged or reduced (depending on the sign of β_2) linearly in proportion to the change of frequency, as shown in Figure 3. The dispersion tuning is a technique using the unevenly spaced resonance

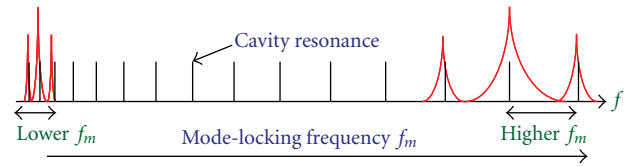

Figure 3: Principle of dispersion tuning: unevenly spaced resonance modes in the dispersive laser cavity.

modes in the dispersive laser cavity. Supposing that we apply a modulation at f_m to the dispersive cavity strongly enough to be mode locked, the laser is obliged to operate at a frequency to meet the mode-locking condition. In the case of Figure 3 where β_2 is negative, lower f_m stimulates lasing at lower frequency, and higher f_m stimulates lasing at higher frequency. Reminding (7) and the harmonic mode locking of Nth order, the change of lasing frequency $\Delta\omega$ and the change of modulation frequency Δf_m should have a relation,

$$\Delta\omega = -\frac{\beta_1}{N\beta_2 F_0}\Delta f_m = -\frac{\beta_1^2 L}{N\beta_2}\Delta f_m = -\frac{n_0^2 L}{c^2 N\beta_2}\Delta f_m. \tag{8}$$

Here we used $\beta_1 = n_0/c$ and n_0 is the refractive index at $\omega = \omega_0$. It is sometimes more useful to rewrite (8) in terms of change of lasing wavelength $\Delta\lambda$. Using relations $\Delta\omega = -2\pi c\,\Delta\lambda/\lambda^2$, $\beta_2 = -\lambda^2 D/2\pi c$, where D is the dispersion parameter, (8) can be transformed to

$$\Delta\lambda = -\frac{n_0^2 L}{c^2 ND}\Delta f_m = -\frac{n_0}{cNDF_0}\Delta f_m = -\frac{n_0}{cDf_{m0}}\Delta f_m, \tag{9}$$

where $f_{m0} = NF_0$, which is the initial modulation frequency to give $\omega = \omega_0$. Thus the lasing frequency or wavelength can be tuned by changing the modulation frequency. This is called the dispersion tuning technique [10, 11]. It is found from (9) that the wavelength shift is more sensitive to the change of modulation frequency when D and f_{m0} are small, which means that the wavelength is not well defined and dispersion tuning is weak.

Wavelength sweep range $\Delta\lambda_{tr}$ is determined by two factors. One is the gain bandwidth, and the other is lasing at the adjacent harmonic mode, $(N-1)$th or $(N+1)$th mode. It happens when the change of modulation exceeds one FSR. From (9), $\Delta\lambda_{tr}$ is expressed as

$$\Delta\lambda_{tr} = \frac{n}{c|D|N} = \frac{1}{|D|Lf_{m0}}, \tag{10}$$

However, (10) means that smaller D, L, and f_{m0} give wider sweep range.

The sweep speed V_{sw} is inversely proportional to the photon lifetime as is the case of conventional swept lasers, that is, the sweep speed is faster when L is small:

$$V_{sw} \propto \frac{1}{L}. \tag{11}$$

Since the laser is mode locked, the output is not in CW, but is pulsed at the repetition rate equal to the modulation

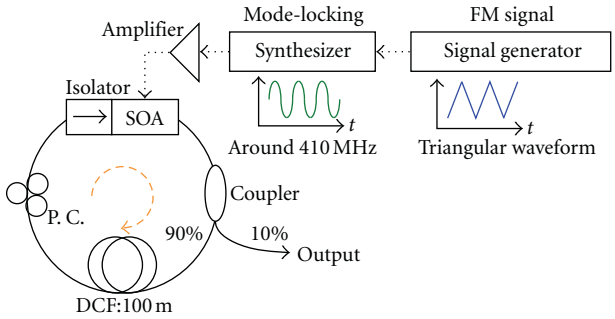

Figure 4: Dispersion-tuned swept fiber ring laser using SOA.

frequency. The pulse is strongly chirped and wide by the intracavity dispersion. The pulse from the mode-locked fiber laser with the intracavity dispersion is expressed with a chirped Gaussian pulse [11], whose spectral half width $\delta\omega$ is given by

$$\delta\omega = \left(\pi \frac{f_{m0}}{\lambda}\right)^{1/2} \left(\frac{8\pi cM}{|D|L}\right)^{1/4}, \quad (12)$$

where M is the modulation depth. This equation means that linewidth can be narrower as f_{m0} is smaller and D and L are larger. However, from (9), smaller f_{m0} increases the instability of lasing wavelength and causes linewidth broadening, which is the most cases in the following experiments. Thus f_{m0} should be as high as the linewidth broadening by (12) is acceptable.

From the above discussions, in order to realize wide and fast tuning with narrow spectral linewidth, D and f_{m0} should be as large as possible, and L should be as small as possible.

3. Swept Fiber Ring Laser Using SOA at 1550 nm and 1300 nm Wavelength Bands

Figure 4 shows a schematic construction of the dispersion tuning-based wavelength-swept fiber ring laser at the 1550 nm wavelength band. The laser is in a ring-laser configuration, and all the devices are pigtailed with single-mode fibers. The polarization-independent SOA module having a 3dB gain bandwidth of 79.7 nm is used as the gain medium of the laser. Active mode-locking is realized by directly modulating the injection current to the SOA with the RF signal from an RF synthesizer. It can reduce the intracavity loss and the cost of external modulator. The triangular signal from a signal generator is input to the RF synthesizer for modulation frequency sweep. In order to provide the chromatic dispersion in the laser cavity needed for the dispersion tuning, we insert a 100m-long dispersion compensating fiber (DCF) having a dispersion parameter of −90 ps/nm/km at $\lambda = 1550$ nm. An isolator in the SOA module ensures unidirectional lasing of the laser cavity. However, 10 % of the light in the laser cavity is output from the 9:1 coupler.

We set the mode-locking frequency at around 410 MHz. It is determined by the RF modulation characteristics of

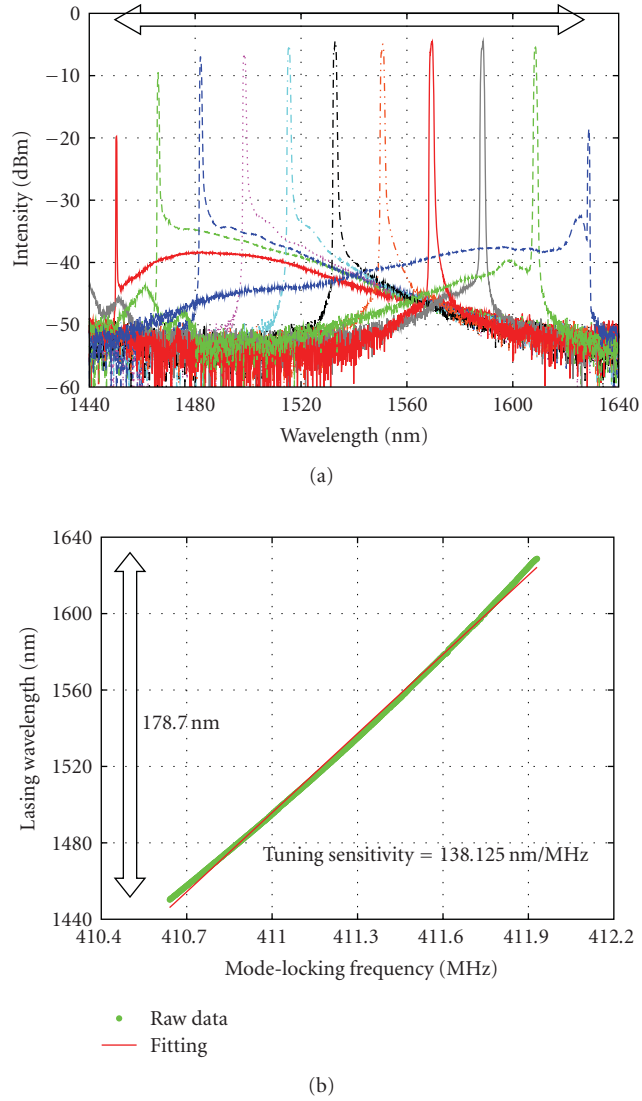

Figure 5: Static tuning characteristics at 1550 nm wavelength band: (a) lasing spectra (b) lasing wavelength again modulation frequency.

the SOA. Figure 5 shows the change of the lasing spectra and the lasing wavelength, respectively, as the mode-locking frequency is changed manually. The results suggest that the lasing wavelength almost shifts linearly toward the longer wavelength as the mode-locking frequency increases. The tuning sensitivity is 138.12 nm/MHz and the static tuning range is as wide as 178.7 nm. The output power is ∼1.3 dBm and the instantaneous linewidth is ∼1.1 nm when the lasing wavelength is 1540 nm. The instantaneous linewidth is almost the same at any wavelengths. Figure 6 is the temporal waveform of the output pulses at the modulation frequency of 400 MHz. It is found that the pulse is very wide, ∼1 ns, because it is strongly chirped by the intracavity dispersion.

The mode-locking frequency at around 410 MHz needs to be linearly modulated with the triangular waveform which is schematically shown in Figure 4 so as to sweep the wavelength linearly. The triangular waveform has two scan

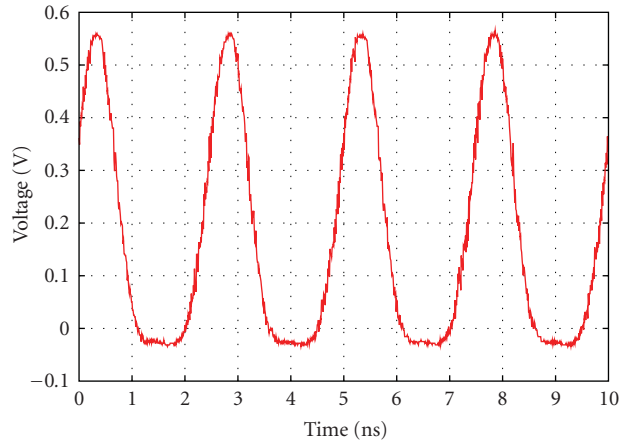

Figure 6: Temporal waveform of the output pulses at the modulation frequency of 400 MHz.

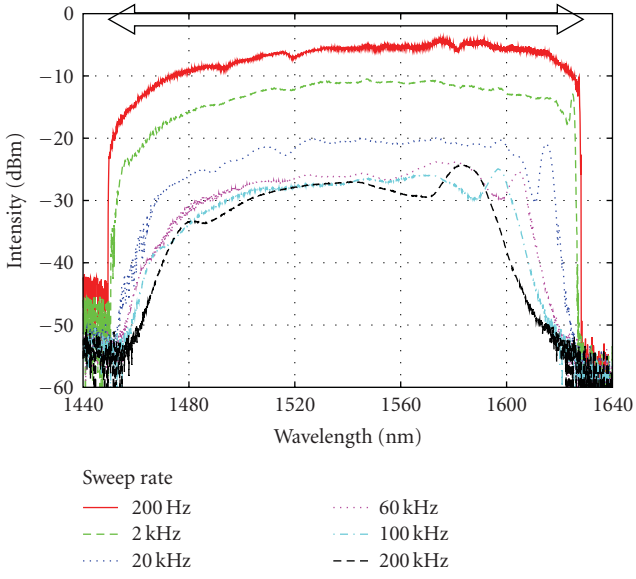

(a)

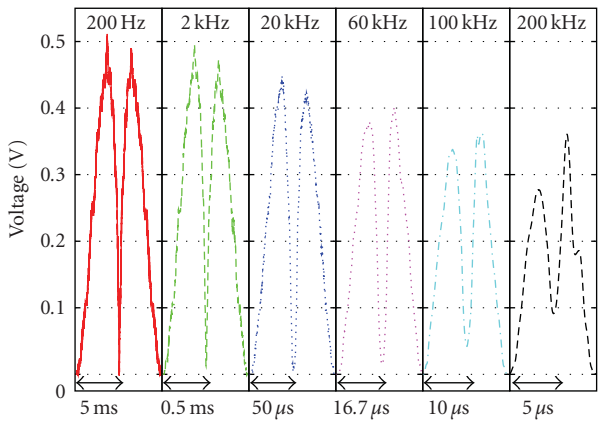

(b)

Figure 7: Dynamic sweep characteristics at 1550 nm wavelength band: (a) Max. hold spectra (b) temporal waveforms at different scan rates.

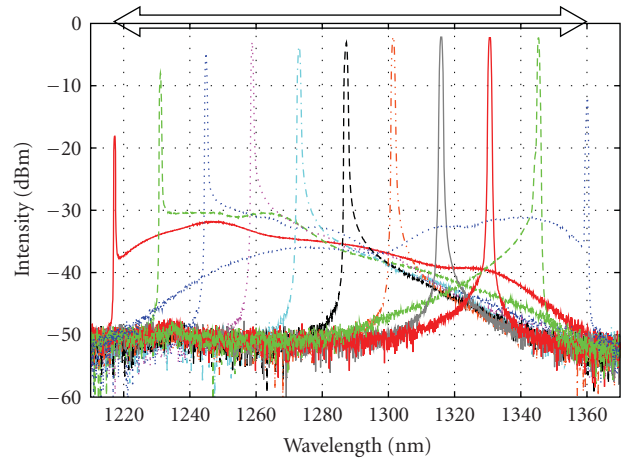

(a)

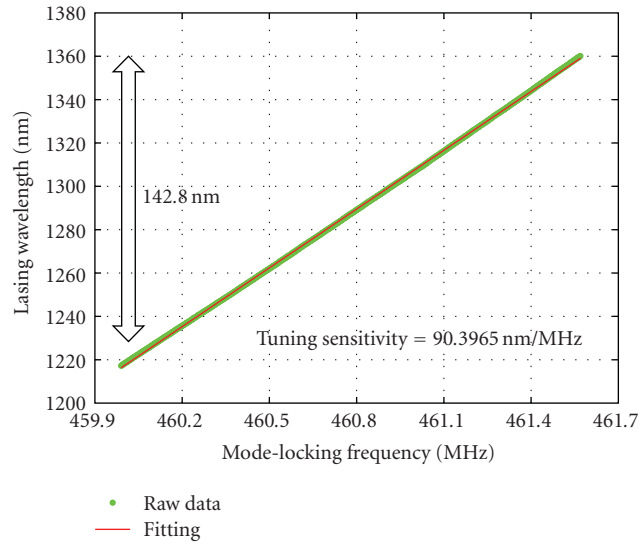

(b)

Figure 8: Static tuning characteristics at 1300 nm wavelength band: (a) lasing spectra (b) lasing wavelength again modulation frequency.

areas, upscan and downscan. In the upscan area, the lasing wavelength shifts-toward longer wavelength. Figure 7(a) shows the peak-hold spectra using a function of the optical spectrum analyzer, and Figure 7(b) shows the temporal waveforms when the scan rate is changed, 200 Hz, 2 kHz, 20 kHz, 60 kHz, 100 kHz, 200 kHz. A dynamic sweep range of over 120 nm is achieved at scan rate over 100 kHz. The difference between the upscan and the downscan can be attributed to the nonlinear effect in SOA [12]. The output power is −1.95 dBm when this laser is swept at scan rate of 200 kHz.

As described earlier, our laser has wide and fast sweep characteristics. Applying this swept laser enables to allocate a large number of FBG array and a dynamic measurement in FBG sensing system. Currently, the tuning rate is determined only by the photon lifetime. Note that higher tuning rate

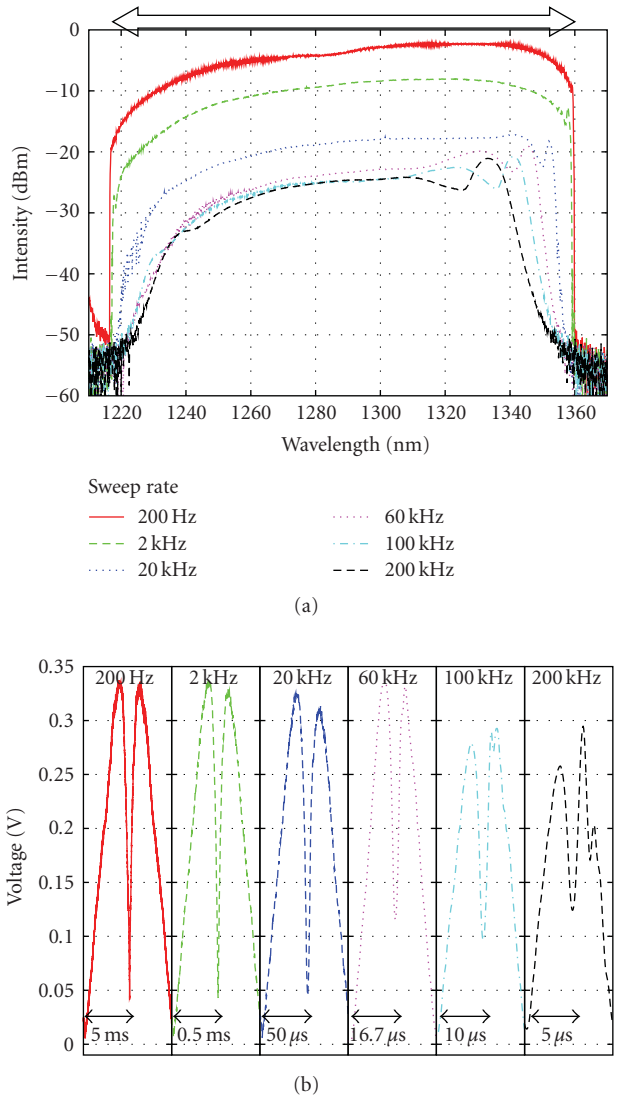

Figure 9: Dynamic sweep characteristics at 1300 nm wavelength band: (a) Max. hold spectra (b) temporal waveforms at different scan rates.

is possible by reducing the cavity length with use of higher dispersive element.

Operation wavelength band can be easily shifted by simply changing the gain medium in our swept fiber lasers. Here we show the swept fiber ring laser using SOA at 1300 nm wavelength band. The experimental setup is the same as in Figure 4, except that the SOA and other devices are replaced by similar devices designed for 1300 nm. We used the same 100m-long DCF as the dispersive medium. The dispersion parameter of DCF is estimated to be around −130 ps/nm/km at $\lambda = 1300$ nm. We chose the mode-locking frequency around 460 MHz.

Figure 8 shows the change of the lasing spectra and the lasing wavelength, respectively, as the mode-locking frequency is changed manually. The tuning range is as wide as 140 nm. The output power is ~ −0.78 dBm and the instantaneous linewidth is ~0.9 nm when the lasing wavelength is 1286 nm. The instantaneous linewidth is almost the same

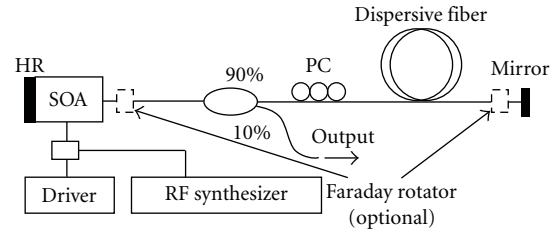

Figure 10: Dispersion-tuned swept fiber linear laser using SOA.

at any wavelengths. Figure 9(a) shows the peak-hold spectra when the modulation frequency is swept by the triangular waveform, and Figure 9(b) shows the temporal waveforms for several scan rates. A dynamic tuning range of over 120 nm is again achieved at scan rate over 100 kHz.

4. Swept Fiber Linear Laser Using SOA at 1550 nm and 800 nm Wavelength Bands

In the previous section, we demonstrated wide and fast wavelength-swept fiber lasers in the ring cavity configuration. The ring lasers, however, require an intracavity isolator to ensure the stable unidirectional lasing. In some wavelength bands, such as 800 nm, isolators are not readily available. By contrast, linear cavity configuration does not require an intracavity isolator, therefore, is versatile in terms of operational wavelength. Here we show that the dispersion tuning is also applicable to the linear lasers, and demonstrate wide and fast wavelength-swept fiber linear laser using SOA at 1550 nm and 800 nm wavelength bands.

The experimental setup of the wide and fast wavelength-swept fiber linear lasers at 1550 nm wavelength band is shown in Figure 10. One end of an SOA is coated with a highly reflective (HR) mirror. Active mode-locking is also realized by directly modulating the injection current to the SOA with the RF signal from an RF synthesizer. The 300m-long DCF, same with that of the ring lasers in the previous section, is inserted in the cavity. Another mirror is placed at the end of DCF. However 10% of the light in the cavity is extracted from the 9:1 coupler as an output light. Since the SOA used in this experiment has polarization dependence, we used two Faraday rotators (FRs), one before the SOA, and the other before the end mirror to form a Faraday rotator mirror (FRM), in order to compensate the polarization fluctuation in the laser cavity [13]. There is no isolator in the cavity.

Figure 11 shows the change of the lasing spectra and the lasing wavelength, respectively, as the mode-locking frequency is adjusted manually. The tuning range is as wide as 110 nm. The output power is ~0.4d Bm and the instantaneous linewith is ~0.7 nm. Figure 12(a) shows the peak-hold spectra, and Figure 12(b) shows the temporal waveforms when the mode-locking frequency is modulated at a different scan rate. A dynamic sweep range of over 100 nm is again achieved at scan rate over 2 kHz. At higher scan rate, 20 kHz, the temporal waveform is degraded. This is because of the limit by the photon lifetime in the cavity.

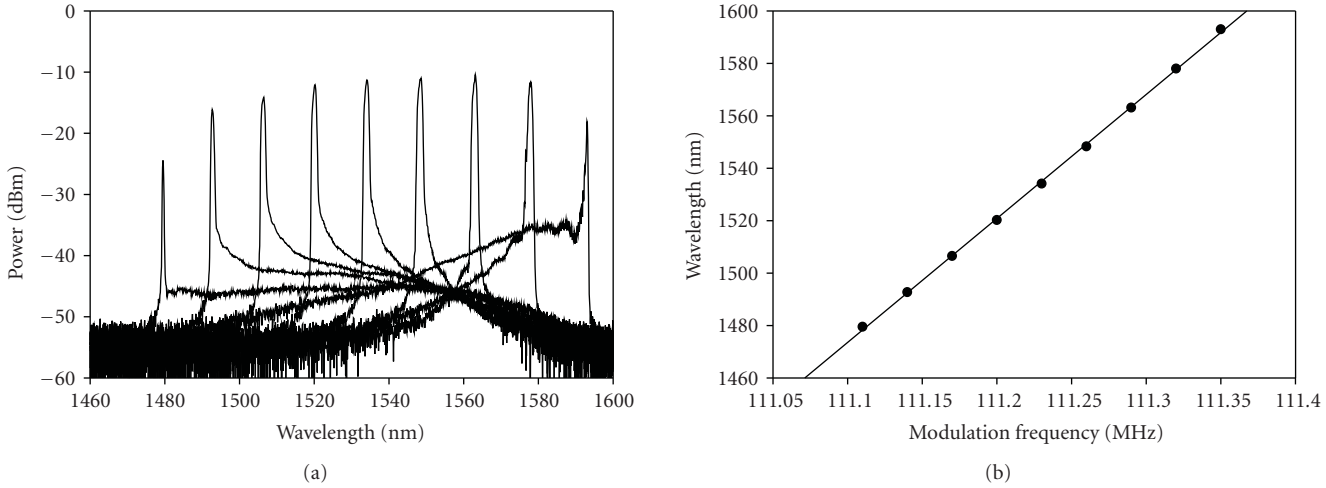

Figure 11: Static tuning characteristics at 1550 nm wavelength band: (a) lasing spectra (b) lasing wavelength again modulation frequency.

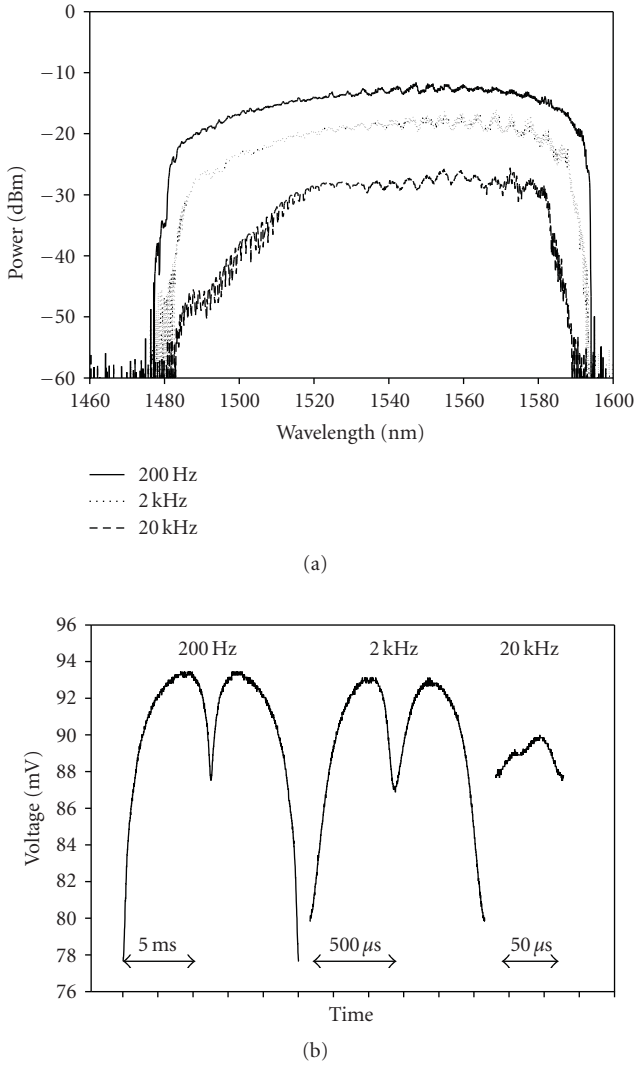

Figure 12: Dynamic sweep characteristics at 1550 nm wavelength band: (a) Max. hold spectra (b) temporal waveforms at different scan rates.

The round trip length in the linear cavity is twice as long as the cavity length, so it corresponds to the case of 600 m-long ring laser. We expect that faster sweep will be possible with the shorter DCF length.

We also composed the wide and fast wavelength-swept fiber linear lasers at 800 nm wavelength band. The experimental setup is basically the same as in Figure 10, except that the SOA and other devices are replaced by similar devices designed for 800 nm, and the FRs are not used since they are not available at this wavelength band. As for the dispersive fiber, we used a 300m-long single mode fiber for 800 nm wavelength band, which has large material dispersion $D \sim -100$ ps/nm/km. Figure 13 shows the change of the lasing spectra and the lasing wavelength, respectively, as the change of mode-locking frequency. The tuning range is around 45 nm, which is limited by the gain bandwidth of the SOA used in the experiment. The output power is ~ -10 dBm and the instantaneous linewith is ~0.67 nm. Figure 14(a) shows the peak-hold spectra, and Figure 14(b) shows the temporal waveforms. A dynamic sweep range is again about 45 nm, achieved at scan rate over 2 kHz. However, the peak-hold spectra are not flat, possibly due to the gain spectrum of the SOA and polarization change as the change of wavelength. Again, at higher scan rate, 20 kHz, the temporal waveform is degraded because of the long cavity length. We plan to address these issues in near future.

5. Swept Fiber Ring Laser Using EDFA at 1550 nm Band

So far, we used SOAs as the gain media, and the direct injection current modulation to the SOA was used for achieving mode locking needed for the dispersion tuning. Advantages of SOAs are the very wide gain bandwidth, and the capability of direct modulation. One drawback is the RF direct modulation characteristics in SOAs. As discussed in Section 2, we should raise the modulation frequency as high as possible for stable wide and fast sweep, preferably

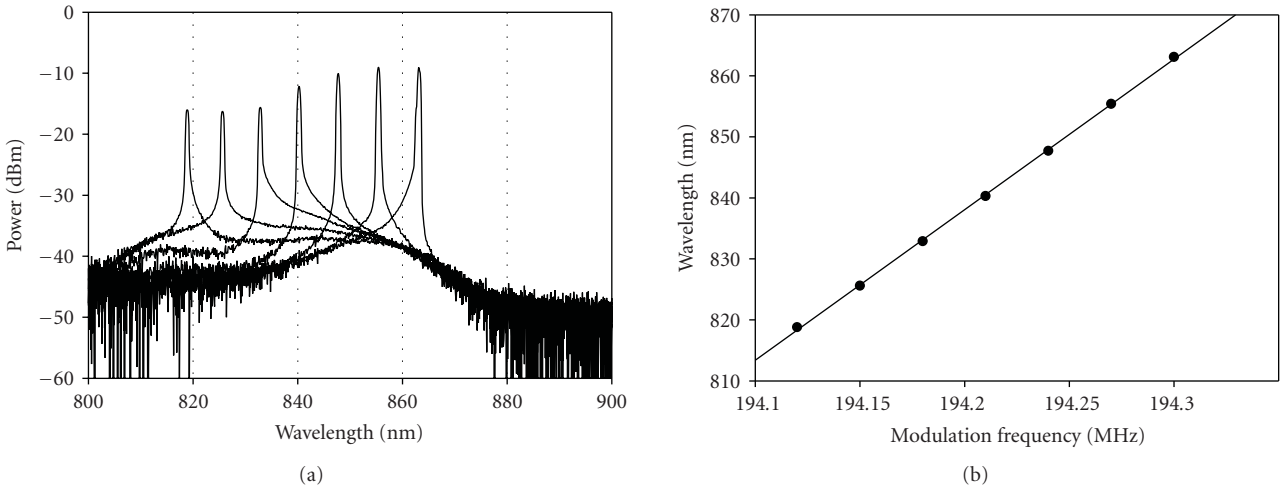

Figure 13: Static tuning characteristics at 800 nm wavelength band: (a) Lasing spectra (b) Lasing wavelength again modulation frequency.

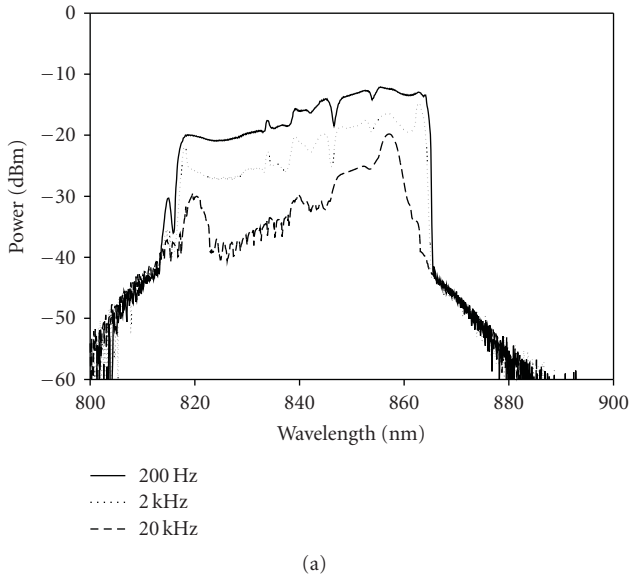

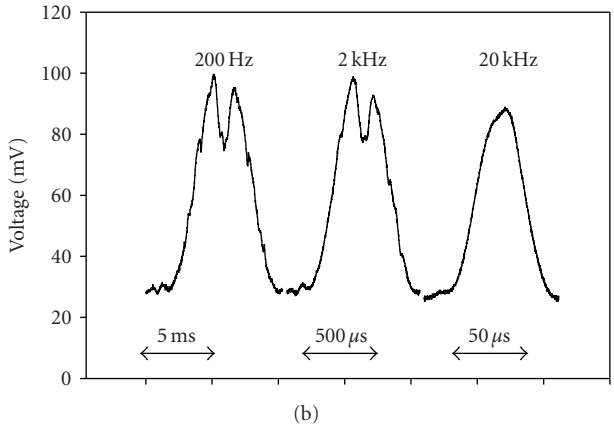

Figure 14: Dynamic sweep characteristics at 800 nm wavelength band: (a) Max. hold spectra (b) temporal waveforms at different scan rates.

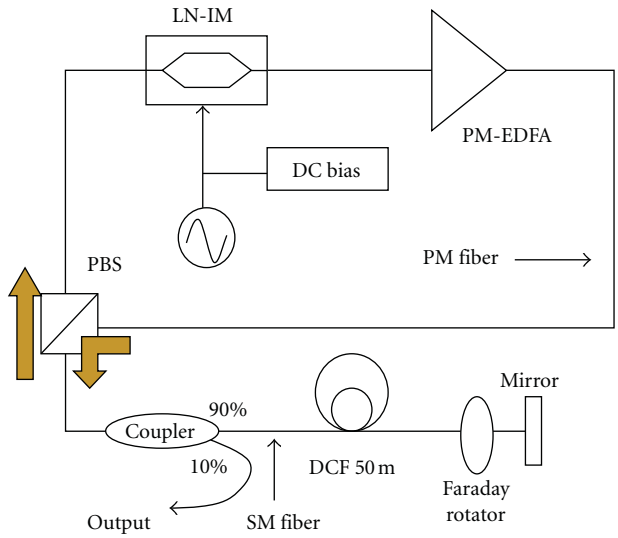

Figure 15: Dispersion-tuned swept fiber ring laser using EDFA.

higher than 1 GHz. However, the SOA chips and surrounding electronics in the module are not normally designed for accepting direct modulation at such high frequency. In the experiments using SOAs, we first measure the RF direct modulation characteristics of the SOA module, which are different one by one, and find the proper modulation frequency "sweet spot" for direct modulation. Another issue is the output power is not high, at best around 3 dBm.

In order to realize high-frequency modulation at high output power, we chose to use an external $LiNbO_3$ intensity modulator as the mode locker, and an EDFA as the gain medium. The experimental setup is shown in Figure 15. Since the intensity modulator has strong polarization dependence, we had to compose the polarization maintaining (PM) type devices, including the EDFA (PM-EDFA). Since we do not have the PM-DCF, we chose to use so-called sigma-laser configuration using a polarization beam splitter (PBS)

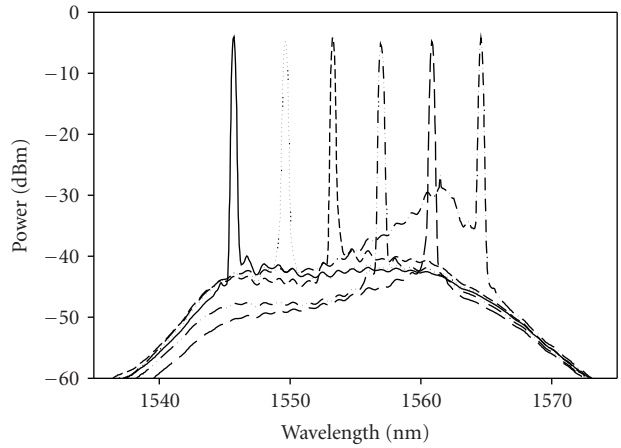

(a)

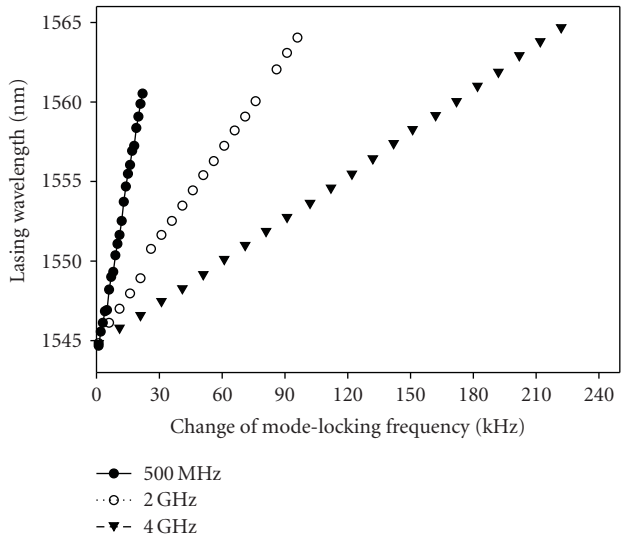

(b)

Figure 16: Static tuning characteristics: (a) lasing spectra (b) lasing wavelength again modulation frequency.

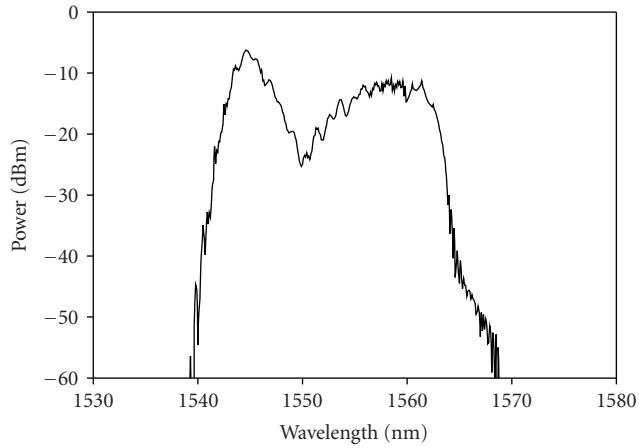

(a)

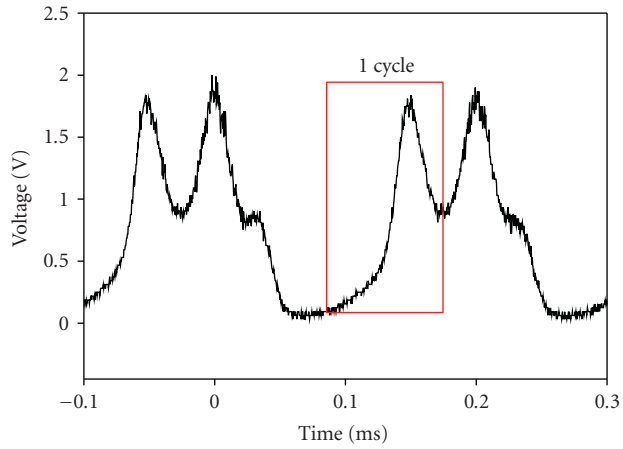

(b)

Figure 17: Dynamic sweep characteristics: (a) Max. hold spectra (b) temporal waveforms at different scan rates.

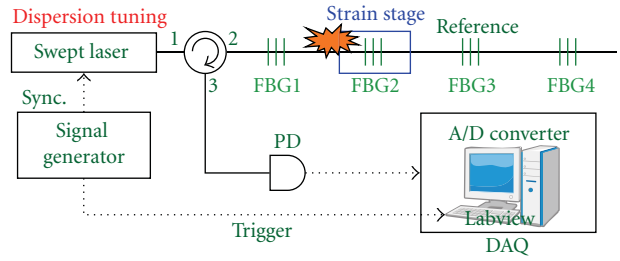

Figure 18: Experimental setup of dispersion-tuned swept-laser based FBG sensor at 1550 nm wavelength band.

and an FRM, and the 50m-long DCF, same with the previous experiments, is placed in between. As the result, the intracavity polarization state is constant over entire wavelength band. Active mode-locking is realized by applying the intensity modulation by the intensity modulator. However, 10 % of the light in the cavity is extracted from the 9:1 coupler as an output light.

Figure 16 shows the change of the lasing spectra and the lasing wavelength, respectively, as the change of mode-locking frequency. The tuning range is not large, around 20 nm, probably due to smaller gain bandwidth of the EDFA and large intracavity loss by the intensity modulator. Since the modulation frequencies are set at arbitrary values, we changed the modulation frequency from 500 MHz to 2 GHz. As shown in Figure 16(b), it is shown that the slope of the lasing wavelength against modulation frequency becomes gentler as the modulation frequency gets higher, and tuning range becomes wider, as expected from (9). Figure 17 shows the peak-hold spectra and the temporal waveforms when the modulation frequency is swept by the triangular waveform. A dynamic sweep range is again about 20 nm, achieved at scan rate of 10 kHz. However, the peak-hold spectra are not flat, possibly due to the remaining polarization change in the cavity as the change of wavelength.

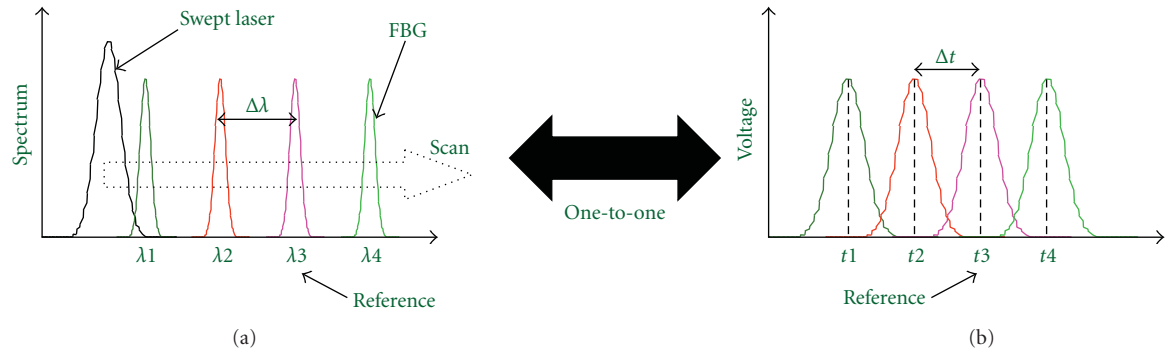

(a) (b)

Figure 19: Sensing of FBG shift in the time domain using the swept laser.

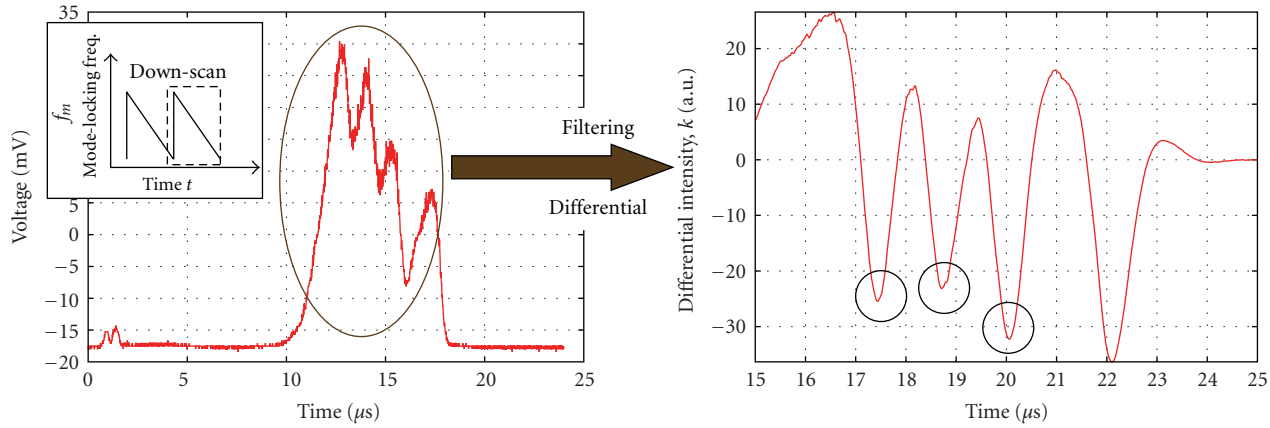

(a) (b)

Figure 20: Temporal waveform, and its derivative waveform of the reflected light from the FBG array.

6. Application to FBG Sensor

The applications of the wavelength-swept laser are further investigated for an FBG sensing system. The experimental setup of our swept-laser based FBG sensor is shown in Figure 18. The swept laser is the SOA-based ring laser at 1550 nm wavelength band described in Section 3. The multiplexed FBG array consists of FBGs having different Bragg wavelengths, FBG1: 1525 nm, FBG2: 1540 nm, FBG3: 1550 nm, FBG4: 1560 nm, having more than 90% reflectivity. The reflected light from the FBG array is led to a photodiode via a circulator. The trigger signal having the same frequency with the sweep signal is used to synchronize the A/D converter. In order to control the A/D-converter and calculate the signals from FBGs, Labview is used. As shown in Figure 19(a), when the optical source is swept, the laser output light scans each FBG. Only the light corresponding to each FBG's Bragg wavelength is reflected and converted to an electrical signal by the photodiode as a sensor signal as shown in Figure 19(b). In this system, we can attribute each pulse in the temporal waveform to the corresponding FBG, and calculate the relative wavelength using the reference FBG. When the reference FBG is set to be FBG3 as shown in Figure 19, the relative wavelength $\Delta\lambda = |\lambda 2 - \lambda 3|$ is estimated from $\Delta t = |t2 - t3|$ by

$$\Delta\lambda = \Delta t \cdot S_s \cdot \Delta\lambda_{tr}, \tag{13}$$

where $\Delta\lambda$ is the relative wavelength from the reference FBG, Δt is the relative time from the reference FBG, S_s is the sweep rate (Hz) of the swept source, and $\Delta\lambda_{tr}$ is the sweep range (nm) of the swept laser. Note that the $\Delta t(\Delta\lambda)$ changes in proportion to the strain added in FBG. In our experiment, in order to avoid errors due to the peak fluctuations in the temporal waveform, the waveform is filtered and differentiated. We track the minimal points in the differentiated waveform to calculate the relative wavelength.

Figure 20(a) shows the temporal waveform of the reflected light from the FBG array. Figure 20(b) is the sensor signal after filtering at 500 kHz and differentiation when the tunable laser source is swept with 40 kHz negative ramp waveform as shown in Figure 20(a). We chose to use only the downscan for interrogation of the FBG array, because the linearity of downscan is better than the upscan, as discussed in Section 3. Measurements at the scan rate of 40 kHz are successfully achieved. Measured relative wavelengths from the reference FBG3 when no strain is applied to FBGs are summarized in Table 1. These results are obtained from

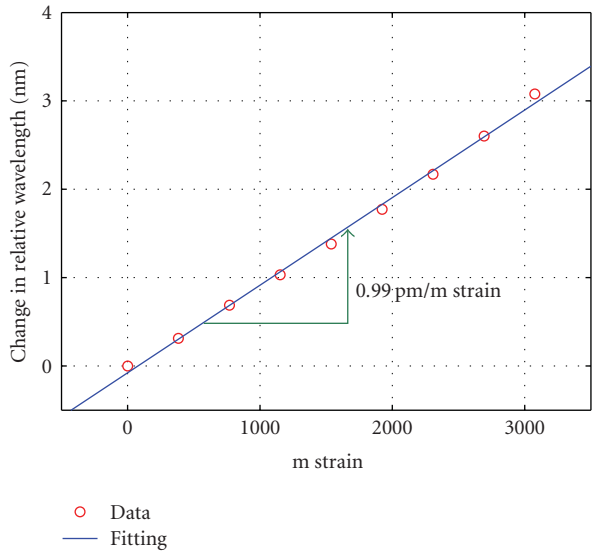

Figure 21: Wavelength shift of FBG2 against applied strain.

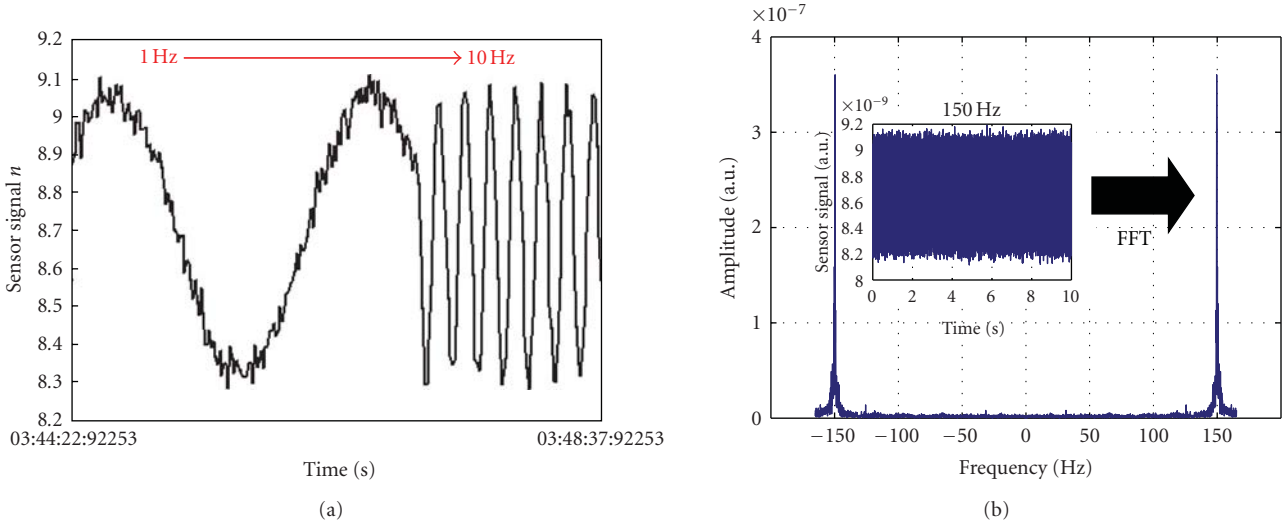

Figure 22: Vibration sensing results: (a) abrupt change from 1 to 10 Hz (b) 150 Hz waveform and its FFT data.

the data obtained for 5 seconds. Each average of relative wavelength from the reference FBG are almost equal to the Bragg wavelength of the FBGs used, and each standard deviation is also very small.

Figure 21 shows the change of relative wavelength when the strain is added to the FBG2 manually, in which the FBG is stretched by a steel slide manual stage. It is observed that the relative wavelength changes linearly as the strain is added. This result indicates that this sensor system works as expected. The slope of the linear-fitting is 0.99 nm/ (m strain).

Figure 22 shows the results of the dynamic sensing when periodical strain is added to the FBG2. The dynamic strain is applied by a PZT stage driven by a sinusoidal waveform from a RF function generator. When the frequency of the strain changes from 1 to 10 Hz, it is confirmed that this sensor can capture the change of the frequency as shown in Figure 22(a). Figure 22(b) indicates that the dynamic strain can be measured correctly when the strain is added with a 150 Hz sinusoidal vibration. The FFT spectrum is calculated by MATLAB software. The resolution of this sensor is currently limited by the instantaneous linewidth of the swept laser since it is larger than the bandwidth of the FBGs, which will be able to be improved in the future. The results show that this system is capable to work accurately and measure transient distortion at a high measurement rate.

7. Conclusion

We reviewed our researches on the wide and fast wavelength-swept fiber lasers. We presented our proposed novel and different type of wide and fast wavelength-tunable fiber

Table 1: Averages and standard deviations of the measured relative wavelengths when no strain is applied to FBGs.

Sensor results\FBG no.	1(m)	2(m)	3(m)	4(m)
Average	23.91n	9.20n	0	9.40n
Standard Deviation	35.37p	28.10p		28.93p

laser. It uses the same gain medium with the conventional swept fiber lasers, but does not use any tunable filters. The tuning mechanism of our swept laser is dispersion tuning technique, which simply modulates the loss/gain in the dispersive laser cavity. By using wideband SOAs, the sweep range could be as wide as ~180 nm. Since the cavity contains no mechanical components, such as tunable filters, we could achieve the very high sweep rate, as high as ~200 kHz. We have realized the swept lasers at three wavelength bands, 1550 nm, 1300 nm and 800 nm, using SOAs along with EDFAs, and in two laser configurations, ring and linear ones. We also succeeded in applying the swept laser for dynamic FBG sensors.

For the further improvement of the scan speed of our laser, the cavity length has to be shorter, and the modulation frequency has to be higher. Our current choice of the dispersion element is the DCF, which satisfies both large dispersion, wide bandwidth, and low loss. Still we need higher dispersion with shorter length. Possible choices might be chirped FBG having very wide band, or photonic crystal fiber designed to have very high dispersion. Short cavity length is also desirable for enhancing the stability of the laser. As for the modulation frequency, currently it is limited by the RF modulation characteristics of the SOA module, as discussed in Section 5, so we expect that SOA modules designed for direct modulation are commercially available. For the further improvement of the sweep range of our laser, wideband SOA is necessary.

The sweep range is determined by two factors, the gain bandwidth and lasing at the adjacent harmonic mode, as discussed in Section 2. The latter factor can be avoided by the proper laser design, so the former factor is the main limiting factor. In the very wide swept laser, another problem will arise that the higher-order dispersion cannot be neglected, and as a result, the change of the lasing wavelength (or frequency) is not in linearly proportional to the change of the wavelength, whose indication has already been observed in Figure 5(b).

The instantaneous linewidth of the swept laser is currently around 1nm, much wider than the value calculated from (12) (~0.1 nm). Thus, as discussed in Section 2, it should be improved by enhancing the modulation frequency. Actually, we have achieved the instantaneous linewidth around 0.2 nm with the modulation frequency of 1 GHz in the first experiment [8].

We succeeded in applying the swept laser for dynamic FBG sensors. Our system is much better in terms of scan speed and sweep range than the existing FBG sensor systems, but its resolution is not yet as good as theirs, mainly due to the large instantaneous linewidth of the swept laser, which has to be improved in future.

Acknowledgment

This work was supported by Grant-in-Aid for Scientific Research (KAKENHI) B 18360163.

References

[1] A. D. Kersey, M. A. Davis, H. J. Patrick, et al., "Fiber grating sensors," *Journal of Lightwave Technology*, vol. 15, no. 8, pp. 1442–1462, 1997.

[2] D. C. Adler, Y. Chen, R. Huber, J. Schmitt, J. Connolly, and J. G. Fujimoto, "Three-dimensional endomicroscopy using optical coherence tomography," *Nature Photonics*, vol. 1, no. 12, pp. 709–716, 2007.

[3] M.-C. Amann and J. Buus, *Tunable Laser Diodes*, Artech House, Norwood, Mass, USA, 1998.

[4] S. Yamashita and M. Nishihara, "Widely tunable erbium-doped fiber ring laser covering both C-band and L-band," *IEEE Journal on Selected Topics in Quantum Electronics*, vol. 7, no. 1, pp. 41–43, 2001.

[5] R. Huber, M. Wojtkowski, K. Taira, J. G. Fujimoto, and K. Hsu, "Amplified, frequency swept lasers for frequency domain reflectometry and OCT imaging: design and scaling principles," *Optics Express*, vol. 13, no. 9, pp. 3513–3528, 2005.

[6] S. H. Yun, C. Boudoux, G. J. Tearney, and B. E. Bouma, "High-speed wavelength-swept semiconductor laser with a polygon-scanner-based wavelength filter," *Optics Letters*, vol. 28, no. 20, pp. 1981–1983, 2003.

[7] R. Huber, M. Wojtkowski, and J. G. Fujimoto, "Fourier Domain Mode Locking (FDML): a new laser operating regime and applications for optical coherence tomography," *Optics Express*, vol. 14, no. 8, pp. 3225–3237, 2006.

[8] S. Yamashita and M. Asano, "Wide and fast wavelength-tunable mode-locked fiber laser based on dispersion tuning," *Optics Express*, vol. 14, no. 20, pp. 9299–9306, 2006.

[9] G. P. Agrawal, *Applications of Nonlinear Fiber Optics*, Academic Press, San Diego, Calif, USA, 2001.

[10] S. Li and K. T. Chan, "Electrical wavelength tunable and multiwavelength actively mode-locked fiber ring laser," *Applied Physics Letters*, vol. 72, no. 16, pp. 1954–1956, 1998.

[11] K. Tamura and M. Nakazawa, "Dispersion-tuned harmonically mode-locked fiber ring laser for self-synchronization to an external clock," *Optics Letters*, vol. 21, no. 24, pp. 1984–1986, 1996.

[12] S. H. Yun, C. Boudoux, M. C. Pierce, J. F. de Boer, G. J. Tearney, and B. E. Bouma, "Extended-cavity semiconductor wavelength-swept laser for biomedical imaging," *IEEE Photonics Technology Letters*, vol. 16, no. 1, pp. 293–295, 2004.

[13] Y. Takushima, S. Yamashita, K. Kikuchi, and K. Hotate, "Polarization-stable and single-frequency fiber lasers," *Journal of Lightwave Technology*, vol. 16, no. 4, pp. 661–668, 1998.

Hindawi Publishing Corporation
Journal of Sensors
Volume 2009, Article ID 312053, 13 pages
doi:10.1155/2009/312053

Review Article

Plastic Optical Fibre Sensors for Structural Health Monitoring: A Review of Recent Progress

K. S. C. Kuang,[1] S. T. Quek,[1] C. G. Koh,[1] W. J. Cantwell,[2] and P. J. Scully[3]

[1] *Department of Civil Engineering, National University of Singapore, Block E1A, #07-03, 1 Engineering Drive 2, Singapore 177576*
[2] *Department of Engineering, University of Liverpool, Brownlow Hill, L69 3GH Liverpool, UK*
[3] *The Photon Science Institute, University of Manchester, Oxford Road, M13 9PL Manchester, UK*

Correspondence should be addressed to K. S. C. Kuang, cveksck@nus.edu.sg

Received 4 March 2009; Revised 24 June 2009; Accepted 30 July 2009

Recommended by Christos Riziotis

While a number of literature reviews have been published in recent times on the applications of optical fibre sensors in smart structures research, these have mainly focused on the use of conventional glass-based fibres. The availability of inexpensive, rugged, and large-core plastic-based optical fibres has resulted in growing interest amongst researchers in their use as low-cost sensors in a variety of areas including chemical sensing, biomedicine, and the measurement of a range of physical parameters. The sensing principles used in plastic optical fibres are often similar to those developed in glass-based fibres, but the advantages associated with plastic fibres render them attractive as an alternative to conventional glass fibres, and their ability to detect and measure physical parameters such as strain, stress, load, temperature, displacement, and pressure makes them suitable for structural health monitoring (SHM) applications. Increasingly their applications as sensors in the field of structural engineering are being studied and reported in literature. This article will provide a concise review of the applications of plastic optical fibre sensors for monitoring the integrity of engineering structures in the context of SHM.

1. Introduction

In recent years, structural health monitoring has attracted significant interest from academia, government agencies, and industries involved in a diverse field of disciplines including civil, marine, mechanical, military, aerospace, power generation, offshore and oil and gas. The aim of SHM is to detect damage initiation and subsequently monitor the development of this damage using structurally-integrated sensors in order to provide early warning and other useful information for successful intervention to preserve the structural integrity of the host. A number of commonly monitored parameters used for SHM applications include the detection or measurement of strain, load, displacement, impact, pH-level, moisture, crack width, vibration signatures, and presence of cracks.

Over the last two decades, optical fibre sensors have attracted substantial attention and shown to be capable of monitoring a wide range of physical measurands for SHM applications. The advantages of optical fibre sensing in engineering structures are well known and these include their insensitivity to electromagnetic radiation (especially in the vicinity of power generators in construction sites), being spark-free, intrinsically safe, non-conductive and lightweight, and also their suitability for embedding into structures. To date, a number of key optical fibre sensors have been reported and their applications for damage detection in composite structures are given in review articles elsewhere [1, 2]. Optical fibre-based sensors such as fibre Bragg gratings (FBG), intensiometric and polarimetric-type sensors and those based on interferometric principles (e.g., Fabry-Perot) have been shown to offer specific advantages in their niche area of applications.

Of the various types of optical fibre sensors, intensiometric sensors represents one of the earliest and perhaps the most direct and basic type of optical fibre sensor used for SHM purposes [1]. Here, the sensing principle is straightforward and relies on monitoring the intensity level of the optical signal as it modulates in response to the measured quantity. Although monitoring of the intensity level of optical signal

has often been cited to be a drawback as a result of possible power fluctuation in the signal level and influence of external environment unrelated to the measured parameter (e.g., micro and macro bending along the fibre length), standard referencing techniques may be used to counter this problem. With the availability of stable and inexpensive light sources and low bend-sensitivity fibres, the intensity-based approach offers excellent commercial prospect for large-scale applications from a cost-effectiveness point of view. In addition, the intensity-based technique is also suitable for frequency analysis in vibration measurements since precise and absolute measurement of the structural strain or displacement values are not required—given that the sensor has sufficient sensitivity to detect the oscillatory nature of the vibration signal.

Plastic optical fibres (POFs) with their large core sizes (diameters ranging typically from 0.25 mm to 1 mm are readily available) and high numerical apertures (0.47) lend themselves well to be used as intensity-based optical fibres sensors. Indeed, many of the POF sensors developed and demonstrated for a variety of SHM applications in recent times are based on intensity modulation using these multi-mode fibres [3–16]. The core of the fibre could be made from polymethymethacrylate (PMMA), polycarbonate (PC), polystyrene (PS) and more recently cyclic transparent optical polymer (CYTOP), which offers the lowest attenuation of 50 dB/km at 650 nm compared to 160 dB/km for PMMA-based POF. The cladding layer of the fibre is generally made of fluorinated polymers. At present, most POF sensors are step-index PMMA-based due to their wider availability and lower cost. Other variants of POFs including multicore fibres, double-step-index fibres, multi-step-index fibres and graded-index fibres have also been introduced to improve the bandwidth and to lower the bending sensitivities (by means of multiple smaller cores and optimising on the refractive index profile). Single-mode POFs are presently obtainable commercially (e.g., Paradigm Optics Inc.) although their availability is still limited worldwide. Bragg gratings, which are commonly applied to single-mode silica fibres using ultra violet laser light to create the interference pattern to induce periodic changes in refractive index of the core, have also been demonstrated on doped plastic optical fibres and undoped bulk PMMA in recent years [17–19]. More recently, micro-structured POF have been introduced and these have received significant attention as a promising class of fibre for new sensor applications [20, 21], achieving unique optical properties via a pattern of holes down the full length of the fibre. Optical properties include enabling single-mode fibre to be made from a single matrix material with characteristics controlled by photonic bandgap effects. Unlike single mode POF, single-mode microstructured POF has a visible loss of around 1 dB/m and are single moded for wide (theoretically endless) range of wavelengths. Bragg gratings [22] and long period gratings [23] have been created within mPOF. Advantages include the possibility of optimising the sensitivities of the different loss features to a range of measurands by adjusting the hole geometry, and using asymmetric microstructures for directional bend sensitivity [24].

In addition to being cheaper than their glass-counterpart, plastic fibres offer better fracture resistance and flexibility compared to bare glass fibres. They also offer ease of termination, safe disposability and ease of handling. It has been reported that plastic optical fibre has an elastic limit of 10% compared to 1% in silica and can withstand strains more than 30% without breakage [25]—this could be a significant benefit for structural health monitoring applications involving large strains greater than that measurable by glass-based fibre sensors. For monitoring internal parameters of a structure, for example, when it becomes desirable to embed sensors within concrete structures, POF sensors offer a possible solution since the extremely alkaline (pH 12) environment of the concrete mixture is known to be corrosive to standard glass fibres [26]. Also, the presence of moisture can weaken the glass core and accelerates crack growth in the fibre. For glass-based sensor, although a polymer coating may be applied in order to protect the glass fibre from the corrosive environment, this will incur additional cost. Finally, glass-based optical fibre sensors are fragile and in general not amenable to rough handling and are highly susceptible to fracture in harsh engineering environment. In view of the advantages associated with plastic optical fibres, intensive research is underway to assess their potential for smart structure and structural health monitoring applications.

2. Recent Development in POF Sensors for SHM

2.1. Intensity-Based POF Sensors for SHM. The ease of monitoring the light intensity level in these large core fibres (typically 1 mm step-index multi-mode type) naturally leads to their development as intensity-based sensors. The availability of in-expensive solid-state light emitters and detectors allows the POF sensors to be conveniently integrated to external set-ups such as control and data acquisition systems. Indeed, the simplicity in design associated with intensiometric measurements has resulted in the various applications of POF sensors not only for SHM but for a variety of other sensing applications [27–29]. POF sensors were demonstrated to have the capability to measure parameters such as strain, curvature, bending displacement as well as for detecting cracks within the structure subjected to either quasistatic or dynamic loading [3–16].

In general two classes of intensity-based sensing have been reported and they are grouped based on whether the optical fibre is an intrinsic or extrinsic sensor. In an intrinsic sensor, modulation of the optical signal is a direct result of the physical change in the optical fibre in response to some measurands (e.g., signal change due to the micro- or macro-bending of the fibre). On the other hand, in an extrinsic optical fibre, the signal modulation takes place outside the optical fibre (e.g., signal change due to the changing gap distance between two cleaved fibre surfaces).

Kuang et al. [3] investigated the use of a low-cost, intensity-based intrinsic POF sensor for monitoring the mechanical response of a number of plastic specimens. In their study, the plastic fibre used (ESKA CK40) was

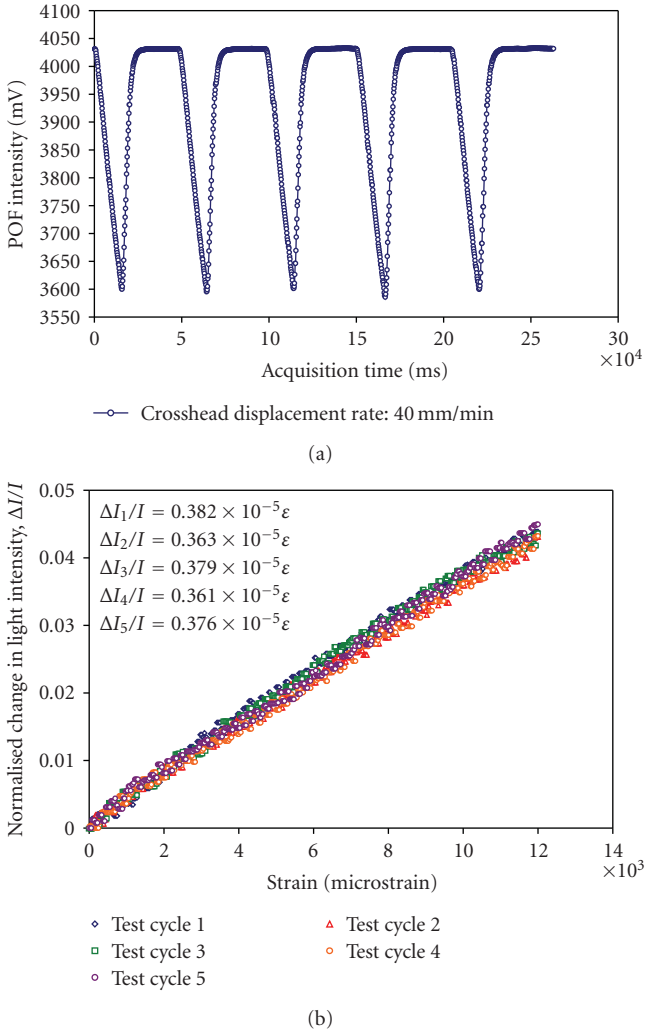

Figure 1: (a) Plot of the POF sensor response under cyclic flexural loading highlighting the stability and responsiveness of the sensor (after [3]). (b) Plot showing the POF sensor signal during a series of tensile tests (after [3]).

a 1 mm diameter multimode step-index type supplied by Mitsubishi Rayon Co. Ltd. By removing a segment of the POF's core and cladding layer over a pre-determined length, the aim was to promote light loss in this region due to reduction in the number of modes undergoing total internal reflection when the fibre was bent. The sensitised region (ranging from 70 mm for smaller specimens to 300 mm for larger ones) was noted to possess directional sensitivity and hence important to ensure the relative planar orientation of the segment of the POF sensor and the direction of loading. The study demonstrated that the POF sensor used exhibited high responsiveness to bending (strain-normalised optical loss coefficient of approximately $1.8 \times 10^{-5}/\mu\varepsilon$) and could be configured to render it sensitive to in-plane axial loads by simply curving the sensing region of the POF in the appropriate orientation with respect to the direction in which the strain is to be measured. Figure 1(a) shows the signal of POF sensor under a cyclical flexural load

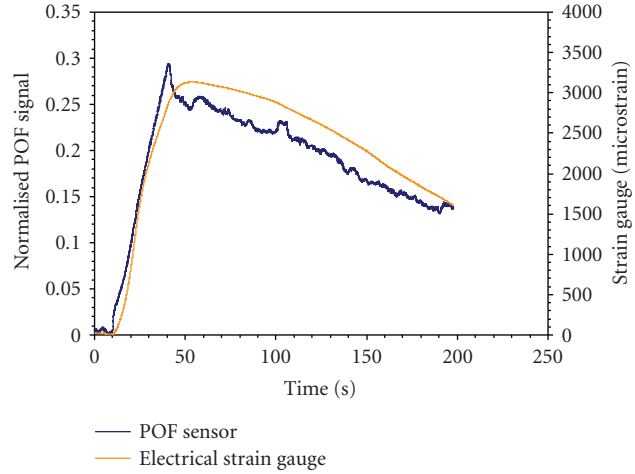

Figure 2: Plot showing the response of the POF sensor following activation of the Ni-Ti sheet (after [34]).

while Figure 1(b) illustrates the repeatability of the sensor configured for tensile strain measurement. Although the tests stopped at bending and tension strains of 0.7% and 1.2% respectively, the ability of the POF to measure higher strain values was expected to be achievable. Strain values up to 15.8% have been reported in a single-mode POF by Kiesel et al. [30, 31] while other studies using standard POF have measured strains up to 45%, although it was noted that depending on strain rate and temperature, the fibre could endure more than 80% strain [32, 33].

The potential use of POF for SHM purposes was also investigated for the dynamic monitoring ability in fibre composites [9, 10]. The upper limit of the frequency tested was 30 Hz (limited by the motor used). Here a POF sensor, identical in terms of theoretical background and operating principle to Kuang et al. [3], was attached to a cantilever-type composite beam to monitor the free vibration of undamaged and damaged specimens following low-velocity impacts. The sensitised POF sensors used was sufficiently sensitive to monitor the change in the damping ratio to characterize the reduction in postimpact flexural modulus and residual strengths of a composite beam with increasing level of impact damage. In the experiment, the POF sensor was able to detect a change in the damping ratio as small as 2.5%. In a later study [34], the POF sensor was applied to a nickel-titanium fibre metal laminate to monitor the morphing response of the hybrid laminate and the POF signal was found to agree well with collocated electrical strain gauges. Following activation of the smart fibre metal laminate (FML) by air through a heat gun, the shape memory alloy (SMA) layers deformed according to the shape it was trained (i.e., curved) and the POF sensor was found to faithfully monitor the flexural response of the smart composite. Figure 2 shows the response of the POF compared to the strain gauge reading.

Further work on the use of an extrinsic POF sensor to monitor the deflection of a smart composite was done by Kuang et al. [35]. The operating principle was straightforward—the sensor relied on the monitoring of the

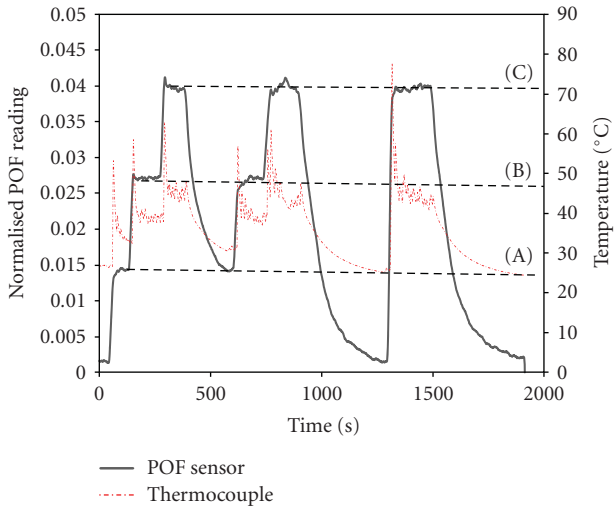

Figure 3: Plot showing the response of the POF sensor highlighting the successful use of the POF data in the control loop to achieve the amount of deflection desired (after [35]).

optical power transmitted through an air-gap between two cleaved optical fibre surfaces. The two fibres were aligned within a housing in which the fibres could slide smoothly. The gap between the cleaved surfaces changes in proportion to the applied strain resulting in the increase or decrease of the transmitted power. A standard red LED (650 nm) and photodiode were used to illuminate and monitor the optical power during the test. Here, thin-film heating technology was introduced to assess their potential for their integration into the smart FML for SMA activation. To provide the sensor feedback signal, the POF sensor was attached to the smart composite allowing the deflection or morphing response of the specimen to be accurately controlled. The POF sensor used here was modified based on a design described in an earlier work [15]. The desired amount of deflection of the beam was pre-set using a controller and the POF sensor reading was used as a feedback signal to achieve the desired deflection. The deflection of the beam specimen was monitored continuously via a data acquisition set-up which logged the POF sensor output simultaneously. Figure 3 shows the data of the POF sensor readings at three different FML beam deflections (A) to (C). The result shows that the FML beam could be controlled accurately to within 3% of the desired deflection using the POF feedback data with very little overshoot.

Another variation of the intensity-based POF sensor for monitoring structural displacement was proposed by Babchenko et al. [4] based on the bending of a multi-looped POF that has sensitised multistructural imperfections on the outer side of its core. The structural imperfections were created on the outer side of the fibre's core by abrading the fibre surface. The imperfections were created in the form of small scratches perpendicular to the curve plane similar in concept to earlier studies [3, 7, 10]. The increased loss of light at the sensitised region due microbending was then related to the amount of displacement. The study used a simple mechanical set-up where the fibre sensor was located between a top and bottom plate connected to a micrometer allowing the amount of bending of the fibre to be controlled. The authors argued that by adding more loops to the fibres and additional imperfections on the apex of the curve section of the POF, an inexpensive POF sensor could be created to monitor a variety of physical measurands, including strain, stress, vibration and pressure although the authors have not conducted any specific studies to show the actual performance of the proposed sensor to monitor the various loading conditions listed.

POF sensors have been applied to concrete structures in the field of civil engineering in view of their ruggedness and ease of handling compared to glass-based fibre sensors. Kuang et al. [11], conducted a series of flexural tests on scaled-specimens where POF sensors were attached to the bottom surface of the beam and showed that the sensors used were of sufficient sensitivity to detect the presence of hair-line cracks as illustrated in Figure 4. A crack width of approximately 0.04 mm was successfully detected using the POF sensor. In order to improve the sensitivity of the POF to beam deflection and crack initiation, a segment of the POF cross sectional profile was removed over a predetermined length (7 cm for a series of scale-model specimens and 30 cm for full-scale specimens) by abrading the surface of the POF using a razor blade. In principle, the sensitisation process increases the loss in mode propagation when the fibre is bent. Exposing the fibre core by removing the cladding layer to create an evanescent field sensor is a well known technique commonly exploited for sensing purposes. Following tests on the scaled-specimen, the authors demonstrated the use of POF sensors to monitor the response of three-meter-long concrete beams subjected to a quasistatic lateral load in a three-point bend set-up. In their study, multimode step-index plastic optical fibres were successfully applied to detect initial cracks in the beam and subsequently to monitor post-crack vertical deflection and finally to detect failure cracks in concrete beam. Figure 5 shows the plot summarising the results of the tests carried out for crack detection in concrete specimens.

In another study related to structural health monitoring of concrete beams, a liquid-filled extrinsic POF sensor design was employed to monitor the central deflection of a concrete specimen in a three-point bend configuration [14]. Here, four extrinsic POF sensors were used—each with a different liquid opacity injected into the housing cavity shown schematically in Figure 6(a). The principle of operation is the same as that described earlier where the transmitted optical power across a gap between two cleaved POF surfaces was monitored and related to the applied load or strain. Instead of an air-gap, the addition of an opaque liquid medium in the cavity of the housing increases the strain sensitivity of the POF sensor (up to approximately 25 times) as shown in Figure 6(b). Following the initiation of crack at the bottom surface of the concrete beam, the electrical strain gauge failed instantly while the POF was able to continue monitoring the response of the beam under the transverse load highlighting the advantage of the POF sensors over electrical strain gauges in this particular

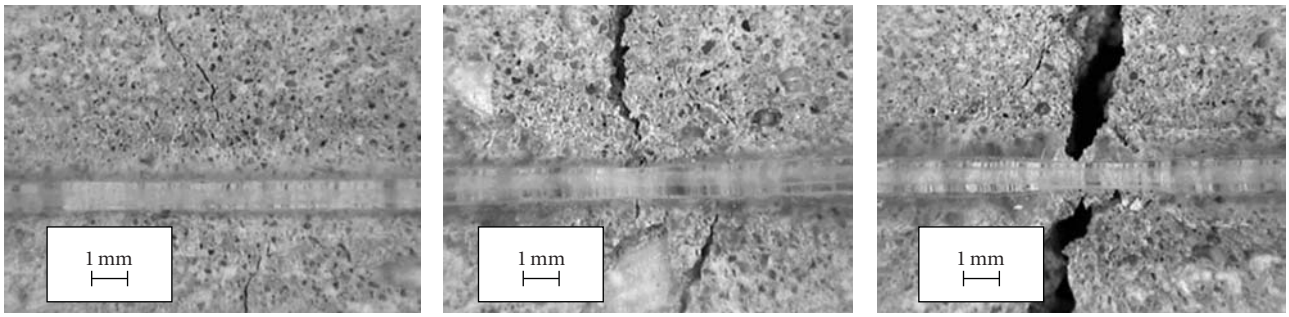

Figure 4: Photomicrographs showing the intersection of the crack in the crack specimens with the POF sensor (after [11]).

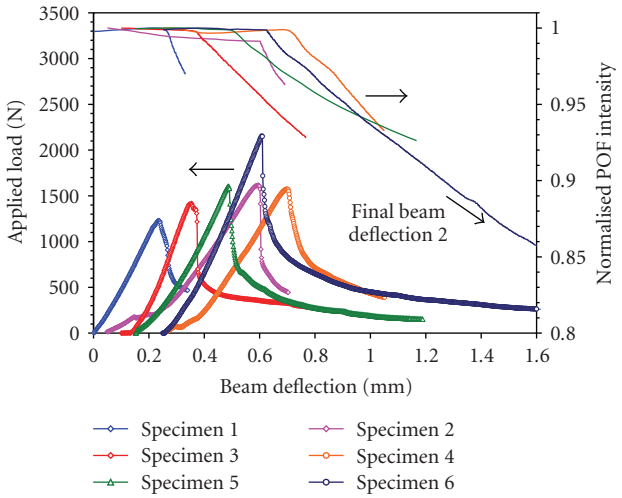

Figure 5: Summary of results for three-point bend tests on concrete specimens (beam deflections for specimens 2–6 have been offset for clarity of presentation) (after [11]).

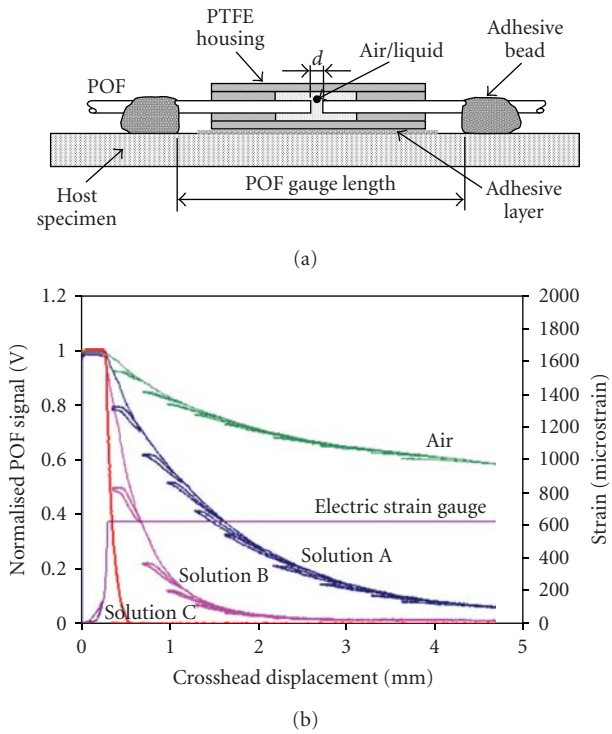

Figure 6: (a) Schematic of extrinsic POF sensor. (b) Plot showing the different POF sensor sensitivities corresponding to the different opacity of liquid used and the response of the electrical strain gauge attached to the bottom side of a concrete beam during a quasistatic cyclic test (after [14]).

application. As shown in Figures 7(a) and 7(b), the collocated electrical strain gauge was damaged at the first crack of the beam and was rendered useless limiting its usefulness for structural health monitoring purposes where surface cracks are frequently encountered. The POF sensors, however, did not appear to be significantly affected by the crack and were able to continue monitoring the loading process even after severe crack damage (crack width of approximately 2 mm and a corresponding POF strain of 4.7%) has taken place in there steel reinforced beam specimen. Since the POF sensor was attached to the beam at the two points (which define its gauge length), the propagation of crack across the sensor has insignificant detrimental effect on its measurement capability.

In view of the potential of the POF sensor for vibration detection, it has also been used in another study on system identification for SHM in a composite beam using genetic algorithm as the parametric search method. An analysis using fast-Fourier transform of the acquired POF vibration signal compared well with a collocated piezofilm sensor and the result showed that the sensor was capable of detecting the shift in the various modal frequencies associated with different system characteristics or damage level [12–14]. The highest frequency detectable in the study was in excess of 1 kHz [12] highlighting the potential of the system for vibration-based structural health monitoring.

In addition to concrete structures, POF sensors have been applied to monitor large strains (defined as greater than 10%) developed in geotextile materials. Kuang et al. [36] reported that the intensity-based sensor used in their work could be customised to monitor strains as high as 40% or more. Based on a previous design [15], the cavity of the housing for this large strain sensor has been readapted and is shown schematically in Figure 8. The basic operating principle of the POF sensor used here relies on measuring

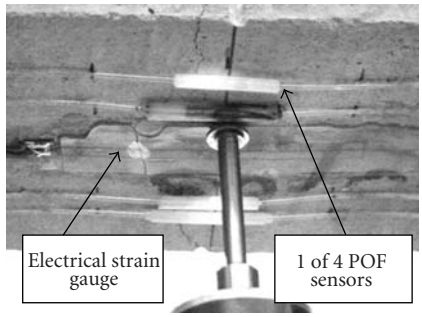

(a)

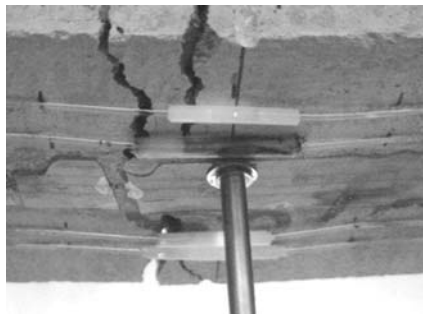

(b)

Figure 7: (a) Photograph showing the crack line across the electrical strain gauge at approximately 0.3 mm beam central deflection. (b) Photograph showing the widening of the crack after several loading cycles—the damage of the electrical strain gauge is evident while the POF sensors continued to monitor the loading process (after [14]).

the displacement of two cleaved fibre surfaces housed within the tube. Since the two ends of the POF were free to move under an applied axial load, the sensor strain measuring capability was not limited to the yield strain or elastic limit of the POF itself. The authors reported that the signal output of the sensor was directly related the separation of the two end faces and the sensor was initially calibrated with a linear variable displacement transducer before being attached to the geotextile host for strain measurement. POFs are available with protective polyethylene jackets and have a good resistance to damage under marine conditions and therefore are suitable candidates for a marine environment. Being inexpensive to produce and interrogate, it was proposed that the POF sensors were more cost-effective than other optical-based sensors such as fibre Bragg grating (FBG) sensors—for comparison, a POF sensor cost less than US$1 while an acrylate-recoated FBG sensor would cost typically US$100. More significantly, an FBG interrogator could range from US$15,000 to US$40,000 while in contrast, it is possible to fabricate an intensity-based system for under US$200 using off-the-shelf parts highlighting the economic attractiveness of the proposed system.

POF has also been embedded in composite materials to monitor damage development. Takeda et al. [5, 6] utilised small diameter multimode POFs (250 μm) for detection of matrix crack in advanced fibre composites. The POFs were

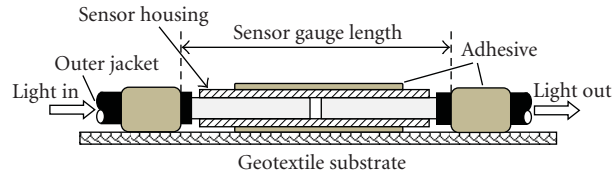

Figure 8: Schematic of POF sensor and location of adhesives (after [36]).

embedded in both unidirectional and cross-ply composite lay-up. The sensors were subjected to the same curing cycle as the composites and the authors successfully demonstrated the possibility of embedding POFs into the fibre composites. This approach relies on changes in the optical power-strain relationship to infer damage. It was reported that when the unidirectional specimen was loaded in the axial direction, the optical power decreases linearly with strain while no damage was observed. In contrast, as a result of the transverse crack in the cross-ply laminate specimen, a non-linear optical response was noted following the initiation of cracks in the specimen. Takeda et al. contended that this observation supported their predicted response and hypothesised that the non-linearity observed in the optical response was an indication of local deformation of POF resulting from the damage in the host and hence demonstrated the viability of the technique for detection of transverse damage in composite materials.

Wong et al. [28] embedded a chemically-tapered POF in a carbon fibre composite to examine the potential for strain measurement. In the study, a POF with taper length of approximately 10 mm was used. Tapering a fibre forms a more sensitive evanescent field sensor because, as the fibre diameter decreases further with strain, the evanescent field penetrates further into the cladding rendering it sensitive to the applied strain. A series of tensile tests was conducted on a composite test beam with an embedded tapered POF sensor. The POF was embedded at the mid-plane of a four-ply woven carbon-fibre epoxy prepreg (Stesapreg EP121-C15-53). The composite lay-up was inserted in a picture frame mould and was processed at 75°C under 3 bar for 8 hours to allow curing of the epoxy matrix. The test specimen was subsequently examined and the POF sensor was found to be capable of withstanding the processing conditions. The authors showed that the embedded POF was capable of monitoring up to 1.4% strain with good repeatability.

Embedding of POF sensors in composite materials requires careful selection of the type of POF material since the processing temperatures vary according to the material system of the composites used. Although certain classes of POF such as polycarbonate and CYTOP are able to sustain higher processing temperatures compared to PMMA POFs without suffering significant optical and structural degradation, the range of composites which could be embedded with POF sensors is clearly limited to the maximum operating temperatures of the chosen POF.

Based on the literature reviewed, it is reasonable to conclude that intensity-based POF sensors offer a simple,

in-expensive yet effective approach in monitoring specific aspect in structural health monitoring, in particular where high-resolution and precise measurements are not key requirements in the application. The concern over the fluctuation of optical intensity due to macrobending along the fibre or other perturbation not related to the measured quantity could be overcome with careful placement of the fibre (if possible) and referencing techniques and hence would not pose a significant barrier to its deployment. It has also been shown in the above review that, the apparent simplicity in sensor design, signal interrogation and acquisition, intensity-based monitoring approach using standard LEDs, photodetectors and low-cost data acquisition units allows users to implement a working system readily without the need for expensive equipment. The ease of handling large core intensity-based POF sensors outside the laboratory environment adds to its attractiveness for health monitoring of engineering structures. The review also provided examples of the use of intensity-based POF sensors for measurement of strain values less than a few hundred microstrains to that exceeding 40%. The sensors were also demonstrated as surface bonded or embedded in structures. These reports highlight the versatility of the intensity-based POF sensors for measurement commonly performed in engineering applications and would indeed be the preferred technique in certain cases of SHM applications following careful consideration of its limitations and benefits.

2.2. OTDR-Based POF Sensors for SHM. Distributed strain sensing using a single fibre enables monitoring over a long section of structure and is highly desirable in structural health monitoring. Optical time-domain reflectrometry (OTDR) is a well known technique in telecommunication for fault analysis and has recently been applied to multi-mode standard POF for strain sensing applications. Despite large fibre core size and hence significant modal dispersion, some success was demonstrated for SHM applications. OTDR sensing exploits the monitoring of the backscatter light in an optical fibre following the launched of a short optical pulse at one end of the fibre. The backscatter signal is recorded as a function of time and then converted to distance measurement. Perturbations, such as strain or defects along the length of the fibre will result in either a peak reflection or loss in the backscatter signal at the location of the perturbation.

Husdi et al. and Nakamura et al. [37, 38] tested two types of PMMA-based multi-mode step-index fibres Eska Premier GH-4001-P and Super Eska SK-40 for the effect of mechanical deformation and temperature on the transmission and reflection properties of these fibres. A commercial photon counting OTDR system (with a position scale resolution of 10 mm) for measuring the very weak backscattering light was used to interrogate the POF sensor. The study showed some interesting effects on the OTDR signal including the response due to (i) a flaw along a fibre (along a 300 m long fibre), (ii) a small bend (bending diameters ranging from 8 mm to 52 mm of a 300 m long fibre), (iii) transverse clamping (clamped over a 50 mm section at a distance 30 m from the input end), (iv) torsional strain (a section of 10 mm was twisted at a distance of 40 m from the input end along a 200 m long cable), (v) axial strain (over a section of 10 cm) and (vi) temperature (a 10 m section at a 300 m long cable was immersed in water of various temperatures). Based on the results, the authors suggested the possibility of discriminating the different types of external perturbation by the specific change in the shapes of the backscattered traces and further detailed investigation will be necessary to correlate the various POF responses to the applied perturbations. The authors argued that if low-cost instrumentation could be developed, the POF-OTDR system will be a competitive candidate for short range distributed SHM.

Fukumoto et al. [39] extended the work on POF-OTDR by conducting a feasibility test of the distributed strain sensor for detecting deformation in wooden structures. In their work, the authors were able to detect the direction and magnitude of deformations at four corners of a rectangular wooden frame. The "memory effect" of the POF was also studied and it was reported that when strain is applied to the POF cable, it could be memorised through the plastic deformation of the core material of the POF, and could be read out using the OTDR even after the strain was removed. The spatial resolution of their set-up was reported to be 5 m for the conventional step-index PMMA POF used (Eska Premier GH-400l-P).

The application of POF using OTDR technology has also been reported elsewhere by Krebber and workers [32, 33, 40]. In their studies, standard SI PMMA POF was integrated into geotextile materials and was shown to be capable of measuring up to 45% strain. Here, it was observed that the level of the backscattered light increases in a non-linear manner with strain up to 16% at locations where strain was applied to the POF. The results concur with that reported by Husdi et al. [37, 38]. Due to the high loss experienced in standard SI PMMA POF (150 dB/km), perfluorinated graded-index (GI) POFs (loss of 30 dB/km) were also studied for distributed strain sensing. It was observed that the length of fibre monitored extended from 100 m for standard PMMA POF to 500 m in these GI-POFs due to the lower modal dispersion in these graded-index fibres [32, 41]. For the GI-POFs studied, it was highlighted that the GI-POF tested exhibit a rather nonlinear backscatter increase up to about 3% strain, above which no further backscatter increase was observed.

In addition to strain monitoring in geotextile materials, the POF was also used for detection of crack opening in masonry structures up to 20 mm in steps of 2 mm [32]. Two displacement transducers were used as reference sensors which monitored the width of the crack opening continuously. The results showed that the OTDR backscatter signal increased in respond to widening crack width (up to 25 mm) highlighting the feasibility of using POF OTDR sensor to detect cracks in masonry ad concrete structures. The POF sensor was integrated into a geotextile and then surfaced attached to a concrete beam specimen with a small pre-crack. The backscatter signal for two textile specimens was found to increase in a reasonably linear manner (approximately

0.05 dB/mm crack width) although the authors highlighted that further tests will need to be conducted to obtain reproducibility in the results.

Although the technique above is excellent for monitoring long, large sections of structures/materials, it is primarily suited for quasistatic measurements since data acquisition and processing time of a few seconds to a few minutes are required particularly if high resolution measurement of extended POF length is important to the user. The use of OTDR technique for measurement of strain would only be meaningful if the strain levels are of the order of 1% and above and a gauge length of tens of centimetre to 1 m. This would be suitable for very large structures with large strains such as the deployment of the POF-OTDR sensor in geotextiles materials as outlined in the review above but may encounter problems if applied to structures with smaller dimension. In addition, the POF OTDR equipment may be prohibitively costly in most situations and hence limited to special niche areas in which their distributed strain monitoring capability is exploited and where their initial investment could be justified.

2.3. Interferometric-Based POF Sensors. Recent progress in the fabrication of single-mode POFs has made possible the use of these fibres for large-strain applications based on interferometric sensing techniques. Here, the principle of operation involves the monitoring of the phase-shift of the propagated light in the test fibre under an applied strain relative to an unstrained reference fibre. The phase-shift is monitored using an interferometric set-up which allows measurement for a limited range of strain values, although it was also reported that using an alternative approach to measuring the phase-shift based on the absolute position time-of-flight telemeter technique has been reported to be useful for strain measurement up to 15.8% strain in a single-mode PMMA fibre [30]. The high precision and immunity to fluctuation due to light source and bends in the fibre are advantages associated with interferometric-based techniques and since single-mode fibres are smaller in diameters compared to their multi-mode counterparts, they are less intrusive in cases where their embedment could lead to discontinuity in the geometrical build-up, for example, as embedded sensors in composite laminates. On the other hand, however, care and skill are required to successfully cleave and couple these single-mode fibres together, particularly in field environment, to ensure minimal coupling losses in addition to the inherent light loss due to the fibre material itself (typically 150 dB/m at 1500 nm).

An initial study by Silva-Lopez et al. [42] reported the sensitivity of dye doped single-mode PMMA fibres to strain and temperature using a Mach-Zehnder interferometric set-up. The study involved the loading of the fibre on a translation stage where the authors reported the phase sensitivity (1.31×10^7 rad/m) of the fibre for strain range of 0–0.04%. Kiesel et al. [30] has conducted further experiments using single-mode POF where the fibres were tested for their strain response to failure in order to determine the calibration coefficients at strain rates from 0.01/min to 3.05/min. The typical failure strains of the POF specimens used was 30%. They reported an upper limit of fringe visibility at 15.8% nominal strain in the fibres used indicating the maximum strain possible for the POF tested using the set-up in their study. The calibrated linear and nonlinear coefficients were found to be 1.37×10^7 rad/m and 3.1×10^6 rad/m, respectively.

Strain measurement based on the fibre stretching of 1 mm diameter multi-mode PMMA POF was demonstrated recently by Poisel [43]. The author monitored the phase shift of a sinusoidal signal in the fibre under various tensile loads (corresponding to increasing extension of the POF from 0 to 500 μm in steps of 50 μm). The interrogation set-up relies on detecting the difference in transit times through the polymer optical fibre (POF) using an electronic phase-shift detector. A resolution of 10 μm extension was reported to be possible under a tensile set-up. The simple system was also shown to be sensitive to bending loads and capable of measuring dynamic loading up to 5 Hz.

These studies have demonstrated the potential of interrogating a section of stretched fibre for strain monitoring. However, there is still limited work to demonstrate the higher dynamic strain measurement capability of the technique (which could be applied for SHM applications). In addition, interferometric sensing in general requires a stable platform due to their susceptibility to vibration-induced noise and hence further work will be required before this approach to POF strain sensing can be applied in real structures.

2.4. Other POF-Based Sensors for SHM Applications. Fibre Bragg grating (FBG) sensors are well known for their capability for strain measurement and the gratings are typically inscribed in silica optical fibres, the fundamentals of which are well documented elsewhere [47, 48]. Briefly, it involves monitoring the shift in the peak or resonance wavelength of either the reflected or transmitted spectrum resulting from an applied strain on the fibre. The possibility of absolute strain measurement and multiplexing capability of grating-based optical fibre sensors has received considerable attention for application in structural health monitoring. For SHM applications, FBG has featured extensively in many published articles for monitoring a variety of physical parameters [1, 2]. Monitoring of strain in this class of fibre sensors relies on detecting the shift in the central wavelength of the reflection spectrum as a response to applied strain.

The ability to induce a periodic refractive-index change in polymer-based optical fibres is a recent development and this has opened up further SHM applications using grating-based sensors since the availability of POF-based FBG sensors offers ease of handling, higher strain sensitivity (1.48 pm/$\mu\varepsilon$ compared to 1.15 pm/$\mu\varepsilon$ for silica-based FBGs at wavelength of 1523 nm) and higher strain limit (up to 3.61% strain compared to 0.5-0.6% strain for silica-based FBGs) [17–19, 45, 46]. Although more work and attention are required to further improve and understand the grating writing process in polymer fibres, their potential for SHM is evident. The possibility of using a POF-based FBG sensor for strain and temperature measurement have been reported and shown to allow strain monitoring up to seven times the measurement

limit of its silica counterpart [45, 46]. The sensor used exhibited good reproducibility and reversibility over the large strain sensing range. In their studies, the authors showed that the polymer FBG sensor was able to sustain up to 3% strain before yielding and by using a combination of polymer and silica FBG, it was possible to discriminate between the effect of temperature and strain on the sensor read-out [46]. Using a matrix inversion technique and solving for change in temperature, $\Delta T = f\{\Delta\lambda_{\text{POF-FBG}}\}$ and change in strain, $\Delta\varepsilon = f\{\Delta\lambda_{\text{Silica-FBG}}\}$ which are formulated using the strain and temperature sensitivities of the POF-FBG and the silica-FBG, respectively, the technique allows the applied strain and temperature to be determined simultaneously.

As a response to the lack of commercial availability of suitable single-mode POF, Krebber et al. [44] demonstrated the use of a tapered multimode standard POF and non-tapered GI-POF for creating grating-based sensors. The authors successfully generated the gratings in the tapered POF (from original 0.75 mm fibre to 0.2 mm) and non-tapered GI-POF specimens which showed strong reflection spectrum at specific locations along the POF using an OTDR technique and reported that it was possible to measure the integral strain along the fibre and to resolve the local strain at various locations.

Writing long period gratings (LPGs) in POFs has been reported recently [19] although there appears to be little published work in the literature on their application for strain sensing. Li et al. reported success of inducing gratings in a highly photosensitive POF core using traditional photo-etching technology together with a low-cost high pressure mercury lamp as the light source but no mechanical test was carried to assess the mechanical response of the sensor produced. The transmission spectrum of the written LPG demonstrated a loss of 3 dB at a peak wavelength of 1568 nm; despite PMMA having peak transmission in the visible spectrum, presumably to interface with optical telecommunications spectrometers and lightsources using with glass optical fibres. For Bragg gratings in the visible spectrum, the required periodicity of refractive index gratings is 183 to 216 nm; for long period gratings, the periodicity is 100 to 500 μm so it can be easily created by direct laser writing. One reason for the lack of published work is due to short supply of good quality commercially available singlemode POF with low loss and doped for photosensitivity, another is the lack of availability of single mode POF connectors since the fibre is produced in non standard diameters.

One of the most recent developments in polymer fibre research which has attracted significant attention is the microstructured POF (mPOF). This type of POF is easy to manufacture with consistent quality, but is not commercially available at present, although it may be available for research groups who are keen to find applications for their mPOFs. Interestingly LPGs have also been fabricated on mPOFs and tested for their mechanical response [49]. mPOF is ideal for FBG and LPG as it is easy to handle, since the mPOF has a large diameter and yet is endlessly singlemoded along its length with low loss compared with single mode POF. In mPOF, the microscopic air channels that run along the length of the fibre defines the light guiding mechanism in contrast to the variations in the refractive index of the fibre material in conventional POF [21]. Two of the main advantages of using LPGs in mPOFs over standard PMMA fibres include the possibility of tuning the sensitivities of the loss features corresponding to the different measurands of interest by altering the hole geometry in mPOFs [21] and the possibility of introducing directional bend sensitivity [24]. LPG has been introduced in mPOFs by mechanical imprinting using a 15 cm long template (with period of 1 mm) placed upon a heated fibre and in their study, Large et al. [25] studied the viscoelastic properties of the mPOF and reported that shift in spectral features for strains up to 8% was possible although above 2% strain a non-linear response was reported to be evident. Below 2% strain, the change in peak wavelength to strain could be computed to be approximately 1.2 pm/$\mu\varepsilon$. The study also showed a non-reversible deformation response due to strain-related creep following a 10 hour constant strain at 3% strain. In addition, the authors also reported a wavelength shift of up to 4 nm due to material relaxation at strains of 6%. In cases where intermittent straining was applied on the mPOF LPG sensor for up to 2% strain, the authors argued that the viscoelastic effects (time, strain rate, and strain magnitude) were small although time-dependent effects such as relaxation during constant strain and strain recovery could become significant. In SHM applications where these limitations are properly understood and deemed acceptable, mPOF LPG sensors may be successfully applied.

Conventionally, fibre Bragg gratings and long-period gratings sensors are interrogated using an optical spectrum analyser to detect the shift in wavelength of the reflected spectrum corresponding to the applied strain and/or temperature. However, the associated interrogation equipment is generally costly, involving the use of optical spectrum analysers and narrow band light sources such as laser diode. In an effort to circumvent the cost barrier to the wider adoption of grating-based sensors, Hwang et al. [49] recently demonstrated an interesting intensity-based set-up which utilizes two long-period fibre gratings and a core mode blocker between the two gratings. Although the fibers used were not polymer-based, this work is highlighted in view of the potential of the technique to be applied for interrogation of POF-based grating sensors. In principle, the core mode blocker acts as a band-pass filter to block the uncoupled light while the light that satisfy the phase-matching condition of the first LPG will be coupled to the cladding mode. The light in the cladding layer would then be effectively coupled back into the core by the second LPG. Strain is then applied on one of the LPGs. The relative change in the resonance wavelengths (change in the degree of spectrum overlap) due to the strain applied on one of the LPGs will result in either increase or decrease in the transmitted optical power. The power is monitored and then calibrated against the applied strain. In their work, the authors were able to show that the intensity transmitted through the fibre increases linearly with strain although the strain sensitivity (1.0×10^{-4} dB/$\mu\varepsilon$) was noted to be three time less than conventional single long-period grating fibre sensor [50]. The authors also noted small fluctuation in the transmitted

Table 1: Sensor performance and other comparison criteria.

POF sensing technology	Type of POF used	Sensor type	Strain resolution	Dynamic range	Relative sensor cost	Relative equipment cost	Key features & remarks
Intensiometric							
[3, 4, 7, 9–11, 14, 28, 34]	SI MMF	Intrinsic	~50 $\mu\varepsilon$	~1.2%	Very low (<US$1/m)	Very low (<US$200)	Simple design; high cost-effectiveness; demonstrated for flexural and axial loading, crack detection in concrete; monitoring low-velocity impact in advanced composites; POF embedded in fibre composites for axial strain measurement; capable of monitoring quasistatic and dynamic loading (~30 Hz or higher).
[12–15, 35, 36]	SI MMF	Extrinsic	~5 $\mu\varepsilon$ (liquid-filled type); ~100 $\mu\varepsilon$ (air-filled type)	~0.12%; ~40% or more	Very low (<US$1/m)	Very low (<US$200)	Simple design; high cost-effectiveness; though strain limit demonstrated up to 40%, higher strains possible; demonstrated for crack detection, monitoring crack-width opening, impact damage, geotextile strain, capable of monitoring quasistatic and dynamic loading (~1 kHz or higher).
OTDR-based							
[37–39]	SI MMF	Intrinsic	~0.5%; Spatial resolution: ~2 m for 50 m POF to 5 m for 100 m POF	~50%–100%	Very low (<US$1/m)	Very high (>US$50,000)	Distributed measurement; High strain measurement, however, POF axial strain *elastic* limit ~5%; general ability to discriminate loading types based on backscatter shape trace; quasistatic measurement only. Demonstrated to be capable of supporting 100% strain applied at 5 locations along a 100 m POF.
[32, 33, 40, 41, 44]	SI & GI MMF	Intrinsic	~0.1% (SI POF); ~2% (GI POF); Spatial resolution: ~0.1–1 m for 100 m (GI POF)	~40%	Very low (<US$1/m)	Very high (>US$50,000)	Distributed measurement of 100 m (SI POF) and 500 m (GI POF); high strain measurement; demonstrated for monitoring geotextile strain, geotextile-retrofitted masonry structures; generally only quasistatic measurement only or very low frequency oscillation (~0.25 Hz) if high-speed OTDR unit used.

Table 1: Continued.

POF sensing technology	Type of POF used	Sensor type	Strain resolution	Dynamic range	Relative sensor cost	Relative equipment cost	Key features & remarks
Interferometric							
[30, 31]	SM POF	Intrinsic	0.05 $\mu\varepsilon$ (for gauge length of 0.1 m)	15.8%	High (~USD$50/m)	High (~USD$6000–USD$7000)	Large strain measuring capability; High measurement precision; less intrusive due to smaller fibre diameter; Difficulty in cleaving and coupling the single mode fibres in the field; strain rate of ~3% strain/min possible.
[43]	SI MMF	Intrinsic	10 $\mu\varepsilon$	500 $\mu\varepsilon$	Very low (<US$1/m)	Low (<US$1000)	Simple concept; demonstrated dynamic monitoring on a rotor blade up to 5 Hz.
Grating-based							
[17, 45, 46]	PMMA; SM POF	Intrinsic	<1 $\mu\varepsilon$	3.6%	Currently not commercially available. Estimated cost: High (~>US$100)	High to very high ~US$10,000–US$30,000 for OSA-based interrogators and broadband light source	Bragg gratings inscribed on in-house made dye-doped PMMA perform with UV-beam; strain measurement conducted by means of simple tension of POF. Scheme proposed allow temperature and strain to be measured simultaneously; depending on interrogator used, the sensor could monitor quasistatic and dynamic loading conditions.
[20–25]	mPOF	Intrinsic	~1 $\mu\varepsilon$	8%	Currently not commercially available. Estimated cost: High >US$100	High to very high ~US$10,000–US$30,000 for OSA-based interrogators and broadband light source	Long period grating mechanically imprinted onto microstructured POF; linear response limited to 2% strain; creeping observed beyond 3%; viscoelastic effects noted above 2% but minimal below 2%; significant material relaxation under constant strain.
[44]	SI MMF; GI MMG;	Intrinsic	Not reported	Not reported	Currently not commercially available.	High to very high ~US$10,000–US$50,000 for spectrometer, OTDR and broadband light source	Grating photo-induced onto tapered 0.2 mm SI-MMF and non-tapered GI POF with UV beam; OTDR used as signal interrogator instead of conventional OSA.
	mPOF	Intrinsic	Not reported estimated: ~0.02%	~1% for initial test	Estimated cost: High >US$100		Long period grating on mPOF integrated to geotextile; length of sensor extended using silica fibres.

power resulting from the unstable LED source though it was unclear whether the observed fluctuation affected the accuracy of the measurements significantly. Despite the lower sensitivity of the system (thought to be due to the broader bandwidth of the LPG relative to a laser diode), small fluctuation in transmitted power, the authors argued that the cost-effectiveness of the proposed sensor system would see its application for interrogation of grating-based sensors. With the possibility of introducing gratings in POFs as outlined by the reports above, it would be interesting to see further developments and field applications in intensity-based POF grating sensors for SHM applications using the technique proposed.

3. Summary and Conclusions

An overview of a selection of articles on the recent progress of the applications of plastic-based optical fibre sensors has been given. A tabulated summary highlighting the major works and a brief comparison of the types of sensors reviewed is shown in Table 1. The overview began with a brief introduction of the technology and sensing techniques used in POF sensors highlighting the various strengths and limitations associated with the different sensing schemes adopted. In view of the ease of handling, low cost and large strain capability of POF, significant interest in their use for structural health monitoring, specifically for measurement of strain, curvature, load, displacement, vibration and crack detection have been demonstrated by various workers. A number of different approaches in sensing interrogation such as intensity-based, interferometric-based, time-of-flight (OTDR-based) and gratings (wavelength-based) have been shown to be feasible for monitoring engineering materials such as concrete, masonry, fibre composites, geotextiles, metals, wood and plastics. There remains much work to be done to fully characterize the POF response to the various physical measurands encountered in SHM applications particularly with the recent development of new POF materials, types and interrogation techniques.

Acknowledgments

Funding by A*STAR-MPA through the National University of Singapore CORE centre under joint Grants no. R-264-000-226-490 and no. R-264-000-226-305 is acknowledged.

References

[1] K. S. C. Kuang and W. J. Cantwell, "The use of conventional optical fibres and fibre Bragg gratings for damage detection in advanced composite structures—a review," *Applied Mechanics Reviews*, vol. 56, pp. 493–513, 2003.

[2] G. Zhou and L. M. Sim, "Damage detection and assessment in fibre-reinforced composite structures with embedded fibre optic sensors-review," *Smart Materials and Structures*, vol. 11, no. 6, pp. 925–939, 2002.

[3] K. S. C. Kuang, W. J. Cantwell, and P. J. Scully, "An evaluation of a novel plastic optical fibre sensor for axial strain and bend measurements," *Measurement Science and Technology*, vol. 13, no. 10, pp. 1523–1534, 2002.

[4] A. Babchenko, Z. Weinberger, N. Itzkovich, and J. Maryles, "Plastic optical fibre with structural imperfections as a displacement sensor," *Measurement Science and Technology*, vol. 17, no. 5, pp. 1157–1161, 2006.

[5] N. Takeda, T. Kosaka, and T. Ichiyama, "Detection of transverse cracks by embedded plastic optical fiber in FRP laminates," in *Smart Structures and Materials 1999: Sensory Phenomena and Measurement*, vol. 3670 of *Proceedings of SPIE*, pp. 248–255, 1999.

[6] N. Takeda, "Characterization of microscopic damage in composite laminates and real-time monitoring by embedded optical fiber sensors," *International Journal of Fatigue*, vol. 24, no. 2–4, pp. 281–289, 2002.

[7] A. Djordjevich, "Curvature gauge as torsional and axial load sensor," *Sensors and Actuators A*, vol. 64, no. 3, pp. 219–224, 1998.

[8] G. Perrone, D. Perla, R. Gaudino, and S. Abrate, "Development of low cost intensity modulated POF based sensors and application to the monitoring of civil structures," in *Proceedings of the 13th Plastic Optical Fibre Conference*, pp. 444–449, 2004.

[9] K. S. C. Kuang and W. J. Cantwell, "The use of plastic optical fibres and shape memory alloys for damage assessment and damping control in composite materials," *Measurement Science and Technology*, vol. 14, no. 8, pp. 1305–1313, 2003.

[10] K. S. C. Kuang and W. J. Cantwell, "The use of plastic optical fibre sensors for monitoring the dynamic response of fibre composite beams," *Measurement Science and Technology*, vol. 14, no. 6, pp. 736–745, 2003.

[11] K. S. C. Kuang, Akmaluddin, W. J. Cantwell, and C. Thomas, "Crack detection and vertical deflection monitoring in concrete beams using plastic optical fibre sensors," *Measurement Science and Technology*, vol. 14, no. 2, pp. 205–216, 2003.

[12] K. S. C. Kuang, M. Maalej, and S. T. Quek, "An application of a plastic optical fiber sensor and genetic algorithm for structural health monitoring," *Journal of Intelligent Material Systems and Structures*, vol. 17, no. 5, pp. 361–379, 2006.

[13] K. S. C. Kuang, S. T. Quek, and M. Maalej, "Detection of impact induce damage in composite beams using plastic optical fibre sensors," in *Proceedings of the 17th KKCNN Symposium on Civil Engineering*, pp. 103–110, 2004.

[14] K. S. C. Kuang, S. T. Quek, and M. Maalej, "Polymer-based optical fiber sensors for health monitoring of engineering structures," in *Smart Structures and Materials 2005: Sensors and Smart Structures*, vol. 5765 of *Proceedings of SPIE*, pp. 656–667, 2005.

[15] K. S. C. Kuang, S. T. Quek, and M. Maalej, "Assessment of an extrinsic polymer-based optical fibre sensor for structural health monitoring," *Measurement Science and Technology*, vol. 15, no. 10, pp. 2133–2141, 2004.

[16] K. S. C. Kuang, S. T. Quek, and W. J. Cantwell, "Use of polymer-based sensors for monitoring the static and dynamic response of a cantilever composite beam," *Journal of Materials Science*, vol. 39, no. 11, pp. 3839–3843, 2004.

[17] P. J. Scully, D. Jones, and D. A. Jaroszynski, "Femtosecond laser irradiation of polymethylmethacrylate for refractive index gratings," *Journal of Optics A*, vol. 5, no. 4, pp. S92–S96, 2003.

[18] G. D. Peng and P. L. Chu, "Polymer optical fiber sensing," in *Optical Information Processing Technology*, vol. 4929 of *Proceedings of SPIE*, pp. 303–311, 2002.

[19] Z. Li, H. Y. Tam, L. Xu, and Q. Zhang, "Fabrication of long-period gratings in poly(methyl methacrylate-co-methyl vinyl ketone-co-benzyl methacrylate)-core polymer optical fiber by use of a mercury lamp," *Optics Letters*, vol. 30, no. 10, pp. 1117–1119, 2005.

[20] M. C. J. Large, L. Poladian, G. W. Barton, and M. A. van Eijkelenborg, *Microstructured Polymer Optical Fibres*, Springer, New York, NY, USA, 2007.

[21] M. A. van Eijkelenborg, M. C. J. Large, A. Argyros, et al., "Microstructured polymer optical fiber," *Optics Express*, vol. 9, pp. 319–327, 2001.

[22] H. Dobb, D. J. Webb, K. Kalli, A. Argyros, M. C. J. Large, and M. A. van Eijkelenborg, "Continuous wave ultraviolet light-induced fibre Bragg gratings in few- and single-moded microstructured polymer optical fibres," *Optical Letters*, vol. 30, pp. 3296–3298, 2005.

[23] M. P. Hiscocks, M. A. van Eijkelenborg, A. Argyros, and M. C. J. Large, "Stable imprinting of long-period gratings in microstructured polymer optical fibre," *Optics Express*, vol. 14, no. 11, pp. 4644–4649, 2006.

[24] H. Dobb, K. Kalli, and D. J. Webb, "Measured sensitivity of arc-induced long-period grating sensors in photonic crystal fibre," *Optics Communications*, vol. 260, no. 1, pp. 184–191, 2006.

[25] M. C. J. Large, J. Moran, and L. Ye, "The role of viscoelastic properties in strain testing using microstructured polymer optical fibres (mPOF)," *Measurement Science and Technology*, vol. 20, no. 3, Article ID 034014, 6 pages, 2009.

[26] K. Murphy, S. Zhang, and V. M. Karbhari, "Effect of concrete based alkaline solutions on short term response of composites," in *Proceedings of the 44th International Society for the Advancement of Material and Process Engineering Symposium and Exhibition*, vol. 44, pp. 2222–2230, 1999.

[27] D. Kalymnios, P. J. Scully, J. Zubia, and H. Poisel, "POF sensor overview," in *Proceedings of the 13th International Plastic Optical Fibres Conference*, pp. 237–244, 2004.

[28] Y. M. Wong, P. J. Scully, R. J. Bartlett, K. S. C. Kuang, and W. J. Cantwell, "Plastic optical fibre sensors for environmental monitoring: biofouling and strain applications," *Strain*, vol. 39, no. 3, pp. 115–119, 2003.

[29] R. J. Bartlett, R. Philip-Chandy, P. Eldridge, D. F. Merchant, R. Morgan, and P. J. Scully, "Plastic optical fiber sensors and devices," *Transactions of the Institute of Measurement and Control*, vol. 22, pp. 431–457, 2000.

[30] S. Kiesel, K. Peters, T. Hassan, and M. Kowalsky, "Calibration of a single-mode polymer optical fiber large-strain sensor," *Measurement Science and Technology*, vol. 20, no. 3, Article ID 034016, 7 pages, 2009.

[31] S. Kiesel, K. Peters, T. Hassan, and M. Kowalsky, "Behaviour of intrinsic polymer optical fibre sensor for large-strain applications," *Measurement Science and Technology*, vol. 18, no. 10, pp. 3144–3154, 2007.

[32] S. Liehr, P. Lenke, K. Krebber, et al., "Distributed strain measurement with polymer optical fibers integrated into multifunctional geotextiles," in *Optical Sensors 2008*, vol. 7003 of *Proceedings of SPIE*, April 2008, article no. 700302.

[33] P. Lenke, S. Liehr, K. Krebber, F. Weigand, and E. Thiele, "Distributed strain measurement with polymer optical fiber integrated in technical textiles using the optical time domain reflectometry technique," in *Proceedings of the 16th International Conference on Plastic Optical Fibre*, pp. 21–24, 2007.

[34] P. Cortes, W. J. Cantwell, K. S. C. Kuang, and S. T. Quek, "The morphing properties of a smart fibre metal laminate," *Polymer Composites*, vol. 29, pp. 1263–1268, 2008.

[35] K. S. C. Kuang, S. T. Quek, and W. J. Cantwell, "Morphing and control of a smart fibre metal laminate utilizing plastic optical fibre sensor and Ni-Ti sheet," in *Proceedings of the 17th International Conference on Composite Materials*, 2009.

[36] K. S. C. Kuang, S. T. Quek, C. Y. Tan, and S. H. Chew, "Plastic optical fiber sensors for measurement of large strain in geotextile materials," *Advanced Materials Research*, vol. 47–50, pp. 1233–1236, 2008.

[37] I. R. Husdi, K. Nakamura, and S. Ueha, "Sensing characteristics of plastic optical fibres measured by optical time-domain reflectometry," *Measurement Science and Technology*, vol. 15, no. 8, pp. 1553–1559, 2004.

[38] K. Nakamura, I. R. Husdi, and S. Ueha, "Memory effect of POF distributed strain sensor," in *Second European Workshop on Optical Fibre Sensors*, vol. 5502 of *Proceedings of SPIE*, pp. 144–147, 2004.

[39] T. Fukumoto, K. Nakamura, and S. Ueha, "A POF-based distributed strain sensor for detecting deformation of wooden structures," in *19th International Conference on Optical Fibre Sensors*, vol. 7004 of *Proceedings of SPIE*, 2008, article no. 700469.

[40] K. Krebber, P. Lenke, S. Liehr, J. Witt, and M. Schukar, "Smart technical textiles with integrated POF sensors," in *Smart Sensor Phenomena, Technology, Networks, and Systems 2008*, vol. 6933 of *Proceedings of SPIE*, 2008, article no. 69330V.

[41] P. Lenke, S. Liehr, K. Krebber, F. Weigand, and E. Thiele, "Distributed strain measurement with polymer optical fiber integrated in technical textiles using the optical time domain reflectometry technique," in *Proceedings of the 16th International Conference on Plastic Optical Fibre*, pp. 21–24, 2007.

[42] M. Silva-Lopez, A. Fender, W. N. MacPherson, et al., "Strain and temperature sensitivity of a singlemode polymer optical fibre," *Optics Letters*, vol. 30, pp. 3129–3131, 2005.

[43] H. Poisel, "POF strain sensor using phase measurement techniques," in *Smart Sensor Phenomena, Technology, Networks, and Systems 2008*, vol. 6933 of *Proceedings of SPIE*, 2008, article no. 69330Y.

[44] K. Krebber, P. Lenke, S. Liehr, et al., "Technology and applications of smart technical textiles based on POF," in *Proceedings of the 17th International Conference on Plastic Optical Fibre*, 2008.

[45] H. Y. Liu, H. B. Liu, and G. D. Peng, "Strain sensing characterization of polymer optical fibre Bragg gratings," in *17th International Conference on Optical Fibre Sensors*, vol. 5855 of *Proceedings of SPIE*, pp. 663–666, 2005.

[46] H. B. Liu, H. Y. Liu, G. D. Peng, and P. L. Chu, "Strain and temperature sensor using a combination of polymer and silica fibre Bragg gratings," *Optics Communications*, vol. 219, no. 1–6, pp. 139–142, 2003.

[47] K. O. Hill, Y. Fuji, D. C. Johnson, and B. S. Kawasaki, "Photosensitivity in optical fiber waveguides, application to reflection filter fabrication," *Applied Physics Letters*, vol. 32, pp. 647–649, 1978.

[48] G. Meltz, G. G. Morey, and W. H. Glenn, "Formation of Bragg grating in optical fibers by a transverse holographic method," *Optics Letters*, vol. 14, pp. 823–825, 1989.

[49] D. Hwang, L. V. Nguyen, D. S. Moon, and Y. J. Chung, "Intensity-based optical fiber strain sensor," *Measurement Science and Technology*, vol. 20, Article ID 034020, 6 pages, 2009.

[50] M. de Vries, V. Bhatia, T. D'Alberto, V. Arya, and R. O. Claus, "Photoinduced grating-based optical fiber sensors for structural analysis and control," *Engineering Structures*, vol. 20, no. 3, pp. 205–210, 1998.

Hindawi Publishing Corporation
Journal of Sensors
Volume 2009, Article ID 720980, 9 pages
doi:10.1155/2009/720980

Research Article

Fabry-Pérot Fiber-Optic Sensors for Physical Parameters Measurement in Challenging Conditions

Éric Pinet

R & D Department, FISO Technologies inc., 500-195 Avenue Saint-Jean-Baptiste, QC, Canada G2E 5R9

Correspondence should be addressed to Éric Pinet, eric.pinet@fiso.com

Received 30 January 2009; Accepted 2 June 2009

Recommended by Christos Riziotis

Optical fiber sensors have unique advantages and distinctive features that make them very attractive for many applications especially those involving challenging conditions where other traditional electrical sensors usually fail. Among the commercially available optical fiber sensors, the Fabry-Pérot sensing technology is probably the most versatile and the most interesting one since a relatively low-cost universal signal conditioner could easily read compatible Fabry Pérot sensors measuring different physical parameters such as strain, temperature, pressure, displacement, or refractive index. This papers details the numerous advantages of this optical sensing technology and also summarizes the operating modes of commercially available signal conditioners and sensors.

1. Introduction

When someone hears the terms "optical fiber," usually the first association that comes to mind is often related to a fast and high-volume modern communication link that helps the expansion of the exploding information data demand created by our "image society driven", by the democratization of the Internet and other new communication technologies. Some others will also associate the optical fibers to their glowing plastic Christmas tree, illuminated by a constellation of stars created at the tip of a myriad of plastic optical fibers which are transmitting the light of a changing color lamp.

Actually very few will think that optical fibers could also be at the core of a sensor technology that already started to take place in our day-to-day life. In that case the fiber optic remains a physical link for the light that travels between the sensor and the signal conditioner, but how the information is coded and translated into useful data will depend on the used technology.

In the last few decades tremendous work has been done by academics and the industry to develop sensing technologies using light properties propagating in optical fibers [1–3] allowing measurements particularly in challenging conditions.

The candidate technologies for monitoring a physical parameter with optical fiber sensor (OFS) can be classified in four main categories relying on the position where the parameter is measured: single-point, long gage, quasi-distributed and distributed [4]. In single-point sensing, the measurement is performed at a defined point along the fiber, usually at or near its end, as the case for most Fabry-Pérot (F-P) sensors. In long gage sensor the measurement is performed along usually 10 cm to 10 m sections of optical fiber, such as for the *SOFO* system [5]. For quasi-distributed OFS, a limited number of sensing points are physically located on the same fiber, as the case for fiber Bragg grating (FBG) dominating this type of sensor. In fully distributed OFS, the optical fiber itself acts as a sensing medium, which could be used to discriminate different positions of the measured parameter along the fiber such as for Raman or Brillouin distributed sensors.

Among the various technologies now commercially available, the Fabry-Pérot white-light interferometry is probably one of the most interesting for point-sensing applications since it is a low-cost solution for multiparameters measurement. This paper describes the advantages of this type of sensor and interrogation technology that is suitable for physical parameters measurement in challenging conditions.

2. Why Use Fabry-Pérot Fiber-Optic Sensors?

Measuring a physical parameter such as temperature, pressure, or strain could sometimes become a real challenge if the environment is not suitable for traditional sensors such as electrical sensors. For instance, in the presence of strong electromagnetic (EM) or microwave (MW) interferences, it could be a headache to shield a thermocouple for accurate and reliable temperature measurement. With an optical sensor such trouble is simply avoided since the encoded light confined in the optical fiber core is not affected by any electromagnetic interference (EMI). So any time such interferences are present in a given application, the optical sensing technology is probably the best solution to select, if not sometimes the only one. For instance, without an optical fiber sensor it would be very tricky to monitor your hot-dog heating in your microwave oven, and you will probably never know that your sausage is hot burning while your bun is still frozen—until you take a bite. If you were a food packaging engineer trying to optimize the heat transfer of a complex microwavable TV dinner or if you were a designer or a programmer of MW oven, having real time temperature data during the MW process may be much more that a simple gadget for hot-dog fans. You may thus probably appreciate using an instrumented microwave work station (MWS) equipped with OFS. As an example, Figure 1 shows temperature experimental data obtained for the heating of a 1 L water bath in a 1200 W commercial microwave oven for the calculation of its peak power according to the protocol described in international standard document [6]. The temperature was measured from 3 different FOT-L temperature sensors connected to OSR interrogator which allows to calculate MW power, even during MW heating. The peak MW power measured experimentally confirms the 1200 W value of the oven manufacturer.

Same measurement problems occur if you were a chemist trying to control critical parameters such as pressure or temperature during a microwave chemistry process, an engineer supervising radio-frequency (RF) wood drying, a physician monitoring the temperature of a critical care patient undergoing a magnetic resonance imaging (MRI) scan, or even if you were a surgeon burning selected tissues with RF instrumented minimally invasive catheters: without an optical sensor you may face big difficulties. Even in extreme environments such as those encountered into nuclear reactors where strong radiations are present, the optical sensors could provide an attractive alternative solution [7, 8].

EMI may not always be constantly present during the measurement to justify the use of OFS. If you were a civil engineer selecting a solution for monitoring a bridge, a dam, or other types of structures over several decades, would you take the risk that a lightning strike destroys or damages permanently your electrical sensors network buried into the structure, or would you use an optical technology [9–14] proven to be unaffected by such unpredictable events? Also as a critical care patient, you would probably feel more secure if you knew that your vital signs such as pressure and temperature are measured with optical sensors [4] that will not give false readings even in the presence of possible EMI generated in modern hospitals crowded by various electrical equipments.

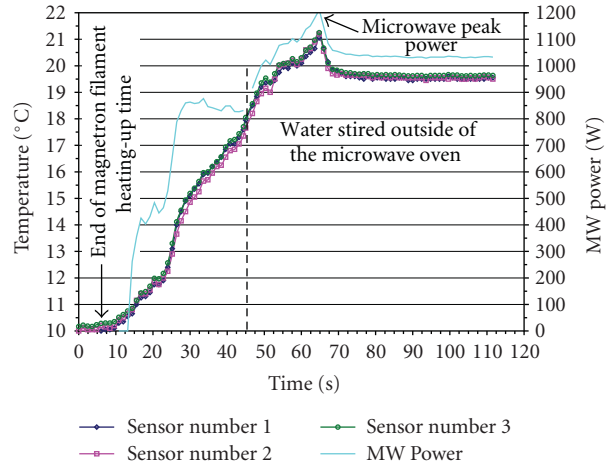

Figure 1: *In situ* measurement of 1 L water bath temperature inside a 1 200 W microwave with 3 FOT-L temperature sensors and OSR interrogator from *FISO Technologies* allows oven power calculation even during microwave heating. The microwave peak power (1200 W) is determined using the protocol described in the IEC-60705 international standard. The end of magnetron filament heating-up time is detected by the start of water bath temperature increase. After 45 seconds (vertical dashed line) when the heating program stops, the door is open and the water is stirred for better temperature uniformity. The temperature rises to a maximum that is used to define the microwave power as stated in the IEC-60705 international standard.

The insensitivity to EMI is not the only advantage of optical sensors. Inversely, since no electricity is used to interrogate the sensor only powered by light, such device is intrinsically safe and naturally totally explosion proof. This may be a great feature if you are working with inflammable gases or liquids or if you want to avoid that the sensor could be a source of electrical discharges or EM field perturbation. For instance, liquid natural gas (LNG) reservoirs are obviously excellent candidates for fiber optical strain, pressure, or temperature sensors. Many other applications could be found in the chemical processing industry or in military applications such as the one involving explosive materials or missiles control.

Another corollary of the fact that light instead of electricity carries the useful information between the sensor and the signal conditioner is the fact that very low attenuation occurs along the optical fiber. Indeed this advantage is truly unique if measurements have to be done in remote locations, as it is often the case for large civil structures such as pipe-lines [15], bridges, tunnels, or dams. Furthermore if the optical fiber has to cross zones with strong EMI, no problem will occur in the transmitted measurement, which is not the case with electrical transmission. For instance, with the Fabry-Pérot sensing interferometry developed by *FISO Technologies*, up to 5 km (expandable to 12 km with custom long-range signal conditioner) could separate measuring

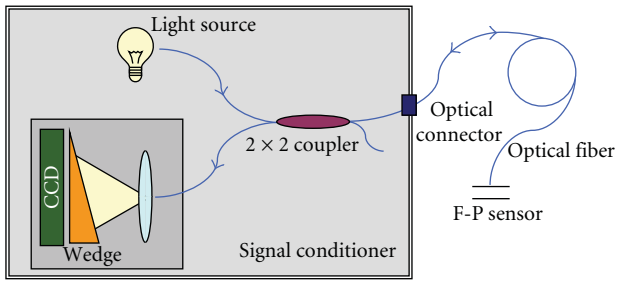

Figure 2: Schematic description of the F-P absolute measurement signal conditioner using white-light interferometry.

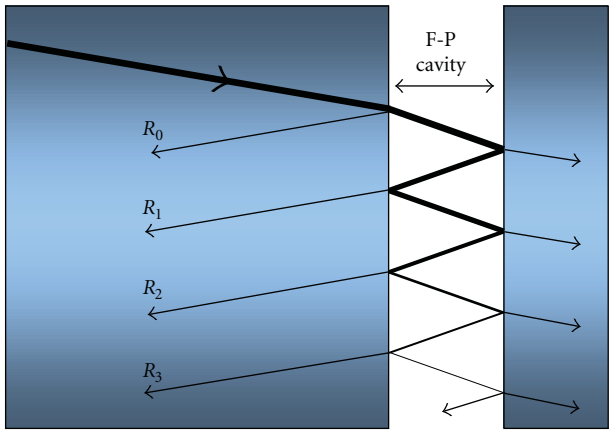

Figure 3: Schematic representation of F-P sensing interferometer showing ray traces obtained from a selected incident angle light beam propagating in the optical fiber core.

and recording locations with the same outstanding sensor sensitivity and accuracy.

Compared to copper wires, glass optical fibers are lighter, and such a property may become an interesting feature for applications where lightweight sensor solutions are a concern such as in aeronautics and more crucially in spatial applications. The fact that glass is a stable inert material that does not corrode is also an advantage for long-term applications in outdoor conditions such as typical for most of civil engineering applications.

Contrary to electrical sensors, most of the optical sensors do not have metal in their construction. In some cases, metals could be used for packaging when this does not present a problem, but an all-glass and polymer sensor has great advantages when interferences with an electromagnetic field are not desirable such as in hospitals during MRI investigations. The materials used in the sensor construction and packaging are also generally biocompatible and chemically inert, which makes optical sensors perfectly suitable for medical or harsh chemical environments applications. Besides its chemical resistance, glass is also very resistant to temperature providing an additional advantage that is very attractive to a lot of challenging applications. Actually, OFS compatible with temperature ranging from cryogenic up to about 450°C is commercially available.

Table 1: Summary of F-P OFS technology advantages.

Design	Environment	Other
Inert materials (glass...)	Cryogenic to high temperature	Biocompatibility and sterilization
Robust packaging	Chemical resistance	Symmetry axis
Light powered	EMI insensitive	Intrinsically safe
Small size	*In situ* monitoring	Light weight
Low attenuation	Remote location	*Low-cost OFS*

If temperature is combined with harsh chemical environment such as the case in oil and gas wells or with strong EMI such as encountered in plasma research, the optical fiber sensing solution is even more attractive.

Besides all the named advantages of F-P OFS which are summarized in Table 1, the one that is probably among the most interesting is the ultraminiature size that can be achieved for such sensors without sacrificing the sensor reliability and precision. Combined with its small size, the geometry of the sensor, which is usually axial, is sometimes an additional interesting advantage. For instance, it is possible to monitor strain in a small bolt almost without changing its mechanical properties: a small hole drilled in its center and filled with a ∅ 230 μm OFS glued strain sensor (FOS-N) will certainly give more accurate measurements than an electrical flat strain gage that could only be installed by creating a flat surface on the bolt and that will definitely create a weak point thus biasing the true strain measurement.

The sensor miniaturization accessible with OFS allows accurate *in situ* measurements exactly where the physical parameter has to be detected in sometimes hard-to-reach areas. This has a major impact in a lot of industries, especially in the medical applications involving minimally invasive diagnostics and therapies [16, 17]. Pressure, temperature, and strain OFS manufactured have found many market niches where their size and reliability were key requirements. For instance, the FOP-MIV pressure sensor (see Figure 4), which is currently mass-produced and assembled using a fully automated assembly line with top quality control, meets all requirements necessary for integration into medical devices [18]. It is thus suitable for many medical applications where miniaturization and sensor global reliability are essential. For instance, it can be integrated into a catheter used for intra-aortic balloon pumping (IABP) therapy [19] which is a life-supporting therapy used in many heart surgical situations [20–22]. The miniature optical sensor can supply an accurate pump triggering signal directly from the *in situ* measured aortic pressure waveform (such as the one simulated in Figure 5(a)). The IABP therapy integrating optical pressure sensors is simplified and is also more reliable since the diameter of the IABP catheters is now reduced to sizes not available with conventional IABP catheters using fluidic transduction pressure monitoring. Such highly valuable miniaturization reduces significantly the occurrence of ischemia, which is the highest risk of this therapy [23].

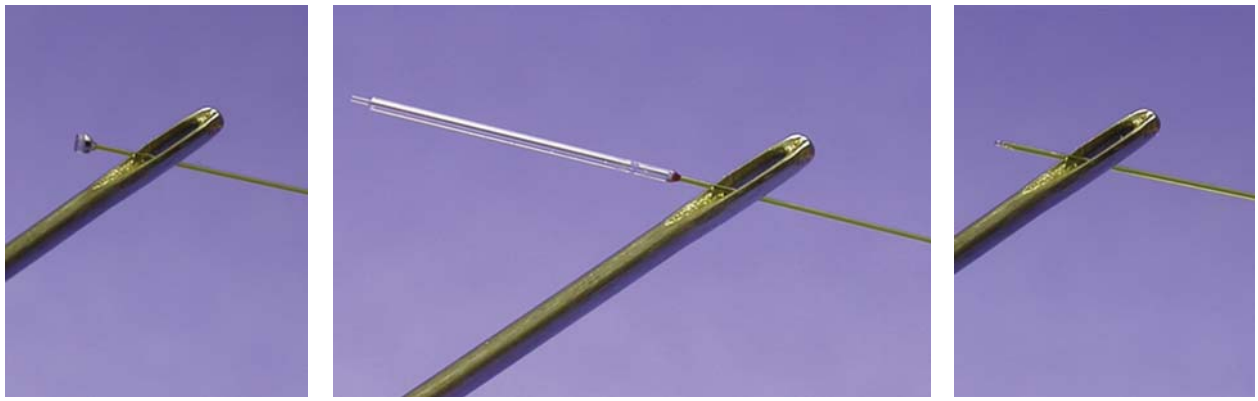

(a) (b) (c)

Figure 4: Examples of bare fiber-optic sensors for medical applications commercially available from *FISO Technologies*. (a) pressure sensor FOP-MIV suitable for mass production (∅ 550 μm), (b) temperature sensor FOT-L (∅ 800 μm), (c) temperature sensor FOT-HERO (∅ 210 μm).

Additional miniaturization of pressure sensor with diameter similar to the one of an optical fiber (∅ 125 μm) [24, 25], currently under development, will push further away the limits achievable with OFS and will open new avenues for minimally invasive *in situ* measurements.

In some cases the selection of an OFS could be driven only by one unique advantage provided by the optical technology, but in some cases a combination of criteria will practically make the choice of OFS the only applicable solution. For instance, in engine testing industry where the motor generates not only a lot of heat in a harsh explosive chemical environment but also a burst of EMI that fools traditional electrical sensors, the use of OFS for monitoring pressure [26, 27], strain cycles, or temperature, with minimal perturbation of the system, is probably a wise approach.

3. How does the Signal Conditioner Work?

Among the fiber-optic point-sensing commercially available technologies, the Fabry-Pérot white-light interferometry is probably the most attractive one. Its greatest advantage is undoubtedly the fact that it offers a low-cost solution for detection of a large variety of physical parameters such as temperature, pressure, strain/force, displacement, and refractive index. All those parameters could be accurately measured with the same universal signal conditioner that has evolved to meet all industrial robustness criteria.

FISO Technologies actually offers two patented technologies [28–30] that are suitable for interrogating Fabry-Pérot sensors. One provides an accurate measurement of the sensor reading (absolute measurement) while the other gives only a measurement of its variations (relative measurement).

Compared to other fiber-optic sensing technologies requiring costly optical source or spectral analysis equipment such as for interrogating FBG sensors, the Fabry-Pérot technology requires inexpensive and simple system instruments as it will be described in the following sections.

3.1. The Absolute Measurement Sensing Technology. The greatest advantage of the first technology is that the measurement is absolute which means that the sensor could be disconnected and reconnected and still give the same reading without any adjustment. Due to light source and detector limitations, such technology is now limited for sampling rates in the kHz range which is however suitable for most industrial practical applications (the recently released FPI-HS allows a 15 kHz sampling rate).

The principle behind this sensing technology, schematized in Figure 2, is actually quite simple although some technical details have to be considered in order to manufacture such device.

A light source, namely, a bright incoherent light source, is first injected and guided into a multimode optical fiber and then into an input of a 2×2 coupler which acts as a 50/50 power splitter. One output is linked to the OFS through an optical connector at the signal conditioner front panel. The second output of the coupler is not used or in some configurations could be connected to a light detector for light source monitoring purposes. Then, the light travels through the lead optical fiber until it reaches its tip, where the OFS is assembled.

The core of the OFS is a Fabry-Pérot interferometer that has been actually well known in the optical scientific community for now more than a century [31]. It has been used in many research applications such as physics and astrophysics notably. It is indeed constituted by two parallel, perfectly flat semireflecting mirrors separated by a given gap. The light passing through a first mirror is reflected back and forth a very large number of times between the two parallel planes as shown in Figure 3. However, at each reflection, a small fraction of the incident beam escapes the interferometer creating a large number of parallel beams of light (R_0, $R_1, \ldots, R_n$) emerging at the same angle at which they entered the interferometer. In the free space, they could be focused to form an image by a converging lens creating a constructive interference by the multiple beams which produce very bright and sharp interference fringes. Their

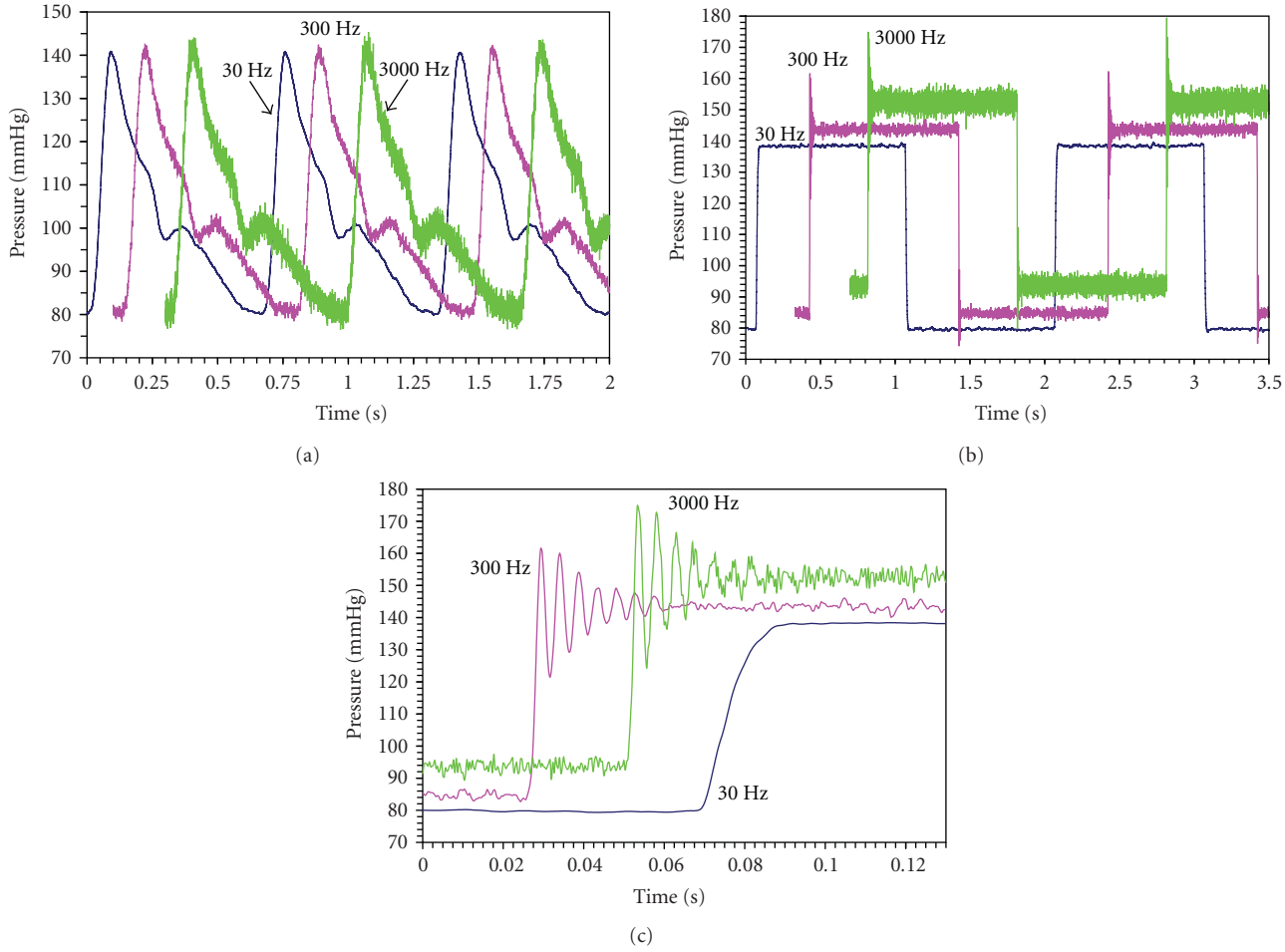

Figure 5: 80–140 mmHg pressure waveforms generated in water with a Bio-Tek 601A pressure simulator and measured by an FOP-M260 pressure sensor connected to a 15 kHz FPI-HS interrogator from *FISO Technologies*. Acquisition rate is set to 3 kHz, and lowpass filter is set to 30 Hz, 300 Hz, and 3000 Hz. (a) Normal aorta waveform, 90 bpm. (b) 0.5 Hz square waveform. Graphs have an offset for better clarity. (c) Detail of previous graph with graphs offset for better clarity to show an increasing pressure impulse.

spacing will depend on the optical path (that is related to the distance separating the parallel planes and the refractive index between those planes) and naturally on the light wavelength. Thus if a physical parameter to be measured by the sensor changes the optical path difference (OPD) of the F-P interferometer, the light escaping the F-P interferometer will be encoded according to this variation.

In the fiber-optic version, the light emerging from the F-P interferometer is not directly focused on a plane to give the interferences mentioned above, but the light beams are rather reinjected into the optical fiber from which they originally came from and they travel back, entering the signal conditioner at the optical connector level. Then, the light is again separated by the 2×2 coupler into two fibers. The light directed back to the light source is lost whereas the other fiber directs the light toward an optical box where the light is spread over a Fizeau wedge that reconstructs the interference pattern which is physically recorded using a charge coupled device (CCD). Due to the fact that white-light is used, all wavelengths are present, and thus destructive interferences occur except for the zero order where all wavelengths are actually constructive. Thanks to the wedge that creates a linear variation of thicknesses, the cross-correlated interference pattern has a maximum intensity at the exact position the optical path difference equals the one created at the F-P sensor, and few lower intensity peaks symmetrically disposed around the central peak (as given by the interferometer cross-correlation function). Thus finding the sensor OPD related to the physical parameter to be measured simply consists of finding the position of the maximum peak in the CCD interference pattern. This robust interferometric method allows accurate and precise F-P cavity length measurement with sub-nanometer range precision over several decades of micrometer span, thus giving a very interesting dynamical range.

3.2. The Relative Measurement Sensing Technology. The second technology, commercialized under the Veloce brand name, only provides a relative measurement: the sensor has to be referenced each time it is optically connected. This technology is best fitted for monitoring very fast occurring

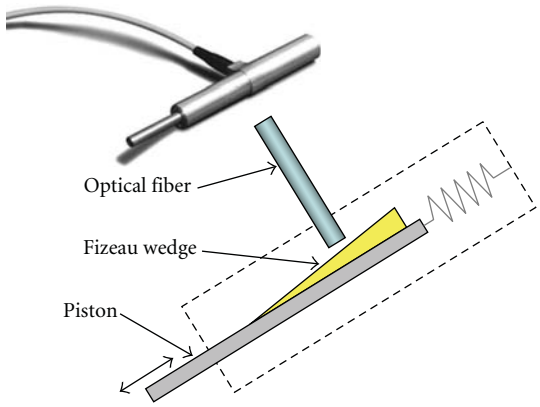

Figure 6: Photo (top left) and schematic representation of FOD displacement sensor from *Fiso Technologies*. As the piston is moving, the optical fiber faces different thicknesses of the Fizeau wedge.

events such as explosions or blasts [32], for instance, or phenomena requiring very high resolution. Thanks to the use of more efficient light sources and detectors, the acquisition rate is much faster than with the other technology: typically 0.2 MHz but it could be extended to 2 MHz if data postprocessing is possible.

In this technology, the light source is actually a bright light emitting diode (LED) that has a narrow wavelength band. Similarly to the previous method, the light is injected into an optical fiber and is guided to the F-P sensor *via* a 2×2 coupler and an optical connector at the signal conditioner front panel. Once returning from the sensor, the coded-light passes again through the connector and the 2×2 coupler, but instead of being directed to an optical box like previously, it is rather again separated into two optical fibers by another 2×2 coupler. Each fiber is directed to a calibrated F-P cavity mounted in front of a photodetector. The calibrated F-P cavities are actually selected so that the two detectors record signals in phase quadrature: that is, if one photodetector records a *cosine* signal, the other would record a *sine* signal for a linear variation of the physical parameter that is measured.

After referencing the sensor at the beginning of the measurement which means selecting an arbitrary phase in the periodic transfer function, the signal treatment algorithm allows tracking the sensor position within this periodic function. Therefore the sensor variation is not limited to a single period, and several orders could be passed without any problem. The only limitation is that the sensor order change should not be faster than the acquisition rate so that the tracking can be performed continuously. In most experimental cases this is obviously not a problem.

4. How Does the Fabry-Pérot Sensor Work?

Most of the Fabry-Pérot optical sensors are constructed around the same idea: they have an F-P interferometer whose OPD changes according to the physical parameter they are designed to measure. The sensor OPD is accurately measured by the signal conditioner of both described technologies absolute or relative measurement. Thanks to an appropriate sensor calibration, this OPD is converted into the appropriate unit corresponding to the sensor type to display a comprehensive value to the end-user.

Although several differences do exist between various commercially available sensor models, they could be briefly summarized by physical parameters categories.

4.1. Strain Sensors. The core sensing part of strain sensors is constituted by two glass fibers, which are ended by perfectly flat surfaces facing each other to constitute the F-P cavity with a given length. Thanks to a microcapillary glass tube that permanently fixes each fiber at a well-defined point few millimeters away from the F-P cavity, this alignment is constantly maintained. The ratio of the F-P cavity length variation to the distance separating the two fixing points is simply the strain measured by the sensor (with unit $\mu\varepsilon$).

To measure the strain of a material, the sensing capillary tube has to be glued or embedded onto or within the material to be studied. Once the material is deformed by a load or by a thermal dilatation, this deformation is transmitted to the capillary tube and thus to the F-P cavity whose length is changing accordingly and is precisely measured by the signal conditioner.

Due to the geometry of this sensor, it is practically not sensitive to transversal strain: only axial strains are thus detected. This is an additional great advantage over traditional electrical strain gages.

With its design, since the glass material used for the optical fibers forming the F-P cavity and the capillary tube is similar, such strain sensor is almost not affected by thermal dilatation: thermal expansion of the fibers is always compensated by thermal expansion of the capillary tube. The only place where such compensation does not occur is at the F-P level, which means that only few micrometers are not thermally compensated. Compared to other commercial OFS strain sensors such as fiber Bragg grating (FBG) that are also commonly used in the industry, Fabry-Pérot strain sensors are at least an order of magnitude less thermally sensitive, making it possible for some applications to avoid temperature measurement for thermal correction purposes.

Beside the bare sensor configuration that has been described here above, *FISO Technologies* also manufacture configurations where the strain sensor has been integrated into robust packaging that could be either welded (SFO-W sensor) on steel structure or directly embedded into cast concrete or similar materials (EFO sensor). Several dynamical ranges are available as standard products ($\pm1000\,\mu\varepsilon$, $\pm2500\,\mu\varepsilon$, and $\pm5000\,\mu\varepsilon$), but customization of this sensor could easily be done to take the best advantage of the whole dynamical range of the signal conditioners. For all these sensors the typical resolution (which also depends on the interrogator used) is 0.01% of full scale.

4.2. Temperature Sensors. Two types of F-P temperature sensors are available commercially: capillary type and refractive index type (see Figure 4).

The design of the capillary type temperature sensor is actually very similar to the above described strain sensor: two flat-ended fibers are assembled in a glass capillary tube to form an F-P cavity. But contrary to the strain sensor, the material of one fiber is selected to have a high coefficient of thermal expansion (CTE). The fiber thermal variation is thus not anymore compensated by the one of the capillary tube.

Also, this tube is encapsulated into a bigger capillary tube to prevent the fact that the sensor sensing part could be affected by strains transmitted through the packaging.

When temperature increases, the thermally sensitive fiber expands, reducing the F-P cavity length. Thanks to factory calibration, this length variation is translated into temperature value.

Several packaging and thermal ranges are available for FOT-L sensors and could be selected depending on the specific needs of the application. Response time of the sensor will of course depend on the selected packaging, but less than 0.5 second is a typical value for a packaged sensor and about 1 millisecond for a bare sensor. A typical accuracy for this sensor is 0.3°C for a medical temperature range (20°C to 85°C) and 1°C for an industrial temperature range (−40°C to 300°C).

Another type of temperature sensor is also available. This time, instead of material thermal dilatation, temperature dependent refractive index is rather used to change the OPD of the F-P sensor. A tiny chip of a semiconductor material with high thermal refractive index dependence and two semireflective surfaces constituting an F-P cavity is assembled at the tip of the lead optical fiber. This solid compact design is actually the smallest optical fiber temperature sensor available on the market (150 μm square). Its sensitivity is about one order of magnitude lower than the capillary type temperature sensor, but due to its extremely low thermal mass, its response time is better than 5 μs for a bare sensor which makes this sensor extremely interesting for fast temperature changes monitoring or for precise spatial point temperature mapping applications.

4.3. Pressure Sensors. Fabry-Pérot pressure sensors, also known as piezometers especially in the civil engineering industry, usually have a similar design. A reflecting deformable membrane is assembled over a generally vacuumed cavity made in a transparent material, thus forming so to speak a small drum. The bottom of the cavity and the inner flat surface of the flexible membrane are forming the sensing F-P cavity. When pressure is applied, the membrane is deflecting toward the bottom of the cavity thus reducing the F-P cavity length. With appropriate sensor calibration, each cavity length corresponds to a pressure value that is displayed with selected appropriate unit.

Several ranges (from ±40 kPa to 0–70 MPa relative to atmospheric pressure) are also available with various packaging alternatives designed to fit various applications. Two major pressure sensor families could be selected among available products at *FISO Technologies*: the FOP-C is a bulky robust sensor with a flexible metal membrane mainly designed for industrial applications requiring medium to high-pressure ranges and the FOP-M family which offers miniature sensors (∅ ~0.25–0.5 mm) manufactured using well-established and well-controlled photolithographic techniques. In this case, the flexible membrane is made of a thin silicon layer bonded to a glass with the cavity. It fits most applications where size and accuracy are important issues. It is available from 40 kPa to 20.7 MPa (full range) and has the highest sensitivity. Some other designs are also available where the optical fiber axis and the flexible membrane are in parallel planes (FOP-MS and FOP-MSL). Such configurations are sometimes useful when routing the optical fiber is difficult in a given application.

Figure 5 shows the waveforms obtained from a 260 μm diameter FOP-M260 pressure sensor measured by an FPI-HS interrogator. This interrogator can have a software configurable acquisition rate up to 15 kHz. In the Figure 5 an acquisition rate of 3 kHz was selected, and different programmable lowpass filters were applied to adjust the output bandwidth. On Figure 5(a), showing a simulated typical 80–140 mmHg aortic pressure waveform [19], it could be seen that a 30 Hz filter provides a smoother profile without distorting the experimental data. If such bandwidth is sufficient for human blood pressure monitoring, it may not be the case for small animals which have faster heartbeat [16]. When higher frequencies are present such as in the 0.5 Hz square waveform presented in Figure 5(b), applying a higher filter allows visualization of fine signal structures that otherwise are smoothed out. It could be seen on the zoom showing the abrupt pressure increase in Figure 5(c) that a ~200 Hz bouncing damping fluctuation is generated in the system by the Bio-Tek 601A pressure simulator at each drastic pressure change. A 300 Hz filter is in that case more appropriate than a 30 Hz filter that eliminates fast pressure variations and is better than a 3 kHz filter (corresponding to no filter since acquisition rate was set to 3 kHz) since data is smoother due to filter averaging. Adapting acquisition rate and output bandwidth (such as possible with the FPI-HS interrogator) allows therefore optimal signal processing.

4.4. Refractive Index Sensors. In some respects, refractive index sensors have a design that is derived from pressure sensors. But in that case the top membrane is not flexible, and the cavity is opened on two sides instead of being sealed and vacuumed. The physical dimension separating the two flat planes, creating the F-P cavity is maintained fixed and opened to the external medium, and so any fluid (gas or liquid) that enters the cavity could change its refractive index and thus will change the OPD of the F-P cavity that is accurately measured by the signal conditioner. Refractive indeces from 1.000 to 1.700, covering a wide range suitable for most liquids and gasses, are typically accessible with a standard FRI sensor with a typical resolution of 10^{-4} RIU. However, custom design could allow higher refractive index ranges if necessary.

Since the open F-P cavity is only few micrometers wide, very opaque fluids could be measured. For instance, you could easily see the increase of refractive index of your black coffee with milk as you dissolve sugar in it. The only

limitation is that the fluid should easily penetrate the F-P cavity, and so viscous fluids or fluids with bubbles will thus be more difficult to measure. But, contrary to other refractive index techniques based on diffraction angles measurements, the F-P refractive index sensor is not much affected by surfaces contamination since it actually measures truly bulk refractive index back and forth through the F-P cavity; so effects of surface contaminant layers are usually negligible compared to the whole optical path.

4.5. Displacement Sensors. F-P displacement sensors have a design quite different from all other described sensors. A Fizeau wedge mounted on a spring loaded axis is positioned in front of the extremity of the lead optical fiber as shown in Figure 6. As the axis is moving, the fiber extremity faces the wedge with variable thickness F-P cavity that could be related, with appropriate calibration, to the linear axis position.

On the standard FOD displacement sensor (see Figure 6), with a range of 20 mm and an accuracy of 2 μm, the optical fiber is normal to the displacement axis. Longer ranges displacement sensors and special sensors with optical fiber in the same direction than the displacement axis are also available.

5. Conclusion

As discussed in this paper, Fabry-Pérot optical sensing technology offers a real variety of sensors for physical parameters (such as strain, temperature, pressure, refractive index, displacement, etc.) that could be interrogated with two commercial families of universal signal conditioners, giving either fast (up to the kHz range) absolute measurements or ultrafast (up to the MHz range) relative measurements.

Such optical sensors have unique advantages that make them suitable for many challenging conditions that sometimes are impossible to address with conventional electrical sensors. They are particularly well adapted in various environments, for instance, in the presence of strong EMI, when there is a risk of explosion or of inflammability, when the temperature is too low or too high or when the chemical environment is really harsh. When other sensors are too bulky or too heavy, when hard-to-reach measuring spots are involved, or when measuring equipments have to be in remote locations, the Fabry-Pérot optical fiber sensors should be considered as a practical solution to problems which sometimes are puzzling the engineers.

One additional reason worth considering is that this field-proven optical sensing technology, commercialized for now more than a decade, is one of the lowest costs on the market. Actually with the recent introduction of its new *Evolution Platform* accepting OEM-ready snap-on DIN-rail modules, *FISO Technologies* now offer to the engineers and scientific community the cost-reduction and quality benefits from high-volume OEM modules and sensors, without sacrificing the possibility for customization and expandability.

With this new democratization of the access to this original and unsurpassed sensing technology for challenging conditions, one can bet that new opportunities and innovative applications will flourish in the very near future, making those optical sensors more and more present in our day-to-day life.

References

[1] D. A. Krohn, *Fiber Optic Sensors: Fundamentals and Applications*, Instrument Society of America, Research Triangle Park, NC, USA, 2nd edition, 1992.

[2] W. J. Bock, I. Gannot, and S. Tanev, Eds., *Optical Waveguide Sensing and Imaging*, NATO Science for Peace and Security Series B: Physics and Biophysics, Springer, Berlin, Germany, 2006.

[3] S. Yin, P. B. Ruffin, and F. T. S. Yu, Eds., *Fiber Optic Sensors*, CRC Press, Boca Raton, Fla, USA, 2nd edition, 2008.

[4] É. Pinet, C. Hamel, B. Glišić, D. Inaudi, and N. Miron, "Health monitoring with optical fiber sensors: from human body to civil structures," in *Health Monitoring of Structural and Biological Systems*, vol. 6532 of *Proceedings of SPIE*, San Diego, Calif, USA, 2007.

[5] D. Inaudi, "Field testing and application of fiber optic displacement sensors in civil structures," in *Proceedings of the 12th International Conference on Optical Fiber Sensors (OFS '97)*, vol. 16 of *OSA Technical Digest Series*, pp. 596–599, Williamsburg, Va, USA, 1997.

[6] International standard IEC 60705:1999 + A1:2004 + A2:2006, "Household microwave ovens—methods for measuring performance," Edition 3.2 (2006-03).

[7] H. Liu, D. W. Miller, and J. Talnagi, "Gamma radiation resistant Fabry-Pérot fiber optic sensors," *Review of Scientific Instruments*, vol. 73, no. 8, p. 3112, 2002.

[8] H. Liu, D. W. Miller, and J. W. Talnagi, "Performance evaluation of Fabry-Pérot temperature sensors in nuclear power plant measurements," *Nuclear Technology*, vol. 143, no. 2, pp. 208–215, 2003.

[9] P. Choquet, R. Leroux, and F. Juneau, "New Fabry-Pérot fiber-optic sensors for structural and geotechnical monitoring applications," *Transportation Research Record*, no. 1596, pp. 39–44, 1997.

[10] M. Quirion and G. Ballivy, "Concrete strain monitoring with Fabry-Pérot fiber-optic sensor," *Journal of Materials in Civil Engineering*, vol. 12, no. 3, pp. 254–261, 2000.

[11] P. Choquet, M. Quirion, and F. Juneau, "Advances in Fabry-Pérot fiber optic sensors and instruments for geotechnical monitoring," *Geotechnical News*, vol. 18, no. 1, pp. 35–40, 2000.

[12] M. Quirion and G. Ballivy, "Laboratory investigation on Fabry-Pérot sensor and conventional extensometers for strain measurement in high performance concrete," *Canadian Journal of Civil Engineering*, vol. 27, no. 5, pp. 1088–1093, 2000.

[13] B. Benmokrane, M. Quirion, E. El-Salakawy, A. Debaiky, and T. Lackey, "Fabry-Pérot sensors for the monitoring of FRP reinforced bridge decks," in *Nondestructive Evaluation and Health Monitoring of Aerospace Materials and Composites III*, vol. 5393 of *Proceedings of SPIE*, pp. 95–102, San Diego, Calif, USA, July 2004.

[14] B. Glišić and D. Inaudi, *Fibre Optic Methods for Structural Health Monitoring*, John Wiley & Sons, New York, NY, USA, 2007.

[15] D. Inaudi and B. Glišić, "Long-range pipeline monitoring by distributed fiber optic sensing," in *Proceedings of the 6th International Pipeline Conference (IPC '07)*, pp. 763–772, Calgary, Canada, September 2007.

[16] C. Hamel and É. Pinet, "Temperature and pressure fiber-optic sensors applied to minimally invasive diagnostics and therapies," in *Optical Fibers and Sensors for Medical Diagnostics and Treatment Applications VI*, vol. 6083 of *Proceedings of SPIE*, San Jose, Calif, USA, February 2006.

[17] É. Pinet, "Medical applications: saving lives," *Nature Photonics*, vol. 2, no. 3, pp. 150–152, 2008.

[18] É. Pinet and C. Hamel, "True challenges of disposable optical fiber sensors for clinical environment," in *Third European Workshop on Optical Fibre Sensors*, vol. 6619 of *Proceedings of SPIE*, pp. 1–4, Napoli, Italy, July 2007.

[19] É. Pinet, A. Pham, and S. Rioux, "Miniature fiber optic pressure sensor for medical applications: an opportunity for intra-aortic balloon pumping (IABP) therapy," in *17th International Conference on Optical Fibre Sensors*, vol. 5855 of *Proceedings of SPIE*, pp. 234–237, Bruges, Belgium, August 2005.

[20] G. A. Maccioli, W. J. Lucas, and E. A. Norfleet, "The intra-aortic balloon pump: a review," *Journal of Cardiothoracic Anesthesia*, vol. 2, no. 3, pp. 365–373, 1988.

[21] D. F. Torchiana, G. Hirsch, M. J. Buckley, et al., "Intraaortic balloon pumping for cardiac support: trends in practice and outcome, 1968 to 1995," *Journal of Thoracic and Cardiovascular Surgery*, vol. 113, no. 4, pp. 758–769, 1997.

[22] J. Litmathe, P. Feind, U. Boeken, and E. Gams, "Mechanical heart support using intraaortic balloon counterpulsation. A retrospective view and current perspectives," *Acta Cardiologica*, vol. 59, no. 2, pp. 159–164, 2004.

[23] P. Menon, P. Totaro, A. Youhana, V. Argano, Z. S. Meharwal, and N. Trehan, "Reduced vascular complication after IABP insertion using smaller sized catheter and sheathless technique," *European Journal of Cardio-Thoracic Surgery*, vol. 22, no. 3, pp. 491–493, 2002.

[24] É. Pinet, E. Cibula, and D. Donlagić, "Ultra-miniature all-glass Fabry-Pérot pressure sensor manufactured at the tip of a multimode optical fiber," in *Fiber Optic Sensors and Applications V*, vol. 6770 of *Proceedings of SPIE*, pp. 1–8, Boston, Mass, USA, October 2007.

[25] E. Cibula, S. Pevec, B. Lenardili, É. Pinet, and D. Donlagić, "Miniature all-glass robust pressure sensor," *Optics Express*, vol. 17, no. 7, pp. 5098–5106, 2009.

[26] R. A. Atkins, J. H. Gardner, W. N. Gibler, et al., "Fiber-optic pressure sensors for internal combustion engines," *Applied Optics*, vol. 33, no. 7, pp. 1315–1320, 1994.

[27] T. Bae, R. A. Atkins, H. F. Taylor, and W. N. Gibler, "Interferometric fiber-optic sensor embedded in a spark plug for in-cylinder pressure measurement in engines," *Applied Optics*, vol. 42, no. 6, pp. 1003–1007, 2003.

[28] C. Belleville and G. Duplain, "Fabry-Pérot optical sensing device for measuring a physical parameter," US patent no. 5202939, 1993.

[29] C. Belleville and G. Duplain, "Fabry-Pérot optical sensing device for measuring a physical parameter," US patent no. 5392117, 1995.

[30] R. Van Neste, C. Belleville, D. Pronovost, and A. Proulx, "System and method for measuring an optical path difference in a sensing interferometer," US patent no. #2004/0075841 A1, 2004.

[31] J. F. Mulligan, "Who were Fabry and Pérot?" *American Journal of Physics*, vol. 66, no. 9, pp. 797–802, 1998.

[32] M. Chavko, W. A. Koller, W. K. Prusaczyk, and R. M. McCarron, "Measurement of blast wave by a miniature fiber optic pressure transducer in the rat brain," *Journal of Neuroscience Methods*, vol. 159, no. 2, pp. 277–281, 2007.

Hindawi Publishing Corporation
Journal of Sensors
Volume 2009, Article ID 982658, 7 pages
doi:10.1155/2009/982658

Research Article

Covalent Attachment of Carbohydrate Derivatives to an Evanescent Wave Fiber Bragg Grating Biosensor

Christopher J. Stanford,[1] Geunmin Ryu,[1] Mario Dagenais,[1] Matthew T. Hurley,[2] Karen J. Gaskell,[2] and Philip DeShong[2]

[1] *Department of Electrical and Computer Engineering, University of Maryland, College Park, MD 20742, USA*
[2] *Department of Chemistry and Biochemistry, University of Maryland, College Park, MD 20742, USA*

Correspondence should be addressed to Mario Dagenais, dage@ece.umd.edu

Received 5 March 2009; Revised 2 July 2009; Accepted 11 August 2009

Recommended by Christos Riziotis

A carbohydrate-based biosensor was prepared by functionalization of the surface of an etched fiber Bragg grating with a glucopyranosyl-siloxane conjugate. Functionalization of the surface with the conjugate resulted in a Bragg grating shift of 24 pm. This shift in the refractive index is consistent with a theoretical shift calculated assuming monolayer coverage of the glucose conjugate on the sensor. The resulting functionalized fiber was shown to interact selectively with concanavalin A (Con A), a glucose binding protein (lectin). Exposure of the glucose-functionalized fiber to peanut agglutinin, a galactosebinding lectin, did not result in a change of the refractive index corresponding to a binding event.

1. Introduction

Biosensors play an increasingly important role in the detection of substances in the environment: they are employed for the detection of viral or bacterial pathogens in the food supply, to biodefense threats such as anthrax, to glucose monitoring of diabetes. [1–7] A variety of biomolecules have previously been attached to silica and related surfaces to provide recognition regimes for biochemical substances, including single strand DNA, antibodies, enzymes, proteins, and cells. In addition to single substrate biosensors, the ability to multiplex biosensors into arrays has provided greater sensitivity to the detection capabilities and array technology has greatly enhanced the study of genomic science, for example.

The functionalization of silica with carbohydrate derivatives, on the other hand, has received skant attention even though carbohydrate-protein interactions at cell surfaces are known to play critical roles in reproduction, infectivity, and tumor metastasis [8–12]. In addition, since many carbohydrate binding events are multidentate in nature and require the simultaneous binding of multiple sugars on the surface of cells, biosensors with a high surface coverage of carbohydrate should provide an ideal platform for the study of carbohydrate-protein interactions. Recently carbohydrate-based biosensors that exploit this multidentate binding have been reported by Izumi and Uzawa [13] and Jelinek and Kolusheva [14]. In addition, Taitt et al. have recently reported a carbohydrate-based array biosensor for use in the detection of toxins in food and clinical fluids [15].

In this paper, we describe the preparation of a carbohydrate-functionalized, etched evanescent wave fiber Bragg grating biosensor and study its binding to the glucose-binding protein (lectin) concanavalin A (Con A). These experiments are the initial step toward the development of carbohydrate-functionalized fibers as biosensors for the detection of carbohydrate binding proteins (lectins). Our immediate goal is to produce a biosensor based on glyco-recognition which should provide distinct advantages over DNA and antibody/antigen sensors. For example, since the binding is analogous to cell-cell recognition, the sensor should occur without the requirement for cell lysis (or other cell preparation methodology). In addition, since cell-cell recognition is known to be fast (seconds) on the biological

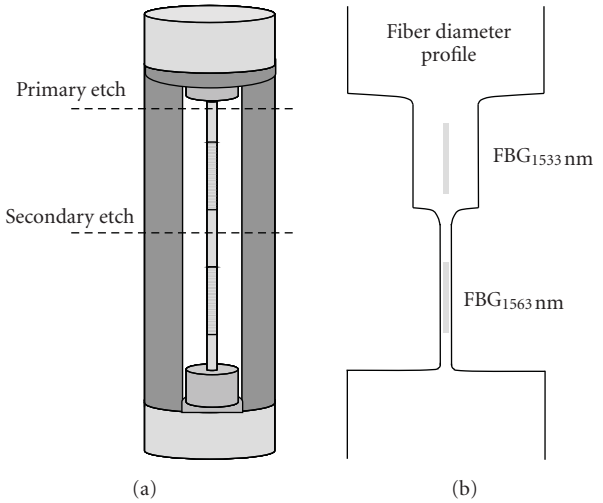

Figure 1: (a) Diagram of the JDSU fiber housing and positions of the etchant during primary and secondary etches; (b) fiber diameter profile after secondary etch.

timescale, one can anticipate that the sensor will function in the same time regime to provide virtually real time analysis of the binding event. Cell-cell recognition is very fast compared to DNA hybridization (hours) and thus the glycosensor may have much faster response times than other types of biological interactions. Once we have demonstrated that a single fiber with one carbohydrate can function as a sensor, then the multiplexing of fibers will be investigated.

2. Experimental Section

2.1. Fiber Optic System. Our fiber optics sensor [16, 17] uses a commercially available (JDSU) single mode photosensitive fiber in which two fiber Bragg gratings (FBGs), with a Bragg wavelength of 1533 and 1563.8 nm, are inscribed in the fiber core. The gratings are about 5 mm long and they have a peak reflectivity of about 30 dB and extremely well-suppressed sidelobes. Measurements from designing a temperature-compensated mount reveal that the JDSU fiber has a thermo-optic coefficient of $9.8 \times 10^{-6}/^{\circ}\mathrm{C}$. The JDSU fiber is a germanosilicate fiber that has been hydrogen loaded to enhance the photosensitivity. Both FBGs are packaged in a single temperature-compensated mount. For an unetched fiber, the temperature sensitivity was measured to be -0.1 pm/°C for temperatures within 10°C from room temperature. The FBG sensors were chemically etched in a two-step process. Fiber etching was conducted in 7 : 1 buffered oxide etch with surfactant from J. T. Baker. Based on the MSDS data sheet, the solution is made up of 0.5%–10% hydrogen fluoride, 40%–70% water, 30%–50% ammonium fluoride, and 0.5%–10% surfactant. The low concentration of hydrogen fluoride and the addition of surfactant reduce the silica etch rate and enhance the surface smoothness, as compared to etching processes utilizing higher hydrogen fluoride concentrations. The etch rate is very stable for a fixed temperature and at 23°C the fiber etches at a rate of 10.9 μm/h. Etch rates vary with temperature and will vary by more than 2% per degree. In a first step, the diameter is reduced from 125 μm to 49 μm. For this operation, the sensor is fully immersed within the etchant for 7 hours. In a second step, the lower grating is immersed in etchant and the upper half of the housing remains in air. The diameter is reduced from 49 μm to the final etch diameter within 3.5–4.5 hours. Even though the etch rates are very uniform and reproducible, the final diameter of the sensor is achieved by monitoring the Bragg wavelength with an optical spectrum analyzer as the fiber is etched. A Bragg wavelength shift of 10.5 nm is measured when the fiber diameter is reduced from 125 μm down to 5 μm. For a fiber diameter of 5 μm, none of the original fiber cladding is left and part of the core is etched away. For small diameters, the sensor becomes very sensitive to a change of the index of refraction of the surrounding liquid. Such enhanced sensitivity to a change of the index of refraction of the surrounding liquid was previously reported by our group [16]. BPM calculations were used to theoretically predict the Bragg shifts due to varying surrounding indices [18]. A sensitivity of about 85 nm for a change of 1 (riu) of the surrounding index of refraction was measured at a surrounding index of 1.4. As the surrounding index increases toward 1.45, a sensitivity of 1063 nm/riu is expected. This sensitivity decreases to about 20 nm/riu as the index of the surrounding liquid is changed to 1.3. In our studies, we take the index of refraction of water and ethanol at 1.55 μm to be 1.319 and 1.356, respectively. For an index of 1.44, we have recently achieved an index change sensitivity of 9.4×10^{-7} in a 3.4 μm diameter sensor [17]. A YSI thermistor with $\Delta T = 0.1^{\circ}\mathrm{C}$ (at room temperature) was immersed in solution near the grating at all times to accurately register the temperature.

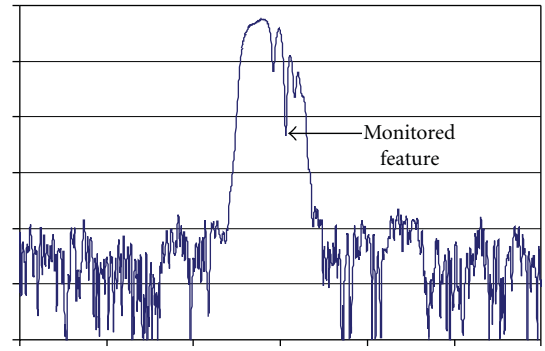

Figure 2: Spectrum of the etched core Fiber Bragg Grating sensor. The feature in the reflection spectrum that is being monitored is also shown.

For the reported experiments, we used a 5 μm diameter etched fiber Bragg grating sensor. We use the broad band amplified spontaneous emission spectrum of an erbium doped fiber amplifier as the broad band source to probe the fiber Bragg reflection spectrum. A typical reflection spectrum of an etched core fiber Bragg grating is shown in Figure 2. As seen, there exist several reflectivity peaks and minima. We use one of the relative minima to monitor the wavelength shift. The feature is very reproducible and shifts

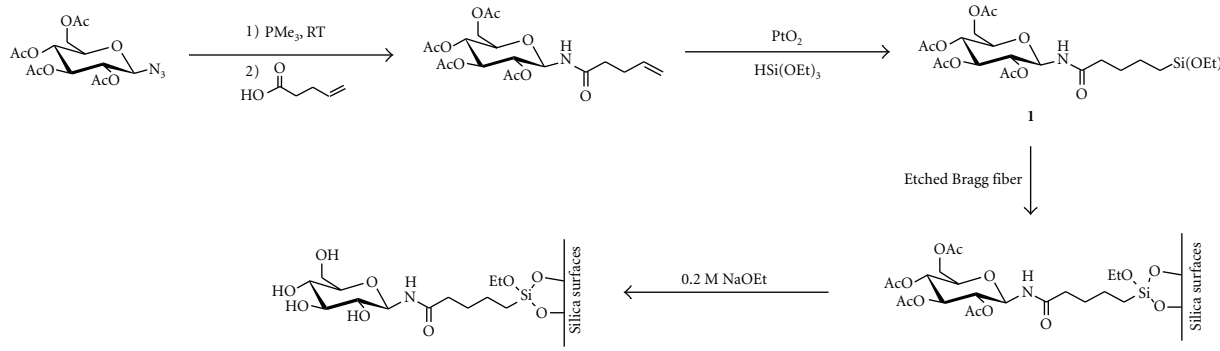

Figure 3: Synthesis of glucose-siloxane conjugate and surface functionalization.

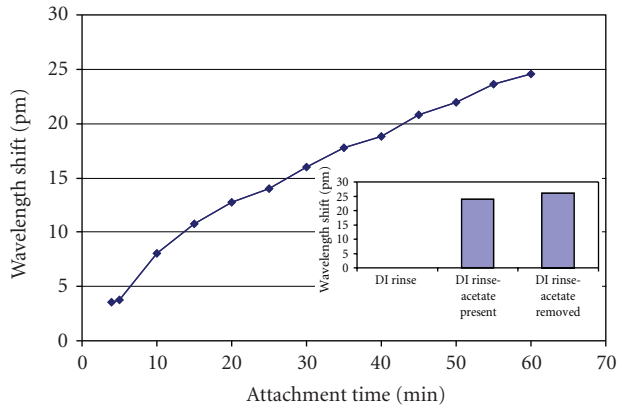

Figure 4: Time dependence of glucose-siloxane (**1**) attachment to the fiber Bragg grating in 95% ethanol. Inset shows the observed wavelength shift after washing the fiber in water.

by the same amount as the peak wavelength. The 3 dB width of the minimum feature is 25 pm. By using an appropriate fitting function, the wavelength shift can be resolved down to 1 pm. This translates to a sensitivity of 1×10^{-5} and 5×10^{-5} in the index change for a surrounding index of 1.4 and 1.3, respectively.

2.2. Synthesis of Glucosyl Siloxane and Functionalization of the Etched Fiber Surface via Glucose Attachment. We have recently developed a general strategy for the synthesis of oligosaccharide conjugates that is the basis for attachment of carbohydrate derivatives to oxidized silica surfaces [19]. Although originally developed for the synthesis of complex glycopeptide derivatives, the methodology summarized in Figure 3 has proven to be viable for the synthesis of a wide variety of glycoconjugates such as glycolipids, glycosylated polyethylene glycol (PEG) derivatives, and glycosyl-siloxanes. For this paper, glucosylamide derivative **1** (Figure 3) was utilized to functionalize the surface of the etched fiber using sol-gel methodology (see Appendix A). Following attachment of **1** to the fiber, the acetate protecting groups were removed by treatment with sodium ethoxide in ethanol at room temperature (see Appendix A).

Although Figure 3 summarizes the method using glucose as the carbohydrate moiety, other monosaccharides (mannose and galactose), disaccharides (maltose, chitobiose, and lactose), trisaccharides (maltotriose and cellotriose), and polysaccharides (cellulose) derivatives have been prepared by this method. These results clearly demonstrate that virtually any polysaccharide cell surface component can be functionalized to a glass fiber using this methodology.

3. Experimental Results

Glucose modified fibers were prepared using the chemistry summarized in Figure 3. A freshly etched fiber was treated with a 10 mM solution of glucose conjugate **1** dissolved in ethanol to yield a fiber whose surface has been modified by the siloxane exchange reaction and results in the attachment of the glucose ligand. Five different experiments were conducted with the identical goal of attaching glucosyl derivative **1** to the fiber via a covalent bond. These results were averaged and are plotted in Figure 4. The error represented by the fluctuations from point to point is less than 2 pm. A growing shift of the Bragg wavelength is observed as attachment of the glucose-siloxane conjugate on the fiber progresses.

The attachment progresses more rapidly at the beginning and then slows down. At the end of the attachment experiment, the sensor was rinsed in ethanol and then rinsed in water. The inset in Figure 4 shows the shift of the fiber Bragg grating peak before and after glucose attachment measured with respect to water. A final shift of 24 pm (as shown in the inset of Figure 4) is measured for the case of glucosyl derivative **1**, which corresponds to a change of the surrounding index of 5.6×10^{-4}. This shift is consistent with the 23 pm time-dependent shift measure from the minima to the observed final value of the shift. If we assume that a solid glucose layer is formed on the fiber of index 1.543 [20], a beam propagation simulation previously discussed in [18] suggests that a layer of thickness about 1 nm is formed, which corresponds to a monolayer of glucose conjugate. When the acetate groups are removed using a 0.2 M solution of sodium ethoxide, a glucose shift with respect to water of 26 pm was registered. This shift is very similar to the shift that was measured for the acetylated glucose on the fiber,

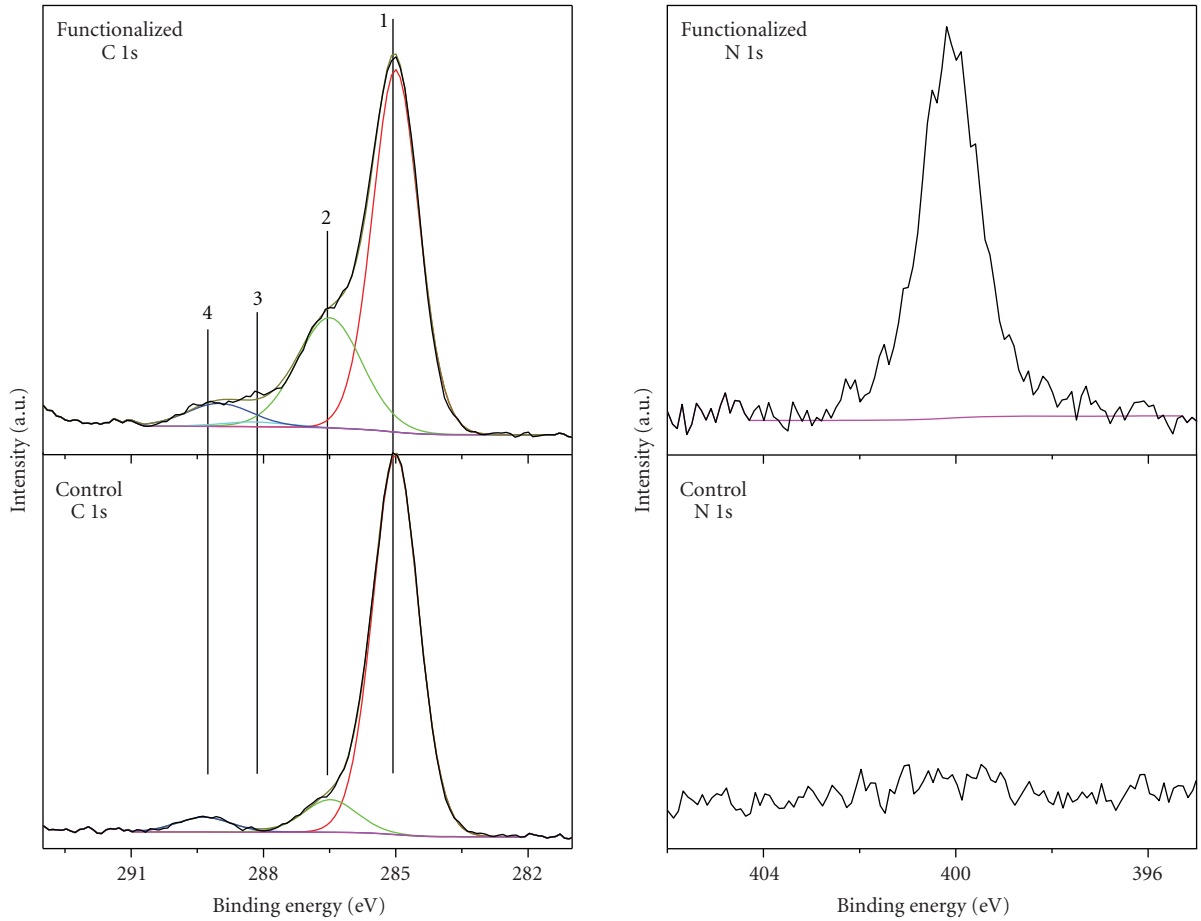

Figure 5: C 1s and N 1s high-resolution X-ray photoelectron spectra for the bare unfunctionalized glass slide (control) and glucose-functionalized glass slide (1 = C–C/C–H, 2 = C–O / C–N, 3 = RC=ON, 4 = OC=OR).

indicating that only a small fraction of the acetate groups has been removed. We have previously reported on the time dependence of the attachment of APTES and APMDS on a fiber [21] and have demonstrated the power of our technique for being able to reach monolayer attachment in a controlled way, as compared to other techniques that do not allow in situ real-time measurement of the functionalization process [22]. Therefore, we conclude that approximately a monolayer of the glucose-siloxane conjugate was attached to the fiber under these conditions.

Attempts to characterize glucose-siloxane **1** attachment to the fiber's surface using X-ray photoelectron spectroscopy (XPS) were inconclusive due to the weak signal obtained from the functionalized fiber. In an effort to demonstrate that glucose-siloxane **1** can be immobilized onto a silica surface, an etched glass slide was functionalized with glucose-siloxane **1** (see Appendix B) and then analyzed by XPS. The larger surface area of the slide provided an increased signal in the XPS spectrum. The high-resolution X-ray photoelectron spectra for bare and functionalized glass slides are depicted in Figure 5 (see Appendix B for experimental details and instrument specifications). The C 1s spectrum of the unfunctionalized glass slide (following the cleaning and etching procedures and washing with water) indicates a small amount of carbon on the surface due to hydrocarbon contamination, with some oxidized carbon due to atmospheric exposure. Notably, there is no nitrogen detected on the surface of the bare unfunctionalized glass slide. However, the XPS spectrum of the glass slide that was treated with glucose-siloxane **1** reveals a well-resolved nitrogen peak at 400.2 eV (~2 atomic % of all elements detected) and increased oxidized carbon species (C=O, C–N, and C–O), which is consistent with the attachment of the protected glucose-siloxane conjugate.

Additional confirmation of the functionalization of the fiber's surface with glucose was demonstrated using a lectin binding assay. Exposure of the glucose-functionalized fiber to a solution of concanavalin A (Con A), a protein known to bind to glucose, at 23°C resulted in a shift of 21 pm in the signal and indicated that binding of Con A had occurred to the fiber (Figure 6). Analogous treatment of the glucose-functionalized fiber with peanut agglutinin, a carbohydrate binding protein that binds to galactose

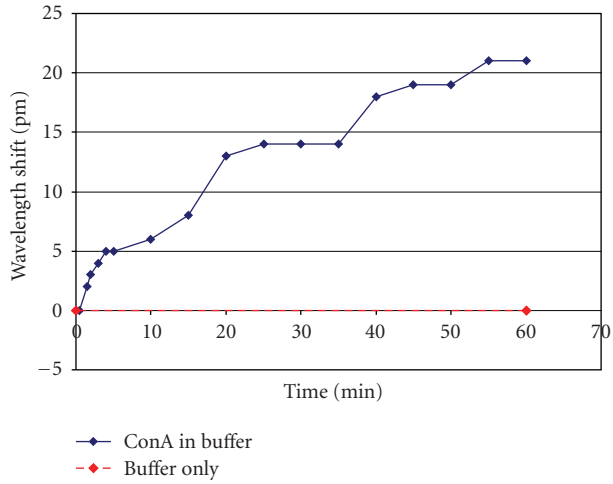

Figure 6: Time dependence of binding of Con A to glucose-functionalized fiber Bragg sensor at 23°C in buffer.

rather than glucose, did not produce a change in the signal of the fiber ($\Delta = 0$ pm). These complementary binding studies employing known lectins, although preliminary, were important on two levels: first, the binding clearly indicated that the surface of the fiber had been functionalized with glucose-siloxane **1** and that treatment with ethoxide had resulted in removal of the acetate protecting groups. More importantly, the binding of well-characterized lectins, carbohydrate-binding proteins, can be determined using the resulting sensor. Accordingly, we anticipate that other lectins whose specificity is unknown can be determined employing analogous methodology with more complex carbohydrate derivatives.

4. Conclusion

An evanescent wave fiber Bragg grating sensor has been prepared and was used to monitor the covalent attachment of a glucose derivative to the surface of the fiber. The observed change in the index was consistent with deposition of approximately a monolayer of the glucose conjugate. After removal of the carbohydrate protecting groups, the lectin concanavalin A was shown to bind to the biosensor. Such probes that rely on cell surface binding events as the basis of the sensing would have distinct advantages over other sensing strategies because (1) the sensors would not require lysis of cells prior to measuring binding and (2) the binding events should occur rapidly, possibly in real time. Subsequent experiments with this and related carbohydrate-functionalized Bragg fiber gratings will be undertaken to demonstrate the scope and limitations of these carbohydrate-functionalized biosensors. Topics to be investigated include temperature and pH stability of the biosensors, specificity of lectin binding to various carbohydrates, the role of tether length on the binding specificity, and the ability to multiplex biosensors to create devices for the detection of important proteins via carbohydrate-protein interactions.

Appendices

A. Preparation of Glucose-Functionalized Fiber

A.1. Synthetic Procedure for Acetylated-β-Glucose-4-Pentenamide. Acetylated glucose-azide was prepared as described in [19]. Acetylated-β-glucose-4-pentenamide was prepared in the following manner: Acetylated glucose-azide (1.0 g, 2.7 mmol) was dissolved in 25 mL of freshly distilled CH_2Cl_2. Diisopropylethylamine (1.0 mL) was added via syringe followed by a 1.0 M solution of trimethylphosphine (3.5 mL, 3.5 mmol) via syringe. Evolution of gas was observed. The reaction mixture stirred at RT for 0.5 hours. 4-Pentenoic acid (0.6 mL, 5.4 mmol) was added via syringe. The reaction mixture stirred at RT for 22 hours. The reaction mixture was then diluted with 125 mL of EtOAc and washed three times with H_2O. The organic layer was collected, dried over $MgSO_4$ and concentrated in vacuo to yield a colorless oil. Purification of the oil by flash chromatography (hexanes: EtOAc, 1 : 1) gave 0.62 g (54%) of acetylated β-glucose-4-pentenamide as a colorless oil. IR (CCl_4, cm^{-1}) 3432 (w), 3080 (w), 2955 (w), 1759 (s), 1709 (s), 1509 (s), 1227 (s), 909 (m); ^{1}H NMR (400 MHz, $CDCl_3$) δ 1.99 (s, 3H), 2.00 (s, 3H), 2.02 (s, 3H), 2.05 (s, 3H), 2.18–2.36 (m, 4H), 3.79 (ddd, J = 9.5, 4.4, 2.2, 1H), 4.05 (dd, J = 12.4, 2.2, 1H), 4.28 (dd, J = 12.4, 4.4, 1H), 4.86 (t, J = 9.5, 1H), 4.98 (dd, J = 10.3, 1.6, 1H), 5.02 (dd, J = 17.3, 1.6, 1H), 5.03 (t, J = 9.5, 1H), 5.23 (t, J = 9.5, 1H), 5.28 (t = 9.5, 1H), 5.70–5.80 (m, 1H), 6.20 (d, J = 9.5, 1H); ^{13}C NMR (100 MHz, $CDCl_3$) δ 20.6, 20.6, 20.7, 20.7, 28.8, 35.6, 61.6, 68.1, 70.5, 72.6, 73.5, 78.1, 115.8, 136.3, 169.5, 169.8, 170.6, 171.0, 172.5; HRMS (FAB) cacld. for $C_{19}H_{28}O_{10}N$ $[M + H]^+$430.1713, found 430.1708.

A.2. Synthetic Procedure for Acetylated β-Glucose-5-(Triethoxysilyl)pentanamide ***1***. Acetylated β-glucose-4-pentenamide (0.43 g, 1.0 mmol) and PtO_2 (0.01 g, 0.05 mmol) were weighed into a vial and dissolved with 1.5 mL of freshly distilled THF. Triethoxysilane (0.9 mL, 5 mmol) was added via syringe in one portion. The vial was flushed with argon and sealed. The reaction mixture stirred at 95°C for 3 hours. The reaction mixture was diluted with 20 mL of EtOH and filtered through a Celite plug. Concentration in vacuo yielded a colorless oil. Purification by flash chromatography (hexanes: EtOAc, 1 : 1) gave 0.42 g of an inseparable mixture of Acetylated β-glucose-5-(triethoxysilyl)pentanamide **1** and the fully hydrogenated amide product. The mol ratio of **1**: hydrogenated product (3 : 1) and percent yields (57% for **1** and 18% for the hydrogenated product) were determined by integration of the ^{1}H-NMR signals at 0.60 ppm (corresponding to the protons on the carbon adjacent to the siloxane group in **1**) and 0.88 ppm (corresponding to the protons on the terminal carbon in the hydrogenated product). IR (CCl_4, cm^{-1}) 3432 (w), 2973 (m), 1755 (s), 1707 (m), 1511 (m), 1224 (s), 956 (w) ^{1}H NMR (**1**, 400 MHz, $CDCl_3$) δ 0.57–0.62 (m, 2H), 1.19 (t, J = 7.0, 9H), 1.35–1.42 (m, 2H), 1.57–1.63 (m, 2H), 1.99 (s, 3H), 2.00 (s, 3H), 2.02 (s, 3H), 2.05 (s, 3H), 2.14–2.20 (m, 2H), 3.77 (q, J = 7.0, 6H), 3.78–3.82 (m, 1H), 4.04 (dd, J = 12.4, 2.0, 1H), 4.28 (dd, J = 12.4, 4.4, 1H), 4.88 (t, J = 9.5, 1H), 5.04 (t, J = 9.5, 1H), 5.22

(t, J = 9.5, 1H), 5.28 (t, J = 9.5, 1H), 6.16 (d, J = 9.5, 1H); ^{13}C NMR (**1**, 100 MHz, $CDCl_3$) δ 10.2, 18.3 (x 3), 20.6, 20.6, 20.6, 20.7, 22.5, 28.4, 36.3, 58.3 (x 3), 61.6, 68.1, 70.5, 72.6, 73.5, 78.1, 169.5, 169.8, 170.6, 171.1, 173.2; ^{29}Si NMR (**1**, 79.5 MHz, $CDCl_3$, externally referenced to TMS at 0 ppm) δ^-45.6; HRMS (FAB) cacld. for $C_{25}H_{43}O_{13}NSiLi$ $[M + Li]^+$ 600.2664, found 600.2694.

A.3. Procedure for the Deprotection of Acetylated Glucose-Siloxane Conjugate Immobilized onto a Bragg Fiber. A Bragg fiber functionalized with glucose-siloxane conjugate **1** was immersed in a 0.2 M NaOEt/EtOH solution for 2.0 hours at 25°C. The fiber was then removed from the sodium-ethoxide solution and rinsed with ethanol followed by Millipore water.

B. Preparation of Glucose-Functionalized Glass Surface and XPS Data

*B.1. Procedure for the Immobilization of Glucose-Siloxane **1** onto an Etched Glass Slide.* A glass cover slip (Fisherbrand Microscope Cover Glass) was immersed in piranha solution (3 : 1 concentrated H_2SO_4: 30% H_2O_2) for 1 hour, rinsed with Millipore H_2O (50 mL), and then immersed in 7 : 1 buffered oxide etch with surfactant from J. T. Baker for 1 hour. The slide was then rinsed with Millipore H_2O followed by sonication in Millipore H_2O for 10 minutes. The sonication process was repeated with fresh Millipore H_2O. The slide was then rinsed with dichloromethane (50 mL) and dried in an oven at 200°C for 1.5 hours. After cooling in a desiccator, a solution of glucose-siloxane **1** dissolved in dichloromethane was added drop wise to one side of the glass slide. After sitting undisturbed under nitrogen atmosphere for 0.5 hour, the glucose-siloxane/dichloromethane solution was reapplied. The glass slide sat undisturbed under nitrogen atmosphere for an additional 0.5 hour. The glass slide was rinsed with dichloromethane (20 mL) and was allowed to sit undisturbed under nitrogen atmosphere overnight.

B.2. Experimental Details for the XPS Analysis of Bare and Glucose-Functionalized Glass Slides. The XPS data was collected on a Kratos Axis 165 X-ray photoelectron spectrometer operating in hybrid mode using monochromatic Al Kα radiation. The instrument maintained a pressure of 5×10^{-9} Torr or better during data collection. The data were collected at a 20° take-off-angle (with respect to the sample plane). Charge neutralization was required to compensate for sample charging. Survey spectra (not shown here) were collected at a pass energy of 160 eV, while high resolution spectra were collected at a pass energy of 20 eV. All spectra were calibrated to the hydrocarbon peak at 285 eV. The C 1s spectra were fit with a Shirley background and peaks of a 30% Lorentzian 70% Gaussian product function.

Acknowledgments

PD acknowledges the generous financial support of the National Science Foundation (NIRT, CHE 0511219478), the Maryland Technology Development Corporation and SD Nanosciences, Inc. for partial support of this study. We gratefully acknowledge shared experimental facilities support for the X-ray Photoelectron Spectrometer from the NSF MRSEC under Grant DMR 05-20471. MTH acknowledges the support of the Graduate Assistance in Areas of the National Need (GAANN) Fellowship.

References

[1] M. Valach and E. Sturdik, "Application of biosensors in monitoring fermentation processes," *Chemicke Listy*, vol. 103, no. 3, pp. 208–215, 2009.

[2] L. C. Shriver-Lake, P. T. Charles, and C. R. Taitt, "Immobilization of biomolecules onto silica and silicabased surfaces for use in planar array biosensors," in *Biosensors and Biodetection, Vol. 2*, vol. 504 of *Methods in Molecular Biology*, pp. 419–440, 2009.

[3] A. Rasooly and K. E. Herold, *Biosensors and Biodetection: Methods and Protocols Volume 2: Electrochemical and Mechanical Detectors, Lateral Flow and Ligands for Biosensors*, Humana Press, Totowa, NJ, USA, 2009.

[4] L. Mi, X. Zhang, W. Yang, et al., "Artificial nano-biocomplexes: effects of nanomaterials on biomolecular reactions and applications in biosensing and detection," *Journal of Nanoscience and Nanotechnology*, vol. 9, no. 4, pp. 2247–2255, 2009.

[5] F. Lu, L. Gu, M. J. Meziani, et al., "Advances in bioapplications of carbon nanotubes," *Advanced Materials*, vol. 21, no. 2, pp. 139–152, 2009.

[6] G. R. Hendrickson and L. A. Lyon, "Bioresponsive hydrogels for sensing applications," *Soft Matter*, vol. 5, no. 1, pp. 29–35, 2009.

[7] G. Blagoi, N. Rosenzweig, and Z. Rosenzweig, "Fluorescence resonance energy transfer-based sensors for bioanalysis," *Fluorescence Sensors and Biosensors*, pp. 93–105, 2006.

[8] L. De Hoff Peter, M. Brill Laurence, and M. Hirsch Ann, "Plant lectins: the ties that bind in root symbiosis and plant defense," *Molecular Genetics and Genomics*, vol. 282, no. 1, pp. 1–15, 2009.

[9] S. Nakahara and A. Raz, "Biological modulation by lectins and their ligands in tumor progression and metastasis," *Anti-Cancer Agents in Medicinal Chemistry*, vol. 8, no. 1, pp. 22–36, 2008.

[10] V. Martos, P. Castreño, J. Valero, and J. de Mendoza, "Binding to protein surfaces by supramolecular multivalent scaffolds," *Current Opinion in Chemical Biology*, vol. 12, no. 6, pp. 698–706, 2008.

[11] T. Horlacher and P. H. Seeberger, "Carbohydrate arrays as tools for research and diagnostics," *Chemical Society Reviews*, vol. 37, no. 7, pp. 1414–1422, 2008.

[12] S. Chen and B. B. Haab, "Antibody microarrays for protein and glycan detection," *Clinical Proteomics*, pp. 101–111, 2008.

[13] M. Izumi and H. Uzawa, "Carbohydrate-based sensing materials for detection of bacterial toxins," *Trends in Glycoscience and Glycotechnology*, vol. 17, no. 95, pp. 107–119, 2005.

[14] R. Jelinek and S. Kolusheva, "Carbohydrate biosensors," *Chemical Reviews*, vol. 104, no. 2, pp. 5987–6015, 2004.

[15] C. R. Taitt, L. C. Shriver-Lake, M. M. Ngundi, and F. S. Ligler, "Array biosensor for toxin detection: continued advances," *Sensors*, vol. 8, no. 12, pp. 8361–8377, 2008.

[16] A. N. Chryssis, S. M. Lee, S. B. Lee, S. S. Saini, and M. Dagenais, "High sensitivity evanescent field fiber bragg grating sensor," *IEEE Photonics Technology Letters*, vol. 17, no. 6, pp. 1253–1255, 2005.

[17] M. Dagenais and C. J. Stanford, "Evanescent fiber bragg grating bio-sensors," in *VLSI Micro- and Nanophotonics: Science, Technology, and Applications*, E.-H. Lee, L. Eldada, M. Razeghi, and C. Jagadish, Eds., Taylor and Francis, London, UK, 2009.

[18] S. S. Saini, C. Stanford, S. M. Lee, et al., "Monolayer detection of biochemical agents using etched-core fiber bragg grating sensors," *IEEE Photonics Technology Letters*, vol. 19, no. 18, pp. 1341–1343, 2007.

[19] F. Damkaci and P. DeShong, "Stereoselective synthesis of a- and b-glycosylamide derivatives from glycopyranosyl azides via Isoxazoline intermediates," *The Journal of the American Chemical Society*, vol. 125, no. 15, pp. 4408–4409, 2003.

[20] X. Cao, B. C. Hancock, N. Leyva, J. Becker, W. Yu, and V. M. Masterson, "Estimating the refractive index of pharmaceutical solids using predictive methods," *International Journal of Pharmaceutics*, vol. 368, pp. 16–23, 2009.

[21] C. J. Stanford, M. Dagenais, J.-H. Park, and P. DeShong, "Real-time monitoring of siloxane monolayer film formation on silica using a fiber bragg grating," *Current Analytical Chemistry*, vol. 4, no. 4, pp. 356–361, 2008.

[22] J. A. Howarter and J. P. Youngblood, "Optimization of silica silanization by 3-aminopropyltriethoxysilane," *Langmuir*, vol. 22, no. 26, pp. 11142–11147, 2006.

Hindawi Publishing Corporation
Journal of Sensors
Volume 2009, Article ID 398403, 10 pages
doi:10.1155/2009/398403

Research Article

Remote System for Detection of Low-Levels of Methane Based on Photonic Crystal Fibres and Wavelength Modulation Spectroscopy

J. P. Carvalho,[1,2] H. Lehmann,[3] H. Bartelt,[3] F. Magalhães,[1,4] R. Amezcua-Correa,[5] J. L. Santos,[1,2] J. Van Roosbroeck,[6] F. M. Araújo,[1] L. A. Ferreira,[1] and J. C. Knight[5]

[1] *INESC Porto, Optoelectronics and Electronic Systems Unit, Rua do Campo Alegre 687, 4169-007 Porto, Portugal*
[2] *Physics Department, Faculty of Sciences, University of Porto, Rua do Campo Alegre 687, 4169-007 Porto, Portugal*
[3] *IPHT, Albert Einstein Straße 9, 07745 Jena, Germany*
[4] *Department of Electrical and Computer Engineering, Faculty of Engineering, University of Porto, Rua Dr. Roberto Frias, s/n 4200-065 Porto, Portugal*
[5] *Department of Physics, University of Bath, Claverton Down, Bath BA2 7AY, UK*
[6] *FOS&S, Cipalstraat 14, B-2440 Geel, Belgium*

Correspondence should be addressed to J. P. Carvalho, joel.carvalho@inescporto.pt

Received 6 March 2009; Accepted 22 June 2009

Recommended by Valerio Pruneri

In this work we described an optical fibre sensing system for detecting low levels of methane. The properties of hollow-core photonic crystal fibres are explored to have a sensing head with favourable characteristics for gas sensing, particularly in what concerns intrinsic readout sensitivity and gas diffusion time in the sensing structure. The sensor interrogation was performed applying the Wavelength Modulation Spectroscopy technique, and a portable measurement unit was developed with performance suitable for remote detection of low levels of methane. This portable system has the capacity to simultaneously interrogate four remote photonic crystal fibre sensing heads.

1. Introduction

1.1. Optical Detection of Methane. Methane is an extremely explosive gas and one of the main constituents of natural gas; so its detection is subject of major importance. The idea of sensing methane by laser absorption was first proposed in 1961 by Moore [1] and later demonstrated by Grant [2] in 1986 using an He-Ne laser. Although methane has a strong absorption line at 3.3 μm, this wavelength region is not suited for optical fibre sensor applications due to the high losses in standard optical fibres and also since it is difficult to fabricate laser diodes operating at wavelengths higher than 2.2 μm at room temperature. In order to effectively use the currently available low-loss optical fibres, remote detection in the near infrared around 1.1–1.8 μm is desirable, where optical fibres have minimum transmission losses (<1 dB/km). Methane has two absorption bands in this region, corresponding to wavelengths of 1.33 μm and 1.65 μm. It was found that the 1.65 μm band of methane absorption is more suitable considering the lower loss of the optical fibre in this region, the fact that the absorption coefficients are larger, and also the circumstance that the spectral widths are broader than those in the 1.33 μm band [3].

Several authors have proposed many configurations using laser diodes, in particular, distributed feedback (DFB) lasers with almost monochromatic emission, having bandwidths much narrower than the individual gas absorption lines. These devices are a suitable solution for optical-based gas sensing since DFB laser technology has reached maturity due to its broad use in telecommunication systems, with the consequent large reduction of the associated costs.

In 1992, Uehara and Tai [4] demonstrated high-sensitivity real time remote detection of methane in air with a DFB operating at 1.65 μm (transmission and reflection schemes). Silveira and Grasdepot [5] presented a methane optical sensor using a 1.31 μm DFB laser and proposed a

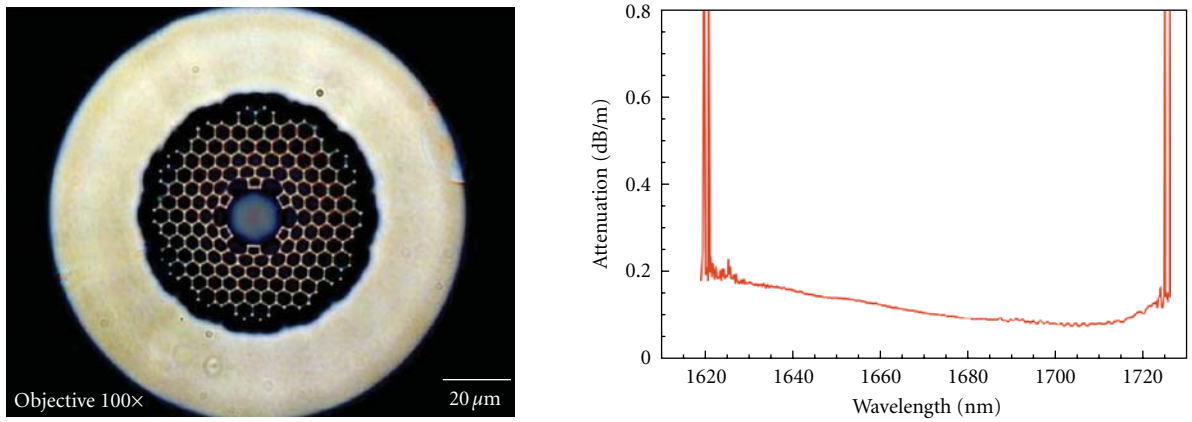

(a) (b)

Figure 1: (a) Optical microscope image of a 7-cell HC-PCF at 1670 nm; (b) spectral fibre transmission.

new type of signal processing technique based on amplitude modulation which provides autocalibration.

The performance limitations of a fibre optic methane sensor using GRIN lenses in either transmission or reflective configurations were examined by Stewart et al. [6]. DFB lasers exhibit very long coherence lengths, and, therefore, multireflections occurring within the gas cells and joints/connectors give rise to interference signals which produce harmonics in the output indistinguishable from the gas signals.

In 2000, Iseki et al. [7] developed a portable remote methane sensor based on frequency modulation using a DFB laser, where a dithering technique is employed, and the first and second derivatives of the absorption line are directly related with the gas concentration.

Chan et al. [8, 9] developed an optical remote sensing system for differential absorption measurement of various inflammable, explosive, and polluting substances employing low-loss optical fibre networks and near-infrared high radiant LED. The highly sensitive technique was achieved employing the power-balanced two-wavelength differential absorption method in the system, which enables direct detection of differential absorption signals for the specific molecule being monitored.

In 2003, Whitenett et al. [10] reported an alternative optical configuration for environmental monitoring applications, namely, the utilization of cavity ringdown spectroscopy using an Erbium Doped Fibre Amplifier (EDFA). This configuration monitors the exponential decay of a light pulse inside a gas chamber that ideally exhibits very high finesse, causing therefore 1/e ring-down time to be very long and very sensitive to small changes in the cavity loss, as induced, for example, by a gas absorber in the cavity.

Photoacoustic spectroscopy (Kosterev et al. [11]) is another technique for detection of absorbing analytes, and it relies on the photoacoustic effect. In this interesting technique, the sample gas is confined in a chamber, where modulated (e.g., chopped) radiation enters via a transparent window and is absorbed by active molecular species. The temperature of the gas thereby increases, leading to a periodic expansion and contraction of the gas volume, synchronous with the modulation frequency of the radiation. This, consequently, produces a pressure wave with amplitude (measured with simple microphones) related to the gas concentration.

Another approach known as multipass transmission absorption spectroscopy can be used and consists of a chamber with mirrors at each end filled with the targeted sample [12]. The beam is folded back and forth through the cell, creating an extended yet defined optical path length in a confined space. Although it presents a high sensitivity, the slow system response to concentration fluctuations and the relatively high volume of the sample required constitute the major disadvantages of this technique.

Other approaches have also been implemented, exploring different types of fibres (e.g., D-fibre) and effects, such as evanescent wave absorption (Culshaw et al. [13]). Their major obstacles, namely, low sensitivity for short interaction lengths, spurious interference effects, and degradation through surface contamination, were analysed (Stewart et al. [14]), and it was determined that the sensitivity of a D-fibre methane gas sensor could be improved by overcoating the flat surface of the fibre with a high index layer, reaching a detection limit lower than 5 ppm (Muhammad et al. [15]).

More recently, several authors proposed new methods for gas detection. Benounis et al. [16] demonstrated a new evanescent fibre sensor based on cryptophane molecules deposited on a PCS (polycarbosilane) fibre. Roy et al. [17] demonstrated a methane sensor based on the utilization of carbon tubes and nanofibres deposited by an electrodeposition technique.

A review of optical sensing methods for methane detection can be found in the work of Magalhães [18].

1.2. Gas Sensing with Photonic Crystal Fibres. The holes in microstructured fibres open up new opportunities for exploiting the interaction of light with gases or liquids. With the possibility of filling the air holes of PCF with gas, with large interaction lengths, new ways to monitor or detect gas are possible. Evanescent field gas sensing in

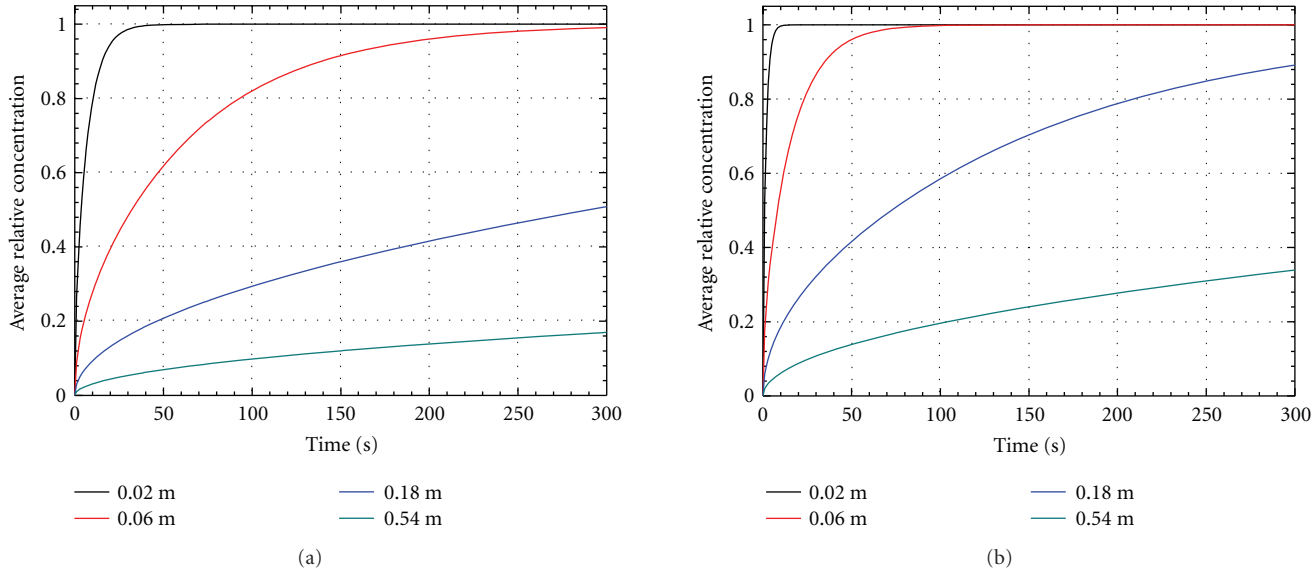

Figure 2: Time-dependence of the average relative methane concentration inside different lengths of HC-PCF with a single open end (a) and two open ends (b).

the holes of PCF (Monro et al. [19]) or in a fibre random hole structure (Pickrell et al. [20]) has been reported. Hoo et al. [21] demonstrated an absorption spectroscopy evanescent wave acetylene detection system based on a 75 cm length PCF sensing head. Another work of the same group presents a design and modelling of a PCF-based structure for gas sensing with enhanced characteristics, relying on the amplifying effect associated with the use of the multicoupling gaps (Hoo et al. [22]).

On the other hand, Ritari et al. [23] studied gas characteristics by monitoring the photonic bandgap parameters within hollow-core PCF. Methane detection at 1670 nm band using hollow-core PCF has been reported (Cubillas et al. [24]). A detection limit of 10 ppm/volume with the system configuration used in the experience is estimated. Cubillas et al. [25] also published a work that describes methane sensing with a hollow-core PCF at 1.3 μm. Other authors studied the characteristics of gas sensing based on evanescent-wave absorption in solid-core by filling the cladding air holes (Cordeiro et al. [26, 27], Li et al. [28]). Side access to the holes of PCF was demonstrated by Cordeiro et al. [27]. The method consists in inserting the liquid or gas to be sensed laterally to the fibre while the tips are optically monitored. An elegant solution to the problem of the long filling time of the gas inside the fibre was proposed by van Brakel et al. [29], using femtosecond-laser drilling microchannels in both hollow and solid core PCFs.

A comprehensive review of optical sensing based on photonic crystal fibres can be found in the work of Frazão et al. [30].

This work reports the development of an optical sensing system for remote sensitive detection of methane based on hollow-core photonic crystal fibres and Wavelength Modulation Spectroscopy (WMS).

2. Sensing System

Hollow-Core Photonic Crystal Fibres (HC-PCF) are structures where the light is guided not by total internal reflection but by a photonic bandgap in the cladding that acts like an insulator for light. The HC-PCF cladding is made with hundreds of periodically spaced air holes in a silica matrix, typically arranged in a honey combed-like pattern. Figure 1(a) shows the cross section of the hollow-core fibre that was used in the experiments. As can be seen, the hollow-core is formed with the suppression of some of such periodically spaced honey combed-like air holes. These fibres exhibit large potential concerning gas sensing since long interaction lengths could be created where light and gas share a common path, therefore, enabling the development of HC-PCF gas sensing heads. This particular fibre is a 7-cell HC-PCF (due to the fact that 7 of those small structures were removed) with a core diameter of 16 μm. To explore the 1.65 μm absorption band of methane, the fibre was designed to have a well defined bandgap in this spectral region. Also, more than 90% of the light propagates in the core, assuring a high field overlap with the gas and therefore enhanced detection sensitivity [31]. The transmission spectrum of this fibre in the region around 1.65 μm is shown in Figure 1(b), obtained using a tuneable laser.

2.1. Diffusion Time. A critical factor in sensing heads projected for detection of dangerous gases is the measurement time. In most cases this is not limited by the intrinsic time constant of the optoelectronic components but by the diffusion time of the gas into the measurement volume. This issue is particularly relevant when these volumes are reduced and accessed only through specific inputs, as is the case when PCF fibres are considered. Therefore, this problem was studied in detail in the context of this work.

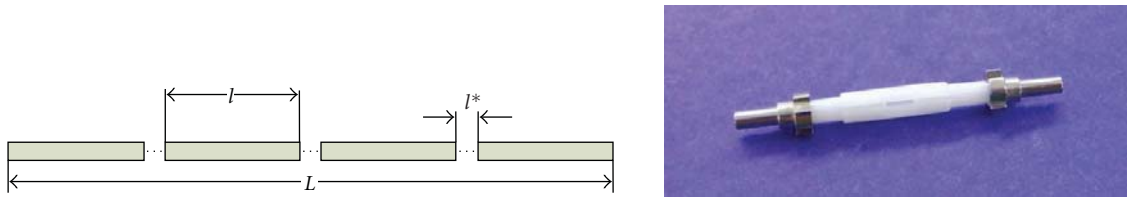

(a) (b)

Figure 3: (a) Project of the sensing head with periodic openings in the PCF fibre; (b) butt-coupling of HC-PCF pieces using standard zirconium ferrules connected with a standard zirconium mating sleeve.

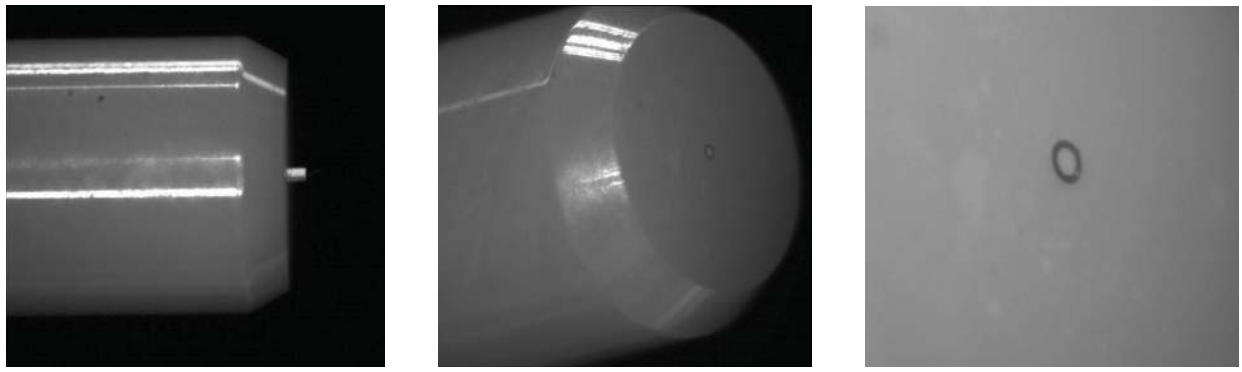

(a) (b) (c)

Figure 4: (a) photo of HC-PCF misaligned with the ferrule; (b) photo of the HC-PCF aligned with the ferrule; (c) detailed photo of the HC-PCF aligned with the ferrule.

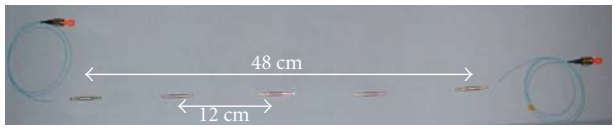

Figure 5: Multisegment sensing head containing 4 segments of HC-PCF.

There is considered an HC-PCF fibre with one open butt-end immersed in a methane atmosphere and the other butt-end closed. Methane gradually penetrates the fibre by diffusion. The diffusion was characterized by the relative concentration of gas inside the fibre averaged over the fibre length. This concentration can be found by integration of local concentration that is obtained by solving the diffusion equation with corresponding boundary conditions. For the average relative concentration the following expression, represented in a form of an infinite sum, was considered [22]:

$$C = 1 - \frac{8}{\pi^2} \sum_{j=1,3,5}^{\infty} \frac{1}{j^2} \exp\left[-\left(\frac{j\pi}{2\ell} \right)^2 D \cdot t \right], \qquad (1)$$

where ℓ is the fibre length, D is the diffusion coefficient of methane, and t is the time. The diffusion coefficient for methane in nitrogen is $2.2 \times 10^{-5}\,\mathrm{m^2 s^{-1}}$ [32]. Using this value, the dependence of the average relative concentration on time for four fibre lengths (0.02, 0.06, 0.18, and 0.54 m) was plotted. The result is shown in Figure 2(a). For the case of the fibre with two open ends, the average relative methane concentration inside the fibre is obtained from (1) with 2ℓ replaced by ℓ, resulting in the dependence given in Figure 2(b). It should be mentioned that on these calculations surface effects were neglected, given the considerably large diameter of the core of the HC-PCF in comparison to the gas molecules size. Table 1 summarizes the results relative to the diffusion time of methane into the HC-PCF with one and two ends open.

Table 1: Theoretical diffusion times to obtain 90% average methane concentration in the core of HC-PCF fibres for different lengths.

	One open end		Two open ends	
ℓ (m)	t (s)	t (min)	t (s)	t (min)
0.02	16	0.27	4	0.07
0.06	136	2.27	34	0.57
0.18	1220	20.33	305	5.08
0.54	10980	183	2745	45.75

This analysis allows to conclude that the length of the fibre used as the sensing head will directly affect the response time of the sensing system, limiting the time that gases may take to diffuse into the holes. As expected, with two open ends the gas diffusion inside the microstructured fibres happens significantly faster compared with the single open end configuration.

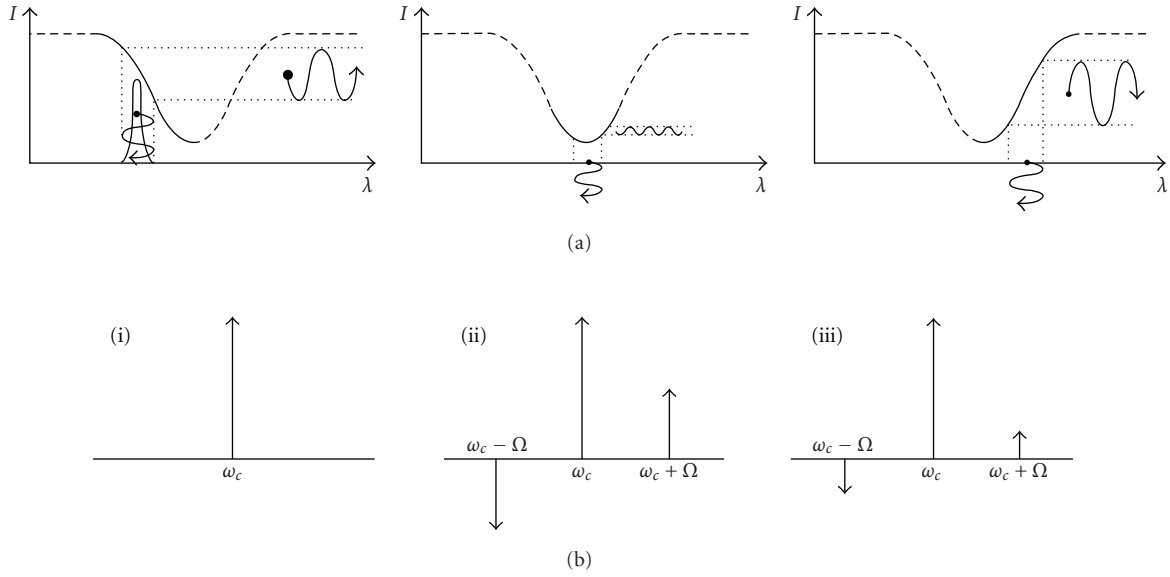

Figure 6: (a) Wavelength modulation converted to amplitude modulation in Wavelength Modulation Spectroscopy; (b) spectral contents of the optical signal: (i) laser unmodulated; (ii) laser modulated with no absorption; (iii) laser modulated with absorption.

2.2. Sensing Head. To optimize the sensing head sensitivity without compromising the response time a structure was devised where there was considered the introduction of periodic openings along the sensing head fibre, as shown in Figure 3(a). The several hollow-core photonic crystal fibre (HC-PCF) pieces are connected through butt-couplings [31]. As previously stated, the length of each segment can be tuned to control the diffusion speed of the gas inside the sensor and hence the response time of the sensor. In turn, the number of segments determines the total fibre length and, therefore, dictates the sensitivity of the sensing head. Standard zirconium mating sleeves, as shown in Figure 3(b), were found suitable for this butt-coupling approach.

The HC-PCF inside the ferrules was aligned using a nanometre resolution positioning stages as can be seen in Figure 4. The diameter of the sleeves is deliberately slightly smaller than the diameter of the ferrules. A slit along the length of the sleeve gives some extra flexibility to the inner diameter and allows the sleeve to act like a small spring (in the radial direction). This mechanism ensures that the ferrules are clamped inside the sleeve, thus optimizing the alignment. Since this is the standard technology for aligning fibre connectors, the technology is well established, and the components are relatively cheap. Furthermore, the slit in the sleeves is also well suited to allow gas in-diffusion through open gaps. Figure 5 shows a chain of different HC-PCF segments connected with this method. This multisegment sensor was placed inside a silica tube that acts like a gas chamber which facilitates greatly the experimental test. The insertion loss of the sensing head is a consequence of the loss induced by each butt joint and can be quantified as presented in a previous work (Carvalho et al. [31]), where there was characterised the optical coupling in a 19-cell HC-PCF with a core diameter, and thus a guided mode behaviour, quite similar to the 7-cell HC-PCF fibre used here. Typically, it was found that the loss in each butt-joint is smaller than 1 dB.

With adequate sensing head packaging, that involves fibre wrapping of several butt-joints segments, which is possible due to the geometrical flexibility of the optical fibre, the volume increase when the number of butt-joint segments increases can follow a slow grow.

2.3. Interrogation Technique. The ability to have sensitive detection of methane with the previously described sensing head requires the consideration of a high-performance interrogation approach. Therefore, the technique Wavelength Modulated Spectroscopy (WMS) was selected in view of its favourable characteristics (Silver [33]). In WMS, the source wavelength is slowly modulated, sweeping the entire absorption peak, and a higher frequency signal (dithering) is superimposed on this signal. As the emission source wavelength slowly scans through the gas absorption line, the wavelength modulation becomes an amplitude modulation, presenting its highest amplitude as it passes in the highest slope points of the absorption peak, as presented in Figure 6(a). As the schemes in this figure indicate, this interrogation method requires that the optical source should have a linewidth significantly smaller than the absorption line of the gas species to be monitored. Considering the detection bandwidth is shifted to higher frequencies where the laser intensity noise is reduced towards the shot noise, and the signal-to-noise ratio is substantially increased, which means better measurement resolution. This concept is similar to that of data encoding in the side bands of a radio transmission carrier wave. Figure 6(b) shows the spectral output of a frequency modulated laser, where there can be seen the carrier frequency ω_c and the side-band frequencies $\omega_c \pm \Omega$. Therefore, when the laser slowly scans through the

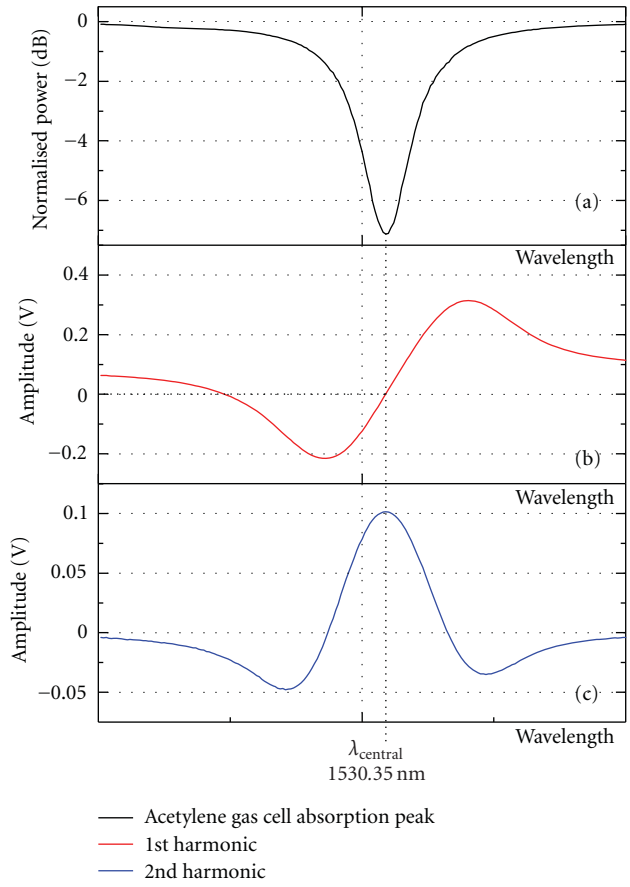

Figure 7: Absorption line of an acetylene gas cell (a) and amplitude of the output signals at the dithering frequency (b) and at double of this frequency (c).

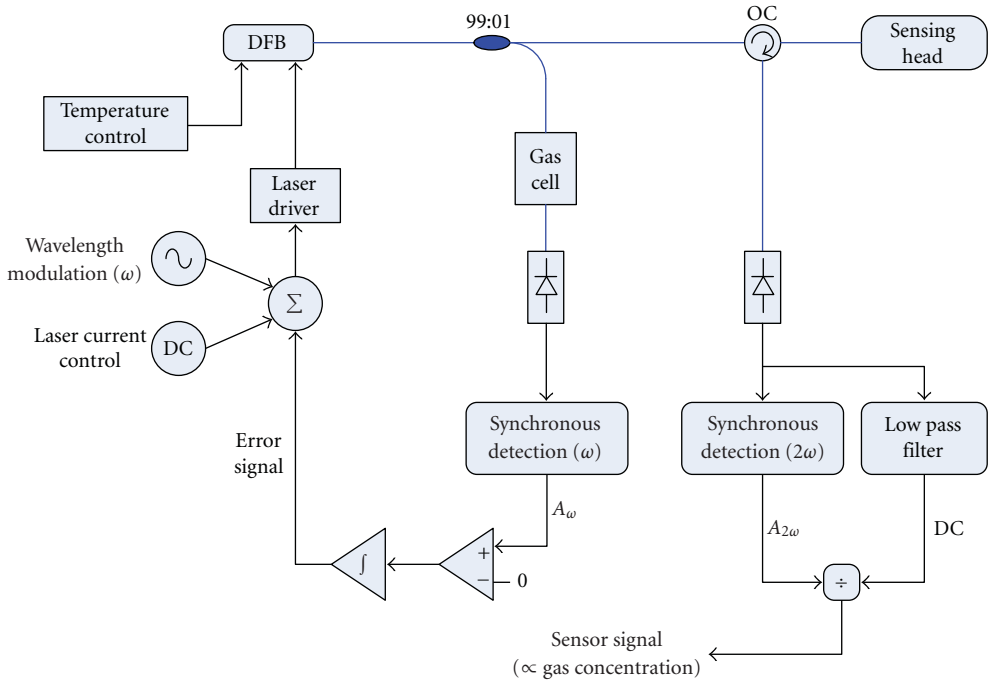

Figure 8: Layout of the Sensing head interrogation based on Wavelength Modulated Spectroscopy.

absorption line, the amount of light absorbed, which by the Lambert-Beer Law is proportional to the gas concentration, is "written" into the side bands. Schematically, this is represented in Figure 6(b) as a decrease in the amplitude of the side bands. Consequently, the absorption information can be retrieved by means of a lock-in amplifier, where a voltage output proportional to gas concentration can be generated.

Some features of this interrogation technique can be better appreciated observing the curves shown in Figure 7. They are relative to the acetylene, the gas that was used in the system development phase because it shows an absorption band around 1530 nm (Figure 7(a); the acetylene strongest absorption peak in the P branch of the $\nu_1+\nu_3$ band), a highly convenient spectral position considering the large range of optical fibre components that can be used in view of its location in the third optical communications spectral window. The interaction between the acetylene (pressure $\approx$200 Torr, $\approx$100% concentration) and the optical field happened in a U-bench with 30 mm length. The laser source used for these experiments was an Avanex-1905 LMI DFB laser optimized for operation at 1530 nm. With the lock-in amplifier locked at the dithering frequency, the output signal is the first derivative of the gas absorption line, and it equals zero when the source wavelength is centred in the absorption peak (Figure 7(b)). The lock-in amplifier output for the second harmonic is the derivative trace of the output at the dithering frequency and reaches a maximum at the peak absorption wavelength (Figure 7(c)). Disabling the slow modulation and stabilizing the source emission wavelength at the absorption peak, the dithering gives rise to a transmitted signal with a frequency that is twice the dithering one and with amplitude that depends on the gas concentration.

This detection method thus converts a frequency modulation into an amplitude modulation. The measured signal will contain both AC and DC components. Fluctuations of the optical power (from the source, fibre bends, etc.) will commonly modify the AC and DC components of the signal; so the ratio of the AC component with the DC component remains fairly unaltered, therefore only affected by the gas concentration. This insensitivity to optical power fluctuations is one of the main advantages of the WMS method.

Figure 8 shows the detailed scheme of the optoelectronic detection technique based in WMS. Ideally, an optical source suited for the WMS method shall have the following properties: high power (assures good signal-to-noise ratios and allows sensor multiplexing), narrow line width (in comparison with the line width of the methane absorption lines), which is also important to enhance the signal-to-noise ratio and tuneable emission wavelength. Distributed Feedback Lasers meet all these demands at affordable cost. A DFB diode can be tuned in wavelength by changing either the temperature or the operating current. While current-tuning is favourable for rapid modulation tasks, thermal tuning has the advantage of providing extremely large mode-hop free tuning ranges. In the configuration presented in the figure, the wavelength of the DFB optical source is modulated with a frequency ω by means of current tuning. The light is then guided through a directional coupler. Part of the light is sent to a reference gas cell whereas the remaining portion of light is sent to a sensing head. The reference cell is used to keep the laser wavelength locked to the gas absorption line. Monitoring of the light from the reference cell happens with a lock-in amplifier working at the modulation frequency, and the resulting signal is feedback to the laser driver. The light coming from the sensor is analyzed for two components. The DC component is filtered out using a lowpass filter, and the doubled frequency amplitude modulated signal is isolated using synchronous detection at 2ω. The information for gas concentration is obtained from the ratio $S = A_{2\omega}/DC$, where $A_{2\omega}$ is the amplitude of the signal synchronously detected at 2ω and DC the continuous level. This relation yields the absorbance and hence the gas concentration. The resulting signal, as previously stated, should be independent of optical power fluctuations.

In order to enable the variation of gas concentrations and to test the implemented setup with the HC-PCF-based sensing heads, a gas chamber was developed (Figure 9). The chamber is hermetically sealed and has one gas input and output as well as a pressure manometer and an optical feedthrough to allow the entrance of fibres. Inside of this chamber there are also two U-benches with different path lengths (30 mm and 6.8 mm).

A LabVIEW application has been developed to control all the signal generation, acquisition as well as all the single processing stages. With a standard computer and a DAQ board a virtual instrumentation workbench has been implemented, with the objective to perform system integration of a portable and customizable system for remote detection of gas species

3. Results

The experimental arrangement implemented to test the gas diffusion time into the HC-PCF is shown in Figure 10(a). Standard SMF transmitted light to the HC-PCF and guided it to the detection unit. After injection of gas into the chamber (a mixture of 5% of methane and 95% of nitrogen), the decay of transmitted light with time caused by the absorbance of the gas inside the HC-PCF was registered. The length of the sensing head HC-PCF was 13.7 cm. The optical source, a DFB laser optimized to work at 1666 nm, was emitting at the strongest methane absorption line in the Q branch of the $2\nu_3$ band (Rothman et al. [34]). The frequency of the dithering signal that modulates the DFB was 500 Hz. To allow gas diffusion, the gap between the input and output SMF and the HC-PCF was guaranteed by the use of angled ferrules (FC/APC) in the side of the standard fibres (Figure 10(b); $x \approx 176\,\mu$m). These ferrules, exhibiting an angle of 8°, were chosen because they do not permit Fresnel (silica-air interface) back reflections to be guided.

The obtained results for methane diffusion inside the HC-PCF are presented in Figure 11. It can be observed that the time taken to achieve 95% of the steady state was about 248 seconds, while the theoretically predicted value (obtained from (1) with 2ℓ replaced by ℓ) was about

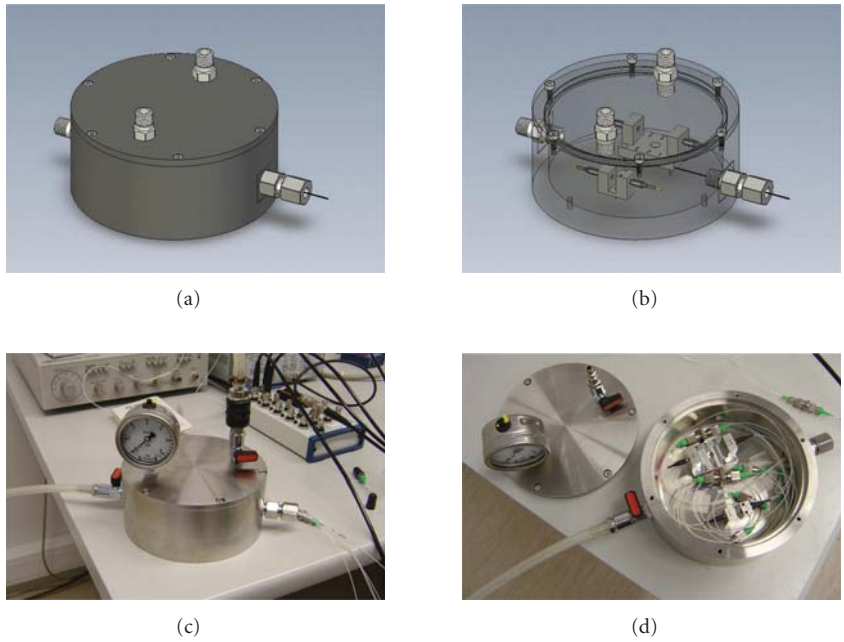

Figure 9: Gas chamber for test of the sensing system: (a) and (b) computer generated pictures; (c) and (d) photographs of the implemented gas chamber (the U-benches shown in (d) were used to test the WMS interrogation technique).

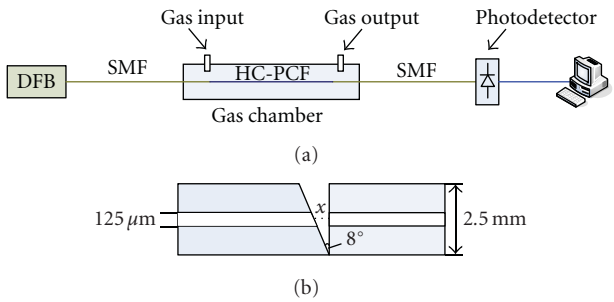

Figure 10: (a) Setup used to measure the diffusion time of gas inside the HC-PCF based sensing head; (b) illustration of the joint between SMF and HC-PCF.

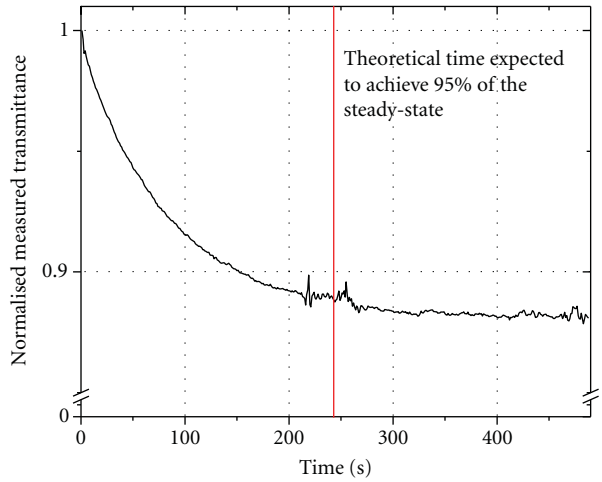

Figure 11: (Experimental results for the diffusion time of 5% of CH_4 inside an HC-PCF with a length of 13.7 cm (two open ends). The theoretical expected value (241 seconds) is shown by the vertical line, while the experimental one is 248 seconds.

241 seconds, thus leading to a relative error of ~2.8%. Therefore, this agreement confirms the reliability of the adopted model.

The detection limit of the methane sensing head can be estimated from the signal-to-noise ratio (SNR) of the demodulated signal. The second harmonic peak at 1000 Hz shows a SNR of ≈50 dB, and it corresponds to a methane concentration of 5%, or 50 000 ppm. In a linear scale, the SNR is ≈316, which means that we are able to detect a concentration smaller by this factor. Therefore, the sensing head with 13.7 cm length and opened in both sides permits a methane detection limit of ≈158 ppm.

If more segments are considered in the sensing head, as shown in Figure 5, the detection limit shall improve proportionally to the increase of the light interaction length with the gas. However, there was noticed the presence of a deleterious effect associated with superficial modes at the boundary of the fibre hollow core. These modes induce interference effects that reduce the signal-to-noise ratio. Research is going on aiming to overcome this problem.

Looking for field application of the R&D above described, an optoelectronic portable measurement unit was developed to measure gas concentration with HC-PCF-based sensors. The portable unit integrates a computer (motherboard, memory, hard-disk, touch-screen, etc.), an optoelectronic board and optical switching capability for multiplexing of four remote photonic crystal fibre sensing

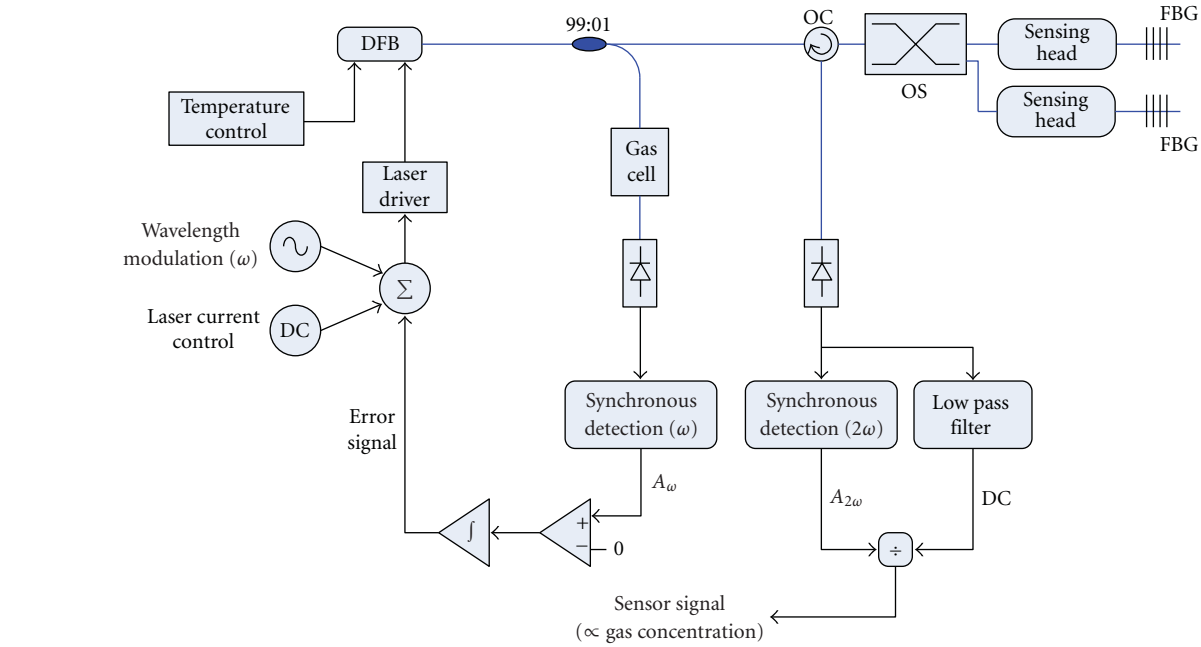

(a)

(b)

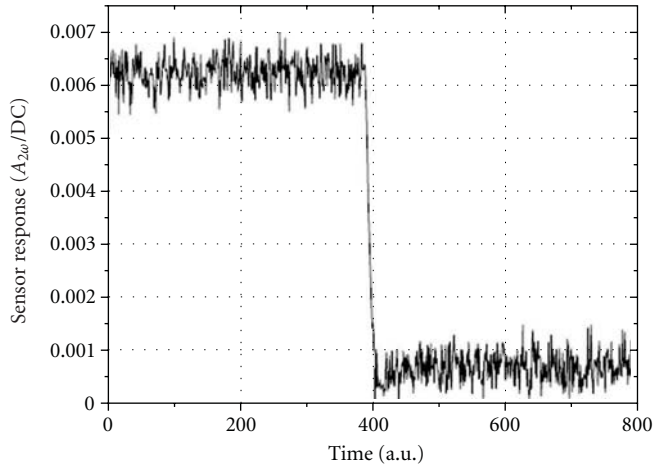

(c)

Figure 12: (a) Diagram of the gas measurement unit prototype; (b) photo of the unit; (c) response for a methane concentration change.

heads. A LabVIEW application was developed to control the measurement unit system which presents a graphical interface to the user. A diagram of the implemented system is presented in Figure 12(a), while Figure 12(b) shows a photo of the equipment. Figure 12(c) gives a unit screen plot representing the system response to a change of methane concentration in the sensing head.

4. Conclusion

This work reported the development of an optical fibre sensing system for detection of low levels of methane, based on a sensing concept that explores the favourable characteristics for gas sensing of hollow-core photonic crystal fibres together with the Wavelength Modulation Spectroscopy interrogation technique. A sensing head structure was designed that is compatible with sensitive methane detection and acceptable measurement time, which is related with the gas diffusion time into the measurement volume. The results obtained confirm the potential of this sensing approach, and aiming field applications a portable measurement unit was developed that has the capacity to simultaneously interrogate four remote photonic crystal fibre sensing heads.

References

[1] C. B. Moore, "Gas-laser frequency selection by molecular absorption," *Applied Optics*, vol. 4, no. 2, pp. 252–253, 1965.

[2] W. B. Grant, "He-Ne and Cw Co2-laser long-path systems for gas-detection," *Applied Optics*, vol. 25, no. 5, pp. 709–719, 1986.

[3] B. Culshaw, G. Stewart, F. Dong, C. Tandy, and D. Moodie, "Fibre optic techniques for remote spectroscopic methane detection—from concept to system realisation," *Sensors and Actuators B*, vol. 51, no. 1–3, pp. 25–37, 1998.

[4] K. Uehara and H. Tai, "Remote detection of methane with a 1.66-μu-M diode-laser," *Applied Optics*, vol. 31, no. 6, pp. 809–814, 1992.

[5] J. P. Silveira and F. Grasdepot, "CH_4 optical sensor using a 1.31 μm DFB laser diode," *Sensors and Actuators B*, vol. 25, no. 1–3, pp. 603–606, 1995.

[6] G. Stewart, A. Mencaglia, W. Philp, and W. Jin, "Interferometric signals in fiber optic methane sensors with wavelength modulation of the DFB laser source," *Journal of Lightwave Technology*, vol. 16, no. 1, pp. 43–53, 1998.

[7] T. Iseki, T. Hideo, and K. Kimura, "A portable remote methane sensor using a tunable diode laser," *Measurement Science & Technology*, vol. 11, no. 6, pp. 594–602, 2000.

[8] K. Chan, H. Ito, and H. Inaba, "Remote-sensing system for near-infrared differential absorption of CH_4 gas-using low-loss optical fiber link," *Applied Optics*, vol. 23, no. 19, pp. 3415–3420, 1984.

[9] K. Chan, H. Ito, H. Inaba, and T. Furuya, "10 km-long fibre-optic remote sensing of CH_4 gas by near infrared absorption," *Applied Physics B*, vol. 38, no. 1, pp. 11–15, 1985.

[10] G. Whitenett, G. Stewart, K. Atherton, B. Culshaw, and W. Johnstone, "Optical fibre instrumentation for environmental monitoring applications," *Journal of Optics A*, vol. 5, no. 5, pp. S140–S145, 2003.

[11] A. A. Kosterev, Y. A. Bakhirkin, and F. K. Tittel, "Ultrasensitive gas detection by quartz-enhanced photoacoustic spectroscopy in the fundamental molecular absorption bands region," *Applied Physics B*, vol. 80, no. 1, pp. 133–138, 2005.

[12] "State-of-the-Art laser-based gas sensing," in *Photonics Spectra*, Laurin Publishing, 2006.

[13] B. Culshaw, F. Muhammad, G. Stewart, et al., "Evanescent wave methane detection using optical fibres," *Electronics Letters*, vol. 28, no. 24, pp. 2232–2234, 1992.

[14] G. Stewart, W. Jin, and B. Culshaw, "Prospects for fibre-optic evanescent-field gas sensors using absorption in the near-infrared," *Sensors and Actuators B*, vol. 38, no. 1–3, pp. 42–47, 1997.

[15] F. A. Muhammad, G. Stewart, and W. Jin, "Sensitivity enhancement of D-fiber methane gas sensor using high-index overlay," *Power Engineering Journal*, vol. 7, no. 3, pp. 115–118, 1993.

[16] M. Benounis, N. Jaffrezic-Renault, J.-P. Dutasta, K. Cherif, and A. Abdelghani, "Study of a new evanescent wave optical fibre sensor for methane detection based on cryptophane molecules," *Sensors and Actuators B*, vol. 107, no. 1, pp. 32–39, 2005.

[17] R. K. Roy, M. P. Chowdhury, and A. K. Pal, "Room temperature sensor based on carbon nanotubes and nanofibres for methane detection," *Vacuum*, vol. 77, no. 3, pp. 223–229, 2005.

[18] F. Magalhães, *Development of gas detection systems based on microstructured optical fibres*, MSc thesis, DEEC/FEUP—Electrical and Computers Engineering, Department of the Faculty of Engineering, University of Porto, Porto, Portugal, 2008.

[19] T. M. Monro, D. J. Richardson, and P. J. Bennett, "Developing holey fibres for evanescent field devices," *Electronics Letters*, vol. 35, no. 14, pp. 1188–1189, 1999.

[20] G. Pickrell, W. Peng, and A. Wang, "Random-hole optical fiber evanescent-wave gas sensing," *Optics Letters*, vol. 29, no. 13, pp. 1476–1478, 2004.

[21] Y. L. Hoo, W. Jin, H. L. Ho, D. N. Wang, and R. S. Windeler, "Evanescent-wave gas sensing using microstructure fiber," *Optical Engineering*, vol. 41, no. 1, pp. 8–9, 2002.

[22] Y. L. Hoo, W. Jin, C. Shi, H. L. Ho, D. N. Wang, and S. C. Ruan, "Design and modeling of a photonic crystal fiber gas sensor," *Applied Optics*, vol. 42, no. 18, pp. 3509–3515, 2003.

[23] T. Ritari, J. Tuominen, H. Ludvigsen, et al., "Gas sensing using air-guiding photonic bandgap fibers," *Optics Express*, vol. 12, no. 17, pp. 4080–4087, 2004.

[24] A. M. Cubillas, M. Silva-Lopez, J. M. Lazaro, O. M. Conde, M. N. Petrovich, and J. M. Lopez-Higuera, "Methane detection at 1670-nm band using a hollow-core photonic bandgap fiber and a multiline algorithm," *Optics Express*, vol. 15, no. 26, pp. 17570–17576, 2007.

[25] A. M. Cubillas, J. M. Lazaro, M. Silva-Lopez, O. M. Conde, M. N. Petrovich, and J. M. Lopez-Higuera, "Methane sensing at 1300 nm band with hollow-core photonic bandgap fibre as gas cell," *Electronics Letters*, vol. 44, no. 6, pp. 403–405, 2008.

[26] C. M. B. Cordeiro, E. M. dos Santos, C. H. B. Cruz, C. J. S. de Matos, and D. S. Ferreira, "Lateral access to the holes of photonic crystal fibers—selective filling and sensing applications," *Optics Express*, vol. 14, no. 18, pp. 8403–8412, 2006.

[27] C. M. B. Cordeiro, M. A. R. Franco, G. Chesini, et al., "Microstructured-core optical fibre for evanescent sensing applications," *Optics Express*, vol. 14, no. 26, pp. 13056–13066, 2006.

[28] S.-G. Li, S.-Y. Liu, Z.-Y. Song, et al., "Study of the sensitivity of gas sensing by use of index-guiding photonic crystal fibers," *Applied Optics*, vol. 46, no. 22, pp. 5183–5188, 2007.

[29] A. van Brakel, C. Grivas, M. N. Petrovich, and D. J. Richardson, "Micro-channels machined in microstructured optical fibers by femtosecond laser," *Optics Express*, vol. 15, no. 14, pp. 8731–8736, 2007.

[30] O. Frazão, J. L. Santos, F. Araújo, and L. A. Ferreira, "Optical sensing with photonic crystal fibres," *Laser & Photonic Reviews*, vol. 2, no. 6, pp. 449–459, 2008.

[31] J. P. Carvalho, F. Magalhães, O. V. Ivanov, et al., "Evaluation of coupling losses in hollow-core photonic crystal fibres," in *Proceedings of the 3rd European Workshop on Optical Fibre Sensors*, vol. 6619, 2007.

[32] D. R. Lide, *CRC Handbook of Chemistry and Physics*, CRC Press, Boca Raton, Fla, USA, 1997.

[33] J. A. Silver, "Frequency-modulation spectroscopy for trace species detection: theory and comparison among experimental methods," *Applied Optics*, vol. 31, no. 6, pp. 707–717, 1992.

[34] L. S. Rothman, D. Jacquemart, A. Barbe, et al., "The HITRAN 2004 molecular spectroscopic database," *Journal of Quantitative Spectroscopy and Radiative Transfer*, vol. 96, no. 2, pp. 139–204, 2005.

Hindawi Publishing Corporation
Journal of Sensors
Volume 2009, Article ID 815409, 4 pages
doi:10.1155/2009/815409

Research Article

Fiber-Optic Aqueous Dipping Sensor Based on Coaxial-Michelson Modal Interferometers

Paola Barrios,[1] David Sáez-Rodríguez,[2] Amparo Rodríguez,[1] José Luis Cruz,[2] Antonio Díez,[2] and Miguel Vicente Andrés[2]

[1] *Instituto de Investigación en Comunicación Óptica (IICO), Universidad Autónoma de San Luis Potosí, Av. Karakorum 1470, 78210 San Luis Potosí, Mexico*
[2] *Departamento de Física Aplicada-ICMUV, Universidad de Valencia, Dr. Moliner 50, 46100 Burjassot, Spain*

Correspondence should be addressed to Miguel Vicente Andrés, miguel.andres@uv.es

Received 1 February 2009; Accepted 9 July 2009

Recommended by Valerio Pruneri

Fiber-optic modal interferometers with a coaxial-Michelson configuration can be used to monitor aqueous solutions by simple dipping of few centimeters of a fiber tip. The fabrication of these sensors to work around 850 nm enables the use of compact, robust, and low-cost optical spectrum analyzers. The use of this type of portable sensor system to monitor sewage treatment plants is shown.

1. Introduction

Since long period gratings (LPGs) were proposed for sensor applications [1]; one can find a significant number of publications where the temperature and strain response of LPG are investigated. Here, we are particularly interested in chemical sensor applications [2], more specifically in refractive index measurements of aqueous solutions. The use of a matched pair of LPG defining an in-line modal interferometer with a coaxial-Mach-Zehnder configuration has been investigated [3] for temperature and strain measurements [4] as well as for chemical applications [5]; this interferometric structure exhibits an enhanced sensitivity to the physical and chemical properties of the surrounding media.

At present, we are specifically interested in the coaxial-Michelson configuration, where a single LPG and a short section of fiber, with its end properly cleaved and coated with a metal, define a compact modal interferometer. This type of interferometer was, first, investigated as a temperature sensor, [6] and, later, refractometric applications have been reported in the 1400–1600 nm wavelength range [7, 8]. The multiplexing of this sensors using low-coherence reflectometry has been also demonstrated [9]. Among the characteristics of this configuration, which is well suited to monitor aqueous solutions using portable sensor systems, we can point out the robustness of the interferometer and the fact that the measurement can be easily performed dipping the fiber tip into the liquid.

Our work is focused on the preparation of LPG-based coaxial-Michelson interferometers at ~850 nm, instead of the 1400–1600 wavelength range, in order to enable the use of compact and low-cost optical spectrum analyzers to extract the information of the sensor. This approach permits easy multiplexing of several sensors if it is required. In addition to the calibration of the sensor response, we demonstrate the application of this type of sensor to monitor sewage treatment plants.

2. Sensor Fabrication and Experimental Arrangement

The LPG is photoinscripted in a hydrogen-loaded germanosilicate fiber using a continuous wave UV laser at 244 nm. The fiber is single mode at 850 nm and has a step index profile, 0.15 numerical aperture, 4 μm core diameter, and 125 μm cladding diameter. The use of a point-by-point writing technique provides a rather flexible choice of the

cladding mode to which the core mode is coupled, since the period can be adjusted precisely. Several LPGs with a period of 313 nm have been fabricated. Figure 1(c) shows the transmission spectrum of one of these LPGs in air, that is, when the fiber is stripped and surrounded by air. The spectra of the LPGs were monitored during the fabrication process, and the depths of the resonances centered at 820 nm and 850 nm were adjusted to be about 3 dB by controlling the length of the grating (7.3 mm). Thus, about a 50% of the power entering the LPG is coupled to the cladding modes LP_{05} and LP_{06} at the resonances of 820 and 850 nm respectively, while the rest of the power remains in the fundamental core mode of the fiber.

Once one LPG is written, the fiber is cleaved at a certain distance L from the end of the LPG (7 cm in our case) and the front surface of the fibers coated with a gold layer by evaporation in a vacuum chamber. In this way, compact and robust coaxial-Michelson interferometers are obtained. Figure 1(a) gives a schematic diagram of the experimental arrangement and a detail of the interferometer. The sensor head is defined by the 7 cm long interferometer, plus the length of the LPG, and the interrogation is carried out by a compact optical spectrum analyzer (OSA) and a superluminescent light emitting diode (SLD); the optical spectrum of the SLD is depicted in Figure 1(b). The OSA that was used in our experiments is manufactured by Ocean Optics (HR4000) and has a resolution of 80 pm and weights 1 kg.

3. Experimental Results and Discussion

Figure 2(a) gives the spectra corresponding to several interferometric fringes within the range 853–870 nm, while Figure 2(b) gives the detail of the fringe centered at 863.5 nm. We can observe in Figure 2 the wavelength shift produced when the sensor head is immersed in water solutions with different concentration of glucose (mass %). The spectrum of the sensor in air is also included. In this example, relatively large concentrations of glucose were used. Measuring the shift of, for example, the interferometric fringe centered at 863.5 nm, one can calibrate the response of the sensor. In fact, one can calibrate the sensor response either in terms of the wavelength shifts of a given fringe or in terms of intensity variations at a given wavelength. Both alternatives are illustrated in Figure 3 for the case of the spectra recorded in Figure 2.

The refractive index of a glucose solution increases about 1.6×10^{-4} per unit of mass % [8]. Thus, the wavelength shifts reported in Figure 2 correspond to refractive index increase of 8×10^{-2}. The optical resolution of the OSA would permit to reach a detection limit of 5%, that corresponds to a refractive index change of 8×10^{-4}. Similar results were obtained with the different sensor heads that were prepared, all with a length $L = 7$ cm. If it is necessary, the detection limit can be improved significantly by coating the fiber with a thin film of a material with higher refractive index than the cladding [10]. The length of the sensor head can be increased, as well, to increase the detection limit. However, any small temperature change might deteriorate dramatically

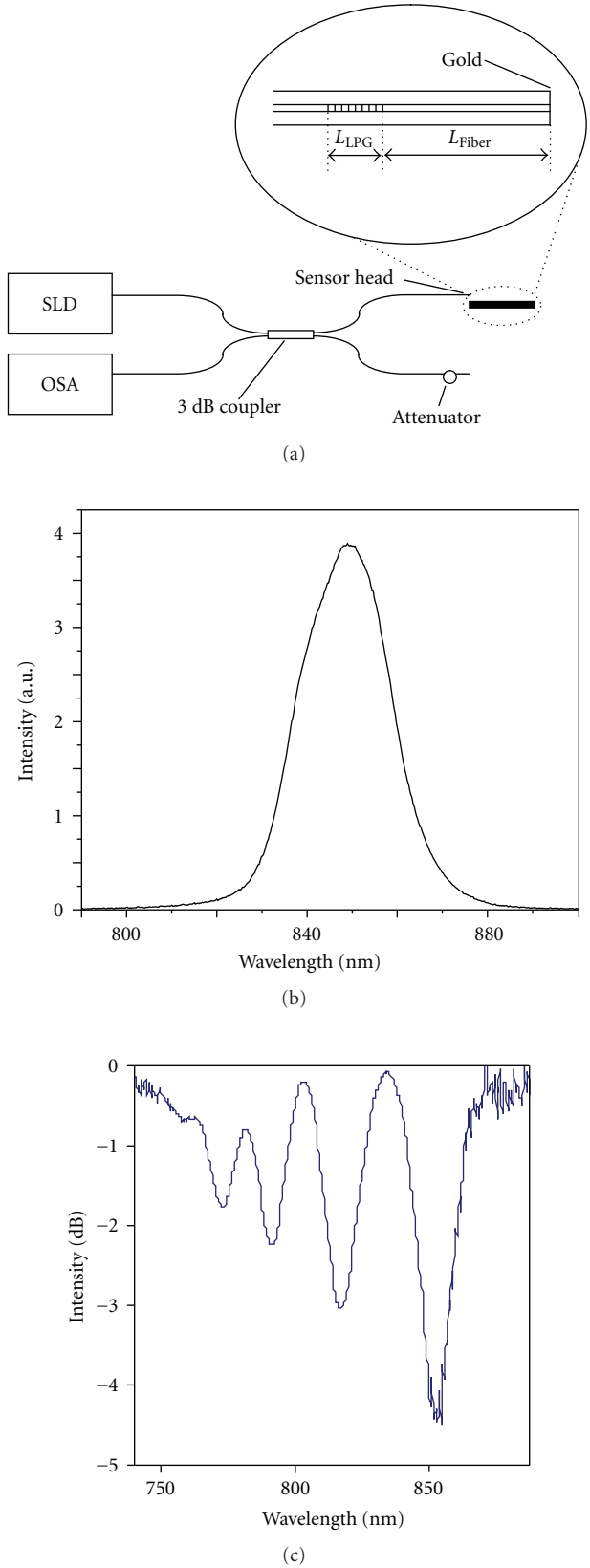

Figure 1: (a) Schematic diagram of the sensor system with a detail of the sensor head. (b) Spectrum of the SLD. (c) Spectrum of one LPG.

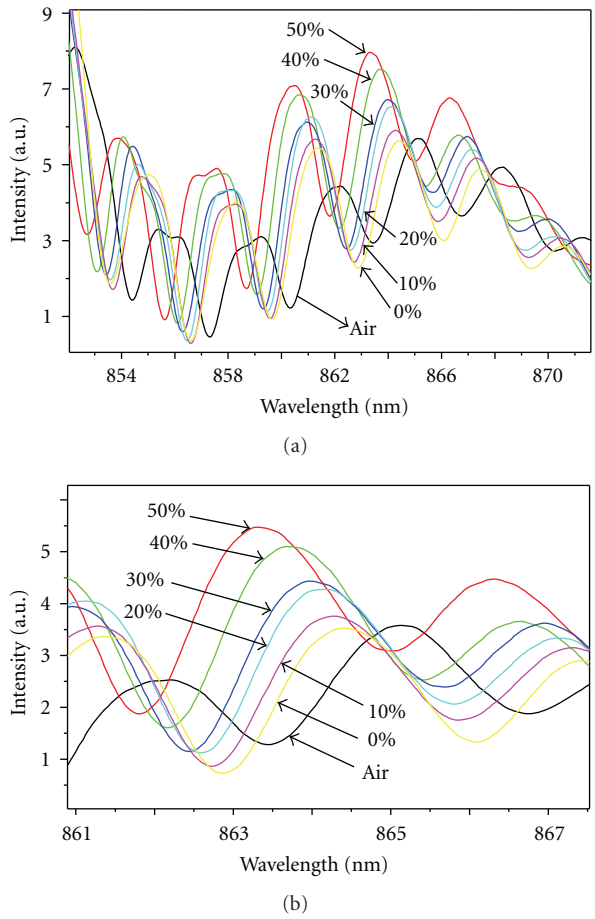

Figure 2: (a) Spectra of several interferometric fringes produced by the sensor head for different glucose concentration (mass %) and when the sensor is in air. (b) Detail of the spectra of the interferometric fringe centered at 863.5 nm.

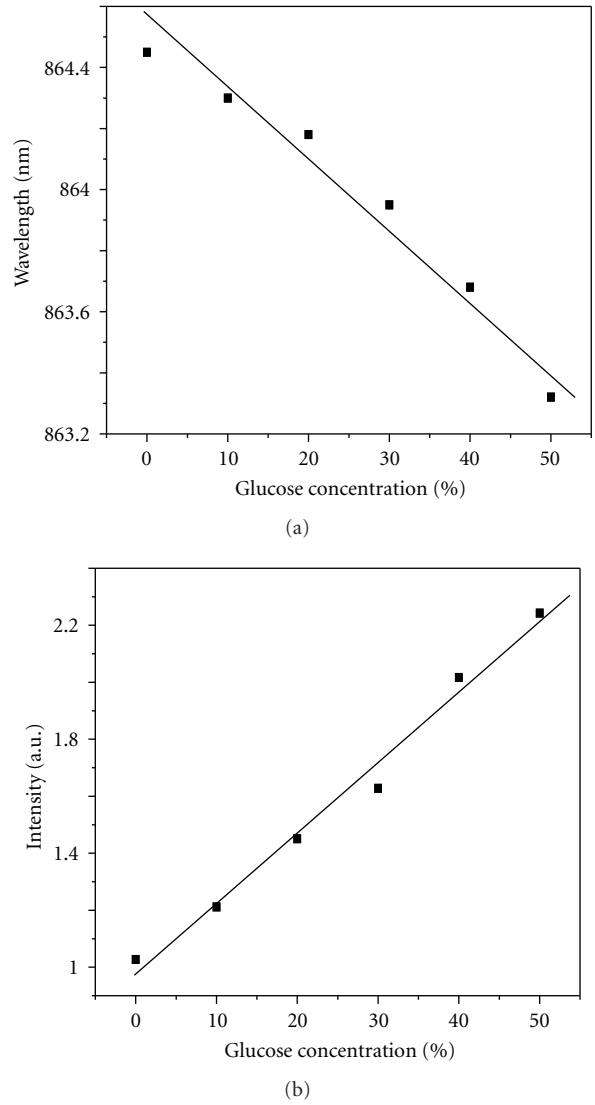

Figure 3: (a) Wavelength shift of the fringe centered at 863.5 nm as a function of the glucose concentration (mass %). (b) Intensity reflected by the sensor head at 863.62 nm as a function of the glucose concentration (mass %).

the detection limit, since, in addition to the temperature drift of the LPG and the interferometer itself, the thermo-optic coefficient of water is relatively high (-8×10^{-5} °C^{-1}). Thus, the use of a reference solution, at thermal equilibrium with the samples to be measured, might be essential to insure the reliability of the measurements in a practical application.

One interesting feature of this type of sensor heads is that the measurement does not rely on the transmission of an optical beam through the solution. This advantage can be exploited to develop chemical sensors for cloudy solutions, as it is the case of sewage. In order to illustrate this application we present in Figure 4 the spectra of the fringe centered at 860.5 nm for 4 different samples of sewage. These samples were taken at the entrance of a sewage treatment plant at different times over one day. All four samples produced a wavelength shift of 750 pm with respect to pure water, which corresponds to a refractive index change of 5×10^{-2}. The four samples were filtered to remove particles in suspension and were measured again. No important changes were observed within the resolution of the sensor heads. The inset of Figure 4 gives the spectra of the same interferometric fringe for the four samples of water after removing the suspended particles.

4. Conclusion

Using single mode fiber at 850 nm, compact and robust coaxial-Michelson modal interferometers have been prepared using a long period grating as an equivalent 3 dB beam splitter. Direct dipping of the sensor head in water solutions permits the measure of small refractive index changes, and, working at 850 nm, low-cost, high-sensitivity, and portable optical spectrum analyzers can be used to interrogate the sensor. The sensor system that has been described here can be used to monitor sewage treatment plants, since the presence of particle in suspension does not deteriorate the response of the sensor.

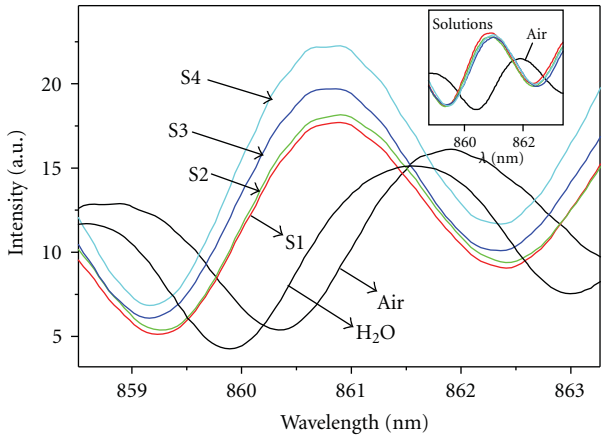

FIGURE 4: Spectra of the interferometric fringe centered at 860.5 nm for air, water, and 4 samples of sewage. The inset gives the fringes after filtering the samples to remove the suspended particles.

Acknowledgments

This work has been financially supported by the Programa de Mejoramiento del Profesorado, Formación y Fortalecimiento de Cuerpos Académicos of México (project UASLP-CA-26) and by the Ministerio de Ciencia e Innovación of Spain (project TEC2008-05490). The authors are grateful to Salvador Guel and Alfonso Lastras for their helpful cooperation.

References

[1] V. Bhatia and A. M. Vengsarkar, "Optical fiber long-period grating sensors," *Optics Letters*, vol. 21, no. 9, pp. 692–694, 1996.

[2] I. Peshko, O. Cherry, T. Rutkevich, B. Hockley, and V. Rubtsov, "Long-period gratings in optical fibres for chemical sensor applications," *Measurement Science and Technology*, vol. 16, no. 11, pp. 2221–2228, 2005.

[3] Y.-G. Han, B. H. Lee, W.-T. Han, U.-C. Paek, and Y. Chung, "Fibre-optic sensing applications of a pair of long-period fibre gratings," *Measurement Science and Technology*, vol. 12, no. 7, pp. 778–781, 2001.

[4] S. K. Abi Kaed Bey, T. Sun, and K. T. V. Grattan, "Simultaneous measurement of temperature and strain with long period grating pairs using low resolution detection," *Sensors and Actuators A*, vol. 144, no. 1, pp. 83–89, 2008.

[5] S. K. Abi Kaed Bey, C. C. C. Lam, T. Sun, and K. T. V. Grattan, "Chloride ion optical sensing using a long period grating pair," *Sensors and Actuators A*, vol. 141, no. 2, pp. 390–395, 2008.

[6] B. H. Lee and J. Nishii, "Self-interference of long-period fibre grating and its application as temperature sensor," *Electronics Letters*, vol. 34, no. 21, pp. 2059–2060, 1998.

[7] P. L. Swart, "Long-period grating Michelson refractometric sensor," *Measurement Science and Technology*, vol. 15, no. 8, pp. 1576–1580, 2004.

[8] D. W. Kim, Y. Zhang, K. L. Cooper, and A. Wang, "In-fiber reflection mode interferometer based on a long-period grating for external refractive-index measurement," *Applied Optics*, vol. 44, no. 26, pp. 5368–5373, 2005.

[9] M. Jiang, Z.-G. Guan, and S. He, "Multiplexing scheme for self-interfering long-period fiber gratings using a low-coherence reflectometry," *IEEE Sensors Journal*, vol. 7, no. 12, pp. 1663–1667, 2007.

[10] I. D. Villar, I. R. Matías, F. J. Arregui, and P. Lalanne, "Optimization of sensitivity in long period fiber gratings with overlay deposition," *Optics Express*, vol. 13, no. 1, pp. 56–69, 2005.

Hindawi Publishing Corporation
Journal of Sensors
Volume 2009, Article ID 645162, 9 pages
doi:10.1155/2009/645162

Review Article

Surface Plasmon Resonance-Based Fiber and Planar Waveguide Sensors

Raman Kashyap[1, 2] and Galina Nemova[1]

[1] *Department of Engineering Physics, Ecole Polytechnique de Montreal, P.O. Box 6079, Station Centre-ville, Montreal, QC, Canada H3C 3A7*
[2] *Department of Electrical Engineering, Ecole Polytechnique de Montreal, P.O. Box 6079, Station Centre-ville, Montreal, QC, Canada H3C 3A7*

Correspondence should be addressed to Raman Kashyap, raman.kashyap@polymtl.ca

Received 29 March 2009; Accepted 26 June 2009

Recommended by Christos Riziotis

Bulk surface Plasmons resonance devices have been researched for several decades. These devices have found a special niche as high-sensitivity refractive index sensor in biomedical applications. Recent advances in guided wave devices are rapidly changing the capabilities of such sensors, not only increasing convenience of use but also opening opportunities due to their versatility. This paper reviews many of these devices and presents some of their salient features.

1. Introduction

The optical performance of metal or metallic gratings dates back to 1902 when Wood discovered absorption anomalies in the response of such structures illuminated by light [1]. Later these absorption anomalies were understood as being caused by the excitation of surface Plasmon-Polaritons along the metal surface. A surface Plasmon-Polariton (SPP) is an electromagnetic excitation at a metal-dielectric interface, which consists of a surface-charge-density oscillation coupled to the electromagnetic fields [2, 3]. The SPP field components have their maxima at the interfaces and decay exponentially in both surrounding a metal layer (usually a few to 10's nm thick) media. In the case of a planar structure the SPP can exist in the form of p-polarized (TM) wave, when the permittivities of two adjacent media have opposite signs, and in the form of s-polarized (TE) wave, when the permeabilities of two adjacent media have opposite signs [4]. Being localised at the metal-dielectric interface, the SPP can serve as a promising tool for sensor applications to investigate the medium near the interface [5–10]. At the present time there are many of different SPP sensors bulk, planar, and fiber geometries.

All these sensors can be characterised by two important parameters: the sensitivity and operating (or dynamic) range. *Sensitivity* is the derivative of the monitored SPP parameter (e.g., resonant angle, wavelength, intensity) with respect to the parameter to be determined (e.g., refractive index). An *operating* (*dynamic*) *range* is the range of values of the parameter to be determined, which can be measured by the sensor. The third important parameter of the sensor is its resolution. The sensor *resolution* is the minimum change in the parameter to be determined, which can be resolved by the sensor. Contrary to the sensitivity and the operating range, the resolution of the sensor depends not only on the sensor properties itself but also on the accuracy with which the sensor is monitored. It means that increasing the accuracy of the interrogation unit one can increase the resolution of the sensor.

2. Surface Plasmon Sensors

In the late sixties, optical excitation of surface plasmons by the method of the attenuated total reflection was demonstrated by Otto [11] (Figure 1(a)). In this scheme there is a finite gap between prism base and metal layer and it is

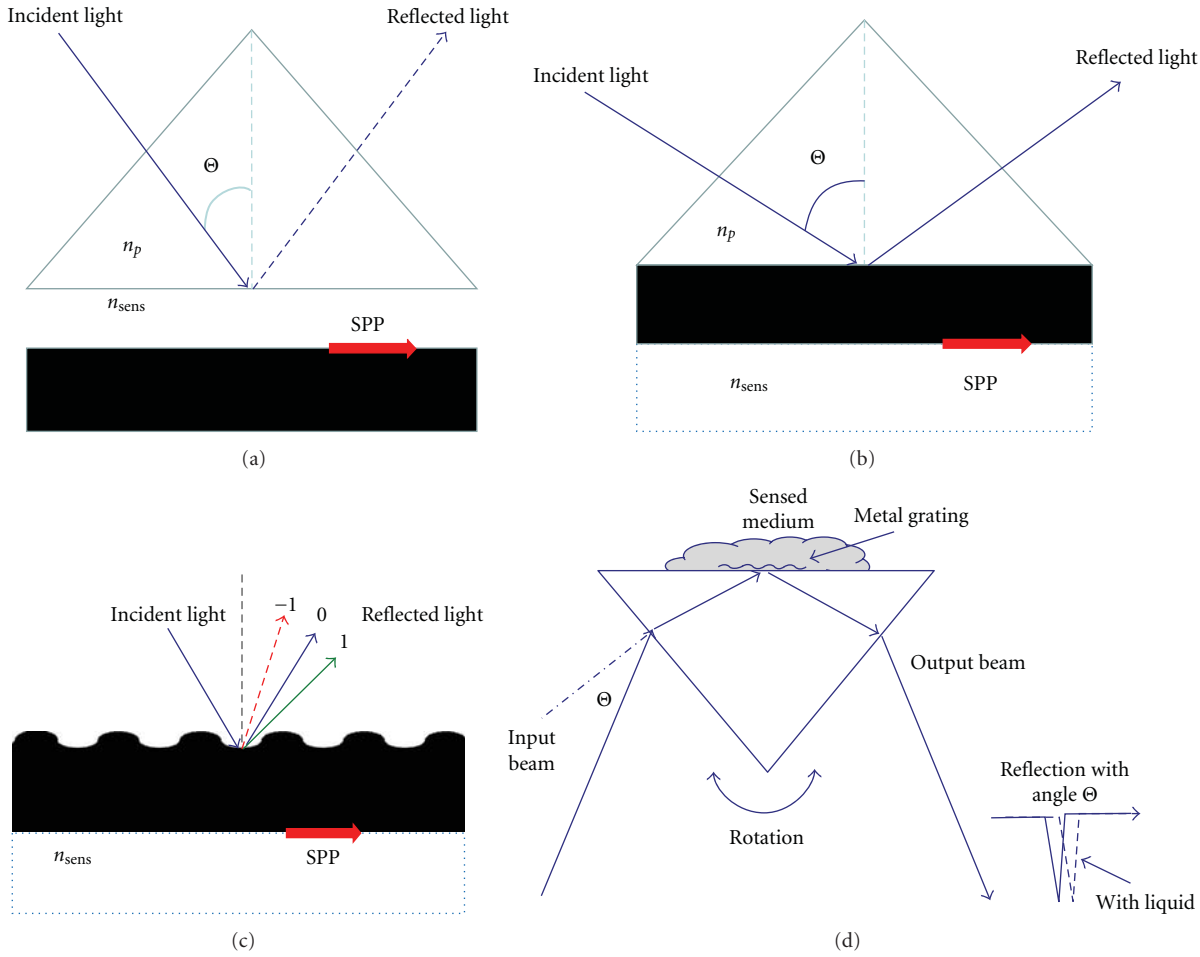

FIGURE 1: (a) Otto configuration for the SPP excitation. (b) Kretschmann configuration for the SPP excitation. (c) Grating coupled SPP system. (d) Practical implementation of an SPP sensor.

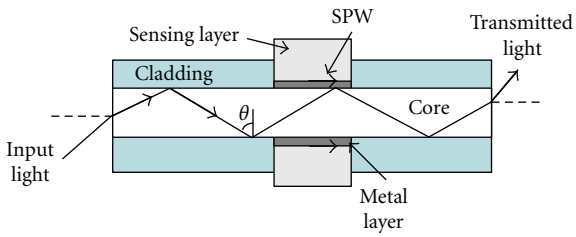

FIGURE 2: One of the widely used Polariton fiber sensor configurations.

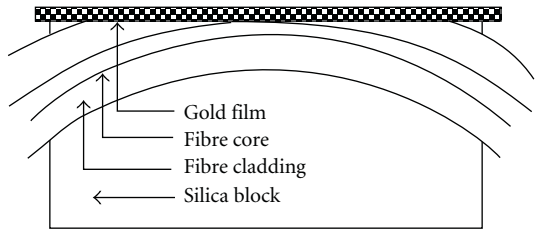

FIGURE 3: Side-polished Polariton fiber sensor.

suitable for surfaces that need to be changed easily. This scheme was modified by Kretschmann and Raether [12] and Kretschmann [13]. In Kretschmann's scheme, a metal layer contacts the prism base (Figure 1(b)). Kretschmann's scheme is one of the most widely used techniques for SPP excitation till now. A scheme with the grating on the top of the structure was also suggested [14] (Figure 1(c)). All these schemes are widely used in sensor application, and a practical configuration is shown in Figure 1(d). The angle, at which the coupling to the Plasmon occurs, changes when a liquid is placed on the surface of the prism. As is clear from Figure 1(d), the angle has to be measured with precision if a high resolution is required. Thus, most of the well-known schemes have elements with a nonplanar geometry and require moving parts and are rather bulky and cumbersome to adjust with high precision. As one can see in Figure 1

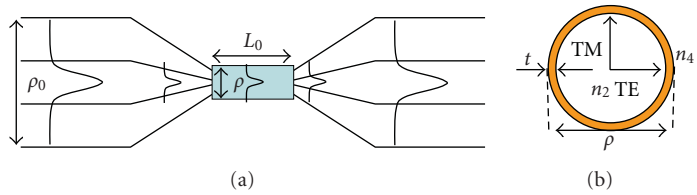

Figure 4: (a) Tapered fiber structure with uniform waist. (b) Cross section of the waist of the fiber with the metal coating.

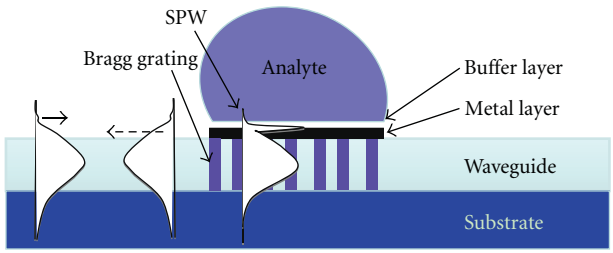

Figure 5: Surface Plasmon resonance sensing structure with Bragg grating.

in these schemes the SPP excitation is based on resonant transfer of the incident photon energy from the free space in the form of *p*-polarized light to a SPP. All these schemes provide the wave-vector matching condition for the incident free space radiation to the SPP with the attenuated total reflection configuration.

3. Guided Wave Surface Plasmon Sensors

Since the SPP excitation with a prism is based on total internal reflection, the coupling prism can be replaced by a waveguide layer of the planar structure of a fiber core to get a compact device easily integrated in any planar or fiber schemes. Indeed propagation of the guided modes in the waveguide layer or in the fiber core is based on total internal reflection. The development of sensors based on the planar and fiber structures began in the early of nineties of last century. During the last two decades, the SPP sensor technique has been widely used for detection of physical, chemical, and biological parameters. We will now present and discuss the most popular, widely used sensor schemes based on fiber or planar structures and review some of the latest ideas in literature.

In the scheme presented in Figure 2 the cladding of the fiber is removed and it is coated with a metal layer, which is surrounded by the sensed medium. However, the radius of the core is very small, and this structure is difficult to fabricate. As an alternative solution a side-polished fiber sensor has also been suggested [15]. This scheme is illustrated in Figure 3. In [16]; a fiber sensor with an asymmetric metal coating on a uniform waist of a single-mode tapered fiber was suggested (a detail is shown in Figure 4). In all these fiber sensors the transmitted guided mode is used in the interrogation process, and a recent review of these fiber sensors can be found in [17].

Planar structures are also widely used for sensor applications. A review of some of these sensors can be found in [18]. In 1999, Ctyroky et al. suggested the use of the reflected guided mode for the monitoring of a sensor [19]. In all these fiber and planar schemes, the sensor element or sensor tool is a surface Plasmon wave (SPW), which has a *hybrid nature*. It consists of the guided mode *coupled* to a surface Plasmon-Polariton as can be seen in Figure 5 [19]. An SPW oscillates in the fiber core or a waveguide layer of the planar structure. Its effective refractive index is only *slightly* different from the effective refractive index of the guided mode supported by the structure without the metal layer. This is because most of the energy is associated with the guided mode and only slightly weighted by Plasmon-Polariton's effective index. This condition means that the hybrid mode is only weakly sensitive to any change in the effective index of the Plasmon, should it be altered by the presence or absence of a surrounding layer.

In 2006, the authors of this paper suggested an improved sensor by the use the "pure" SPP as opposed to the hybrid mode [20]. Contrary to SPW, in this "pure" SPP, almost all the energy is concentrated at the metal-dielectric interfaces.

The "pure" SPP decays exponentially away from the metal surface, including a waveguide layer of the sensor structure. The difference between effective refractive index of the guided mode and effective refractive index of the "pure" SPP is thus large and requires a special scheme to excite the "pure" SPP. This is done with a grating, which allows the wave-vector matching condition to be met. The advantage of using the grating is that it decouples the coupling scheme from the second important parameter—the overlap integral between the guided exciting mode and the "pure" SPP. Since almost all energy of the "pure" SPP is concentrated at the metal-dielectric interface, this scheme is extremely sensitive to small changes in the refractive index of the sensed medium. The value of the change in the effective refractive index of the "pure" SPP caused by the change in the refractive index of the sensed medium depends on the parameters of the structure. A full theoretical model of a hollow core fiber with the Bragg grating imprinted in its waveguide layer (Figure 6) may be found in [21].

Other planar structures with Bragg gratings imprinted into the waveguide layer or the use of a corrugated Bragg grating engraved on the top of the metal layer have also been considered [22, 23]. In these structures the Bragg grating excites a counter-propagating SPP, that is, in the opposite direction to the incident guided mode (Figure 7).

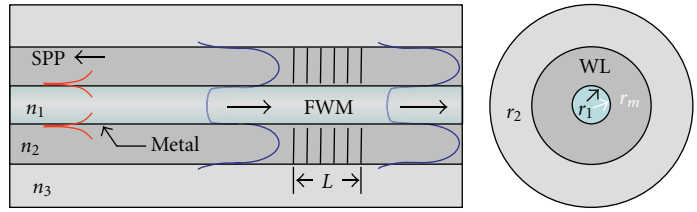

Figure 6: (a) Hollow core sensing structure with Bragg grating. (b) Cross section of the sensor.

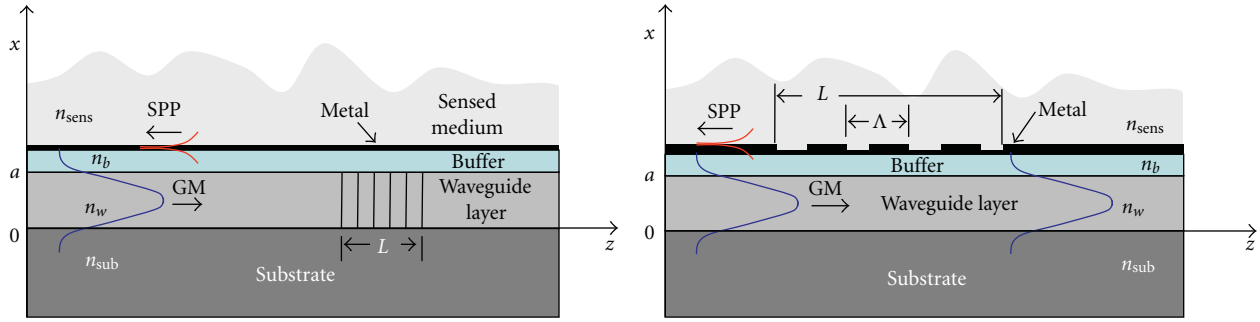

Figure 7: Planar SPP sensor with (a) Bragg grating imprinted into the waveguide layer and (b) Bragg grating engraved on the top of the metal layer.

The guided mode transmitted through the Bragg grating can then be used in the interrogation process. The sensitivity of the structure is characterized by the shift in the wavelength of the grating transmission dip versus the refractive index of sensed medium. The sensitivity of these sensors is ~250 nm/RIU (refractive index units) for optimised structures. This sensitivity does not depend on the Bragg grating (imprinted in the waveguide layer or engraved on the top of the metal layer) used for exciting the counter-propagating SPP.

To increase the sensitivity of the sensor, the Bragg grating may be replaced by a long period grating (LPG) (Figure 8). In these sensor structures the guided mode propagating in the waveguide layer of the structure excites a copropagating SPP. The LPG may be imprinted into the waveguide layer or engraved on the top of the metal layer. The guided mode transmitted through the LPG is then used to interrogate the sensor. The sensitivity of these structures is ~1100 nm/RIU.

The increase in the sensor's sensitivity may be easily explained, by comparing the LPG to the Bragg grating. Indeed, the larger grating period of the LPG is a result of the *difference* between the propagation constants of the guided and SPP modes. On the other hand the shorter period Bragg grating for exciting the counter-propagating SPP is a result of the *sum* of the propagation constants of the guided and SPP modes, since the SPP and the guided modes propagate in opposite directions. Any small change in the refractive index of the surrounding medium (n_{sens}) induces a larger fractional change in the LPG-based sensor as it changes the SPP's propagation constant; that is, if δn is the change in the SPP's effective refractive index for a change in n_{sens}, then the fractional change in the mismatch is

$$\frac{\delta n}{(n^p - n^g)}, \tag{1}$$

where n^p and n^g are the effective indexes of the SPP and guided modes, respectively. In the counter propagating scheme with the Bragg grating, a small change in the propagation constant of the SPP has a smaller fractional influence on the sum of the propagation constants of the SPP and the guided mode as

$$\frac{\delta n}{(n^p + n^g)}. \tag{2}$$

The ratio of the sensitivities of the LPG and the SPG sensors is therefore

$$r \approx \frac{n^p + n^g}{n^p - n^g}. \tag{3}$$

In (3), the ratio r is greater than unity, indicating an enhanced sensitivity for the LPG (copropagating) compared to the SPG-based sensor (counter-propagating).

In all schemes presented in Figures 6, 7, and 8, the intensity of the guided mode transmitted through the grating is used to acquire the information concerning the sensed medium. A novel approach to monitor a planar refractive index sensor with the "pure" SPP used as a sensor tool was suggested in [24]. A variation of this type of sensor may

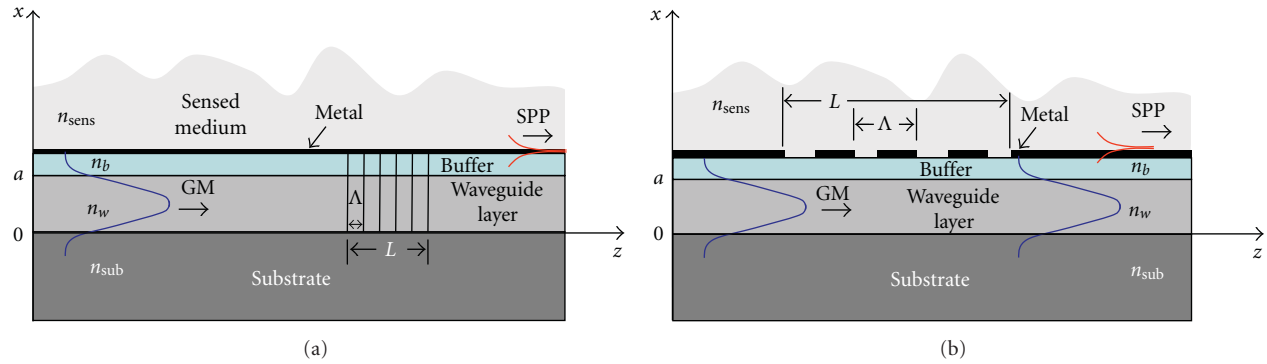

FIGURE 8: Planar SPP sensor with (a) LPG imprinted into the waveguide layer and (b) LPG engraved on the top of the metal layer.

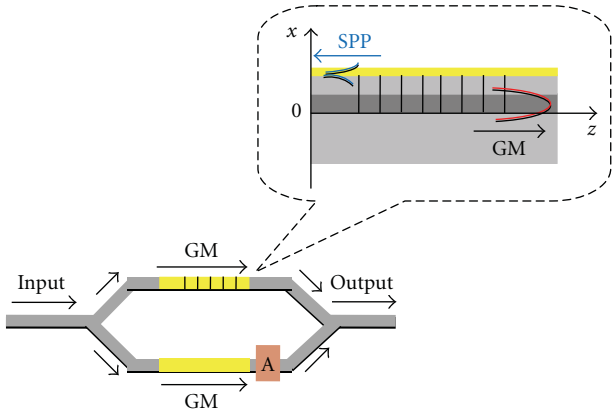

FIGURE 9: GM is the guided mode, and **A** is an attenuator. Insertion illustrates the MZI branch with the Bragg grating. The other MZI branch is identical to the shown one, but without the grating. The SPP travels in the opposite direction if an LPG is used.

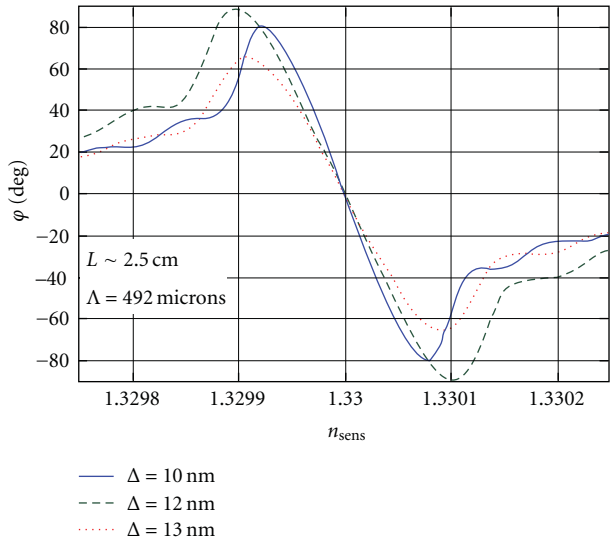

FIGURE 10: Dependence between the refractive index of the sensed medium (n_{sens}) and the phase of the guided mode transmitted through the grating (φ) for three structures with the thickness of the metal layer $\Delta = 10$ nm, $\Delta = 12$ nm, and $\Delta = 13$ nm.

also be found in [25] but is based on the *hybrid* SPP mode. This new interferometric approach is based on the detection of the *phase* of the guided mode transmitted through the grating (Figure 9). Close to the resonance condition, which corresponds to the excitation of the "pure" SPP, a very small changes in the refractive index of the sensed medium causes a dramatic change in the phase of the guided mode transmitted through the grating. The phase detection of the guided mode is performed by a simple integrated optical Mach-Zehnder interferometer (MZI). The sensitivity of the sensor can be characterised by $dn_{sen}/d\varphi$ (RIU/°), where $d\varphi$ is the change in the phase of the guided mode transmitted through the grating, and dn_{sen} is the change in the refractive index of the sensed medium causing the phase change.

The sensitivity of the optimised sensor is $\sim 8 \times 10^{-7}$RIU/° with a linear slope for a refractive index change of 10×10^{-4}, at the operating refractive index of, $n_{sen} = 1.33$ (Figure 10), common for many biological applications. It is important to note that if parameters of the planar structure used in the sensor structure presented in Figure 7(a) are identical to the parameters of the planar structure presented in Figure 9, the sensitivity of the sensor is ~250 nm/RIU. If the Optical Spectrum Analyzer (OSA), used as an interrogation unit, has a resolution 0.01 nm, the resolution of the sensor presented in Figure 7(a) is $\Delta n_{sen}^{min} \approx 4 \times 10^{-5}$. The value of the transmission dip in the guided mode transmission spectrum changes with the change in the refractive index of the sensed medium restricting the dynamic range of this device. The dynamic range of this sensor is defined as the range within which the value of the transmission dip changes in the interval ±0.1 around the chosen value of the transmission dip equal to 0.3 (i.e., 30% dip in transmission) for $n_{sen} = 1.33$. Roughly estimated, this dynamic range turns out to be an interval Δn_{sen} ~0.01.

Interferometric methods enable detection of phase changes below $2\pi \times 10^{-3}$ radians [26]. Using this value as a limit, the resolution of the SPP-interferometer of the sensor, based on phase interrogation and presented in Figure 9, is calculated to be $\Delta n_{sen}^{min} \approx 3 \times 10^{-7}$. The resolution of this sensor is thus extremely high, but the dynamic range, which can be characterised by the linear dependence in Figure 10, is small Δn_{sen} ~0.0005. It is therefore important to remember

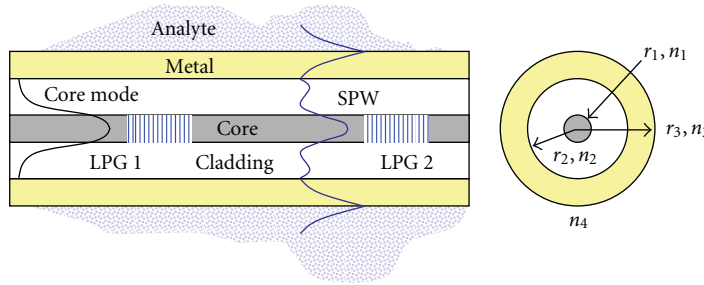

Figure 11: A dual LPG-based SPR sensor. The first LPG couples a guided mode to a particular cladding mode which has a small SPP component (the hybrid mode). The second step is the recoupling of the hybrid surface Plasmon wave back to the guided mode at the output of the fibre. A phase change is imparted by the introduction of the analyte, which detunes the coupling at the second LPG, resulting in an amplitude change at the output [27].

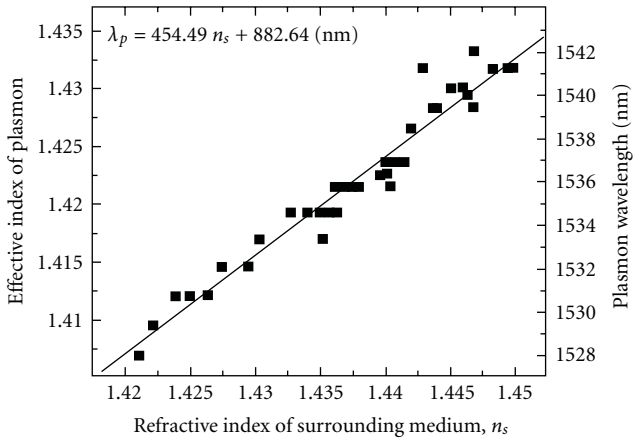

Figure 12: The tilted grating assisted SPR sensor. The guided mode is scattered into a set of counter-propagating cladding modes via the tilted grating. Some are coupled to the SPP in the thin gold layer deposited on the fiber. The introduction on the analyte on the surface of the metal coating changes the details of the resonances spectra at the output [28, 29].

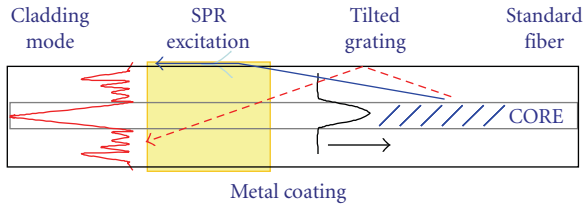

Figure 13: Refractive index of an analyte determined from the changes in the intensities of the cladding mode resonances (Adapted from [28]).

that in the suggested scheme, the Bragg grating is used for exciting the SPP. This means that the excited SPP propagates in an opposite direction to the guided mode (Figure 9). If the Bragg grating is replaced by an LPG, the SPP will copropagate with the guided mode. In the latter case the sensitivity of the sensor can be increased by approximately an order of magnitude; however the dynamic range will be correspondingly reduced by a factor of ten.

Another type of waveguide SPP sensor based on the hybrid mode is shown in Figure 11 [27]. Part of the guided mode is first excited into a cladding mode which then couples to a surface Plasmon-Polariton in the metal layer surrounding the fiber. Any change in the SPP via a refractive index change in the sensed analyte is translated into a phase shift in the propagating cladding hybrid mode, detuning the coupling back into the fundamental guided mode in the core at the second LPG. Thus, the transmitted signal suffers a change in the amplitude through interference of the guided and cladding modes. The overlap of the excited cladding mode with the SPP is small, as seen in Figure 11: the surface Plasmon hybrid-mode has a substantial amount of its energy associated with the guided mode and is therefore intrinsically less sensitive to the surrounding liquid than the "pure" SPP scheme proposed in [20–24]. The second LPG couples the cladding hybrid mode back into the core mode for direct detection.

The use of a tilted grating to excite an SPP in a standard telecommunications fiber has some advantages as the system is quite robust. This has been demonstrated [28] and is shown in Figure 12. The scheme relies on the detailed spectra in transmission of the series of counter-propagating cladding modes scattered by the tilted grating, some of which are coupled to the SPP in a thin gold metal layer on the surface of the fiber. The resonance peaks are predominantly defined by the geometric dimensions of the fiber [30] and *not* by the refractive index of an analyte in contact with the metal layer. This makes the interpretation of the data a bit complicated as there is no *shift* in the resonance peaks, but a redistribution of the energy amongst the peaks, as the phase-matching to the SPR shifts to a different wavelength, and there is no "allowed" mode for the geometry of the fiber. In practice, each cladding mode has some bandwidth, and therefore the amplitude of the coupled mode changes. Using this scheme, it is possible to determine the refractive index of the analyte. Figure 13 shows a measurement result [30], with a resolution of 466 nm/RIU. Allsop et al. [29] demonstrated a similar sensor with a germanium-silver metal layer and tilted Bragg grating but with a much lower resolution (3.4 nm/RIU) compared to the results presented in [27].

More recently, a "holey" fibre was proposed as an SPR gas sensor in the THz frequency regime [31]. This scheme,

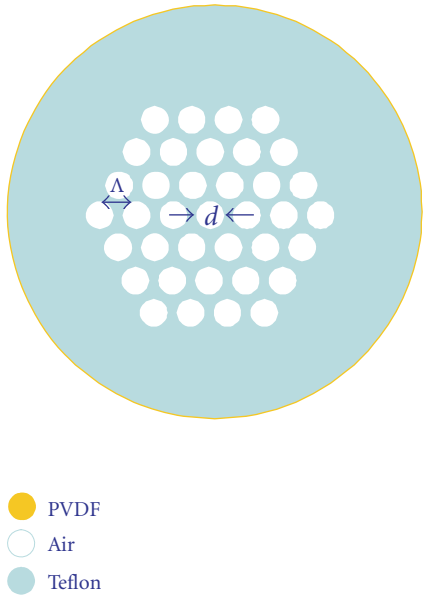

Figure 14: A proposal for a PVDF coated Teflon fibre SPR gas sensor (Adapted from [31]).

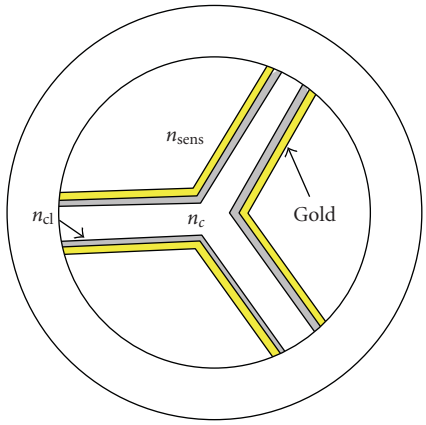

Figure 15: The cross-section of a proposed three section *hybrid mode* SPR sensor [32] in silica glass fiber.

shown in Figure 14, uses a Teflon fibre with a series of holes to introduce a gas into the sensor. The THz guided mode in the Teflon is coupled to the SPP in a ferroelectric outer layer (polyvinylidene: PVDF). The gas introduced into the holes shifts the resonance between the guided mode and the SPP in the THz regime and is thus detected.

Hautakorpi et al. [32] have recently proposed an alternative scheme based on a modified microstructured fiber used by Huy et al. [33]. In this proposal, a *hybrid* SPP mode is excited in the gold layer. The waveguide is a fiber nanowire of refractive index, n_c, supported by three, 120 degree separated strands of glass wires in a multistructured optical fibre. The nanowire mode is thus exposed to three gold-coated surfaces separated from the core by a thin layer of lower refractive index n_{cl}. The liquid to be sensed with a refractive index, n_{sens} is introduced into the three hollow sections as

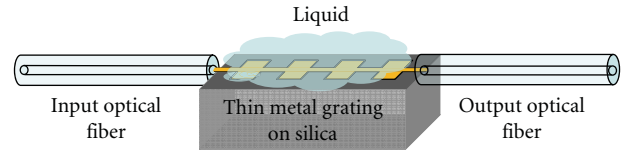

Figure 16: End-fire coupled SPP using a thin SPP *waveguide*. The optical fiber excites the SPP directly, and the metal grating ensures phase-matching [34]. By reducing the lateral dimension, one of the major problems of SPPs, that is, transmission loss, is greatly ameliorated and light can be coupled into the output fiber for making measurements.

shown in Figure 15. Designed to operate at ~550 nm, the refractive index resolution of this sensor is calculated to be $\sim 10^{-4}$. Assuming a minimum measurement capability of 0.1 nm, the sensitivity of the sensor is estimated to be 100 nm/RIU.

In a very elegant scheme using end-fire coupling Jetté-Charbonneau et al. [34] demonstrated in- and out-coupling of an SPP. One of the major hurdles in SPP excitation and out-coupling is propagation loss in the metal. By reducing the transverse dimensions, it is possible to "squeeze" the Plasmon in the transverse dimension. The result of this squeezing is the spreading of the energy into the dielectric, in which the absorption loss is negligible. Using such a scheme, a thin metal layer with a narrow lateral dimension imbedded into a dielectric, end-fire in- and out-coupling was successfully demonstrated. This allows the SPR to propagate centimetres, rather than microns, as is the case for normal SPPs. Figure 16 shows this type of a sensor.

4. Conclusions

As a result of overcoming the propagation loss for SPPs, it is likely that many more waveguide devices will be seen in the future. Several of the fabrication challenges, however, still remain. These include processing of the devices through photolithography and plasma deposition. The metal layer thickness is an important parameter which determines sensitivity, resonance coupling, handling, and robustness of the sensors. Ideally, the metal layers could be printed directly onto plastic substrates and integrated into polymer waveguides or optical fibers. The mass production of these plug-in slides or entirely disposable waveguide sensors is quite conceivable in the near future. Multiple-use of some of these sensors is possible, whilst others will have to remain single-use. For medical applications, it is desirable to have single-use devices to avoid cross contamination, which then demand that the devices should be cheap enough to become disposable. However, it is clear that waveguide-based SPP sensors have many advantages of compactness, ease of in- and out-coupling, high sensitivity, and no moving parts. For clinical use, the instruments have to be not only low cost but reliable as well. The advances in waveguide SPP sensors will certainly have an impact in reducing costs of traditionally expensive surface Plasmon resonance sensor instruments, based, for

example, on the highly reliable Kretchmann technique, and therefore should be available commercially in the near future.

Acknowledgments

The first author acknowledges support from the Government of Canada's Canada Research Chairs Program as well as the Canadian Natural Science and Engineering Research Council's Strategic Grants program.

References

[1] R. W. Wood, "On a remarkable case of uneven distribution of light in a diffraction grating spectrum," *Proceedings of the Physical Society of London*, vol. 18, no. 1, pp. 269–275, 1902.

[2] H. Raether, *Surface Plasmons*, Springer, Berlin, Germany, 1988.

[3] H. Raether, *Surface Plasmons on Smooth and Rough Surfaces and on Gratings*, Springer, Berlin, Germany, 1988.

[4] K. Park, B. J. Lee, C. Fu, and Z. M. Zhang, "Study of the surface and bulk polaritons with a negative index metamaterial," *Journal of the Optical Society of America B*, vol. 22, pp. 1016–1023, 2005.

[5] C. Nylander, B. Liedberg, and T. Lind, "Gas detection by means of surface plasmon resonance," *Sensors and Actuators*, vol. 3, pp. 79–88, 1982.

[6] H. Kano and W. Knoll, "Locally excited surface-plasmon-polaritons for thickness measurement of LBK films," *Optics Communications*, vol. 153, no. 4–6, pp. 235–239, 1988.

[7] H. Kano and W. Knoll, "A scanning microscope employing localized surface-plasmon-polaritons as a sensing probe," *Optics Communications*, vol. 182, no. 1–3, pp. 11–15, 2000.

[8] D. Kim, "Effect of the azimuthal orientation on the performance of grating-coupled surface-plasmon resonance biosensors," *Applied Optics*, vol. 44, no. 16, pp. 3218–3223, 2005.

[9] S. Patskovsky, A. V. Kabashin, M. Meunier, and J. H. T. Luong, "Silicon-based surface plasmon resonance sensing with two surface plasmon polariton modes," *Applied Optics*, vol. 42, no. 34, pp. 6905–6909, 2003.

[10] S. Patskovsky, A. V. Kabashin, and M. Meunier, "Properties and sensing characteristics of surface-plasmon resonance in infrared light," *Journal of the Optical Society of America A*, vol. 20, pp. 1644–1650, 2003.

[11] A. Otto, "Excitation of nonradiative surface plasma waves in silver by the method of frustrated total reflection," *Zeitschrift für Physik*, vol. 216, no. 4, pp. 398–410, 1968.

[12] E. Kretschmann and H. Raether, "Radiative decay of non radiative surface plasmons excited by light," *Zeitschrift für Naturforschung. Teil A*, vol. 23, pp. 2135–2136, 1968.

[13] E. Kretschmann, "Decay of non radiative surface plasmons into light on rough silver films. Comparison of experimental and theoretical results," *Optics Communications*, vol. 6, no. 2, pp. 185–187, 1972.

[14] I. R. Hooper and J. B. Sambles, "Surface plasmon polaritons on narrow-ridged short-pitch metal gratings in the conical mount," *Journal of the Optical Society of America A*, vol. 20, pp. 836–843, 2003.

[15] J. Homola and R. Slavik, "Fiber-optic sensor based on surface plasmon resonance," *Electronics Letters*, vol. 32, pp. 480–482, 1996.

[16] D. Monzon-Hermandez, J. Villatoro, D. Talavera, and D. Luna-Moreno, "Optical-fiber surface-plasmon resonance sensor with multiple resonance peaks," *Applied Optics*, vol. 43, no. 6, pp. 1216–1220, 2004.

[17] A. K. Sharma, R. Jha, and B. D. Gupta, "Fiber-optic sensors based on surface plasmon resonance: a comprehensive review," *IEEE Sensor Journal*, vol. 7, pp. 1118–1129, 2007.

[18] J. Homola, S. S. Yee, and G. Gauglitz, "Surface plasmon resonance sensors: review," *Sensors and Actuators B*, vol. 54, no. 1, pp. 3–15, 1999.

[19] J. Ctyroky, F. Abdelmalek, W. Ecke, and K. Usbeck, "Modelling of the surface plasmon resonance waveguide sensor with Bragg grating," *Optical and Quantum Electronics*, vol. 31, no. 9, pp. 927–941, 1999.

[20] G. Nemova and R. Kashyap, "Fiber-Bragg-grating-assisted surface plasmon-polariton sensor," *Optics Letters*, vol. 31, no. 14, pp. 2118–2120, 2006.

[21] G. Nemova and R. Kashyap, "Modeling of plasmon-polariton refractive-index hollow core fiber sensors assisted by a fiber Bragg grating," *Journal of Lightwave Technology*, vol. 24, no. 10, pp. 3789–3796, 2006.

[22] G. Nemova and R. Kashyap, "Theoretical model of a planar integrated refractive index sensor based on surface plasmon-polariton excitation," *Optics Communications*, vol. 275, no. 1, pp. 76–82, 2007.

[23] G. Nemova and R. Kashyap, "A compact integrated planar-waveguide refractive-index sensor based on a corrugated metal grating," *Journal of Lightwave Technology*, vol. 25, no. 8, pp. 2244–2250, 2007.

[24] G. Nemova, A. V. Kabashin, and R. Kashyap, "Surface plasmon-polariton Mach-Zehnder refractive index sensor," *Journal of the Optical Society of America B*, vol. 25, pp. 1673–1677, 2008.

[25] A. K. Sheridan, R. D. Harris, P. N. Bartlett, and J. S. Wilkinson, "Phase interrogation of an integrated optical SPR sensor," *Sensors and Actuators B*, vol. 97, no. 1, pp. 114–121, 2004.

[26] A. V. Kabashin, V. E. Kochergin, and P. I. Nikitin, "Surface plasmon resonance bio- and chemical sensors with phase-polarisation contrast," *Sensors and Actuators B*, vol. 54, no. 1, pp. 51–56, 1999.

[27] Y.-J. He, Y.-L. Lo, and J.-F. Huang, "Optical-fiber surface-plasmon-resonance sensor employing long-period fiber gratings in multiplexing," *Journal of the Optical Society of America B*, vol. 23, no. 5, p. 80, 2006.

[28] Y. Y. Shevchenko and J. Albert, "Plasmon resonances in gold-coated tilted fiber Bragg gratings," *Optics Letters*, vol. 32, no. 3, pp. 211–213, 2007.

[29] T. Allsop, R. Neal, S. Rehman, D. J. Webb, D. Mapps, and I. Bennion, "Generation of infrared surface plasmon resonances with high refractive index sensitivity utilizing tilted fiber Bragg gratings," *Applied Optics*, vol. 46, no. 22, pp. 5456–5460, 2007.

[30] R. Kashyap, *Fiber Bragg Gratings*, section 4.7., Academic Press, 1999.

[31] A. Hassani and M. Skorobogatiy, "Surface Plasmon resonance-like integrated sensor at terahertz frequencies for gaseous analytes," *Optics Express* , vol. 16, no. 25, p. 20206, 2008.

[32] M. Hautakorpi, M. Mattinen, and H. Ludvigsen, "Surface-plasmon-resonance sensor based on three-hole microstructured optical fiber," *Optics Express*, vol. 16, no. 12, pp. 8427–8432, 2008.

[33] M. C. P. Huy, G. Laffont, V. Dewynter, et al., "Three-hole microstructured optical fiber for efficient fiber Bragg grating

refractometer," *Optics Letters*, vol. 32, no. 16, pp. 2390–2392, 2007.

[34] S. Jetté-Charbonneau, R. Charbonneau, N. Lahoud, G. Mattiussi, and P. Berini, "Demonstration of Bragg gratings based on long-ranging surface plasmon polariton waveguides," *Optics Express*, vol. 13, no. 1, p. 4679, 2005.

Hindawi Publishing Corporation
Journal of Sensors
Volume 2009, Article ID 607647, 12 pages
doi:10.1155/2009/607647

Review Article

Planar Bragg Grating Sensors—Fabrication and Applications: A Review

I. J. G. Sparrow,[1] P. G. R. Smith,[1] G. D. Emmerson,[1] S. P. Watts,[1] and C. Riziotis[2]

[1] *Stratophase Ltd, Unit A7, The Premier Centre, Premier Way, Romsey SO51 9DG, UK*
[2] *Theoretical and Physical Chemistry Institute, The National Hellenic Research Foundation (NHRF), 48 Vassileos Constantinou Avenue, 11635 Athens, Greece*

Correspondence should be addressed to I. J. G. Sparrow, ian.sparrow@stratophase.com

Received 5 April 2009; Accepted 13 July 2009

Recommended by Valerio Pruneri

We discuss the background and technology of planar Bragg grating sensors, reviewing their development and describing the latest developments. The physical operating principles are discussed, relating device operation to user requirements. Recent performance of such devices includes a planar Bragg grating sensor design which allows refractive index resolution of 1.9×10^{-6} RIU and temperature resolution of 0.03°C. This sensor design is incorporated into industrialised applications allowing the sensor to be used for real time sensing in intrinsically safe, high-pressure pipelines, or for insertion probe applications such as fermentation. Initial data demonstrating the ability to identify solvents and monitor long term industrial processes is presented. A brief review of the technology used to fabricate the sensors is given along with examples of the flexibility afforded by the technique.

1. Introduction

A wide range of optical sensing technologies exist and are subject to intensive development due to a number of driving factors. In the fields of process control and automation for example, there is a desire to monitor concentrations and compositions in real time without the risk of damaging or contaminating high-value product. It is common for such applications to occur in volatile or flammable environments where spark-free or intrinsically safe technology is a prerequisite. Whilst there are many fields with disparate motivations and sensing requirements, they do in many ways share a common goal, that of rapid, accurate, and safe detection in a potentially harmful environment.

Existing review papers discuss the broad range of optical sensing technologies [1] and the motivations for using an integrated optical format in terms of compatibility with microfluidics [2]. In this paper we concentrate on a review of results on planar Bragg grating sensors which are a recent addition to the field and offer attractive advantages.

A detailed description of the range of different techniques and technologies available from the generic class of "optical sensors" would form an extensive review and could include a vast array of applications from particle counting to vibration detection. Therefore the various optical sensor technologies may be segmented in a wide number of ways, but it is helpful to distinguish between sensors in which the light does not physically pass into the measurand material (such as a Bragg grating sensor for strain) and sensors in which the optical field does pass into the measurand. In this paper we are concerned with the latter type of device. It is further useful to consider the means by which the light interacts; this may be either through the refractive index of the measurand or via an absorption or other energy exchanging interaction with the measurand. In that sense we can choose to characterise both types of linear properties of the light interacting in the material via a complex refractive index ($n^* = n - i\kappa$) where n is the real index at a particular wavelength and κ represents the absorption. There are, of course, nonlinear interactions too, such as the Raman effect—which are outside of the scope of this paper.

By thinking in terms of the complex refractive index we can choose to classify techniques into either ones that make use of the imaginary part ($i\kappa$) such as absorption

spectroscopy, and those that make use of the real part of the index (n) such as refractometry. In these terms we see that absorption spectroscopy can be viewed as investigating how ($i\kappa$) varies with wavelength. However, in this paper we are primarily interested in those techniques that make use of the refractive index properties of the measurand, and particularly techniques in which the light interaction in the sensor and measurand modifies the modal properties of the light. A modal picture is familiar in fibre optics where a mode represents a solution to the laws of electromagnetic propagation that is constant in form along an invariant refractive index structure. This modal concept is distinct from refractive index properties (such as are used in a refractometer) in which the light propagation is effectively free space like with refraction occurring at a set of discrete boundaries. Thus from the huge possible range of sensor technologies we are led to consider firstly those that primarily sense the real part of the refractive index and then specialise to those techniques in which modal interactions are used.

Within this category of modal devices the most familiar devices make use of surface plasmon resonance [3] and provide a well-established technology [4, 5]. Such plasmon devices are well established in literature; for a recent review of plasmonics the book by Maier [6] provides a wealth of information. Plasmon-based sensors are used in a number of commercial instruments produced by companies such as Biacore, Biosensing Instruments Inc, Sensata, and ICx Nomadics. In a Plasmon type sensor the light propagation and modal properties are strongly dependent on the properties of a thin film of a metallic conductor (most commonly gold), in which the modal coupling properties are modified by the refractive index of the surrounding dielectric (the measurand).

In contrast to SPR sensors, the types of devices in this paper make use of dielectric waveguides in which there are no metallic elements and in which the modal properties are dominated by the real part of the refractive index of the waveguide and of the measurand. The most familiar format for such a device is an optical fibre sensor. A recent review article can be found [7] which covers the whole area of fibre sensing. In this review we are specifically interested in devices in which guidance occurs by total internal reflection in a higher index core, and where the waveguide structure is processed to allow light to interact with a measurand fluid. This interaction causes a change in optical path length, which can be sensed in a number of ways but typically is either interferometric or via a change in the response of a grating structure. More recently, researchers have started to exploit the advantages of planar integration as a way to allow enhanced functionality devices to be made in which microfluidics and multiple sensor elements can be incorporated into a single device. Such devices have a common physical operating principle, in that they all operate by having a dielectric waveguide in which the propagating mode is allowed to partially interact with the measurand, and where the optical path change associated with that interaction is measured. For example work by Heideman et al. [8] describes the operation of a Mach-Zehnder sensor which measures fringe changes in the interferometer output; in contrast early work by Tiefenthaler [9] used a surface grating to measure water absorption on a planar waveguide. More recently work by Schroeder et al. [10] showed how multiple gratings at different operating wavelengths may be used to measure and correct for temperature variation and also gain information on the variation of refractive with wavelength; however, this device used a side-polished fibre embedded in a block, which is not simple to fabricate.

A relatively small number of Bragg grating-based devices have been considered and implemented in planar form. They have been demonstrated in a variety of different material platforms such as in polymers [11–14], Sol-gel systems [15], Silicon-on-Insulator SOI [16, 17], Lithium Niobate [18], and Silica-on-Silicon [19, 20].

The wave-guiding and grating structures in Bragg-based optical sensors have been fabricated with a number of approaches leading to sensing elements with ridge waveguides [21], UV written waveguides and gratings [19, 20], corrugated/etched Bragg gratings [22, 23], or even Bragg gratings through selective precipitation of nanoparticles [24].

However a very limited number of designs have been proved viable in terms of commercialisation. Recently, Stratophase Ltd has commercialised a direct UV writing technology following its original development at the University of Southampton [19, 20]. The method allows the inscription of waveguides and gratings onto planar substrates. This technique enjoys the benefits of planar integration and ease of applying microfluidics and also makes use of telecommunication grade single mode fibre components and measurement technology allowing for tremendous refractive index sensitivity while exploiting the temperature compensation advantages first demonstrated by Schroeder et al. [10].

Moving on from consideration of the physical mechanisms, in the context of the work presented here, perhaps the most widely used tool is the benchtop refractometer upon which samples taken from processing steps are analysed in a lab to determine solution concentrations or sugar, alcohol, or solvents. Inline variants of this style of equipment have started to reach the market in recent years so that offline measurements may be replaced with at-line or inline measurements to save time, money and reduce safety and contamination concerns. Generally these tools require an electrical signal at the point of measurement which can be problematic in volatile environments which require intrinsically safe equipment to minimise the risk of explosion.

This paper presents a review of recent advances that have been made in the development of an optical sensor that has proven to be suitable in the application areas described above. The sensor, an evanescent wave device based on planar Bragg gratings, offers both the required sensitivity for concentration measurements and process monitoring and is also suited to industrial environments where robust and reliable devices must be installed. The all optical measurement means that there is no ignition risk, making the technology highly suitable for volatile environments. Additionally, because the underlying principles are the same as those used in the field of telecommunications, multiple

devices may be networked and multiplexed over very large distances. Multiple devices located at separate and distant locations can easily be monitored from a single analysis base station to maximise convenience and minimise cost.

To describe the sensing technology, an overview of the fabrication technique and its advantageous features is given. This is followed by an analysis of the device sensitivity to refractive index and temperature. To complete the presentation two examples of industrial applications are given.

2. Background

The core technology of the sensors discussed here is that of the Bragg grating, a structure that has been known for decades and has always been recognised as having the potential for use as a sensing element. Most commonly employed in optical fibres, the Bragg grating reflects optical wavelengths according to the following relation:

$$\lambda_B = 2\Lambda n_{\text{eff}}, \tag{1}$$

where λ_B is the Bragg wavelength at which maximum reflectivity occurs. Λ provides the period of the refractive index modulation that defines the grating. The effective index of the waveguide that contains the Bragg grating, n_{eff}, is a combined refractive index of the core and cladding that the optical mode interacts with.

From this equation it can be seen that as the material surrounding the Bragg grating changes, variation in the effective refractive index causes the reflected wavelength to shift. This forms the basis of the use of Bragg gratings as sensors and is shown conceptually in Figure 1.

The specific devices that will be outlined in the subsequent discussion use the technique of UV writing. This approach is highly flexible and has been highly refined for the creation and postfabrication trimming [25] of optical devices suitable for, amongst other applications, the telecommunications industry.

The sensors described here are fabricated using a unique extension to the UV writing technology known as Direct Grating Writing which simultaneously creates a waveguide and a Bragg grating in a planar substrate.

Early work on the conversion of the UV written substrates into liquid sensors has been presented along with demonstrations of their use as tunable filters and refractometers. Whilst this early work highlights some of the opportunities for such devices, the level of development was not initially suited towards full commercial exploitation.

Such planar Bragg grating devices are appealing for sensing applications for several reasons.

(1) Multiple wavelengths may be used offering the possibility for analyte identification through optical dispersion measurements and also providing a range of evanescent field penetration depths which may provide additional information on the dimensions of biological entities.

(2) Multiple separate sensing regions may be incorporated onto a single sensor chip. This can be an advantage particularly in immunoassay-based biodetection where it is advantageous to test for multiple different targets simultaneously without the need for duplication of equipment or time delays.

(3) The monolithic silicon chip-based design is robust, requires no electrical signal, is resistant to a wide range of chemicals, and is thus suitable for deployment in a wide range of environments.

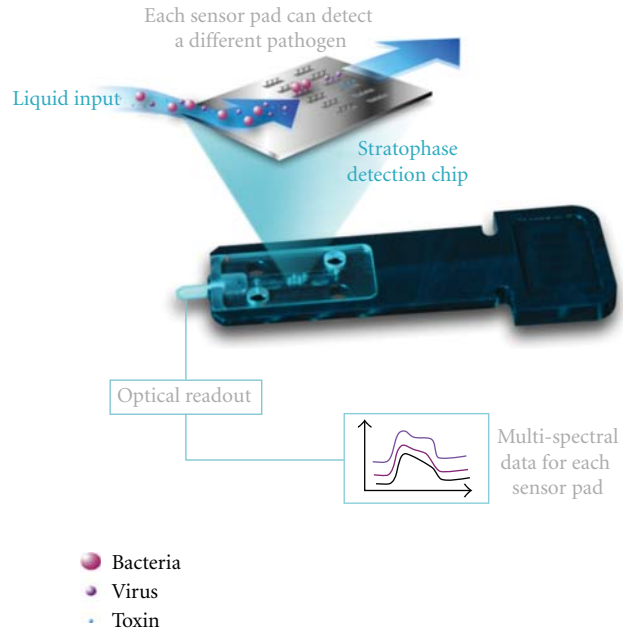

Figure 1: Representation of the interaction between liquid and a Stratophase sensor chip that is mounted in a microfluidic cell. In this case a functionalised chip for the purposes of specific biological detection is shown.

In order to get the maximum possible performance from a Bragg sensor the optical interrogation method is critical. Many industrial applications require multiple measurements to be made 24 hours per day, and so relatively high capital cost can be tolerated as the cost is shared. For top end performance the interrogation can come at a relatively high financial cost although technology improvements and commercial competition provide a strong drive for cost reduction over time. Additionally, the devices presented here are designed to operate in the telecommunications wavelength band. As such it is possible to have sensors positioned at up to several kilometre distances from the optical source. More advantageous still, signals from multiple sensors at different locations may be multiplexed in such a way as to have many sensors all monitored by a single read-out unit. Thus the cost per sensor, which is often more important than total cost, is dramatically reduced. Furthermore, the cost per *measurement* is lower still because of the opportunity to incorporate multiple sensing regions on a single chip.

In addition there is the possibility to integrate the sensing element with the interrogation system by deploying, for example, Bragg grating or Arrayed Waveguide Gratings

[26–28] within the same chip, a technology that is highly compatible and readily available in the Silica-on-Silicon platform. This combination could lead to compact and self-contained sensing systems.

3. Fabrication of Sensors

3.1. UV Writing. In a method similar to prior work [29] and shown in Figure 2, Bragg gratings and waveguides are written into a three-layer silica on silicon substrate using the DGW technique.

The UV writing process utilises the photosensitivity of Germanium doped silica. Exposure of the silica to UV light at 244 nm causes an increase in the refractive index. The three layer samples are fabricated by flame hydrolysis deposition such that the silica is deposited onto a silicon substrate. The middle layer is doped with germanium to provide a photosensitive layer that may be exposed to UV to raise the refractive index.

High-pressure hydrogen loading is used as a method of enhancing the photosensitive response immediately prior to UV exposure. Similar techniques are used in the fabrication of fibre Bragg gratings prior to UV exposure for grating inscription. The planar samples are placed into hydrogen at 120 bar for three days in order to allow hydrogen to diffuse through to the glass layer, that is, to act as the waveguide core. After hydrogen loading chips may be kept for many days in dry ice before UV writing. Once removed from cold storage they may be kept at room temperature for in excess of an hour before out-diffusion of hydrogen becomes a significant issue. The initial out-diffusion of hydrogen can result in a slight change of Bragg wavelength due to a reduction in photosensitivity over time. This may be compensated for with a well-controlled UV writing process if required. However in this application it is not the UV writing process that determines sensitivity to refractive index. It is in fact the later processing stages of etching and over-layer deposition described in Section 3 that determine overall performance. Thus long UV writing times may be used, and complex structures may be written without the need for any other special precautions.

Controlled, localised irradiation of the silica with a sufficiently high fluence after hydrogen loading allows well-defined waveguide structures to be created. For the work reported here, a frequency doubled argon-ion laser is used to produce the UV beam for irradiation. The beam is conditioned and focussed down to a five micron diameter spot in a fixed location. Samples for UV writing are mounted on an air-bearing translation stage which allows three dimensional movement of the photosensitive substrate to a spatial resolution better than 10 nm.

The most direct method of creating a waveguide is to simply translate the sample at a constant speed under the UV beam at a constant power. However, to allow the inscription of both Bragg gratings and waveguides this simple arrangement is extended. Using a beam splitter and carefully positioned mirrors an interferometer is created such that the UV beam is recombined to create an interference pattern. This pattern, when incident on a photosensitive sample, will create a corresponding refractive index modulation in the core layer. The period of the interference pattern is set to be 530 nm, a period which when combined with the refractive index of the core layer can be used to create a Bragg grating reflecting at 1550 nm.

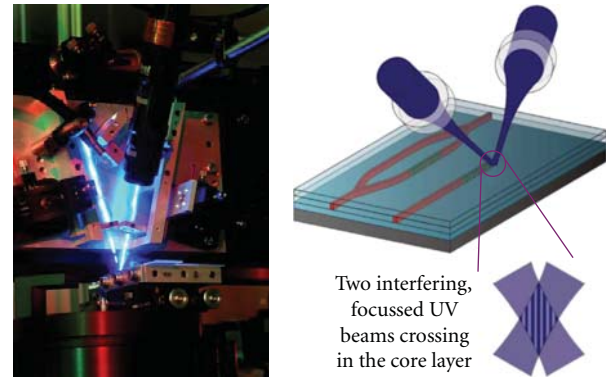

Figure 2: Photographic and diagrammatic representation of the UV writing process with crossing UV beams focussed onto the photosensitive substrate.

The interference pattern cannot simply be translated across the sample to create a Bragg grating. A static exposure would, in effect, create a very short Bragg grating of just a few grating planes in length. However, upon translating the sample this refractive index modulation would be "smeared out" in the direction of translation. This destroys the periodic refractive index modulation resulting in a uniform increase in the refractive index. Thus, translation of the sample beneath a continuous UV spot results in the formation of an unmodulated waveguide. To create, a Bragg grating the UV beam must be modulated as the sample is translated under the UV beams. Monitoring the position of the sample as it is translated and briefly turning on the UV beam every time the sample has moved by one grating period causes the pattern of refractive index modulation to be repeatedly written into the sample. This occurs in such a way that each pattern is shifted by precisely one period relative to the previous one. In other words, as the sample is translated a Bragg grating is written into the sample. To change from Bragg grating to waveguide the UV beam is simply returned to its former nonmodulating state. In this way, a single process may be used to write both waveguides and Bragg gratings into a sample in a single but highly flexible process. Accurate control of the UV switching is achieved by using the high precision position information from the translation stages to drive an acousto-optic modulator.

3.2. Grating Parameters. A number of parameters may be controlled in order to tailor the Bragg gratings and waveguides. The primary factor in UV writing is the fluence used to write the waveguide and grating structures. A higher UV power (or a lower translation speed) gives a higher fluence, resulting in larger changes in refractive index.

The relationship between translation speed and the rate at which the UV beam is modulated plays an important role in the creation of Bragg structures. Variation of the duty cycle can be used to control the strength of the Bragg grating. Duty cycle refers to the percentage of time that the UV beam is turned on in the process of writing a Bragg grating. Previously, the modulation of the UV beam whilst the sample is translated was discussed. The duration of this modulation as a percentage of the Bragg period gives the duty cycle. A duty cycle of 100 percent results in a waveguide with no refractive index modulation whilst a duty cycle of 0 percent results in no refractive index change being written into the sample whatsoever.

It is desirable for the average refractive index of a Bragg grating to be close to, if not identical to, the waveguide at either end of the grating. Although the link between UV power and induced refractive index change is not perfectly linear, to a close approximation fluence and duty cycle may be used to index match waveguides and gratings very simply. A grating written with a 50-percent duty cycle with a given UV power must be translated under the UV beam at half the speed used for a waveguide written with the same power. This gives the same fluence and therefore approximately the same average refractive index in both the grating and waveguide. Similarly a 90-percent duty cycle grating would be translated at 90 percent of the waveguide translation speed to "fluence match" the two structures. This simple relation is possible because the waveguides and gratings are being written into a "blank" substrate where no waveguide exists beforehand. In the case of fibre Bragg gratings this is slightly different as the gratings are added to a pre-existing waveguide, and so the average index of the waveguide and fibre cannot be the same unless special extra steps are taken.

Duty cycle may also be used to change the strength of the Bragg gratings written. Generally speaking, a higher duty cycle results in a lower contrast between the grating planes resulting in a more response with a more narrow bandwidth than one written with lower duty cycles.

An additional degree of flexibility may be achieved by modulating the UV beam at a rate very slightly different to the intrinsic period of the UV intensity modulation. The cumulative effect of the multiple UV exposures used to create a grating produces a grating with a period that is equal to the period between exposures, not the intrinsic period of the interference pattern. [30]. In this way, gratings may be written spanning hundreds of nanometer using exactly the same process.

Refinement of the UV writing process has allowed an immensely flexible technique for waveguide and grating production to be developed. Using specially developed software packages it becomes a simple matter to create scripts which when loaded into the UV writing system can produce straight and curved waveguides with sophisticated grating structures at multiple wavelengths in a single process. Not only can bespoke waveguide and grating designs be rapidly created without the need for expensive phase masks but also no clean room facilities are needed, making the overall infrastructure requirements low.

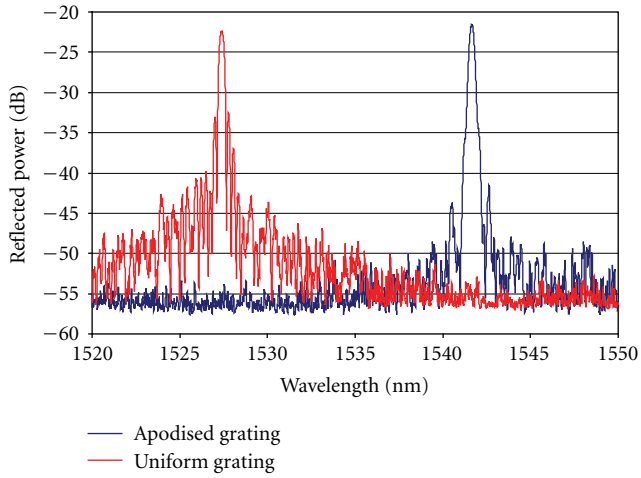

Figure 3: Comparison of reflection spectra of uniform and apodised gratings.

Some examples of grating spectra that may be written using this process are given below. All structures were created using the same proprietary software package to create the required grating responses.

Figure 3 compares a straightforward uniform grating with another grating of similar properties but which has been apodised using a cosine squared function. The reduction in sidelobes is clear albeit at the expense of a slightly broader reflection peak.

As the gratings are written in a manner that is close to being plane by plane, it is straightforward to achieve high levels of control of the grating structure along its length. For example, phase shifts may be inserted in order to achieve a sharp dip in the reflection response which may in some cases be advantageous when determining the centre wavelength of peaks. Such a spectrum is shown in Figure 4.

Periodic spacing of phase shifts can be used to generate more elaborate grating structures which provide multiwavelength responses. An example of this is given in Figure 5, which is a demonstration of a superstructured grating providing over 15 wavelengths that may be used for sensing purposes over a 130 nm wavelength span. This grating, just 4 mm in length, opens up opportunities to measure refractive index over sufficiently wide ranges to allow dispersion characterisation and thus material fingerprinting to be performed.

This approach may be extended, as shown in Figure 6, to use multiple superstructured gratings that are interlaced such that they allow a greater spectral density of measurements to be performed from a compact device which is again written in a single step onto a single device that is just millimetres in dimensions.

Drawing on the technology of fibre Bragg gratings it should be possible, if required, to fully control the spectral properties of Bragg gratings through the use of novel design strategies employed in fibres [31] and then implement them through the DGW fabrication technique. This advantage gives this particular planar platform further flexibility to

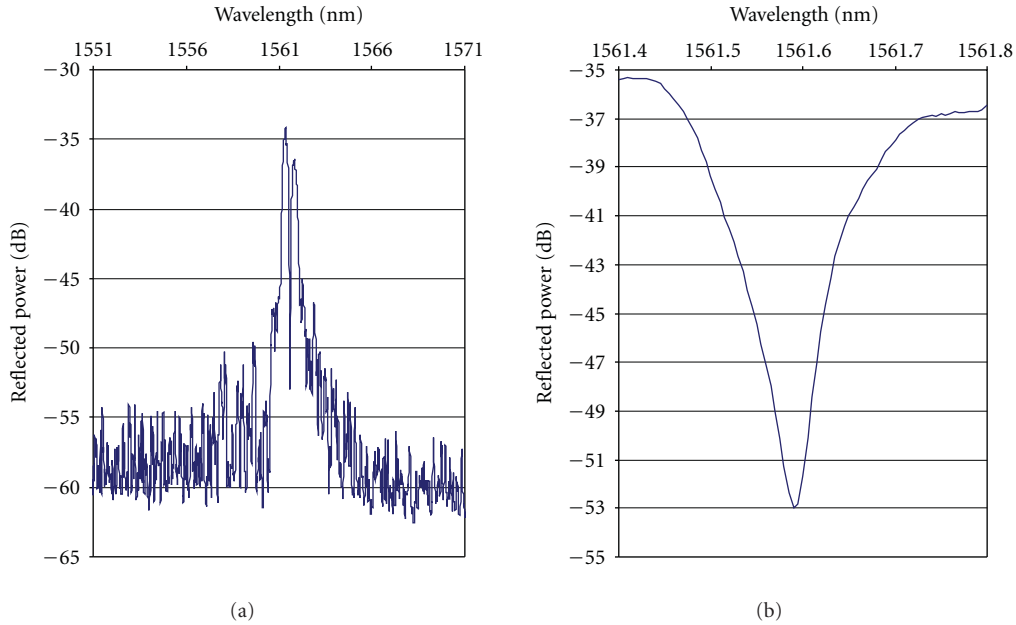

Figure 4: Example of a phase-shifted Bragg grating with a deep transmission dip written by DGW. The grating used here has a total length of 3 mm.

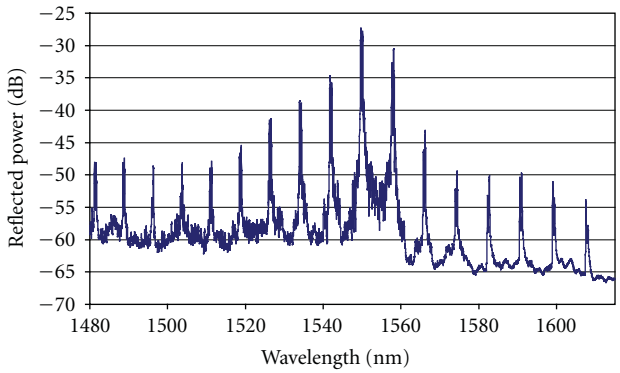

Figure 5: Wide span reflection spectrum of a superstructured grating written into a planar sensor chip.

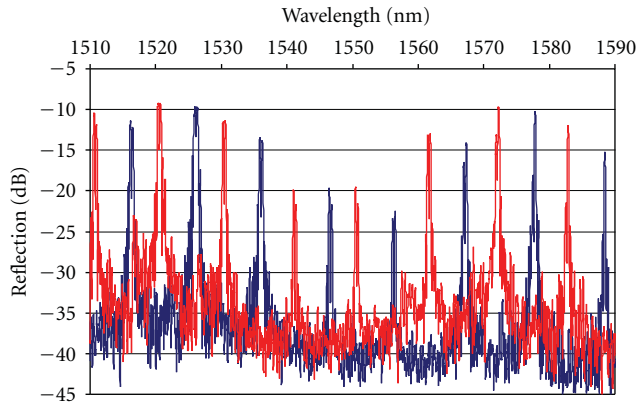

Figure 6: Reflection spectra of two interlaced superstructure Bragg gratings on separate waveguides. These allow multiple wavelengths to be measured in a single sensing region on a single chip.

develop customised purpose-oriented sensors combined in a compact integrated form.

3.3. Creating a Sensor. In their as-written state, the UV written samples are intrinsically sensitive to temperature or stress and can be used as sensors in a manner comparable to that widely used in fibre sensing [7]. To exploit the advantages of the planar geometry this temperature sensing ability may be combined with multiple liquid refractive index sensing regions. Conversion to a sensor uses relatively simple principles. The Bragg wavelength of a grating is determined by the effective index of the waveguiding structure in which the grating is defined. In other words the combined refractive indices of the waveguide core and cladding play a key role in setting the wavelength or wavelengths at which the Bragg grating operates. If we remove the upper cladding and replace it with something else, the effective index and thus the Bragg wavelength is changed. In this way, the device can now be made into a sensor. Liquid that is used to replace the upper cladding in the vicinity of the Bragg grating will control the Bragg wavelength. As the properties of that liquid change, so the Bragg wavelength changes.

The cladding over the sensor gratings is removed using a wet etch. The etchant is delivered to the silica surface using a microfluidic flow cell which allows the chemical to come into contact with only the areas of the chip where etching is required. The Bragg response is monitored throughout the etching process to ensure that the etch is allowed to proceed until sufficiently deep to ensure that the cladding is removed but that it is stopped before the response is degraded by

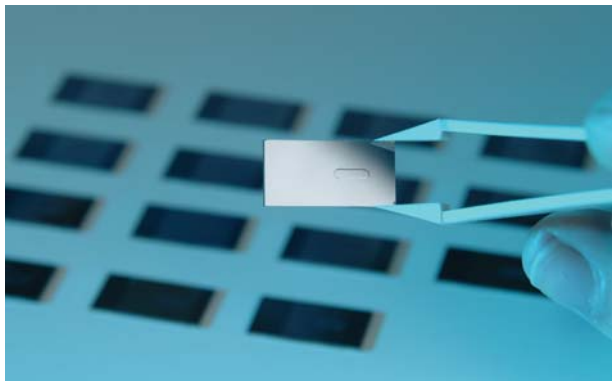

Figure 7: An etched sensor chip before fibre pigtailing. The sensing region is seen as a small oval towards the right hand end of the chip.

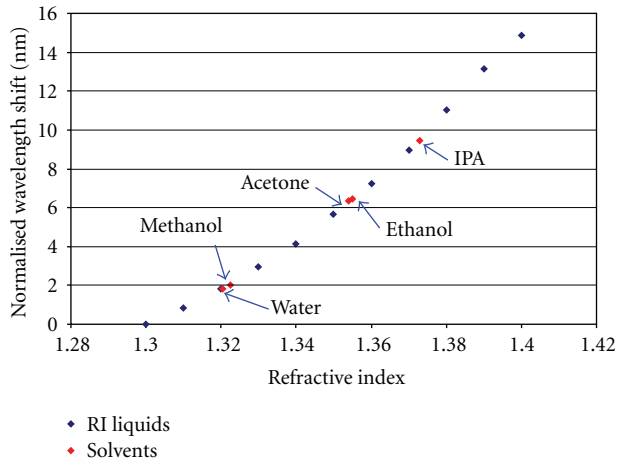

Figure 8: Sensitivity curve showing variation in Bragg wavelength with refractive index.

removal of the waveguide core. Temperature measurement gratings are left unetched such that they are immune to changes in the refractive index of any liquids above them.

Following etching, the penetration depth of the optical mode into the liquid analyte is relatively low. To extend the penetration further, a high-index overlayer may be applied to the etched surface [32]. This has the effect of lifting the optical mode up towards the analyte, resulting in a much higher penetration depth and a much greater sensitivity to refractive index. A number of methods and materials may be used to achieve this effect depending on the desired upper surface material and the required refractive index sensitivity. To date several materials have been utilised including, silica, silicon nitride, silicon oxynitride, fluorinated polymers, titania, zirconia, and alumina. The different materials all require different processing steps and results in different end products.

To perform measurements the etched and overlayered chips are pigtailed using single mode fibre, and optical spectra are obtained with the use of commercially available Bragg grating interrogators.

Figure 7 shows a photograph of a typical sensor chip after fabrication but before optical fibre pigtailing. The etched window containing the sensing region can be seen as a small oval to the right of the chip. Temperature measurement gratings are embedded in the left-hand side of the chip.

It should be noted that the process of etching the chip and subsequently adding a high-index overlayer brings about a very high level of birefringence in the Bragg grating section of the device. In many applications this would not be tolerable as it would cause large amounts of polarisation dependence. Here, the effect is sufficiently large that TE and TM modes can be independently resolved. This means that instead of requiring polarisation control to obtain a reliable mode of operation, the more simple route of using an unpolarised optical source can, if desired, be taken.

Similarly, whilst overall optical loss would in many applications be required to be minimal, it is of less concern here. It is critical to measure changes in Bragg wavelength as accurately as possible but this is not dependant on the optical power that is reflected.

4. Refractive Index Sensitivity

The ability to detect changes in refractive index depends on two key aspects when using a Bragg grating device. Firstly and most obviously, the rate at which the Bragg wavelength varies with refractive index, the intrinsic sensor sensitivity, must be considered. Secondly, the resolution and accuracy to which the Bragg wavelength can be determined must be taken into account.

To address the first of these considerations, a simple sensitivity curve may be generated. Such a curve is shown in Figure 8 where Cargille refractive index liquids are used on the sensor chips, and the resultant Bragg wavelengths are measured. It must be noted that there is a very slight uncertainty in this data as the RI liquids are quoted at 589 nm, not at 1550 nm used here. As a result of material dispersion, there will be small but currently unknown offset between the RI values quoted in this graph and their true values.

It is easy to see that over a refractive index span of 1.30 to 1.40 the Bragg wavelength shifts by approximately 15 nm, giving rise to a particularly high sensitivity to refractive index. The sensitivity of this device increases at higher refractive indices as expected [20]. The gradient of the curve provides the sensitivity measured in refractive index units (RIUs) per nanometre. At an index of 1.31 the sensitivity shown is 92 RIU/nm rising to 155 RIU/nm at an index of 1.36. The upper end of the curve shown here gives a sensitivity of 193 RIU/nm at a refractive index of 1.39. At analyte refractive indices much above 1.40 this particular device ceases to act as a waveguide. The combined effect of the high-index overlayer and the refractive index of the analyte means significant modal mismatch occurs as the light travels into the etched window region, and all of the optical mode is lost to the overlayer and analyte with the result that the Bragg signal is completely lost.

In addition to the RI liquid data shown on Figure 8, data points associated with several solvents are included. These data points were obtained by simply using the relevant

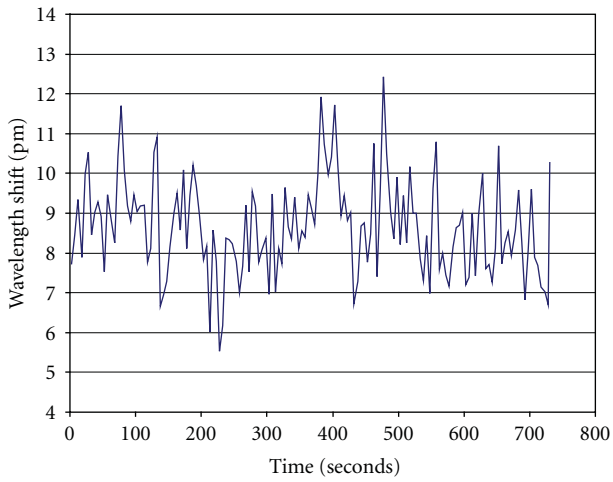

Figure 9: Steady-state Bragg wavelength determination showing subpicometre stability.

solvent as the analyte on the sensor. The measured Bragg wavelength allows the solvent data points to be interpolated onto the existing RI curve such that the measured RI of the solvents can be determined. Clearly the five solvents, namely, water, methanol, acetone, ethanol, and isopropyl alcohol, can all be easily resolved and thus identified by measurement of the Bragg wavelength. These liquids represent just a small subset of the liquids that may be monitored in this way.

The second factor in determining refractive index resolution is that of the measurement technique. Firstly, an optical spectrum must be obtained in an easy to manipulate format. Within this spectrum the Bragg reflection must be identified and the centre wavelength determined. A number of Bragg grating interrogators are available in an off the shelf configuration, typically operating in wavelengths between 1500 and 1600 nm. The stability and repeatability of the interrogators is of obvious importance as is the reliability of the centre wavelength determination from the reflection spectrum.

Using a simple weighted average calculation on a reflection peak a quick and easy measurement of centre wavelength may be made. Figure 9 shows the result of such a calculation on a single Bragg reflection from a sample made according to the techniques outlined earlier. The chip was held at a constant 35°C using a PID temperature controller in a stable environment such that the Bragg wavelengths of the peaks would remain constant as no external changes were permitted. Measuring the Bragg wavelength for a period of time allows an estimate of the stability and the calculation to be made.

This data shows that over the 12 minute section in the graph the wavelength varies by a maximum of 0.7 pm representing excellent stability. Each data point shown is the mean wavelength of 5 seconds worth of data collected from single Bragg reflection peak. A common method of quoting the stability is to multiply the standard deviation of the data set by three, a calculation which provides a stability of just 0.36 pm.

With the assumption that any change in wavelength greater than 0.36 pm should be the smallest change in wavelength that can be resolved with this combination of chip, interrogator, and analysis technique, we can determine the refractive index resolution. Figure 8 allowed the sensitivity to refractive index to be measured at 193 RIU/nm; so with a wavelength resolution of 0.36 pm we obtain a refractive index resolution of just 1.9×10^{-6} RIU. Further time-averaging may allow this to be further improved but this would come at the expense of data update rate which in many applications is an important parameter.

5. Temperature Measurement

As mentioned earlier, the UV written chips may be used as temperature sensing devices as well as refractive index sensors by choosing to leave one or more of the Bragg gratings unetched. In this case thermal expansion of the silica brings about a change in the Bragg period and therefore in the Bragg wavelength.

Using a temperature controlled and stabilised environment a sensor chip was ramped up and down between multiple temperatures and allowed to stabilise at five degree intervals. Both the Bragg wavelength and the actual chip temperature were recorded throughout the process. Temperature was measured using a 100 Ω PRT monitored using a Measurement Computing USB-Temp module. This data is shown in Figure 10 with the data points between stable temperatures being removed for clarity. The steps in output as the temperature was ramped up and down are easily seen. In order to see the relationship between temperature and wavelength the data is replotted in Figure 11 where a linear relationship between temperature and wavelength is clear. Whilst this graph appears to show only nine data points, there is in fact over twenty five thousand points plotted. The points are very closely clustered due to the stability of the temperature and therefore wavelength.

The data in Figure 11 yields a temperature coefficient for this unetched grating of 0.011 nm per °C, which when using the wavelength resolution of 0.36 pm derived earlier gives a temperature resolution of just 0.03°C. This resolution is easily equal to that obtainable by many electrical methods and is made more attractive as the optical nature of the measurement will not be compromised in electrically noisy environments which may degrade the signals from PRT and thermistor type devices. Additionally, this temperature measurement technique is entirely compatible with the refractive index sensing technology as well as being safe for use in volatile or flammable environments.

6. Real World Measurement Techniques

One of the great challenges in creating a sensor technology is the conversion from development laboratory experiment into a robust, easy to use package suitable for real world applications. The packaging needs to meet end-user requirements and be sufficiently robust to allow installation by

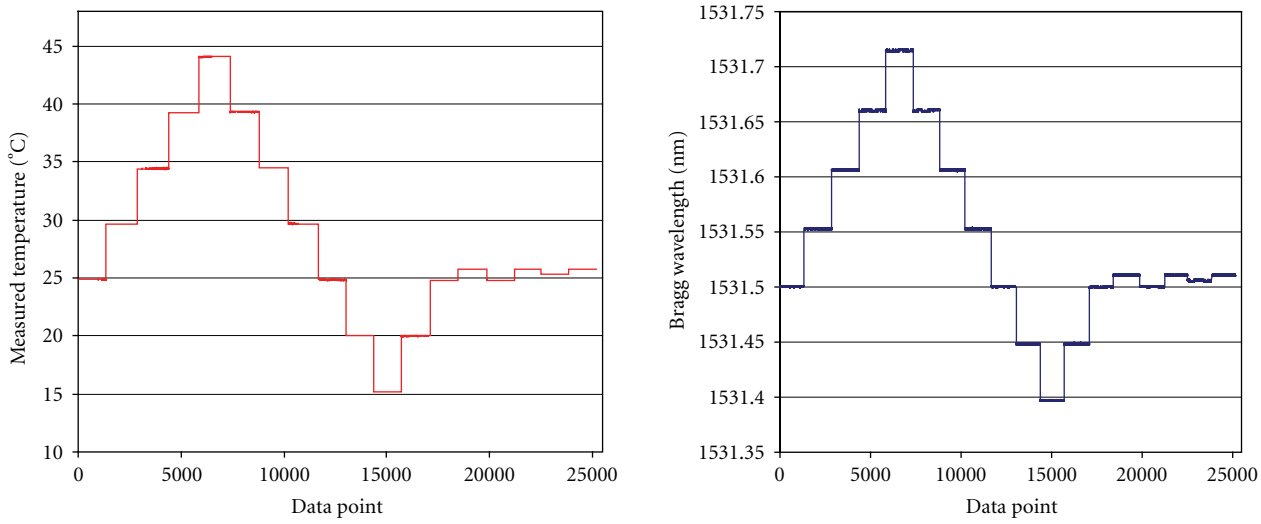

Figure 10: Variation in temperature (left-hand graph measured using PRT) and corresponding Bragg wavelength (right-hand graph) over time. Data points recorded at a rate of 2 Hz.

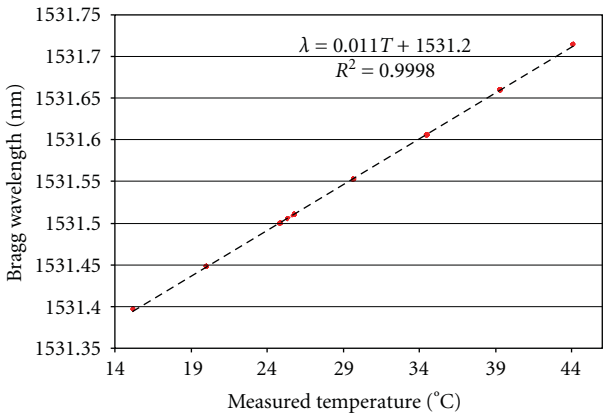

Figure 11: Relationship between temperature and Bragg wavelength. Note that over twenty five thousand data points are plotted on this graph but that high precision temperature measurement results in data points being closely clustered.

Figure 12: Industrial sensor cell for high-volume flow applications.

unskilled workers but retain the performance of the laboratory prototypes. To this end, the sensor technology discussed above has been integrated into a variety of application specific packages which allow the liquids for analysis to be easily delivered to the sensing region.

6.1. High-Flow Industrial Process Control Flow Cell. Monitoring pipelines in a process can be an invaluable tool for protecting the overall process integrity in many applications. An unknown or uncontrolled concentration of reagents entering a process at any point may severely compromise or totally write-off a complete processing batch. In order to allow pipeline contents to be measured in situ and in real time, Stratophase has defined a series of sensor chip products (Figure 12) that have been designed into a robust stainless steel unit designed for incorporation into high-flow, high pressure pipelines. The industrial process control (IPC) flow cells are designed to accept standard 1/4″ Swagelok fittings and pipes and allow liquid pressures up to 6 bars to be used.

6.2. Reaction Vessel Insertion Probe. Many applications, particularly those requiring fermentation processes for pharmaceutical, biofuel, or food and beverage must monitor their reactions in large reaction vessels or in multiple bench-top bioreactors. In these applications, a flow cell configuration is not always suitable as it requires a portion of the liquid to be tapped off from the main tank and pumped through a separate sensing loop. Instead, insertion probes are commonly used to allow sensors to be pushed through the walls or lids of the reaction vessels. A common solution uses a standard form-factor, typically with a Pg13.5 thread to allow sensors to be screwed into standard ports fitted to the fermenters or reactors. A probe-housing compatible with standard ports has been designed to allow the planar

Figure 13: Probe sensor for in-vessel monitoring applications.

Bragg sensors discussed here to be used in an insertion probe format (Figure 13). The probes may be used in static or retractable housings and require only an optical fibre connection to access the sensor data.

7. Example Applications

Using the inline flow cell and insertion probe formats, the planar Bragg grating devices are capable of monitoring many aspects of process evolution over many weeks. Whilst the focus of this paper has so far been on the sensitivity to refractive index, it is more common to require an insight into changes in a process due to concentration variation or biological growth rather than in absolute refractive index. Even the smallest change in the properties of a liquid will result in a refractive index change regardless of whether the change is due to temperature, concentration, or other reaction events. By measuring both temperature and RI simultaneously and detailed picture of process evolution may be obtained.

7.1. Real Time Monitoring of Fermentation Processes. The process of fermentation using yeast to convert sugar to alcohol is as old as it is commercially important. The presence of sugars, nutrients, and final alcohol content are the key factors of interest, and the variation of these may be observed through refractive index change. To demonstrate this capability the IPC flow cell described above was plumbed into a standard fermentation process using a pump to circulate the fermenting liquid over a sensor. Tracking the variation in Bragg wavelength over a number of weeks reveals clear events that correlate to distinct phases of the process. Figure 14 shows how the sensor output varies with the process evolution over several weeks. The refractive index output of the sensor is shown on the left-hand axis and is plotted in units of nanometres and provides the change in Bragg wavelength over time. These units are used rather than conversion to refractive index units as it is overall insight into the fermentation process that is desirable, not the absolute refractive index at any given moment. In contrast, the output of the sensor that provides temperature has been calibrated into degrees C.

During the initial stages it is clear that the Bragg wavelength drops steadily due to the reduction in sugar concentration as it is consumed by the yeast. Following this initial activity the rate of change of concentration decreases as more and more of the sugar is consumed, and the sensor output indicates that a steady state has been achieved. Between about 500 and 700 hours of process time several fining agents are added to the brewing liquid in order to assist in separating out the yeast and from the liquid product of interest. This causes step changes in both positive and negative directions as the decrease in suspended particles is reduced and as further chemicals are added, respectively. In the final stages, additives to improve flavour and mouth-feel are added to the liquid, causing a distinct change in the sensor output.

The lower trace on the graph, which corresponds to the right-hand axis, shows the optically measured temperature variation and allows events in the liquid sensor trace to be decoupled from temperature effects. For example, at about 500 hours of processing time a fault in the environmental temperature controls caused an oscillation of several degrees in the temperature. This is reflected in the upper fermentation trace. Other key events in the fermentation trace are known to be "real" effects of the process and not due to environmental changes as they are not mirrored by the temperature reference data.

These steps show that the processes may be monitored continuously in real time. Perhaps more importantly, they also show that additive or sugar concentration may be measured throughout the process such that remedial action may be immediately taken should the process deviate from the required path.

7.2. Industrial Feedstock Monitoring. Another example application is in the protection of pharmaceutical production from contamination of the feedstock. A solvent that is contaminated with another product may significantly affect process yield and efficiency, ultimately costing large sums of money. By monitoring the supply of liquids prior and throughout the process, errant steps may be avoided.

Figure 15 shows the output of a sensor mounted into an IPC flow block and connected to an ethanol supply line. Contamination of the ethanol with water at regular intervals causes the clear steps in sensor output to jump. The large changes shown here make it clear that very small amounts of water contamination (approximately 0.1% by volume) may be detected.

8. Summary

In this paper we have provided a review of the capabilities of planar waveguide Bragg sensors. Starting with the background physical principles we have shown how different types of refractive index sensor may be considered to operate on common principles and then indicated the advantages

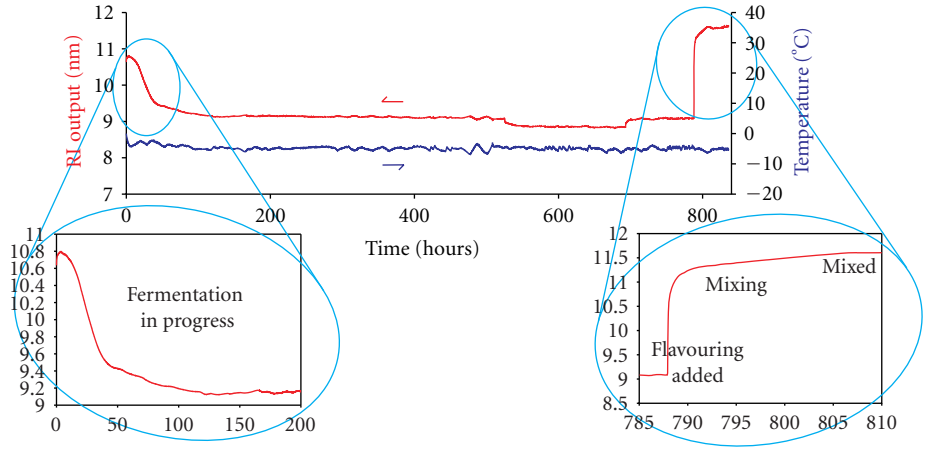

Figure 14: Sensor measurement of refractive index and temperature over several weeks during fermentation process. Close-up sections show the initial consumption of sugars and the addition of chemical flavouring.

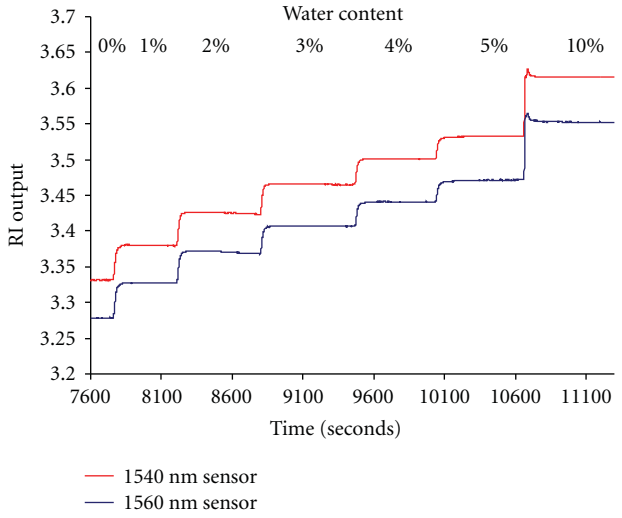

Figure 15: Sensor output as ethanol with small variable water content flows over sensing region.

of using a Bragg grating-based device using a modal light confinement approach. We have reviewed in detail the fabrication and packaging routes for such devices and given examples of their behaviour in a range of industrial applications. Data presented shows refractive index sensitivity of order 1.9×10^{-6}, and corresponding temperature resolution of 0.03°C. The devices offer the advantages of temperature self-referencing and a microfluidic based silica-on-silicon platform.

References

[1] X. Fan, I. M. White, S. I. Shopova, H. Zhu, J. D. Suter, and Y. Sun, "Sensitive optical biosensors for unlabeled targets: a review," *Analytica Chimica Acta*, vol. 620, no. 1-2, pp. 8–26, 2008.

[2] P. Dumais, C. L. Callender, J. P. Noad, and C. J. Ledderhof, "Microchannel-based refractive index sensors monolithically integrated with silica waveguides: structures and sensitivities," *IEEE Sensors Journal*, vol. 8, no. 5, pp. 457–464, 2008.

[3] J. Ctyroky, F. Abdelmalek, W. Ecke, and K. Usbeck, "Modelling of the surface plasmon resonance waveguide sensor with Bragg grating," *Optical and Quantum Electronics*, vol. 31, no. 9, pp. 927–941, 1999.

[4] G. Nemova and R. Kashyap, "A compact integrated planar-waveguide refractive-index sensor based on a corrugated metal grating," *Journal of Lightwave Technology*, vol. 25, no. 8, pp. 2244–2250, 2007.

[5] G. Nemova and R. Kashyap, "Theoretical model of a planar integrated refractive index sensor based on surface plasmon-polariton excitation," *Optics Communications*, vol. 275, no. 1, pp. 76–82, 2007.

[6] S. A. Maier, *Plasmonics: Fundamentals and Applications*, Springer, New York, NY, USA, 2007.

[7] B. Culshaw and A. Kersey, "Fiber-optic sensing: a historical perspective," *Journal of Lightwave Technology*, vol. 26, no. 9, pp. 1064–1078, 2008.

[8] R. G. Heideman, G. J. Veldhuis, E. W. H. Jager, and P. V. Lambeck, "Fabrication and packaging of integrated chemo-optical sensors," *Sensors and Actuators B*, vol. 35, no. 1–3, pp. 234–240, 1996.

[9] K. Tiefenthaler and W. Lukosz, "Integrated optical switches and gas sensors," *Optics Letters*, vol. 9, no. 4, pp. 137–139, 1984.

[10] K. Schroeder, W. Ecke, R. Mueller, R. Willsch, and A. Andreev, "A fibre Bragg grating refractometer," *Measurement Science and Technology*, vol. 12, no. 7, pp. 757–764, 2001.

[11] F. Ouerghi, W. Belhadj, F. Abdelmalek, M. Mejatty, and H. Bouchriha, "Polymer thin films and Bragg grating structures based temperature and pressure integrated effects," *Thin Solid Films*, vol. 485, no. 1-2, pp. 176–181, 2005.

[12] C. Wochnowski, M. Abu-El-Qomsan, W. Pieper, et al., "UV-laser assisted fabrication of Bragg sensor components in a planar polymer chip," *Sensors and Actuators A*, vol. 120, no. 1, pp. 44–52, 2005.

[13] C. Wochnowski, M. T. Kouamo, W. Pieper, et al., "Fabrication of a planar polymeric deformation Bragg sensor component by excimer laser radiation," *IEEE Sensors Journal*, vol. 6, no. 2, pp. 331–338, 2006.

[14] K. J. Kim and M. C. Oh, "Flexible Bragg reflection waveguide devices fabricated by post-lift-off process," *IEEE Photonics Technology Letters*, vol. 20, no. 1–4, pp. 288–290, 2008.

[15] T. Pustelny, I. Zielonka, C. Tyszkiewicz, P. Karasinski, and B. Pustelny, "Impressing technology of optical Bragg's gratings on planar optical sol-gel waveguides," *Opto-Electronics Review*, vol. 14, no. 2, pp. 161–166, 2006.

[16] V. M. N. Passaro, R. Loiacono, et al., "Design of Bragg grating sensors based on submicrometer optical rib waveguides in SOI," *IEEE Sensors Journal*, vol. 8, no. 9-10, pp. 1603–1611, 2008.

[17] S.-L. Tsao and C.-P. Peng, "An SOI Michelson interferometer sensor with waveguide Bragg reflective gratings for temperature monitoring," *Microwave and Optical Technology Letters*, vol. 30, no. 5, pp. 321–322, 2001.

[18] D. Runde, S. Brunken, C. E. Ruter, and D. Kip, "Integrated optical electric field sensor based on a Bragg grating in lithium niobate," *Applied Physics B*, vol. 86, no. 1, pp. 91–95, 2007.

[19] I. J. G. Sparrow, G. D. Emmerson, C. B. E. Gawith, and P. G. R. Smith, "Planar waveguide hygrometer and state sensor demonstrating supercooled water recognition," *Sensors and Actuators B*, vol. 107, no. 2, pp. 856–860, 2005.

[20] I. J. G. Sparrow, G. D. Emmerson, C. B. E. Gawith, P. G. R. Smith, M. Kaczmarek, and A. Dyadyusha, "First order phase change detection using planar waveguide Bragg grating refractometer," *Applied Physics B*, vol. 81, no. 1, pp. 1–4, 2005.

[21] X. Dai, S. J. Mihailov, C. L. Callender, C. Blanchetiere, and R. B. Walker, "Ridge-waveguide-based polarization insensitive Bragg grating refractometer," *Measurement Science & Technology*, vol. 17, no. 7, pp. 1752–1756, 2006.

[22] S.-M. Lee, K.-C. Ahn, and J. S. Sirkis, "Planar optical waveguide temperature sensor based on etched Bragg gratings considering nonlinear thermo-optic effect," *KSME International Journal*, vol. 15, no. 3, pp. 309–319, 2001.

[23] A. V. Dotsenko, A. L. Diikov, and T. A. Vartanyan, "Label-free biosensor using an optical waveguide with induced Bragg grating of variable strength," *Sensors and Actuators B*, vol. 94, no. 1, pp. 116–121, 2003.

[24] H. Nishiyama, Y. Hirata, I. Miyamoto, and J. Nishii, "Formation of periodic structures by the space-selective precipitation of Ge nanoparticles in channel waveguides," *Applied Surface Science*, vol. 253, no. 15, pp. 6550–6554, 2007.

[25] M. Svalgaard, K. Faerch, and L.-U. Andersen, "Variable optical attenuator fabricated by direct UV writing," *Journal of Lightwave Technology*, vol. 21, no. 9, pp. 2097–2103, 2003.

[26] P. Cheben, E. Post, S. Janz, et al., "Tilted fiber Bragg grating sensor interrogation system using a high-resolution silicon-on-insulator arrayed waveguide grating," *Optics Letters*, vol. 33, no. 22, pp. 2647–2649, 2008.

[27] A. J. Willshire, P. Niewczas, and J. R. Mcdonald, "A cyclic arrayed-waveguide-grating-based fiber-optic sensor interrogation system," *IEEE Photonics Technology Letters*, vol. 18, no. 18, pp. 1904–1906, 2006.

[28] G. Z. Xiao, P. Zhao, F. G. Sun, Z. G. Lu, Z. Zhang, and C. P. Grover, "Interrogating fiber Bragg grating sensors by thermally scanning a demultiplexer based on arrayed waveguide gratings," *Optics Letters*, vol. 29, no. 19, pp. 2222–2224, 2004.

[29] G. D. Emmerson, S. P. Watts, C. B. E. Gawith, et al., "Fabrication of directly UV-written channel waveguides with simultaneously defined integral Bragg gratings," *Electronics Letters*, vol. 38, no. 24, pp. 1531–1532, 2002.

[30] C. B. E. Gawith, G. D. Emmerson, S. G. McMeekin, et al., "Small-spot interference pattern for single-step 2D integration and wide wavelength detuning of planar Bragg gratings," *Electronics Letters*, vol. 39, no. 14, pp. 1050–1051, 2003.

[31] R. Feced, M. N. Zervas, and M. A. Muriel, "An efficient inverse scattering algorithm for the design of nonuniform fiber Bragg gratings," *IEEE Journal of Quantum Electronics*, vol. 35, no. 8, pp. 1105–1115, 1999.

[32] G. R. Quigley, R. D. Harris, and J. S. Wilkinson, "Sensitivity enhancement of integrated optical sensors by use of thin high-index films," *Applied Optics*, vol. 38, no. 28, pp. 6036–6039, 1999.

Hindawi Publishing Corporation
Journal of Sensors
Volume 2009, Article ID 470175, 11 pages
doi:10.1155/2009/470175

Research Article

Design and Fabrication of Slotted Multimode Interference Devices for Chemical and Biological Sensing

M. Mayeh,[1,2] J. Viegas,[1,2,3,4] P. Srinivasan,[5] P. Marques,[3,4] J. L. Santos,[3,4] E. G. Johnson,[1,2] and F. Farahi[1,2]

[1] *Department of Physics and Optical Science, University of North Carolina at Charlotte, Charlotte, NC 28223, USA*
[2] *Center for Optoelectronics and Optical Communications, University of North Carolina at Charlotte, NC 28223, USA*
[3] *INESC Porto, Rua do Campo Alegre 687, 4169-007 Porto, Portugal*
[4] *Departamento de Física, Faculdade de Ciências da Universidade do Porto, 4169-007 Porto, Portugal*
[5] *College of Optics and Photonics, University of Central Florida, Orlando, FL 32816, USA*

Correspondence should be addressed to M. Mayeh, mmayeh@uncc.edu

Received 2 February 2009; Accepted 5 May 2009

Recommended by Christos Riziotis

We present optical sensors based on slotted multimode interference waveguides. The sensor can be tuned to highest sensitivity in the refractive index ranges necessary to detect protein-based molecules or other water-soluble chemical or biological materials. The material of choice is low-loss silicon oxynitride (SiON) which is highly stable to the reactivity with biological agents and processing chemicals. Sensors made with this technology are suited to high volume manufacturing.

1. Introduction

During the last decade there has been a rapidly growing interest in integrated optical sensors because of their many advantages over the nonplanar optical sensors. Many of integrated optical sensors (IOSs) primarily allow for sensitive, real-time, label-free, and on-site measurements of very small changes of biological and chemical parameters of species. There are different methods for IO sensing and the majority of them imply a change of the optical properties of the sensing, area such as its refractive index and thickness, which will be translated into a change in output intensity of optical sensor. In nearly all integrated optical sensors it is the change of effective index of refraction, N_{eff}, that is utilized, and in some cases measurement methods rely on the phenomenon of optical interference [1]. That is clearly visible in the so-called interferometric sensors in which the output beam of the sensing waveguide interferes with a reference beam. Between the sensors in which they work, based on interference concept, here are a few to mention: Mach-Zehnder interferometers (MZIs) [2–6], Young interferometer [7–9], and Michelson [10], of course resonator-type sensors also rely on interference such as ring resonator [11, 12] and Fabry-Perot resonator [13]. The typical resolution of these classes of sensors is in the order of 10^{-7}–10^{-5} refractive index units (RIUs). The most widespread sensing scheme is surface-plasmon resonance (SPR) [14] in which biochemical interaction on the surface of a grating translates into the changes of refractive index and will be monitored by resonance behavior of a guided wave at the surface of a thin metal film. Recently some sensing schemes based on surface-plasmon interference have been proposed [15, 16]. For these types of sensors typical resolution is in the order of 10^{-6}–10^{-5}. The grating coupler has been realized in the area of IO sensors as well, using wavelength interrogation or angular interrogation [17–20]. In many cases an improved resolution of the sensor is obtained at the expense of limited operating range.

In this paper a novel type of IO sensor has been introduced. This sensor is based on a slotted multimode interference (MMI) waveguide in which the changes in refractive index are read out as change in output intensity. Due to its compactness, robustness, large operating range, and high sensitivity, the proposed device is a novel contribution to the field of optical sensing. MMI-based optical devices have been widely used for a variety of sensing purposes among them

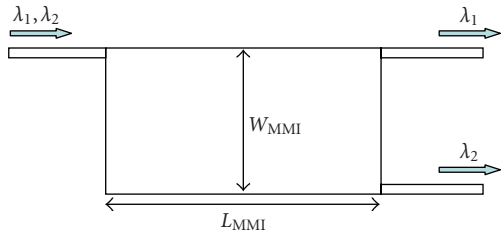

Figure 1: Schematic configuration of a, MMI coupler.

temperature [21] and chemical/biological sensors [22, 23] but in the best of our knowledge, slotted MMI devices have never been investigated for sensing applications.

This work describes the design and optimization parameters of the proposed device as well as the detailed description of fabrication process. The performance of the device in terms of sensitivity to bulk refractive index changes of covering medium has been experimentally investigated. The preliminary experimental results demonstrate the applicability of this specific configuration to detection of wide range of chemicals and biological species.

2. Design

Multimode interference (MMI) device compromises single mode input and output waveguides and a multimode region. This waveguide region is typically single mode in the transverse direction and multimode in lateral direction. Figure 1 shows a schematic configuration of a simple off-center-fed MMI [24].

The MMI region supports many lateral modes. The input signal excites these modes, which propagate with different phase velocities along the length of the MMI region and become out of phase. The input field will reproduce itself when the superposition of the modes in the MMI region matches the original modal distribution at the input plane. This condition occurs at planes where the phase differences among the excited modes are integral multiples of 2π, which allows the excited modes to constructively interfere and reproduce the input's modal distribution. The propagation distance at which this occurs is known as the self-image length and is described in (1):

$$L_\pi = \frac{4n_{\text{core}} W_{\text{eff}}^2}{3\lambda}. \quad (1)$$

The self-image length depends upon the wavelength (λ) and the polarization of the light, as well as upon parameters of the device such as refractive index (n_{core}) and width (W_{eff} which is slightly larger than MMI width).

Recently Mackie and lee [25] have introduced a new modification in MMI region which reduces the self- imaging length. The modification involves introducing one or more slots along the entire longitudinal length of the MMI region (Figure 2(b)). The term "slot" refers to a narrow subregion of the MMI region, with a specific width and position that has a different effective refractive index than the rest of the

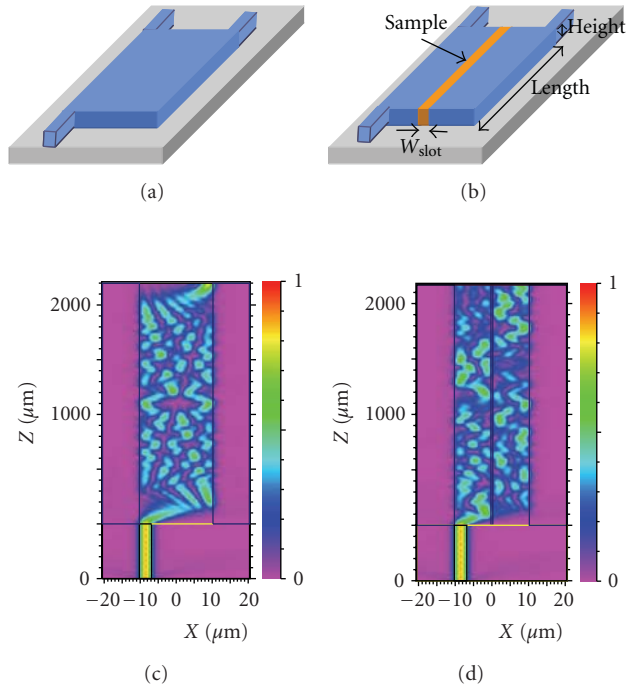

Figure 2: Schematic representation of (a) a simple MMI and (b) a MMI with one slot of width (W_{slot}). (c) Top view of field distribution in a MMI device with no slot and (d) one slot.

MMI region. A single centered slot with the right parameters such as refractive index of slot, width and separation of the slot reduces the self-imaging length by a factor of 2 and does so without adversely affecting the performance. Introducing N slots reduces the self-imaging length by a factor of $N + 1$. Figures 2(a) and 2(b) represent a simple and one-slot ($N = 1$) MMI. The field propagation along both devices is depicted in Figures 2(c), and 2(d), assuming a fused quartz wafer as the substrate ($n_{\text{clad}} = 1.445$) and SiON as core material ($n_{\text{core}} = 1.49$). The refractive index of the sample fluid film to be analyzed is 1.45, and it completely fills the slots. The operating wavelength is 1300 nm, and the width of the slot (W_{slot}) is set to 520 nm. Length of the MMI region (Length) is 2.2 mm, and the height of waveguide is to 2.5 μm.

As each mode of the MMI region propagates, it acquires a modal phase delay, given by (2):

$$\phi_m = \frac{\pi . p^2 z}{L_\pi}, \quad (2)$$

where p is the mode number, z is the propagation distance, and L_π is the self-imaging distance for the MMI without a slot. For slotted MMI regions, each mode also acquires an extra phase delay from the slots. This extra phase delay depends upon z, δn (the difference in effective refractive index between the slot region and the rest of the MMI region), the slot width W_{slot}, and the value of the mode across the slot. One can approximate the last parameter as the value of the mode at the center of the slot. In fact, the extra phase delay from a slot will be zero for modes that have nodes (i.e., are zero) at that slot position. Self-imaging

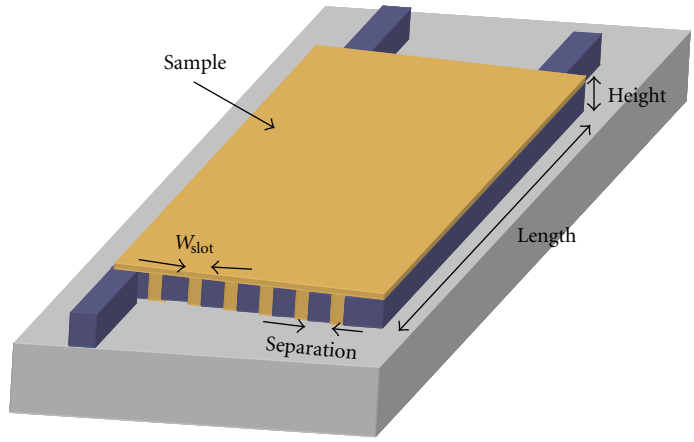

Figure 3: Schematic representation of a MMI with six-slots of equal widths (W_{slot}) which are separated by equal distances.

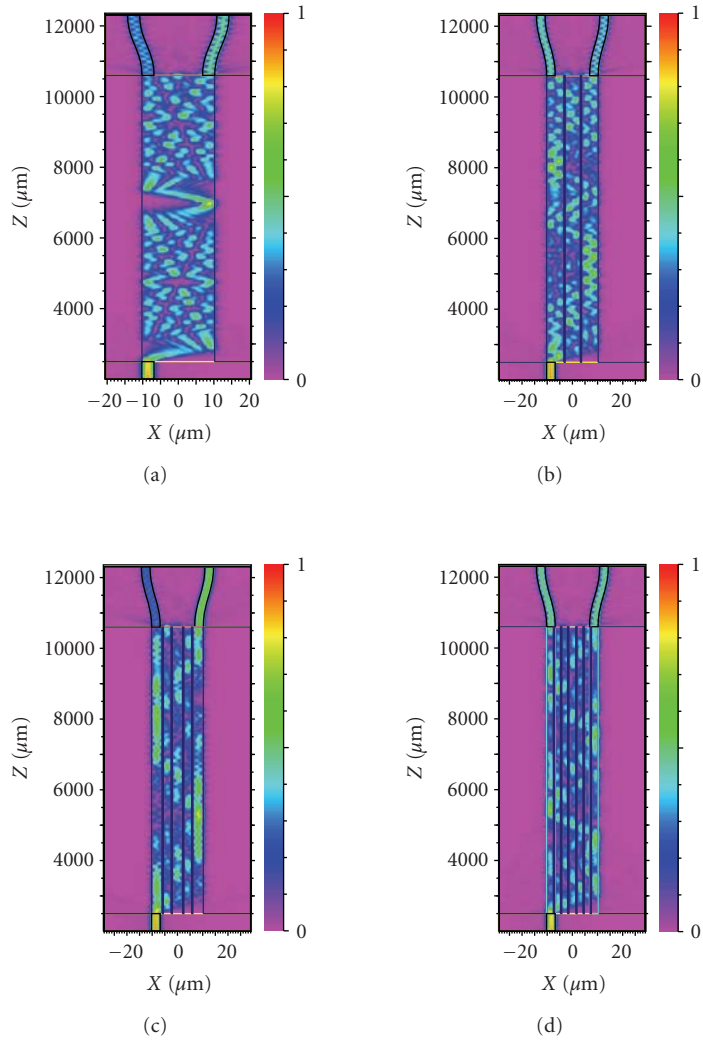

Figure 4: Top view of field distribution in a MMI device with even number of slots: (a)–(d), zero slot to six-slots.

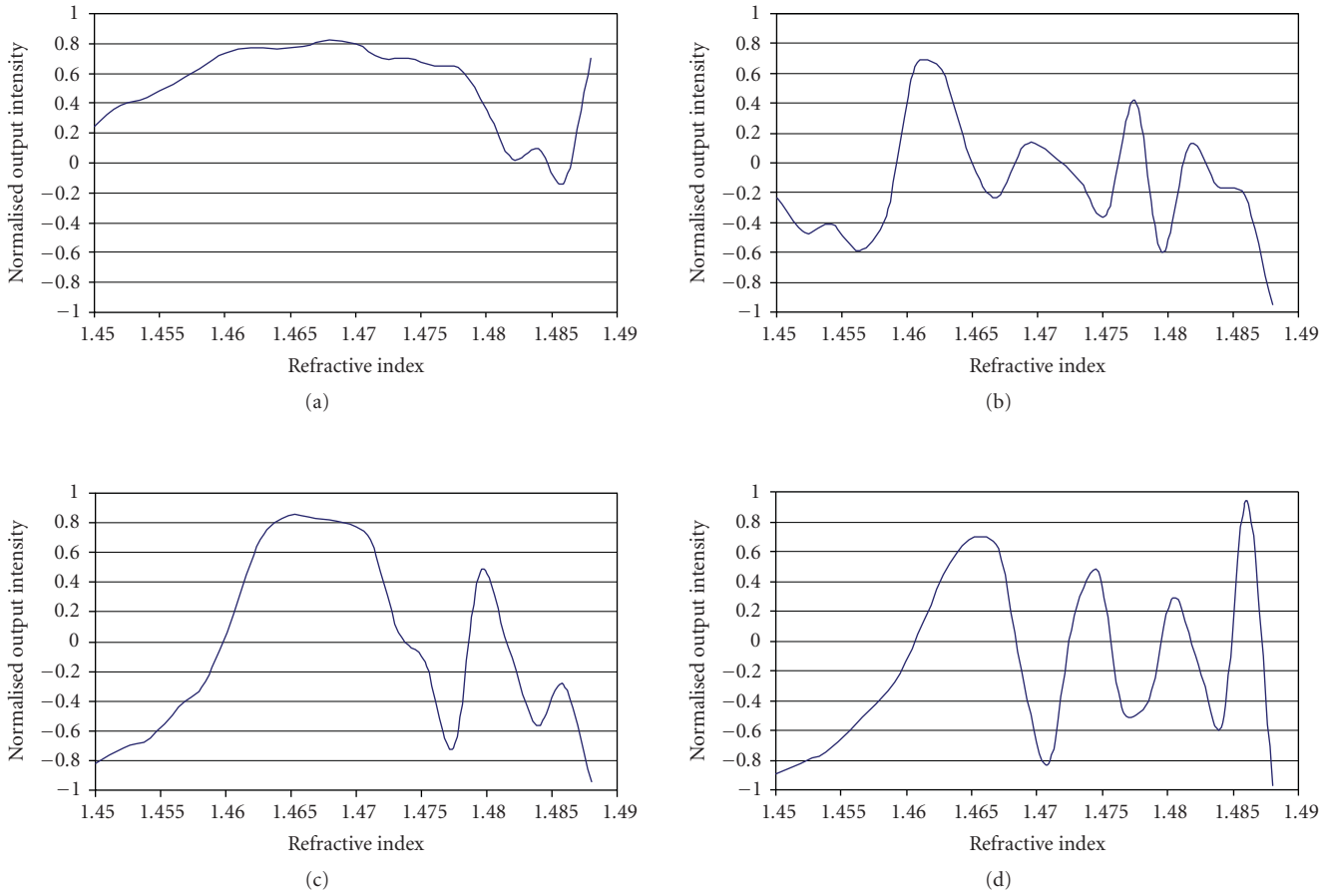

Figure 5: Normalized differential outputs of (a) zero-, (b) two-, (c) four-, and (d) six-, slot MMI response to different cover liquids refractive index.

occurs whenever the difference in total phase delay between all successive modes is either an odd multiple of π resulting in inverted image (cross state) or else an even multiple of π resulting in noninverted image (bar state).

Slotted MMIs waveguides have raised a lot of interest due to their potential as MMI devices for separation/combination of wavelength/polarization, powersplitting, and novel types of MMI switches [25] but they have never been used for sensing purposes. This paper investigates the potential sensing application of this class of devices. Figure 3 represents a MMI with six-slots of equal widths which are placed symmetrically relative to the center of device.

In our design, we assumed a glass wafer as the substrate ($n_{\text{clad}} = 1.445$) and SiON as core material ($n_{\text{core}} = 1.49$). The fluid film to be analyzed forms the cladding and completely fills the slots. Therefore, we studied the behavior of the device for a typical range of refractive index of many solvents, which ranges between 1.33 for water and 1.5 for protein solution [26, 27]. The experimental results presented in this paper focuses on materials with index of refraction of around 1.5 and the operating wavelength of 633 nm. Experiments are in progress for the same device dimensions for refractive index of around 1.3 and operating wavelength of 1300 nm. It should be mentioned that wavelengths greater than 1300 nm are not ideal choices, since most of the liquid-based samples contain water in which they strongly absorb signals at these wavelengths. Slots widths are set to 520 nm value that can be realized in a reproducible way when using our SiON technology. Since the sensitivity of the sensor is proportional to L_{sensor}, the long sensing structure would be desired. In our design, the length of the device is 8.1 mm. The height of SiON waveguide is optimized to 2.5 μm.

Every sensor application is characterized by its own specific set of requirements. Because integrated optical sensors are most competitive if high resolution is required, we will focus on this aspect and analyze the resolution prospects of the slotted MMI sensor. Resolution is defined as the smallest change in bulk refractive index that can be detected and measured by the complete sensing system. In slotted MMI sensor, more variation in field distribution has been observed for higher number of slots as the refractive index of sensing material varies.

Figure 4 represents the field propagation in MMIs with even number of slots with the parameters mentioned and n_{liquid} is set to 1.48. As depicted in Figure 4, two arbitrary

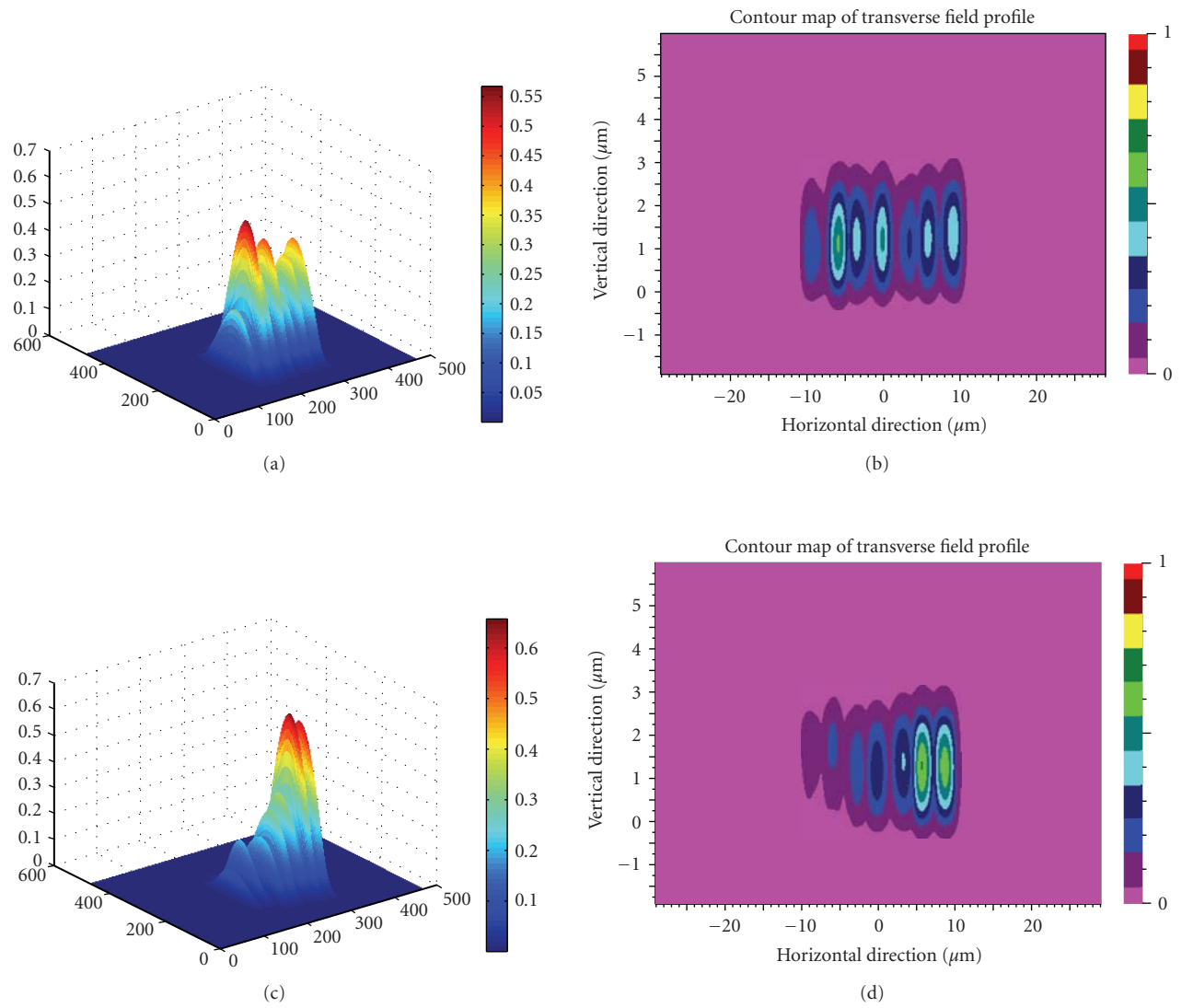

FIGURE 6: (a) and (b) 3D power distribution and 2D cross-section image of a Six-slot MMI sensor with cover liquid refractive index of 1.468 at $\lambda = 633$ nm. (c) and (d) 3D power distribution and 2D cross-section image with cover index of 1.465848 at $\lambda = 633$ nm. (Horizontal axis and vertical axis are width of the device and output intensity, respectively, with the arbitrary units).

positions at the end face of the slotted MMI sensor have been selected to study the behavior of the field distribution with the change in the refractive index of covering material for different number of slots. The output signal is the relative differential intensity defined as $\Delta P = (P1 - P2)/(P1 + P2)$, where $P1$ is the power in the right output and $P2$ corresponds to power in the left output. Relative differential intensity was plotted versus refractive indices of sample material and presented in the graph of Figure 5. As the number of slots increases more oscillations will appear in the output signal, corresponding to an increase in responsivity of sensor for a small range of refractive index. The most oscillations have been detected for the highest number of slots. For six-slot MMI we can distinguish three maxima and minima, which oscillate from -1 to 1 in a small range of refractive index where 1 differential output corresponds to all power in right-hand output port of MMI and -1 corresponds to all power in left-hand port.

Rather than limiting ourselves to only two data points in the output side, we could monitor the intensity distribution at every point of the output face. Figure 6 represents the intensity distribution at the endface of a six-slot MMI sensor with the material parameters and dimensions as defined above while the refractive index of top liquids is 1.4682 and 1.465848. Figures 6(a) and 6(c) present a 3D intensity profile at the output end of device if the refractive indexes of sensing materials are 1.4682 and 1.465848, respectively. Figures 6(b) and 6(d) represent the cross-section of intensity distribution for two different refractive indexes of 1.4682 and 1.465848, respectively. A significant change in the output profile could be observed only if the refractive index of the covering material was changed by 2×10^{-3}.

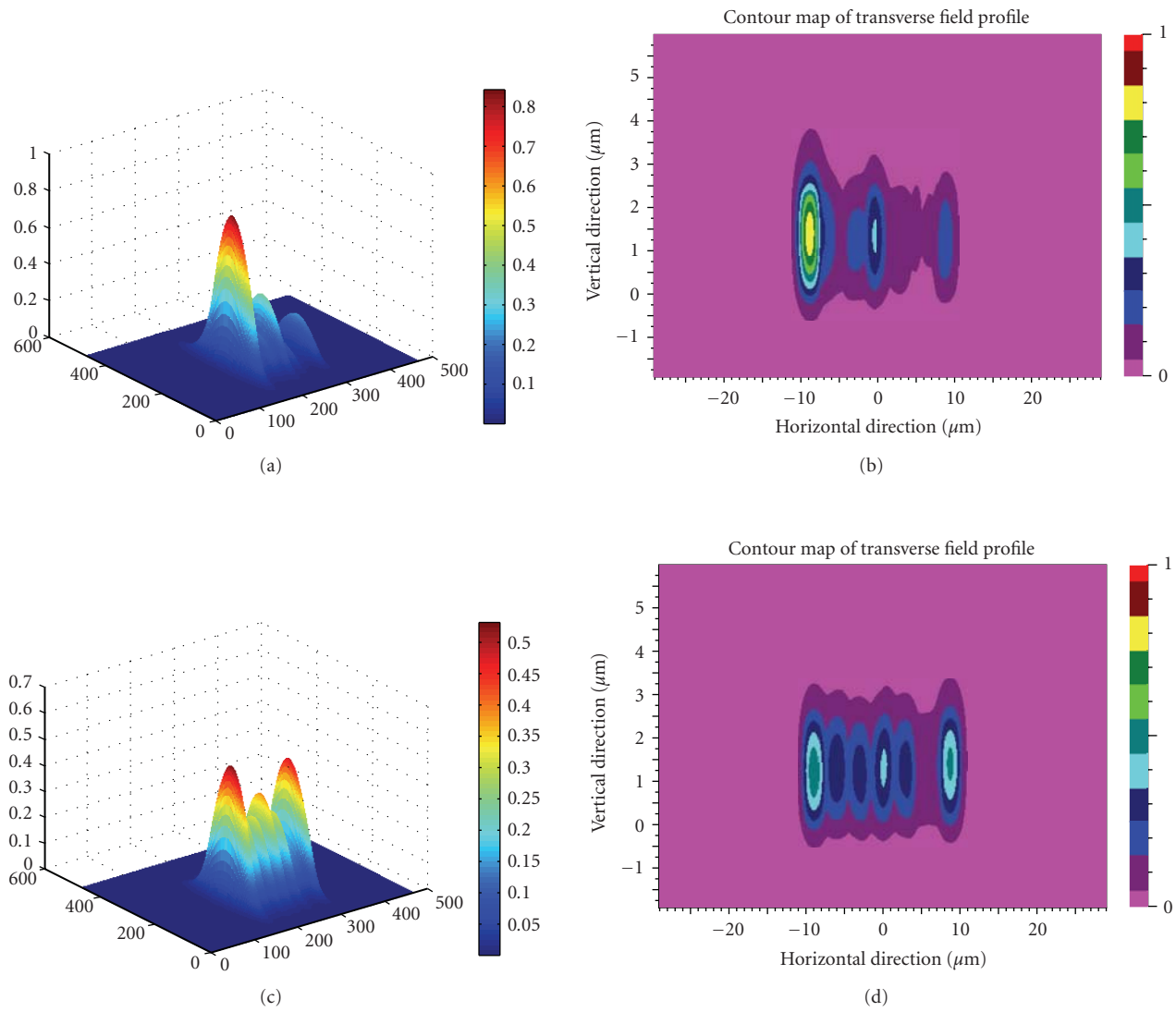

Figure 7: (a) 3D power distribution and (b) 2D cross-section image of a six-slot MMI sensor with cover liquid refractive index of 1.468 at $\lambda = 780$ nm. (c) 3D power distribution and (d) 2D cross-section with cover index of 1.465848 at $\lambda = 780$ nm.

As Figure 5 shows, the response of slotted MMI devices is periodic in general which could lead to measurement ambiguity. In order to resolve this potential problem, we have investigated a wavelength interrogation method in which more than one wavelength at any time should be used so that the combination of sensor response at these wavelengths would lead to a unique value of refractive index.

In order to analyze this solution we simulated the behavior of the six-slotted MMI device used to obtain the results of Figure 6 at two new wavelengths. Therefore, we maintained the same material properties, dimensions, and covering liquid indices; however, the operating wavelengths are of 780 nm and 800 nm.

The results are illustrated in Figures 7 and 8.Comparison of the results of Figures 8 and 9 illustrates that for any given refractive index the near field intensity profile of the sensor output depends on the operating wavelength. However, when the intensity profiles at two wavelengths of 780 nm and 800 nm are simultaneously obtained, a unique and unambiguous value for the index of refraction could be determined.

Further investigations showed that this device is capable of detecting very small variation of refractive index. A very simple signal detection scheme could conservatively recognize index variation in the order of 10^{-5}. Graph in Figure 9 represents the normalized differential output intensity between the first and sixth waveguides (from left to right) as the refractive index of cover liquid changes between 1.465652 and 1.466436 with step size of 9.8×10^{-5}. The theoretical predictions agree well with the experimental results, as will be demonstrated later.

3. Fabrication

Different technologies are being employed for producing IO sensors which depend on the application. The SiON

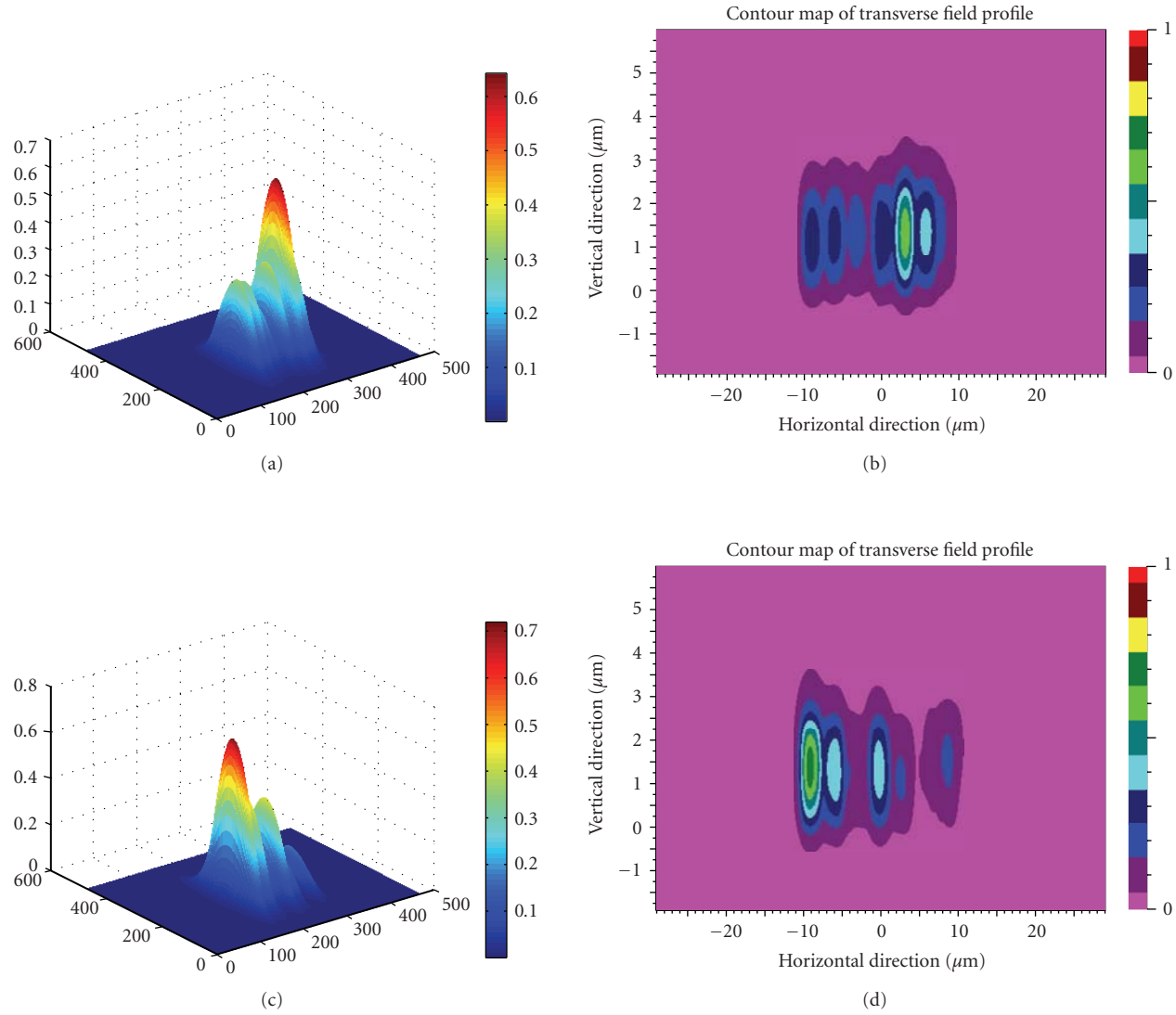

Figure 8: (a) 3D power distribution and (b) 2D cross-section image of a Six-slot MMI sensor with cover liquid refractive index of 1.468 at $\lambda = 800$ nm. (c) 3D power distribution and (d) 2D cross-section image with cover index of 1.465848 at $\lambda = 800$ nm.

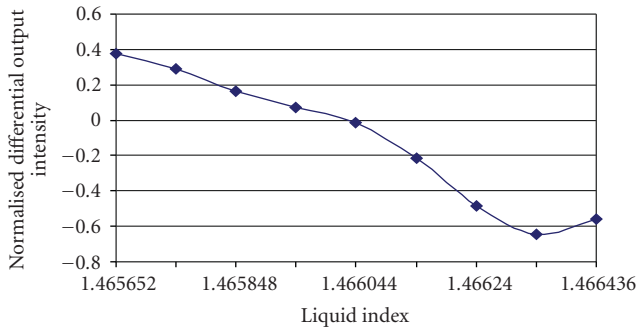

Figure 9: Normalized differential output intensity between waveguides one and six (from left to right) versus refractive index of liquid ($\lambda = 633$ nm).

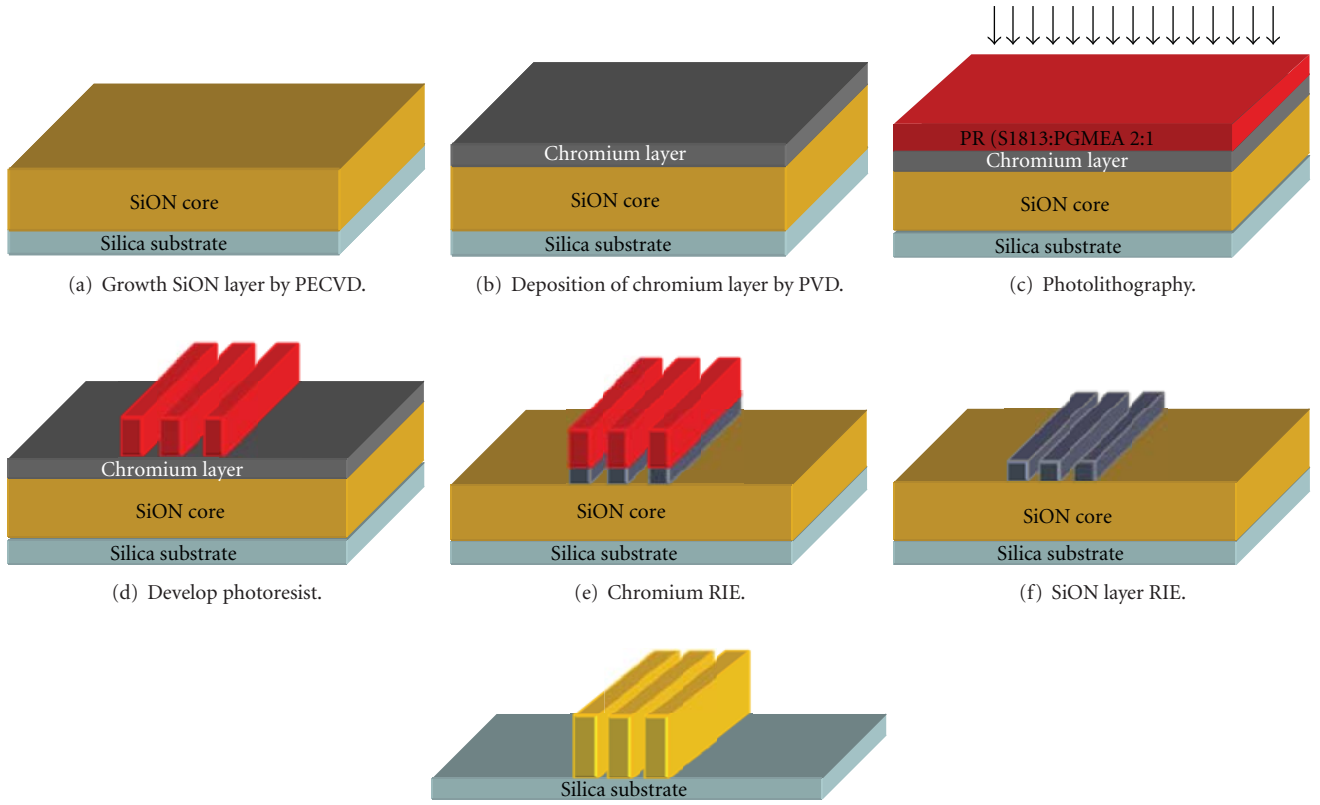

(a) Growth SiON layer by PECVD.
(b) Deposition of chromium layer by PVD.
(c) Photolithography.
(d) Develop photoresist.
(e) Chromium RIE.
(f) SiON layer RIE.
(g) Wet chromium etch.

Figure 10: Fabrication process of slotted MMI sensor.

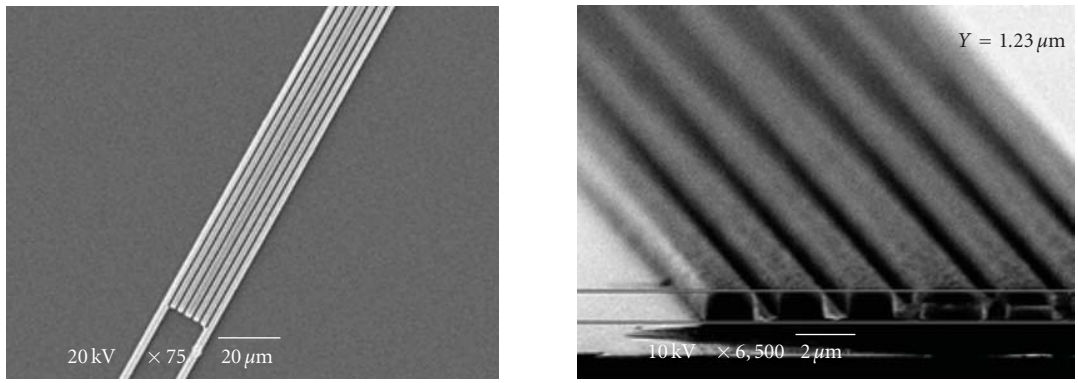

(a) (b)

Figure 11: SEM view of slotted MMI device. (a) Top view: 750×, (b) cross-section 6500×.

technology [28–30], indiffusion of glass [31], and polymer technology [32] are few to name. Between them, the SiON technology is the large range of wavelengths from visible to near infrared. With a precise control of process during reactive ion etching (RIE), SiON provides us with a high quality, straight sidewall which is required to our application. The chemical inertness of SiON makes this material a good candidate to avoid the reactivity with biological agents and processing chemicals. Finally, SiON growth and processing parameters have been well studied so that the desired characteristics required for this proposed sensor could be readily achieved.

Sensor is structured in the multilayer stacks deposited on top of a silica substrate. SiON has been deposited by plasma enhanced chemical vapor deposition (PECVD), and the refractive index has been tailored by mixing different gas concentrations (SiH_4, N_2O, and NH_3). Patterns are created by photolithography and have been developed and etched by RIE using C_4F_8 and O_2. Figure 10 represents the fabrication process of slotted MMI sensor which will be discussed

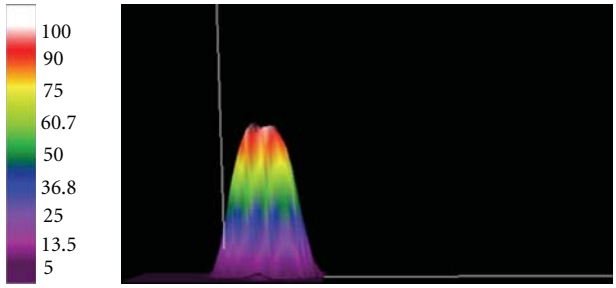

Figure 12: 3D beam profiler image of 6-slot MMI sensor at wavelength of 633 nm and liquid refractive index of 1.465652 covering the sensor. (Horizontal axis and vertical axis are MMI width and intensity distribution along the MMI width with arbitrary units).

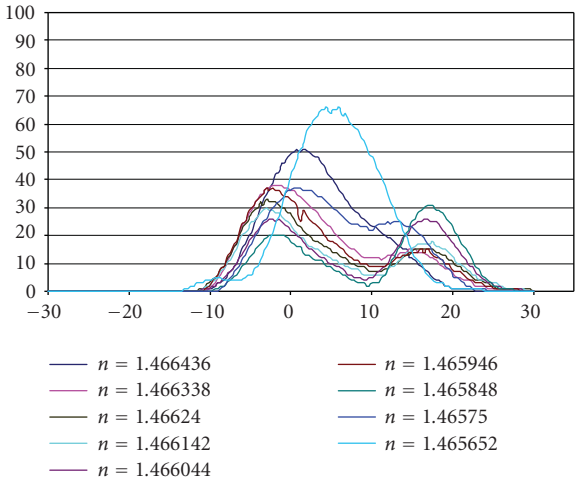

Figure 13: Power distribution along the endface of 6 slot MMI sensor for 9 different refractive indexes of cover medium. . (Horizontal and vertical axis are MMI width and output intensity, respectively, with arbitrary units).

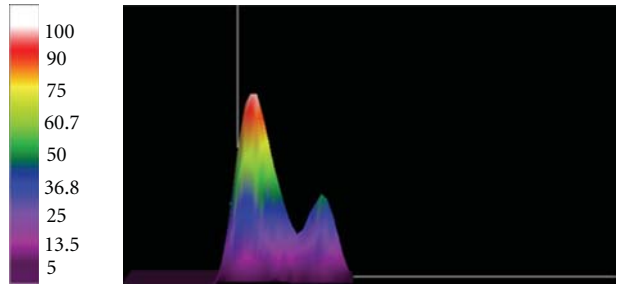

(a)

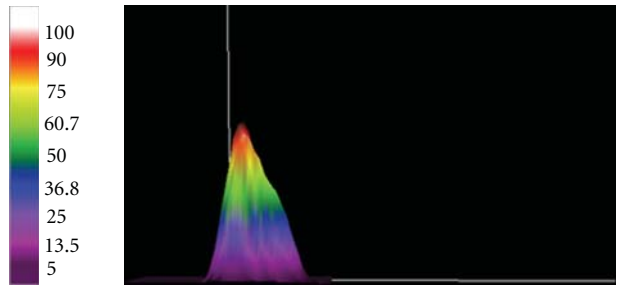

(b)

Figure 14: Three-dimensional far-field intensity distribution of output of six-slot MMI for refractive index of liquid (a) 1.466240 and (b) 1.466436 (Wavelength of 633 nm). (Horizontal axis and vertical axis are MMI width and intensity distribution along the MMI width, respectively, with arbitrary units).

in more details as we proceed. First a 2.5 μm-thick SiON waveguide layer with refractive index of 1.49 was grown on a quartz wafer using PECVD. A thin layer of chromium deposited on SiON using PVD-Lesker 75 tools to a thickness of 120 nm. To define the slotted MMI, a positive photoresist S1813 diluted in PGMEA with the ratio 2 : 1 was spun on the chromium layer. Pattern has been transferred by a stepper tool, with a projection aligner with a reduction factor of 5. After exposure and development of the resist, the pattern was transferred into the 120 nm-thick chromium layer by liftoff. The resist layer acted as an etch mask for the underlying Cr layer by reactive ion etching (RIE) in O_2–Cl_2 plasma. The chief advantage of dry Cr. etch is that it etches anisotropically, which significantly reduces the chrome etch undercut. As a consequence, the critical dimension (CD) bias is greatly reduced and resolution improves [33]. Finally the Cr layer was used as a mask in a second RIE step to transfer the slotted MMI structure into the SiON waveguide layer. C4F8/O2, 80/5 sccm-based plasmas are used for selective etching of high aspect ratio trenches in SiON. Additives such as oxygen are often used to optimize the process [34, 35]. In the last step fused silica wafers were cut in 1 in^2 chips with a high-speed saw, followed by a polishing step. Some Scanning Electron Microscope (SEM) pictures of the devices are shown in Figure 11. The cross-section of device shows an almost perfect rectangular trenches and straight, smooth side walls.

4. Experiments

Each chip containing 10 devices was mounted on a translation stage. Light from a He–Ne at 633 nm was launched into a single mode fiber and coupled to the input waveguide of the MMI sensor. The light output from sensor was imaged on a BeamPro (Photon Inc.) camera. Over the depth of focus of the imaging lens the output signal is integrated; therefore, the intensity profile obtained with this method should be considered to be the far-field distribution of the device, while the simulations of Figures 6, 7, and 8 represent the near-field intensity profile.

A liquid with refractive index of 1.4682 at 633 nm wavelength and temperature coefficient of 0.000392/°C (Gargille certified) were used as sensing material. The cover refractive index was changed in very small steps between 1.4632 and 1.4682 by an infrared thermal emitter source element. BeamProfiler software (version 2.84) was used to monitor the

far-field intensity distribution as the refractive index changes and is compared with values published in literatures [2–20]. Figure 12 shows a 3D far-field intensity profile of the output end of six-slot MMI sensor with the dimensions and device parameters mentioned in fabrication section with the cover liquid's refractive index of 1.465652 at the wavelength 633 nm.

The change in refractive index has been carried out by heating the covering medium using infrared thermal emitter source, while real-time intensity change of the output endface is being monitored and stored in very small steps by camera and software. Figure 13 plots power distribution along the MMI width at the wavelength of 633 nm for nine different refractive indices with $\delta n_{\text{cover}} = 9.8 \times 10^{-5}$. For the sake of clarity, not all n measured are shown in this Figure. Graphs show a noticeable change in distribution of power, as the refractive index of cover medium changes by the order of 10^{-5}.

Figure 14 shows a 3D image of intensity distribution for two different cover indices in the far-field. As depicted, the intensity distribution pattern at the output shifts as the refractive index increases from (a) 1.466240 to (b) 1.466436.

Results of Figure 13 verify a resolution of the order of 10^{-5} for change in the refractive index, as estimated in the theoretical section. This resolution implies a control of the temperature of the sensor and liquid system within 0.2°C, assuming typical thermo-optical coefficients of liquids of interest in biochemical and chemical monitoring. This could be overcome by developing a calibration process and implementing a dual wavelengths interrogation method. Although the results presented in this paper are for the refractive indices of around 1.46, this device could be easily used for much lower refractive index range, around 1.33, to detect water-soluable chemical. In such a case all the device parameters and dimensions should remain the same, but the operation wavelength would be at 1300 nm. This wavelength is below the absorption spectrum of water.

At this point no assessment of the repeatability of the fabrication process has been done, but all devices on a single chip were functional. Further study should be conducted to compare their performance characteristics. Another aspect of this project that requires further investigation is the development of a practical calibration method. As Figures 6–8 illustrate, the dynamic range of slotted MMI sensors can be enhanced if two or more wavelengths are incorporated to overcome the ambiguity problem. Another solution that is being considered is to develop an image processing tool to identify the power distribution associated with a unique index of refraction.

5. Conclusion

A novel configuration of integrated optical sensors based on slotted MMI structures has been proposed and demonstrated. The results confirmed that higher number of slots in the multimode area increases the sensitivity of device to the change in bulk refractive index of sensing species. Material of choice was SiON which is a robust material in terms of interaction with detectable chemicals comparing to sol-gels, and the technology for depositing SiON has been already developed. A maximum resolution of 9.8×10^{-5} RIU at a specific operating regime is expected.

References

[1] P. V. Lambeck, J. van Lith, and H. J. W. M. Hoekstra, "Three novel integrated optical sensing structures for the chemical domain," *Sensors and Actuators B*, vol. 113, no. 2, pp. 718–729, 2006.

[2] R. G. Heideman, R. P. H. Kooyman, and J. Greve, "Performance of a highly sensitive optical waveguide Mach-Zehnder interferometer immunosensor," *Sensors and Actuators B*, vol. 10, no. 3, pp. 209–217, 1993.

[3] R. G. Heideman and P. V. Lambeck, "Remote opto-chemical sensing with extreme sensitivity: design, fabrication and performance of a pigtailed integrated optical phase-modulated Mach-Zehnder interferometer system," *Sensors and Actuators B*, vol. 61, no. 1, pp. 100–127, 1999.

[4] B. Drapp, J. Piehler, A. Brecht, et al., "Integrated optical Mach-Zehnder interferometers as simazine immunoprobes," *Sensors and Actuators B*, vol. 39, no. 1–3, pp. 277–282, 1997.

[5] G. L. Duveneck, M. Pawlak, D. Neuschäfer, et al., "Novel bioaffinity sensors for trace analysis based on luminescence excitation by planar waveguides," *Sensors and Actuators B*, vol. 38, no. 1–33, pp. 88–95, 1997.

[6] P. Hua, B. J. Luff, G. R. Quigley, J. S. Wilkinson, and K. Kawaguchi, "Integrated optical dual Mach-Zehnder interferometer sensor," *Sensors and Actuators B*, vol. 87, no. 2, pp. 250–257, 2002.

[7] A. Brandenburg, "Differential refractometry by an integrated-optical Young interferometer," *Sensors and Actuators B*, vol. 39, no. 1–3, pp. 266–271, 1997.

[8] G. H. Cross and Y. Ren, "Youngs fringes from vertically integrated slab waveguides: applications to humidity sensing," *Journal of Applied Physics*, vol. 86, no. 11, pp. 6483–6488, 1999.

[9] A. Ymeti, J. S. Kanger, J. Greve, P. V. Lambeck, R. Wijn, and R. G. Heideman, "Realization of a multichannel integrated Young interferometer chemical sensor," *Applied Optics*, vol. 42, no. 28, pp. 5649–5660, 2003.

[10] W. Faubel, B. S. Seidel, and H. J. Ache, "Trace analysis of water pollutants by photothermal phase shift spectroscopy with an integrated optical micro-interferometer," *Optical Engineering*, vol. 35, no. 12, pp. 3555–3561, 1996.

[11] X. Fan, I. M. White, H. Zhu, J. D. Suter, and H. Oveys, "Overview of novel integrated optical ring resonator bio/chemical sensors," in *Laser Resonators and Beam Control IX*, vol. 6452 of *Proceedings of SPIE*, San Jose, Calif, USA, January 2007.

[12] C. A. Barrios, K. B. Gylfason, B. Sánchez, et al., "Slot-waveguide biochemical sensor," *Optics Letters*, vol. 32, no. 21, pp. 3080–3082, 2007.

[13] E. Krioukov, D. J. W. Klunder, A. Driessen, C. Otto, and J. Greve, "Refractive index sensing using an integrated optical microcavity," *Optics Letters*, no. 7, pp. 512–514, 2002.

[14] J. Homola, S. S. Yee, and G. Gauglitz, "Surface plasmon resonance sensors: review," *Sensors and Actuators B*, vol. 54, no. 1, pp. 3–15, 1999.

[15] G. Nemova, A. V. Kabashin, and R. Kashyap, "Surface plasmon-polariton Mach-Zehnder refractive index sensor," *Journal of the Optical Society of America B*, vol. 25, no. 10, pp. 1673–1677, 2008.

[16] X. Wu, J. Zhang, J. Chen, C. Zhao, and Q. Gong, "Refractive index sensor based on surface-plasmon interference," *Optics Letters*, vol. 34, no. 3, pp. 392–394, 2009.

[17] S. Grego, J. R. McDaniel, and B. R. Stoner, "Wavelength interrogation of grating-based optical biosensors in the input coupler configuration," *Sensors and Actuators B*, vol. 131, no. 2, pp. 347–355, 2008.

[18] K. Cottier, M. Wiki, G. Voirin, H. Gao, and R. E. Kunz, "Label-free highly sensitive detection of (small) molecules by wavelength interrogation of integrated optical chips," *Sensors and Actuators B*, vol. 91, no. 1–3, pp. 241–251, 2003.

[19] J. Piehler, A. Brandenburg, A. Brecht, E. Wagner, and G. Gauglitz, "Characterization of grating couplers for affinity-based pesticide sensing," *Applied Optics*, vol. 36, no. 25, pp. 6554–6562, 1997.

[20] http://www.microvacuum.com.

[21] A. Irace and G. Breglio, "All-silicon optical temperature sensor based on Multi-Mode Interference," *Optics Express*, vol. 11, no. 22, pp. 2807–2812, 2003.

[22] K. R. Kribich, R. Copperwhite, H. Barry, et al., "Novel chemical sensor/biosensor platform based on optical multimode interference (MMI) couplers," *Sensors and Actuators B*, vol. 107, no. 1, pp. 188–192, 2005.

[23] D. A. May-Arrioja, P. L. Wa, J. J. Sánchez-Móndragon, R. J. Selvas-Aguilar, and I. Torres-Gomez, "A reconfigurable multimode interference splitter for sensing applications," *Measurement Science & Technology*, vol. 18, no. 10, pp. 3241–3246, 2007.

[24] L. B. Soldano and E. C. M. Pennings, "Optical multi-mode interference devices based on self-imaging: principles and applications," *Journal of Lightwave Technology*, vol. 13, no. 4, pp. 615–627, 1995.

[25] D. M. Mackie and A. W. Lee, "Slotted multimode-interference devices," *Applied Optics*, vol. 43, no. 36, pp. 6609–6619, 2004.

[26] M. Noto, M. Khoshsima, D. Keng, I. Teraoka, V. Kolchenko, and S. Arnold, "Molecular weight dependence of a whispering gallery mode biosensor," *Applied Physics Letters*, vol. 87, no. 22, Article ID 223901, 3 pages, 2005.

[27] H. El-Kashef, "Necessary requirements imposed on polar dielectric laser dye solvents," *Physica B*, vol. 279, no. 4, pp. 295–301, 2000.

[28] K. Wörhoff, P. V. Lambeck, and A. Driessen, "Design, tolerance analysis, and fabrication of silicon oxynitride based planar optical waveguides for communication devices," *Journal of Lightwave Technology*, vol. 17, no. 8, pp. 1401–1407, 1999.

[29] K. Wörhoff, P. V. Lambeck, H. Albers, O. F. Noordman, N. F. Hulst, and Th. J. Popma, "Optimization of LPCVD silicon oxynitride growth to large refractive index homogeneity and layer thickness uniformity," in *Micro-optical Technologies for Measurement, Sensors and Microsystems II and Optical Fiber Sensor Technologies and Applications*, vol. 3099 of *Proceedings of SPIE*, pp. 257–268, Munich, Germany, June 1997.

[30] L. Wosinski, *Technology for photonic components in silica/silicon material structure*, Ph.D. thesis, Royal Institute of Technology (KTH), Stockholm, Sweden, 2003.

[31] S. I. Najafi, *Introduction to Glass Integrated Optics*, Artech House, Boston, Mass, USA, 1992.

[32] L. Eldada, "Optical communication components," *Review of Scientific Instruments*, vol. 75, no. 3, pp. 575–593, 2004.

[33] P. Buck and B. Grenon, "A comparison of wet and dry chrome etching with the CORE-2564," in *Photomask Technology and Management*, vol. 2087 of *Proceedings of the SPIE*, 1993.

[34] A. Sankaran and M. J. Kushner, "Etching of porous and solid SiO_2 in Ar/c-C_4F_8, O_2/c-C_4F_8 and Ar/O_2/c-C_4F_8 plasmas," *Journal of Applied Physics*, vol. 97, no. 2, Article ID 023307, 10 pages, 2005.

[35] A. Sankaran and M. J. Kushner, "Integrated feature scale modeling of plasma processing of porous and solid SiO_2. I. Fluorocarbon etching," *Journal of Vacuum Science and Technology A*, vol. 22, no. 4, pp. 1242–1259, 2004.